CONTRACT JPL 952534

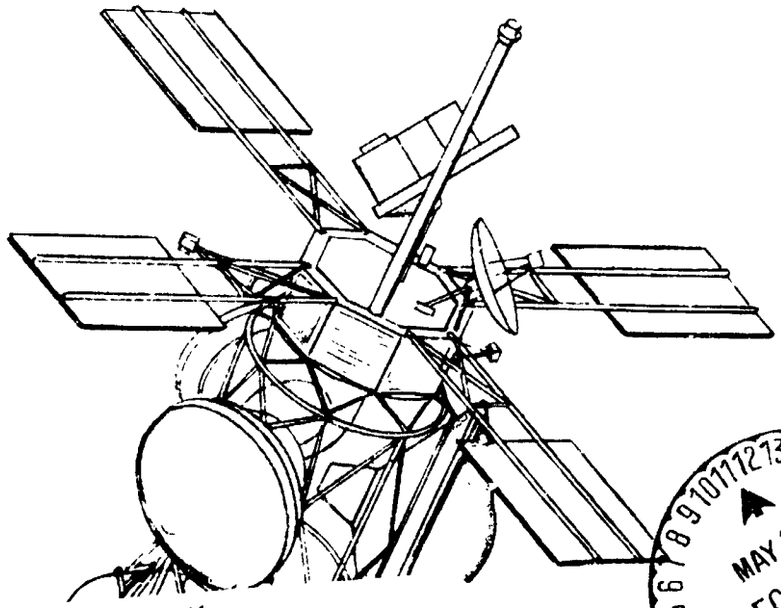
1975 VENUS MULTIPROBE MISSION STUDY

FINAL STUDY REPORT

VOLUME II
TECHNICAL STUDIES AND ANALYSIS

APRIL 1970

MCR-70-89 (Vol II) Copy No.



MAY 1970
RECEIVED
NASA STI FACILITY
INPUT BRANCH

N70-26151 (ACCESSION NUMBER)
737 (PAGES)
CR-109632 (NASA CR OR TMX OR AD NUMBER)
(THRU)
(CODE)
31 (CATEGORY)
FACILITY FORM 602

MARTIN MARIETTA CORPORATION

MCR-70-89 (Vol II)

Contract JPL 952534

1975 VENUS MULTIPROBE MISSION STUDY
FINAL REPORT
March 1970

Volume II
TECHNICAL STUDIES AND ANALYSIS

Approved

Stephen J. Ducsai,
Study Manager

MARTIN MARIETTA CORPORATION
Denver Division
Denver, Colorado

FOREWORD

This report has been prepared in accordance with requirements of Contract JPL 952534 to present data and conclusions resulting from a six month study effort performed for the Jet Propulsion Laboratory by the Martin Marietta Corporation. Volume I contains the Introduction, Summary and Conclusions, Volume II contains details of the Technical Studies and Analysis, and Volume III contains the Appendixes.

CONTENTS

		Page
Foreword		ii
Contents		iii
Symbols and Abbreviations		xxviii thru xxxiv
I.	Definition of Requirements	I-1
	A. Scientific Mission Requirements	I-1
	1. Scientific Objectives and Instruments	I-1
	2. Instrument Grouping by Target Zone	I-4
	3. Required Altitude Coverage and Sample Intervals	I-11
	B. Operational Requirements	I-14
	C. Environmental Requirements	I-15
	1. Flight Article Acceptance Testing	I-15
	2. Subsystem Fabrication and Assembly	I-15
	3. Sterilization	I-15
	4. Planetary Vehicle Assembly and Checkout	I-16
	5. Launch and Boost	I-16
	6. Interplanetary Cruise	I-16
	7. Entry into the Venus Atmosphere	I-17
	8. Balloon Floating in the Venus Atmosphere	I-17
	D. Probe Configuration Requirements	I-18
	1. Probe Classification from Science Objectives	I-18
	2. Non-Science Constraints Affecting Probe Configuration	I-20

E. Sterilization Criteria and Requirements I-20
F. Requirements Documentation I-21
1. Study Ground Rules and Constraints Document I-22
2. Science Questions I-22
3. System Design Criteria I-24
G. References I-25
II. Definition of Trajectories and Environmental Models II-1
A. Interplanetary Transfer Trajectory . . . II-1
B. Probe-Planetary Deflection Strategies . . II-11
C. Probe-Planetary Entry Trajectories . . . II-42
D. Probe-Planetary Descent Trajectories . . II-50
E. Trajectory Accuracy Analysis II-70
F. Planetary Vehicle - Baseline Flyby and Impacting Trajectories II-89
G. Baseline Engineering Model Atmospheres II-95
1. NASA SP-8011 Model Atmospheres . . . II-95
2. Mariner and Venera Data II-100
3. Recommended Study Models II-100
H. Baseline Scientific Models II-113
I. Entry Condition Selection and Environment Data II-115
J. References II-117
III. Entry Probe Synthesis III-1
A. Selection of a Baseline Mission III-1
1. General Description of the Mission Effectiveness Model III-1
2. Straight Mission Evaluation III-2
3. Identification of Inadequately Answered Science Questions III-2

4. Identification of Nonproductive Instruments III-2
5. Evaluation of a Large Number of Missions III-3
6. Establishment of Targeting Priorities III-3
7. Establishment of an Instrument Preference List III-6
8. Summary of Mission Effectiveness Evaluation III-7
B. Baseline Mission - Large Probe III-11
1. Large Probe Science Capabilities . . III-11
2. Engineering Mechanics - Large Descent Probe III-20
3. Mission Analysis III-47
4. Telecommunications and Data System - Large Probe III-49
5. Power System - Large Ballistic Probe III-75
C. Baseline Mission - Small Ballistic Probes III-82
1. Small Probe Science Capabilities . . III-82
2. Engineering Mechanics - Small Descent Probe III-88
3. Mission Analysis III-98
4. Telecommunications and Data System III-107
5. Power System - Small Ballistic Probe III-114
6. Sequencer for Small Probes (Baseline) III-114
D. Baseline Mission - High-Cloud Probe . . . III-116
1. High-Cloud Probe Science Capabilities III-116
2. Engineering Mechanics - High-Cloud Probe III-119

3. Mission Analysis III-132

4. Telecommunications and Data System - High-Cloud Probe III-132

5. Power System - High-Cloud Probe . . . III-137

6. Sequencer for Cloud Probe III-141

E. Optional Missions Probe Configurations. . III-143

1. Optional Probes Science Capabilities III-143

2. Engineering Mechanics - Optional Balloon Probes III-144

3. Mission Analysis III-155

4. Telecommunications Systems - Optional Probe Configuration III-164

5. Data System - Optional Probe Configuration III-174

6. Power System, Balloon Probes III-178

7. Sequencers for Balloon Probes III-181

F. References III-184

IV. Planetary Vehicle Synthesis IV-1

A. Baseline Flyby Mission IV-1

1. Engineering Mechanics IV-2

2. Telecommunications System IV-9

3. Data System - Common Capsule Adapter (CCA) IV-9

4. Power System IV-10

5. Common Capsule Adapter Sequencer . . IV-12

B. Baseline Direct Impact Mission IV-13

1. Engineering Mechanics IV-13

2. Telecommunications System IV-15

3. Data System - Common Capsule Adapter (CCA) IV-17

4. Power System IV-18

5. Common Capsule Adapter Sequencer . . IV-18

C. Optional Mission Planetary Vehicle Configuration IV-19
1. Engineering Mechanics IV-19
2. Telecommunications System IV-23
3. Power System IV-23
4. Common Capsule Adapter Sequencer . . IV-23
D. Modifications to the Spacecraft IV-24
1. Systems Engineering Requirements . . IV-24
2. Structural Modifications IV-24
3. Midcourse Propulsion Modifications. . IV-26
4. Thermal Control Modifications IV-27
5. Attitude Control System Modifications IV-27
6. Telecommunications Modifications . . IV-31
7. Power Modifications IV-31
8. Sequencer IV-31
V. Systems Engineering Supporting Studies . . . V-1
A. Baseline Mission Profile V-1
1. Prelaunch Operations V-1
2. Launch V-4
3. Planetary Vehicle Separation V-4
4. Interplanetary Cruise V-5
5. Preseparation V-5
6. Capsule Separation and Spin-Up . . . V-6
7. Probe Deflection V-7
8. Probe Coast and Despin V-8
9. Probe Entry and Aeroshell Deceleration V-9
10. Probe Parachute Deceleration V-10
11. Probe Terminal Descent V-11
12. Spacecraft and Common Capsule Adapter V-11

B. Mission Functional Flow V-12

C. Mission Sequence of Events V-20

1. Planetary Vehicle Sequence of Events V-20

2. Entry Capsule Sequence of Events . . V-20

D. Flyby Missions versus Direct Impacting Missions V-24

1. Configuration Effects V-24

2. Mission Operation V-25

3. Implementation Effects V-25

E. Sterilization and Decontamination V-26

1. Sterilization Criteria and Requirements V-26

2. System Assembly and Test Sequence . . V-28

3. General Operational Approach V-28

4. Planetary Contamination Allocation. . V-31

5. Sterilizable Equipment Survey Results V-32

F. Planetary Vehicle System Interfaces . . . V-34

1. Capsule Systems to Spacecraft Interfaces V-35

2. Planetary Vehicle to Launch Vehicle Interfaces V-38

G. Potential Problem Areas and Uncertainties V-39

1. Descent Probes V-39

2. Balloon Probes V-40

3. Planetary Vehicle V-42

H. Technology Development Required V-42

I. References V-43

VI. Science Supporting Studies VI-1

A. Science Mission Trades VI-1

B. Science Mechanization VI-17

1. General Objectives VI-17

2. General Considerations for Science Mechanization VI-18

3. Experiment Mechanization . . . . . VI-20 thru VI-58

VII. Electronic Systems Supporting Studies VII-1

A. Propagation Losses in the Venus Atmosphere VII-1

B Multipath Analysis VII-19

C. Optimum Processing of the Turnaround Ranging Signal VII-39

D. Position Determination, Balloon Probes . VII-59

1. Ranging - Polarization Fix VII-59

2. Ranging - Microwave Radiometer Fix VII-70

E. Probe Antenna Selection VII-73

F. Electrical Power System VII-95

G. Pyro System VII-118

1. Pyro Subsystem Functions VII-118

2. Pyro Subsystem Design Criteria . . . VII-119

H. References . . . . . VII-121 thru VII-123

VIII. Engineering Mechanics Supporting Studies . . VIII-1

A. Thermal Control VIII-1

1. Cruise Phase VIII-3

2. Postseparation Phse VIII-9

3. Descent Phase VIII-13

4. Thermal Control of Individual Science Instruments VIII-27

5. Atmospheric Thermophysical Properties VIII-31

6. Convective Heat Transfer Coefficients VIII-34

7. Phase Change Material Mechanization . VIII-41
8. Alternative Design Approaches VIII-45
B. Structural/Mechanical System VIII-50
1. Entry Aeroshell Structural Design . . VIII-50
2. Heat Shield VIII-53
3. Pressure Vessel Analysis VIII-54
4. Planetary Vehicle Structure VIII-65
C. Decelerator Design VIII-66
1. Decelerator Design Criteria VIII-66
2. Decelerator Flight Test Experience . VIII-67
3. Decelerator Design Trade Studies . . VIII-69
4. Supersonic Decelerator Design VIII-76
D. Attitude Control System Studies VIII-79
1. Probe ACS VIII-79
2. Spacecraft ACS VIII-79
E. Probe Deflection Propulsion VIII-85
F. Planetary Vehicle Propulsion System . . . VIII-87
G. Terminal Descent Dynamics and Antenna Pointing Angle VIII-87
1. Terminal Descent Dynamics Criteria . VIII-87
2. Spin Requirements VIII-100
H. Subsonic Descent Capsule Aerodynamics Design Data VIII-101
I. Balloon Design VIII-106
1. Balloon Design Criteria VIII-106
2. Balloon Design Data VIII-106
J. References VIII-110

LIST OF FIGURES

Figure		Page
I-1	Venus as Seen from Earth on October 31, 1975, Type II 5/30 LD	I-7
I-2	Schematic Representation of Target-Instrument Matrices	I-9
I-3	Temperature Profiles for Venus	I-12
II-1	1975 Earth-Venus Trajectory Parameters	II-2
II-2	Entry Velocities	II-3
II-3	Titan IIIC Payload Capabilities	II-5
II-4	Communications Range	II-6
II-5	1975 Type I Venus Encounter, Locus of V_{HE} Vectors	II-7
II-6	1975 Type II Encounter Geometry, Locus of V_{HE}	II-8
II-7	Direct Communications Link Limitations	II-10
II-8	Entry Flight Path Angle	II-12
II-9	Impact Parameter	II-14
II-10	Periapsis Radius	II-15
II-11	Path Curvature	II-16
II-12	Local Velocity	II-17
II-13	Accessible Regions, R_p = 100 and 3000 km	II-19
II-14	Accessible Regions, R_p = 3200 and 4500 km	II-20
II-15	Accessible Regions, R_p = 6252 and 7050 km	II-21
II-16	Accessible Regions, R_p = 9000 km	II-22
II-17	Effect of Periapsis Radius	II-24
II-18	Time of Flight, Retro Deflection	II-25
II-19	Time of Flight, Forward Deflection	II-27
II-20	Angle of Attack Contours	II-31

Figure		Page
II-21	Angle of Attack Contours	II-32
II-22	Angle of Attack Contours	II-33
II-23	Angle of Attack Contours	II-34
II-24	Angle of Attack Contours	II-35
II-25	Angle of Attack Contours	II-36
II-26	Angle of Attack and Deflection Angle	II-37
II-27	Deflection Parameter Selection	II-38
II-28	Mission Operating Sequence	II-41
II-29	Altitude as a Function of Flight Path Angle	II-45
II-30	Altitude as a Function of Ballistic Coefficient	II-46
II-31	Effect of Entry Angle and Ballistic Coefficient	II-47
II-32	Effect of Entry Angle and Ballistic Coefficient	II-48
II-33	Density Profiles	II-51
II-34	Terminal Velocity	II-54
II-35	Descent Time from 6130 km Radius	II-55
II-36	Altitude-Time Profile	II-56
II-37	Altitude-Velocity Profile	II-57
II-38	Small Probe Time Profile	II-58
II-39	Small Probe Velocity Profile	II-59
II-40	Large Probe Time Profile	II-60
II-41	Large Probe Velocity Profile	II-61
II-42	Cloud Probe Time Profile	II-62
II-43	Cloud Probe Velocity Profile	II-63
II-44	Altitude-Time Profile (V5M)	II-64
II-45	Altitude-Velocity Profile (V5M)	II-65
II-46	Small Probe Time Profile	II-66
II-47	Small Probe Velocity Profile	II-67

Figure		Page
II-48	Time to M = 0.5	II-79
II-49	Deceleration Altitudes	II-80
II-50	Range to M = 0.5	II-81
II-51	Time Sensitivity to Path Angle Errors	II-82
II-52	Range Sensitivity to Path Angle Errors	II-83
II-53	Deceleration Altitudes	II-85
II-54	Venus as Seen from Earth on October 31, 1975, Type II 5/30 LD	II-91
II-55	Spacecraft Velocity vs Radius (Impact and Flyby)	II-92
II-56	Spacecraft Velocity History	II-94
II-57	Kinetic Temperature vs Altitude	II-96
II-58	Mass Density vs Altitude	II-97
II-59	Pressure vs Altitude	II-98
II-60	Pressure Profiles for Venus Lower Atmosphere	II-101
II-61	Temperature Profiles for Venus Lower Atmosphere	II-102
II-62	Comparison of Mariner/Venera Data and Various Models	II-103
II-63	Comparison of Pressure Profiles from Mariner Data and SP-8011	II-104
II-64	Comparison of Density Profiles from Mariner Data and SP-8011	II-105
II-65	Comparison of Temperature Profiles from Mariner Data and NASA SP-8011	II-106
II-66	Density Profiles above Cloud Tops	II-107
II-67	Temperature Profiles above Cloud Tops	II-108
II-68	Temperature Profiles in Lower Atmosphere	II-109
II-69	Pressure Profiles in Lower Atmosphere	II-110
II-70	Density Profiles in Lower Atmosphere	II-111
II-71	Temperature Profiles for Venus	II-114

Figure		Page
II-72	Typical Entry Heat Pulse	II-116
III-1	Mission Value vs Number of Instruments for 54 Mission Configurations	III-4
III-2	Target Values as a Function of ψ for Three Great Circles	III-5
III-3	Mission Value vs Number of Instruments for Optimum Missions	III-9
III-4	Number of Upper Atmosphere Measurements from 2 Planet Radii	III-14
III-5	Number of Measurements from Entry	III-15
III-6	Deceleration vs Altitude for Large Probe	III-16
III-7	Deceleration vs Time for Large Probe	III-17
III-8	Number of Measurements vs Altitude	III-18
III-9	Number of Samples vs Altitude	III-19
III-10	Ambient Temperature History, Large Descent Probe	III-21
III-11	Inboard Profile, Large Ballistic Descent Probe	III-23
III-12	Internal Arrangement, Large Ballistic Descent Capsule	III-25
III-13	Descent Probe Tradeoffs	III-31
III-14	Sensitivity of Altitude for Reaching Subsonic Velocity to Ballistic Coefficient	III-36
III-15	Aeroshell Parametric Weight Data	III-37
III-16	Dynamic Pressure and Band Line Temperature	III-39
III-17	Summary of Heat Shield Unit Weights	III-41
III-18	NASA Ground Test Simulation Capability and Baseline Mission Entry Conditions	III-42
III-19	Large Probe Descent Profile	III-50
III-20	Large Probe Descent Profile, Subsolar	III-51
III-21	Telemetry Data Handling, Large Probe (Baseline with Impacting Spacecraft)	III-70
III-22	Telemetry Data Formats, Large Probe (Baseline)	III-71

Figure		Page
III-23	Deceleration vs Altitude for Small Probes . . .	III-84
III-24	Deceleration vs Time for Small Probes	III-85
III-25	Number of Measurements vs Altitude, Small Probe	III-86
III-26	Number of Samples vs Altitude, Small Probe . .	III-87
III-27	Ambient Temperature History, Small Descent Probe	III-90
III-28	Inboard Profile, Small Ballistic Descent Probe	III-91
III-29	Internal Arrangement, Small Descent Capsule . .	III-93
III-30	Small Probe Descent Profile, South Pole	III-101
III-31	Small Probe Descent Profile, South Pole	III-102
III-32	Small Probe Descent Profile, Antisolar	III-103
III-33	Small Probe Descent Profile, Antisolar	III-104
III-34	Telemetry Data Handling, Small Probes (Baseline)	III-111
III-35	Telemetry Data Format, Small Probes (Baseline)	III-112
III-36	Number of Measurements vs Altitude, High-Cloud Probe	III-117
III-37	Number of Samples vs Altitude, High-Cloud Probe	III-118
III-38	Ambient Temperature History, High-Cloud Probe	III-121
III-39	Inboard Profile, High-Cloud Probe	III-123
III-40	Internal Arrangement, High-Cloud Probe Instrumentation Canister	III-125
III-41	Entry Parameters Selection	III-128
III-42	Influence of Targeting and Survival Depth on Cloud Probe Design	III-130
III-43	High-Cloud Probe Descent Profile, South Pole	III-134
III-44	High-Cloud Probe Descent Profile, South Pole	III-135

Figure		Page
III-45	Telemetry Data Handling, High-Cloud Probe (Baseline and Option 2)	III-139
III-46	Telemetry Data Formats, High-Cloud Probe (Baseline and Option 2)	III-140
III-47	Inboard Profile, Balloon Probe	III-146
III-48	Internal Arrangement, Buoyant Station Balloon Probe	III-147
III-49	Balloon Probe Entry Weight vs Survival Time	III-154
III-50	Balloon Probe Entry Weight vs Superpressure	III-154
III-51	Balloon Probes (LSMT) Descent Profile	III-160
III-52	Balloon Probes (LSMT) Descent Profile	III-161
III-53	High-Cloud Probe Descent Profile, Antisolar	III-162
III-54	High-Cloud Probe Descent Profile, Antisolar	III-163
III-55	Telemetry Data Handling, Balloon Probe (Baseline Option)	III-176
III-56	Telemetry Data Formats, Balloon Probe (Baseline Option)	III-177
IV-1	Planetary Vehicle/Booster Integration, Baseline	IV-5
IV-2	Impacting Spacecraft Configuration	IV-14
IV-3	Planetary Vehicle/Booster Integration, Option 1	IV-21
IV-4	Sensitivity of ACS Gas Weight and Spacecraft Battery Weight to Maneuver Time	IV-30
V-1	Multiple Probe Systems Top Level Diagram	V-2
V-2	Composite Diagram of Systems	V-3
V-3	Functional Flow Diagram Baseline Mission Phase	V-13
V-4	Phases 5.0 and 6.0	V-14
V-5	Phases 7.0 and 8.0	V-15
V-6	Phase 9.0	V-16
V-7	Phase 11.0	V-17
V-8	Phases 11.3 and 11.4	V-18

Figure		Page
V-9	Phase 12.0	V-19
VI-1	Terminal Velocity in MMC Lower Density Model Atmosphere	VI-3
VI-2	Descent Time from 6130-km Radius in MMC Lower Density Model Atmosphere	VI-4
VI-3	Sample Time Intervals Required to Obtain 200-m Altitude Interval	VI-5
VI-4	Sample Time Intervals Required to Obtain 500-m Altitude Interval	VI-6
VI-5	Sample Time Intervals Required to Obtain 1000-m Altitude Interval	VI-7
VI-6	Sample Time Intervals Required to Obtain 2000-m Altitude Interval	VI-8
VI-7	Sample Time Intervals Required to Obtain 5000-m Altitude Interval	VI-9
VI-8	Altitude Intervals Obtained with 300-sec Sample Time	VI-10
VI-9	Altitude Resolution for Large Probe	VI-11
VI-10	Number of Measurements vs Altitude for Large Probe	VI-12
VI-11	Altitude Resolution for Small Probes	VI-13
VI-12	Number of Measurements for Small Probes	VI-14
VI-13	Altitude Resolution for Small Probes	VI-15
VI-14	Number of Measurements for High-Cloud Probes	VI-16
VI-15	Mounting of Cloud Particle Counter on High-Cloud Probe	VI-33
VI-16	Cloud Particle Counter in Ballistic Probe . . .	VI-34
VI-17	Installation of Evaporimeter-Condensimeter . .	VI-37
VI-18	Temperature Probes Optimized for Low and High Atmospheric Densities	VI-43
VI-19	Integration of Radar in Ballistic Probe	VI-48
VI-20	High-Pressure Sampling with Two Valves	VI-50

Figure		Page
VI-21	Single Mass Spectrometer Leak	VI-50
VI-22	Dual-Stage Pressure Reduction for Mass Spectrometer	VI-50
VI-23	Concept for Cloud Particle Transport with Collector Outside Probe Wall	VI-54
VII-1	Refractibility of Neutral Venus Atmosphere . .	VII-3
VII-2	Ray-Trapping Geometry	VII-5
VII-3	Pointing Error for Several Model Atmospheres	VII-8
VII-4	Defocusing Loss for Several Model Atmospheres	VII-10
VII-5	Zenith Attenuation, 2.3 GHz	VII-12
VII-6	Upper and Lower Bounds for Attenuation	VII-13
VII-7	Attenuation, Lower Atmosphere, 6050-km Surface	VII-14
VII-8	Defocusing and Attenuation Loss vs Elevation for Several Departure Angles	VII-16
VII-9	Combined Attenuation and Defocusing Loss vs Departure Angle, Nominal and Worst-Case Atmospheres	VII-17
VII-10	Surface Angle vs Departure Angle, Nominal and Worst-Case Atmospheres	VII-18
VII-11	Communications Geometry	VII-20
VII-12	"Flat Planet" Communications Geometry	VII-21
VII-13	Reflection Coefficients vs Incidence Angle . .	VII-23
VII-14	Direct and Multipath Spectra, Descending Probe, 10 m/sec, $\theta = 70°$	VII-27
VII-15	Multipath Signal Strength and Required Carrier Fading Margin, Cloud Probes	VII-33
VII-16	Multipath Signal Strength and Required Fading Margin, Balloon Probes	VII-36
VII-17	Ranging Code Spectrum	VII-40
VII-18	Autocorrelation Function Ranging Sequence Filtered to 0.7 MHz Bandwidth	VII-43

Figure		Page
VII-19	Performance of a Rectangular Filter, Relayed Ranging Signal	VII-45
VII-20	Intermodulation Loss, Weak Signals in Gaussian Noise	VII-50
VII-21	Filtered and Unfiltered Waveforms	VII-52
VII-22	Intermodulation Loss, SNR = 1.0	VII-53
VII-23	Limiter Loss, Baseband Limiting	VII-55
VII-24	Optimum Transponder Bandwidth	VII-58
VII-25	Radiation Pattern, Balloon Antenna System	VII-60
VII-26	Position Determination by Ranging and Polarization	VII-62
VII-27	Range-Polarization Coordinates Centered on the Subearth Point	VII-63
VII-28	Range-Sun Zenith Angle Coordinates	VII-63
VII-29	Position Error, Range-Polarization Fix	VII-67
VII-30	Antenna Temperatures, Sun and Galaxy, as Seen from Venus, 20° Beamwidth	VII-72
VII-31	0.6 λ Annular Slot Antenna	VII-74
VII-32	Four-Arm Equiangle Spiral on a Cone Antenna	VII-76
VII-33	Radiation Pattern	VII-79
VII-34	Radiation Pattern, 1.2 λ Annular Slot on an 8.0 Circular Ground Plane; Peak Gain, 7.0 db λ	VII-83
VII-35	Radiation Pattern, Four Arm Cavity-Backed Spiral, Difference Mode; Peak Gain 5.0 db	VII-85
VII-36	Annular Slot and Ring Array of 0.5 λ Slots, 1.2 λ Diameter	VII-86
VII-37	Radiation Pattern, 0.5 λ Cavity Helix; Peak Gain, 8 db	VII-87
VII-38	Radiation Pattern, Balloon Antenna System	VII-89
VII-39	Cavity Helix-Annular Slot Antenna Combination	VII-90
VII-40	Radiation Patterns, Equiangular Spiral on a Cone Antenna	VII-91

Figure		Page
VII-41	Cell Voltage vs Percent Capacity, Ag-Zn Battery	VII-97
VII-42	Typical Battery Energy Densities for Ag-Zn Batteries	VII-98
VII-43	Typical I-V Characteristics as a Function of Solar Irradiance at Constant Temperature	VII-103
VII-44	Voltage-Current Characteristics vs Cell Temperature	VII-104
VII-45	Venus Probe Solar Radiation Environment	VII-106
VII-46	Coordinate Nomenclature	VII-107
VII-47	50 mb Incident Flux vs Zenith Angle (at 5 Optical Depths)	VII-110
VII-48	500 mb Incident Flux vs Zenith Angle (at 20 Optical Depths)	VII-111
VII-49	50 mb Probe Solar Array	VII-114
VII-50	500 mb Probe Solar Array	VII-115
VIII-1	Planetary Vehicle Characteristics	VIII-5
VIII-2	Computer Plot of Planetary Vehicle Surfaces	VIII-6
VIII-3	Probe Cruise Temperature vs α/ϵ	VIII-8
VIII-4	Large Probe Postseparation Thermal Model	VIII-11
VIII-5	Postseparation Cooling of Large Probe	VIII-12
VIII-6	High-Cloud Probe Thermal Network	VIII-13
VIII-7	High-Cloud Probe Temperature History	VIII-15
VIII-8	Thermal Model Used in Descent Probe Thermal and Structural Design Program	VIII-21
VIII-9	Influence of Probe Geometry and Insulation Thickness on Probe Weight	VIII-24
VIII-10	Variation in Thermal Structural Weights with Insulation Thickness	VIII-25
VIII-11	Sensitivity of Descent Probe Weight to Design Parameter Variation	VIII-26
VIII-12	Sensitivity of Descent Probe Weight to Subsonic Descent Profile	VIII-28

Figure		Page
VIII-13	Radar Altimeter Thermal Model	VIII-30
VIII-14	Radar Altimeter Temperature History	VIII-32
VIII-15	Exterior Insulation Temperatures	VIII-34
VIII-16	Small Probe Descent Velocity Profile	VIII-36
VIII-17	Small Probe Descent Conditions	VIII-37
VIII-18	Location and Reynolds Number at which Flow Becomes Turbulent on the Small Probe	VIII-38
VIII-19	Small Probe Heat Transfer Coefficients	VIII-40
VIII-20	Small Probe Outer Pressure Shell Temperature Profile and Film Coefficient Distribution	VIII-42
VIII-21	Sensitivity of Payload Temperatures to PCM Coupling	VIII-44
VIII-22	Aeroshell Parametric Weights	VIII-51
VIII-23	Comparative Aeroshell Structure Weights for 6.0-ft Diameter	VIII-52
VIII-24	Decelerator Flight Test Experience	VIII-68
VIII-25	Terminal Velocity vs m/C_DA	VIII-70
VIII-26	Parachute Weight	VIII-71
VIII-27	Parachute Weight Penalty vs Terminal Velocity	VIII-72
VIII-28	m/C_DA vs Parachute Weight Penalty	VIII-73
VIII-29	Effect of Dynamic Pressure on Parachute Weight	VIII-75
VIII-30	Characteristic Ballute Drag	VIII-78
VIII-31	Solid Rocket Motor Performance	VIII-86
VIII-32	Antenna Pattern and Communications Angle	VIII-88
VIII-33	Normal and Axial Force Coefficients for Cones	VIII-92
VIII-34	Cone Pitch Damping Coefficients	VIII-93
VIII-35	Cone Damping Characteristics	VIII-94
VIII-36	Probe Response to Disturbance	VIII-95

Figure		Page
VIII-37	Horizontal Gust Effects at 30 km Altitude . .	VIII-97
VIII-38	Horizontal Gust Effects at Various Altitudes	VIII-98
VIII-39	Communications Angle Disturbance	VIII-99
VIII-40	Cone Total Drag Coefficient	VIII-103
VIII-41	Cone Subsonic Center of Pressure	VIII-104
VIII-42	Longitudinal Static Stability Margin	VIII-105
VIII-43	Balloon Probe Design Superpressure	VIII-109

LIST OF TABLES

Table		Page
I-1	Basic Questions Concerning Venus.	I-2
I-2	List of Observables Derived from Questions. .	I-3
I-3	Instruments and Characteristics Specified by RFP.	I-5
I-4	Recommended Additional Instruments.	I-6
I-5	Primary and Secondary Target Zones vs Instruments	I-10
I-6	Desired Altitude Sample Intervals	I-13
I-7	Design Atmospheres.	I-17
I-8	Balloon Floating Environments	I-18
II-1	Atmosphere Model Effects on Entry	II-49
II-2	Drag Coefficient vs Mach Number	II-52
II-3	Sensitivities for Venus Probes, R_p = 2800 km.	II-72
II-4	Sensitivities for Venus Probes, R_p = 12,600 km	II-72
II-5	Sensitivities for Venus Probes, R_p = 3200 km.	II-75
II-6	Sensitivities for Venus Probes, R_p = 9000 km.	II-75
II-7	Far Side and Near Side Entry Conditions . . .	II-77
II-8	Entry Dispersions	II-87
II-9	Launch, Interplanetary Cruise, and Encounter Parameters for Venus.	II-90
II-10	NASA SP-8011 Models of Venus Atmosphere (1968).	II-99
II-11	Summary of Model Surface Conditions	II-112
III-1	Preference List	III-8
III-2	Baseline Large Probe Instrument Complement. .	III-12
III-3	Large Ballistic Probe Weight Summary.	III-27
III-4	Design Information for Descent Probes	III-34
III-5	Venus Large Ballistic Probe Design Data . . .	III-48
III-6	RF Components, 1972 Technology, DSN Frequencies	III-53

Table		Page
III-7	Link Calculations, Downlink, Large Probe, Impacting Spacecraft Option	III-56
III-8	Link Calculations, Downlink, Large Probe, Noncoherent Signaling	III-57
III-9	Link Calculations, Downlink, Latge Probe, Flyby Spacecraft Option	III-63
III-10	Link Calculations, Uplink, Descent Probes, Data Transmission Mode, Two-Way Doppler Channels.	III-64
III-11	Telemetry Measurement List 1, Large Probe (Baseline).	III-67
III-12	Telemetry Measurement List 2, Large Probe (Baseline).	III-68
III-13	Telemetry Measurement List 3, Large Probe (Baseline).	III-69
III-14	Buffering Requirements for Large Probe Data System.	III-73
III-15	Weight and Power Summary, Large Ballistic Probe, Impacting Spacecraft Option	III-76
III-16	Weight and Power Summary, Large Ballistic Probe, Flyby Spacecraft Option.	III-77
III-17	Timing Precision, Large Probe Sequencing. . .	III-81
III-18	Baseline Small Probes Instrument Complement.	III-83
III-19	Small Ballistic Probe Weight Summary.	III-95
III-20	Venus Small Probe (South Pole) Entry Probe Design Data	III-99
III-21	Venus Small Probe (Antisolar) Entry Probe Design Data	III-100
III-22	Sensitivities for Far Side Entries.	III-106
III-23	Link Calculations, Downlink, Small Probes . .	III-108
III-24	Telemetry Measurement List, Small Probes (Baseline).	III-110
III-25	Entry Data Store and Read Times for Small Probes.	III-113

Table		Page
III-26	Buffering Requirements for Small Probe Data System	III-114
III-27	Weight and Power Summary, Small Ballistic Probe	III-115
III-28	Baseline High-Cloud Probe Instrument Complement	III-119
III-29	High-Cloud Probe Weight Summary	III-122
III-30	Venus High-Cloud Probe (South Pole) Entry Probe Design Data	III-133
III-31	Link Calculation, Downlink, High-Cloud Probes	III-136
III-32	Measurement List, High-Cloud Probe (Baseline or Option 2)	III-138
III-33	Buffering Requirements for Cloud Probe Data System	III-141
III-34	Weight and Power Summary, High-Cloud Probe	III-142
III-35	Balloon Probes Instrument Complement	III-144
III-36	Balloon Probe Weight Summary, 500 mb Configuration	III-149
III-37	Balloon Probe Weight Summary. 50 mb Configuration	III-156
III-38	Venus Balloon 50 mb Entry Probe Design Data	III-157
III-39	Venus Balloon 500 mb Entry Probe Design Data	III-158
III-40	Venus High-Cloud Probe (Antisolar) Entry Probe Design Data	III-159
III-41	Link Calculation, Uplink, Balloon Probes, Two-Way Doppler Channel	III-167
III-42	Link Calculation, Downlink, Balloon Probes, Data Transmission Mode	III-168
III-43	Link Calculation, Uplink, Balloon Probes, Ranging	III-169
III-44	Link Calculation, Downlink, Balloon Probes, Ranging	III-170
III-45	Link Calculation, Downlink, Balloon Probes, Polarization Experiment Mode	III-171

Table		Page
III-46	Measurement List, Balloon Probe (Baseline Option 1 or 2).	III-175
III-47	Weight and Power Estimate, 500 mb Balloon Probe	III-179
III-48	Weight and Power Estimate, 50 mb Balloon Probe	III-180
III-49	Heating Power Sources, 50 mb Balloon.	III-182
III-50	Timing Precision, Balloon Probe Sequencing. .	III-183
IV-1	Planetary Vehicle Weight Summary.	IV-4
IV-2	Typical Measurement List for CCA Cruise Telemetry	IV-9
IV-3	Weight and Power Summary, Electronics and Power System, Planetary Vehicle CCA, Baseline Flyby Mission.	IV-12
IV-4	Link Calculation, Downlink, Spacecraft. . . .	IV-16
IV-5	Weight and Power Summary, Electronics and Power System, Planetary Vehicle CCA, Baseline Direct Impact Mission.	IV-18
IV-6	Planetary Vehicle Weight Summary, Option 1. .	IV-20
IV-7	Planetary Vehicle Weight Summary, Option 2. .	IV-20
IV-8	Weight and Power Summary, Electronics and Power System, Planetary Vehicle CCA, Optional Missions.	IV-23
IV-9	Moment of Inertia Summary, Baseline Planetary Vehicle	IV-28
V-1	Probe Separation and Deflection	V-7
V-2	Baseline Mission Entry Parameters	V-9
V-3	Aeroshell Loads	V-9
V-4	Parachute Deceleration Phase.	V-11
V-5	Planetary Vehicle/Capsule Separation Capsule Sequence Functions.	V-21
V-6	Capsule Sequence Functions.	V-23
V-7	Venus Probe(s) Sterilizable Hardware.	V-33

Table		Page
VI-1	Summary of Information about Instruments. . .	VI-19
VI-2	Science Mechanization	VI-21
VII-1	Ray Trapping Angles and Radii, First Method .	VII-6
VII-2	Ray Trapping Angles and Radii, Second Method.	VII-6
VII-3	Annular Slot (0.6 λ diameter) Antenna Specification.	VII-93
VII-4	Cavity Helix Antenna Specification.	VII-93
VII-5	Annular Slot (1.2 λ diameter) Antenna Specification.	VII-94
VII-6	Four-Arm Spiral on a Cone Antenna Specification.	VII-94
VII-7	Ag-Zn Battery Power System.	VII-102
VII-8	Solar Array Weight Estimates.	VII-116
VII-9	Battery Weight Determination.	VII-117
VIII-1	Component Temperature Limits.	VIII-2
VIII-2	Balloon Probe Environments.	VIII-16
VIII-3	Summary of Cases Run for Single-Wall Concept.	VIII-46
VIII-4	ACS Propellant Usage Summary.	VIII-81

ABBREVIATIONS AND SYMBOLS

A	reference area, ft^2
	ampere, electrical unit of current
	atmosphere (pressure) (1 atmosphere = 1.013×10^6 dynes/cm^2)
	(subscript) ambient
ACS	attitude control system
A/D	analog to digital
AGC	Aerojet-General Corporation
Alt.	altitude
	altimeter
AMU	atomic mass unit
AS	antisolar
A/S	aeroshell
AVCO	AVCO Systems Division
B	impact parameter, km
	ballistic coefficient, slugs/ft^2
	bandwidth
	(subscript) body
b	bar, (pressure) (1 bar = 10^6 dynes/cm^2)
	bit
bps	bits per second
C	capacity (battery, ampere hours)
C_3	injection energy, km^2/sec^2

c	free space propagation velocity of light (10^{10} cm/sec)
°C	temperature, degrees Celsius
CAP, CAPS	capsule
CCA	common capsule adapter
CCAS	common capsule adapter sequencer
CC&SS	command, control, and sequencing system
C_D	drag coefficient
cg	center of gravity
cm	centimeter
CP	center of pressure
c_p	specific heat
D	diameter
db	decibel
dbm	decibels above 1 milliwatt
DLA	declination of launch asymptote
DSIF	Deep Space Instrumentation Facility
DSN	Deep Space Net
E	electrical voltage
	modulus of elasticity
	(subscript) entry
e	eccentricity
EJ	(subscript) deflection-ejection
ETO	ethylene oxide

EMI	electromagnetic interference
E/NO	signal-to-noise ratio
F	solar flux
	frequency, Hz
FTS	flight telemetry system (S/C)
°F	temperature, degrees Fahrenheit
f	(subscript) flight
GSFC	Goddard Space Flight Center
G	(subscript) gust
G.	(prefix) giga (1×10^9)
g	acceleration of gravity, Earth
	(subscript) gas
H	altitude
	(subscript) horizontal
HE	(subscript) (V_{HE} - hyperbolic excess velocity)
h	heat transmission coefficient
hr	hour
Hz	Hertz
I	electrical current
	moment of inertia
i	inclination to ecliptic
IR	infrared
JPL	Jet Propulsion Laboratory

°K	temperature, degrees Kelvin
k	thermal conductivity
	(prefix) kilo (1×10^3)
km	kilometer
LRC	Langley Research Center
LSMT	light side morning terminator
M	Mach number
	(prefix) Mega (1×10^6)
m	mass
	meter
	(prefix) milli- (1×10^{-3})
mb	millibar
MCD	main chute deployment
MMC	Martin Marietta Corporation
MMCL	MMC Lower (Atmosphere)
mps	meters per second
N	refractivity
N	(subscript) noise
n	index of refraction
NASA	National Aeronautics and Space Administration
P	pressure
p	roll rate

PCM	phase change material
	pulse code modulation
P/L	payload
PLL	phase lock loop
Pr	Prandtl number
psf	pounds per ft^2
psi	pounds per $in.^2$
psia	pounds per $in.^2$ (absolute)
PV	planetary vehicle
q	dynamic pressure
R	radius
°R	temperature, degrees Rankine
RA	right ascension
Re	Reynolds number
S/C	spacecraft
SNR	signal-to-noise ratio
SP	South Pole
SS	subsolar
T	time
TRW	Thompson Ramo Woolridge
TWT	traveling wave tube
UV	ultraviolet

V	velocity
	volume
	electrical voltage
	(subscript) vertical
W	watts
X	displacement
α	solar absorptivity
α_E	maximum angle of attack
Γ	polarization
γ_E	entry angle
Δ	(prefix) increment of change
ϵ	2.71828
	dielectric constant
	infrared emissivity
θ_o	solar zenith angle
θ	(see ψ)
λ	wavelength
	longitude
μ	micron
	(prefix) micro (1×10^{-6})
	gravitational constant of Venus (1.147223×10^{16} ft^3/sec^2) (3.248596×10^5 km^3/sec^2)
	viscosity
π	3.1416

ρ	density
σ	standard deviation
	Stefan-Boltzmann constant
τ	application angle $\left(\text{for } \Delta V_{EJ}\right)$
ϕ	latitude
ϕ_t	trap angle of communications ray
ψ	(θ and ψ are two departure angles of straight line communications rays that bound the true, curved path)
ω	angular velocity,
	frequency, radians per second
$\sim$	approximately
$\propto$	varies as
$\frac{\partial(y)}{\partial(x)}$	(partial derivative) sensitivity of y to changes in x

I. DEFINITION OF REQUIREMENTS

A. SCIENTIFIC MISSION REQUIREMENTS

1. Scientific Objectives and Instruments

The primary objective of the Venus Multiprobe Mission is to perform an extensive exploration of the atmosphere and clouds of Venus by entering suitably instrumented probes at significantly different locations over the planet. The goal of such an exploration is to provide as much information as possible relevant to the set of basic questions concerning the physics, chemistry, and dynamics of the atmosphere and clouds on Venus. These questions are listed on Table I-1. These questions, derived from previous studies (Ref I-1 and I-2),* form the basis for establishing specific mission requirements or tasks that the mission must accomplish.

The basic questions were first translated into a set of physical observables or measurements that would provide the relevant information within the framework of the mission concept and the available instrumentation. These observables, listed in Table I-2, were reviewed by JPL and a set of general priorities was established as follows:

Priority 1 - Composition and distribution of the clouds;
Priority 2 - Atmospheric circulation from just above the cloud layer and below;
Priority 3 - Vertical structure of the atmosphere, particularly in regions;
Priority 4 - Upper atmosphere definition.

*References cited in each chapter appear in the last section of each chapter.

Table I-1 Basic Questions Concerning Venus*

WHAT IS THE DISTRIBUTION AND CHEMICAL COMPOSITION OF THE CLOUDS? (PRIORITY 1) ● Are the clouds composed of condensed vapors or of solid particles? ● If the cloud particles are solids, are they ice crystals (or other condensables) or dust? ● If the clouds are dust, is the dust the result of volcanic eruption or of surface disintegration? ● What size are the particles? ● Are the clouds uniformly distributed **vertically** in the atmosphere, or are there several cloud layers?
WHAT IS THE GENERAL CIRCULATION PATTERN OF THE ATMOSPHERE? (PRIORITY 2) ● Is there any variation of the vertical temperature or compositional profiles with latitude? ● Are the polar regions cooler than the equatorial region? ● What is the physics of interaction between the clouds and atmospheric heat sources? ● Is the high surface temperature due to a greenhouse effect, to convective heating, or to what effect? ● To what extent is the atmosphere responsible for a redistribution of surface or internal material? ● What is the variation in temperature between the dayside and the nightside? ● Are there high-speed winds on Venus?
WHAT IS THE COMPOSITION OF THE ATMOSPHERE? (PRIORITY 3) ● Are the minor constituents uniformly mixed throughout the atmosphere? ● Can any constituents condense to form liquids on the surface of the planet? ● Are argon, neon, or nitrogen present in the atmosphere, and what is their origin? ● How is the abundance of these gases related to that of the major constituent CO_2? ● What ionic species are present in the upper atmosphere? ● What is the photochemistry of the upper atmosphere?
*The scientific objectives for the Venus entry mission were specified in terms of these questions from JPL Section Document 131-03.

Table I-2 List of Observables Derived from Questions

0.1	Determine the planetocentric radius (or altitude above a reference sphere) of the probe during the subsonic portion of its descent.
0.2	Determine the planetocentric radius of the probe during the supersonic/hypersonic portion of its descent.
1.1	Identify the ionic species present in the upper atmosphere and determine their number density profiles.
1.2	Identify the neutral gas constituents in the upper atmosphere and determine their number density profiles.
1.3	Determine the electron number density and electron temperature profiles in the upper atmosphere.
1.4	Determine the UV radiation flux profiles at several wavelengths.
1.5	Determine the number densities and sizes of any cloud or haze particles versus altitude above the main cloud top.
1.6	Determine the wind shear profiles above and through the tops of the main cloud deck.
1.7	Determine the composition of any cloud or haze particles above the main cloud tops.
2.0	Determine pressure, temperature and density profiles from above the clouds to the surface over several widely separated points on the planet.
2.1	Identify the minor atmospheric constituents and determine their number density profiles.
2.2	Determine the precise ($\pm$0.5%) concentration of CO_2 at several altitudes between cloud tops and surface.
2.3	Determine the abundances and isotopic ratios of the rare gases, e.g., N_e^{20}, N_e^{22}, A^{36}, A^{38}, A^{40}, etc.
2.4	Locate the top of the visible cloud layer with respect to pressure, temperature, and radius over several widely separated points on the planet.
2.5	Locate (with respect to pressure, temperature, and radius) and determine the vertical extent of all cloud layers between the surface and cloud tops.
2.6	Determine the chemical composition of the cloud particles in each cloud layer.
2.7	Determine the number density and size distribution of the cloud particles versus altitude within each cloud layer.
2.8	Determine the physical state (liquid, solid) of the cloud particles versus altitude in each cloud layer.
2.9	Determine the visible radiation fluxes (direct, diffuse) at several wavelengths versus altitude over several widely separated points on the light side.
2.10	Determine the upward and downward thermal IR radiation fluxes at several wavelengths versus altitude over several widely separated points on the planet.
2.11	Determine the general circulation pattern of the atmosphere at several altitudes.
2.12	Determine the horizontal and vertical wind profiles near the subsolar and antisolar points and a pole.
2.13	Determine the magnitude and frequency spectrum of the turbulence versus altitude near the subsolar, polar and antisolar points.
2.14	Search for transient light phenomena during descent.

These priorities were used to guide mission design by indicating which questions should receive most emphasis. However, the priorities were not used as a basis for exclusion of instruments or objectives to alleviate mission design problems.

Having defined the observables, the next task was to specify the conditions required for their satisfactory accomplishment with the available instrumentation (Table I-3). This entailed, for each observable, a definition of the instrumental techniques, the required target zones, altitude coverage, and altitude sampling intervals. In addition, value functions indicating the relative values of instruments, targets, altitudes, and sampling intervals were defined for each observable for use in the mission effectiveness modeling. These definitions were collected into a science criteria document (Appendix C).

It was found that additional instrumentation would be required to accomplish all of the objectives. Since some of these would have a significant effect on the probe system designs as well as on the science accomplishment, the instruments shown in Table I-4 were added to those of Table I-3.

2. Instrument Grouping by Target Zone

A target zone is defined as the area within 20° to 30° of the target because our present state of knowledge of Venus does not justify a more precise statement. Figure I-1 shows Venus as it would appear from Earth on the arrival date for the baseline mission (October 31, 1975). The regions probed by Mariners and the Veneras were not considered as candidate targets for this study. The primary targets are as identified by: (1) Subsolar; (2) Antisolar; and (3) South Pole.

Table I-3 Instruments and Characteristics Specified by RFP

INSTRUMENT	VOLUME ($in.^3$)	WEIGHT (lb)	POWER (w)	SAMPLING INTERVAL, (m)	WORD SIZE (bits)	WORDS per SAMPLE	BITS per SAMPLE
Accelerometers (4)	24	1.9	4.0	(t = 0.2 sec	10	4	40
Pressure Gages (5) (Switched)	10	0.8	0.1	300	8	1	8
Temperature Gage (Range-Switched)	15	0.8	0.2	300	8	1	8
Neutral Particle Mass Spectrometer (1-90 AMU)	280	10	10-20	1000	15	40	600
Thermal Radiometer	18	3	3	100	7	2	14
Solar Radiometer	100	4	3	1000	10	120	1200
Nephelometer	100	4	3	100	8	2	16
Cloud Particle (No., Density, Size)	500	8	10	100	10	8	80
Cloud Particle Composition (3-100 AMU)	500	20	50-60	7000	16	100	1600
Evaporimeter-Condensimeter	70	2	10	1500	8	57	456
Aititude Radar	50	3	18	400	7	1	48
Drift Radar	50	3	18	150	8	6	48

Table I-4 Recommended Additional Instruments

Instrument	Weight (lb)	Power (w)	Objectives
70-km Altitude/Drift Radar	15	30	Provide unambiguous altitude reference for other measurements
Transponder	5.3 (2.0)	1.5 (0.5)	Determine probe line of sight velocity & range; Determine probe line of sight velocity
Surface Impact Indicator (300-m range)	0.75	3	Locate surface, determine whether signal loss is due to impact
Accelerometers	--	--	Determine wind shear and turbulence profiles in lower atmosphere. Range switch entry accelerometers
Balloons (50 mb and 500 mb)	--	--	Determine circulation pattern near cloud tops
Ion Mass Spectrometer	8	4	Provide upper atmosphere measurements from entry probe when flyby spacecraft mode is elected
Neutral Mass Spectrometer	10	20	↓
Electron Density Probe	3	3	
UV Photometer	2	1	

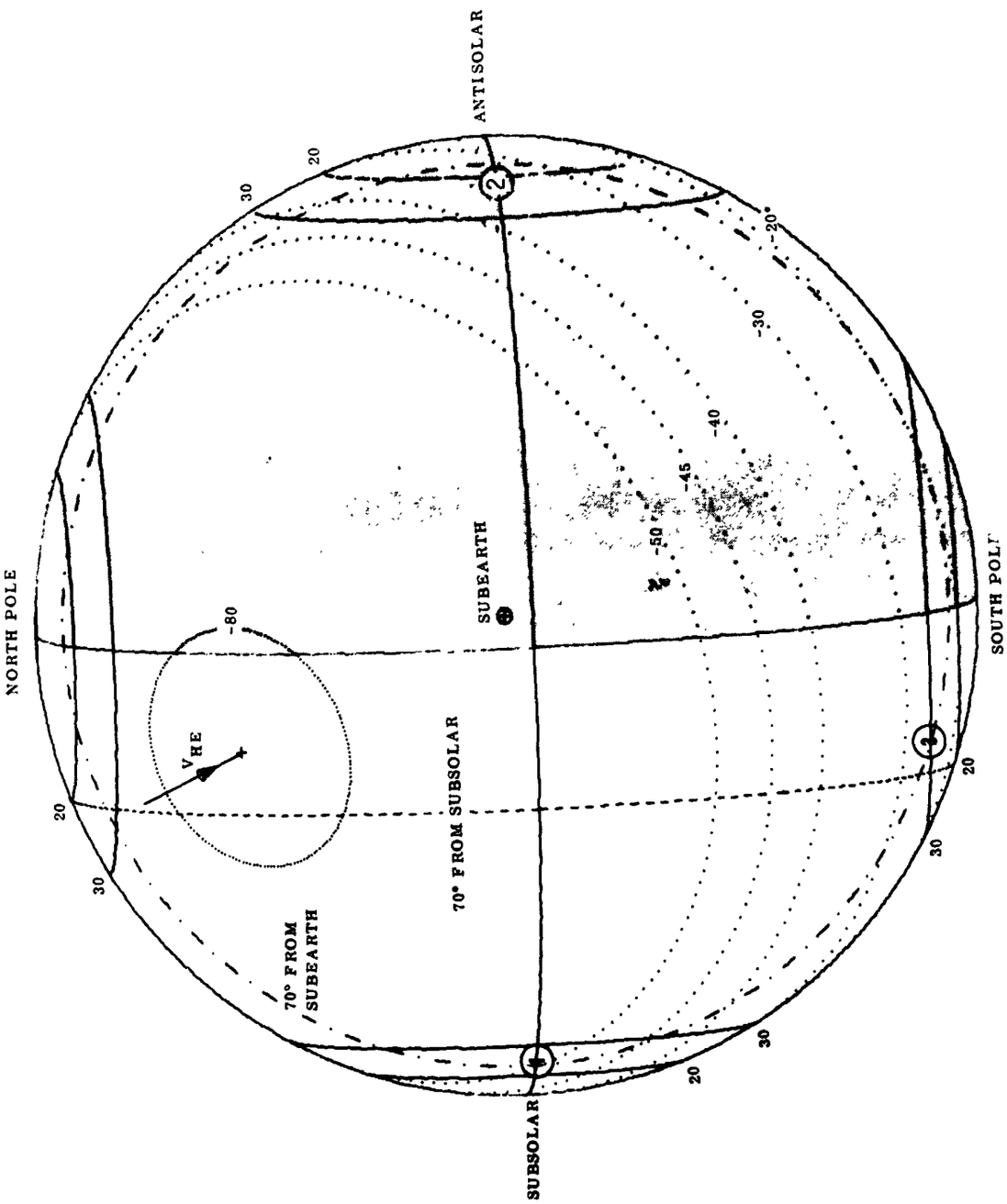


Fig. I-1 Venus as Seen from Earth on October 31, 1975, Type II 5/30 LD

The primary target zones dictated by the scientific objectives are the subsolar zone, a pole, and the antisolar zone in that order. Secondary targets include the lightside of the morning terminator, the opposite pole, and the evening terminator (which was excluded by the direct earth communications constraint). The subsolar zone is an important target since most of the solar energy is deposited there and it represents a source for the circulation. The greenhouse effect requires that some solar radiation reach the surface; measurements at the subsolar point would confirm or deny this. The poles and/or the antisolar regions are the coolest places on the planet and one or both will therefore represent a sink for the circulation. The arguments for the subsolar, polar, and antisolar regions being the primary targets are fairly straightforward; they are the most different points on the planet, the furthest apart, the furthest removed from the regions probed by Mariner and Venera, and are the source and sinks for the circulation. The choice of which of these is most important is a subjective one; a spectroscopist might choose the subsolar region, while a proponent of ice caps might choose the pole. However, considering the question observable by observable, results in the choice of the subsolar region, because the most observables require the delivery of most instruments for the most different reasons.

For each of the observables there is a set of one or more desired targets and a set of applicable instruments. These can be arranged into a target/observable matrix and an instrument/observable matrix, as shown schematically in Fig. I-2. A cross plot of these two matrices results in an instrument/target matrix as shown in Table I-5. This matrix represents an "ideal" grouping of instruments for the various targets and indicates that sending all of the instruments to at least the first three targets is required by the objectives. However, while this would indeed be ideal, there is some redundancy that allows sending only some of the instruments to the polar and antisolar targets.

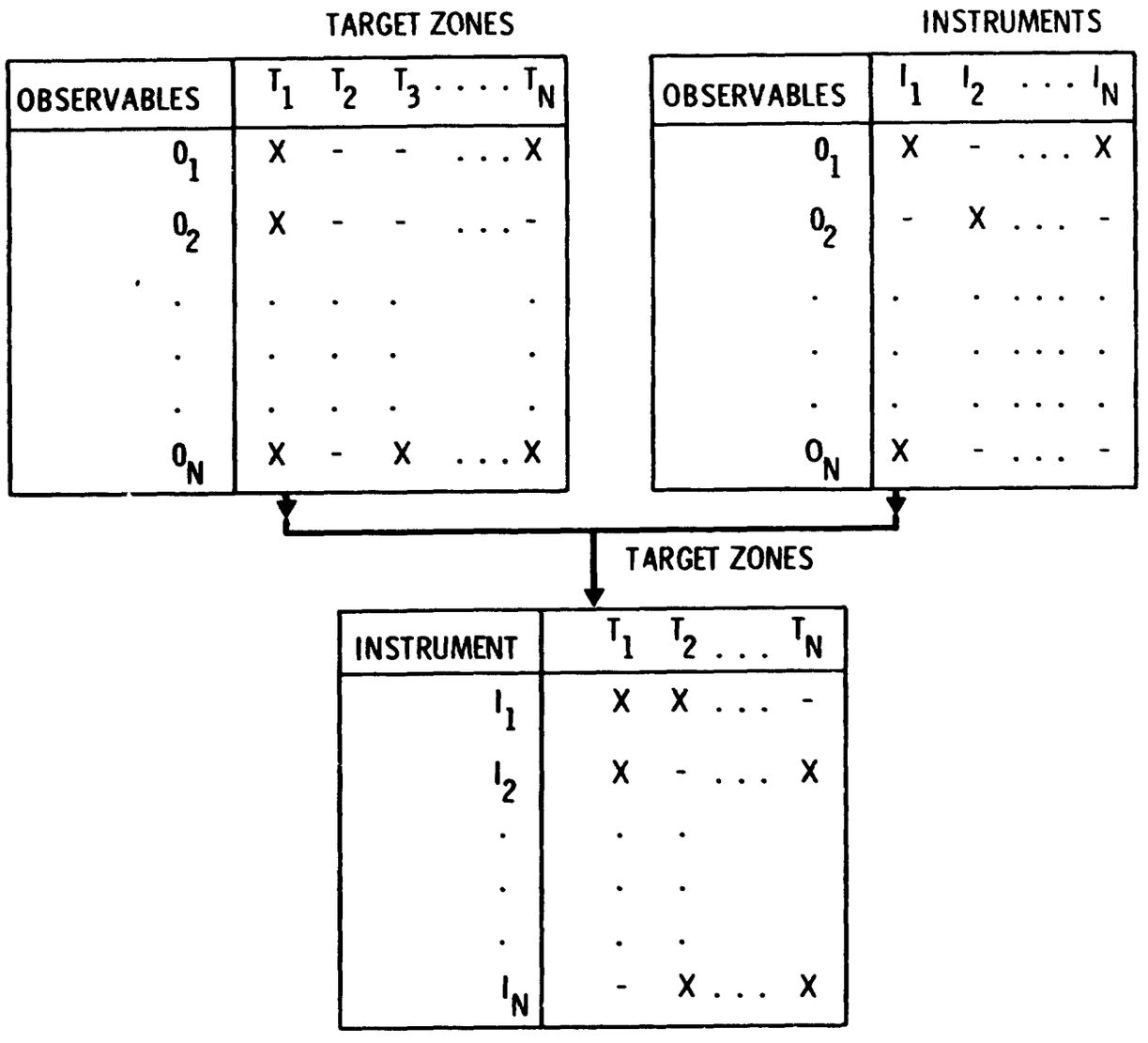


Fig. I-2 Schematic Representation of Target-Instrument Matrices

Table I-5 Primary and Secondary Target Zones vs Instruments

Instrument	Sub-solar	Polar (N or S)	Anti-solar	Evening Terminator	Morning Terminator
Accelerometer	X	X*	X	*	*
Pressure Sensors	X	X	X	*	*
Temperature Sensors	X	X	X	*	*
Solar Radiometer	X	*		*	*
Thermal Radiometer	X	X	X	*	*
Gas Mass Spectrometer	X	X	X	*	*
Cloud Composition	X	X	X	*	*
Cloud Particle Size	X	X	X	*	*
Nephelometer	X	X	X	*	*
Evaporimeter/Condensimeter	X	X	X		
Altitude and Drift Radar (70 km)	X	X	X	*	*
Balloons	X	X	X		
Transponder	X	X	X	*	*
Ion Mass Spectrometer	X	*		*	*
High Altitude Neutral Mass Spectrometer	X	*		*	*
Electron Density Probe	X	*		*	*
UV Photometer	X	*		*	*

Note: X, primary target;
*, secondary target.

For example, having established a pressure-altitude reference with the pressure sensors and large radar on the subsolar probe, pressure sensors alone on other probes would serve as altimeters (assuming the surface and levels of constant pressure are spherical). Also, a good determination of the cloud composition profile referenced to the pressure, temperature, mass spectrometer, and evaporimeter/condensimeter measurements at the subsolar target would permit at least an indirect determination of the cloud composition at other points using the evaporimeter/condensimeter measurements alone. Thus, the condition that all instruments be delivered to all primary targets can be relaxed with only a small degradation in accomplishing the objectives. The relaxed condition is then that all instruments be delivered to at least one primary target (preferably subsolar) and only some (most) be delivered to the neighborhood of a pole and the antisolar point. If additional capability is available, there is a choice between sending the full instrument complement to more than one of the primary targets or sending the smaller instrument group to one of the secondary targets (lightside of the morning terminator or the opposite pole) as well as the pole and antisolar. In the first case, a more comprehensive vertical coverage is obtained at two primary targets, while in the second case a more comprehensive horizontal coverage is obtained. The final choice depends on how well the objectives can be accomplished with the (feasible) probe systems needed for delivery. The mission effectiveness model has proven very useful in helping evaluate various missions.

3. Required Altitude Coverage and Sample Intervals

Figure I-3 summarizes our present knowledge of the atmosphere of Venus along with some speculation on the lower clouds. The regions of primary importance to the objectives are indicated at the right of the Fig. I-3. Table I-6 summarizes the desired altitude sample intervals for these ranges. Appendix C gives the intervals for each observable.

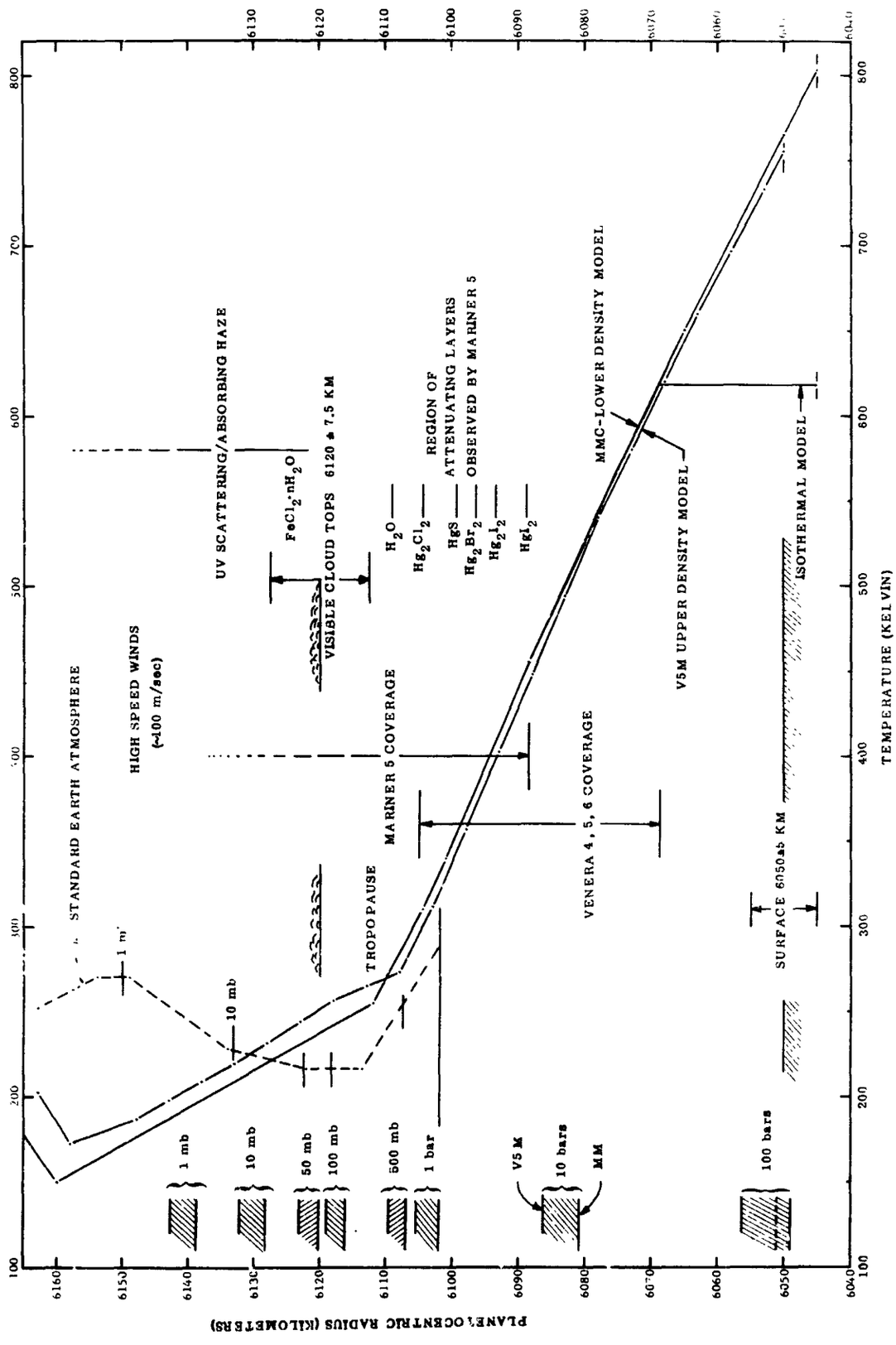


Fig. I-3 Temperature Profiles for Venus

Table I-6 Desired Altitude Sample Intervals

INSTRUMENTS	RFP SAMPLING INTERVALS (m)	BITS PER SAMPLE	MIN SAMPLE ANALYSIS TIME (sec)	RECOMMENDED SAMPLING INTERVAL (meters)	AT NOMINAL RADIUS (km)
Nephelometer	(averages)	16	< 5	200	
Thermal Radiometer	100	14	< 5	to	6120
Cloud Particle		80	< 5	500	
Temperature	300	8	< 1	200	6100 - 6130
Pressure		8	< 1	to	6045 - 6070
				500	
Mass Spectrometer	1000	600	10 - 60	1000 to 2000	~6120
Solar Radiometer	1000	1200	-	1000	~6120
Radar Altimeter (70 km)	(1000)	56	< 10		
Evaporimeter/Condensimeter	1500	456	60 -300	1000 2000	~6120
Cloud Composition	7000	1600	> 300	~5000	above 6110 & below 6085
				~2000	between 6110 & 6085
Accelerometer (for turbulence, shears)	-	-	-	~500	6130>R>6080 or more or less

B. OPERATIONAL REQUIREMENTS

To provide the science instruments with the most advantageous sampling conditions, certain requirements are imposed on the operational modes of the entry probes. These deal primarily with providing the proper sampling altitude and velocity and reflect directly on probe design and operation. The requirement to place entry probes at significantly different planet locations places specific requirements on the operational mode of the planetary vehicle and probes during separation and deflection operations. Factors influenced most are the ejection radius, attitude requirements at probe separation, deflection impulse requirements, and the resulting atmospheric entry operations.

The directed use of the Titan IIIC launch vehicle has not affected operational modes. It has lifted payload constraints that could have otherwise restricted choices of various mission operations. The operation is affected by the flyby and direct impact spacecraft modes, and both cases are discussed.

The required use of direct-link communications and compatibility with the projected capability has also affected the system operation and methods of providing adequate data links have been defined.

The entry probes have not been required to survive surface impact and no operational or configuration provisions are included.

All these operational requirements have been combined with configuration, science, and environmental requirements. Operational procedures and sequences have been written that define operations consistent with hardware definitions.

C. ENVIRONMENTAL REQUIREMENTS

Entry Capsule systems must be designed to withstand all adverse environments to be encountered during performance of the mission. This includes the requirements that are associated with the following phases of system development and mission performance:

1) Flight article environmental testing;
2) Subsystem fabrication and assembly;
3) Sterilization;
4) Planetary Vehicle system assembly and checkout;
5) Launch and boost;
6) Interplanetary cruise;
7) Entry into the Venus atmosphere;
8) Floating in the Venus atmosphere (Balloon Probes only).

The environments in these phases can not be entirely separated from each other. Each must be considered in relation to the others and also in relation to the characteristics of the particular configuration or subsystem.

1. Flight Article Acceptance Testing

The environmental levels for qualification testing must account for the uncertainties in operational environments plus a nominal margin of safety.

2. Subsystem Fabrication and Assembly

These operations should be performed in clean rooms of Class 100,000, or better.

3. Sterilization

Subsystems will be cleaned to a Class 100 level, moved to a Class 100 clean room, and decontaminated with ethylene oxide. Final installation of flight batteries, propulsion, and pyrotechnics will be made. Biocanisters will be installed and terminal heat sterilization will be performed.

4. Planetary Vehicle Assembly and Checkout

Environmental protection will be provided throughout assembly and checkout. For the case of the impacting spacecraft, an overall biocanister will be installed and the assembly will be resterilized with ethylene oxide. A protective cover will be required for transport to the launch pad. For transporter design, it is important that transport shock loads not exceed any levels for which the subsystems have been qualified. Mating of the Planetary Vehicle to the Launch Vehicle and installation of the Payload Fairing will take place in the Universal Environmental Shelter.

5. Launch and Boost

The dynamic loads during launch and boost are dependent on the distribution of mass within the Planetary Vehicle, the stiffness of supporting members, and the aerodynamic forces on the Payload Fairing. Boost venting of the Payload Fairing will occur and this will require venting of the Planetary Vehicle. Venting of the overall biocanister for the impacting spacecraft will require special consideration. The residual turning rates from the Launch Vehicle combined with the dynamic forces of Planetary Vehicle separation (including the biocanister for the impacting spacecraft) must not exceed the ability of the spacecraft attitude control system to recover ($\pm$50 mrad/sec about any axis).

6. Interplanetary Cruise

The most significant space environmental effects are due to absorption of thermal energy from the sun and radiation into space. Thermal analyses and design of thermal control systems, supported by preflight testing, will provide assurance of system operability of Entry Capsule systems. Modifications of the spacecraft must also be verified to the extent that they are different from configurations that have previous flight history.

7. Entry into the Venus Atmosphere

Environmental conditions during entry are functions of the descent profile for each probe and the reference atmosphere. The range of atmospheres for design is represented by the "V5M Atmosphere" and the "MMC Lower Atmosphere," both of which are discussed in Chapter II, Sections G and H and in Appendix F. When interpreted in terms of probe design parameters the worst-case atmospheres are as shown in Table I-7.

Table I-7 Design Atmospheres

Design Parameter	Worst-Case Atmosphere
1. Ballistic Coefficient Selection	Entry in the Reference MMC Lower Atmosphere
2. Bit Rate	Same as 1.
3. Structure	Descent in the V5M Atmosphere
4. Thermal Control	Same as 3.
5. Atmospheric RF Attenuation	Same as 3.
6. Operating Life	Same as 3.

8. Balloon Floating in the Venus Atmosphere

The balloon probes of Options 1 and 2 will float in the Venus atmosphere for indefinite periods of time. Float altitude pressures will be at 500 mb (Option 1) or at 500 mb and 50 mb (Option 2). Ambient temperatures for the MMC Lower Atmosphere (worst case) are shown in Table I-8. It will be a requirement on the thermal control subsystems of the gondolas to maintain internal temperatures so that a range of 40°F to 120°F is not exceeded for electronic components and a range of 40°F to 130°F is not exceeded for batteries.

Table I-8 Balloon Floating Environments

Floating Altitude Pressure (mb)	Ambient Temperature (°F)	Maximum Super Pressure (mb)	Maximum Skin Temperature (Subsolar) (°F)
500	60	84	150
50	-30	10.5	60

D. PROBE CONFIGURATION REQUIREMENTS

Entry probe configuration requirements are constrained by the science objectives, and other constraints that were identified in the statement of work.

1. Probe Classification from Science Objectives

Examination of the science instruments, sampling intervals, and target zones shows a need to simultaneously gather data on the vertical structure of the atmosphere at dispersed targets. This can be accommodated by a group of ballistic probes. A second need is to emphasize investigation of the high clouds with a probe design that traverses this region much slower than is feasible with ballistic probes. Finally, the need for atmospheric circulation data can only be fulfilled with balloons floating in the atmosphere for extended periods of time.

In all cases, probe design must be compatible with survival in the designated environments and must not allow contamination of regions conducive to life.

a. Ballistic Probe Configuration Requirements - The ballistic probes must collect data during entry, and the descent profile through the atmosphere to the surface must be compatible with data collection and transmission. It is desirable to provide low descent velocities in the upper atmosphere, with a velocity increase permissible in the lower atmosphere. Stability in the lower

atmosphere indicates the use of cone shapes. Instrument containers must be designed to provide pressure protection to 150 bars. Thermal protection to 900°F in the lower atmosphere can be provided by the use of insulation and phase change material. The basic configuration is then largely determined by the terminal descent requirements, and to these must be added the requirements associated with the higher altitudes and entry.

The ballistic probes must be at subsonic velocity for data collection at an altitude for 6120 km. This requires deploying a parachute above that altitude, in addition to the aeroshell and heat shield required for entry.

One ballistic probe must be larger in size than the others to accommodate the added instruments to the subsolar target.

b. High Cloud Probe Configuration Requirements - The high cloud probes must be designed to be subsonic and operable at an altitude of 6130 km and to remain operable to 6100 km. Operation is not required below 6100 km. There is no requirement for pressure protection of operating instruments. The significant requirements of light weight, and low ballistic coefficient at the range of operating altitudes can be based on a canister suspended from a parachute. A lower ballistic coefficient during the entry phase is required for the high cloud probes than for the ballistic probes and this implies an entry diameter that is relatively large with respect to the longitudinal axis.

c. Balloon Probe Configuration Requirements - The balloon probes have no requirement for collection of science data before balloon deployment. Pressure protection will not be required for operating instruments, though thermal protection must be considered. The size of the entry probe is largely determined by the storage tanks for the inflation gas, and this volume then determines the minimum dimensions of the aeroshell. The weight of the operating

configuration can be greatly reduced from the entry configuration by jettisoning the decelerator and inflation systems. Two balloons floating at different ambient pressures will require significantly different floating volumes, and inflation gas, with subsequent differences in entry size and weight.

2. Non-Science Constraints Affecting Probe Configuration

The specified requirements to use the Titan IIIC launch vehicle, and the version of the Mariner spacecraft known as AVCO Configuration 20a, both imply maximum total weights to be considered. Weight distribution between probes is subject to tradeoff analyses. In addition, maximum launch dimensions are fixed by the Titan IIIC Payload Fairing. To a somewhat lesser degree, maximum dimensions are also controlled by the interfaces with the spacecraft when permissible orientations and acceptable maneuver capabilities are considered. Technology requirements, including components of 1972 state of the art, sterilization, heat shield requirements definition, and definition of the Venus atmosphere also provide constraints for probe configurations. In the main, these non-science constraints have their major effects on the total system with some variations of treatment between probes of different types.

E. STERILIZATION CRITERIA AND REQUIREMENTS

The mission shall be consistent with NASA planetary quarantine policy specified in NASA Management Manual 4-4-1 (Ref I-3), which for this mission is interpreted to mean that the region of the atmosphere that might be conducive to life forms shall not be contaminated.

For purposes of this study:

1) The system shall be assembled in clean rooms at specified levels of assembly;
2) All hardware entering the planet's atmosphere must be capable of withstanding ETO exposure in accordance with JPL Specification No. VOL-50503-ETS (Ref I-4);
3) Selected probe equipment (e.g., heat shield and other elements that might outgas or vent to the atmosphere) must be capable of withstanding heat sterilization as defined in JPL Specification No. VOL-50503-ETS (Ref I-4);
4) The planetary entry systems shall be enclosed in a bacteriological barrier to maintain cleanliness and sterility. After decontamination, the enclosure shall not be opened within any portion of the Earth's atmosphere that might recontaminate the entry system;
5) Adherence to items covered in Chapter V, Section E.1 shall apply only to the entry probes. (Note: Exclusion of the spacecraft at this time is for purposes of this study only.)

F. REQUIREMENTS DOCUMENTATION

The Venus Multiple Probe Study was performed within technical constraints, and in accordance with technical requirements, specified in the requirements of JPL Letter 622-MMH:sb, dated March 13, 1969 (Ref I-5). Technical requirements were invoked by the following sections:

1) Statement of Work; (Appendix A)
2) Designation of Technical Documents for RFP GR-2-3971.

During the study, a series of four Technical Directive Memorandums (TDMs) were received, dated September 17, 1969, September 29, 1969, October 3, 1969, and October 26, 1969. The TDMs identified technical areas where study emphasis was desired and provided additional criteria. A Midterm Oral Briefing at JPL on December 2, 1969 and several technical coordination meetings with JPL personnel completed the technical framework under which the study was conducted. TDMs are contained in Appendix C, Volume III.

1. Study Ground Rules and Constraints Document (MCR-69-519)

Study Ground Rules and Constraints Document (Ref I-6) issued by Martin Marietta consolidated requirements received from JPL and provided early internal direction to personnel engaged in the study. This document is Appendix I in Volume III.

a. Content of MCR-69-519 - The *Study Ground Rules and Constraints Document* provided ground rules for mission definition and synthesis of systems to perform the Venus mission, in addition to ground rules for conduct of the study.

b. Use of MCR-69-519 - The early issuance of MCR-69-519 enabled "snortform" reference to a larger mass of technical data that was not expected to change during the course of the study.

2. Science Questions

The Statement of Work referred to JPL Section Document 131-03 *Science Criteria for Venus Entry Missions*. The essence of this document was to pose a series of questions to serve as representative objectives for Venus exploration and to define instrumentation that would be suitable for a 1975 mission.

a. Venus Exploration Questions - A group of three major questions was further subdivided into a total of 18 secondary level questions. The three major questions were:

1) "What is the composition of the atmosphere?" (Six secondary questions were in this subgroup;)

2) "What is the distribution and chemical composition of the clouds?" (Five secondary questions were in this subgroup;)

3) "What is the general circulation pattern of the atmosphere?" (Seven secondary questions were in this subgroup.)

The 18 questions, backed up by discussion of instrumentation requirements and instrument characteristics, provided a baseline for the initiation of system synthesis.

b. Observable Objectives - Martin Marietta responded to the Venus exploration questions by compiling a list of 22 "Observable Objectives" directed toward determining the physical properties of the Venus atmosphere. The effect of this list of objectives was to make the transition from a question to be answered to an objective to be achieved. The list of observable objectives was coordinated with JPL, and was used within the study group as the governing document with regard to design for science. It was also used for comparisons of science achievement for different missions.

c. Value Curves for Science Objectives - In support and amplification of the Observable Objectives, value curves were constructed for the purpose of correlating instrument performance in the Venus atmosphere as a function of target location, altitude range, sampling intervals, and other comparable parameters. These curves aided in assessing the merits of competing designs and provided insight into methods for system improvement.

3. System Design Criteria

The *Study Ground Rules and Constraints Document* and the *Science Criteria for Venus Entry Missions* documents were invariant during the course of the study. In contrast there was a need for a document to serve as a repository for "current" design approaches no matter how rapidly the changes might occur. This document was regarded as a system level specification that was in the early stages of development.

The processes of writing, coordinating, interpreting, and revising this document provided a level of detail design direction that would not have been attainable otherwise.

a. Trial Mission System Design Criteria - An original release and a Revision A of the System Design Criteria defined the requirements applicable to the trial mission.

b. Baseline Mission System Design Criteria - Following the Midterm Oral Briefing, the Baseline Mission with Options 1 and 2 was defined and two in-process releases, were made to the System Design Criteria.

G. REFERENCES

I-1. "A Venus Multiple-Entry-Probe Direct-Impact Mission -- Scientific Objectives and Technical Description." Goddard Space Flight Center, Greenbelt, Maryland, January 1969.

I-2. R. J. Mackin, Jr., et al.: "Scientific Questions for the Exploration of the Terrestrial Planets and Jupiter." TM-33-410. Jet Propulsion Laboratory, October 1, 1968.

I-3. *NASA Unmanned Spacecraft Decontamination Policy.* NASA Management Manual 4-4-1. September 1963.

I-4. *Environmental Specification, Voyager Capsule Flight Equipment Type Approval and Flight Acceptance Test Procedures for the Heat Sterilization and ETO Decontamination Environments.* JPL Specification No. VOL-50503-ETS. January 2, 1966.

I-5. "Request for Proposal (RFP) No. GR-2-3971, Study of a Venus Entry Mission." JPL Letter 622-MMH: sb, March 13, 1969.

I-6. *Study Ground Rules and Constraints Document.* MCR-69-519. Martin Marietta Corporation, Denver, Colorado, October 3, 1969. Appendix I.

I-7. Statement of Work, Appendix A.

I-8. *Science Criteria for Venus Entry Missions.* JPL Section Document 131-03. Appendix B.

II. DEFINITION OF TRAJECTORIES AND ENVIRONMENTAL MODELS

A. INTERPLANETARY TRANSFER TRAJECTORY

The interplanetary trajectories for the Venus Entry Mission Study are limited to mission opportunities in 1975. The launch vehicle is assumed to be the Titan IIIC and the launch azimuths are assumed to be between 90 and 114°.

The general requirements for a Venus mission in 1975 are presented in Fig. II-1 as a function of launch and encounter date and are plotted from JPL-generated computer tabulations (Ref II-1). The energy requirements are presented as C_3 values. The hyperbolic excess velocity, V_{HE}, also is shown and can be related to the entry velocity at Venus as noted in Fig. II-2. For this study the entry radius is assumed at 6300 km to be consistent with the heating technology data of Ref II-2. The constants used in all computations are noted in Ref II-3.

Two areas of constraint are shown in Fig. II-1. The first of these assumes that the declination of the launch asymptote (DLA) is always less than ±36°. Regions of greater DLAs are not available for the Venus Entry Mission Study. This constraint is consistent with the nominal downrange azimuth capabilities from the Eastern Test Range (ETR) of 90 to 114° and the Titan IIIC launch vehicle. Other azimuths can be used if overflight conditions are acceptable and downrange tracking ships are properly located. For this study the launch azimuth constraint does not appear to be a limiting factor since larger values of the DLA will generally result in C_3 values too large for a significant science payload.

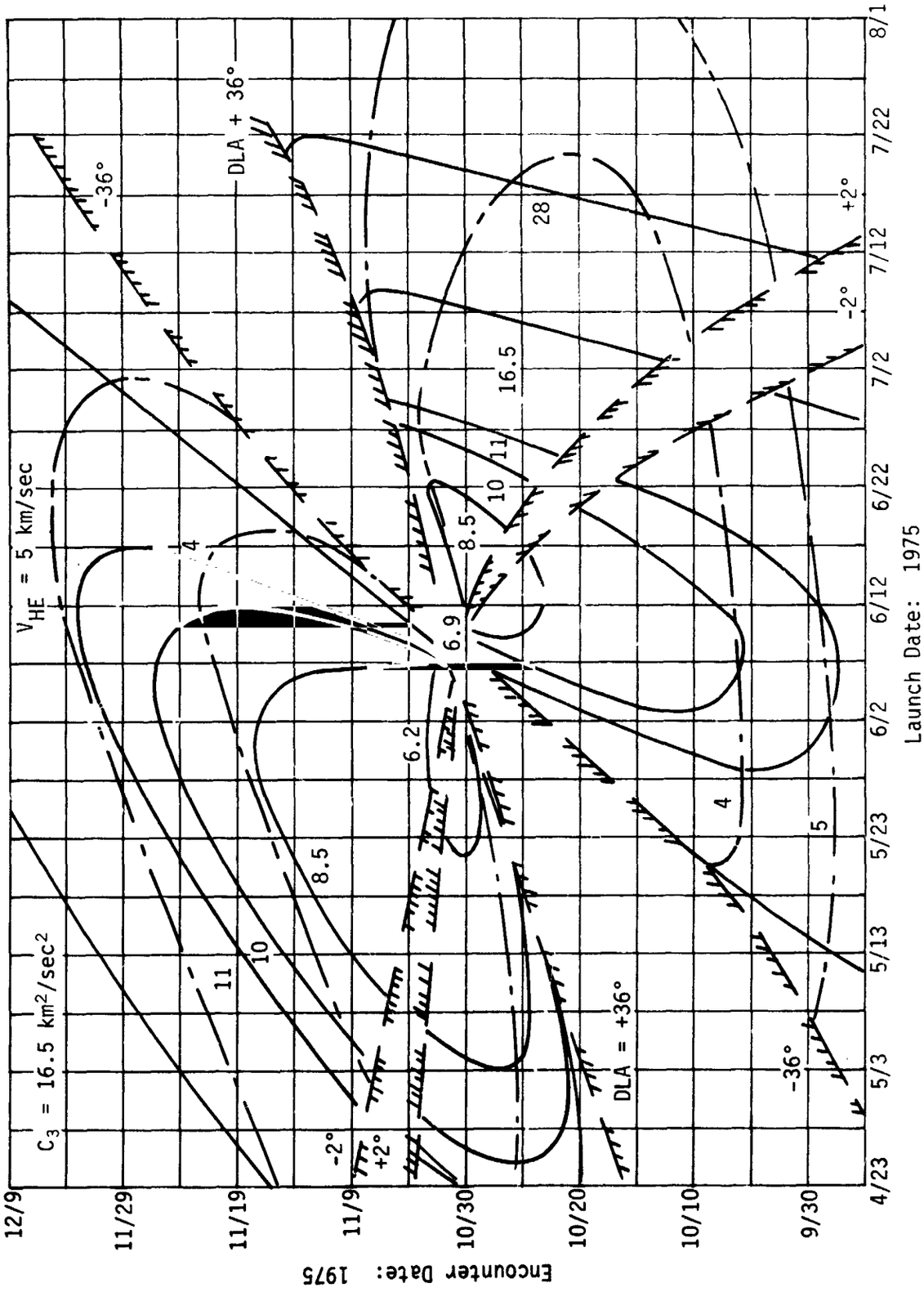


Fig. II-1 1975 Earth-Venus Trajectory Parameters

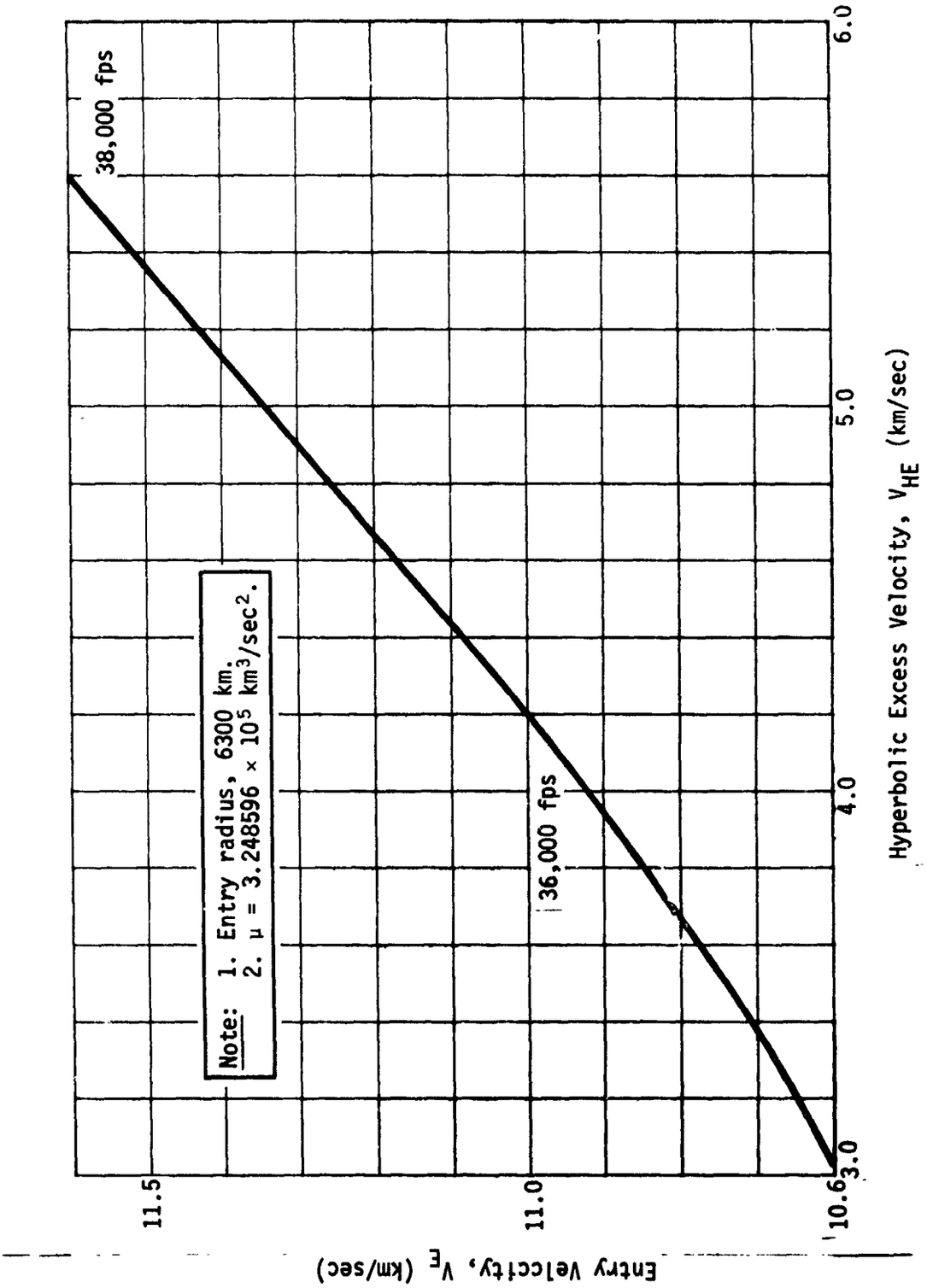


Fig. II-2 Entry Velocities

The second constraint noted in Fig. II-1 is the assumption that the DLA must always be greater than ±2° for navigational accuracy. This assumption has been discussed and agreed on with JPL. It does not appear to create a situation that would significantly affect the mission choices, and therefore no further effort will be expended to justify this assumption.

The launch vehicle for the Venus Entry Mission Study is assumed to be the Titan IIIC as defined in Ref II-4. The payload capabilities of this vehicle are summarized in Fig. II-3 as a function of C_3 requirements. The performance is based on a launch from ETR to direct injection at a 100-n-mi altitude above the Earth. Data are shown for both 90 and 114° launch azimuths. A payload fairing of 1668 lb is assumed with separation from the flight vehicle occurring 280 sec after launch. A maximum payload capability is also shown in Fig. II-3 based on the minimum C_3 values of Fig. II-1 required to assure at least a 20-day launch period. The parametric studies identified no constraints with respect to launch window, launch period, or parking orbit coast time requirements within the specified constraints for the Venus Study.

The communications systems depend on distance as one parameter. This range is presented in Fig. II-4 as a function of arrival date. Direct communication between the probes and Earth is a requirement of this study. To accomplish this direct communication the probe is assumed to be limited to an area within 70° of the subearth point at encounter. Therefore to aid in selecting targeting parameters, Fig. II-5 and II-6 present the latitude and longitude of the V_{HE} and subearth point at encounter for Type I and Type II trajectories, respectively. The communications mask also is shown as a function of encounter date. Latitude and longitude are measured from the Venus orbit plane and the subsolar point respectively in this case.

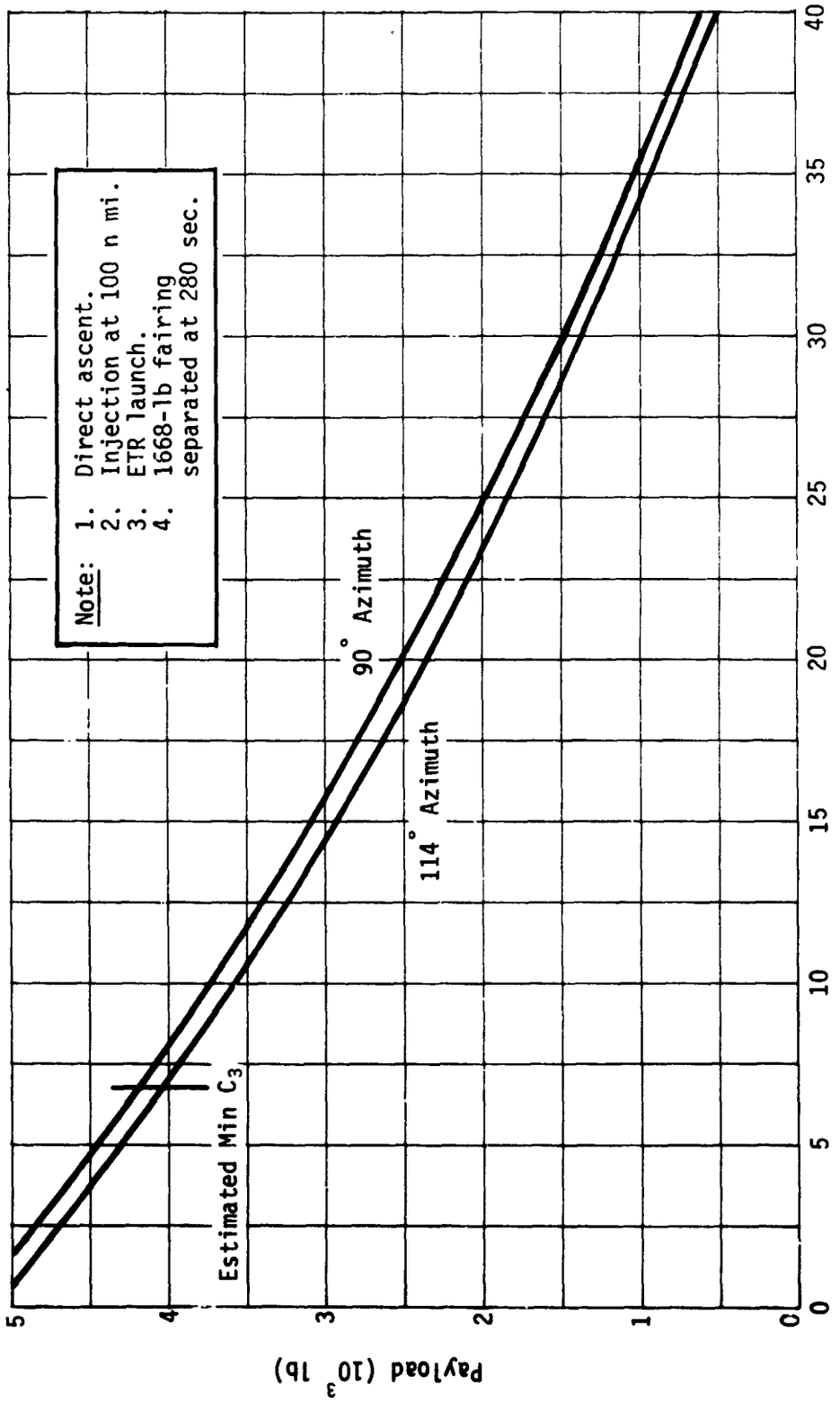


Fig. II-3 Titan IIIC Payload Capabilities

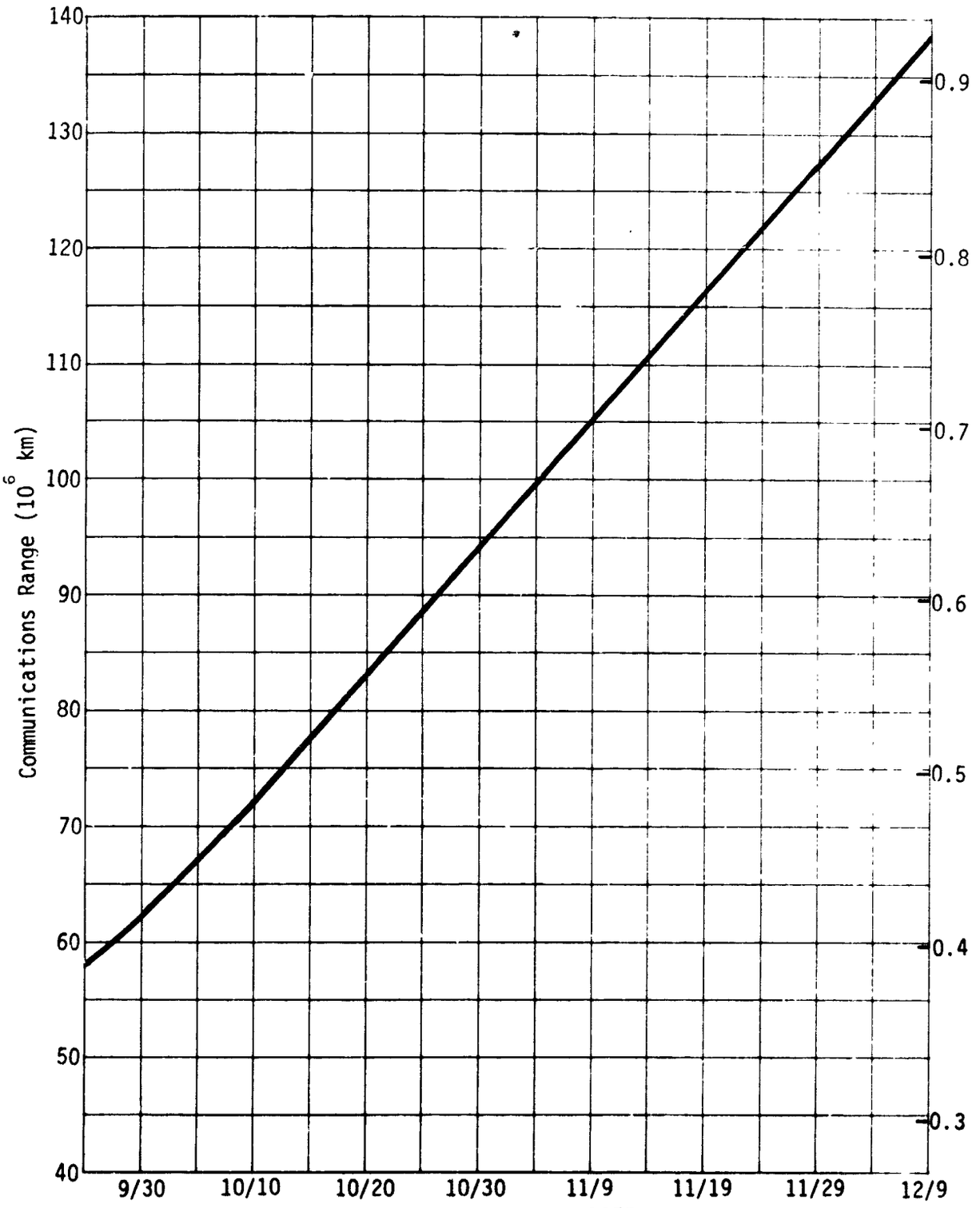


Fig. II-4 Communications Range

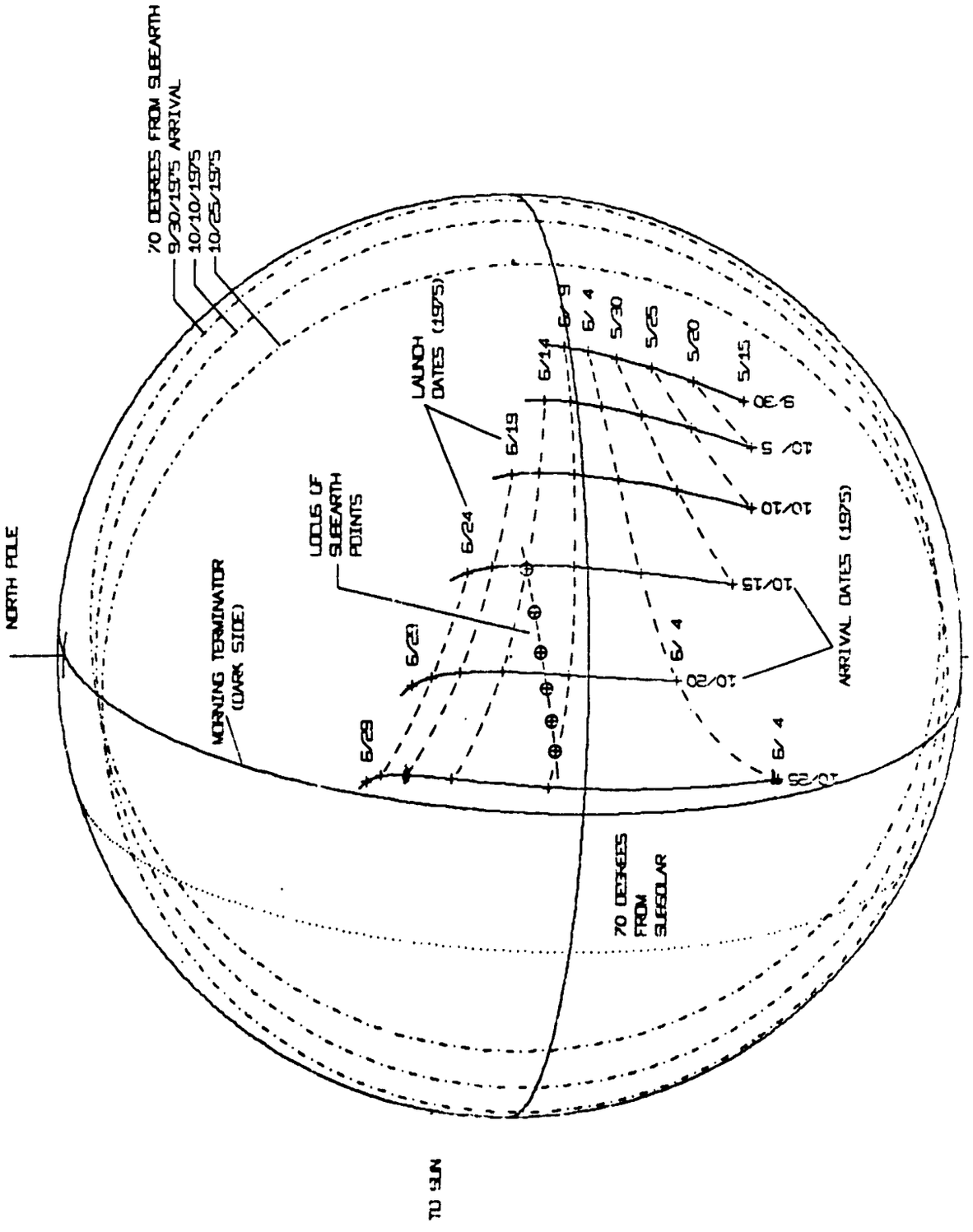


Fig. II-5 1975 Type I Venus Encounter, Locus of V_{HE} Vectors

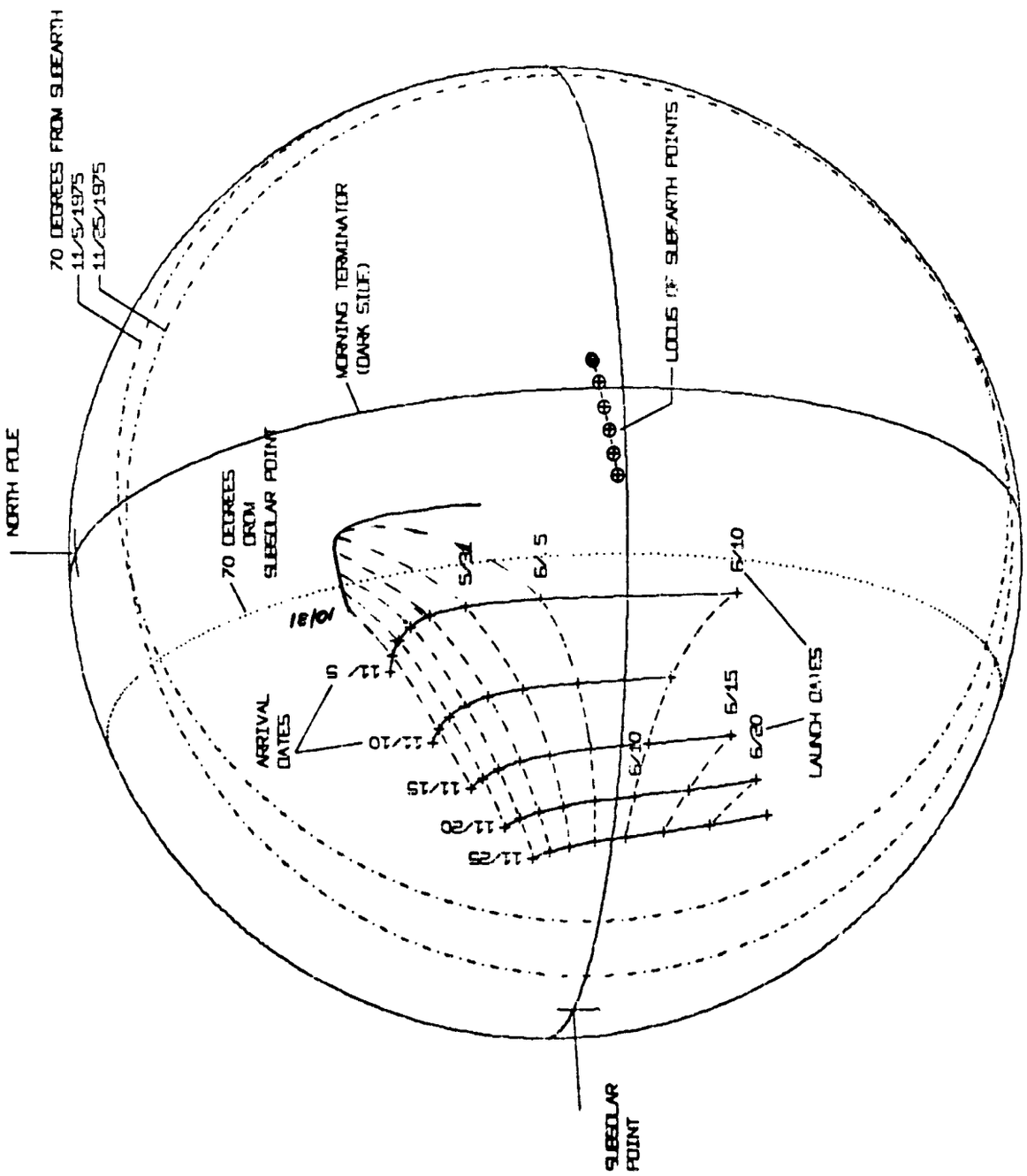


Fig. II-6 1975 Type II Encounter Geometry, Locus of V_{HE}

Figure II-7 presents the limitations on encounter geometry established to meet the requirements of a direct communications link. The position of the V_{HE} relative to the subsolar point and the 70° communications mask is shown as a function of encounter date. To communicate directly with a target within 20° of the subsolar point requires encounter dates later than November 6, 1975. However, certain tradeoffs are considered. An encounter date of October 31, 1975 will move the communications mask to 24 to 25° from the subsolar point, which does not unduly compromise the science experiments. This particular encounter date permits a 20-day launch period at low values of C_3 and maximizes the payload. The V_{HE} position for the 20-day launch period is shown in Fig. II-6 and moves very little during that period. Other encounter dates show considerable movement and therefore require a more complicated deflection and targeting scheme. The October 31, 1975 encounter day exhibits nearly constant deflection and entry parameters for all launch dates. The entry velocity also is near minimum for Type II trajectories and all of the desired target areas are within direct communications capabilities.

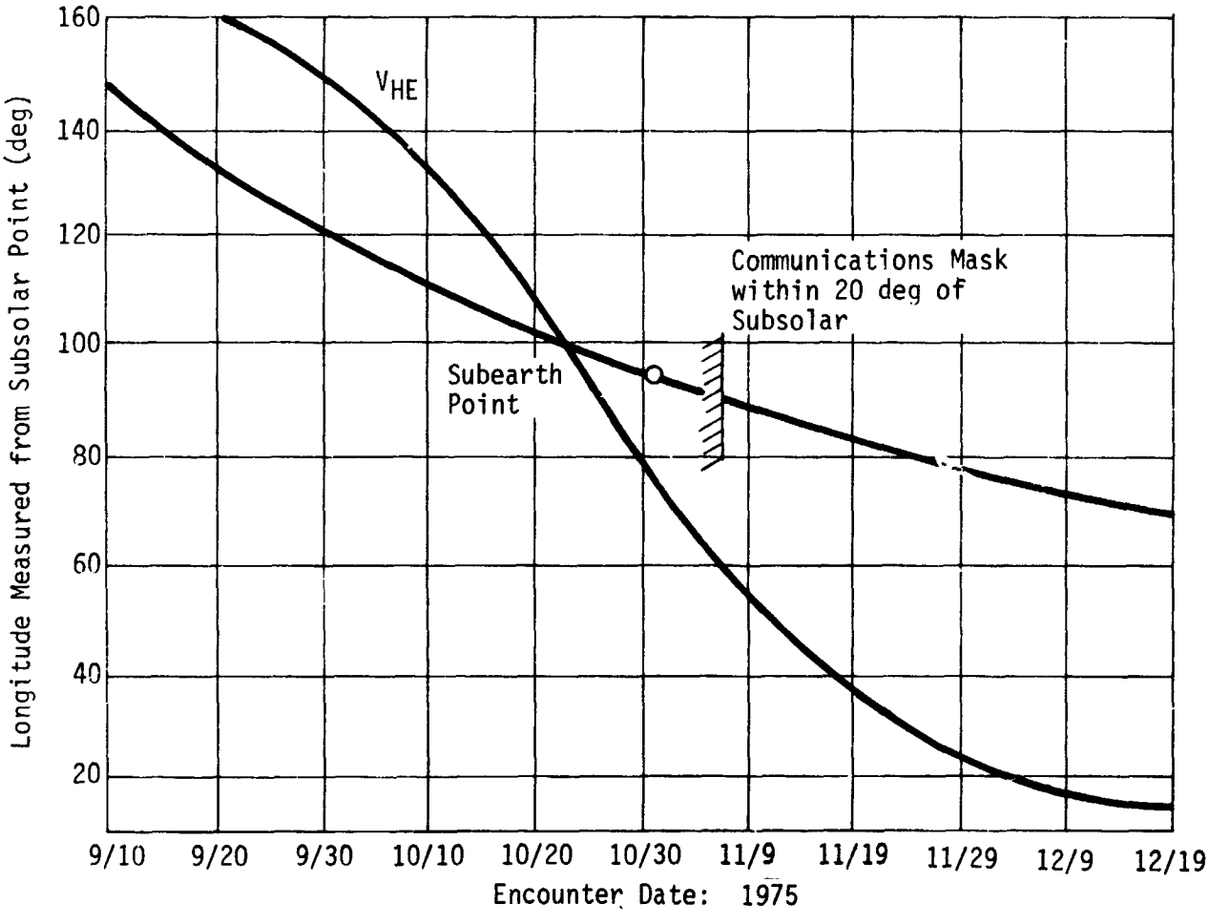


Fig. II-7 Direct Communications Link Limitations

B. PROBE-PLANETARY DEFLECTION STRATEGIES

To provide separation between the spacecraft path and the scientific probe trajectories some technique must be used to deflect the probes from the spacecraft path. A deflection system is required and can be of a mechanical nature (springs), cannon type, or rocket type. The impulse requirements and directions are independent of the type of system and are presented parametrically in this section. The data define the flight paths from deflection to entry. The deflection radius is a parameter in the study and entry is assumed to occur at a radius of 6300 km. Since direct communications with the Earth are required, lead time is not a parameter in this study. Staggering the entry times for communications, however, may be a desirable concept and capabilities and penalties for varying flight times are noted. The impulse requirements are relatively small and the times of application short. For this reason the study considers impulsive velocity increments and does not consider finite burning time effects. The parameters considered are radius of deflection maneuver, radius of periapsis, deflection velocity increment, deflection application angle, and magnitude of the V_{HE}. The results are presented in terms of flight times, entry flight path angle and displacement from the V_{HE}, angle of attack at entry and aim point conditions for various periapsis radii.

Certain quantities and conditions are established by the geometry of the problem and are not affected by the deflection parameters. The hyperbolic excess velocity vector, V_{HE} is specifically located by the launch and arrival date for the mission. To achieve selected targets the incoming vehicles must be displaced from the V_{HE}. This displacement from the V_{HE} along with the magnitude of the V_{HE} defines the entry flight path angle, as noted in Fig. II-8.

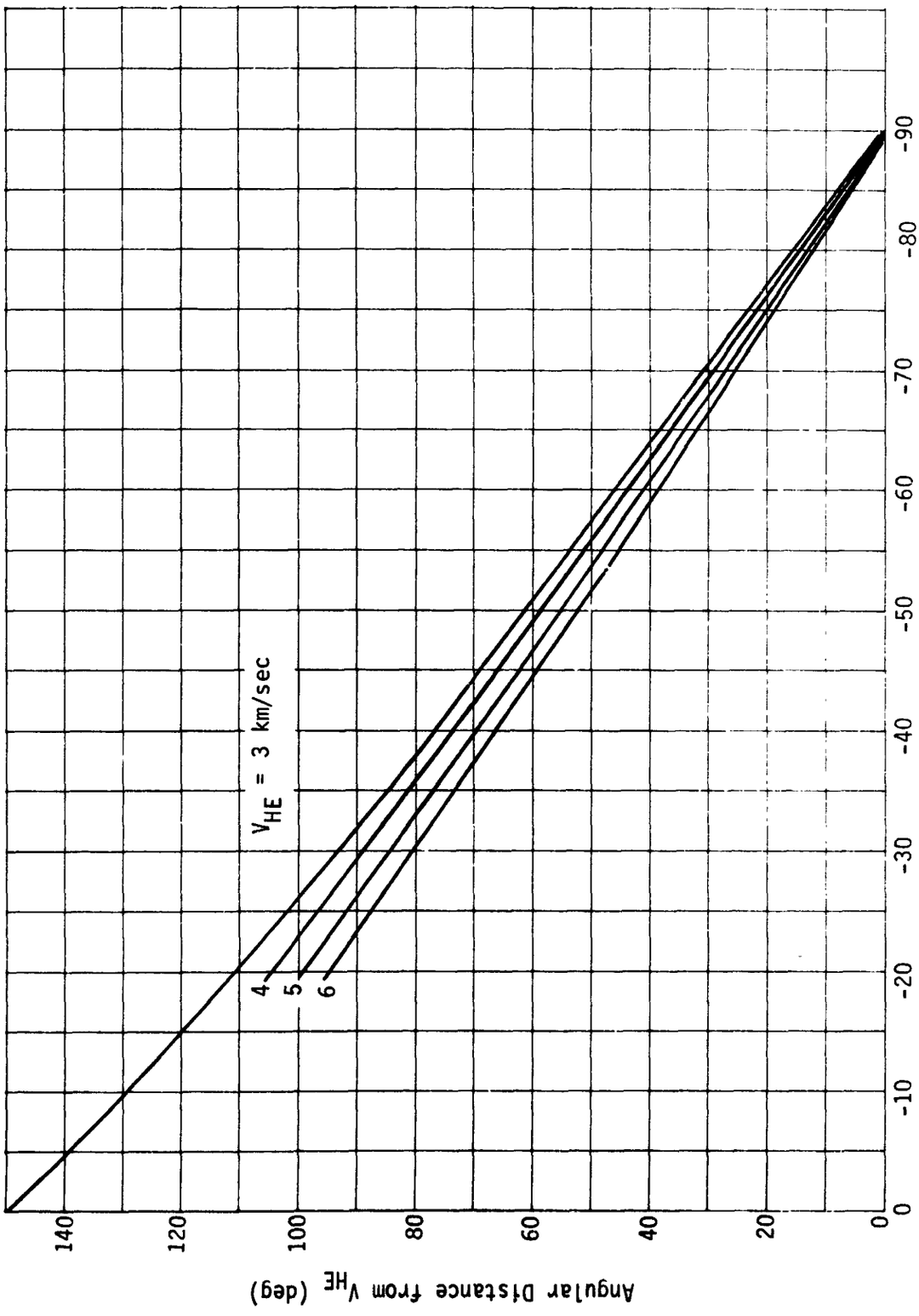


Fig. II-8 Entry Flight Path Angle

The data shown are for an entry radius of 6300 km and take into account the path curvature resulting from the gravity effects of Venus. Also, Fig. II-8 indicates that certain areas are not available for direct entry. For a V_{HE} = 3 km/sec the entry flight path becomes zero at a displacement of 150° from the V_{HE}. The path grazes the entry radius at this point and the region beyond the point is unavailable for direct entry. Therefore, a circle of 30° radius with its center located 180° from the V_{HE} is not available for direct entry targeting in this case. Since a minimum entry angle generally is imposed on actual systems the unaccessible region will be somewhat larger than indicated.

Definition of the magnitude of the V_{HE} and either the entry flight path angle or the target displacement from the V_{HE} will yield the impact parameter, B. This impact parameter is shown in Fig. II-9 as a function of the entry flight path angle. Using the impact parameter and the V_{HE} value, we can define the periapsis radius as shown in Fig. II-10.

As the planet is approached, the local gravity tends to bend the approach path toward the center of the planet and increase the velocity. The magnitude of the bending effect is presented in Fig. II-11 as a function of the value of V_{HE} and displacement from the V_{HE}. The displacement is measured on a surface at a radius of 6300 km from the center of the planet. Generally the curvature will produce an angle of attack on a vehicle whose axis is fixed in inertial space. The vehicle orientation, however, can be selected to yield a zero angle of attack at entry. The variation in local velocity is presented in Fig. II-12 as a function of V_{HE} and distance from the planet. The increase in velocity becomes significant at radii less than 10^6 km. The deflection velocity requirements will increase as the velocity to be deflected increases. At greater radii the velocity is essentially constant. For this reason all deflection maneuvers will be achieved at radii greater than 10^6 km.

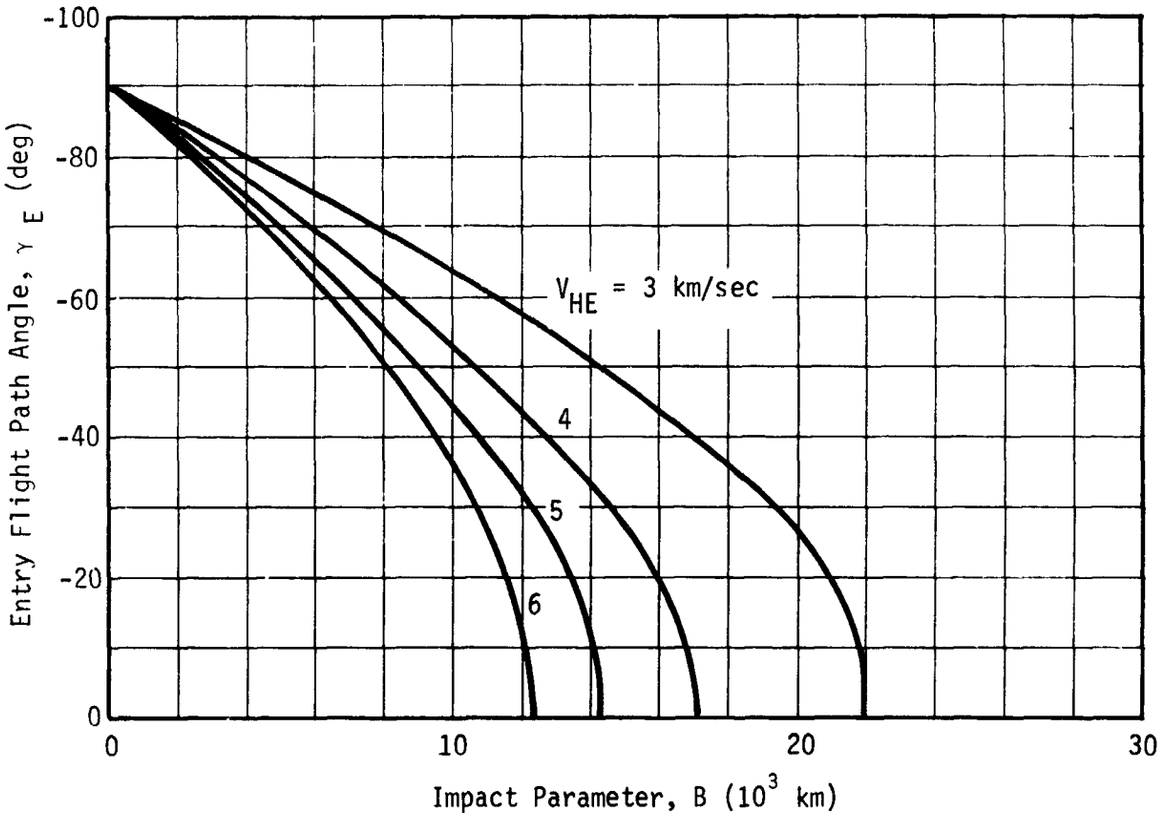


Fig. II-9 Impact Parameter

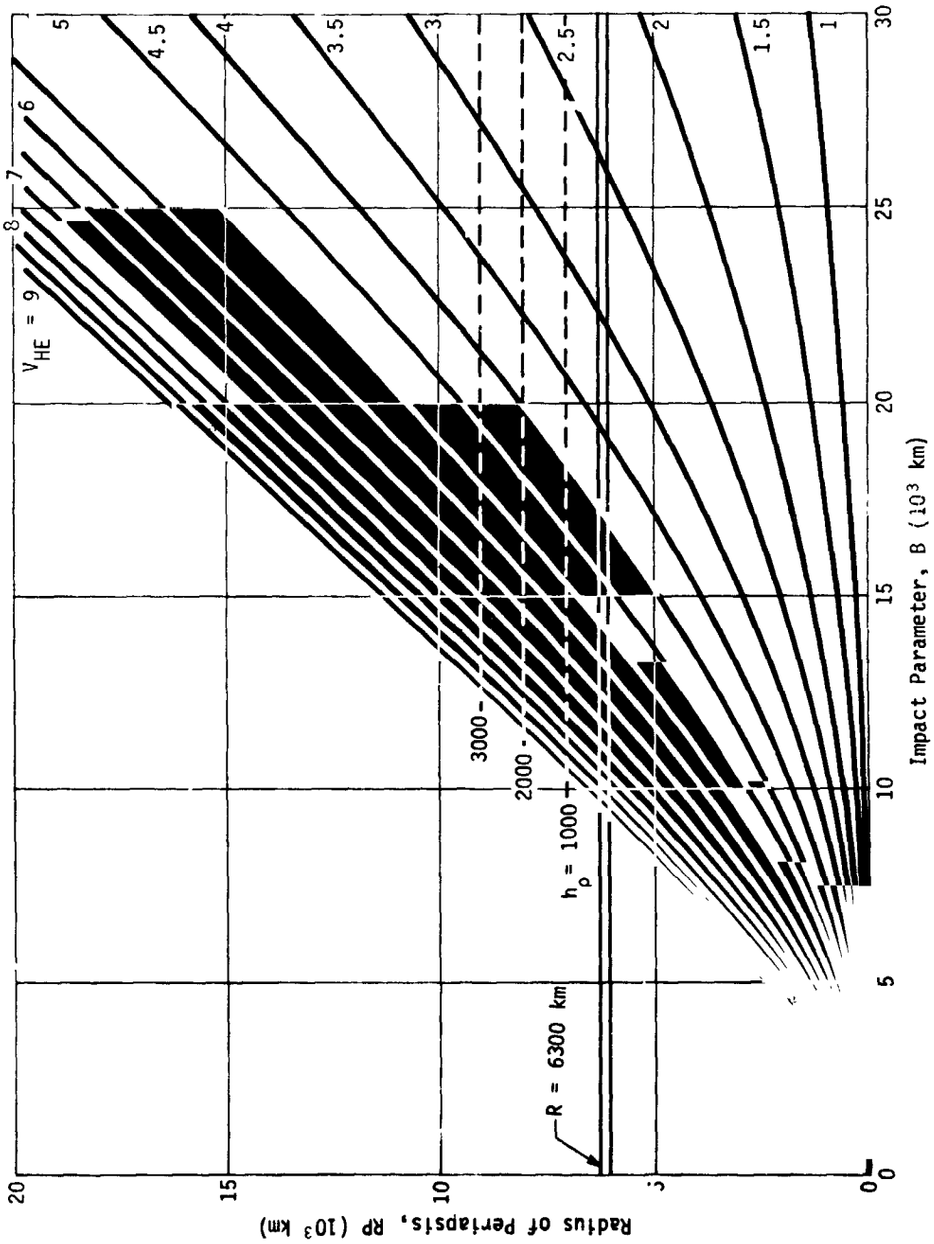


Fig. II-10 Periapsis Radius

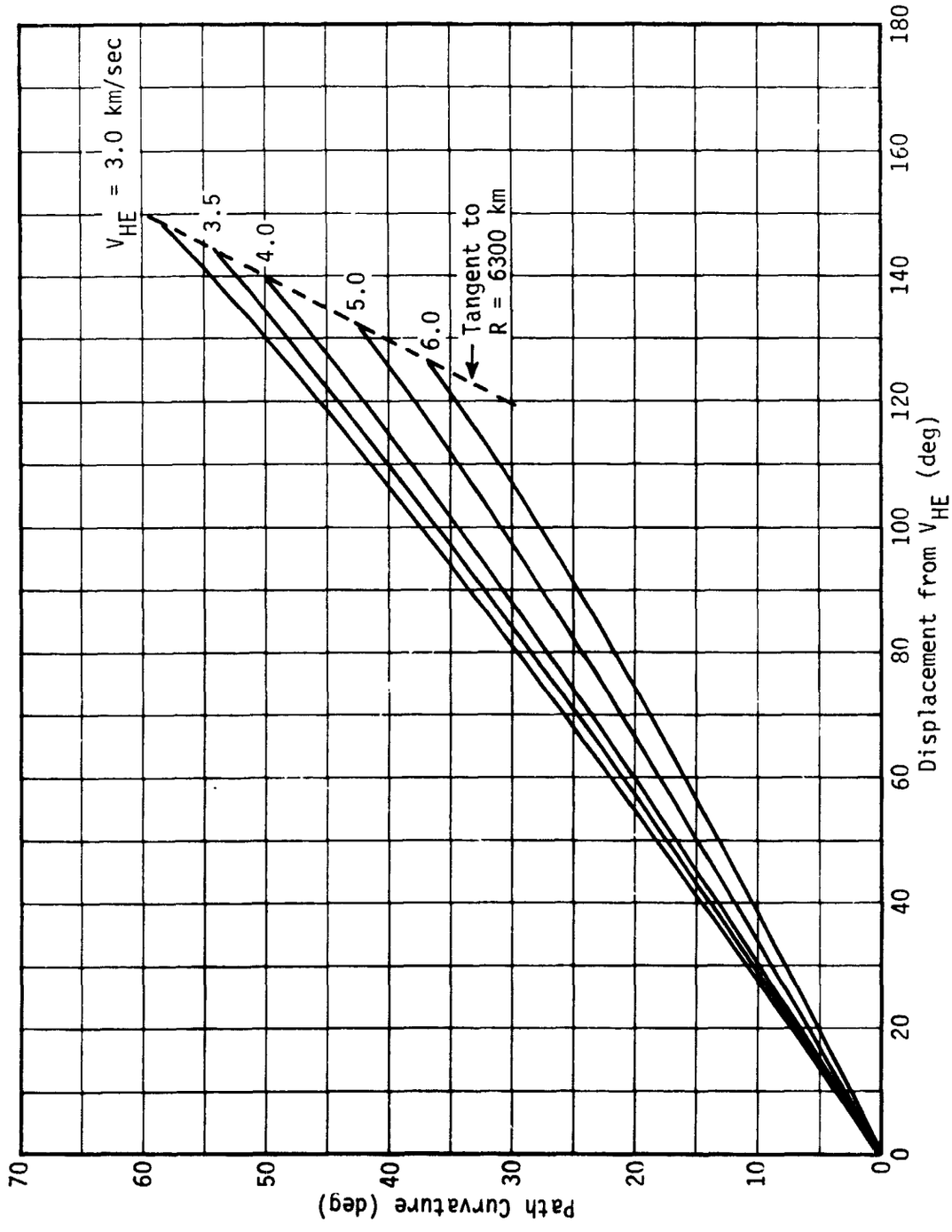


Fig. II-11 Path Curvature

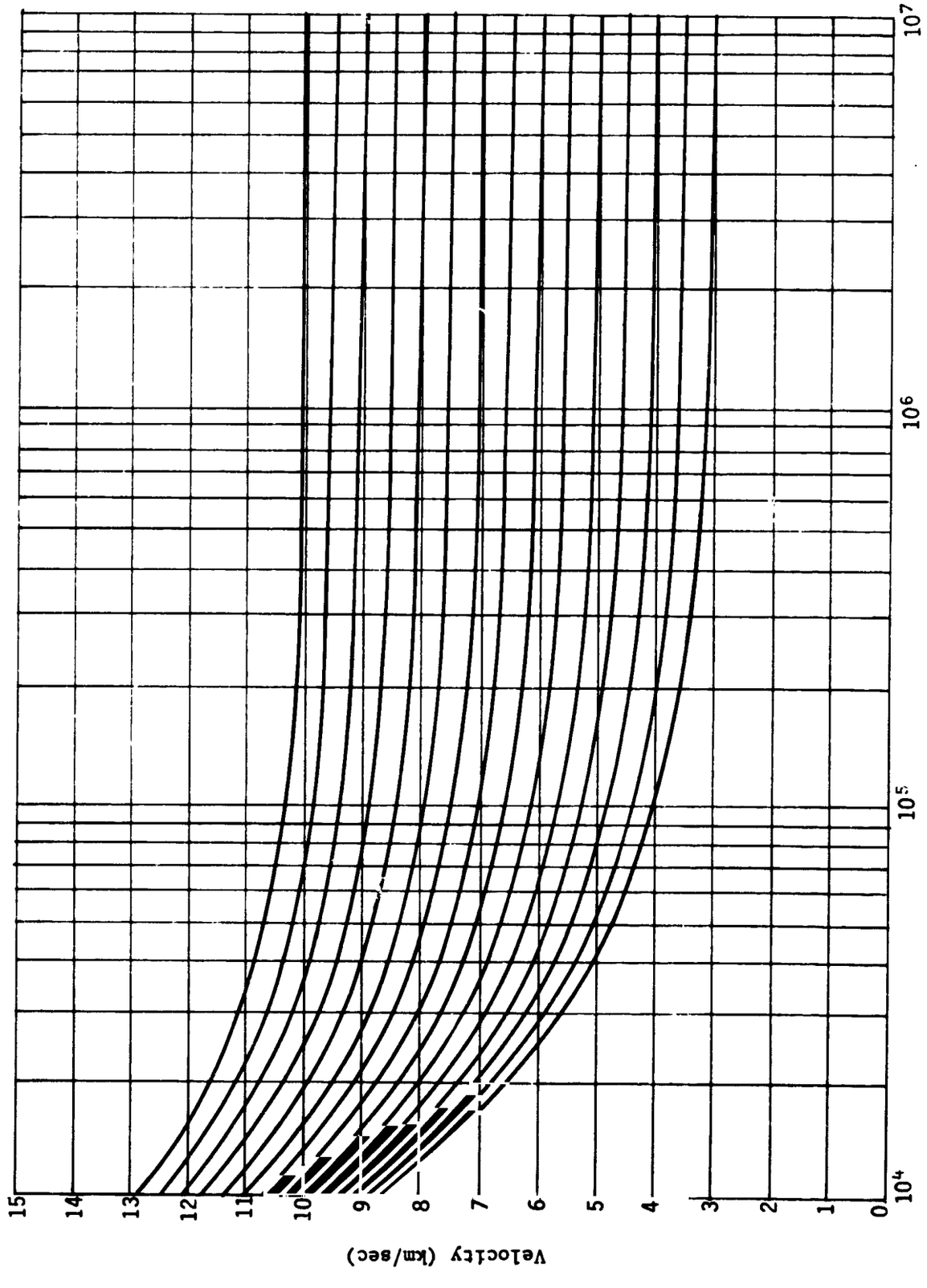


Fig. II-12 Local Velocity

The simplest and most direct deflection maneuver is to apply the deflection impulse normal to the approach velocity vector. This application neither speeds up nor slows down the probe approach velocity, but does maximize the displacement from the spacecraft path for a given impulse. The radius from the center of the planet to the application point influences the velocity increment requirements and the time of flight. To achieve a specific target point by deflecting from a given path with V_{HE} and periapsis radius identified, the expression

$$R_{EJ} \times \Delta V_{EJ} = \text{Constant}$$

defines the variation in velocity increment with application radius. The time of flight from deflection to entry is directly proportional to the radius to the deflection maneuver. The entry angle parameters (γ and α) of the selected target point are essentially unchanged.

Setting the radius to the deflection maneuver at 10^6 km, we now investigate the other parameters and their effects on entry conditions. Figures II-13 thru II-16 present the maximum downrange and crossrange capabilities ($\tau = 90°$) as a function of velocity increment and periapsis radius of the approach path. Crossrange is achieved by a roll angle to either side of the spacecraft approach plane. The figures show a flat representation of the planet surface with downrange and crossrange measured from the location of the incoming V_{HE}. Only half the map is presented for each condition since crossrange capabilities are symmetrical. The coordinates for the V_{HE} are defined in Chapter II.A for launch date, arrival date and trajectory type. The region of $\gamma_E \leq -20°$ is shown on each figure. This entry angle condition is assumed to be the minimum acceptable to avoid skipout and account for possible entry angle dispersions. The location of this boundary was discussed earlier in terms of displacement from the V_{HE}. The region enclosed by this boundary is assumed to be inaccessible for probe targeting.

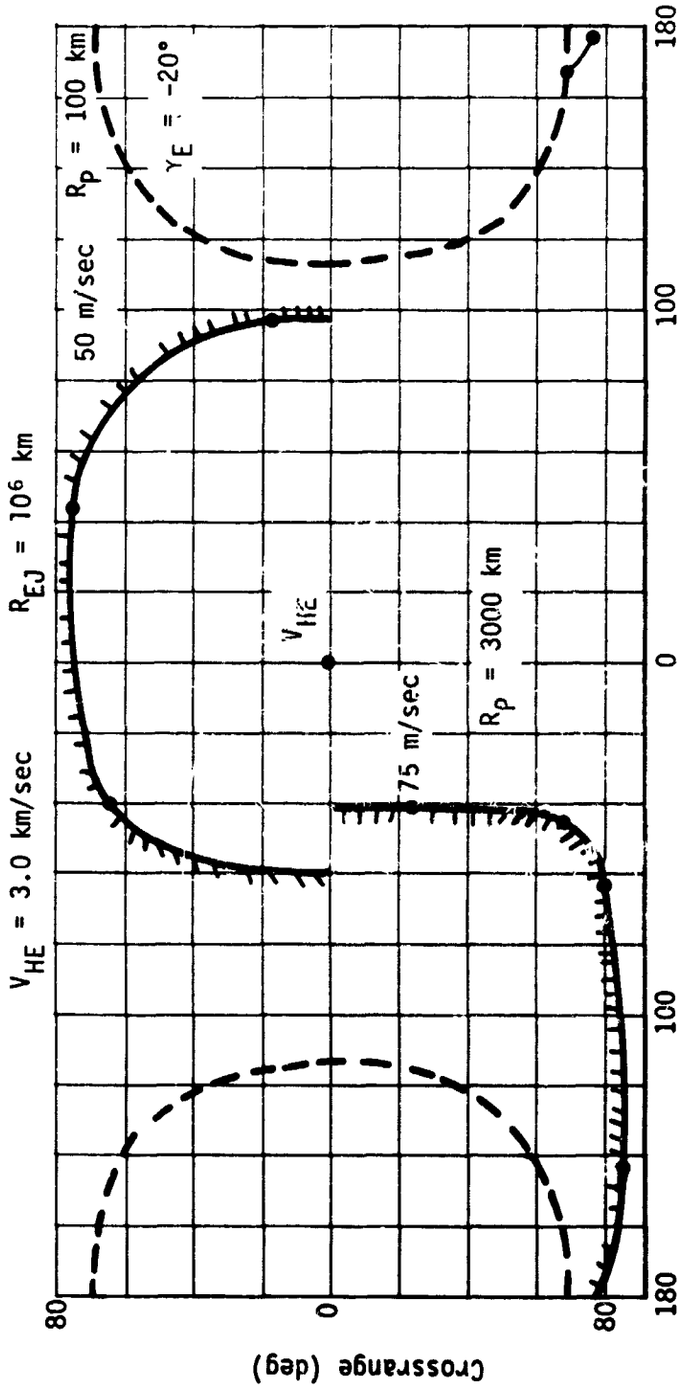


Fig. II-13 Accessible Regions, R_p = 100 and 3000 km

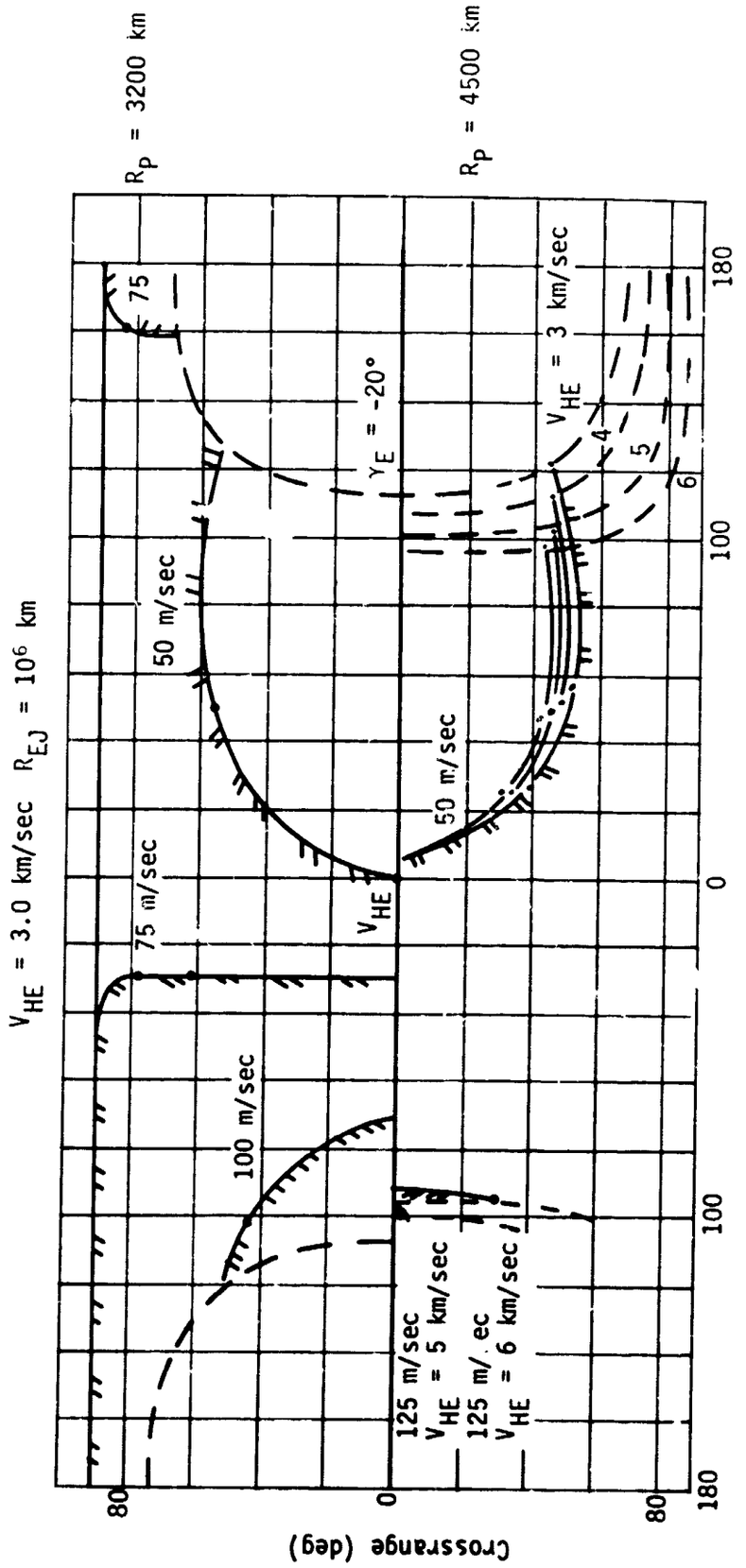


Fig. II-14 Accessible Regions, R_p = 3200 and 4500 km

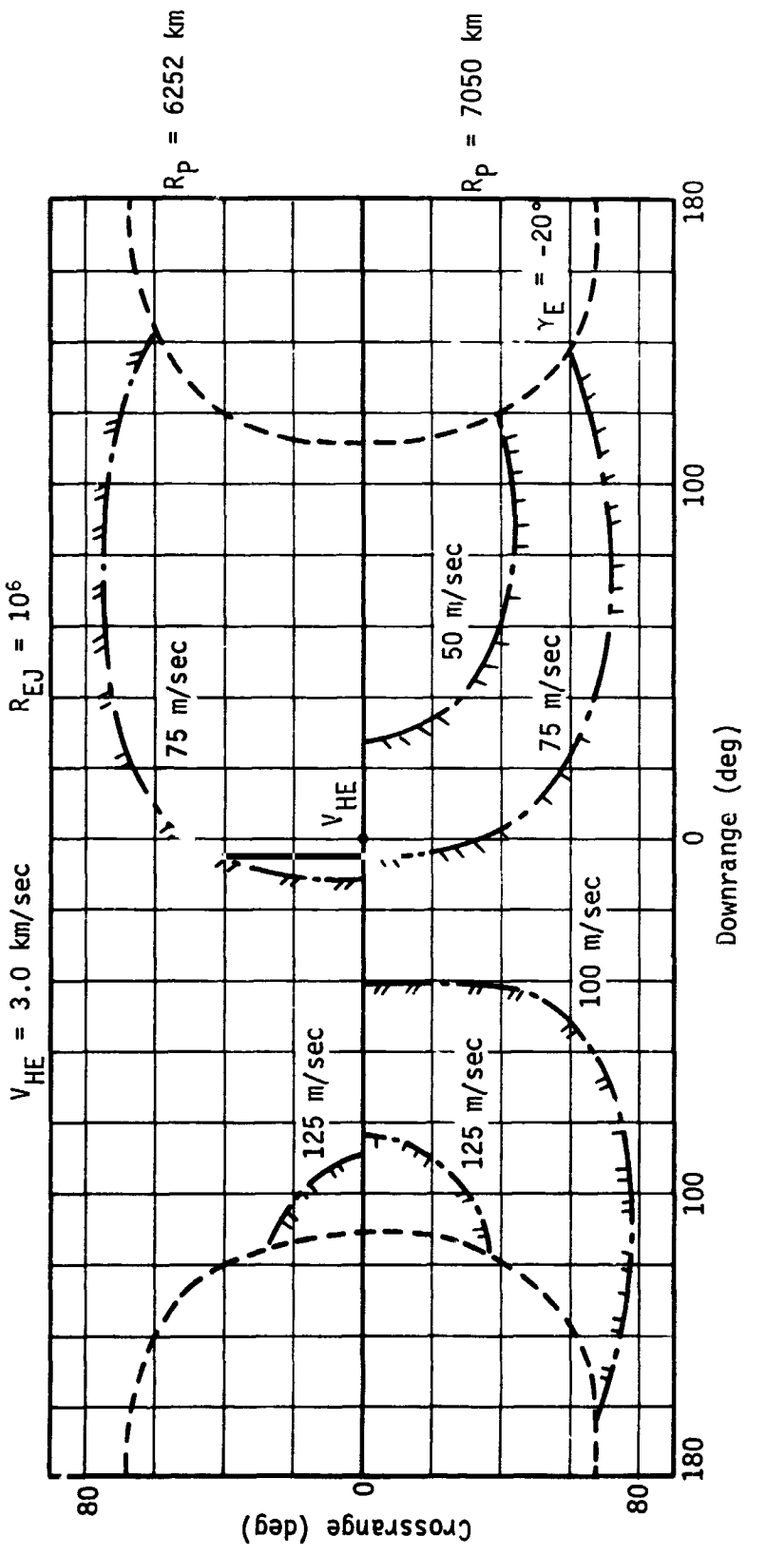


Fig. II-15 Accessible Regions, R_p = 6252 and 7050 km

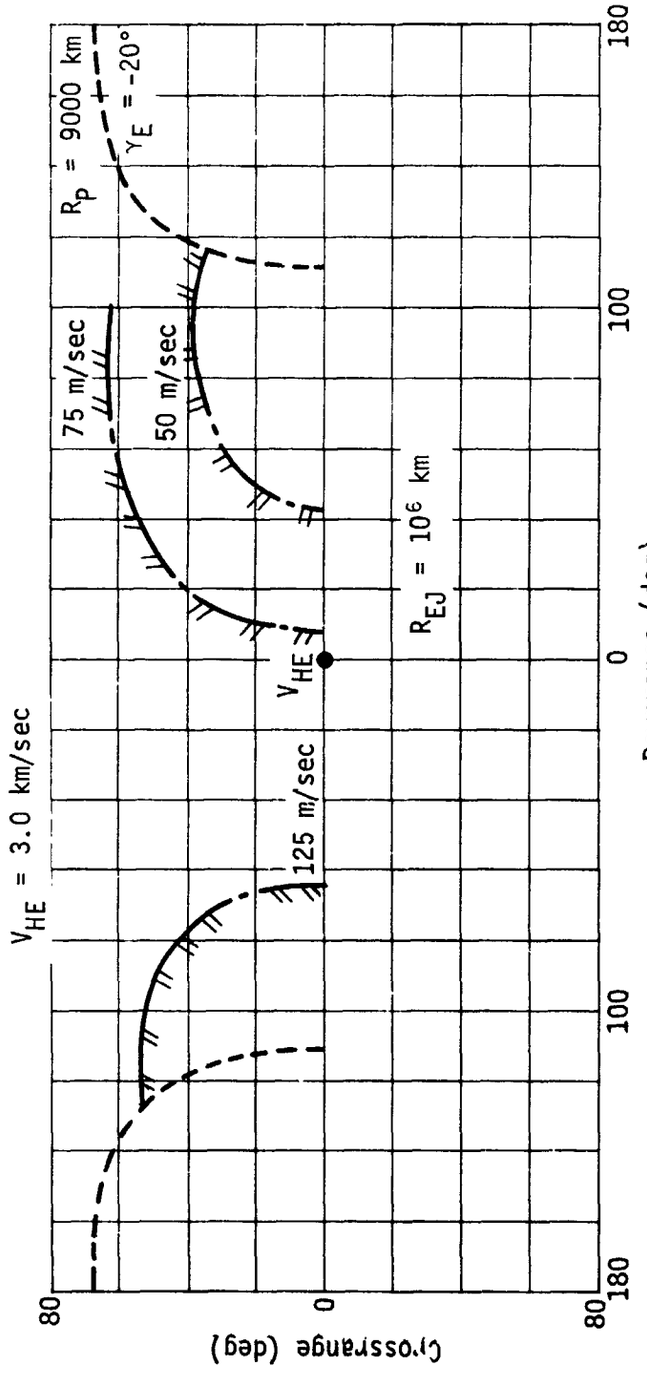


Fig. II-16 Accessible Regions, R_p = 9000 km

The value of V_{HE} is assumed to be 3 km/sec for each figure except Fig. II-14 where the effects of various V_{HE} values are presented. Increasing the V_{HE} moves the $\gamma_E \leq -20°$ boundary and all other entry angle contours toward the V_{HE}. This is a result of the decreased path bending experienced. As noted earlier increasing the velocity reduces the effectiveness of planet gravity until, as a limit, infinite velocity passes the planet in a straight line and entry angles of 0° occur 90° from the V_{HE}. The accessible regions for a given deflection velocity capability are not affected significantly by V_{HE}. Downrange capability does not appear to change and the crossrange capability is reduced slightly with increasing V_{HE}. Note that deflection velocity increments of about 125 m/sec are required to reach all targets where $\gamma_E > -20°$ and the radius of periapsis yields an impacting approach path.

Now consider the effect of varying the periapsis radius of the approach path. Figure II-17 presents the downrange and crossrange capabilities as a function of periapsis radius and deflection velocity increment. For the case of a direct $(\gamma_E = -90°, R_P = 0)$ impact the accessible regions for a given deflection velocity capability are distributed in a circle about the V_{HE}. As the periapsis radius increases the accessible regions become ellipses with the major axis located in the downrange direction. Both downrange and crossrange capability are reduced and the accessible area is located downrange from the V_{HE}. Increasing the available velocity increment increases the area that can be targeted.

The time of flight from deflection maneuver to entry is shown as a function of the deflection radius in Fig. II-18 for retro thrusting deflection. The 90° deflection angle case is shown as a single line for all deflection velocity increments since the probe approach velocity is neither slowed down nor speeded up by

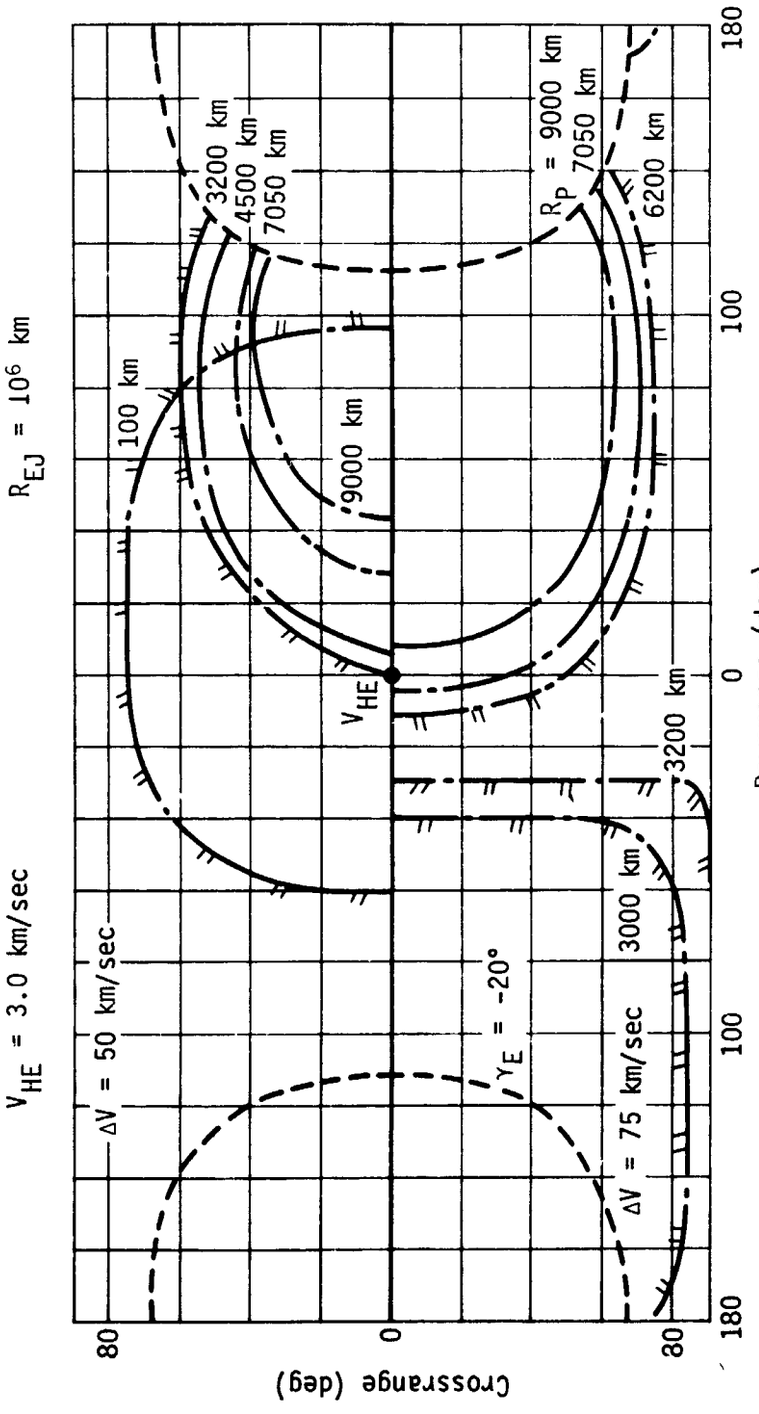


Fig. II-17 Effect of Periapsis Radius

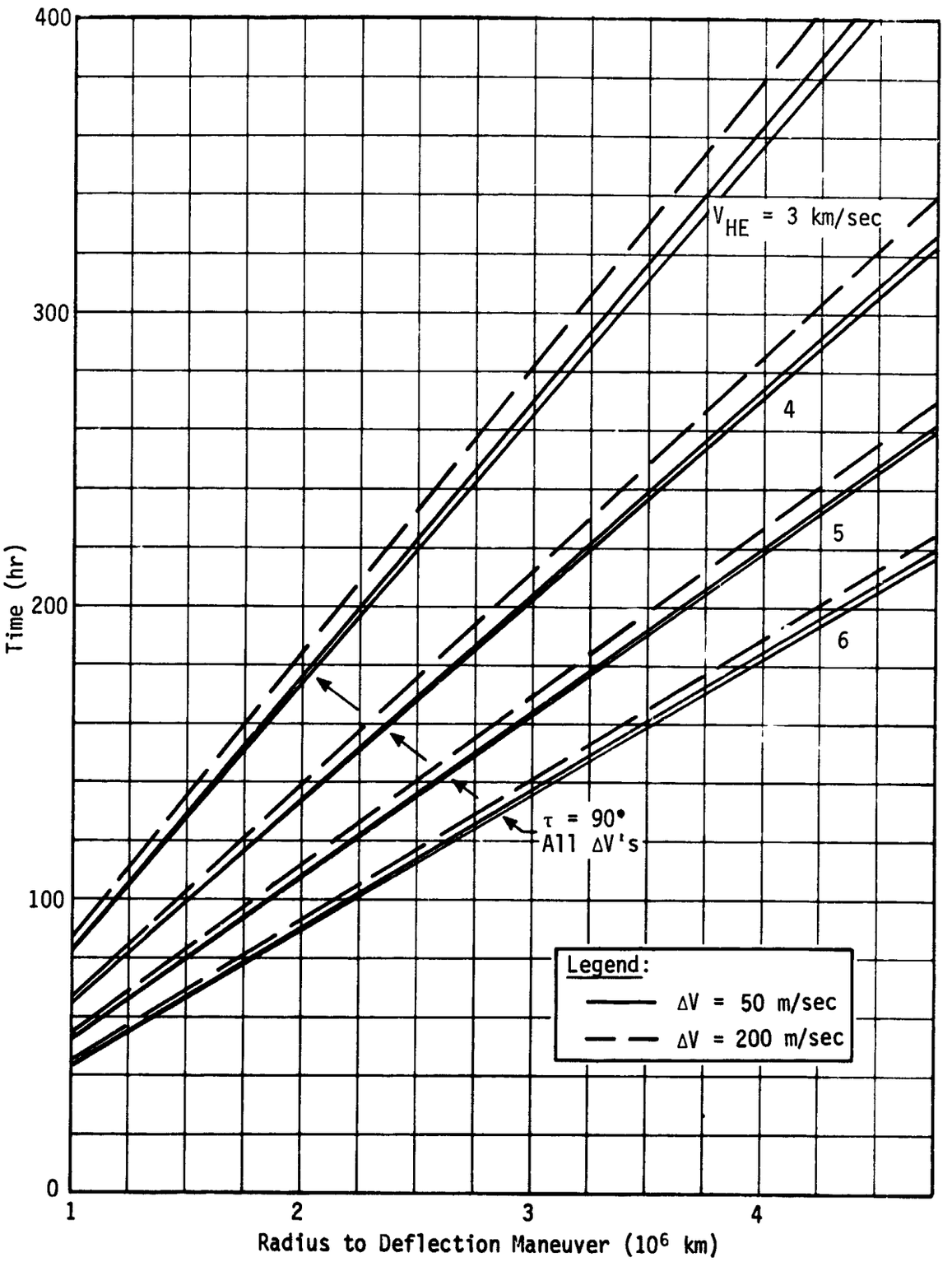


Fig. II-18 Time of Flight, Retro Deflection

this maneuver and, therefore, the time of flight is not changed. Time variations for other deflection angles near 20° are shown for velocity increments of 50 m/sec and 200 m/sec. The effect of various V_{HE} values is shown also. The time of flight is relatively insensitive to periapsis radius or target location displacement from the V_{HE}. Figure II-19 presents dimilar data for forward thrusting deflection maneuvers.

One additional consideration, angle of attack at entry, must be investigated to complete the picture of maximum deflection techniques. The deflection angle generally establishes the orientation of the probe in inertial space because the thrust axis is usually aligned with the probe spin axis. A more sophisticated probe with self-contained active altitude control systems could yield any desired orientation. However, with the spin system and a 90° deflection angle, the angle of attack at entry will be large. The bending of the approach path discussed earlier will be added to the deflection angle of 90°. Since path curvature to targets 70 to 100° from the V_{HE} is about 30°, the entry angle of attack at these targets would be between 60 and 120°. The range of values results from different deflection directions. Deflection toward the planet center reduces the angle of attack from the 90° deflection angle and deflection away from the planet center increases the angle of attack. Deflection to the side results in entry angles nearly equal to the deflection angle.

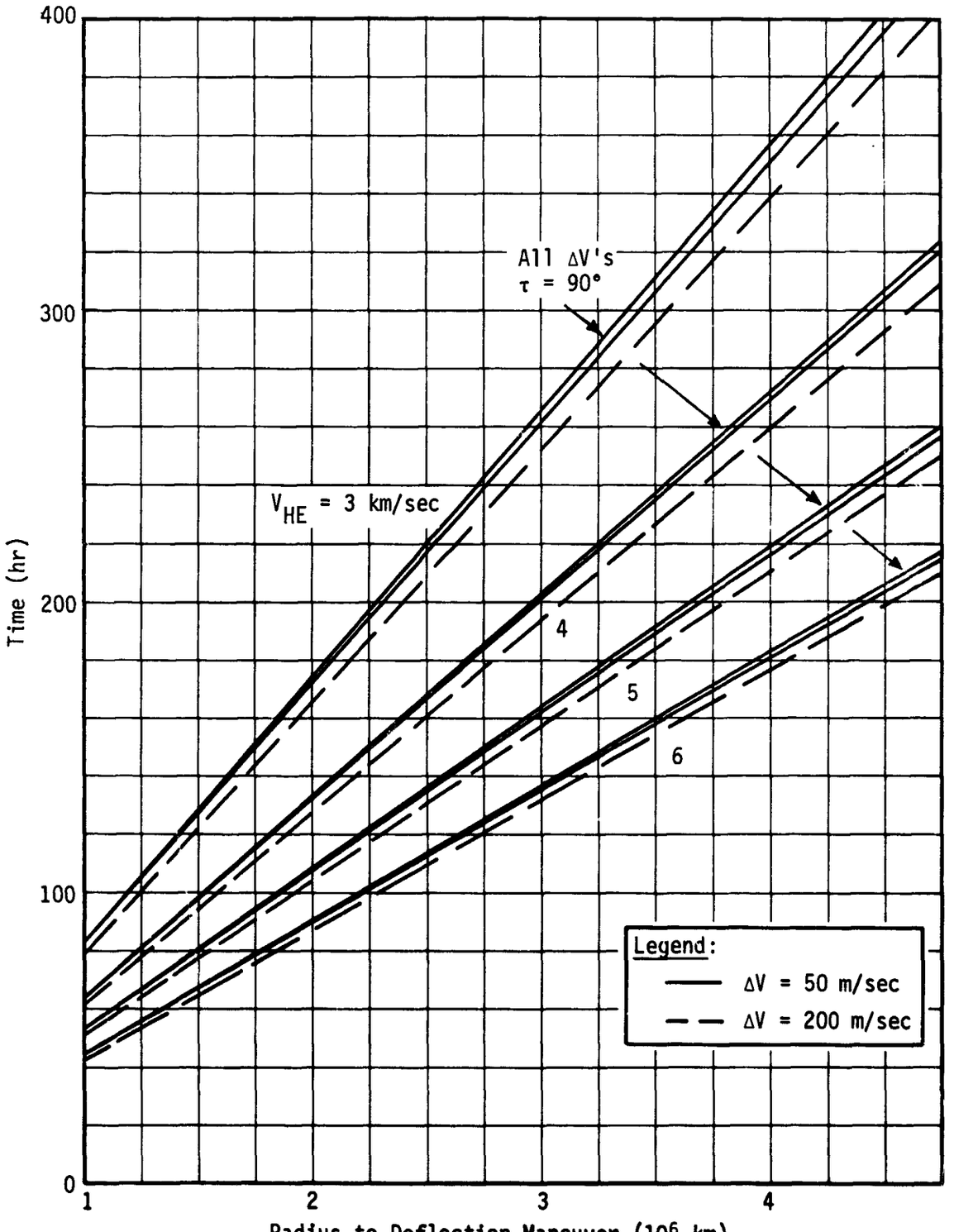
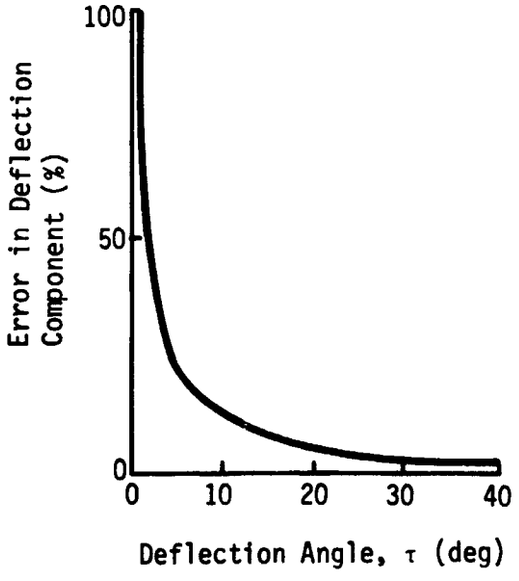


Fig. II-19 Time of Flight, Forward Deflection

Maximum deflection for a given velocity increment is seldom the only consideration in defining the deflection strategy. A requirement for staggered entry times may establish different velocity increments and application angles. Low entry angles of attack may be required. A single deflection system design may be desired for several probes resulting in a fixed velocity increment capability with targeting achieved by varying the deflection radius and deflection angle. This part of the report investigates the alternatives and decision factors in selecting a deflection strategy other than to achieve maximum displacement.

First consider limits on the deflection angle. The 90° deflection angle achieves maximum displacement for a given velocity increment. The effect of pointing errors are a minimum at 90° and become very large at 0°. A 1° pointing error will produce errors in the normal component of the deflection velocity as noted in the following sketch.



Thus an error of ½° in pointing is equivalent to a 2½% error in the deflection component of velocity at deflection angles of 20°. Pointing errors of ½° or more overshadow velocity errors at deflection angles of 40° or less. To maintain relatively low sensitivities the minimum deflection angle is set at >20° or <160°. At this point the sensitivities are no longer increasing linearly.

Figures II-18 and II-19 show how the flight time can be varied using two levels of velocity increment at deflection angles near 20°. The variation for other deflection angles is represented by time difference between a 90° deflection angle and a specific velocity increment line. Time and angle of attack are the only differences between retro and forward deflection if deflection angle and velocity increment are the same. Range, entry path angle, and other parameters are unchanged.

The entry angle of attack contours can be plotted in the downrange and crossrange coordinate system. These data are presented in Fig. II-20 thru II-26 for different periapsis radius and deflection velocity increments. The deflection angle is that which is required to achieve a given angle of attack at a specific target location. This angle is not shown but will be discussed later. As the velocity increment increases, the constant angle of attack contour grows in area and moves toward the V_{HE}. The center of these areas would have a zero angle of attack. In this case the approach path curvature would be exactly equal to the deflection angle. This condition only occurs for a forward deflection toward the planet center. The constant angle of attack contours are concentric like the constant entry angle and maximum deflection contours and for $R_p > 0$ are biased downrange from the V_{HE}. As the periapsis radius is reduced the contours become more circular and will be concentric about the V_{HE} for $R_p = 0$. The side nearest the V_{HE} is affected most by deflection velocity increment changes

because the deflection angle is larger on the near side resulting in more of the velocity being used for displacement. Variations in the velocity increment cause greater range variations at the large deflection angles than at the small ones.

Figure II-26 also shows the relative deflection angles for achieving displacements with a given velocity increment. The deflection angle contours are concentric also. The center of the deflection angle pattern is located downrange from the center of the angle of attack pattern so that larger deflection angles are required for the same angle of attack on the side near V_{HE} than on the far side.

The effect of the radius to the deflection maneuver on angle of attack is related to the effect on deflection angle. The deflection angle and angle of attack decrease directly with increasing radius and constant ΔV. Increasing the V_{HE} reduces the path curvature and moves the angle of attack = 0° conditions away from the V_{HE}. Other angle of attack contours are moved away from the V_{HE} in a similar fashion. Size of contours does not change.

To achieve a specific target location the target coordinates are located in the map (Fig. II-27) and the parameters of γ, α, ΔV are plotted for fixed R_{EJ}, V_{HE} and R_P. The angle of attack varies only slightly along the entry angle contour and increasing the deflection velocity increment with fixed deflection angle increases the crossrange for a given angle of attack. The deflection angle is set at 20° to maintain angles of attack of less than 50° and to avoid large dispersions associated with smaller deflection angles. The target locations are shown and the resulting deflection velocity increment requirements are noted. The deflection velocities for the flyby mission shown are approximately 40 m/sec greater than the impacting case.

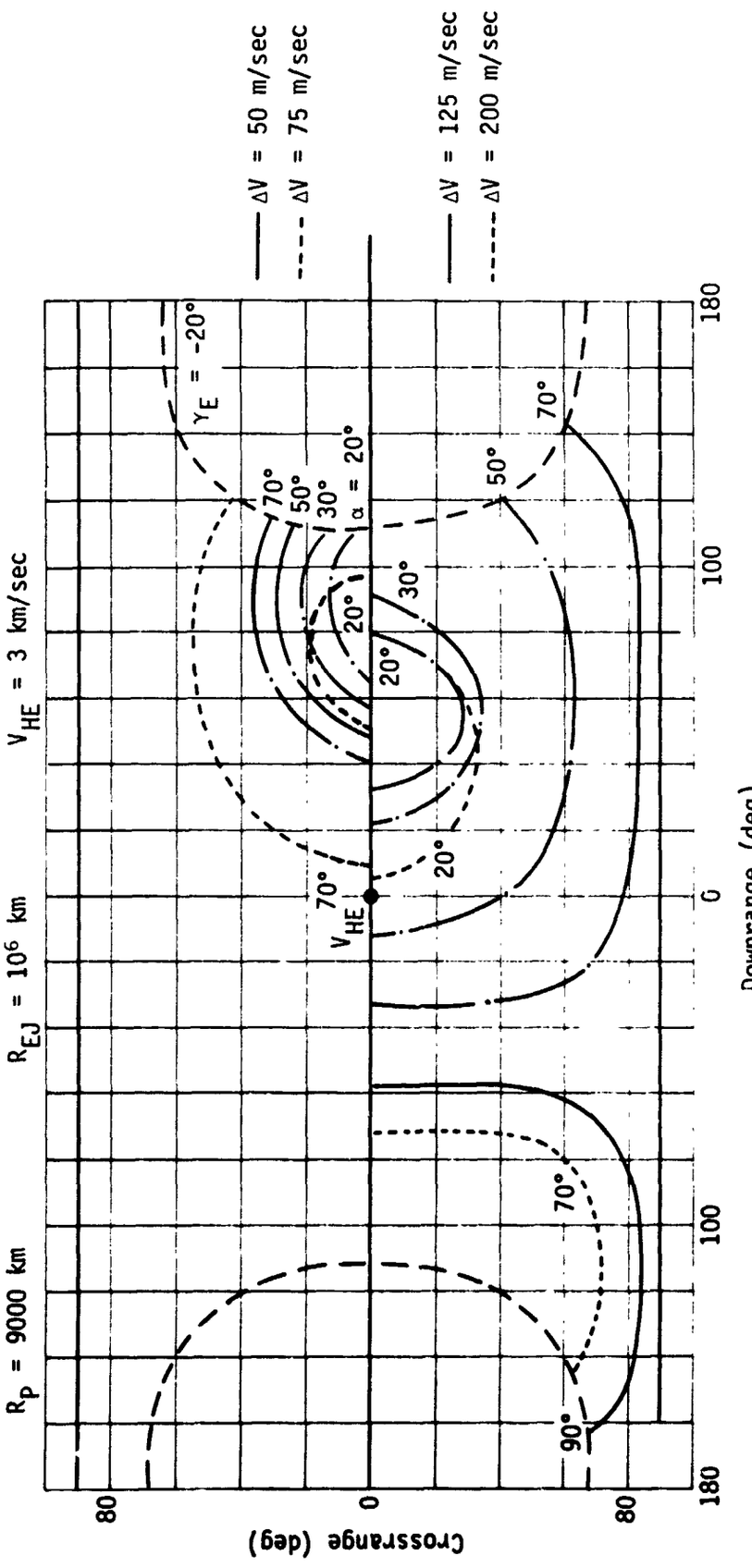


Fig. II-20 Angle of Attack Contours

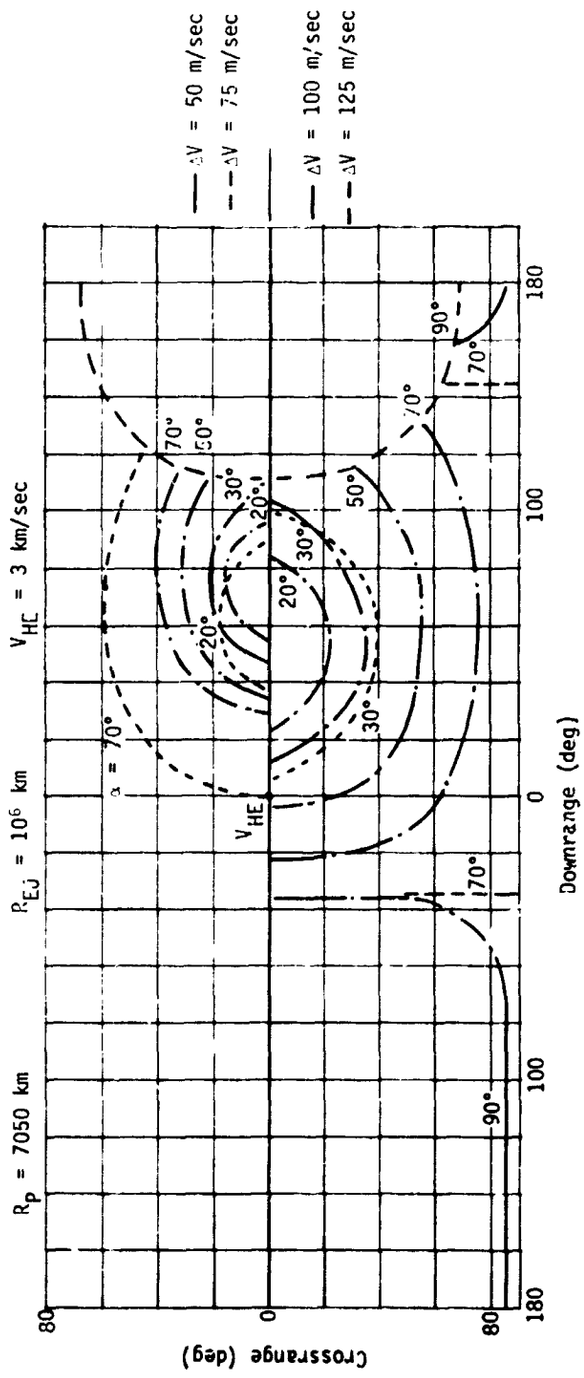


Fig. II-21 Angle of Attack Contours

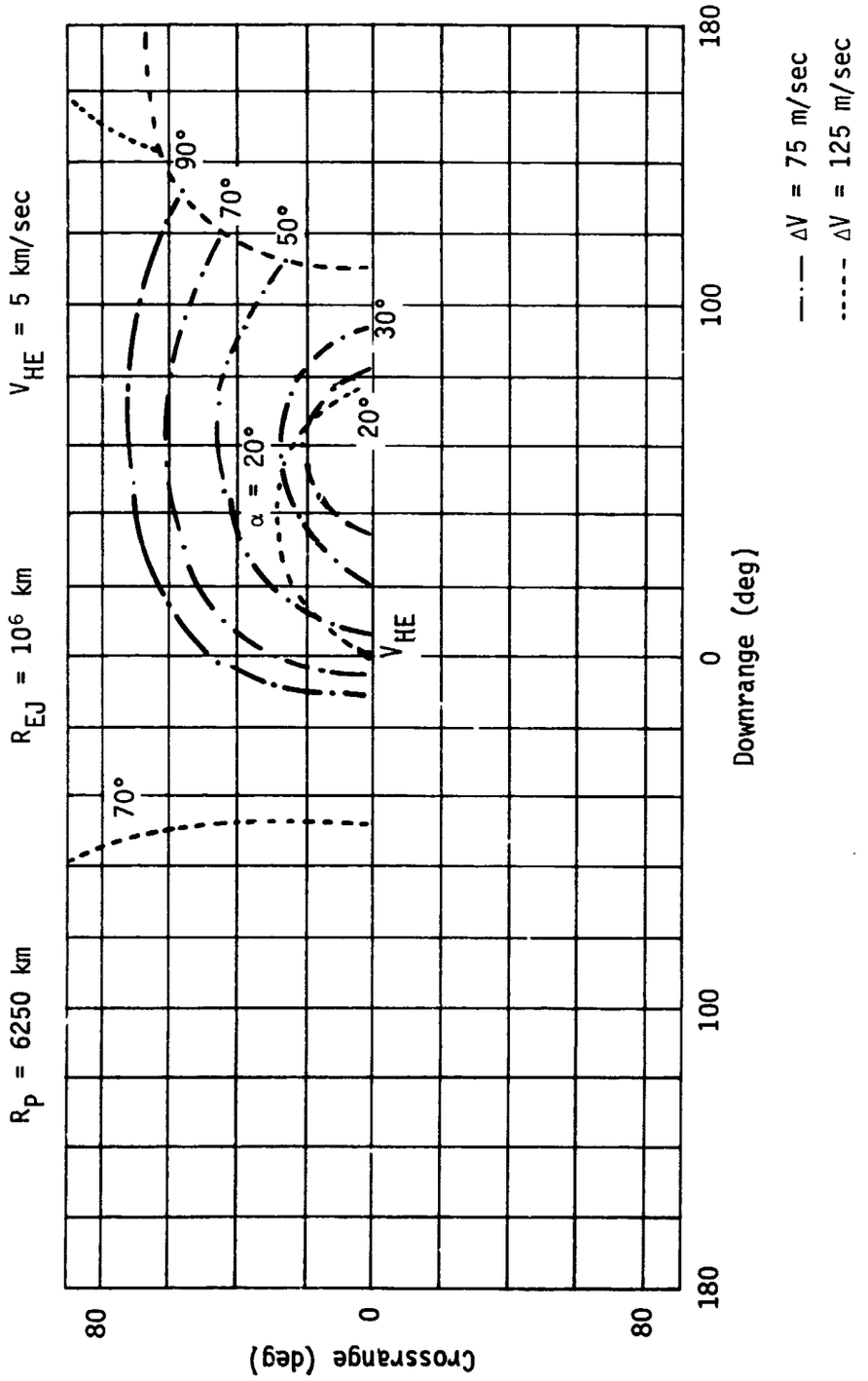


Fig. II-22 Angle of Attack Contours

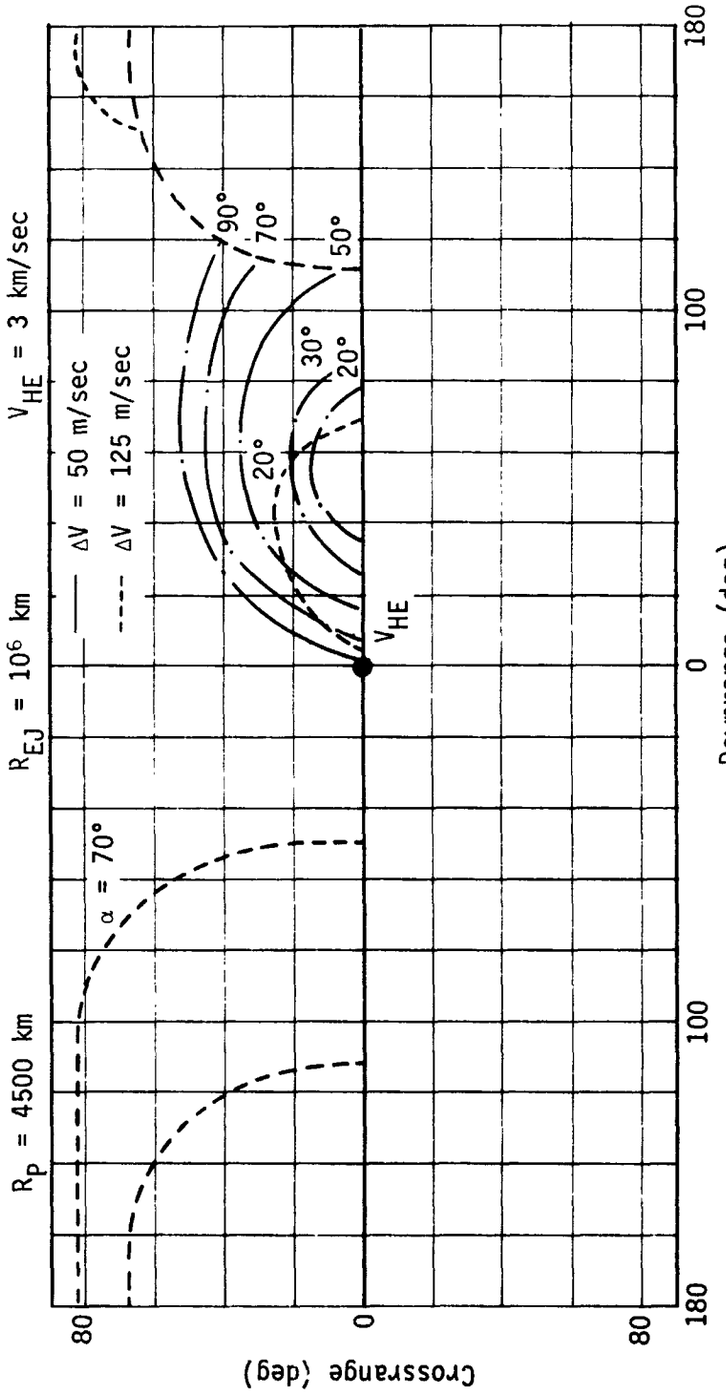


Fig. II-23 Angle of Attack Contours

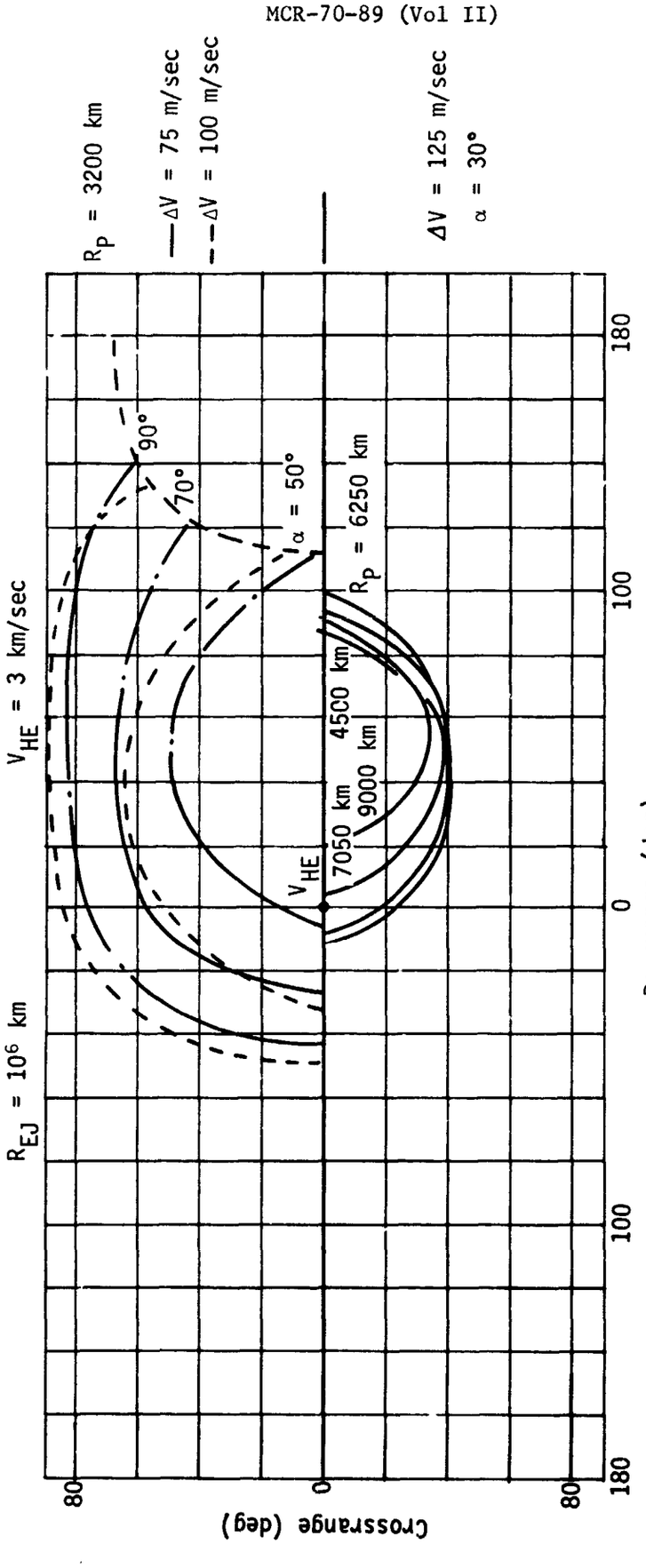


Fig. II-24 Angle of Attack Contours

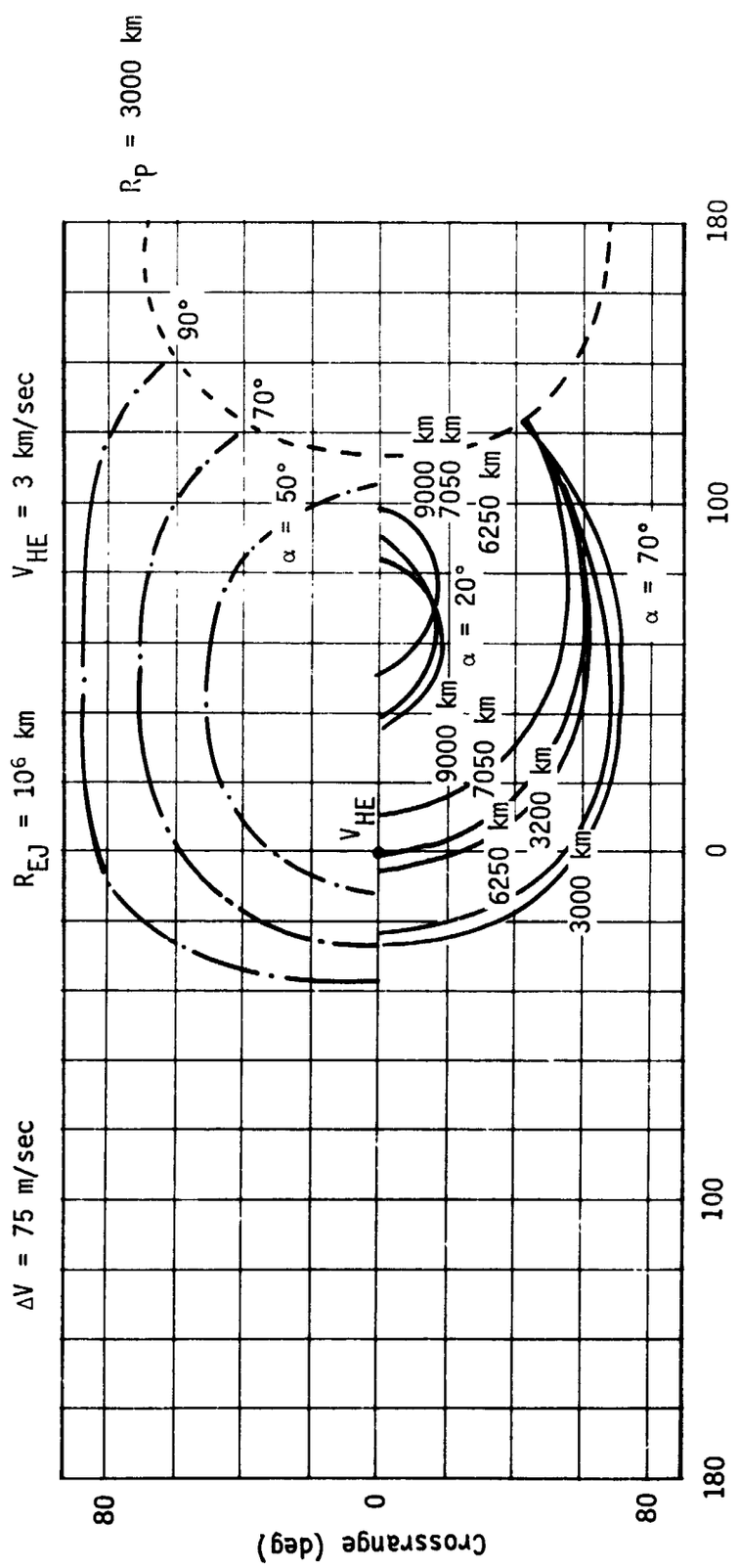


Fig. II-25 Angle of Attack Contours

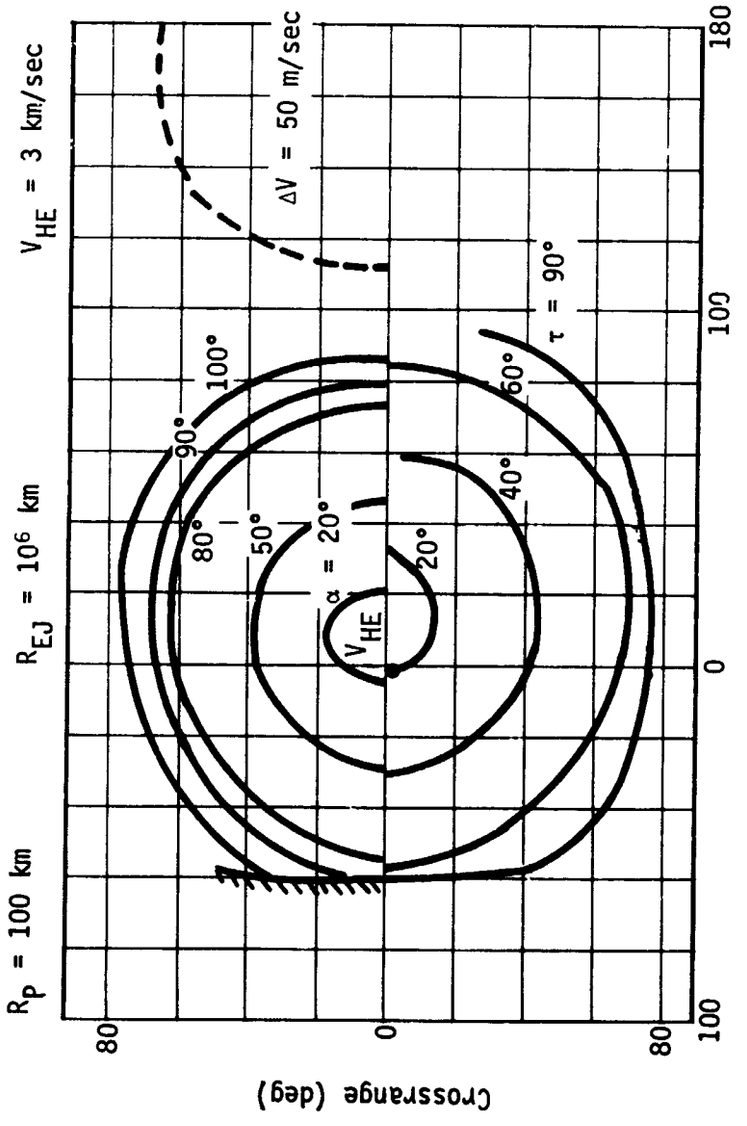


Fig. II-26 Angle of Attack and Deflection Angle

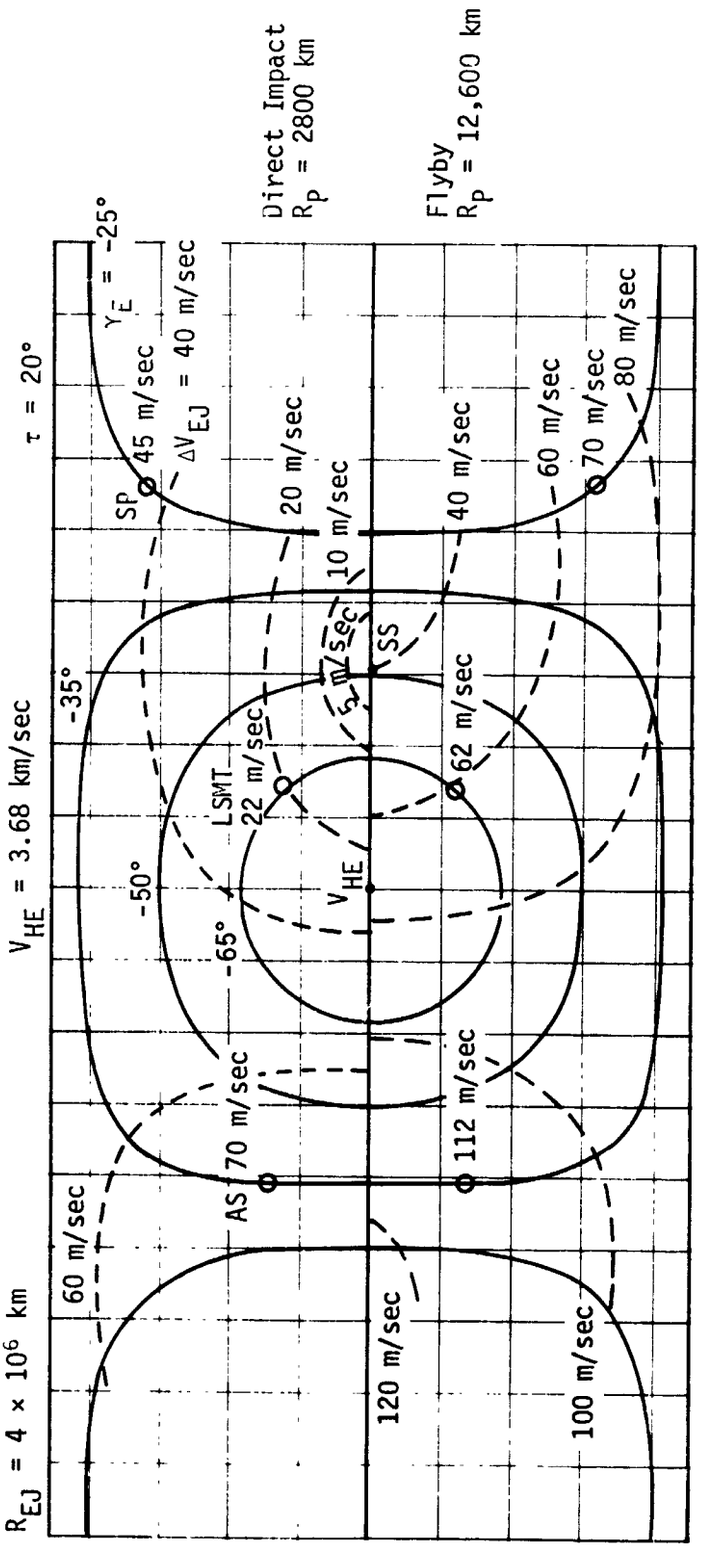


Fig. II-27 Defection Parameter Selection

Now consider the entry times that result from these deflection quantities. Figure II-28 presents the operating sequence of the probes for both flyby and impacting missions. The balloon operating times were moved to the end of the mission by retro thrusting for their velocity increment. Other adjustments to the operating times were accomplished by varying the velocity increment from Fig. II-27 by a few meters per second and the deflection angle about 1°. The data shown are representative of the mission operating sequence where only two probes can be interrogated at a time and can be adjusted for other requirements.

Staggering the time of deflection and therefore the radius to the deflection maneuver has no significant effect on the entry parameters or on the operating sequence where the total time spread is 4 hr or less.

From the data presented the following conclusions and observations can be stated:

1) The minimum deflection radius is 10^6 km in order to maintain low deflection velocity increments and error sensitivities;
2) The minimum entry flight path angle is assumed to be -20° to avoid skipout. This assumption considers possible entry angle dispersions to ensure being larger than the actual boundary of about -8°;
3) Maximum deflection maneuvers use deflection angles of 90° and generally result in large angles of attack unless corrected by an active attitude control system;
4) A period of several hours can be reasonably achieved between initial probe entry and final probe entry;
5) A minimum deflection angle of 20° is established to maintain reasonable sensitivity to pointing errors;

6) When velocity increment and deflection angle are constant, the differences in retro deflection and forward deflection are primarily in time to entry. Depending on the installation of the impulse system the angles of attack will be different by 180°;
7) Time from deflection to entry is relatively insensitive to periapsis radius.

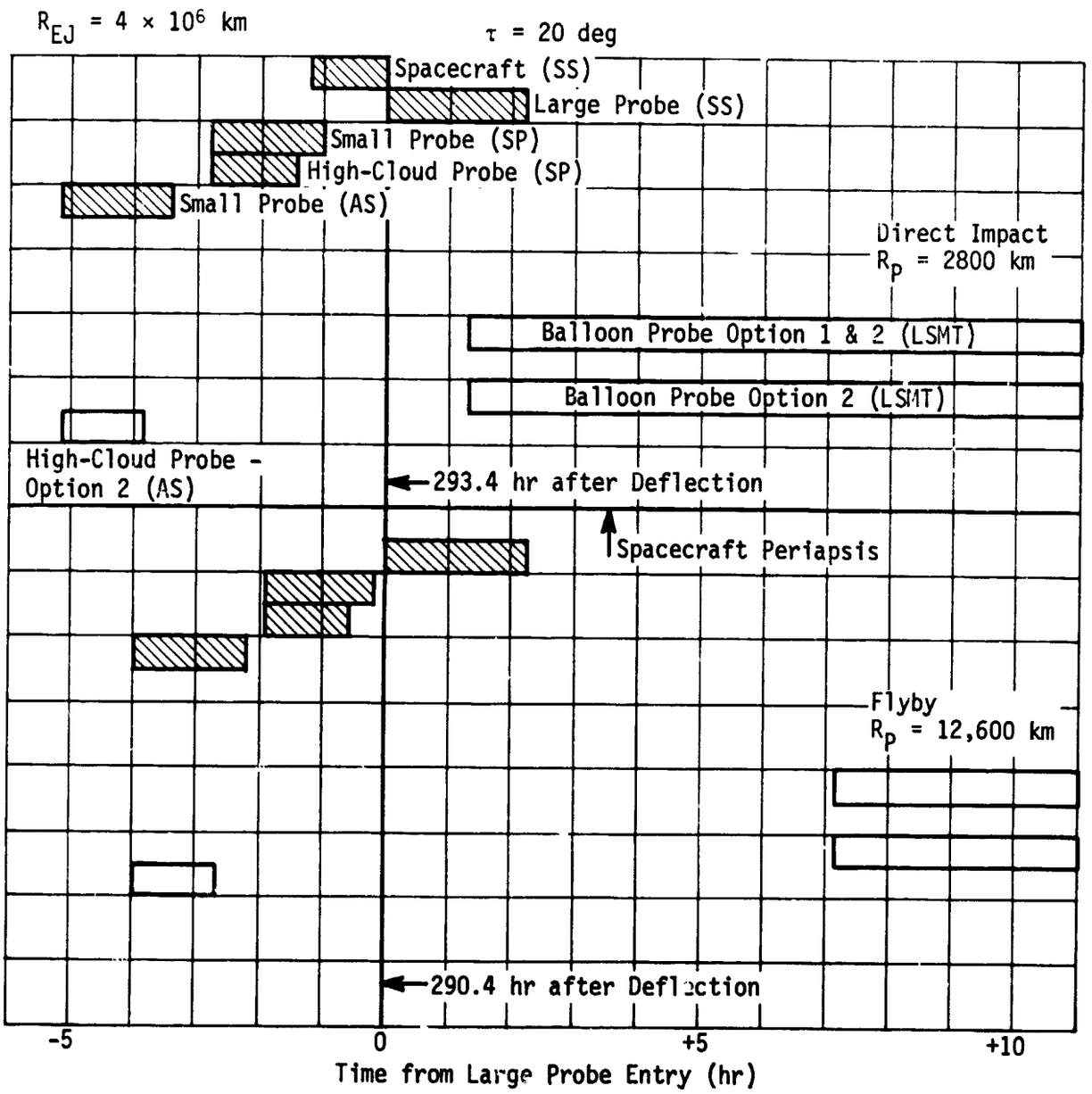


Fig. II-28 Mission Operating Sequence

C. PROBE-PLANETARY ENTRY TRAJECTORIES

The planetary entry trajectories are designed to yield entry environments within the aerothermal design contraints and to decelerate the probe to velocities compatible with science data acquisition at the required altitudes. Parametric entry data are presented in Appendix H (Vol III). The results and conclusions derived from the parametric study are presented here.

A lower limit on the entry flight path angle is imposed by the large entry dispersions associated with the skip-out boundary. The skip-out boundary is defined as the velocity-flight path angle combinations at entry altitude which produce a 0° flight path angle at circular orbit speed during the in-atmosphere portion of the entry trajectory. These velocity flight path angle combinations will not result in actual skip-out into orbit, but the boundary thus computed provides a limit at which large range dispersions and flight path sensitivity begins. For this study the MMC-Lower Density Model provides the largest angle. This angle is -7.8° at 35,500 fps (10.8 km/sec) and -7.9° at 36,000 fps (10.96 km/sec).

No rigid upper limit on entry velocity and flight path angle have been established for this study. JPL, in Ref II-2, defines NASA ground test capability limits for heat shield testing (see Fig. E-17, Appendix E), but states that exceeding these capabilities shall not be the basis of excluding any entry conditions. However, since entry velocities greater than 36,000 fps (10.96 km/sec) do not appear to be required, this value is adapted as a limit for the parametric studies. The entry altitude for Ref II-2 is 815,000 ft (248.4 km) and is therefore compatible with the data presented in the entry parametric plots. The entry flight path angles extend to -90°. Ballistic coefficients up to

0.8 slugs/ft^2 are considered since higher values are not consistent with probe configuration requirements.

From the parametric observations of Appendix H it can be shown that entry behavior trends can be predicted readily. Some of these trends are noted below. The time to any event above M = 0.5 is proportional to the inverse of the sine of the entry angle. The altitude of occurrence is affected slightly with the effect more noticeable at higher altitudes. Steeper entry angles produce lower altitudes for a specific event through a tendency to penetrate the atmosphere deeper. The altitude change is nearly linear with flight path angle. The altitude and time of occurrence of events above M = 0.5 are reduced slightly and in a linear manner with increasing entry velocity. The entry velocity effects on time and altitude of occurrence are generally negligible. The quantities such as maximum velocity, dynamic pressure, and deceleration are increased proportional to the entry velocity. Ballistic coefficients significantly affect only the value of dynamic pressure. Time increases and altitude of occurrence decreases slightly with B_E. The time increases because of the increased depth of penetration. This occurs as the result of a more dense entry body.

Now consider the objective of decelerating to reasonable velocities above the cloud tops to achieve effective experiment operation. Figures II-29 and II-30 present the altitude for achieving M = 1.0 and M = 0.7 as a function of entry ballistic coefficient and flight path angle. The entry velocity is 36,000 fps (10.96 km/sec); however, as noted above, the data are applicable to all velocities in the vicinity of 36,000 fps. Figure II-31 presents these data in the form of velocity profiles that indicate how small altitude variations effect the velocity significantly above M = 1.0. Also, it can be noted that the altitude of

occurence becomes less sensitive to entry angle as the Mach number approaches 0.5 (low altitudes). Dynamic pressure lines have been noted for reference. These lines are parallel to the terminal conditions of velocity and altitude where weight is equal to drag, and represent the change in velocity as a function of density required to maintain a constant dynamic pressure and therefore constant drag where the drag coefficient and area are fixed. The deceleration data can be presented in a carpet plot as noted in Fig. II-32.

The different atmosphere models are compared in Appendix H and should present no significant variations other than the altitude of occurrence of events, and therefore some time variations. Previous studies of potential Venus atmosphere models show no variations other than the altitude spread as noted in the density comparisons and the attendant time change required to reach a new altitude. Table II-1 presents the data for the MMC-Lower Density Model and the V5M. The altitude of events is different in the two models by 11,000 to 13,000 ft (3.4 to 4.2 km). The time differences are negligible and the different values of maximum deceleration and dynamic pressure can be attributed mainly to a lack of a precise match of maximum value and printout interval in the digital simulation of the trajectory.

The entry portion of the flight for Venus is well ordered and occurrences and events are easily and accurately predicted. This portion of the trajectory yields initial conditions for the descent portion of the path and establishes criteria for the initial decelerator design. The sensitivities of the entry and descent profiles to errors in initial conditions at entry are discussed in Section E of this chapter.

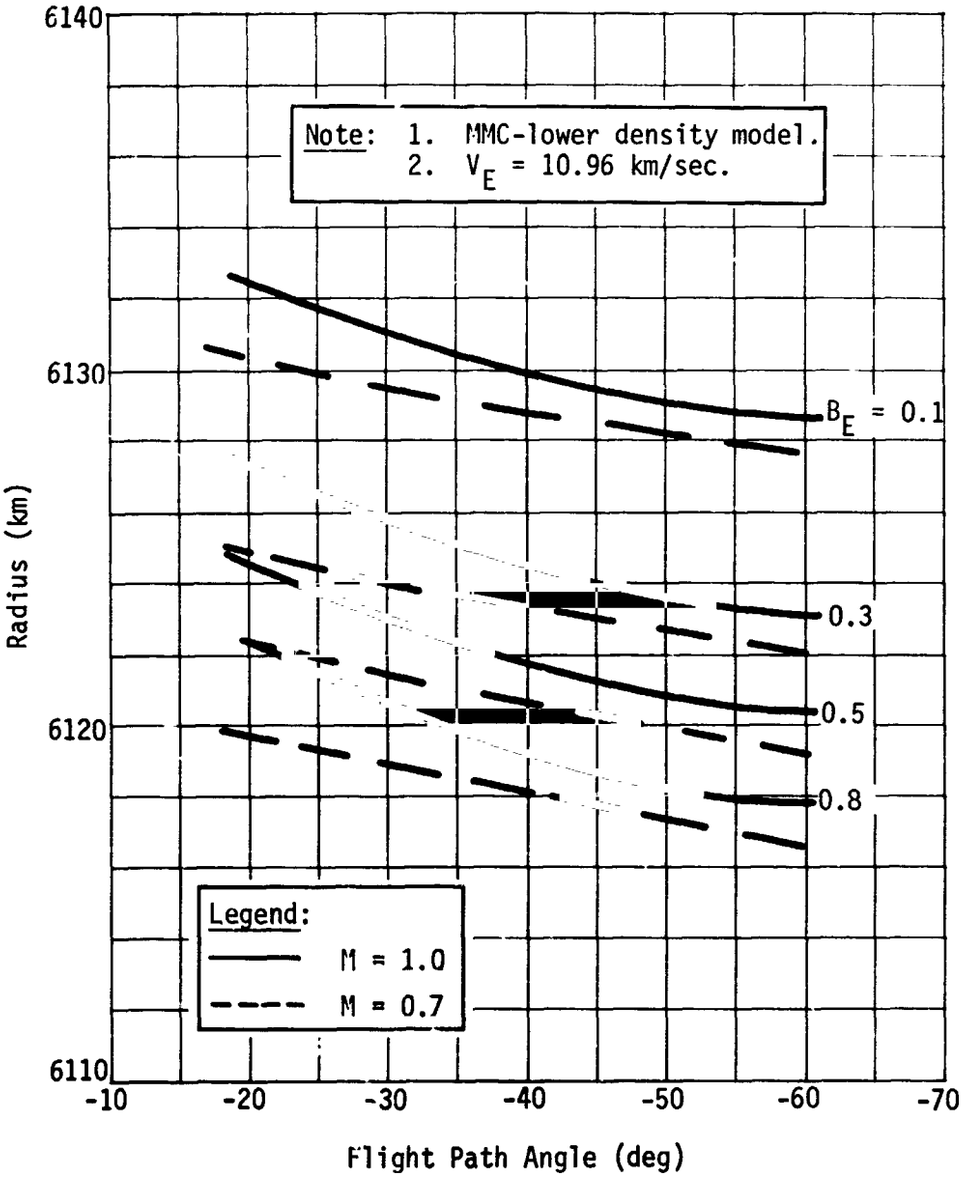


Fig. II-29 Altitude as a Function of Flight Path Angle

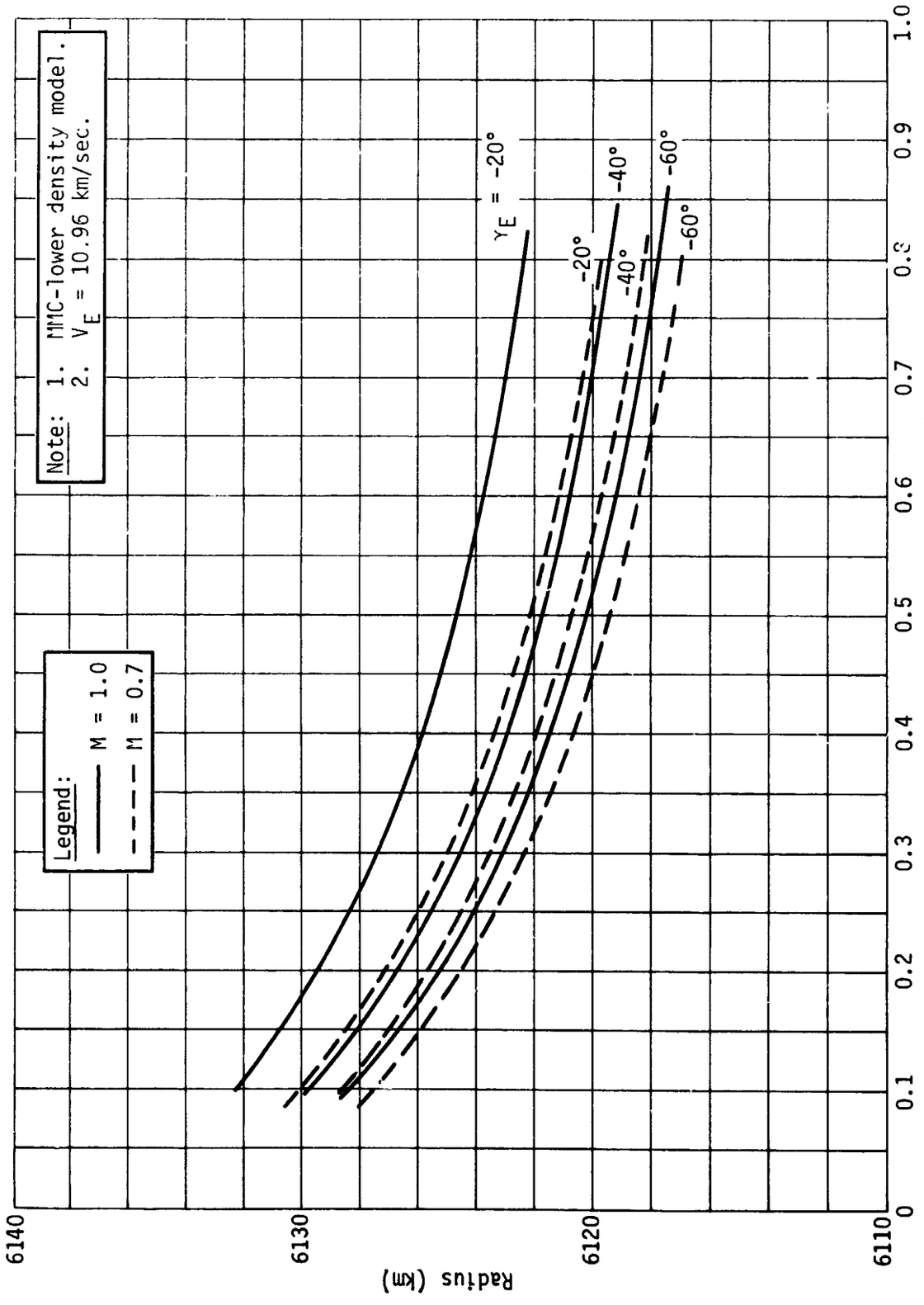


Fig. II-30 Altitude as a Function of Ballistic Coefficient

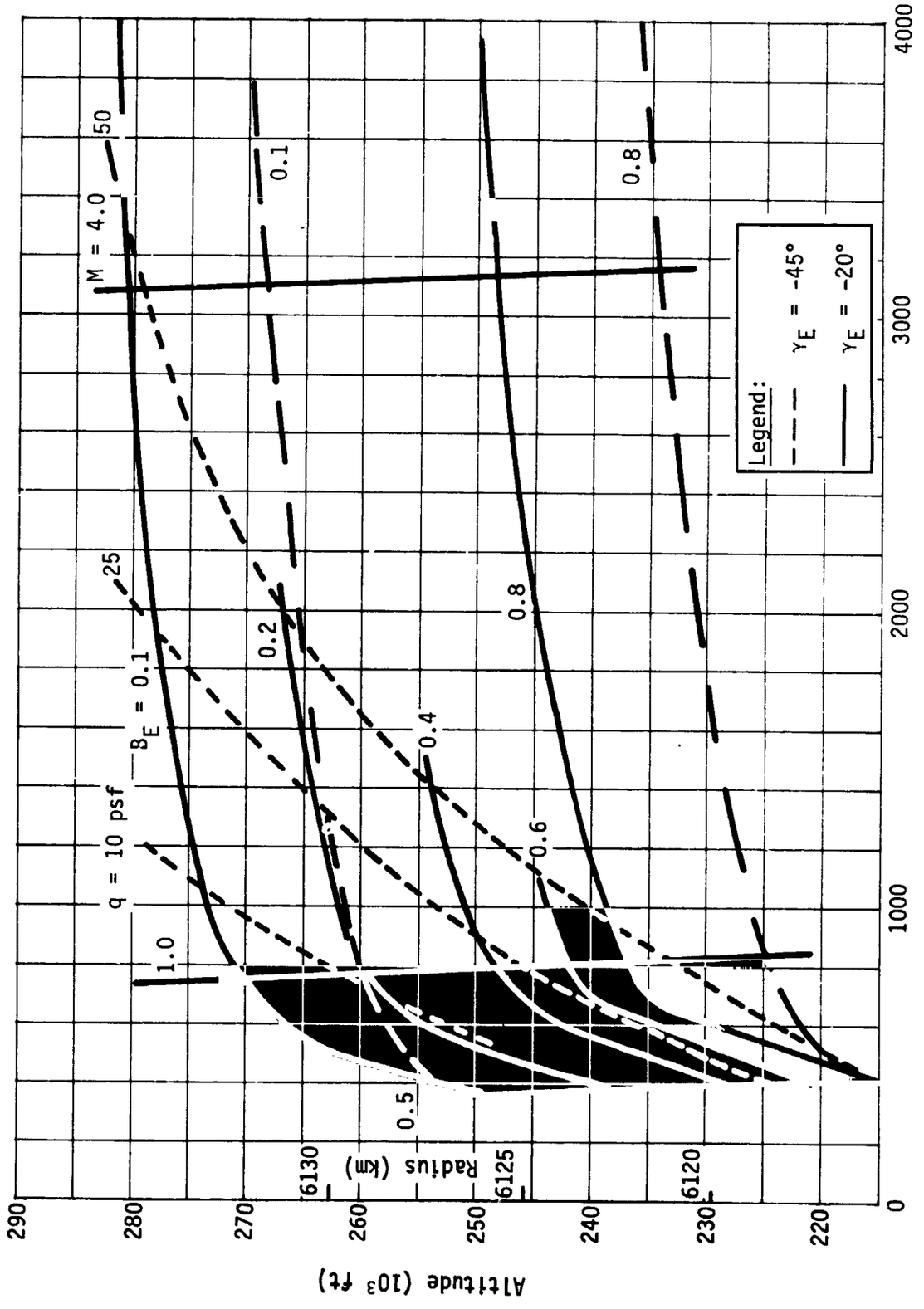


Fig. II-31 Effect of Entry Angle and Ballistic Coefficient

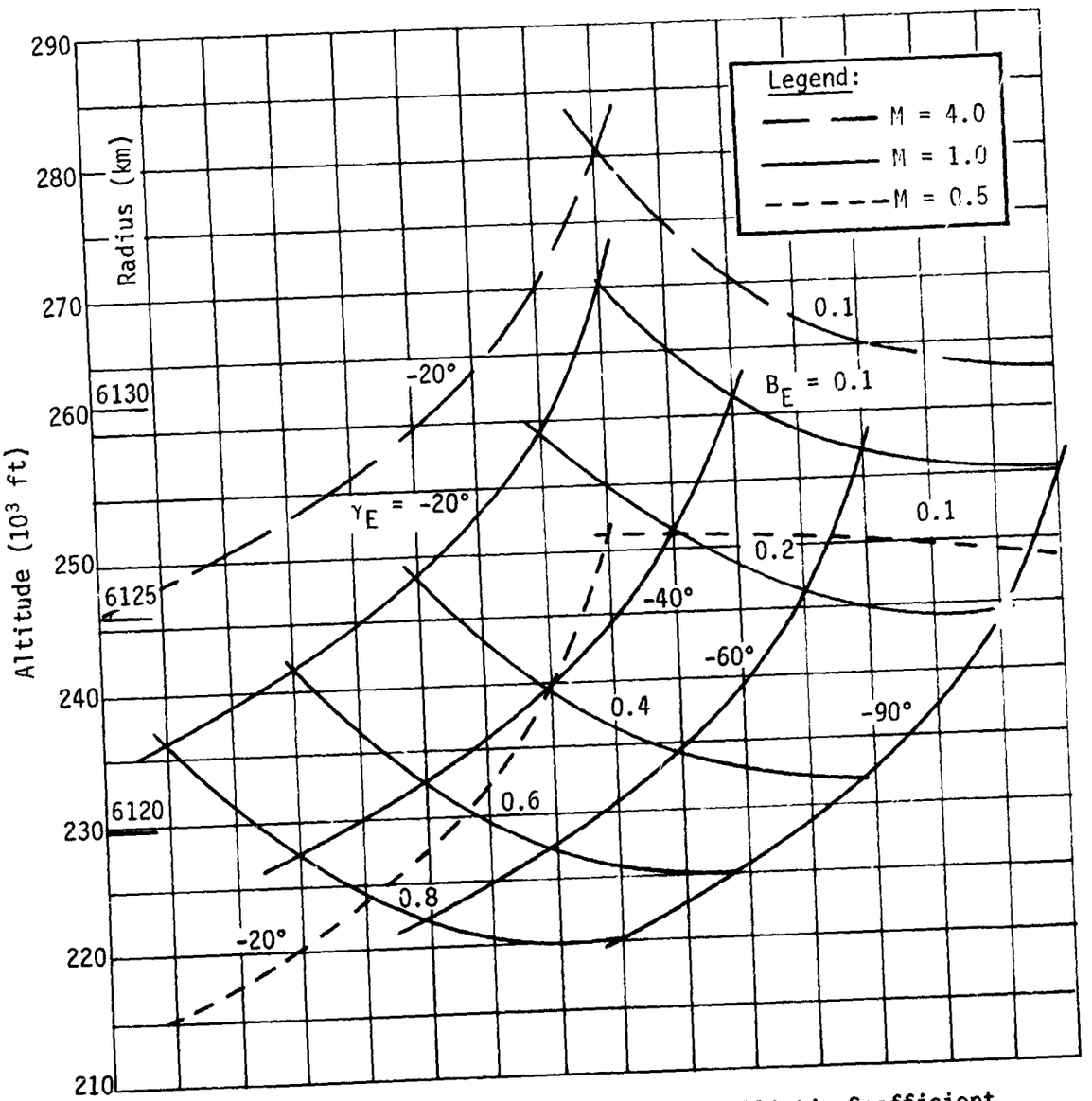


Fig. II-32 Effect of Entry Angle and Ballistic Coefficient

Table II-1 Atmosphere Model Effects on Entry

	Lower Density Atmosphere	V5M Atmosphere
Maximum Dynamic Pressure (psf)	4,343	4,118
Maximum Deceleration (g)	337	320
Altitude of Maximum Dynamic Pressure and Deceleration (ft)	275,835	288,981
Time of Maximum Dynamic Pressure and Deceleration (sec)	21.5	20.9
Altitude of g = 0.1 (ft)	384,148	409,523
Time of g = 0.1 (sec)	16.9	15.9
Altitude of M = 1.0 (ft)	237,622	248,866
Time of M = 1.0 (sec)	33.4	33.4
Altitude of M = 0.5 (ft)	227,587	238,319
Time of M = 0.5 (sec)	55.1	55.5

Note: Entry at 815,000 ft altitude and 36,000 fps. Typical values: $B_E = 0.4$, $\gamma_E = -45°$.

D. PROBE-PLANETARY DESCENT TRAJECTORIES

This section presents parametric descent trajectory data for the Venus Multiple Probe Study. Both the MMC-Lower atmosphere and the V5M atmosphere are used in this analysis to arrive at descent times and relative velocities that define the scientific instrumentation operating times. For the MMC-Lower atmosphere model terminal velocity and time of descent data are presented. Profiles of altitude versus velocity and altitude versus time are presented for both model atmospheres.

The following descent trajectory vehicle and planetary data are used.

1) Planetary radius (no oblateness) = 19,849,040 ft, 6050 km;
2) Planetary gravitational constant = 1.1472308×10^{16} ft^3/sec^2 (3.248596×10^5 km^3/sec^2);
3) Initial vehicle altitude above reference surface = 262,467 ft (80 km);
4) Initial vehicular planetocentric longitude and latitude = 0°.

The descent trajectories have been computed using the UD208 (Ref II-5), a point mass simulation model, on the CDC 6500 computer. A nonrotating planet is assumed. Additional constants and related information may be found in Ref II-3.

The MMC-Lower atmosphere and the V5M atmosphere used in this analysis are from Ref II-6. Figure II-33 gives a density-altitude comparison between these atmospheres. The V5M model, for the same atmospheric density, represents an altitude difference of 7 to 8 km over the MMC-Lower model near the surface.

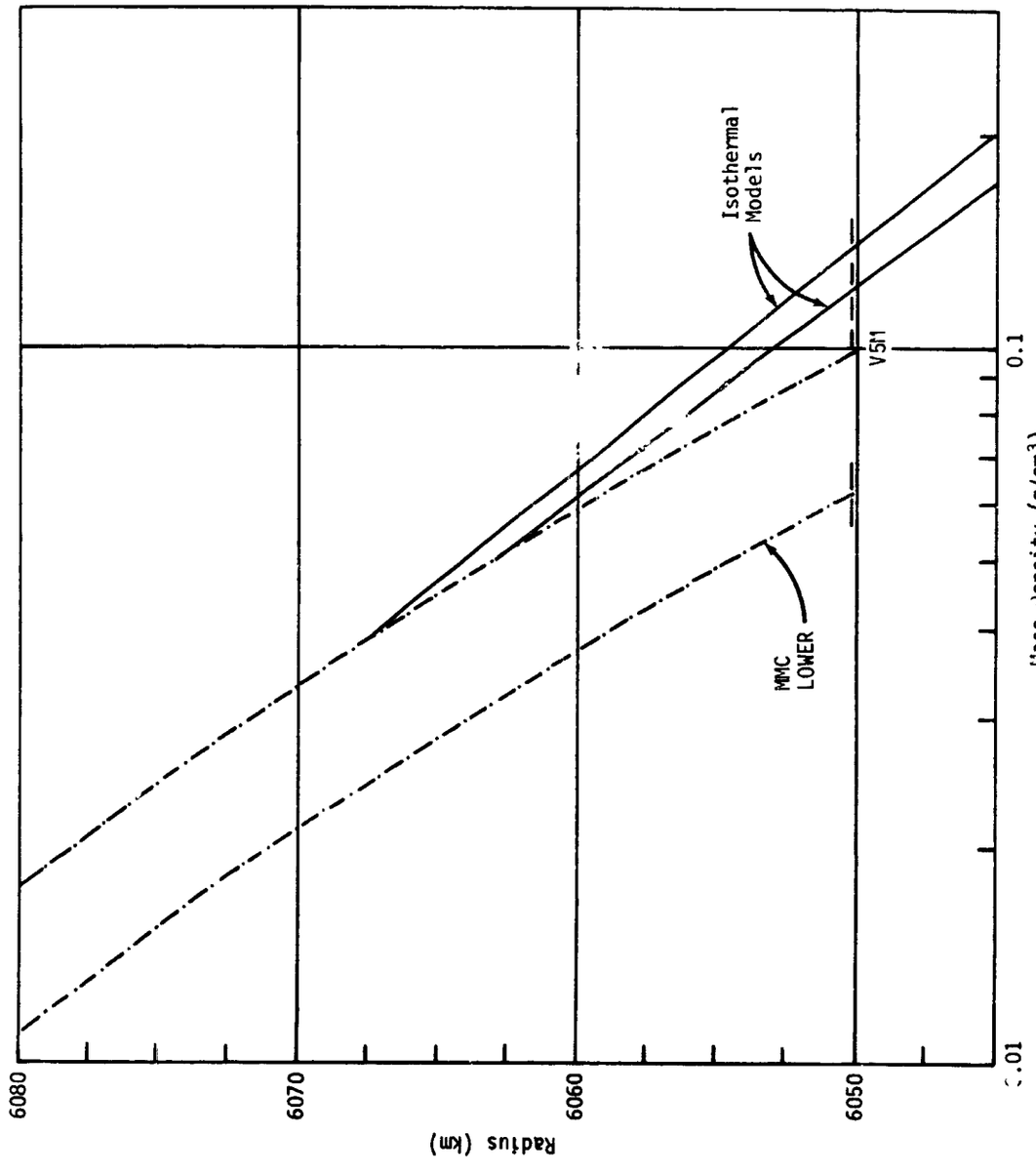


Fig. II-33 Density Profiles

The vehicle descent trajectory start conditions are peculiar to each probe and are chosen to satisfy particular scientific data-gathering requirements. Basically, however, the start altitudes are below 262,000 ft and the initial relative velocities are less than Mach = 1. The initial conditions are obtained from the entry studies of Section C of this chapter.

The descent vehicle ballistic coefficients (B_E) used ranged between 0.005 slug/ft^2 and 5.0 slug/ft^2 where

$$B_E = \frac{M}{C_D A}$$

where

M = mass of descent probe (slugs),

C_D = aerodynamic drag coefficient,

A = cross-sectional reference area of probe (ft^2).

Table II-2 gives C_D as a function of the local Mach No. The corresponding reference area used is 0.0206 ft^2 for M > 0.5, and 0.0311 ft^2 for M < 0.5.

Table II-2 Drag Coefficient vs Mach Number

Mach No.	C_D
0.	1.
0.5	1.02
1.0	1.25
1.5	1.48
2.0	1.52
3.0	1.53
5.0	1.51
100.	1.51

Figure II-34 shows the terminal velocity profiles as a function of the ballistic coefficient. These are computed using the MMC-Lower atmosphere and the assumption that the local drag is equivalent to the weight. The results compare precisely with the CDC 6500 runs. Figure II-35 gives the descent time from 6130 km (radius) as a function of the ballistic coefficient, also for the MMC-Lower atmosphere.

Figures II-36 and II-37 show the altitude-time and the altitude-velocity profiles for unstaged descents. These descent families reflect a range of ballistic coefficients between 0.1 and 5.0 slug/ft^2.

Figures II-38 and II-39 show descent data for a small probe in which the ballistic coefficient is 0.4 to Mach No. = 1, 0.01 to 6110 km (radius), and 2.0 slug/ft^2 to surface impact. A range of entry flight path angles (-25° to -50°) is reflected in these plots. From Fig. II-39 it can be seen that after staging at M = 1.0 the probes are at terminal velocities.

Figures II-40 and II-41 show descent data for a large probe that exhibits a β_E of 0.4 from entry to Mach 1, 0.1 to 6080 km, and 3.0 slug/ft^2 to surface. These figures show the effects of both Venus model atmospheres.

Figures II-42 and II-43 present descent data for cloud probes in both model atmospheres. These probes have ballistic coefficients of 0.2 from entry to Mach 4, 0.12 to Mach 1, and 0.005 slug/ft^2 down to 6100 km.

Figures II-44 and II-45 give altitude-time and altitude-velocity profiles for unstaged Venus descent probes. A range of ballistic coefficients between 0.01 and 5.0 slug/ft^2 is reflected in these plots. Figures II-46 and II-47 present descent data for a small probe in the V5M model atmosphere. The ballistic coefficients for this probe are 0.4 form entry to Mach 1, 0.01 to 6110 km, and 2.0 slug/ft^2 to surface impact.

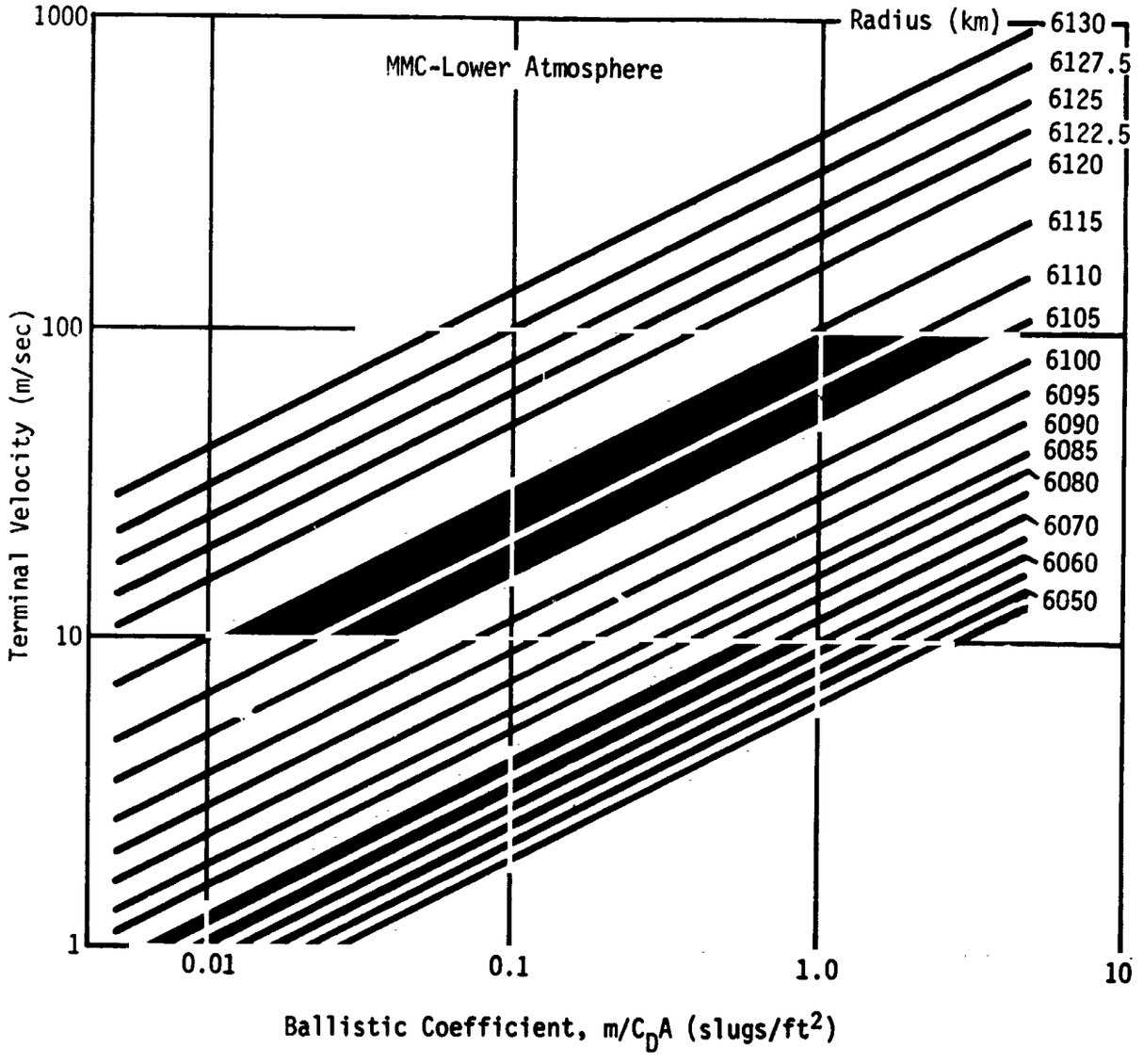


Fig. II-34 Terminal Velocity

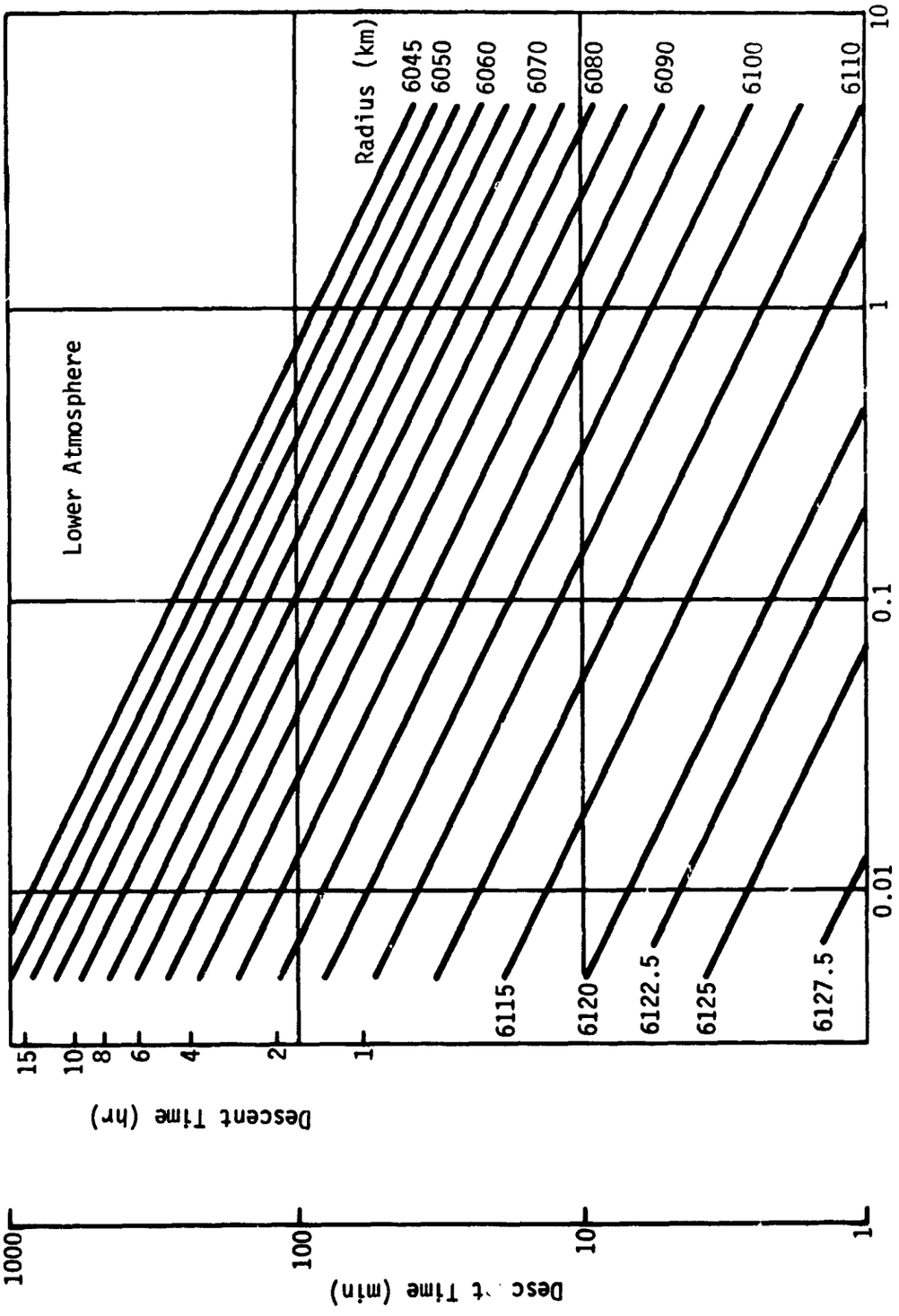


Fig. II-35 Descent Time from 6130 km Radius

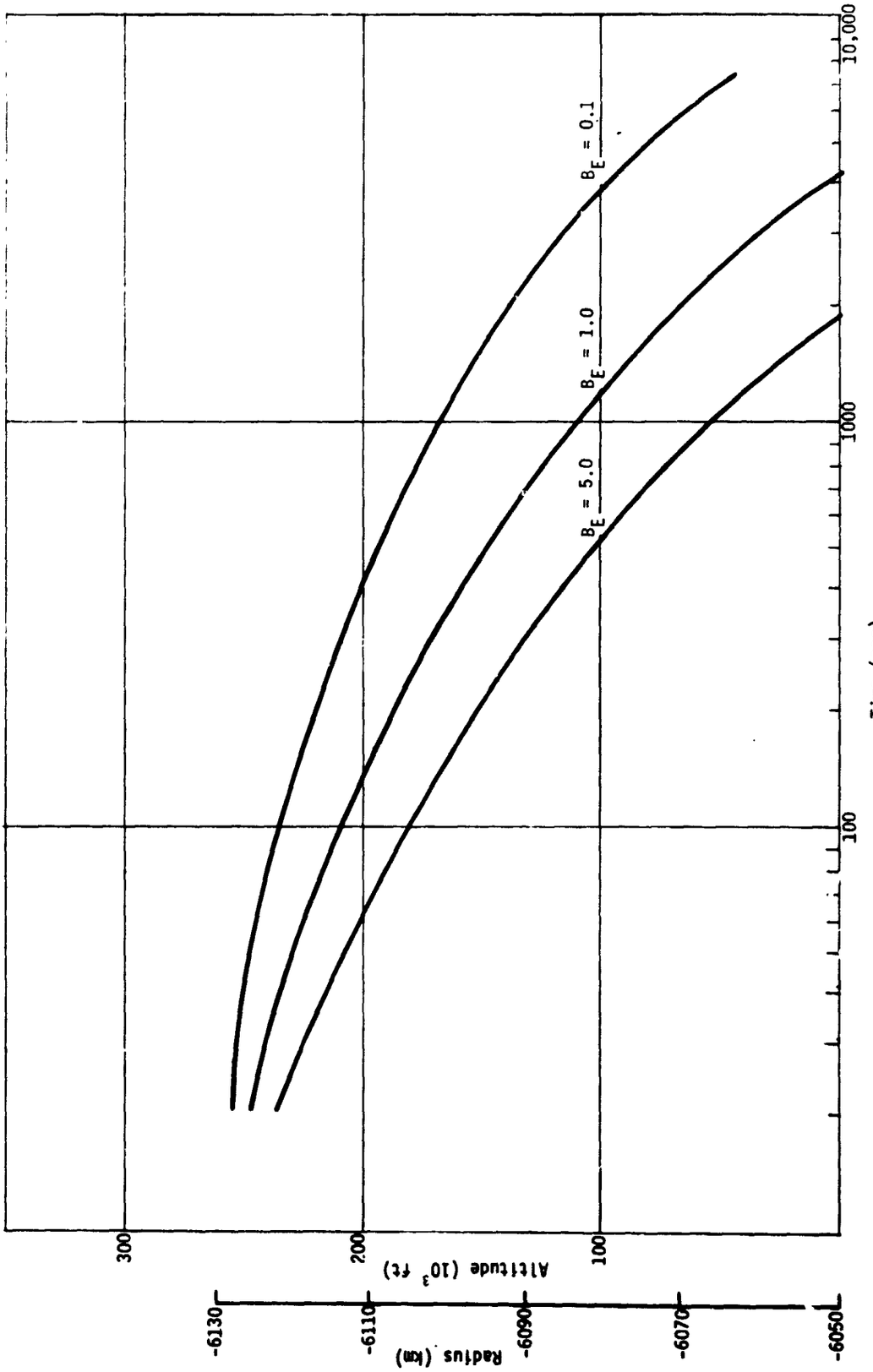


Fig. II-36 Altitude-Time Profile

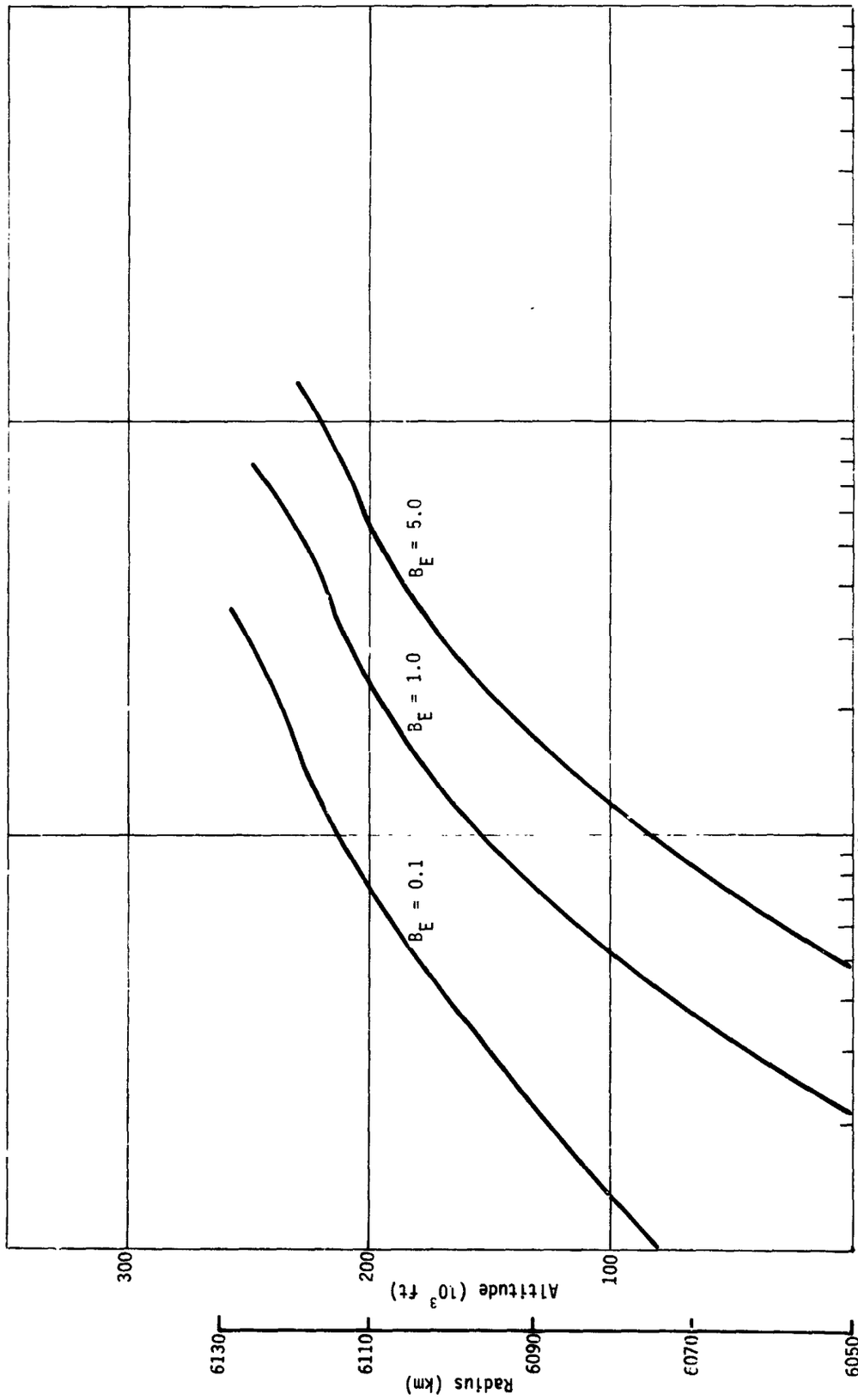


Fig. II-37 Altitude Velocity Profile

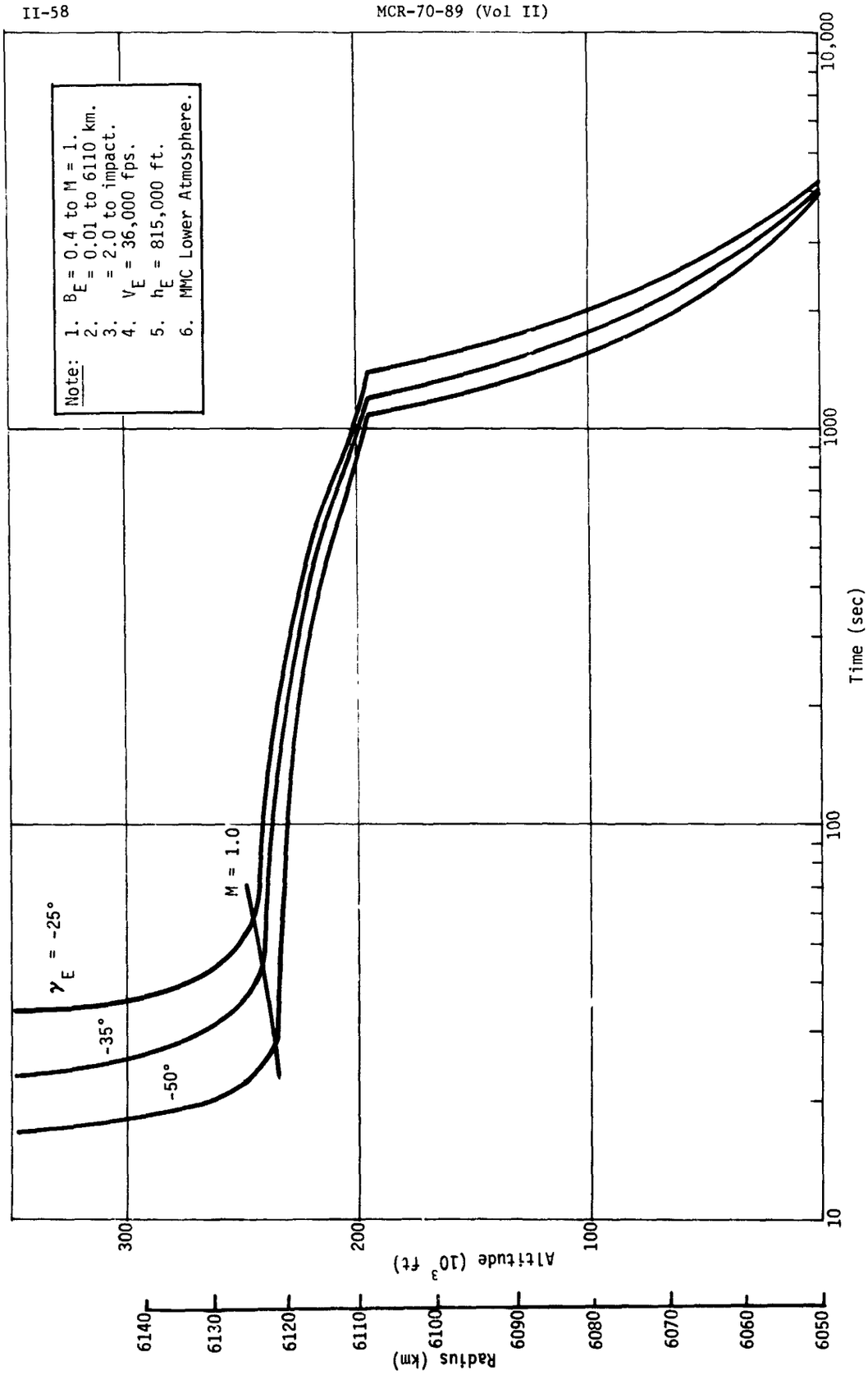


Fig. II-38 Small Probe Time Profile

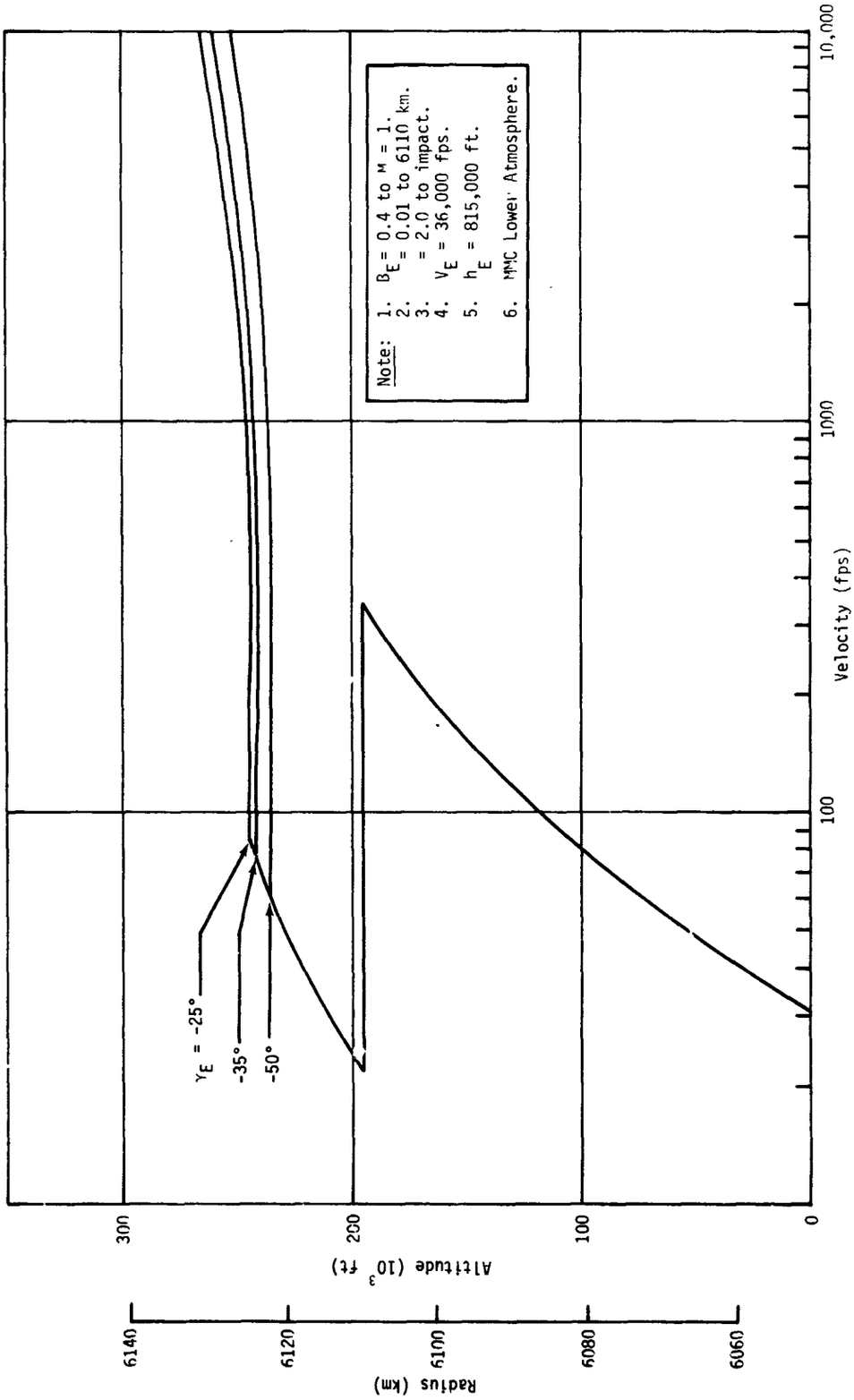


Fig. II-39 Small Probe Velocity Profile

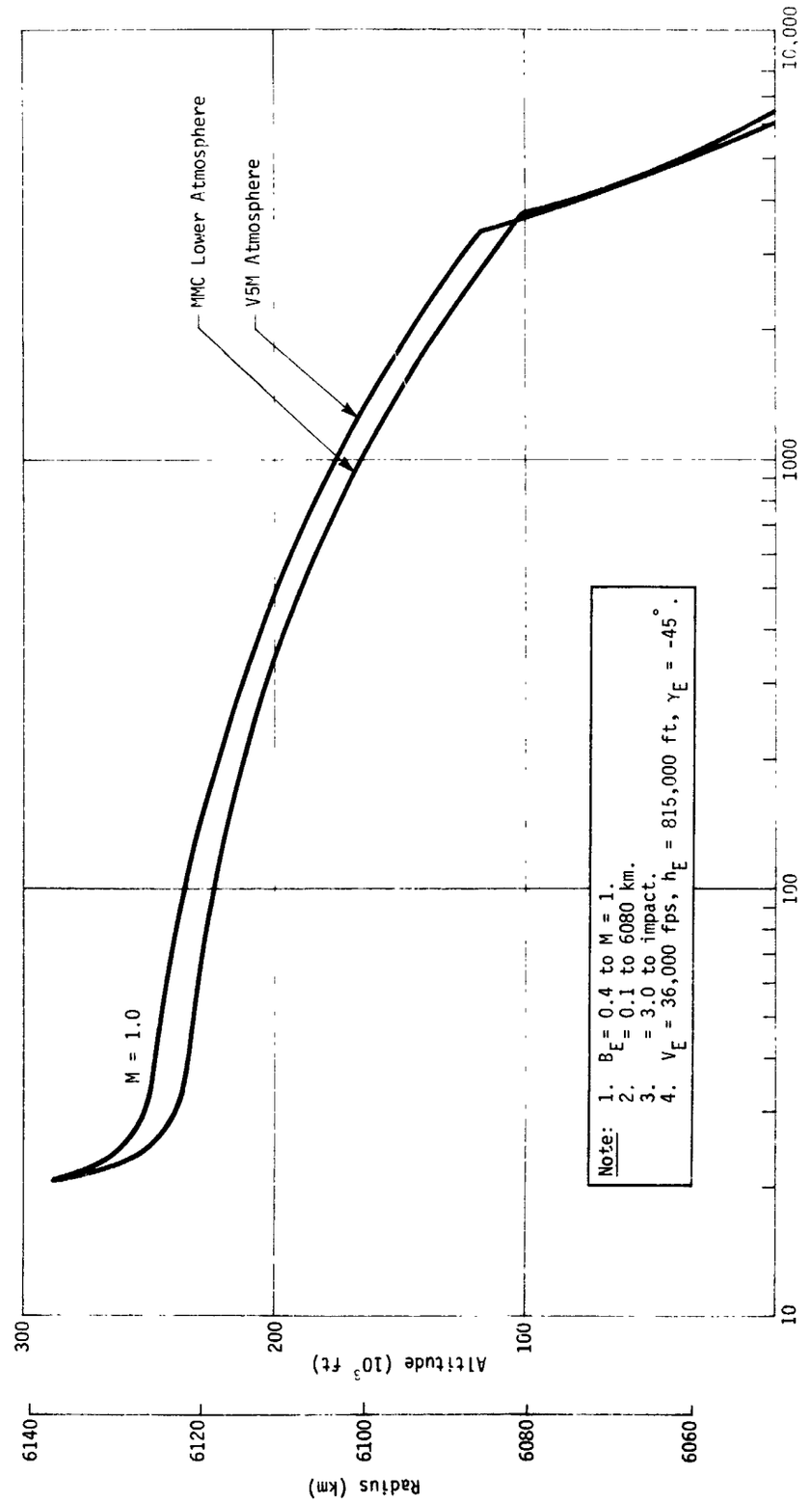


Fig. II-40 Large Probe Time Profile

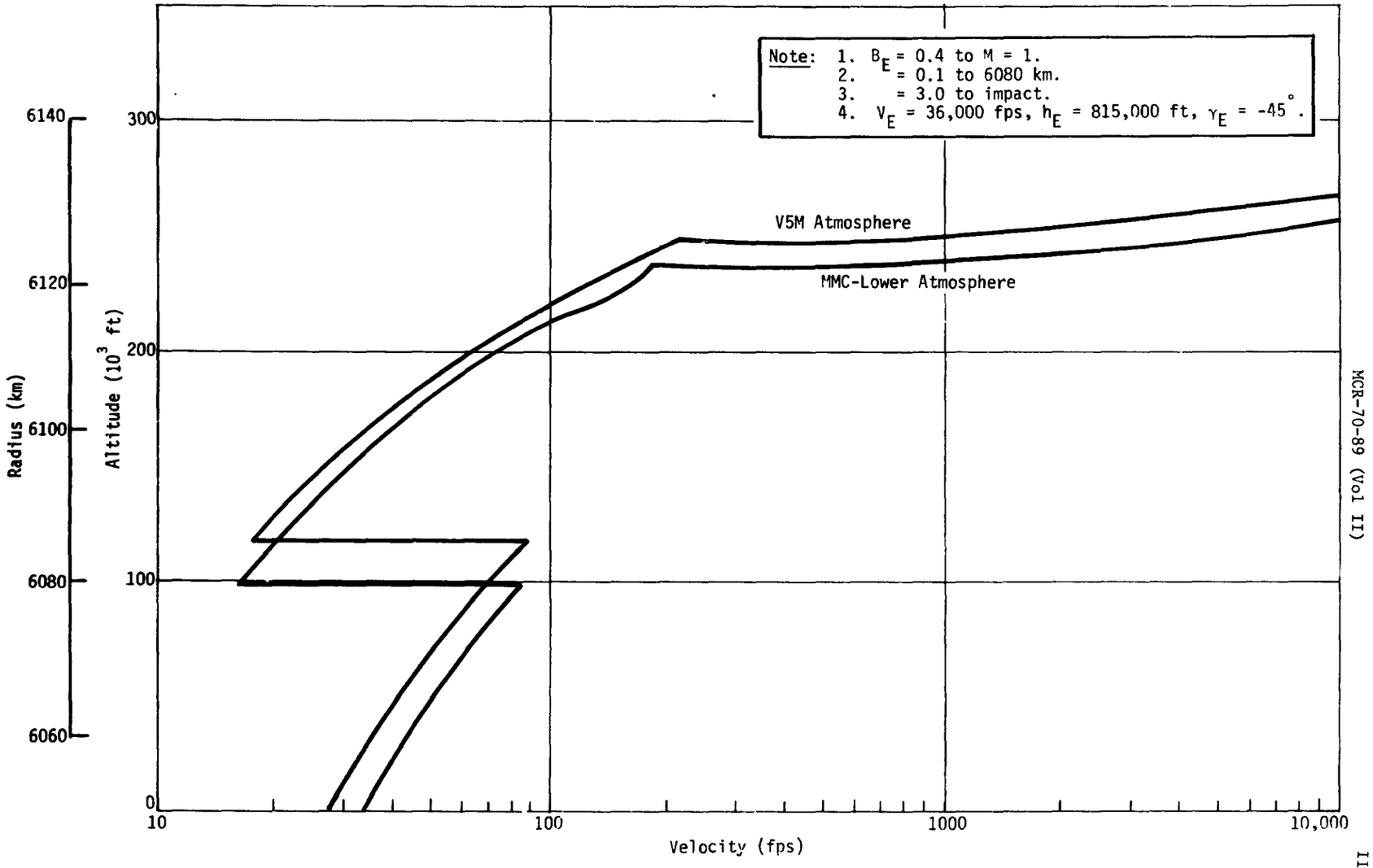


Fig. II-41 Large Probe Velocity Profile

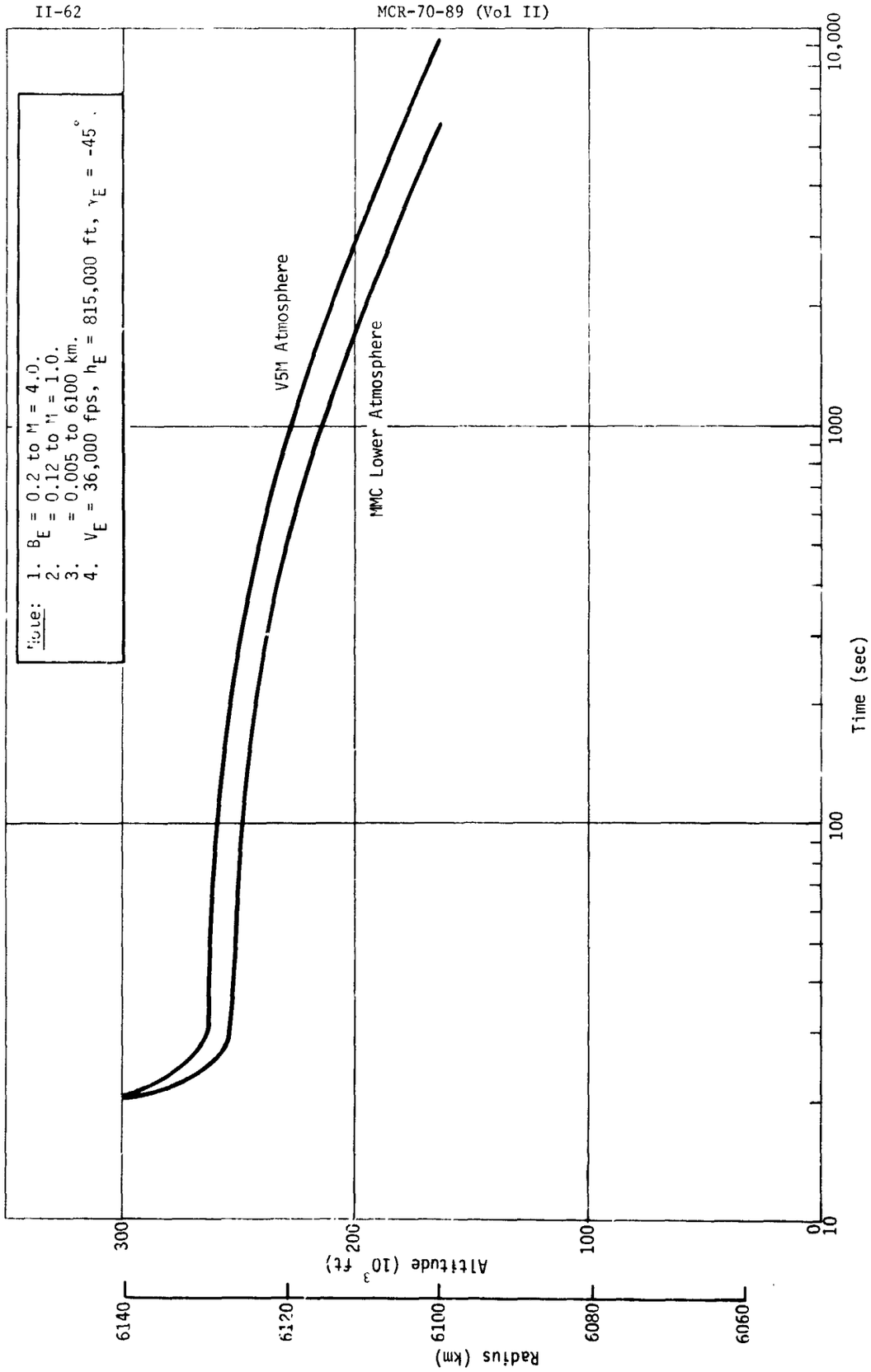


Fig. II-42 Cloud Probe Time Profile

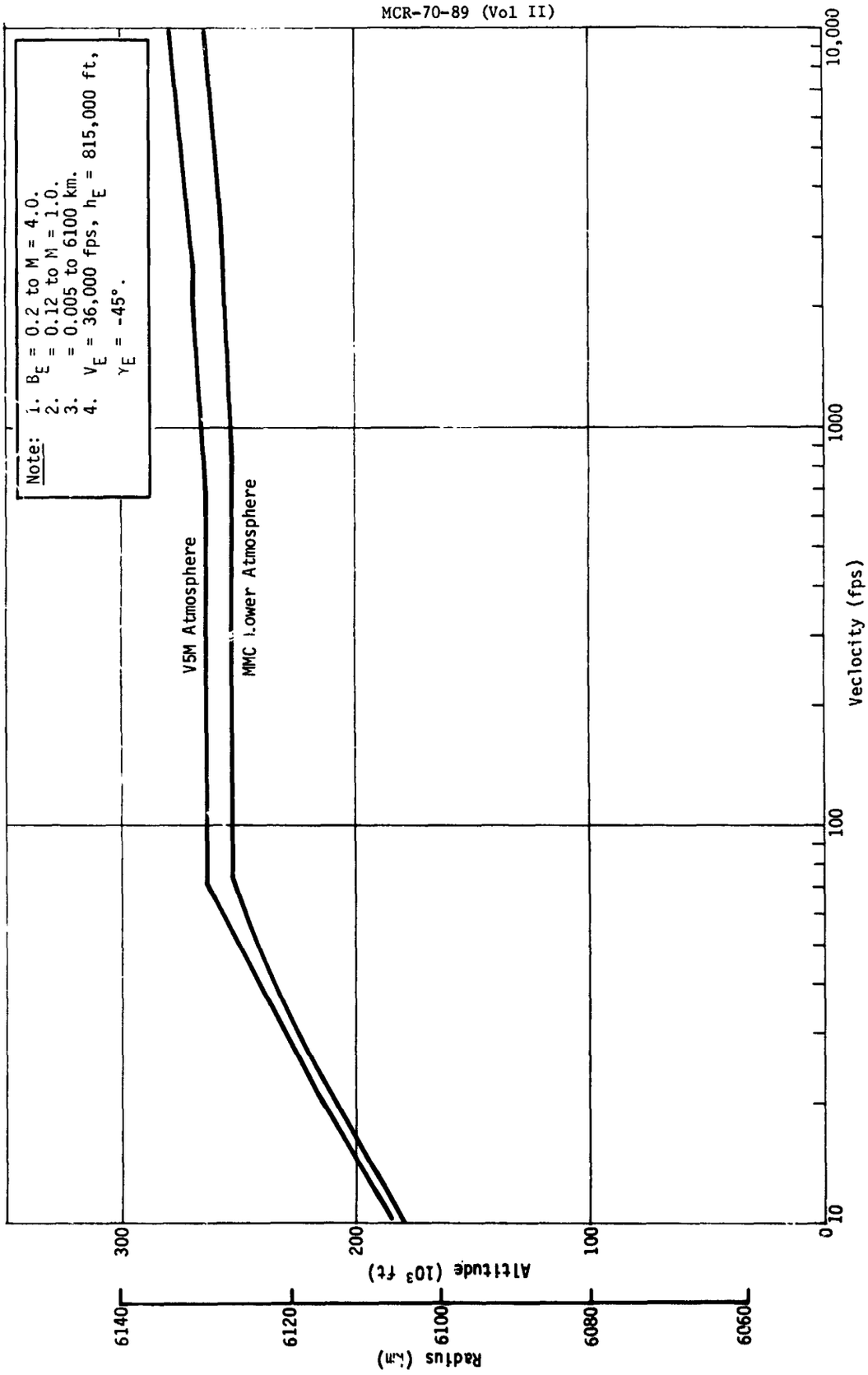


Fig. II-43 Cloud Probe Velocity Profile

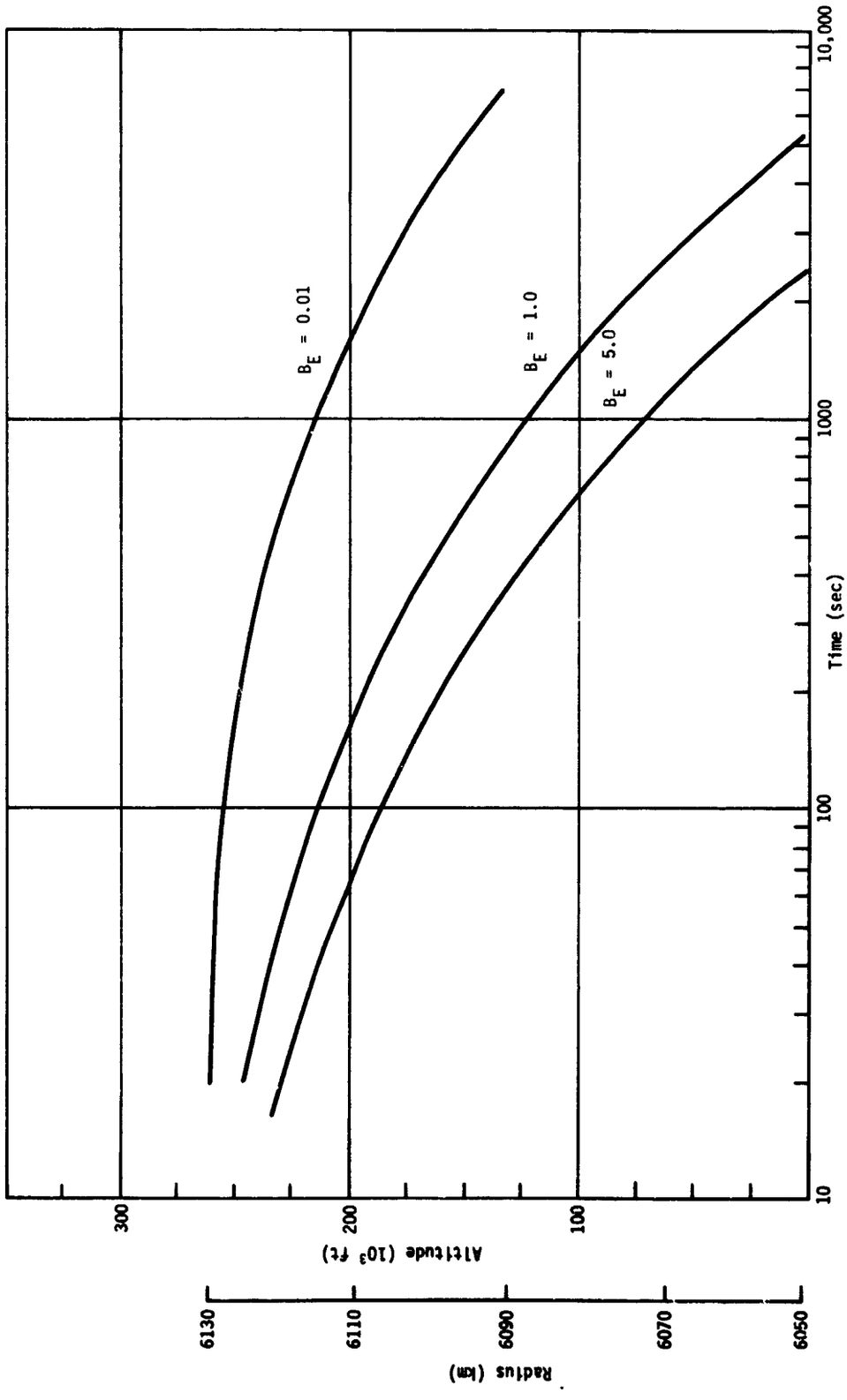


Fig. II-44 Altitude-Time Profile (VSM)

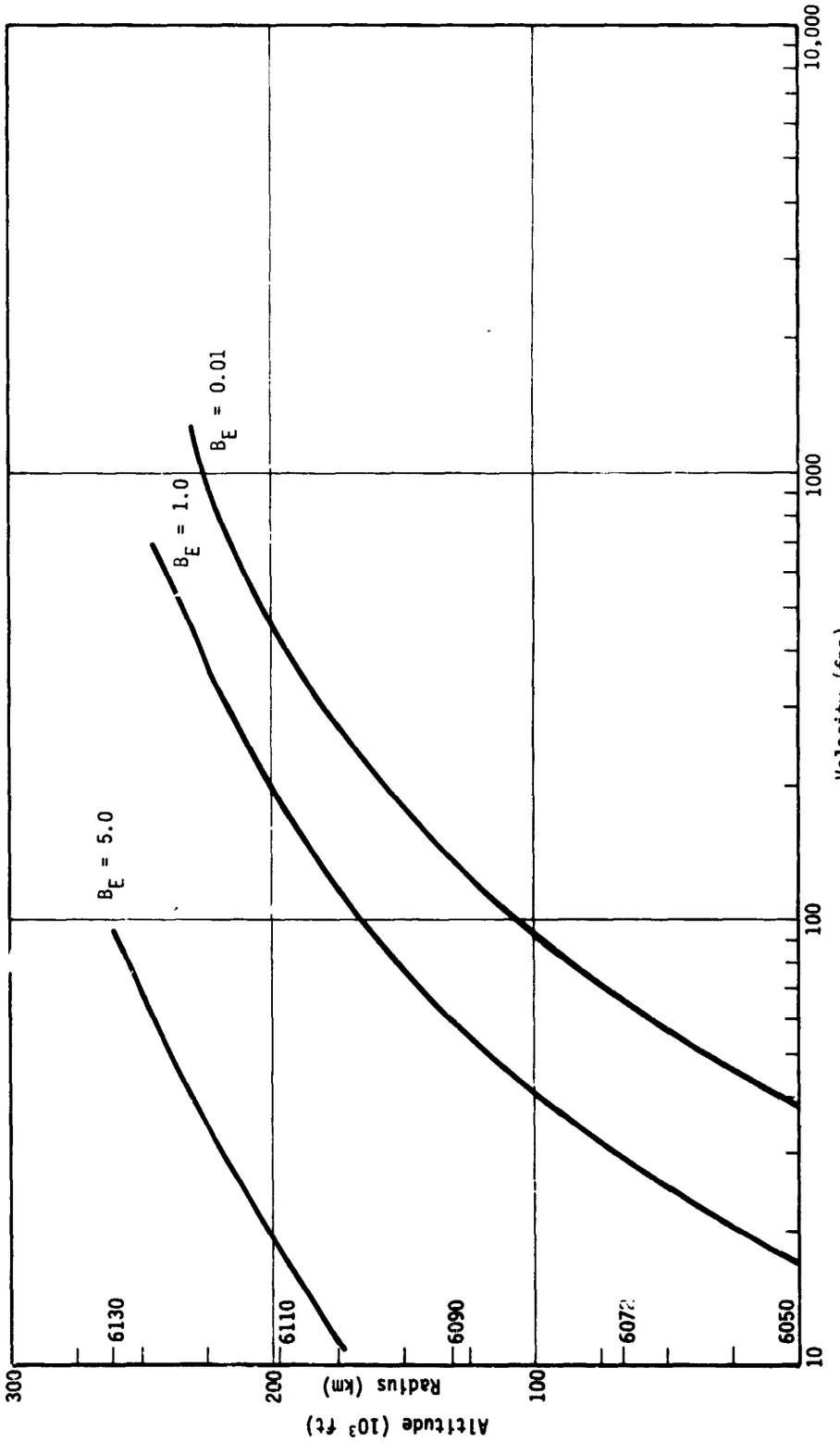


Fig. II-45 Altitude-Velocity Profile (V5M)

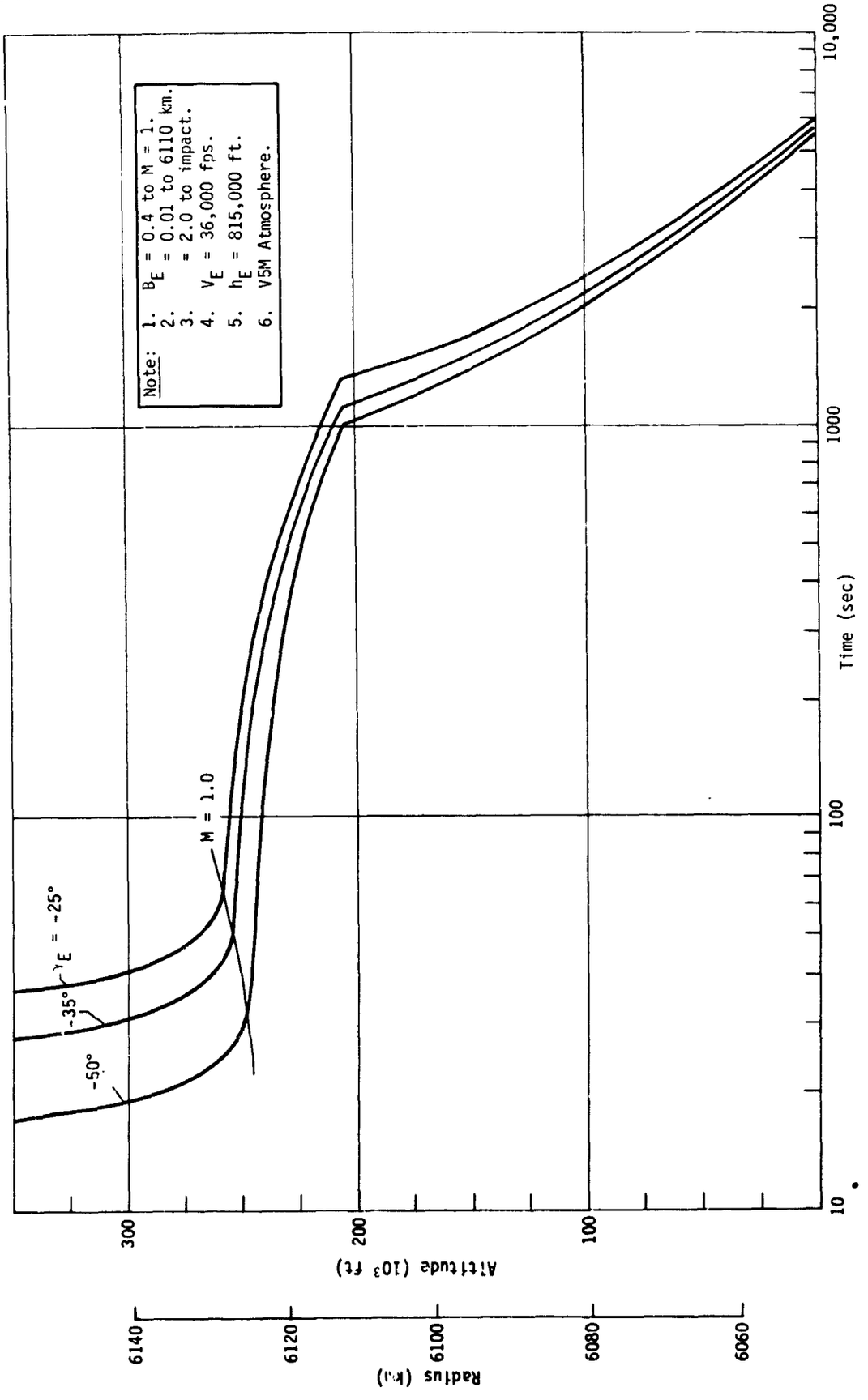


Fig. II-46 Small Probe Time Profile

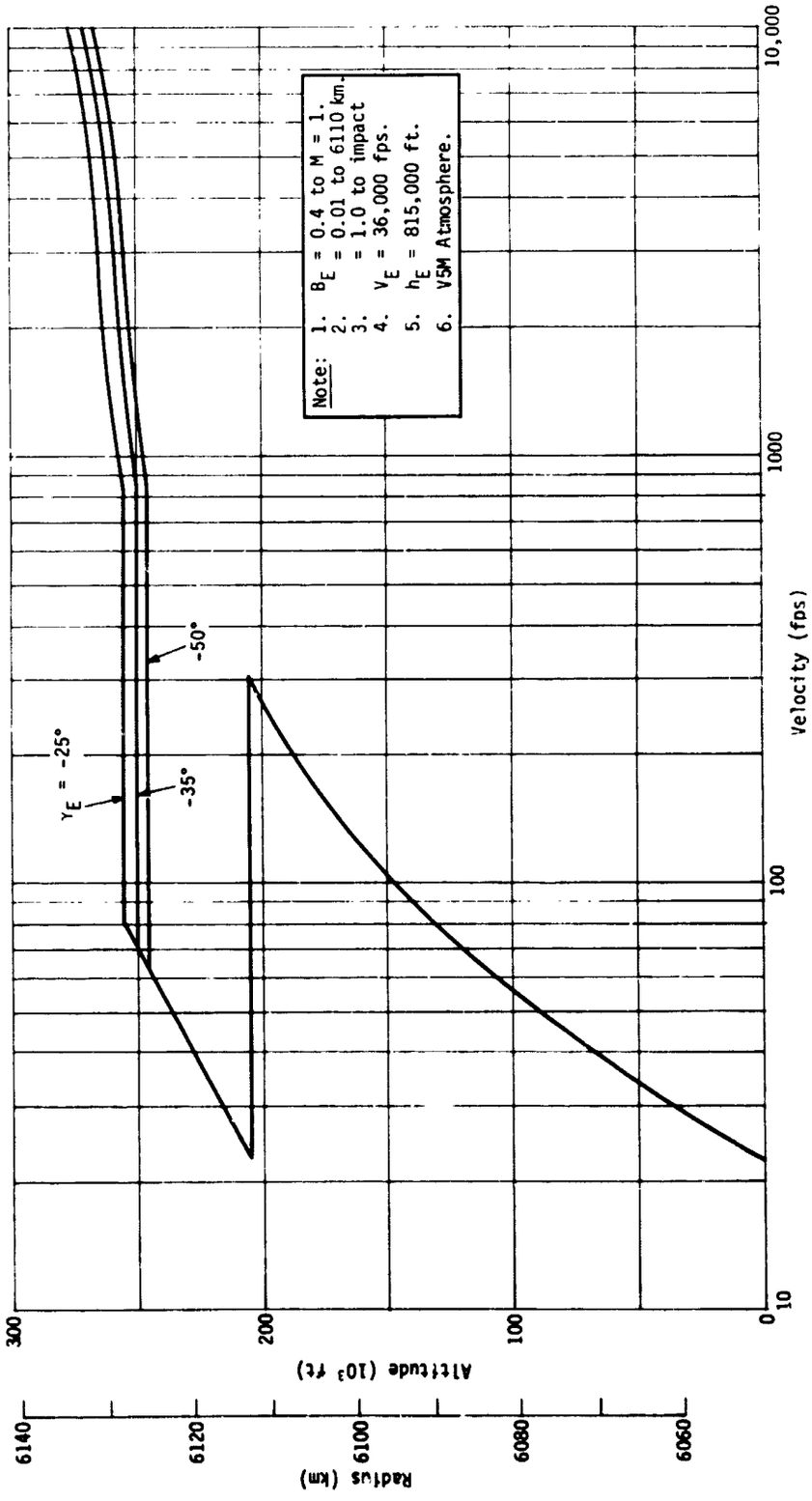
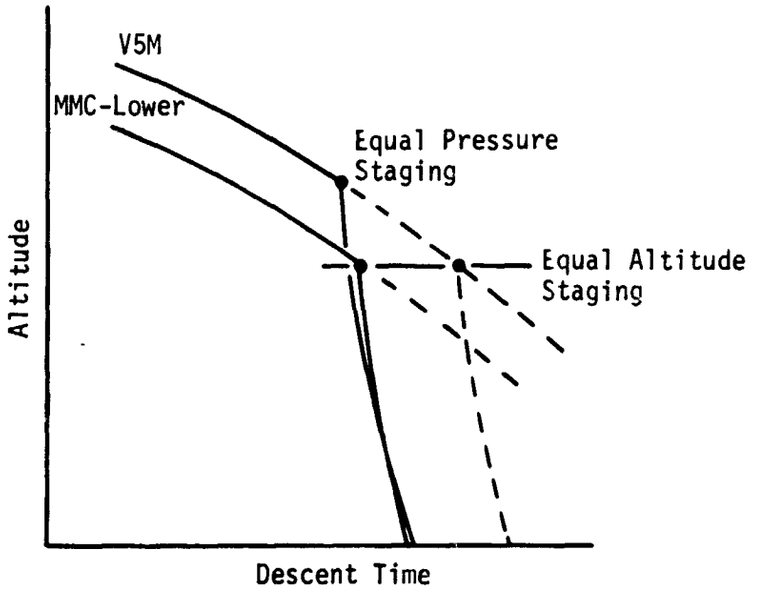


Fig. II-47 Small Probe Velocity Profile

The descent profiles are terminal velocity profiles and can be defined for a wide range of conditions rapidly. The descent time becomes the only error parameter in the absence of a definable wind structure. Range is zero since the flight path is vertical. Staging of the probes will introduce local accelerations or decelerations of short duration. These do not significantly affect the descent times.

The staging events must be referenced to some measurable quantity -- altitude or pressure. Variations in the atmosphere models must be considered in selecting the staging point. The following sketch indicates the different techniques.



The descent time difference for staging at equal pressure in both models is about 8 minutes. Similarly, staging at equal altitudes yields 22 minutes difference in descent time between the two atmosphere models. Therefore, staging at equal pressure is recommended.

For the small probe, the total entry and descent time difference between entry angles of -25 and -50° is approximately 6 minutes.

The science data rate requirements set probe descent velocities at 6130 km near 100 m/sec. Relating to Fig. II-33 and II-34, the ballistic coefficient for this condition should be near 0.1 slug/ft^2. The total descent time to the surface, however, for a low ballistic coefficient is quite large. Therefore, staging to a high ballistic coefficient (1.0 slug/ft^2 or larger) after 15 to 20 minutes is desirable to keep the descent time near 1 hr.

E. TRAJECTORY ACCURACY ANALYSIS

The various trajectory phases contribute in some degree to the final position and time errors at impact. These errors must be defined to ensure proper experiment operations and a satisfactory communications link. The sensitivities of each trajectory phase are evaluated in this section and discussed along with their impact on staging techniques, targeting, deflection strategy, etc.

The parametric data for the various trajectory phases have been presented in Sections A thru D of this chapter. These data have been used in defining the error sensitivities. The data of Section A establish the dates, arrival geometry, and arrival parameter magnitudes. The uncertainty in these data are assumed on the basis of other studies and a short survey of the literature. The initial errors are in the injection quantities at earth departure. The initial aim point at Venus is biased far enough from the planet to ensure a miss if no further maneuvers are performed. Tracking data refine our knowledge of position and velocity. Midcourse maneuvers retarget our aim point closer to the planet and reduce the dispersions at encounter. Post-midcourse tracking will further reduce the uncertainties in our knowledge of position and velocity at encounter. The midcourse propulsion system on the spacecraft must be sized to correct for the full range of injection errors and to nominally achieve the desired encounter aim point. The actual propulsion sizing and maneuver scheduling is a basic design problem on the spacecraft and is beyond the scope of this study. From the literature (Ref II-7) it appears that one midcourse correction for the case presented could provide final encounter within 2500 km of the target point. If we assume that this is a sphere about the target point and that the velocity is known to within 0.5 cm/sec (Ref II-8) then the sensitivities indicate no significant ΔV increment (less than 6.0 m/sec at $\tau = 20°$) must be provided to meet the targeting requirements. Two midcourse corrections

could improve the spacecraft accuracy. The knowledge of position from tracking data for the October 31, 1975 arrival has been defined from representative trajectory simulations as an ellipse of semimajor axis equal to 112 km (1σ) and semiminor axis equal to 21 km (1σ). This ellipse is oriented with its semimajor axis approximately 90° to the T-vector. It is the effect of these uncertainties on entry conditions that is discussed in this section along with the deflection maneuver execution errors, atmosphere model variations, and configuration uncertainties.

The errors in initial position and in deflection maneuver execution result in errors in entry time, flight path angle, velocity, and range. The in-plane entry condition sensitivity to the initial condition and execution errors are presented in Table II-3 for impacting trajectories and Table II-4 for flyby paths. The entry dispersions due to the initial condition errors are generally much smaller than those due to the execution errors. The sensitivity to R_{EJ} is negligible for any reasonable ΔR_{EJ}. For a ΔV_{HE} of 0.5 cm/sec the sensitivity to this parameter also is negligible. The periapsis radius does exhibit a significant error in specific cases. If the original position uncertainty of 2500 km is translated to an error in perapsis radius, then this error is about 1000 km and substantial range errors exist. For the case where the spacecraft is targeted to near the subsolar point $\left(\gamma_E = -50°\right)$ this means about a ±15° downrange error, a ±0.2° crossrange error, and approximately a ±10° error in entry flight path angle. Other quantities are affected in a negligible manner.

Table II-3 Sensitivities for Venus Probes, R_p = 2800 km

Near Side Entries $\tau = \pm 20°$ $R_{EJ} = 4 \times 10^6$ V_{HE} = 3.6 km/sec

	γ_E = -25°				γ_E = -35°				γ_E = -50°				γ_E = -65°			
	ΔR (deg)	T (hr)	V_E (m/sec)	γ_E (deg)	ΔR (deg)	T (hr)	V_E (m/sec)	γ_E (deg)	ΔR (deg)	T (hr)	V_E (m/sec)	γ_E (deg)	ΔR (deg)	T (hr)	V_E (m/sec)	γ_E (deg)
$\frac{\partial(\ )}{\partial R_{EJ}(km)}$	14.39×10^{-6}	74.9×10^{-6}	0	8.562×10^{-6}	6.9×10^{-6}	74.9×10^{-6}	0	4.235×10^{-6}	0.02×10^{-6}	75.0×10^{-6}	0	-0.038×10^{-6}	-5.3×10^{-6}	74.9×10^{-6}	0	-3.426×10^{-6}
$\frac{\partial(\ )}{\partial V_{HE}^{km/sec}}$	-10.28	-75.4	343	-2.896	-7.66	-75.5	342	-1.748	-4.86	-75.8	341	-0.789	-2.65	-75.3	342	-0.151
$\frac{\partial(\ )}{\partial R_p km}$	2.7618×10^{-2}	1.4×10^{-4}	0	$+1.691 \times 10^{-2}$	1.9438×10^{-2}	1.0×10^{-4}	0	$+1.225 \times 10^{-2}$	1.3961×10^{-2}	0.6×10^{-4}	0	$+0.9083 \times 10^{-2}$	1.1543×10^{-2}	0.4×10^{-4}	0	$+0.768 \times 10^{-4}$
$\frac{\partial(\ )}{\partial \tau deg}$	-2.833	-0.020	+0.02	-1.734	-1.322	-0.011	+0.01	-0.8330	+0.0118	0	0	+0.00757	+1.0158	-0.002	+0 02	+0.6742
$\frac{\partial(\ )}{\partial \Delta V\ m/sec}$	4.735	-0.048	0.33	2.899	3.29	-0.055	0.33	2.075	-2.270	-0.0.	0.33	+1.477	-1.889	-0.077	0.32	-1.254

Table II-4 Sensitivities for Venus Probes, R_p = 12,600

Near Side Entries $\tau = \pm 20°$ $R_{EJ} = 4 \times 10^6$ V_{HE} = 3.6 km/sec

	γ_E = -25°				γ_E = -35°				γ_E = -50°				γ_E = -65°			
	ΔR (deg)	T (hr)	V_E (m/sec)	γ_E (deg)	ΔR (deg)	T (hr)	V_E (m/sec)	γ_E (deg)	ΔR (deg)	T (hr)	V_E (m/sec)	γ_E (deg)	ΔR (deg)	T (hr)	V_E (m/sec)	γ_E (deg)
$\frac{\partial(\ )}{\partial R_{EJ}^{km}}$	-32.73×10^{-6}	$+74.3 \times 10^{-6}$	0	-20.07×10^{-6}	-27.0×10^{-6}	$+74.2 \times 10^{-6}$	0	-16.93×10^{-6}	-24.73×10^{-6}	$+74.1 \times 10^{-6}$	0	-16.11×10^{-6}	-25.8×10^{-6}	$+73.9 \times 10^{-6}$	0	-17.18×10^{-6}
$\frac{\partial(\ )}{\partial V_{HE}^{km/sec}}$	5.8	-74.7	343	7.35	3.78	-74.6	344	5.74	3.32	-74.2	345	4.583	4.08	-73.8	346	4.241
$\frac{\partial(\ )}{\partial R_p km}$	1.62×10^{-2}	0.8×10^{-4}	0	0.996×10^{-2}	1.15×10^{-2}	0.5×10^{-4}	0	0.729×10^{-2}	0.83×10^{-2}	0.4×10^{-4}	0	0.543×10^{-2}	0.689×10^{-2}	0.2×10^{-4}	0	0.459×10^{-2}
$\frac{\partial(\ )}{\partial \tau deg}$	+5.88	+0.016	+0.06	+3.637	+4.98	+0.010	+0.07	+3.161	+4.64	+0.001	+0.09	+3.036	+4.88	-0.009	+0.11	+3.259
$\frac{\partial(\ )}{\partial \Delta V\ m/sec}$	-4.14	-0.092	+0.33	-2.553	-3.04	-0.087	+0.33	-1.923	-2.24	-0.081	+0.33	-1.459	-1.86	-0.076	+0.33	-1.239

Additional spacecraft maneuvers would improve the accuracy and possibly could correct the large initial condition errors to the order of 300 km or the equivalent to 120 km error in radius of periapsis. This reduces the in-plane downrange errors and flight path angle errors to about ±1.7° and ±1°, respectively. It is interesting to note that the range errors are generally about 50% larger than the flight path angle errors.

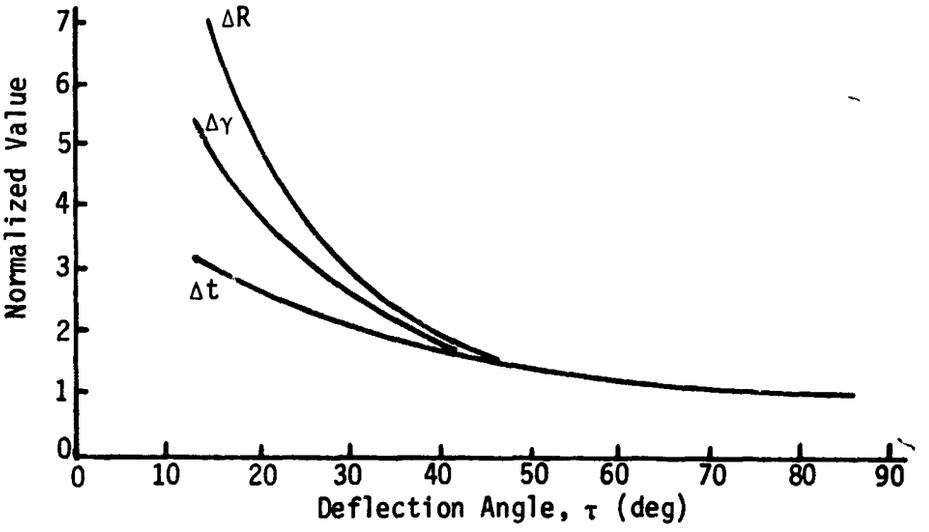
The maneuver execution accuracy is assumed to yield pointing within 0.75° (1σ) and velocity within 1% of the total (1σ). To apply these to a sample case, consider entry at a polar point on October 31, 1975. The entry angle is -25° and the required deflection velocity increment is 45 m/sec applied at an angle of 20° from the V_{HE}. The velocity error would be 0.45 m/sec and would yield a range error of ±2.14° and an entry flight path angle error of ±1.3°. The errors in entry velocity and time can be neglected for most analyses. The errors in knowledge of the initial position of the deflection maneuver add ±1.1° of range error and ±0.68° of entry angle error.

The error in deflection angle results in ±2.14° error in range and ±1.3° error in path angle. Again entry velocity and time errors are very small and can be neglected for most missions.

If the in-plane errors are root-sum-squared, the resultant error is ±3.23° (1σ) in downrange, and ±1.96° (1σ) in flight path angle. Crossrange errors due to initial conditions are reduced to near zero because of the focusing effect of planetary gravity. Execution errors yield the significant crossrange dispersions, which are in the order of ½ the downrange errors. Crossrange is achieved by the equivalent of a pitch and roll maneuver. Similar to the pitch angle considerations of Section B, velocity increments are the most significant parameters at roll angles of 40° or larger, and pitch angles of 20 deg. For the -25° entry angle case the crossrange sensitivities are approximately 2°/m/sec and

less than 1.5°/deg pointing error. These sensitivities yield maximum crossrange errors near ±1.7° (RSS 1σ). The roll maneuver effectively reduces the execution downrange errors directly as a function of the cosine of the roll angle.

The error variation with deflection angle is of the nature noted in the following sketch,



which indicates that deflection angles less than about 20° are not desirable from an error standpoint.

Other periapsis radii have been investigated and the error sensitivities for 3200 km and 9000 km are presented in Table II-5 and II-6, respectively. The -50° entry exhibits near minimum sensitivities at R_p = 2800 km because nominal entry occurs without deflection impulse. Other periapsis radius would increase the deflection maneuver and generally increase the sensitivities. For entries at angles of -25° and -35° the periapsis radius for direct targeting is greater than 2800 km and the sensitivities tend to first decrease and then increase as periapsis radius increases.

Table II-5 Sensitivities for Venus Probes, R_p = 3200 km

Near Side Entry $\tau = \pm 20°$, $R_{EJ} = 4 \times 10^6$ km, V_{HE} = 3.6 km/sec

	γ_E = -25°				γ_E = -35°				γ_E = -45			
	ΔR (deg)	T (hr)	V_E (m/sec)	γ_E (deg)	ΔR (deg)	T (hr)	V_E (m/sec)	γ_E (deg)	ΔR (deg)	T (hr)	V_E (m/sec)	γ_E (deg)
$\frac{\partial(\ )}{\partial R_{EJ}^{km}}$	11.62×10^{-6}	76.7×10^{-6}	0	7.07×10^{-6}	4.79×10^{-6}	76.7×10^{-6}	0	2.97×10^{-6}	0.474×10^{-6}	76.7×10^{-6}	0	0.275×10^{-6}
$\frac{\partial(\ )}{\partial V_{HE}^{km/sec}}$	-10.07	-78.6	+335	-2.455	-7.66	-78.6	+335	-1.603	-5.51	-79.0	+334	-0.86
$\frac{\partial(\ )}{\partial R_p^{km}}$	2.615×10^{-2}	1.4×10^{-4}	0	1.596×10^{-2}	1.841×10^{-2}	1.0×10^{-4}	0	1.155×10^{-6}	1.452×10^{-2}	0.7×10^{-4}	0	0.931×10^{-2}
$\frac{\partial(\ )}{\partial \gamma^{deg}}$	-2.304	-0.017	0.02	-1.4068	-0.9559	0.008	0.01	-0.60025	-0.0851	0	0.01	-0.05462
$\frac{\partial(\ )}{\partial \Delta V^{m/sec}}$	+4.7722	-0.050	0.32	+2.91064	3.314	-0.057	0.32	+2.08096	2.6014	-0.062	0.31	+1.67031

Table II-6 Sensitivities for Venus Probes, R_p = 9000 km

Near Side Entry R_p = 9000 km, τ = -20°, $R_{EJ} = 4 \times 10^6$ km, V_{HE} = 3.6 km/sec

	γ_E = -25				γ_E = -35				γ_E = -45			
	ΔR (deg)	T (hr)	V_E (m/sec)	γ_E (deg)	ΔR (deg)	T (hr)	V_E (m/sec)	γ_E (deg)	ΔR (deg)	T (hr)	V_E (m/sec)	γ_E (deg)
$\frac{\partial(\ )}{\partial R_{EJ}^{km}}$	-17.75×10^{-6}	$+76.3\times10^{-6}$	0	-10.88×10^{-6}	-16.2×10^{-6}	$+76.2\times10^{-6}$	0	-10.23×10^{-6}	-16.41×10^{-6}	$+76.2\times10^{-6}$	0	-10.60×10^{-6}
$\frac{\partial(\ )}{\partial V_{HE}^{km/sec}}$	-1.11	-78.3	+336	+3.031	-1.17	-78.2	336	2.470	-0.65	-77.9	336	2.250
$\frac{\partial(\ )}{\partial R_p^{km}}$	1.7773×10^{-2}	$+0.9\times10^{-4}$	0	1.086×10^{-2}	1.2611×10^{-2}	$+0.6\times10^{-4}$	0	0.7925×10^{-2}	0.9973×10^{-2}	0.5×10^{-4}	0	0.6409×10^{-2}
$\frac{\partial(\ )}{\partial \tau(deg)}$	3.279	+0.009	0.03	+2.011	3.039	0.007	0.04	+1.916	3.1005	0.003	0.06	1.998
$\frac{\partial(\ )}{\partial \Delta V\ m/sec}$	-4.381	-0.096	0.32	-2.679	-3.076	-0.091	0.32	-1.936	-2.466	-0.086	0.32	-1.586

Table II-7 presents two other unique conditions. The antisolar target site $\left(\gamma_E = -35°\right)$ requires a deflection maneuver that moves the entry point across the center of planet (far side entry) and increases the sensitivities significantly. What these sensitivities mean in terms of actual entry dispersions for specific probe designs is discussed in Chapter III, Section C. The sensitivities can be reduced by decreasing the ΔV_{EJ} and increasing the application angle while maintaining acceptable entry angles of attack. A 5° change in τ is accompanied by a 15 m/sec change in ΔV_{EJ}.

Table II-7 also presents data for a retro thrusting deflection maneuver. The data indicate no substantial differences from the forward thrusting case.

The entry phase has as its objective the deceleration of the probe to low velocities at altitudes compatible with experiment operation. The accuracy of this entry path is influenced by errors in the initial entry position, entry velocity, entry flight path angle, entry ballistic coefficient, and atmosphere model being considered. The resulting errors are those of range, time of flight, altitude of specific velocities and dynamic loads and decelerations. Entry is assumed to start at an altitude of about 250 km above the surface radius of 6050 km. Winds and planetary rotation are ignored. Downrange errors in degrees of arc at entry are essentially translated into identical downrange errors of impact. Entry and descent geometry does not change the central angle of travel. Crossrange errors at entry tend to be reduced at impact because of the great circle nature of the descent path. At a point 90° downrange from the initial point, the crossrange errors would be reduced to zero. This 90° downrange point is a node of the nominal trajectory path and the path perturbed in crossrange. Errors in time of entry propagate directly to impact.

Table II-7 Far Side and Near Side Entry Conditions

$R_{EJ} = 4 \times 10^6$ km $\qquad$ $V_{HE} = 3.6$ km/sec

	Far Side Entry: $\gamma = -35°$, $\tau = -20°$				Near Side Entry: $\gamma_E = -65°$, $\tau = -160°$			
	ΔR (deg)	T (hr)	V_E (m/sec)	γ_E (deg)	ΔR (deg)	T (hr)	V_E (m/sec)	γ_E (deg)
Impact R_p = 2800 km								
$\frac{\partial(\ )}{\partial R_{EJ}\,km}$	58.13×10^{-6}	74.0×10^{-6}	0	36.802×10^{-6}	-5.23×10^{-6}	-75.3×10^{-6}	0	-3.394×10^{-6}
$\frac{\partial(\ )}{\partial V_{HE}\,km/sec}$	-10.45	-73.2	347	-3.471	-2.57	-76.1×10^{-6}	340	-0.109
$\frac{\partial(\ )}{\partial R_p\,km}$	-1.903×10^{-2}	-0.9×10^{-4}	0	-1.208×10^{-2}	1.15×10^{-2}	0.4×10^{-4}	0	0.764×10^{-2}
$\frac{\partial(\ )}{\partial \tau\,deg}$	-11.108	-0.090	0.15	-7.1140	1.0135	0.009	-0.02	0.6732
$\frac{\partial(\ )}{\partial \Delta V\ m/sec}$	3.2139	-0.053	0.33	2.0354	-1.9173	0.166	-0.32	-1.2737
Flyby R_p = 12600 km								
$\frac{\partial(\ )}{\partial R_{EJ}\,km}$	93.07×10^{-6}	$+73.3 \times 10^{-6}$	0	$+59.07 \times 10^{-6}$	-25.11×10^{-6}	$+75.9 \times 10^{-6}$	0	-16.571×10^{-6}
$\frac{\partial(\ )}{\partial V_{HE}\,km/sec}$	-20.99	-71.8	350	-10.214	4.94	-77.7	337	4.864
$\frac{\partial(\ )}{\partial R_p\,km}$	-1.14×10^{-2}	-0.6×10^{-4}	0	-0.728×10^{-2}	0.677×10^{-2}	0.2×10^{-4}	0	0.449×10^{-2}
$\frac{\partial(\ )}{\partial \tau\,deg}$	-18.043	-0.14	+0.24	-11.448	-4.906	-0.041	+0.11	-3.243
$\frac{\partial(\ )}{\partial V\ m/sec}$	3.167	-0.054	-0.33	+2.011	-1.944	0.067	-0.32	-1.2889

Entry velocity has no significant effect on the altitude of occurrence of events or time of flight. The time of flight varies less than 1 sec for each 456 m/sec (1500 fps). The maximum dynamic pressure and deceleration are directly functions of the entry velocity. The range to a specific event (i.t., M = 0.5) is insensitive to the entry velocity varying less than 0.00001°/m/sec.

The entry path angle accuracy is an important parameter. The trajectories with smaller entry angles are more sensitive to errors than the trajectories with steep entry angles. A lower limit of -20° has been established to ensure that the entry path does not encounter the large range sensitivities associated with trajectories near the skipout boundary as defined in Section C of this chapter. The maximum dynamic pressures and decelerations are a function of the sine of the entry angle. The time of occurrence of these maximums is a function of the inverse of the sine of the entry angle. The time to M = 0.5 is shown in Fig. II-48. The altitude of occurrence of an event is only slightly affected by the entry angle; the altitude for M = 1 varying about 4 km (13,000 ft) for entry angles between -30° and -90°. This variation is shown in Fig. II-49. The events at lower altitudes exhibit less altitude variation. The range from entry to M = 0.5 is defined in Fig. II-50. The time of flight and range sensitivity to entry angle errors are presented in Fig. II-51 and II-52. The altitude of event occurrence sensitivity to entry angle errors is always less than 0.15 km/deg.

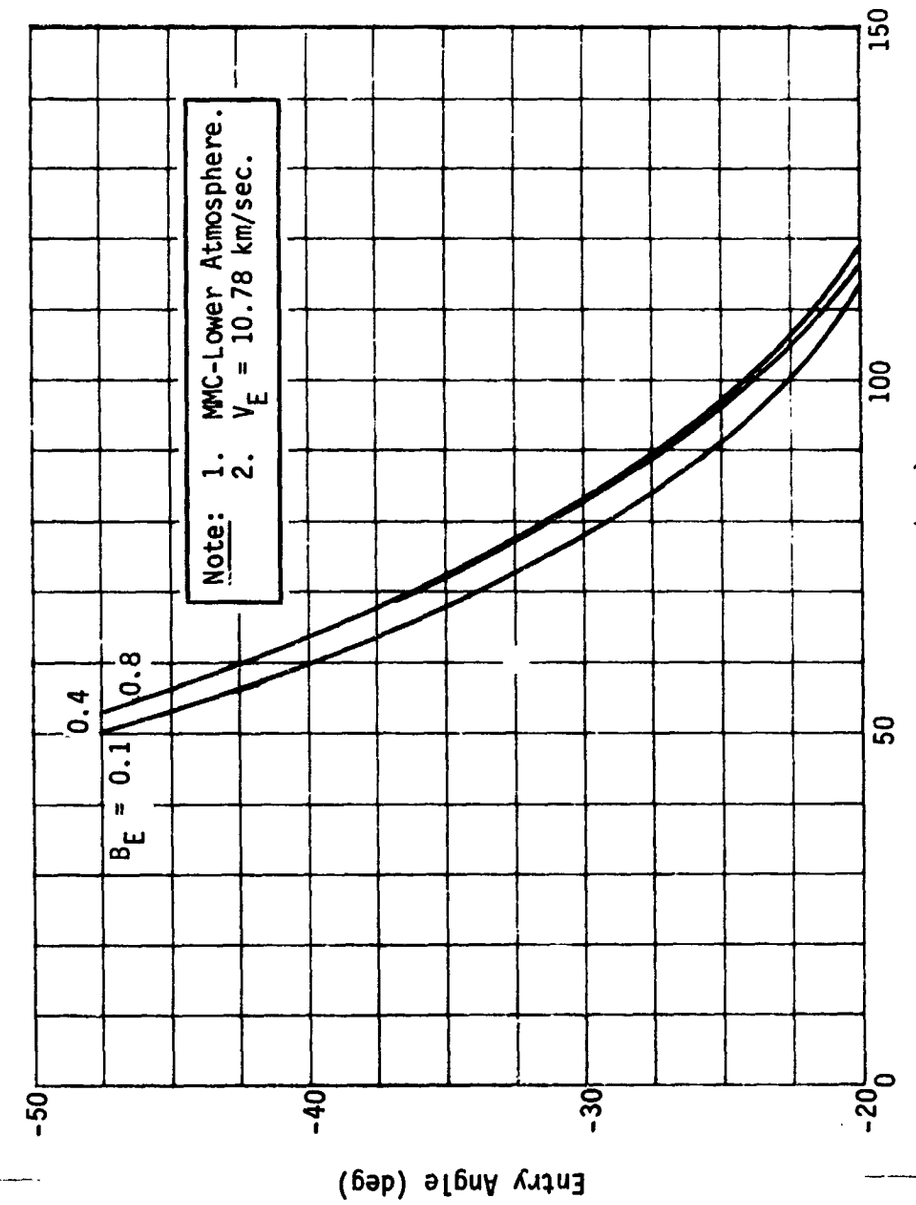


Fig. II-43 Time to M = 0.5

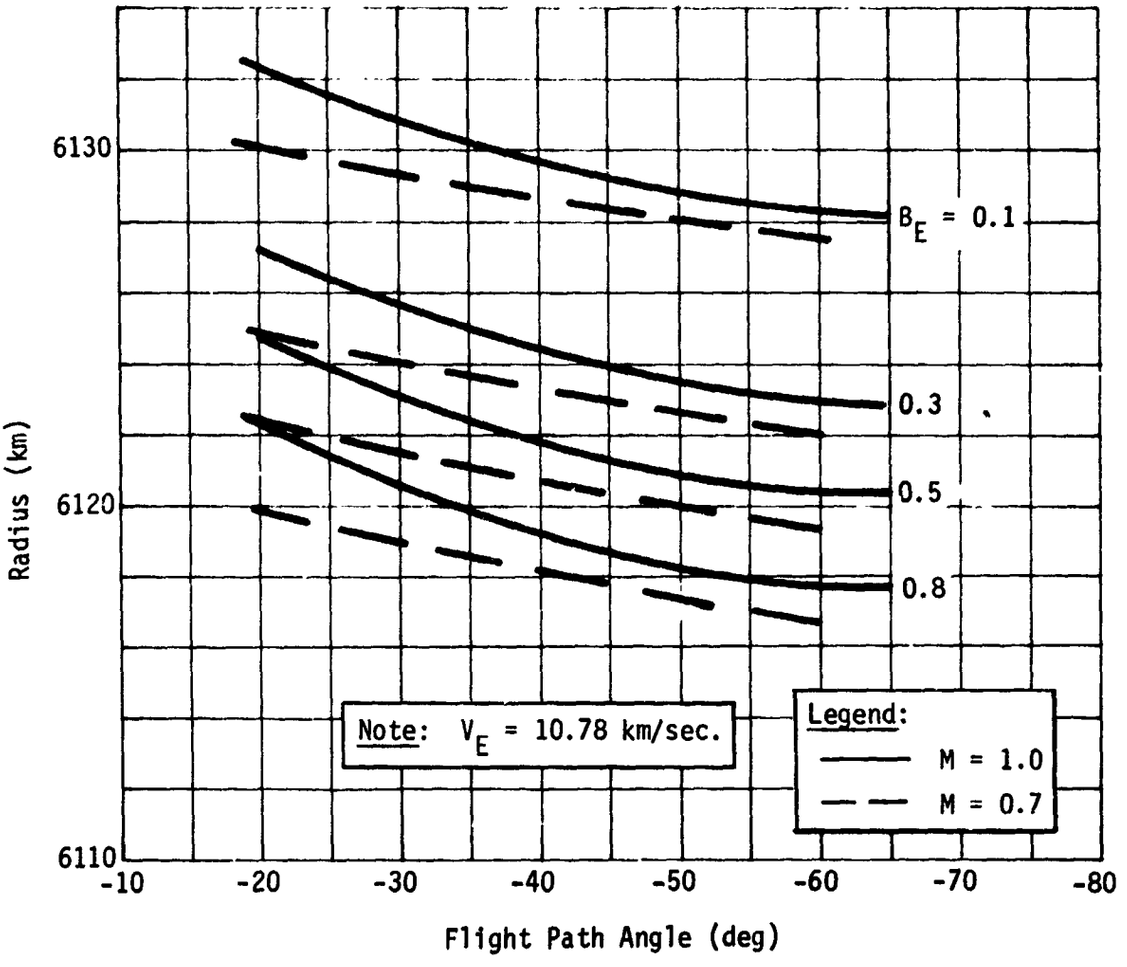


Fig. II-49 Deceleration Altitudes

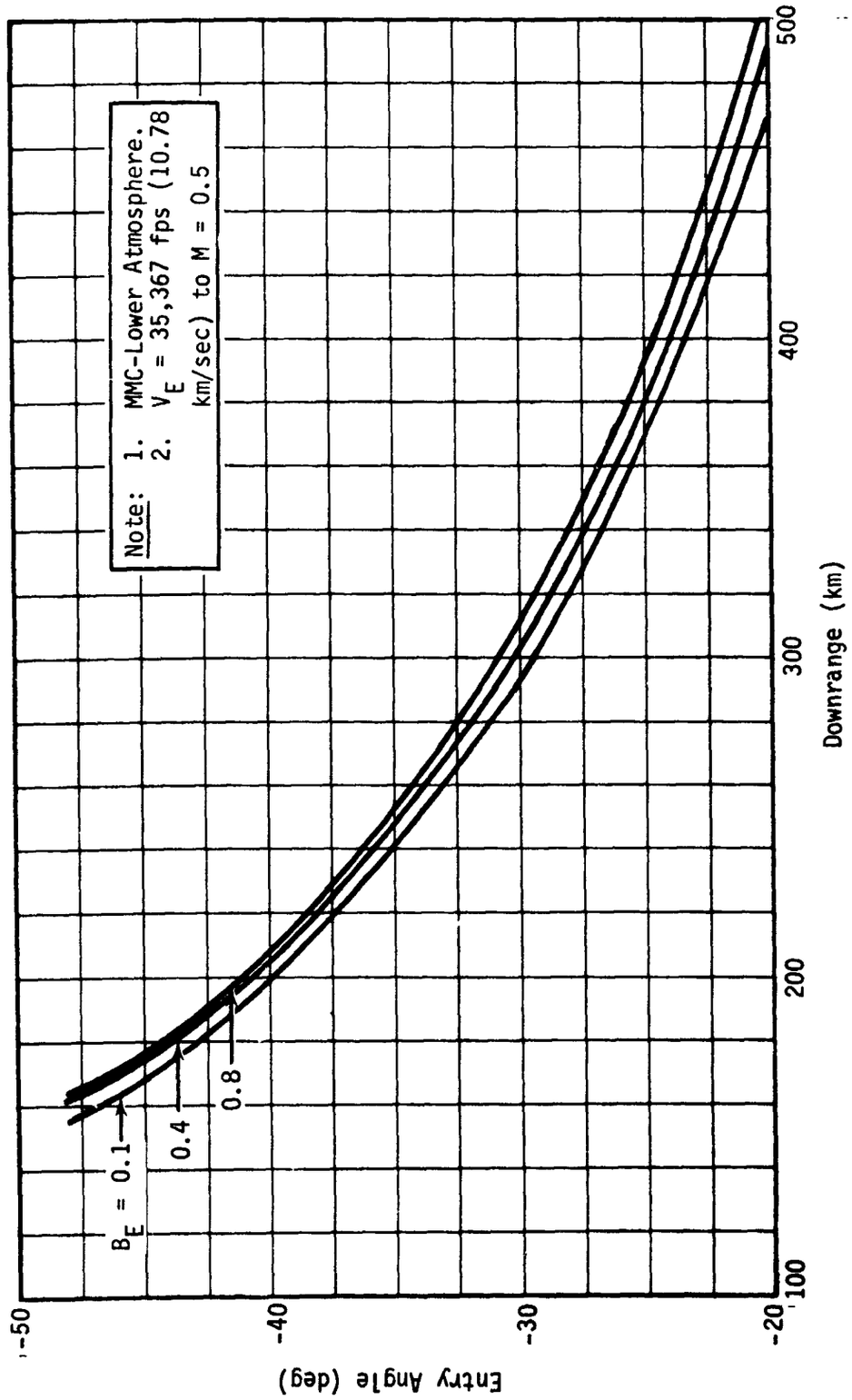


Fig. II-50 Range to M = 0.5

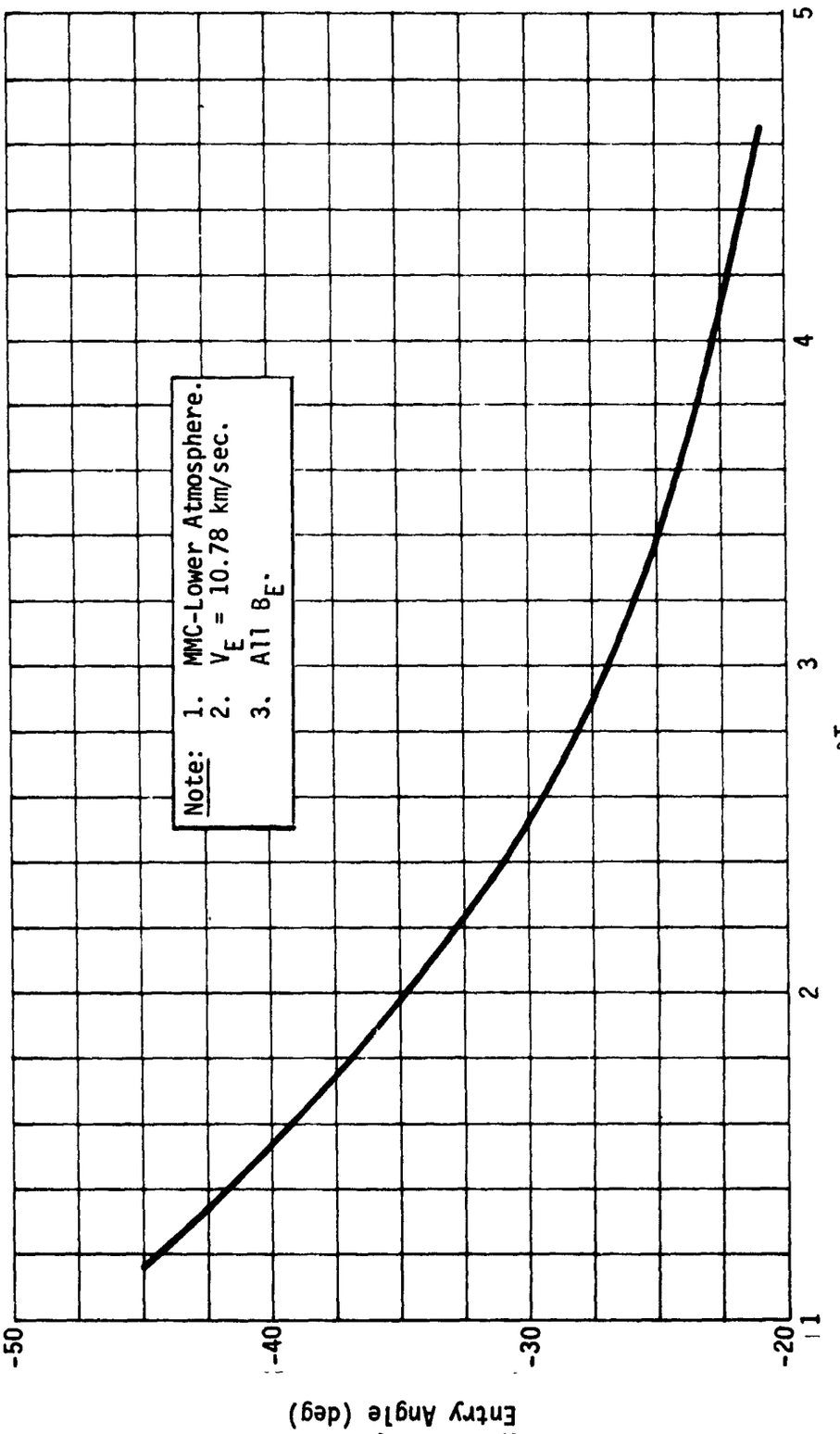


Fig. II-51 Time Sensitivity to Path Angle Errors

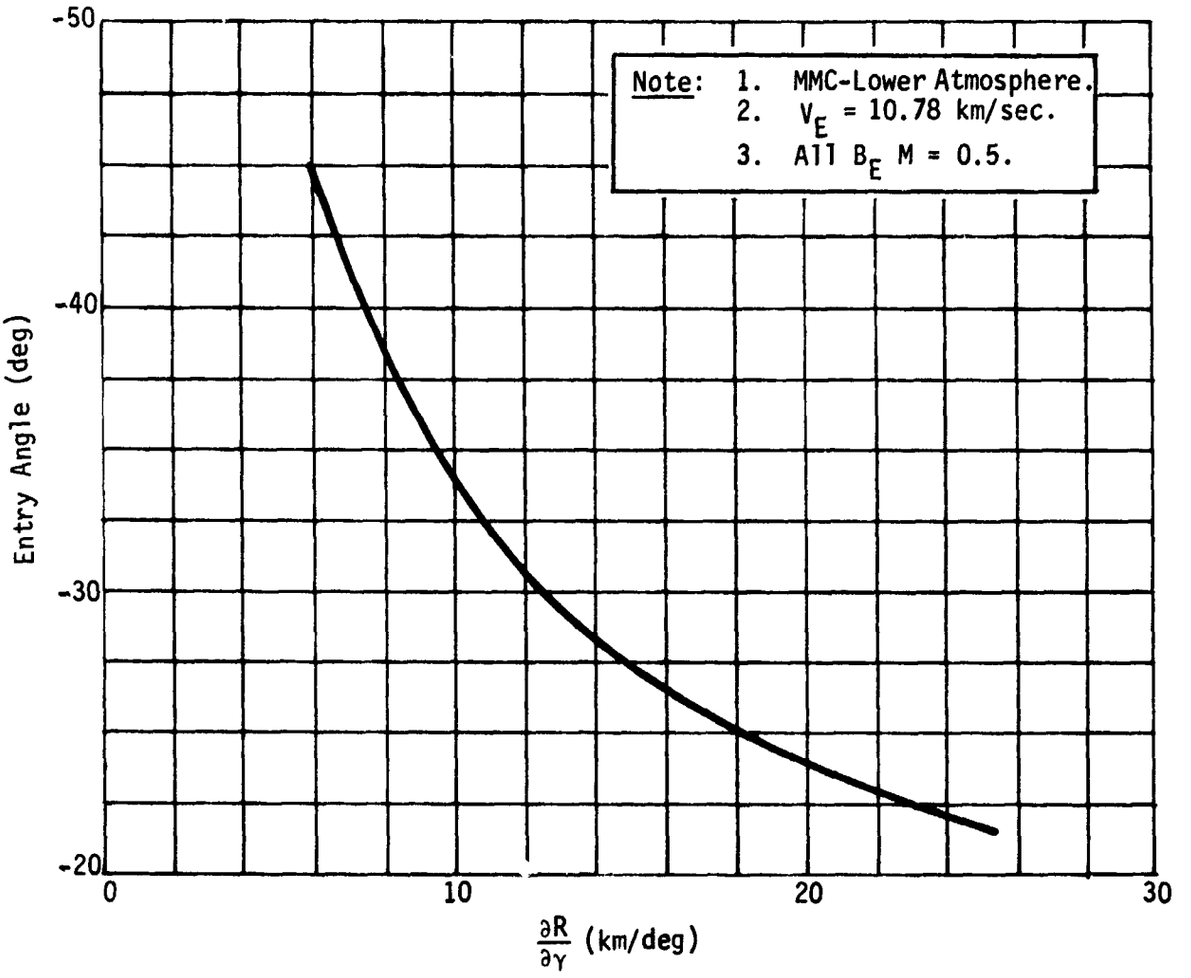


Fig. II-52 Range Sensitivity to Path Angle Errors

The ballistic coefficient has very little effect on the maximum deceleration. The maximum dynamic pressure increases with increasing B_E. The ballistic coefficient exhibits no effect on the range and time-of-flight sensitivities of Fig. II-51 and II-52. However, the absolute values of range and time of flight vary slightly with B_E; increasing with increasing B_E. The time of flight variation is of the order of 4.4 sec/slug/ft^2 at entry angles of -30°. A 10% error in B = 0.4 results in less than 0.2 sec in time. The effect on range is about 0.14°/slug/ft^2 at -30° and less than 0.05°/slug ft^2 at -60°. The altitude of occurrence of an event varies as shown in Fig. II-53. The altitude of M = 1.0 varying on the order of 10 km for B_E's varying from 0.1 to 0.8. The entry angle does not significantly affect the sensitivities and altitude variation of lower and higher events does not change significantly.

Different atmospheres affect the descent profile principally in the altitudes of events and the attendant time variations. The atmosphere models create a maximum altitude variation at M = 0.5 of 3.4 to 4.2 km (11,000 to 13,000 ft) which results in time errors of 0.4 to 0.6 sec. The range variation to M = 1.0 is 0.02° for B - 0.4 at -25° γ_E.

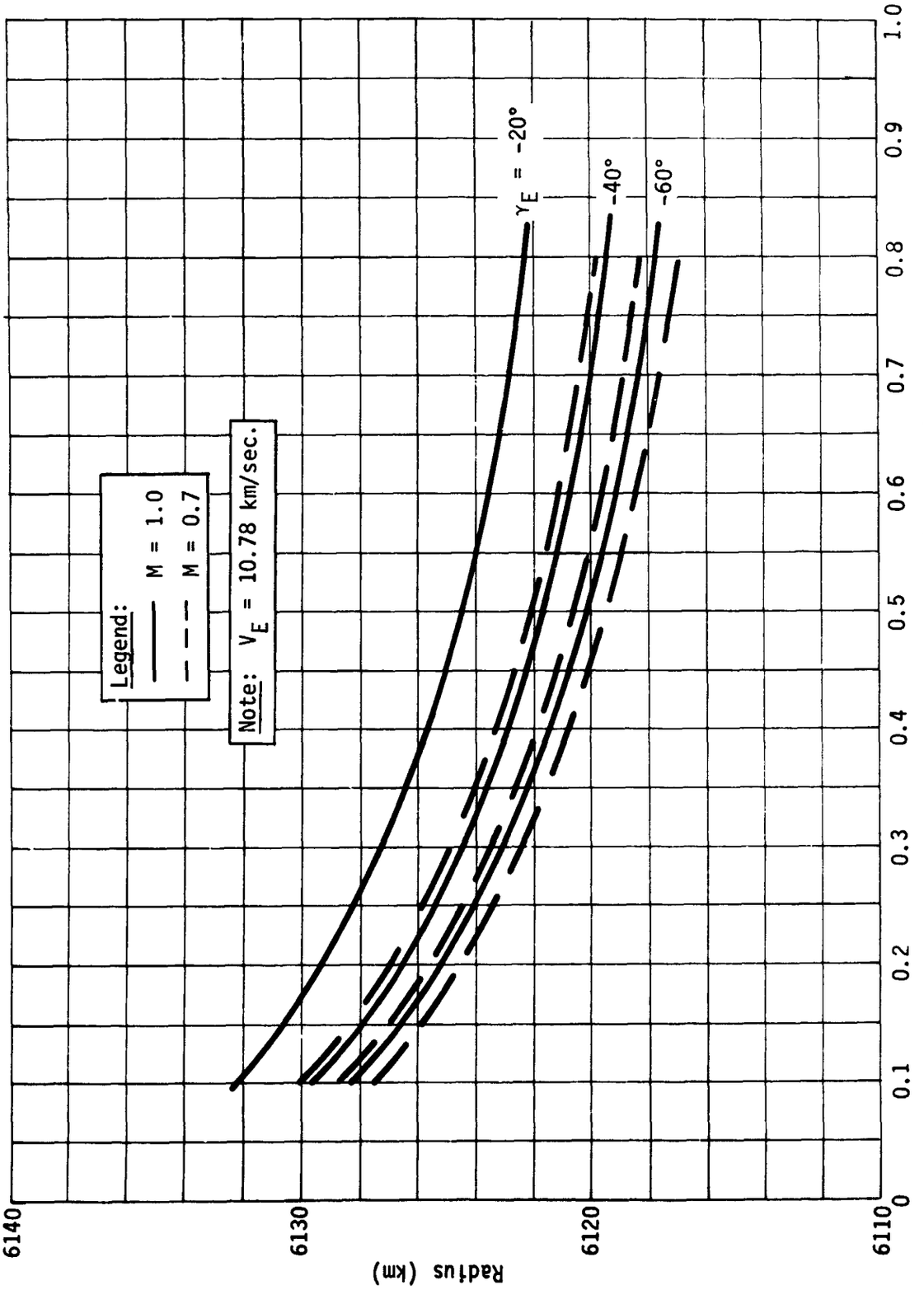


Fig. II-53 Deceleration Altitudes

Hence for the entry portion of flight the principal errors result from range variations due to entry angle errors and altitude variations from atmosphere model differences. Entry velocity errors create no significant errors during the entry profile. Similarly the ballistic coefficient errors are not significant during entry. The entry angle errors produce between 5 and 18 km of range error for each degree of entry angle error. This is equivalent to 0.05 to 0.18° of range and is negligible. The differences in atmosphere models result in 3 to 4 km difference in altitudes to start descent. On top of this, a g sensor good to 0.01 g will result in about 0.1 km altitude difference. Time and range differences are negligible.

The entry error sensitivities are defined in Table II-8 where a range of values indicates the variation for entry angles between -20°and -60°. The atmosphere effects are for differences between the lower density model and the V5M. The deceleration values indicate the sensing accuracy for events sequenced from specific deceleration points near 0.1 g.

The descent portion of the flight path is essentially vertical and at terminal velocity. Therefore, in the absence of winds, the descent portion of the flight does not contribute to range dispersions. Only velocity and time-of-flight dispersions result from descent condition errors. These dispersions are a result of uncertainty in the altitude of initial deceleration conditions, subsequent staging ballistic coefficients, and the altitudes of staging. The altitudes of deceleration and staging are affected by the method of initiating the operations and the atmospheric model variations. The uncertainty in initial deceleration conditions includes range, altitude, and time of flight. The range errors and time of flight errors will map directly to impact.

Table II-8 Entry Dispersions

Error Source	Sensitivity	Value
ΔV_E	$\frac{\partial t}{\partial V_E}$	0.00219 sec/m/sec
	$\frac{\partial R}{\partial V_E}$	<0.00001 deg/m/sec
	$\frac{\partial h}{\partial V_E}$	0
$\Delta \gamma_E$	$\frac{\partial t}{\partial \gamma_E}$	1 to 3 sec/deg
	$\frac{\partial R}{\partial \gamma_E}$	5 - 25 km/deg or 0.05 to 0.25°/deg
	$\frac{\partial h}{\partial \gamma_E}$	0.075 to 0.15 km/deg
ΔB_E	$\frac{\partial t}{\partial B_E}$	2.4 to 4.4 sec/slugs/ft^2
	$\frac{\partial R}{\partial B_E}$	0.05 to 0.14°/slug/ft^2
	$\frac{\partial h}{\partial B_E}$	1.4 km/slug/ft^2
ΔAtmosphere Model	$\frac{\partial t}{\partial A}$	0.6 sec
	$\frac{\partial R}{\partial A}$	0.02°
	$\frac{\partial h}{\partial A}$	3.4 to 4.2 km
Increasing Deceleration	$\frac{\partial t}{\partial g}$	10 sec/g (at 0.1 g)
	$\frac{\partial R}{\partial g}$	1°/g (at 0.1 g)
	$\frac{\partial h}{\partial g}$	48.6 km/g (at 0.1 g)
Decreasing Deceleration	$\frac{\partial t}{\partial g}$	50 sec/g (at 0.1 g)
	$\frac{\partial R}{\partial g}$	0.03°/g (at 0.1 g)
	$\frac{\partial h}{\partial g}$	9.1 km/g (at 0.1 g)

The uncertainty in the ballistic coefficient is a result of uncertainties in size, weight, and drag coefficient. A 10% error in ballistic coefficient will yield a 5% error in local terminal velocity, and therefore a 5% error in total descent time.

Staging presents a transient period that is so short in time and small in altitude that it is ignored in this analysis. Typical times for these transients are 5 to 30 sec and typical altitude ranges are less than 1.8 km.

The altitude of staging is a function of the means of sensing the staging conditions. Staging could be done at equal altitudes based on radar altimeter data or similar instrumentation. If the atmosphere model varied from the lower density to the upper density case for this study then the time of flight would vary by 35% when staging was at equal altitudes. Staging at equal pressures can be used, and in this case the staging times would vary only slightly since the altitudes for equal pressure are separated by about 3 km.

In this case staging would occur earlier in the more dense model offsetting the longer distance to descend and slower terminal velocities at equivalent altitudes.

It appears that a deflection strategy can be defined which, when coupled with reasonable spacecraft guidance and navigation accuracies, will yield in-plane entry position errors of less than ±6° (1σ) and entry angle errors of less than ±4.0° (1σ). The arrival time can be off by about ±6 minutes. The entry conditions will not affect these results, but can yield an initial descent altitude that is about ±4 km in error. The descent time will be affected by the initial altitude error and, depending on the subsequent staging, the time differences can be significant. Descent parameters such as ballistic coefficient also affect the time. Each particular probe is examined to define this effect.

F. PLANETARY VEHICLE - BASELINE FLYBY AND IMPACTING TRAJECTORIES

The planetary vehicle approaches the planet Venus in the plane containing the V_{HE}, the $\gamma_E = -50°$ subsolar target point, and the planet center. The baseline launch, interplanetary cruise, and encounter trajectory parameters are noted in Table II-9. The encounter geometry is presented in Fig. II-54. For the October 31, 1975 arrival date the cone angle near encounter is about 80° and the clock angle is 315°.

The radius of periapsis affects the deflection maneuver, the impact parameter and the targeting accuracies. For a flyby trajectory, the periapsis radius will be greater than the 6300 km radius of the planet and its significant atmosphere. The accuracy analysis of Section E indicates that a 1000 km error in periapsis radius can result from one midcourse correction. More than one correction will reduce the error in periapsis radius to 100 km or less. To assure a nonimpacting path the flyby case is defined at a periapsis radius of 12,600 km. The periapsis point will be toward the light side of the planet in the plane defined above.

For the impacting planetary vehicle the periapsis radius is established as 2800 km. This radius yields a planetary vehicle entry at $\gamma_E = -50°$ near the subsolar point (point 1, Fig. II-55) without utilizing a deflection maneuver.

A review of key differences between the planetary flyby and impacting cases indicates that the flyby path requires about 40 m/sec more ΔV_{EJ} for each deflection maneuver and results in entry angles of attack up to 15° less than the impacting case (Fig. II-27 and II-25, respectively). For similar targeting requirements the time staggering is less favorable for the flyby case than for the impacting case (Fig. II-28). The target dispersions are greater for the flyby path than for the impacting path.

Table II-9 Launch, Interplanetary Cruise, and Encounter Parameters for Venus

LAUNCH PARAMETERS	
LAUNCH VEHICLE	TITAN III C WITH XX25 PAYLOAD FAIRING (25FEET. OVERALL LENGTH)
LAUNCH PERIOD	5/15/75 TO 6/4/75
SPACECRAFT	MODIFIED MARINER 69
PAYLOAD WEIGHT	4000 LBS
FAIRING SEPARATION	280 SECONDS
LAUNCH AZIMUTH	114 DEGREES (MAX)
PARKING ORBIT ALTITUDE	100 NAUTICAL MILES
INTERPLANETARY CRUISE PARAMETERS	
TRAJECTORY	TYPE II
DECLINATION OF LAUNCH ASYMPTOTE	
DLA	5.4 TO 8.7 DEGREES
RIGHT ASCENSION	167-155 DEG (APPROX)
INJECTION ENERGY. C3	6.8 KM2/SEC2
FLIGHT TIME	159/149 DAYS
PERIHELION RADIUS	107.800.000 KM
ECCENTRICITY	0.170
INCLINATION TO ECLIPTIC	0.4-7.0 DEGREES (APPROX)
CENTRAL ANGLE OF TRAVEL	200-184 DEGREES (APPROX)
ENCOUNTER PARAMETERS	
VENUS ARRIVAL DATE	10/31/75 (CONSTANT)
EXCESS VELOCITY. VHE	3.68 KM/SEC
DEC OF VHE VECTOR	37.5 DEGREES (APPROX)
RA OF VHE VECTOR	69-76 DEGREES (APPROX)
TRUE ANOMALY AT ARRIVAL	7 - 4 DEGREES (APPROX)
COMMUNICATION RANGE	95.000.000 KM

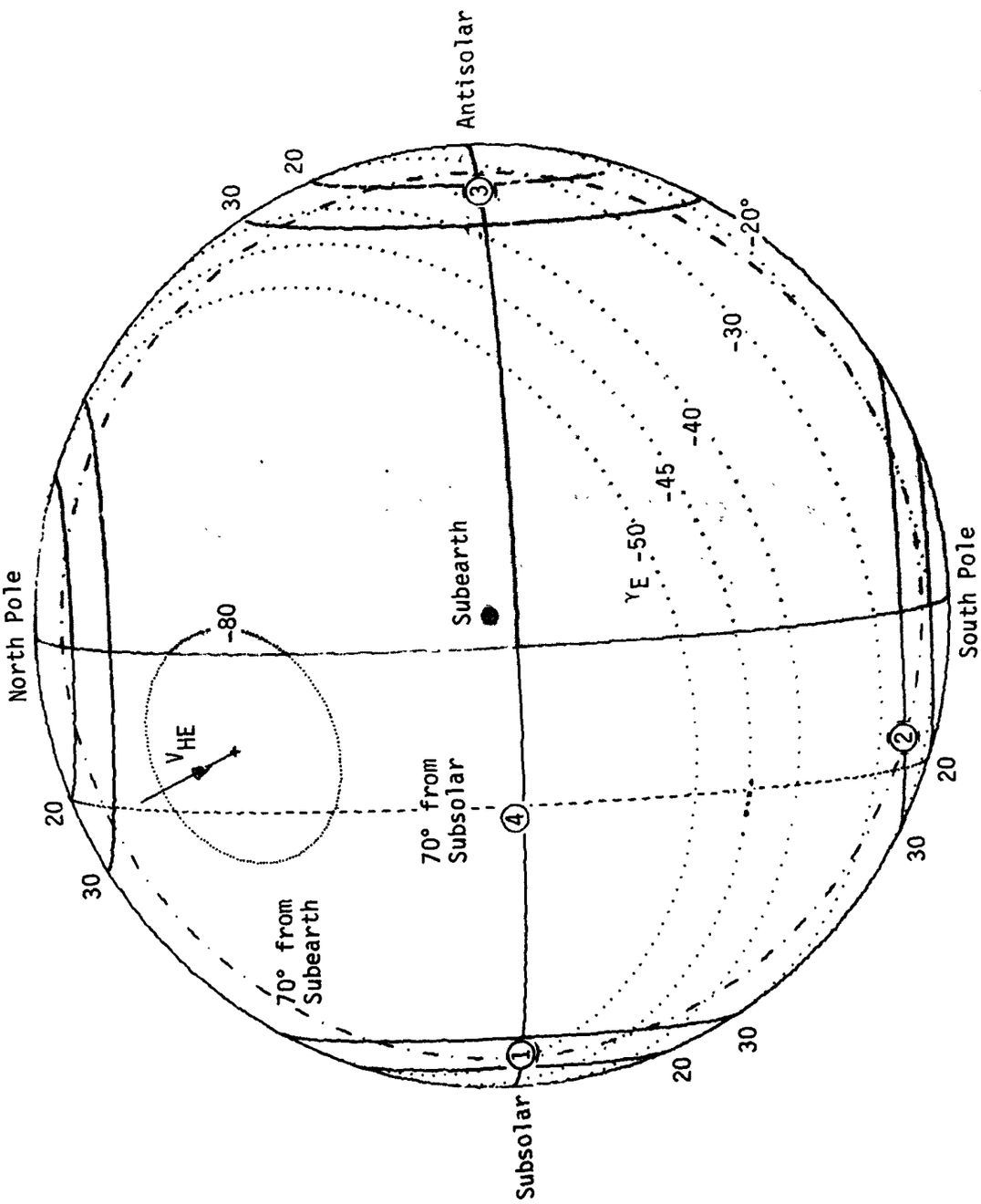


Fig. II-54 Venus as Seen from Earth on October 31, 1975, Type II 5/30 LD

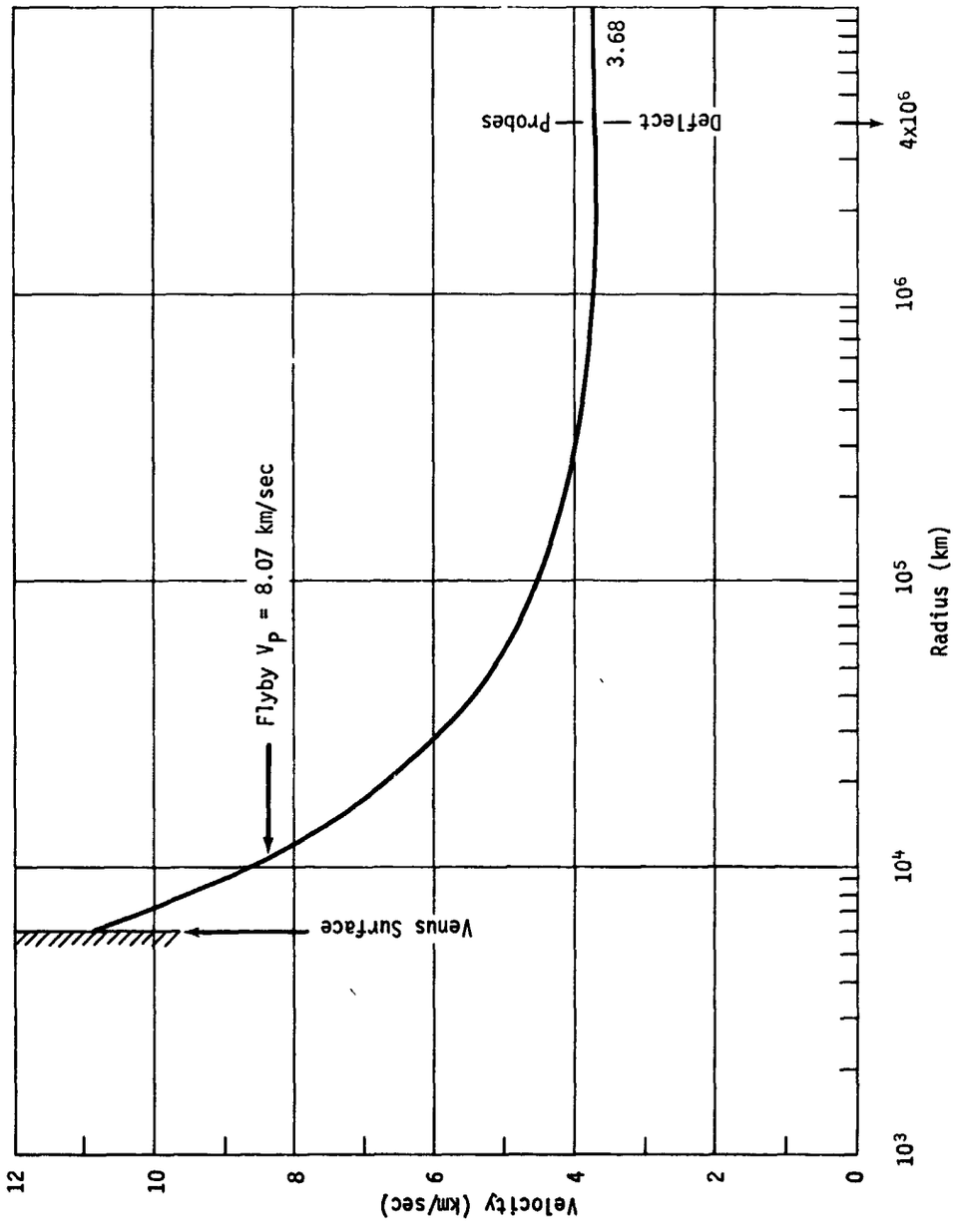


Fig. II-55 Spacecraft Velocity vs Radius (Input and Flyby)

The planetary vehicle reaches periapsis 293.9 hr after the deflection maneuver and the large probe enters 290.4 hr after deflection. For the impacting case both Planetary Vehicle and large probe enter 293.3 hr after deflection.

The variation in velocity as the planet is approached is noted in Fig. II-55 for both flyby and impacting spacecraft. This velocity variation yields the times shown on Fig. II-56. From these data the time to various radii can be defined. The time to 2 Venus radii is about 14 minutes and the time to 5 Venus radii is about 1 hr for the impacting case.

Planetary vehicle entry dispersions for the impacting case are defined in Chapter III, Section B.

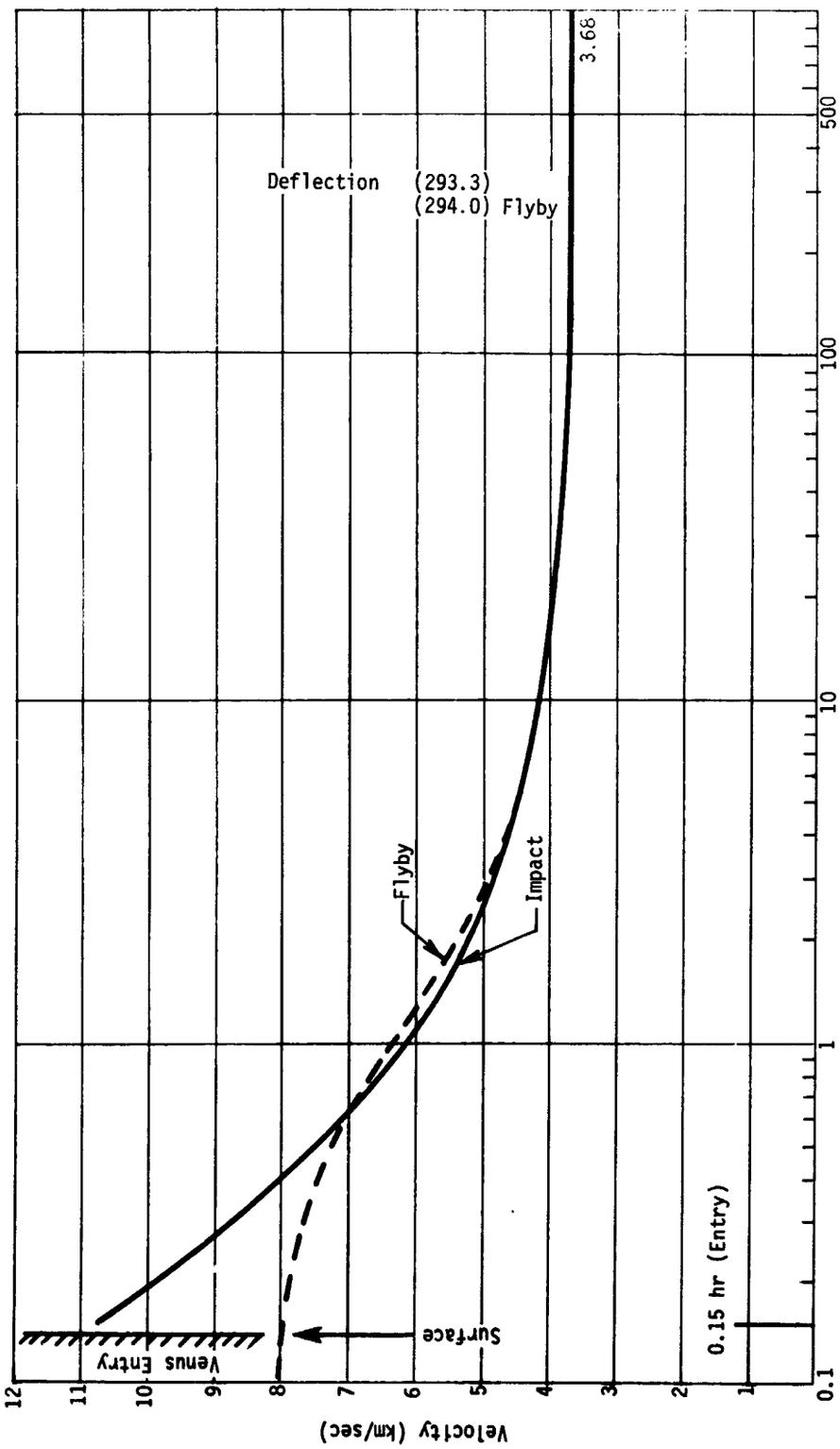


Fig. II-56 Spacecraft Velocity History

G. BASELINE ENGINEERING MODEL ATMOSPHERES

The Statement of Work required a "definintion of ... planetary environment models for development of the baseline mission design. The entry and descent requirements shall be based on the Venus environment models specified ... (in NASA SP-8011) ... for a nominal surface pressure range of 70 to 150 earth atmospheres." It further states that "the atmospheric parameter range for which the entry probe systems must be capable of accomplishing mission requirements shall be determined by tradeoff of subsystem design penalties and the most probable ranges of parameters. Final selection of the baseline range for the probe system design shall be reviewed and approved by JPL."

1. NASA SP-8011 Model Atmospheres

The atmospheric structure for the six models given in NASA SP-8011 is illustrated in Fig. II-57 thru II-59. Table II-10 lists some basic data for these models. Note that the surface pressure is 16.7 bars at 6078 km radius for models V2, V4, and V6, while it is 169 bars at 6048 km radius for models V1, V3, and V5. As can be seen from Fig. II-57, above about 6190 km the temperature profiles for models V1, V3, and V5 are essentially the same as those for models V2, V3, and V5, respectively, while all models have about the same profile below 6190 km. Further examination of the figures shows that models V2 and V5 represent extremes in all cases.

Models V2 and V5 must be modified to encompass the nominal surface pressure range of 70 to 150 earth atmospheres. Figure II-60 shows the pressure profiles in the lower atmosphere for models V2 and V5. The most straightforward modifications entail extrapolating the model V2 adiabatically down to 70 atmospheres

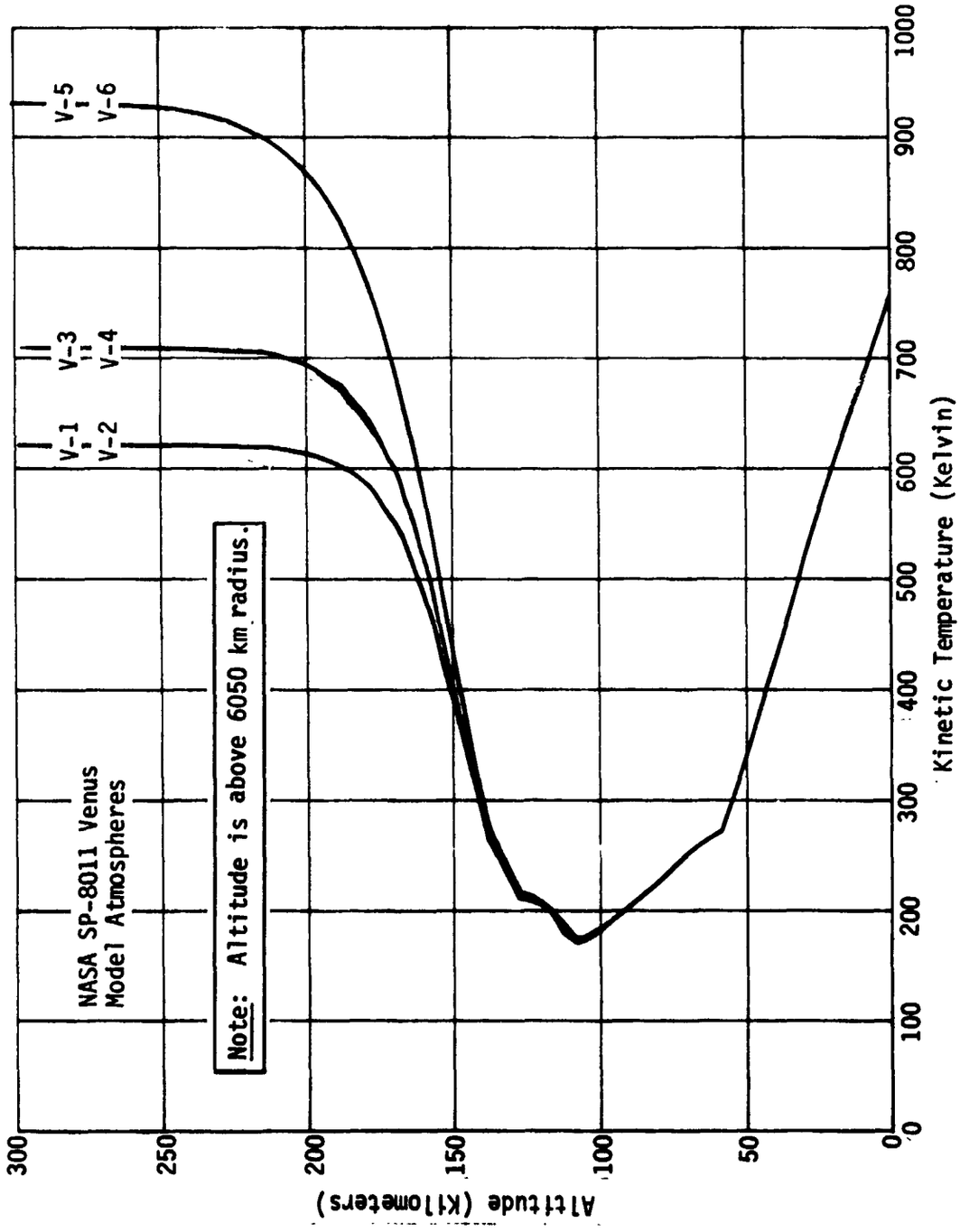


Fig. II-57 Kinetic Temperature vs Altitude

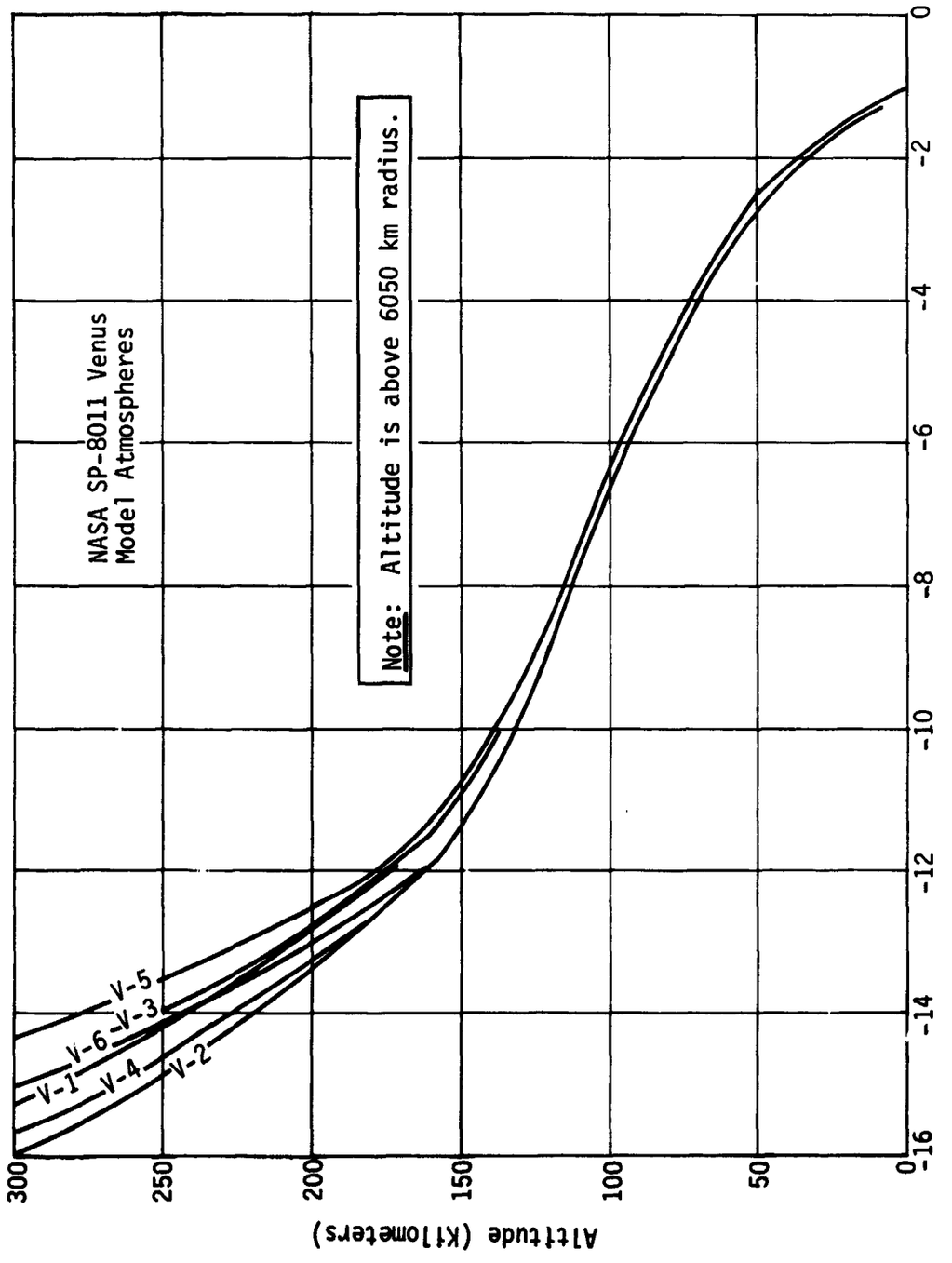


Fig. II-58 Mass Density vs Altitude

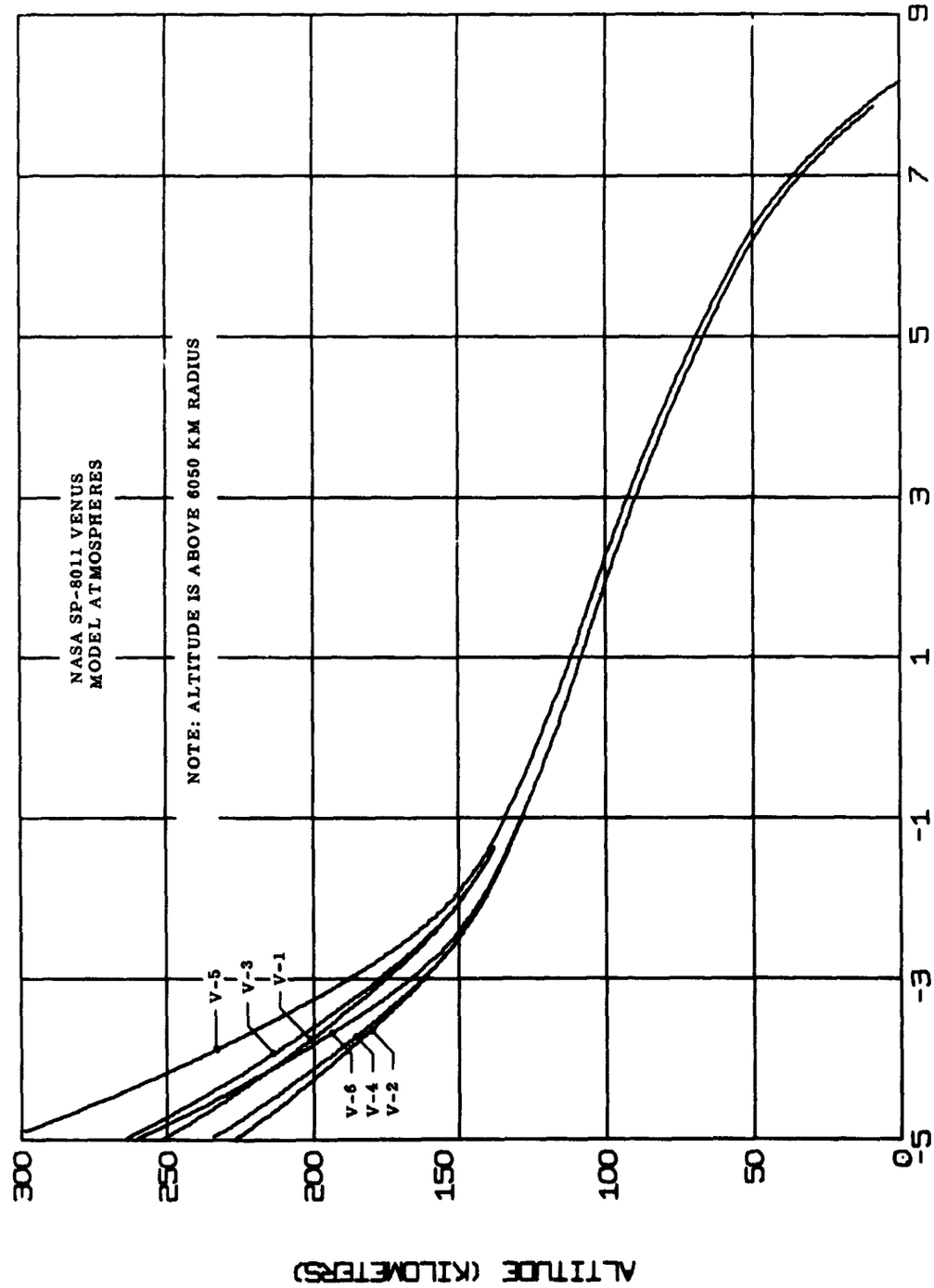


Fig. II-59 Pressure vs Altitude

Table II-10 NASA SP-8011 Models of Venus Atmosphere (1968)

PARAMETERS	Minimum Solar Activity		Mean Solar Activity		Maximum Solar Activity	
	High Density (Model V-1)	Low Density (Model V-2)	High Density (Model V-3)	Low Density (Model V-4)	High Density (Model V-5)	Low Density (Model V-6)
Planetary Radius (km)	6048	6078	6048	6078	6048	6078
Surface Gravity (cm/sec^2)	888.1	879.4	888.1	879.4	888.1	879.4
Surface Pressure (atm)	167	16.4	167	16.4	167	16.4
Surface Temperature (°K)	770	534	770	534	770	534
Exospheric Temperature (°K)	625	625	710	710	931	931
Below the Turbopause						
1. Composition (percent by volume)						
N_2	10		10		10	
CO_2	90	100	90	100	90	100
2. Molecular Mass (grams/gram-mole)	42.4	44.0	42.4	44.0	42.4	44.0
At the Turbopause						
1. Composition (percent by volume)						
N_2	10		10		10	
CO_2	87.73	99.98	87.73	99.98	87.73	99.98
CO	1.125		1.125		1.125	
O	1.125		1.125		1.125	
He	0.01	0.01	0.01	0.01	0.01	0.01
H_2	0.01	0.01	0.01	0.01	0.01	0 01
2. Molecular Mass (grams/gram-mole)	41.9	44.0	41.9	44.0	41.9	44.0
3. Density ($grams/cm^3$)	3.6×10^{-11}	3.6×10^{-11}	3.6×10^{-11}	3.6×10^{-11}	3.6×10^{-11}	3.6×10^{-11}

and terminating the model V5 at 150 atmospheres as shown in Fig. II-60 and II-61. For convenience, the surface radii in the two modified models are taken as 6059 km for V2M and 6050 for V5M, resulting in surface pressures of 7188 bars (70.95 atm) for V2M and 150.07 bars (148.12 atm) for V5M. Appendix F gives a tabulation of the pressure, temperature, and density for these modified models.

2. Mariner and Venera Data

The Mariner 5 S-band occultation experiment has provided a radius referenced refractivity profile of the Venus atmosphere between about 6085 and 6130 km radius. From these data and a knowledge of the composition from Veneras 4, 5, and 6, the density, pressure, and temperature profiles can be computed. Figures II-62 thru II-66 illustrate the profiles computed from the Mariner data and compare them to other models. As can be seen, the GSFC 3609 model and the MMC-Lower model agree well with the data, but lie outside the range of the SP-8011 models.

3. Recommended Study Models

In order to ensure deceleration to low speeds above the cloud tops, it was recommended that a model which bounds the Mariner/Venera data be used for the entry and descent studies. This model (MMC-Lower) is shown in Fig. II-64 thru II-70 and is tabulated in Appendix F. The model assumes a composition of 95% CO_2 and 5% N_2 (M = 43.21 g/g-mole) at all altitudes. The linear temperature profile approximates the Mariner 5 95% CO_2 data and an adiabatic extrapolation to a surface at 6045 km radius as shown in Fig. II-65 and II-68. The resulting lower atmosphere pressure and density profiles are shown in Fig. II-69 and II-70.

The models MMC-Lower and V5M were approved by JPL as representing the baseline range of atmospheric parameters for use in the system design studies. The V2 model was not used in the study.

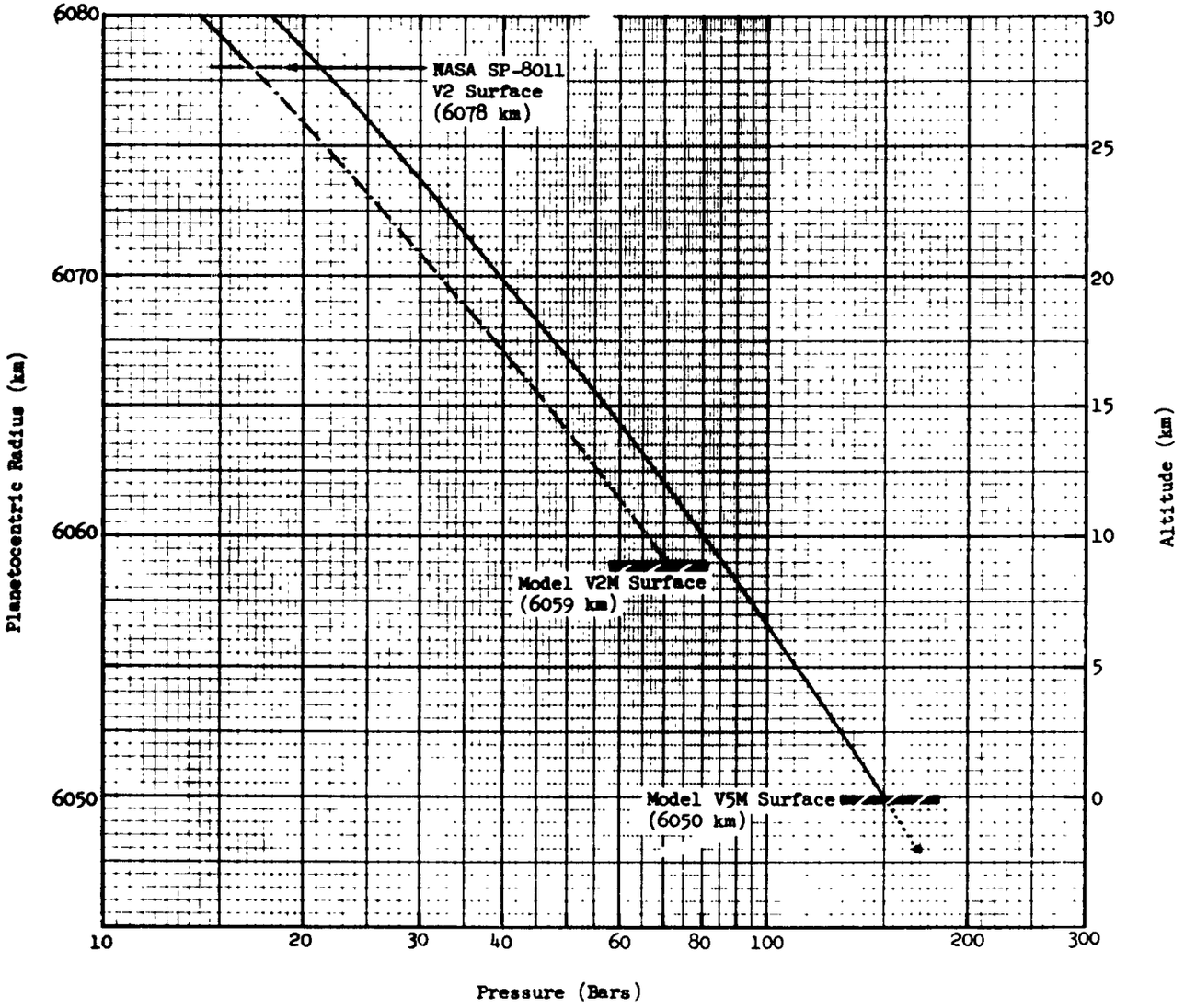


Fig. II-60 Pressure Profiles for Venus Lower Atmosphere

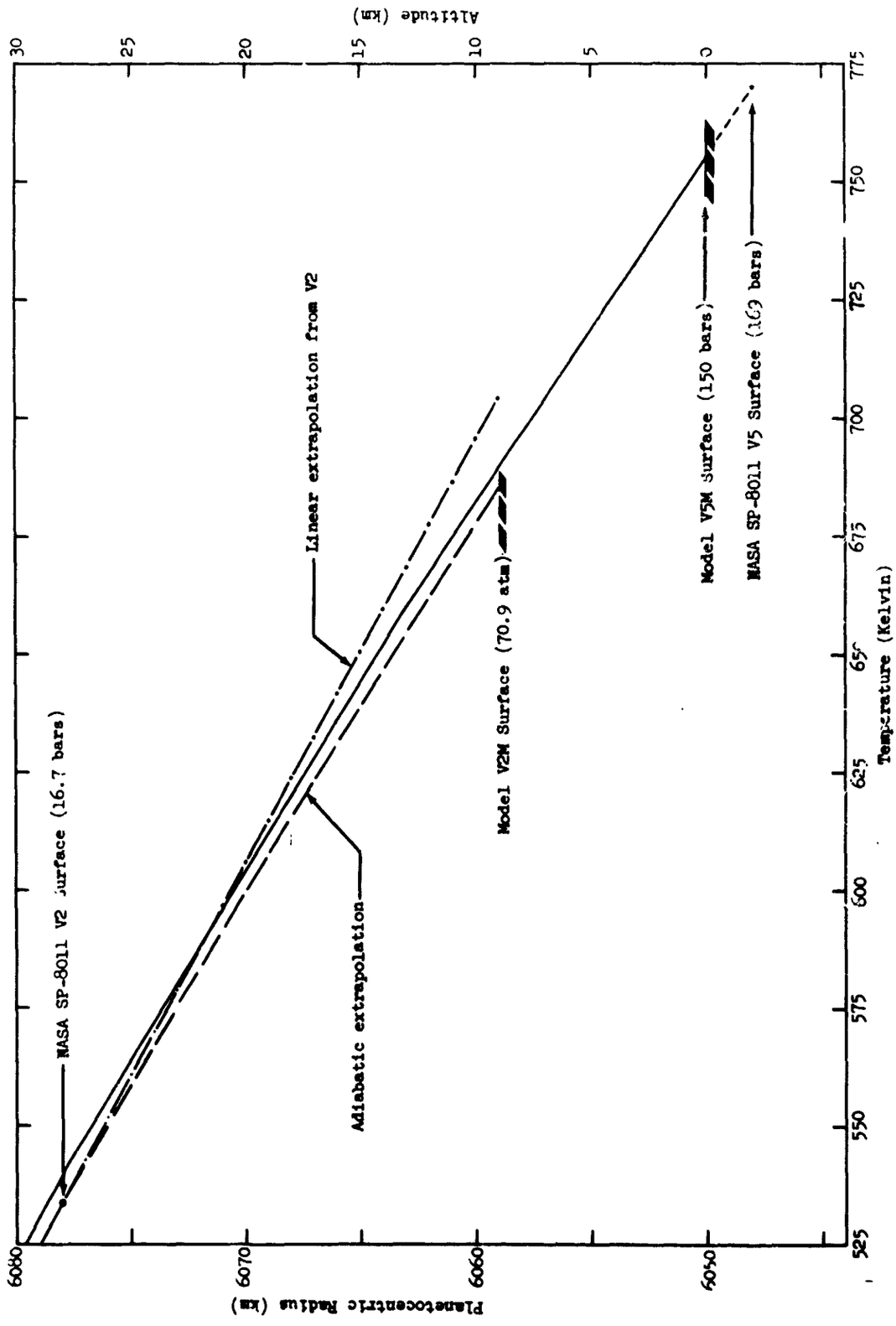


Fig. II-61 Temperature Profiles for Venus Lower Atmosphere

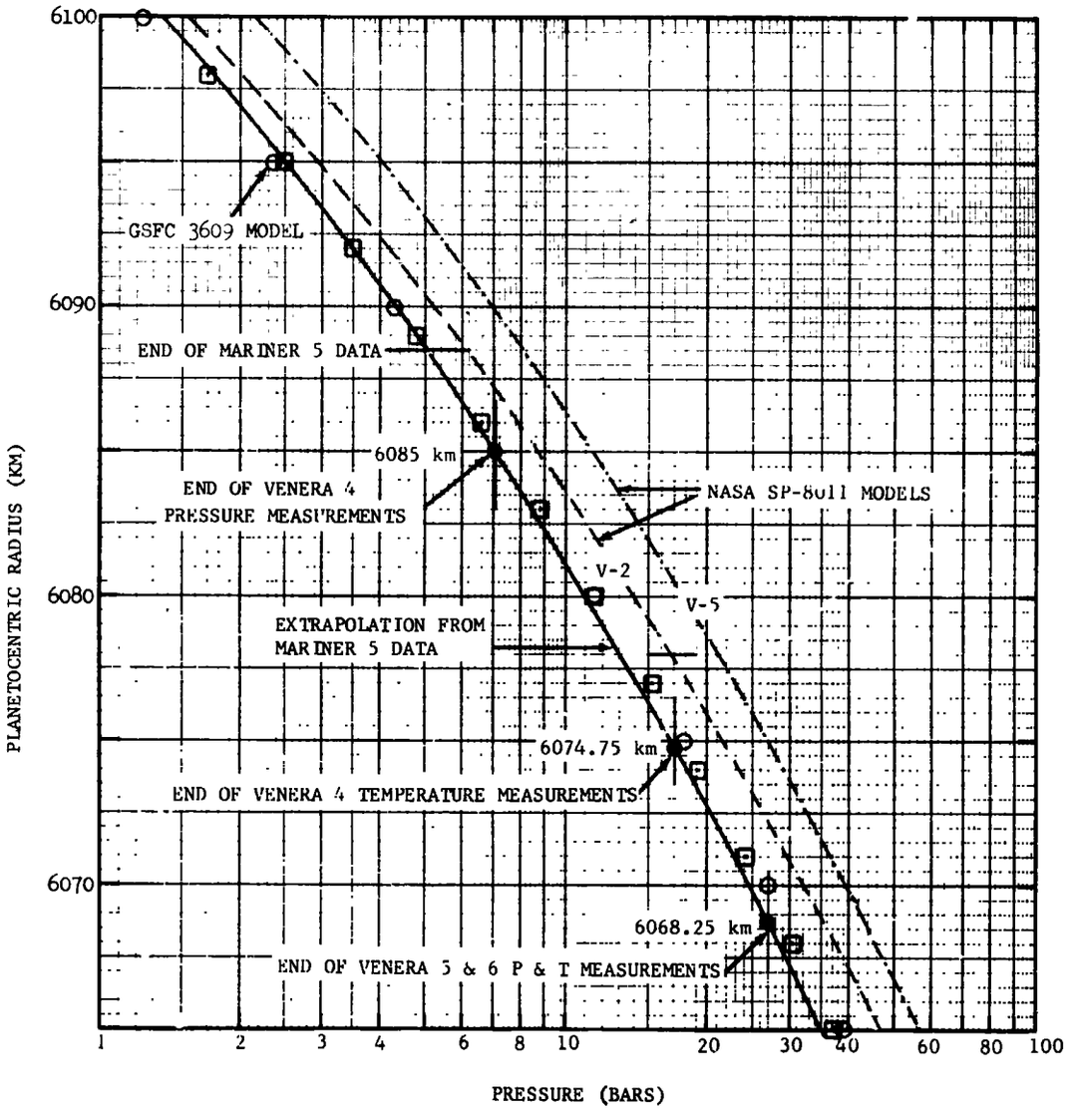


Fig. II-62 Comparison of Mariner/Venera Data and Various Models

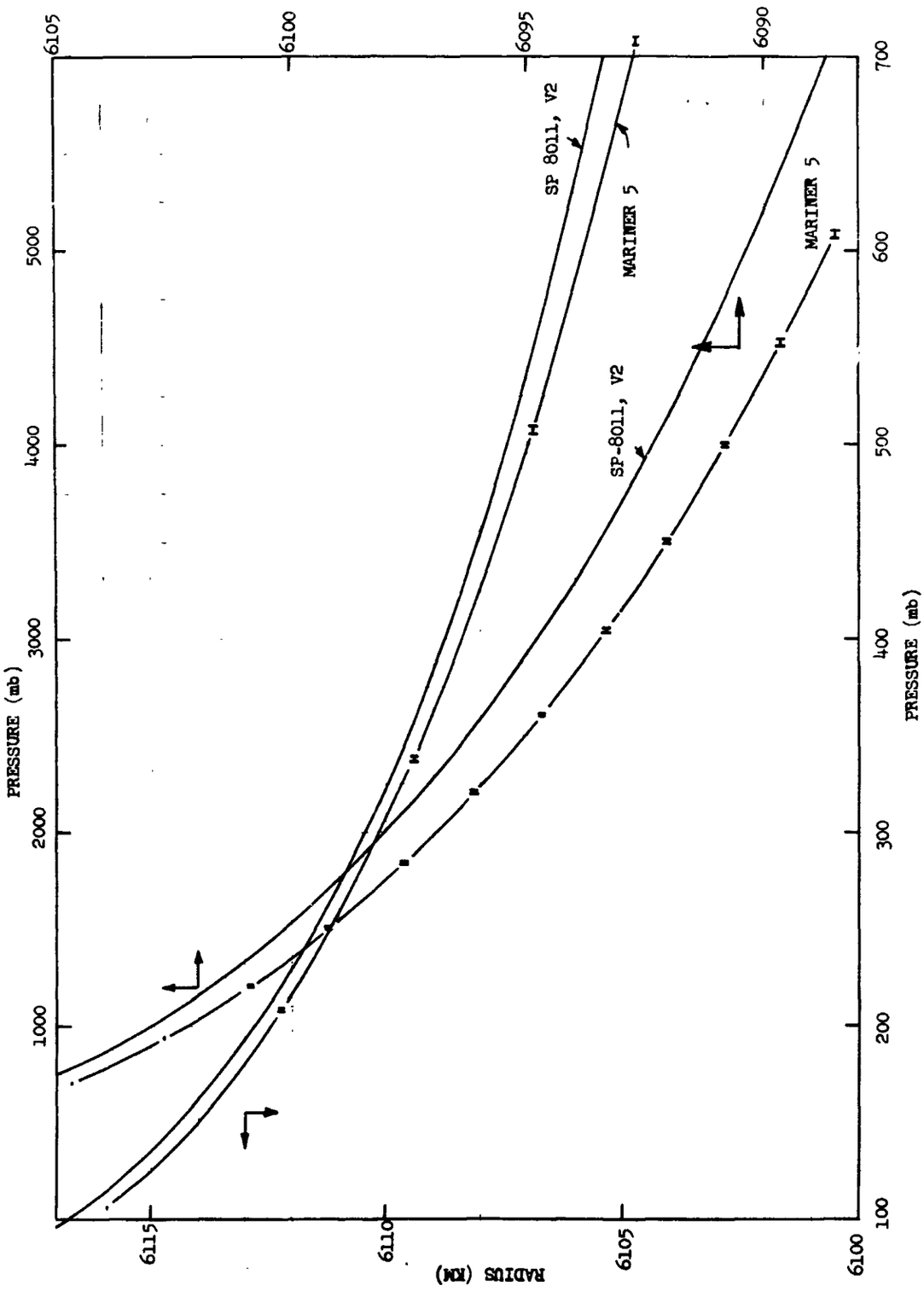


Fig. II-63 Comparison of Pressure Profiles from Mariner Data and SP-8011

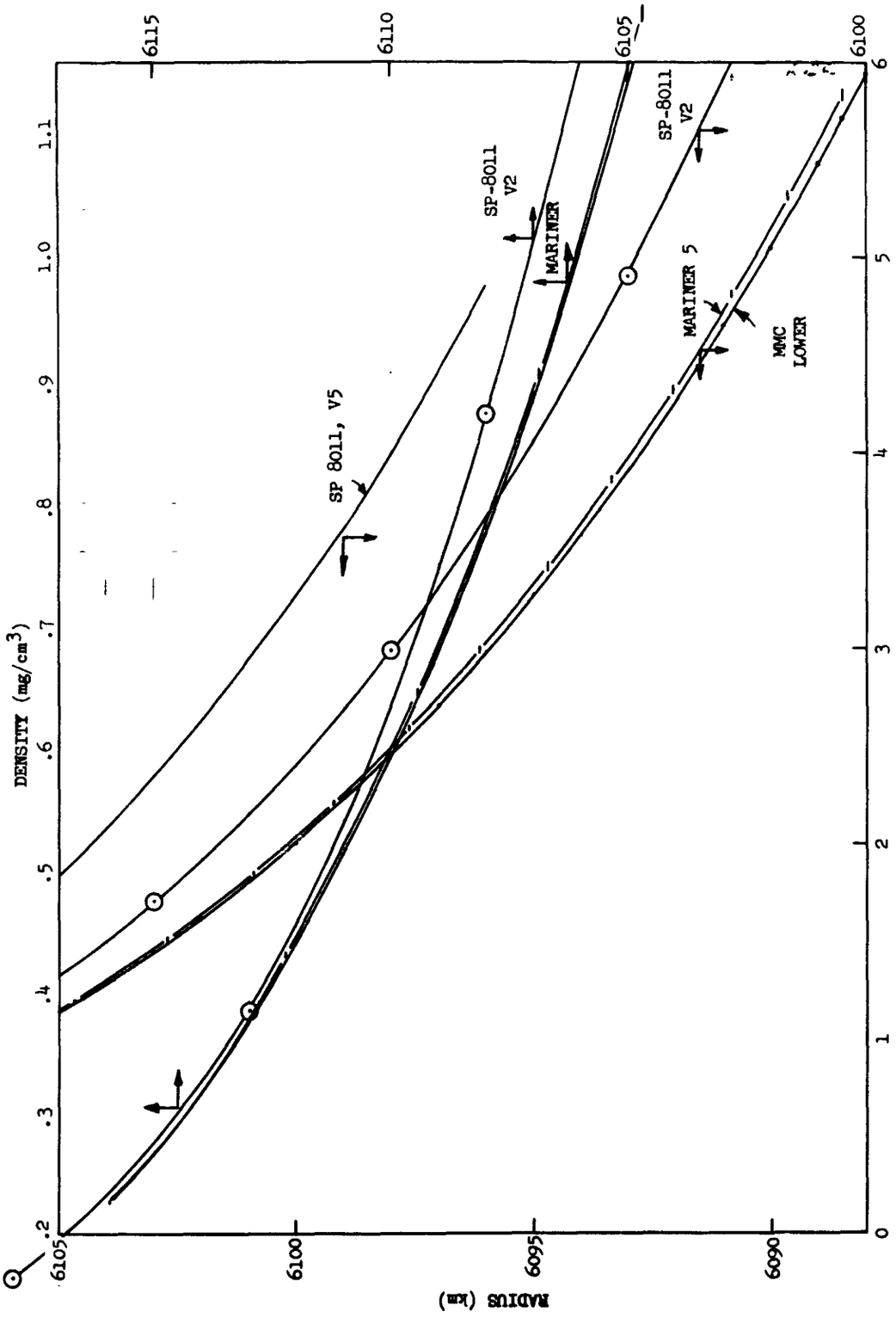


Fig. II-64 Comparison of Density Profiles from Mariner Data and SP-8011

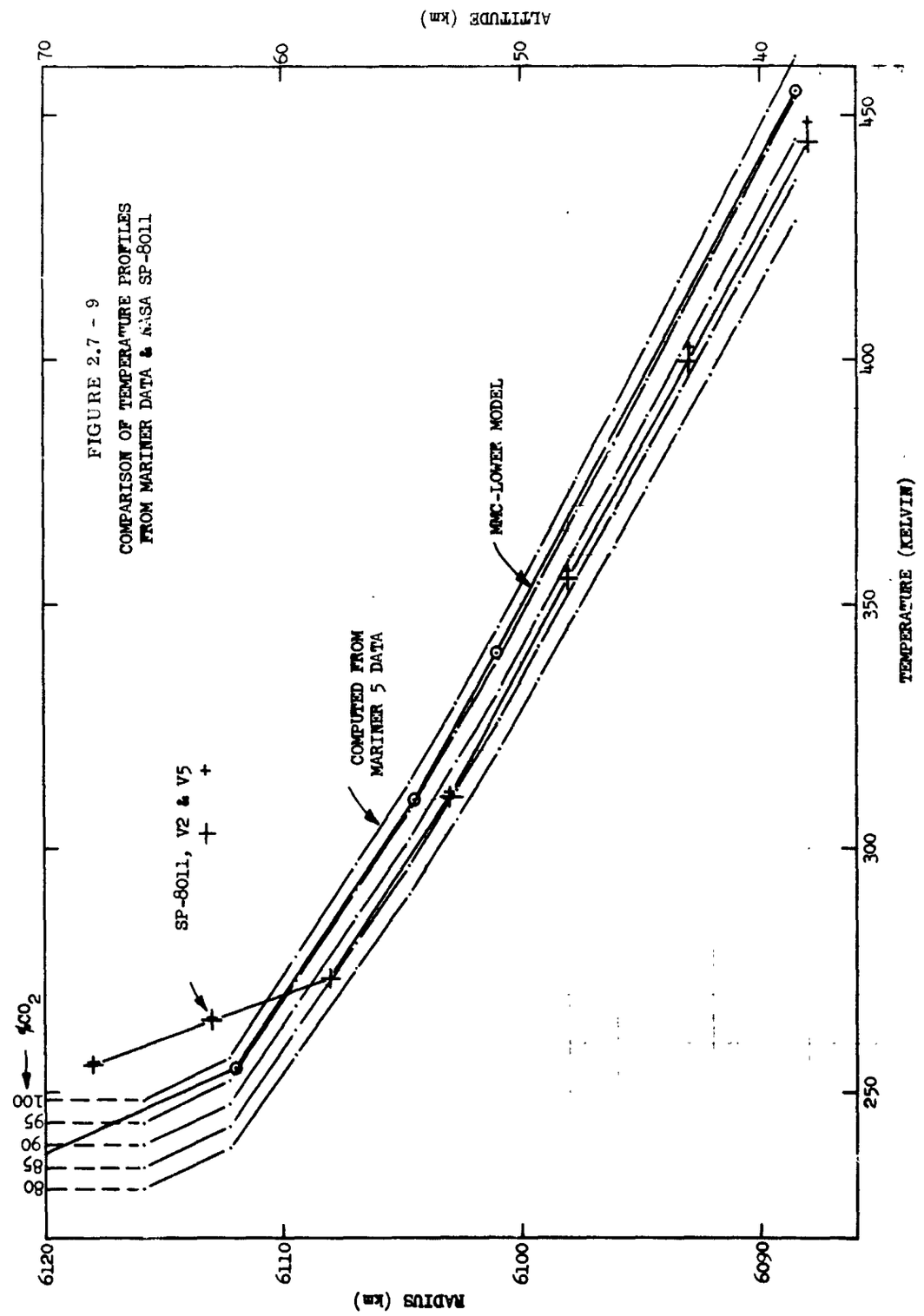


Fig. II-65 Comparison of Temperature Profiles from Mariner Data and NASA SP-8011

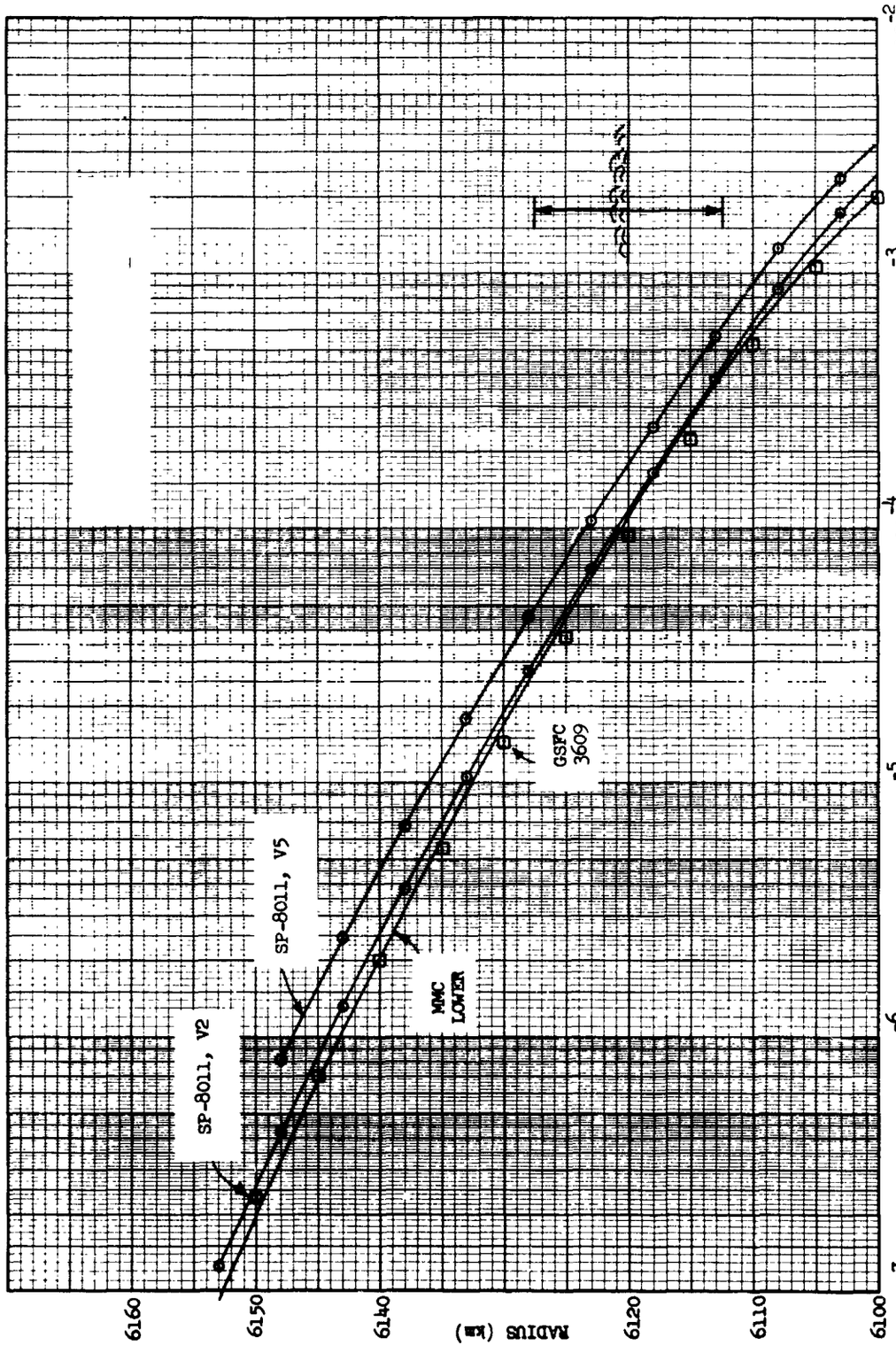


Fig. II-66 Density Profiles above Cloud Tops

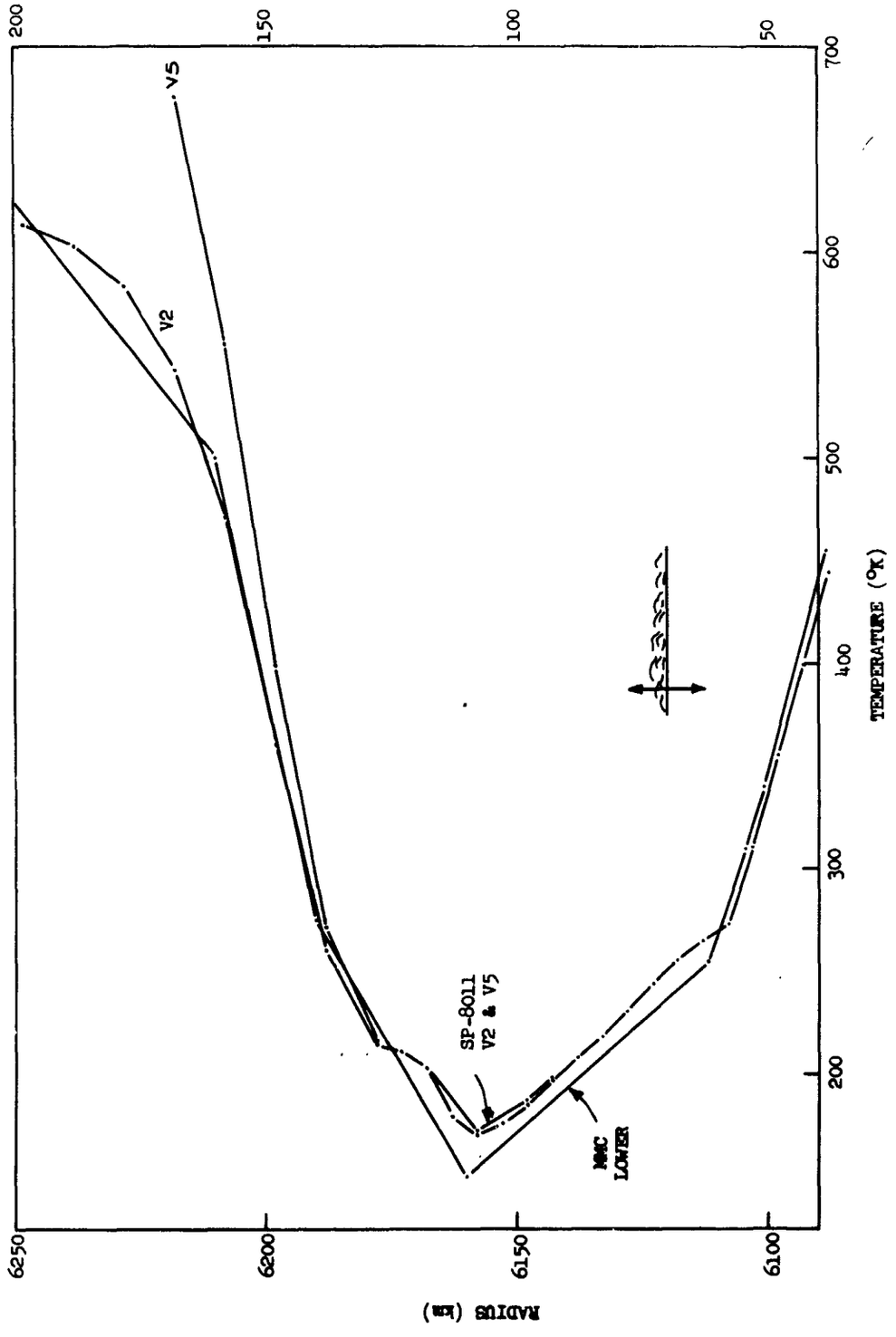


Fig. II-67 Temperature Profiles above Cloud Tops

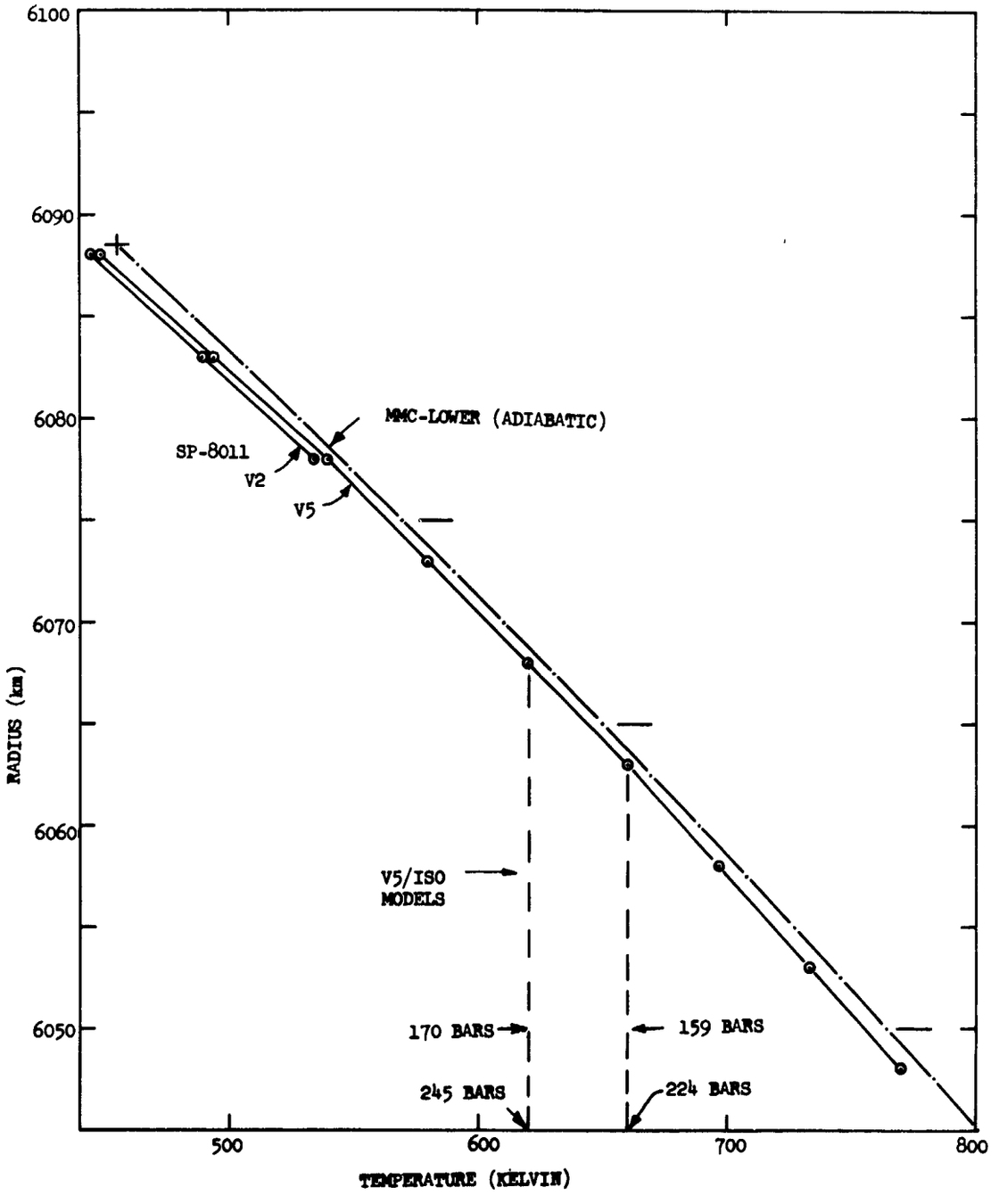


Fig. II-68 Temperature Profiles in Lower Atmosphere

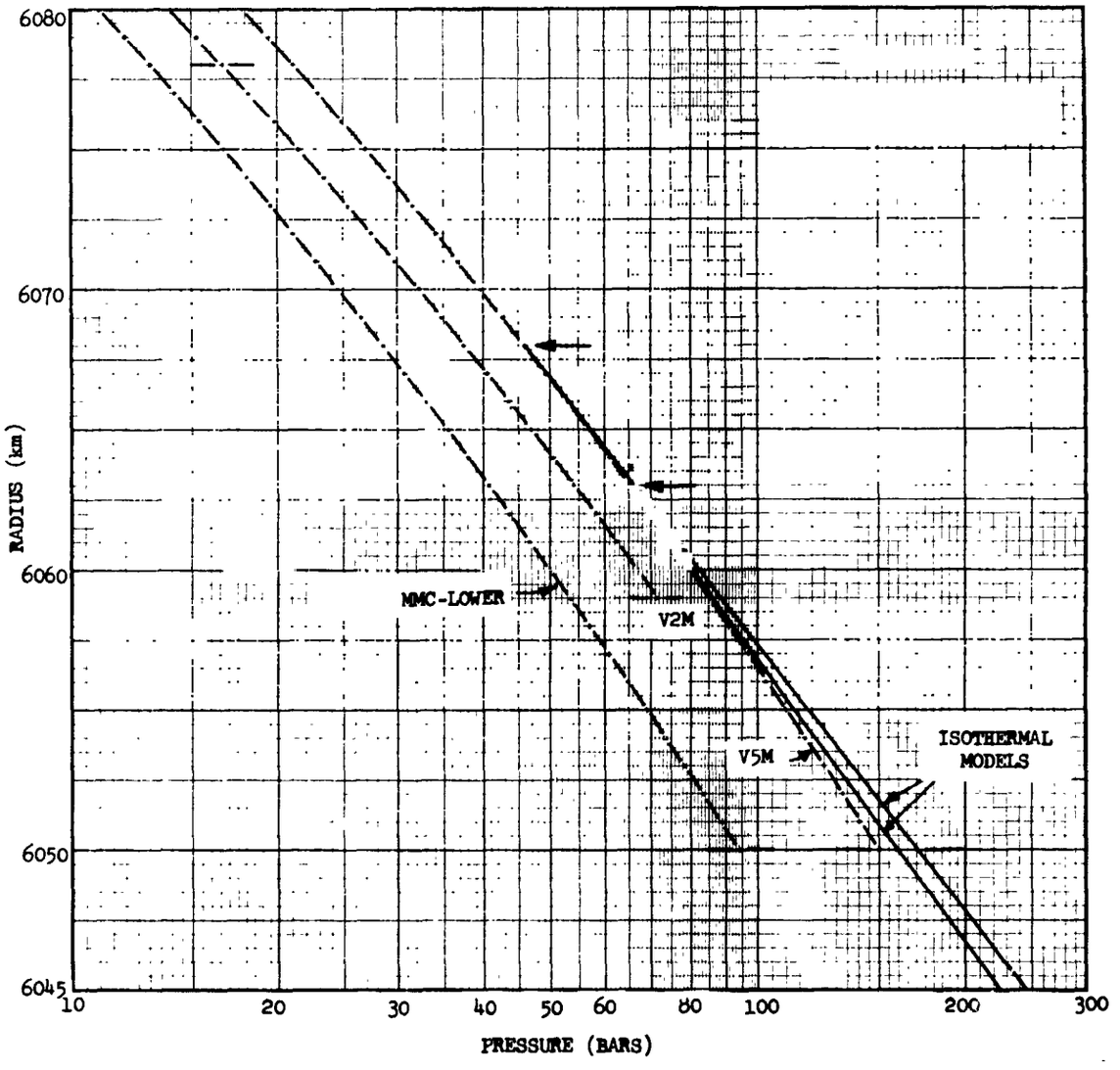


Fig. II-69 Pressure Profiles in Lower Atmosphere

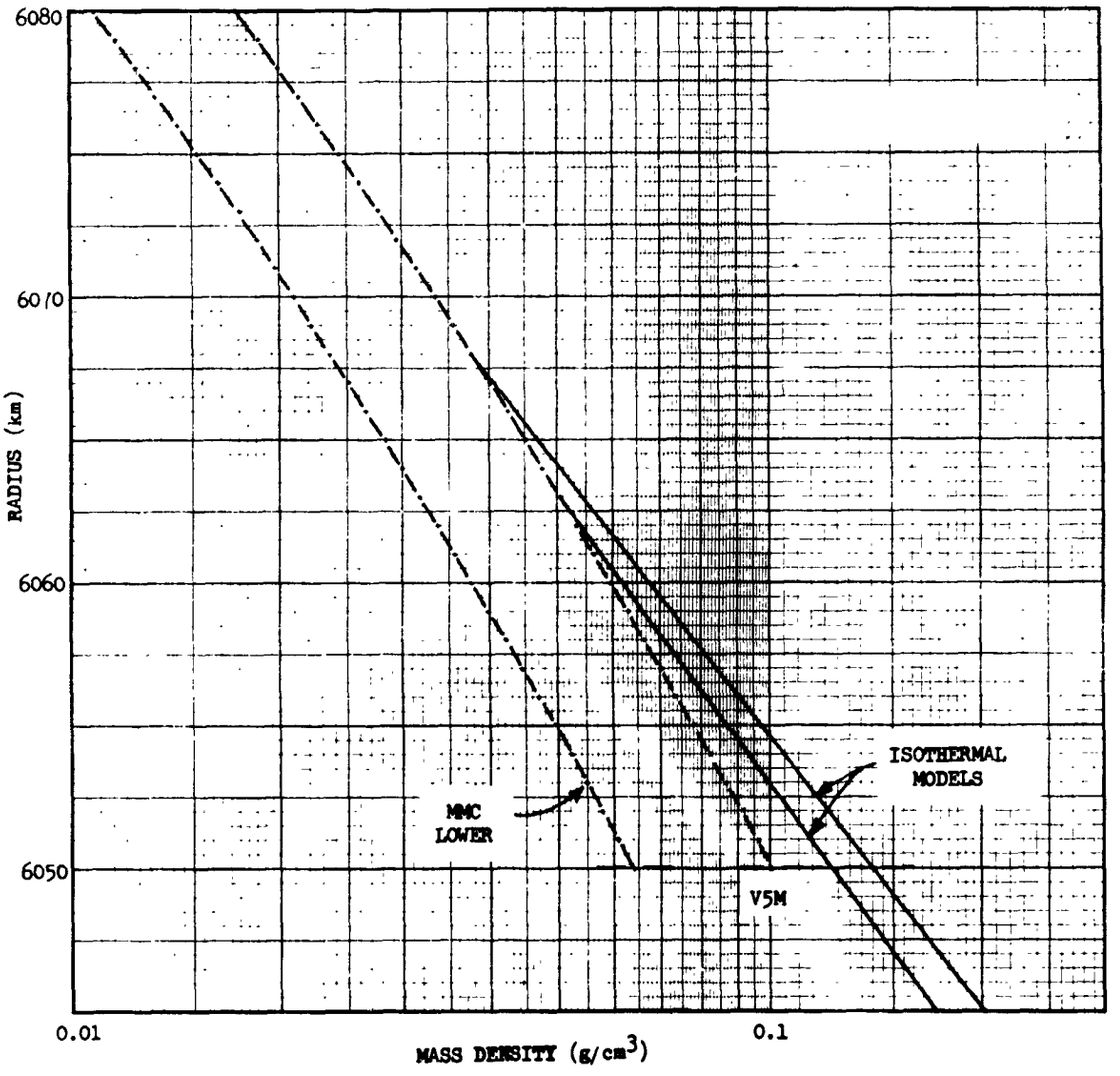


Fig. II-70 Density Profiles in Lower Atmosphere

The surface conditions for these models are summarized in Table II-11, and a tabulation of the model atmosphere parameters is given in Appendix F.

Table II-11 Summary of Model Surface Conditions

Model	Radius (km)	Temperature (°K)	Pressure (bars)	Density (g/cm^3)
V5M	6050	755.32	150.07	1.0132×10^{-1}
MMC-Lower	6045	803.33	126.60	9.1902×10^{-2}
MMC-Lower	6050	765.00	94.314	6.4072×10^{-2}
MMC-Lower	6055	726.66	69.241	4.9520×10^{-2}

H. BASELINE SCIENTIFIC MODELS

A more detailed description of the atmosphere and clouds of Venus than given in the previous section is desirable for the definition of the science mission requirements and the instrument mechanization studies. Figure II-71 summarizes the two mode' atmospheres used in the study. The visible cloud tops are located at 6120 ± 7.5 km as determined from earth-based observations. Other earth-based observations indicate the presence of a tenuous haze extending some 40 km above this level. Dark patches observed in the blue (indicating clearings in this aerosol) move parallel to the equator in the direction of rotation with velocities up to 100 m/sec. A Doppler shift corresponding to this same velocity has been observed in the blue also. These velocities probably refer to the regions above the cloud tops.

The candidate cloud compostions are indicated in Fig. II-71. Measurements from earth indicate several orders of magnitude less H_2O than measured by the Veneras below the clouds. Apparently, there is some sort of trapping mechanism for H_2O below the visible cloud tops. According to Kuiper, the visible clouds are partially hydrated $FeC\ell_2$. The lower clouds of mercury compounds have been predicted by Lewis; their existence seems to have been verified by the Mariner S-band attenuation data.

Below the Venera coverage (∿6070 km), little is known of the atmosphere. There is some evidence for an isothermal layer near the surface as indicated in Fig. II-71, but more recent analyses indicate it is much less extensive than shown, if it exists at all.

The surface radius is 6050 ± 5 km as determined by earth-based radar measurements. While the radar altimeters on Veneras 5 and 6 indicated a 10 to 15 km altitude difference between two points 300 km apart, the earth-based radars can detect no features larger than 1 to 2 km in the equatorial regions.

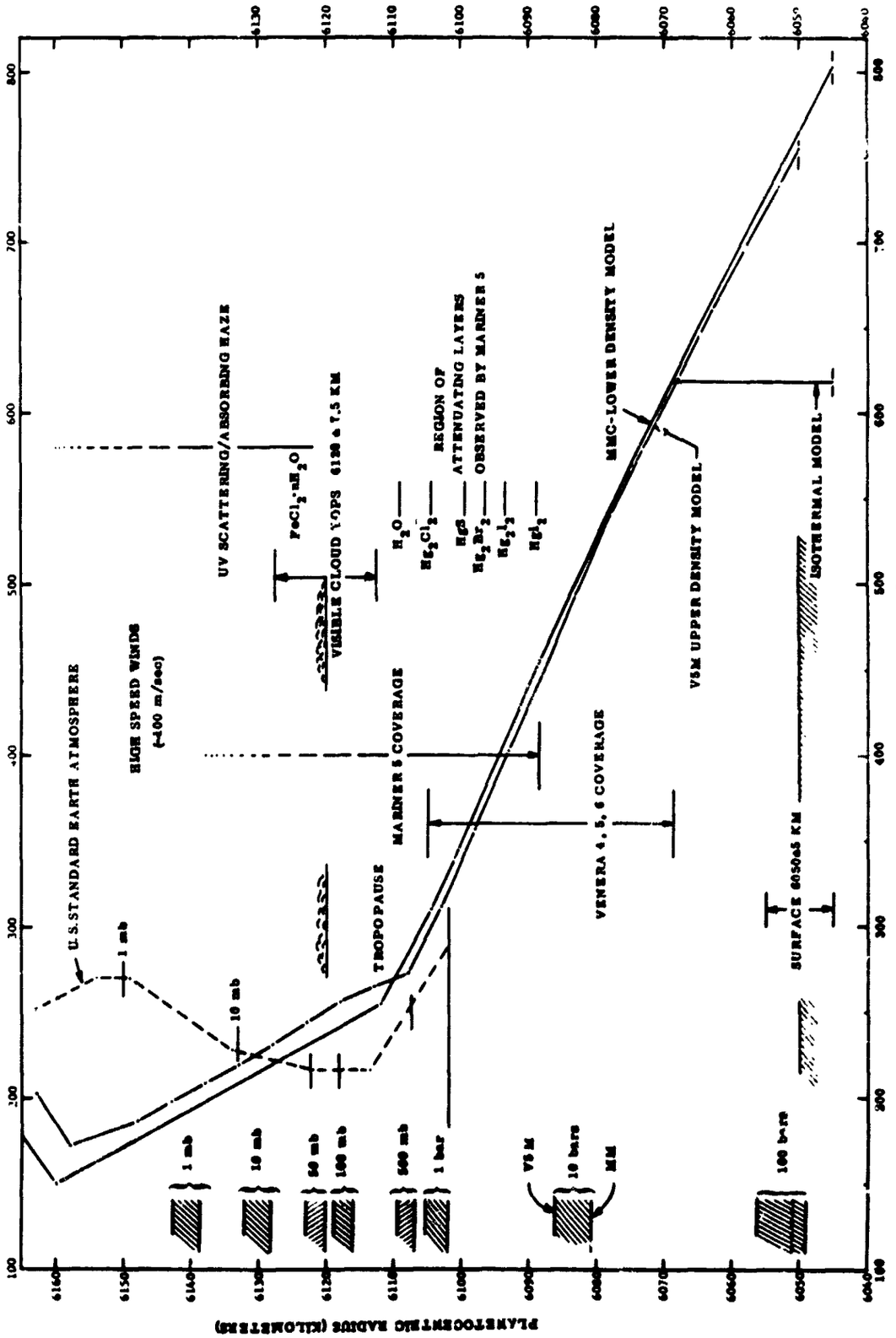


Fig. II-71 Temperature Profiles for Venus

I. ENTRY CONDITION SELECTION AND AEROTHERMAL ENVIRONMENT DATA

As discussed in the preceding sections, establishment of entry conditions is influenced by targeting considerations from the standpoint of science value, communications mask, and accuracy. Probe design considerations, of course, also influence the selection of entry conditions. Entry velocity, path angle, and ballistic coefficient affect probe design to varying degrees through their influence on:

1) Peak dynamic pressure and deceleration;
2) Peak and total heat load;
3) Altitude at which subsonic velocities and low dynamic pressures are reached.

The weight sensitivity of the aeroshell structure and heat shield to variations in items 1) and 2) over the range of interest of this study has been found not to be a controlling factor. This is due partly to the large payload capability of the Titan III Launch Vehicle. Aeroshell structural weight data are given in Chapter III, Section A. JPL-provided unit weight data for the heat shield design is given in Chapter III, Section A and a typical aerothermal environment plot is shown in Fig. II-72. NASA heat shield test capability limits are shown in Appendix B-3 but were not used to constrain the designs (final design entry conditions turned out not to exceed these test capabilities in terms of peak heating rate and pressure).

Item 3) above, however, was found to have a very significant impact on entry angle and ballistic coefficient selection due to considerations of deploying science instruments and controlling their descent rate. Consequently this factor plus the targeting to the locations of scientific interest and also staying within

a 70° communication mask angle (90° for nondescent probes), essentially controlled the entry conditions for the study. Specific considerations for each probe are discussed in the probe synthesis sections that follow.

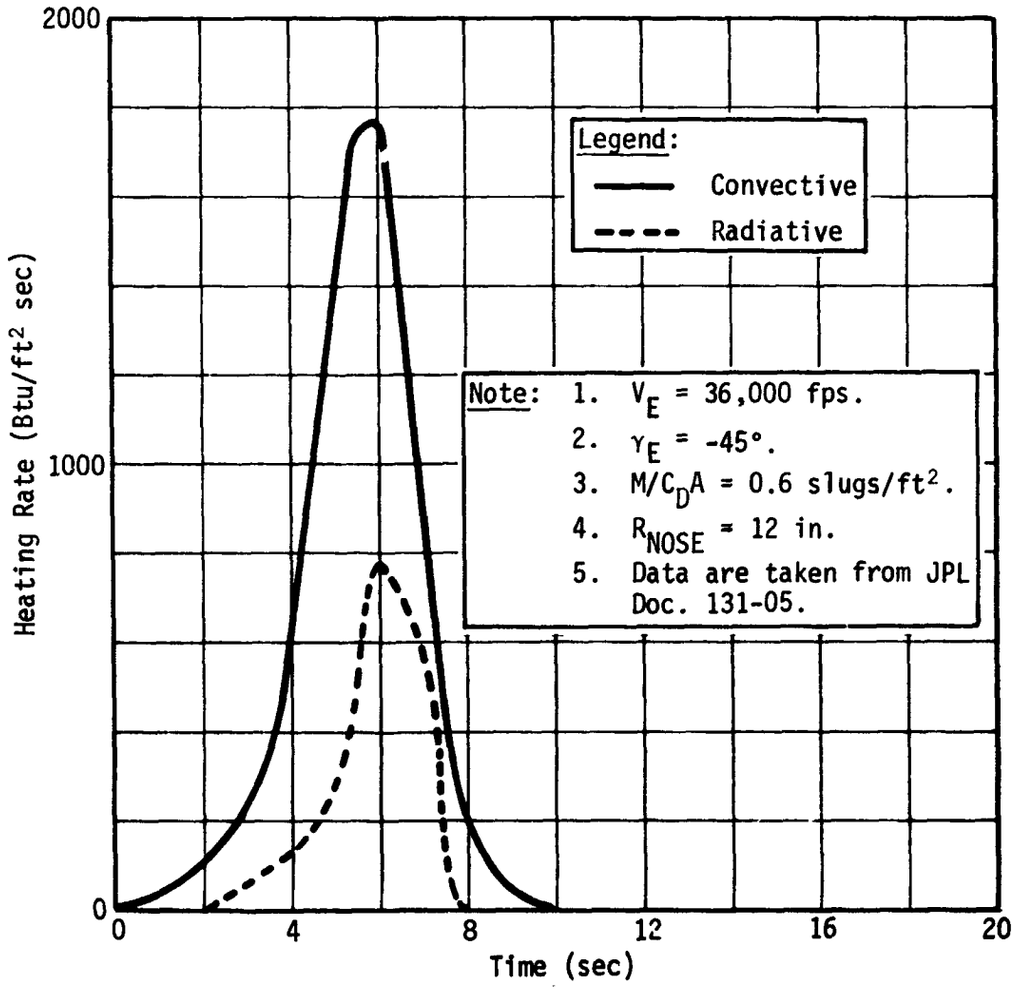


Fig. II-72 Typical Entry Heat Pulse

J. REFERENCES

II-1. JPL-generated computer tabulations for 1975 launch opportunities for Venus mission.

II-2. *Venus Entry Heat Shield Design Requirements and Technology Limits*. JPL Section Document 131-05, August 13, 1969.

II-3. *Constants and Related Information for Astrodynamic Calculations 1968*. JPL TR-32-1306, July 15, 1968.

II-4. *Titan III-C Launch Vehicle Performance for Venus Entry Mission Study*. JPL Section Document 131-04, March 3, 1969.

II-5. W. E. Wagner and W. R. Garner: *Near Planetary Flight Analysis (UD208)*. ER1346J, Martin Marietta Corporation, June 1964.

II-6. A. R. Barger: *Venus Planetary Environment Models, Part I, Atmosphere Models for Use in Entry and Descent Studies of a Multiple Probe Mission*. MCR-69-48. Martin Marietta Corporation, September 1969.

II-7. *Mariner Venus 67 Final Project Report: Volume II Midcourse Maneuver through End of Mission*. JPL Technical Report 32-1203, May 1, 1969.

II-8. D. Stechert: "Navigation Measurement Requirements for Direct Jupiter Missions." Martin Marietta Memo, December 19, 1969.

III. ENTRY PROBE SYNTHESIS

The configurations of the Baseline Mission Entry Probes were synthesized by progressing from consideration of optimum ways of meeting the science requirements within the technical constraints. This process involved the use of an effectiveness model that had been developed for, and verified on, the trial mission. The model and the trial mission are described in Volume III, Appendixes E and G. This section gives a brief summary of the use of the model followed by Entry Probe configuration requirements for the Baseline Mission and also for Optional Missions 1 and 2.

A. SELECTION OF A BASELINE MISSION

Two tasks inherent in the Venus study were the development of the capability of measuring the effectiveness with which a given mission configuration would be able to answer the question that formed the science objectives, and a methodology of incorporating the results of this measurement into appropriate changes in that configuration. This section describes the uses of the Venus probe evaluation model and the methods by which this model was used to help select the baseline mission.

1. General Description of the Mission Effectiveness Model

The Venus mission effectiveness model is a digital program designed to provide a rapid evaluation of a mission configuration, in accordance with constant criteria, and with a validity limited by the detail of the science requirements. A description of the science criteria, along with the required instruments, target sites, and sampling intervals is given in Appendix D, Volume III.

2. Straight Mission Evaluation

The purpose of the evaluation model is to accept a mission description and to quickly determine the efficiency with which that mission answers the science questions that form the mission science objectives. A secondary purpose is to provide a simple method of changing the input configuration to observe the resulting change in the science value and to determine the sensitivities to that change. Note that numerical values obtained have little intrinsic worth in themselves, and only in the context of a comparison between two or more configurations do the evaluations have significance.

3. Identification of Inadequately Answered Science Questions

In this mode of operation, the model found its greatest use. Once a question was isolated as being inadequately answered, the cause must be found. There are three primary causes of poor question performance -- inadequate sampling, inappropriate targeting, or an important instrument missing from the probe. In some cases, the low question value was never adequately corrected because of a combination of long cycling time on an instrument that was required to be sampled at a given delta height at a radius where sufficient deceleration was not feasible. The design of the High Cloud Probe was based directly on this kind of consideration.

4. Identification of Nonproductive Instruments

In another class of problems it was desired to reduce the complexity or instrument weight while affecting the total mission value as little as possible. An output summary of accumulated instrument value was very helpful for this purpose. The values of this particular output were the total value contributed by each individual instrument. A survey of the output generally disclosed one or more instruments that are contributing little or

nothing to the mission value. Such an instrument could obviously be removed from the mission without significantly changing the total mission value.

5. Evaluation of a Large Number of Missions

The model was first used to evaluate a large number of configurations with the purpose of finding trends that might aid in the selection of a baseline configuration. When the value determined for each of these configurations was plotted as a function of the number of instruments used, a large spread in the effectiveness was noted. Figure III-1 is a plot of the value achieved by 54 of these configurations as a function of the number of instruments used. There is so much variance in the results that a single general conclusion might be drawn that an acceptable baseline configuration must lie close to the upper bound of these plots.

6. Establishment of Targeting Priorities

Some of the missions included the same instrument-probe complements and showed a large difference in effectiveness, due solely to targeting. It was apparent that some method of treating targeting as an independent parameter was desirable.

The target value subroutine was run independently from the model to find the target value for each question at a set of points distributed across the planet surface. The average of the value for all the questions gives a numerical priority for the various planet locations. Figure III-2 is a plot of these average target values as a function of ψ (distance from subsolar point) for three great circles passing through the equator at the morning and evening terminators and across the pole. These curves provide the following target zone priorities:

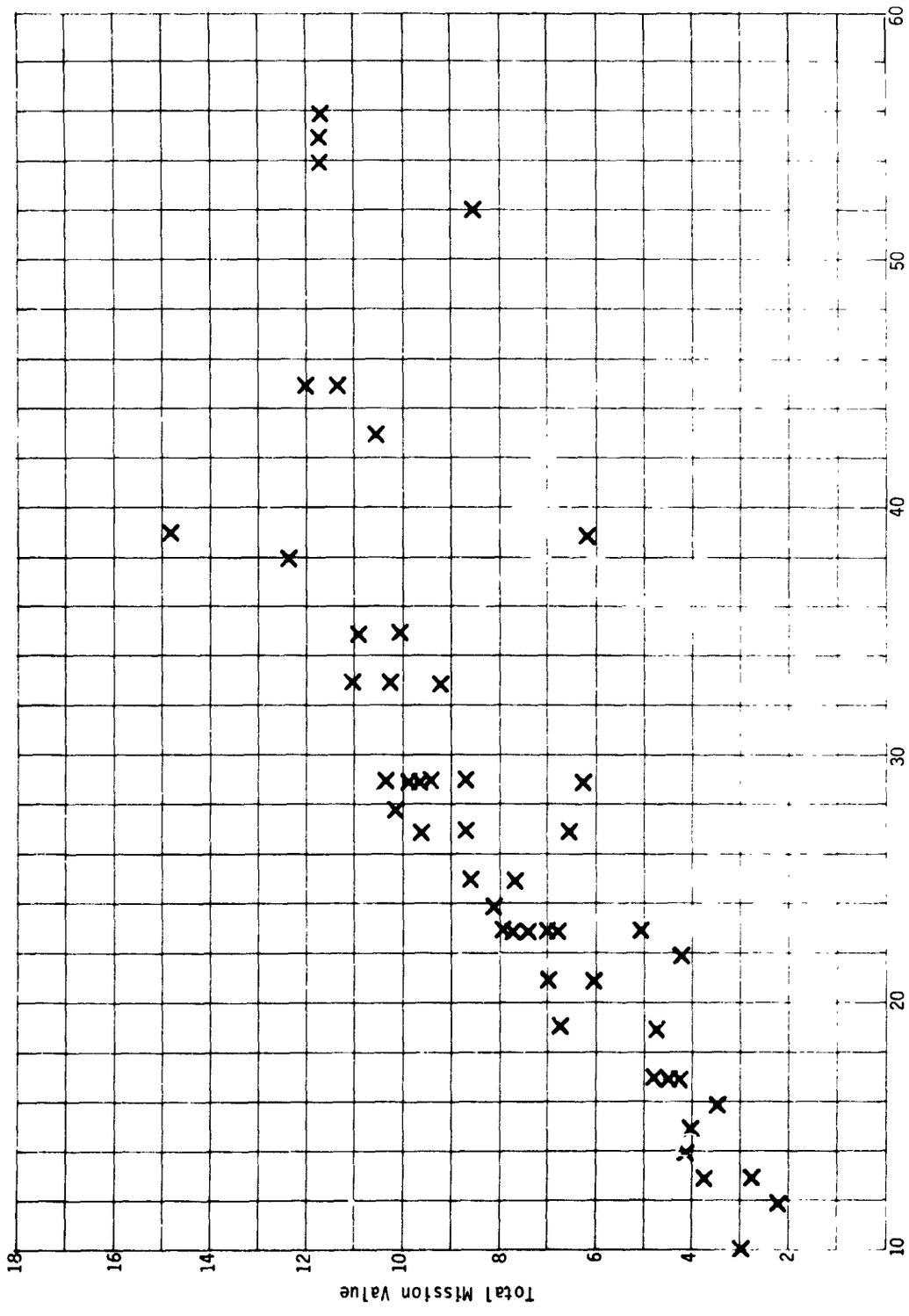


Fig. III-1 Mission Value vs Number of Instruments for 54 Mission Configurations

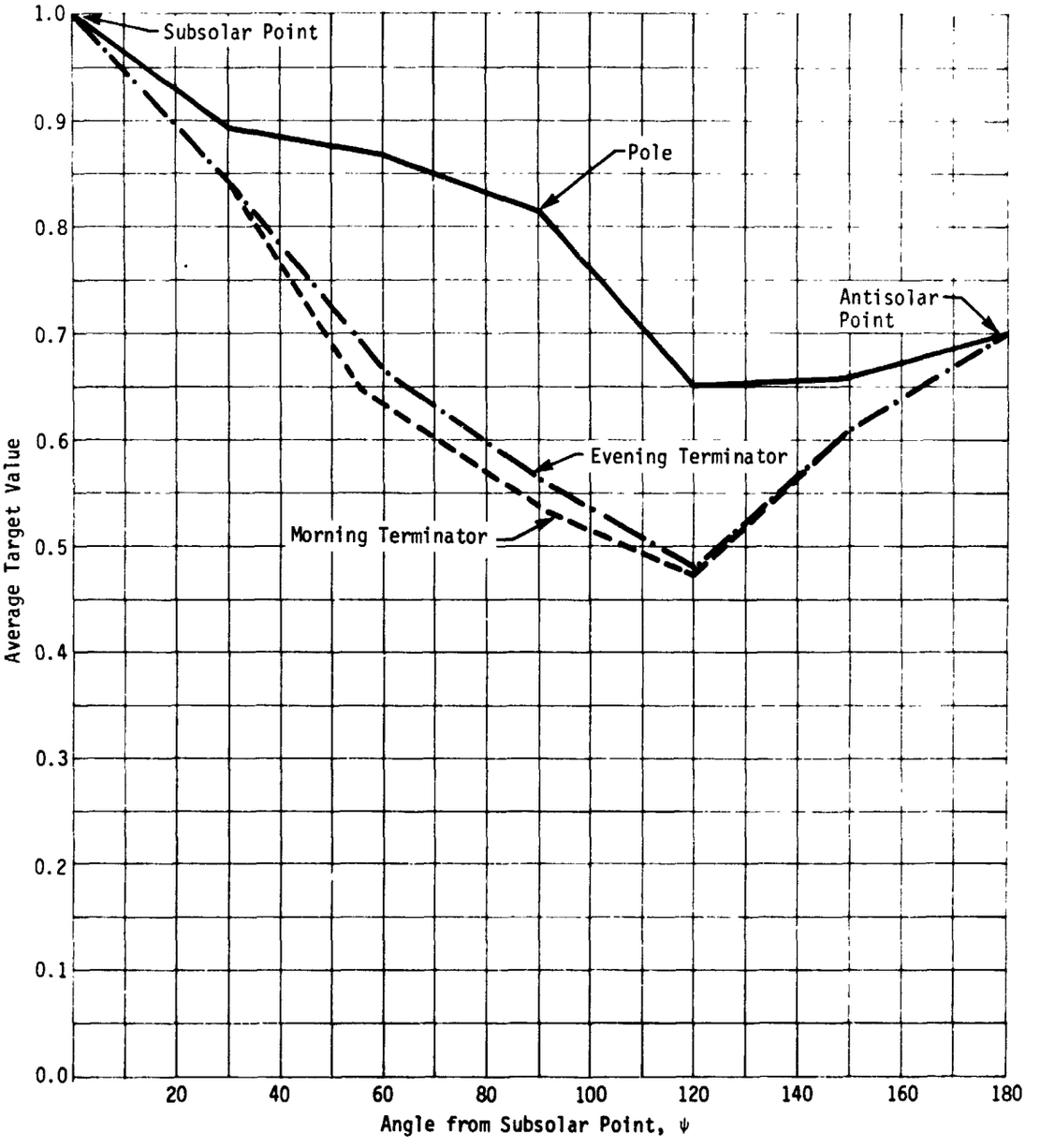


Fig. III-2 Target Values as a Function of ψ for Three Great Circles

Subsolar	1.000
Pole	0.817
Antisolar	0.700
Morning Terminator	0.536

Once this targeting priority was established it was desirable to establish a similar priority or order of preference for adding instruments to a mission.

7. Establishment of an Instrument Preference List

The maximum contribution to the value of a given question can be calculated for a given instrument using the probe instrument value equations described in Appendix E, Volume III. However, the value computed depends in all cases on the existence of other instruments. The reason for this interdependence is the nonlinear manner in which the value contributed by each instrument accumulates toward the total question value. Some assumptions were required about the order in which instruments are included on the probes. These assumptions were later established as correct by an iterative process. The following assumptions were used in the construction of the preference list:

1) A pressure and a temperature gage is assumed as a prerequisite for any probe. This is justified by the involvement of the pressure gage in every question and the temperature gage in a majority of questions;
2) The 70-km radar is assumed as a prerequisite for the first probe which, due to the target priority, is assumed to go to the subsolar point. The radar is required to establish an altitude reference.

Three other assumptions of instrument order were based on the number of questions with which the particular instruments were involved. These assumptions are:

1) The UV photometer (involved in three questions) will be added to a probe prior to either the ion mass spectrometer or the high altitude mass spectrometer, which are involved in two questions only;
2) The nephelometer (involved in two questions) which will be added prior to the thermal radiometer;
3) The accelerometer which is involved in three questions will be added prior to transponder (involved in two questions), which will be added prior to the drift radar (involved in answering one question).

Once the above assumptions have been made, the value increment added by a particular instrument can be calculated making proper use of the summation scheme indicated for that particular question. When the possible contributions of all instruments have been calculated for the four possible target zones, by adding the contributions to individual questions, a preference list of instruments can be found by simply placing the values in descending orde .

The resulting preference list is given in Table III-1.

8. Summary of Mission Effectiveness Evaluation

The mission effectiveness evaluations can best be summarized by viewing a plot of total mission value achieved as a function of the number of instruments used in the mission. Figure III-3 is a plot of a family of such curves. The solid line entitled "Instrument Preference Curve" is a plot of the values calculated in generating the preference list. These values are optimistic because they assume altitude references of unity, whereas the altitude reference can be no greater than 0.9 unless a radar is included. The three dashed curves are plots of actual computer runs for three conditions of degradation. The top curve labeled "Altitude Reference Degradation" is the same as the preference

Table III 1 Preference List

Subsolar	Polar	Antisolar	Terminator
Pressure Temperature 70-k Radar 1. UV Photometer 2. Mass Spectrometer			
	Pressure Temperature 3. Mass Spectrometer		
4 Electron Probe 5. Cloud Composition 6. Cloud No. Size			
		Pressure Temperature 7. Mass Spectrometer	
8. Solar Radiometer			
	9. Solar Radiometer		
10 Accelerometer 11. High Altitude Mass Spectrometer			
	12. Cloud Composition		
		13 Cloud Composition	
	14. Cloud No. Size		
		15. Cloud Size	
	16. Accelerometer		
17. Ion Mass Spect.			
		18. Accelerometer	
19. Thermal Radiometer			
	20. Thermal Radiometer		
		21. Thermal Radiometer	
22. Nephelometer			
	23. Nephelometer		
		24. Nephelometer	
	25. Drift Radar		
		26. Drift Radar	
27. Evap/Condens			
	28. Evap/Condens		
		29. Evap/Condens	
30. Transponder			
	31. Transponder		
		32. Transponder 33. Solar Radiometer	
			Pressure Temperature 34. Solar Radiometer
	35. UV Photometer 36. Electron Probe 37. Ion Mass Spectrometer		
			38. Accelerometer
	39. High Altitude Mass Spectrometer		
		40. Electron Probe	
			41. Electron Probe
		42. UV Photometer	
			43. UV Photometer
		44. Ion Mass Spectrometer	
			45. Ion Mass Spectrometer
		46. High Altitude Mass Spectrometer	
			47. High Altitude Mass Spectrometer

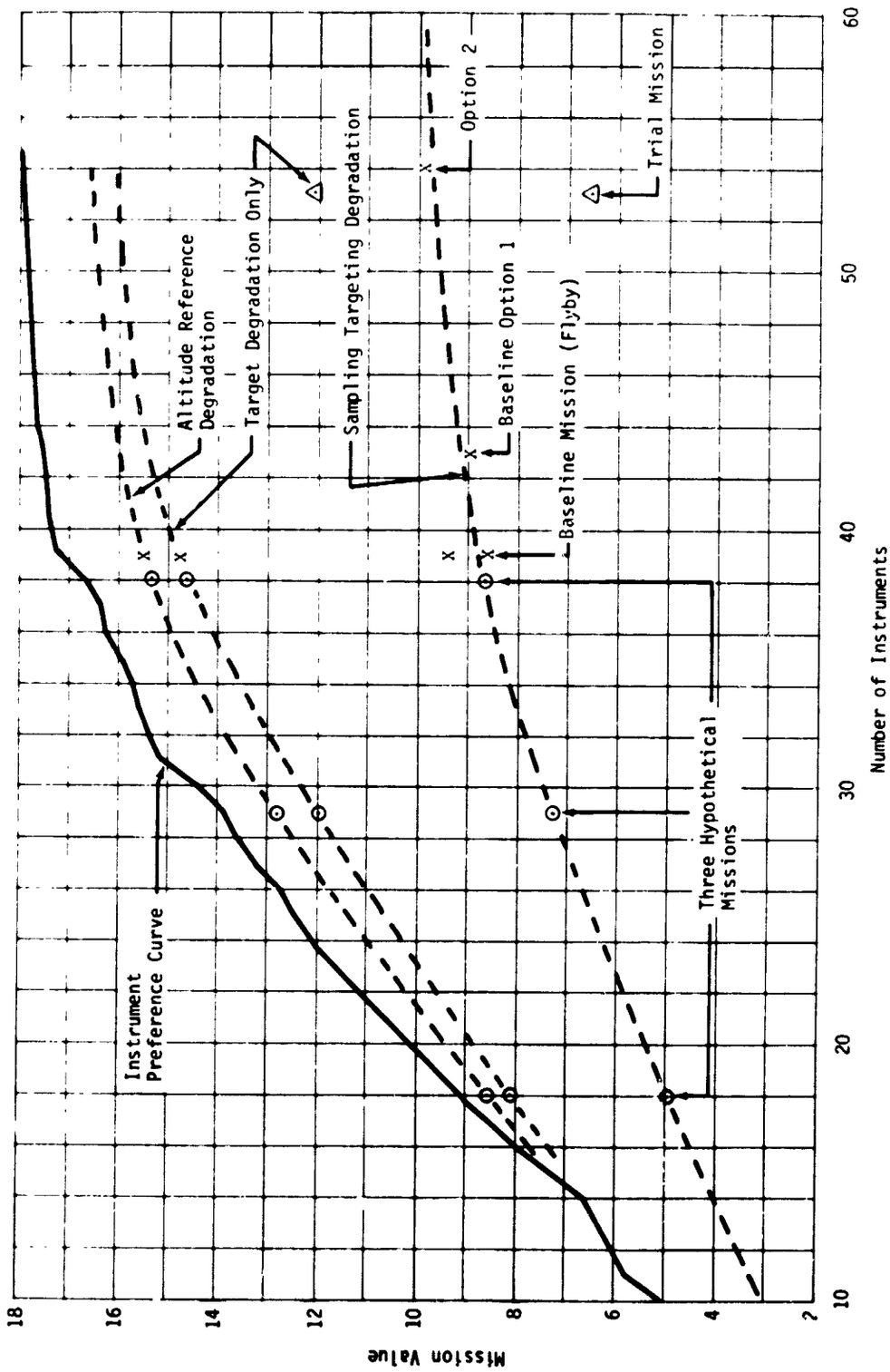


Fig. III-3 Mission Value vs Number of Instruments for Optimum Missions

curve except for the assumption noted above. The dashed family of curves was plotted from three hypothetical mission configurations as well as the baseline and the two options to the baseline.

The first conclusion that may be drawn from Fig. III-3 is that the baseline mission and its options fall on a curve representing the optimum value per instrument.

A second conclusion is that the baseline mission is found at the knee of the curve and that further weight and complexity expended toward the same set of science objectives will produce less science value per instrument added.

B. BASELINE MISSION - LARGE PROBE

The configuration selection process identified the need for a probe to serve as a reference by providing a data profile from entry to impact while carrying the largest instrument complement to the most valuable target (subsolar). The instrument complement includes all of the instruments carried by any other probe, and in addition, includes the extreme altitude science instruments for use with a flyby spacecraft. In the case of an impacting spacecraft mission, the data return from the large probe will serve as the principal complement to the data collected by the spacecraft. Irrespective f the spacecraft mission, the large probe provides the reference for all other probes. Because of its importance to the mission, the design of the large probe is discussed first.

1. Large Probe Science Capabilities

The large probe system was defined to provide a comprehensive altitude profile of the atmosphere, clouds, and dynamics near the subsolar point from the cloud tops to the surface. The instrument complement is listed in Table III-2. Note that the radar altimeter has a 70-km range. The upper atmosphere instruments are located on the large probe aeroshell and ejected at 0.1 g increasing in the event a flyby spacecraft mode is elected. In the case of an impacting spacecraft mode (see Chapter IV, Section B), these instruments are located on that vehicle. The flyby spacecraft mode is assumed in the descriptions below. The lower density MMC Model Atmosphere is used since it represents a worst case for the data profiles. If pressure rather than radius is used as a reference, events occur at about the same pressure level in either of the extreme model atmospheres.

Table III-2 Baseline Large Probe Instrument Complement

Instrument	Bits Per Sample	Sample Time Interval (sec)	Altitude Sample Interval at 6120 km (m)	Total Number of Measurements
Pressure	8	10	290	778
Temperature	8	10	290	778
Mass Spectrometer	600	60	1640	129
Solar Radiometer	200	10	290	778
Thermal Radiometer	16	10	290	778
Nephelometer	16	10	290	778
Cloud Particle Size and Number	80	10	290	778
Evaporimeter/Condensimeter	456	30	850	259
Cloud Particle Composition	1800	300	6570	26
70-km Altitude and Drift Radar	60	30	850	259
Accelerometer (1)	10	1	29.4	7788
Transponder	--	continuous	--	--
				(approx)
Ion Mass Spectrometer	200	10.0	--	76
Neutral Mass Spectrometer	600	10.0	--	76
Electron Density and Temperature	30	0.5	--	1500
UV Photometer	10	1.0	--	760
Accelerometers (4) Entry	4 × 10	0.2	--	4 × 130

The upper atmosphere instruments begin sampling at 2 planet radii (12,100 km). Sample time intervals shown in Table III-2 result in the measurement profiles shown in Fig. III-4 and III-5. Shock formation occurs at a density of about 10^{12} particles/cm^3 or about 6180 km radius, just below the ionospheric electron density peak at 6192 km radius. A deceleration of 0.1 g increasing occurs just after shock formation and serves as a trigger to eject the upper atmosphere instruments. The data from these instruments are transmitted in real time (Chapter III, Section C).

Upon sensing 0.1 g increasing, each of the four accelerometers is sampled 5 times/sec through deceleration until the parachute deployment is complete. These data, stored for transmission during parachute descent, provide information on the atmospheric structure through the region indicated in Fig. III-6. The deceleration time history is shown in Fig. III-7.

Parachute deployment, initiated at 2.7 g decreasing, is assumed to be complete by 6122 km (34 mb). Sampling of all other instruments begins at this point and a single accelerometer is sampled once per second until impact. The number of measurements and the altitude sampling intervals obtained with each of the instruments are shown in Fig. III-8 and III-9.

The parachute is released at 7 bars ($\sim$6085 km radius) after passing through the layered structure indicated by Mariner 5. The altitude sampling intervals are somewhat larger than nominal just after parachute release, but rapidly improve as the probe descends. At 50 bars ($\sim$6060 km radius) the sampling rate is halved to ensure data transmission through the thick atmosphere. Adequate sampling intervals are obtained due to the low descent velocity.

The physical arrangement of the instruments on the large probe is illustrated in Fig. III-12 shown in the following subsection. More detailed discussions of the instrument mechanizations will be found in Chapter VI, Section B and Appendix A.

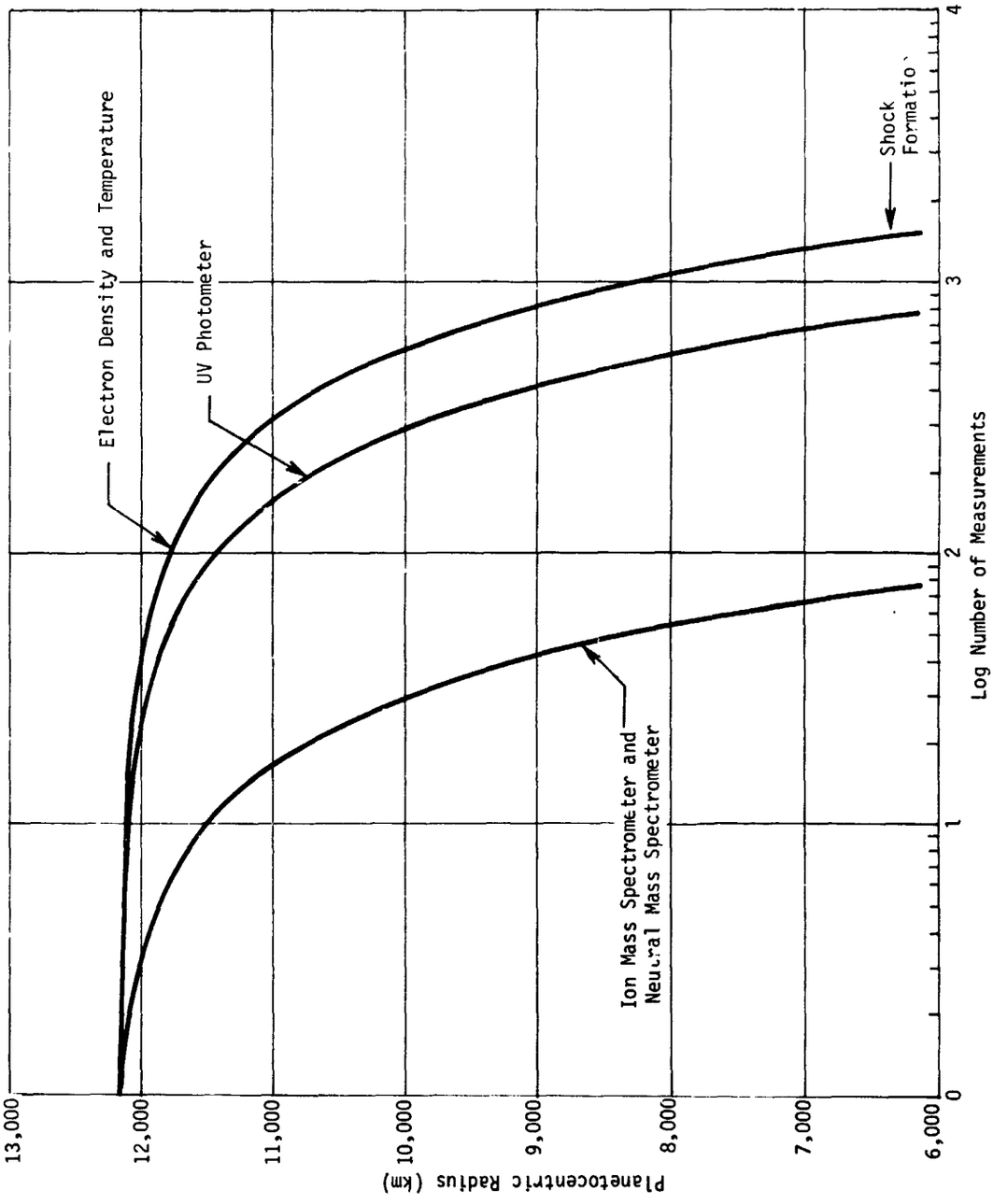


Fig. III-4 Number of Upper Atmosphere Measurements from 2 Planet Radii

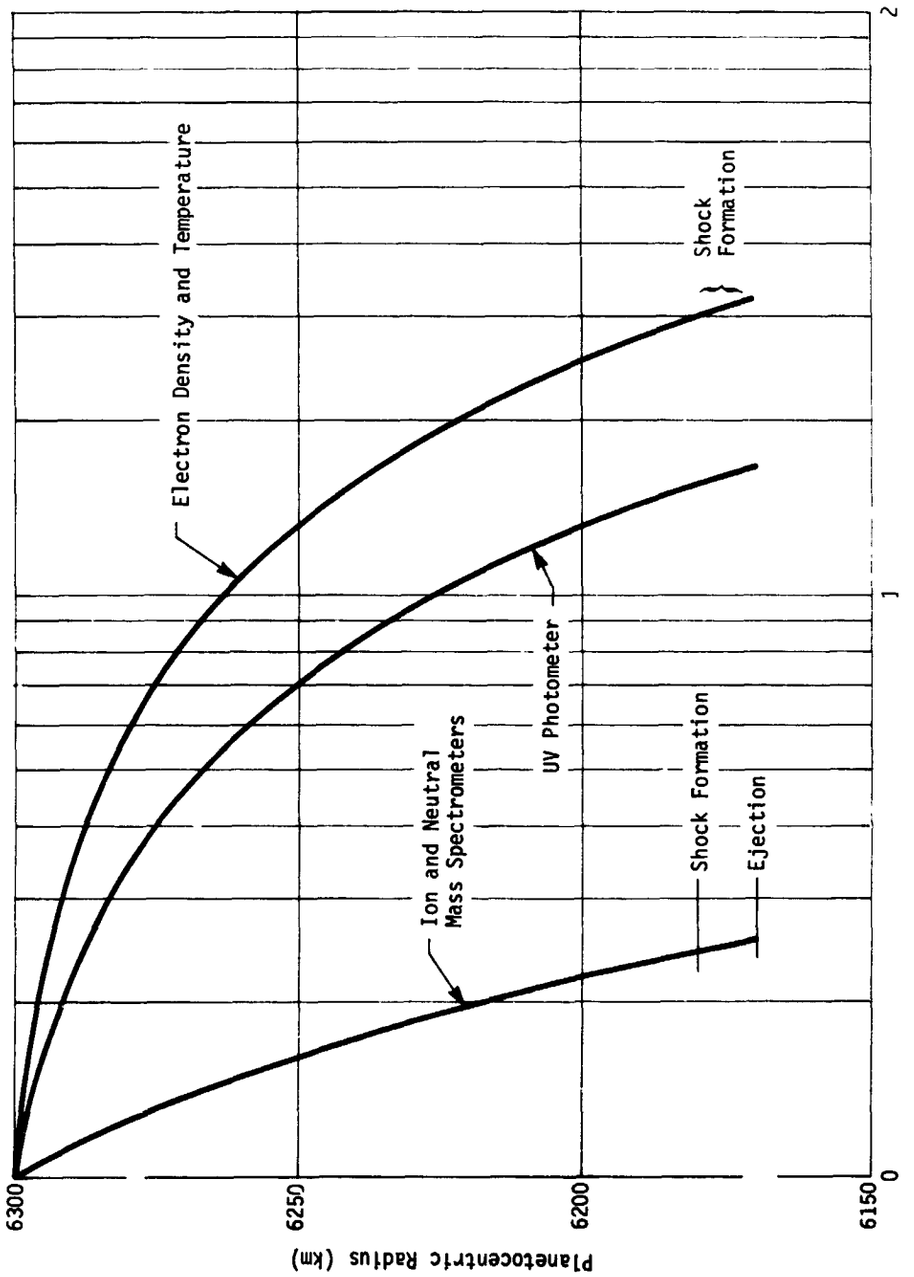


Fig. III-5 Number of Measurements from Entry

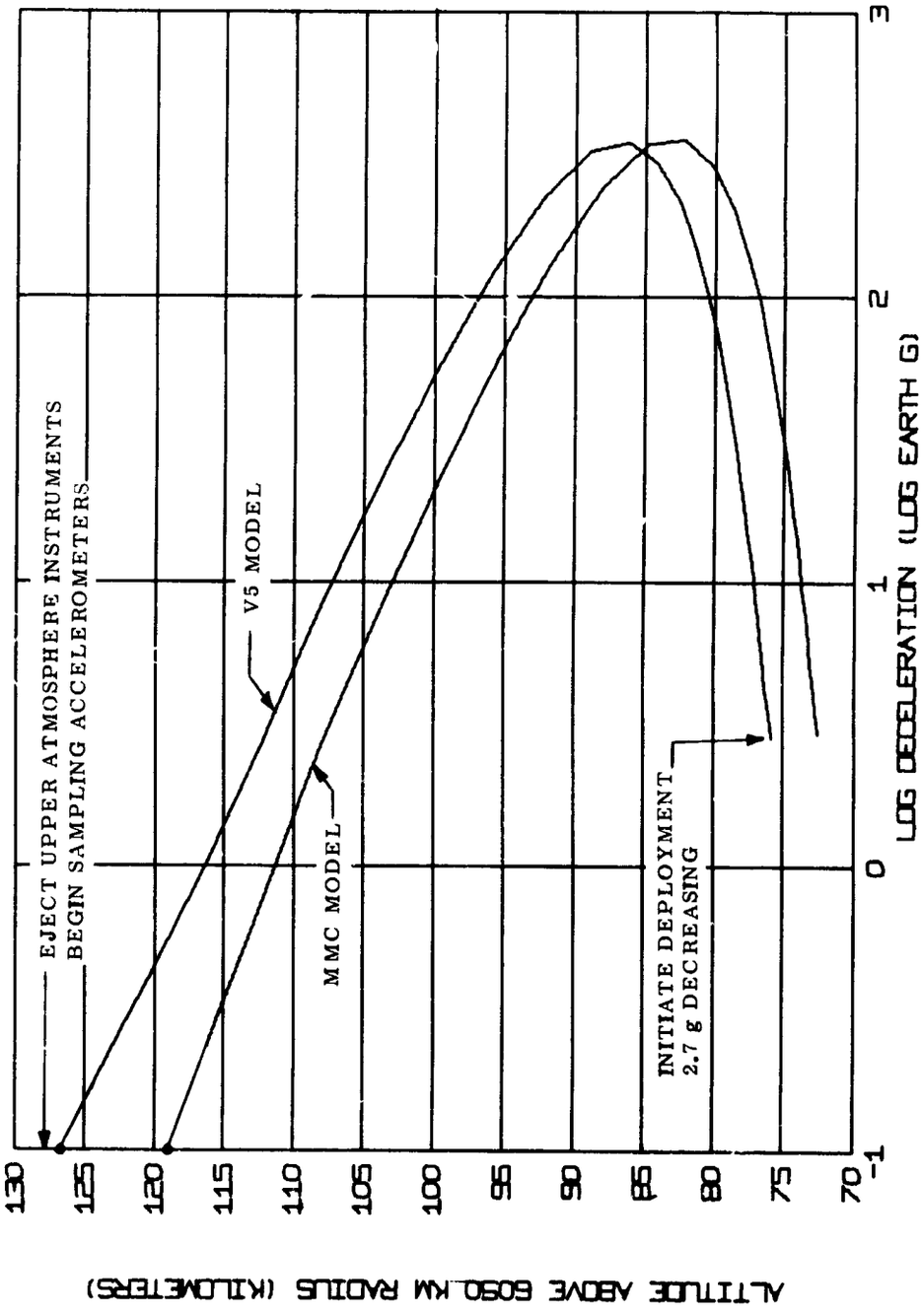


Fig. III-6 Deceleration vs Altitude for Large Probe

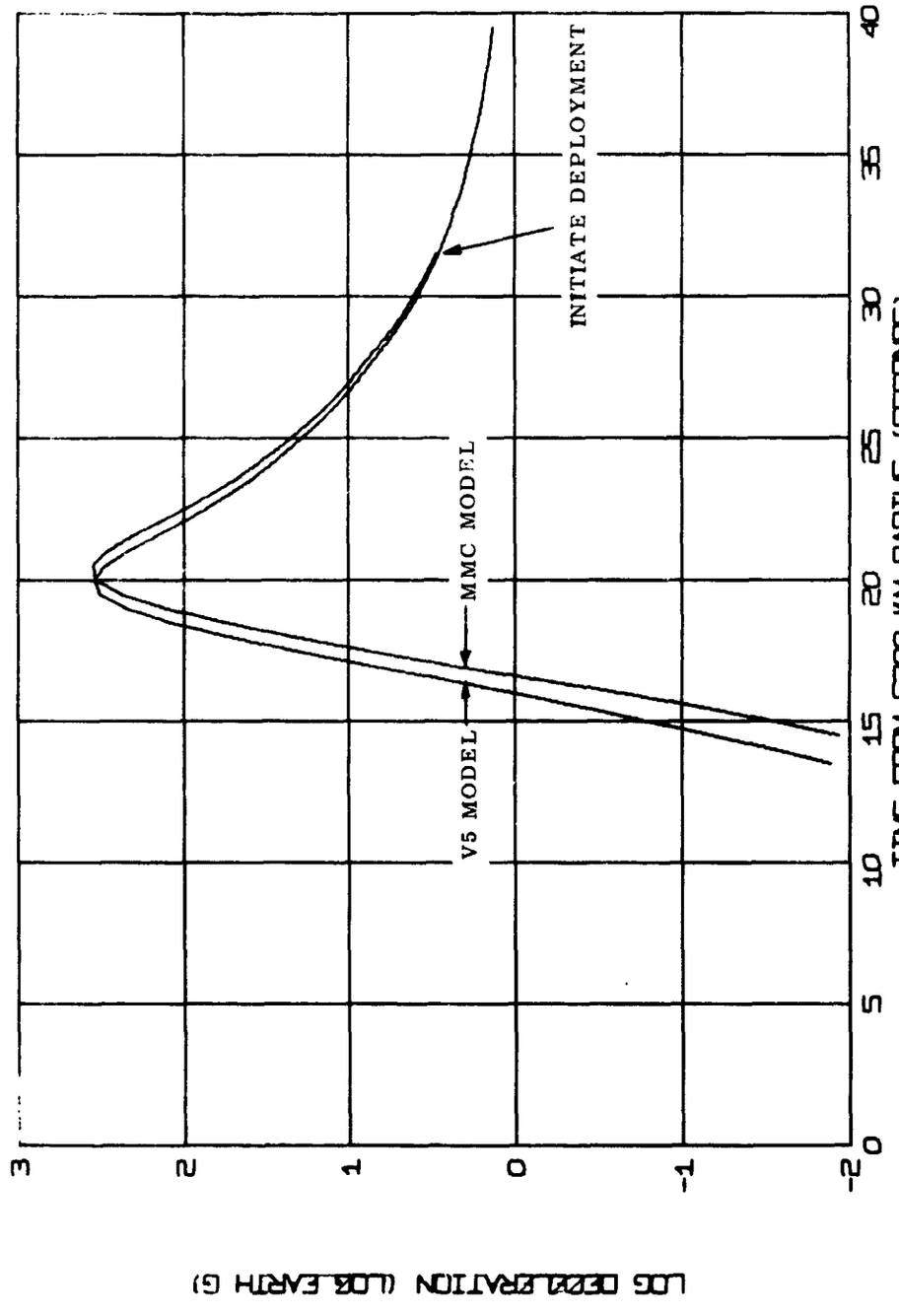


Fig. III-7 Deceleration vs Time for Large Probe

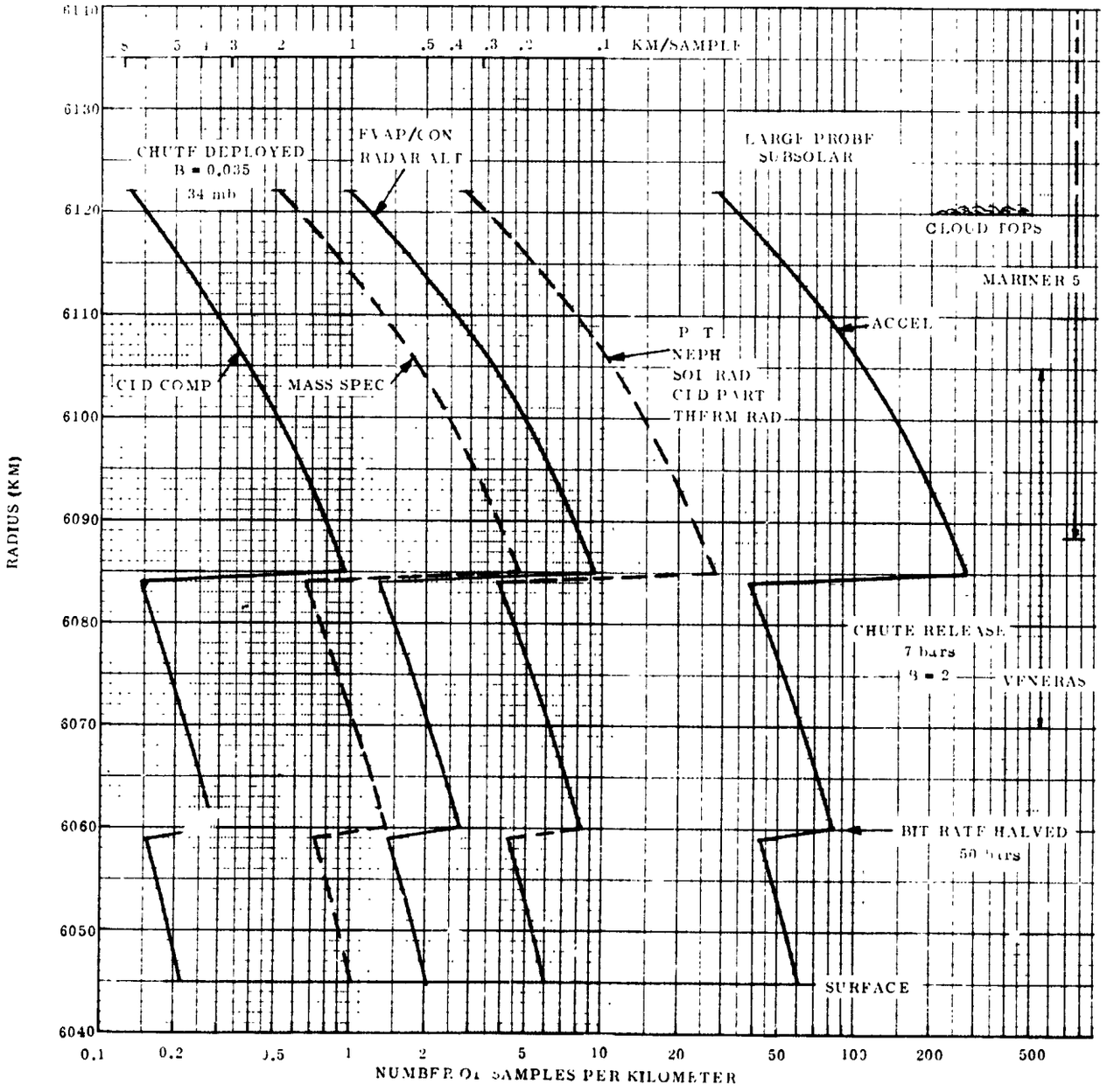


Fig. III-8 Number of Measurements vs Altitude

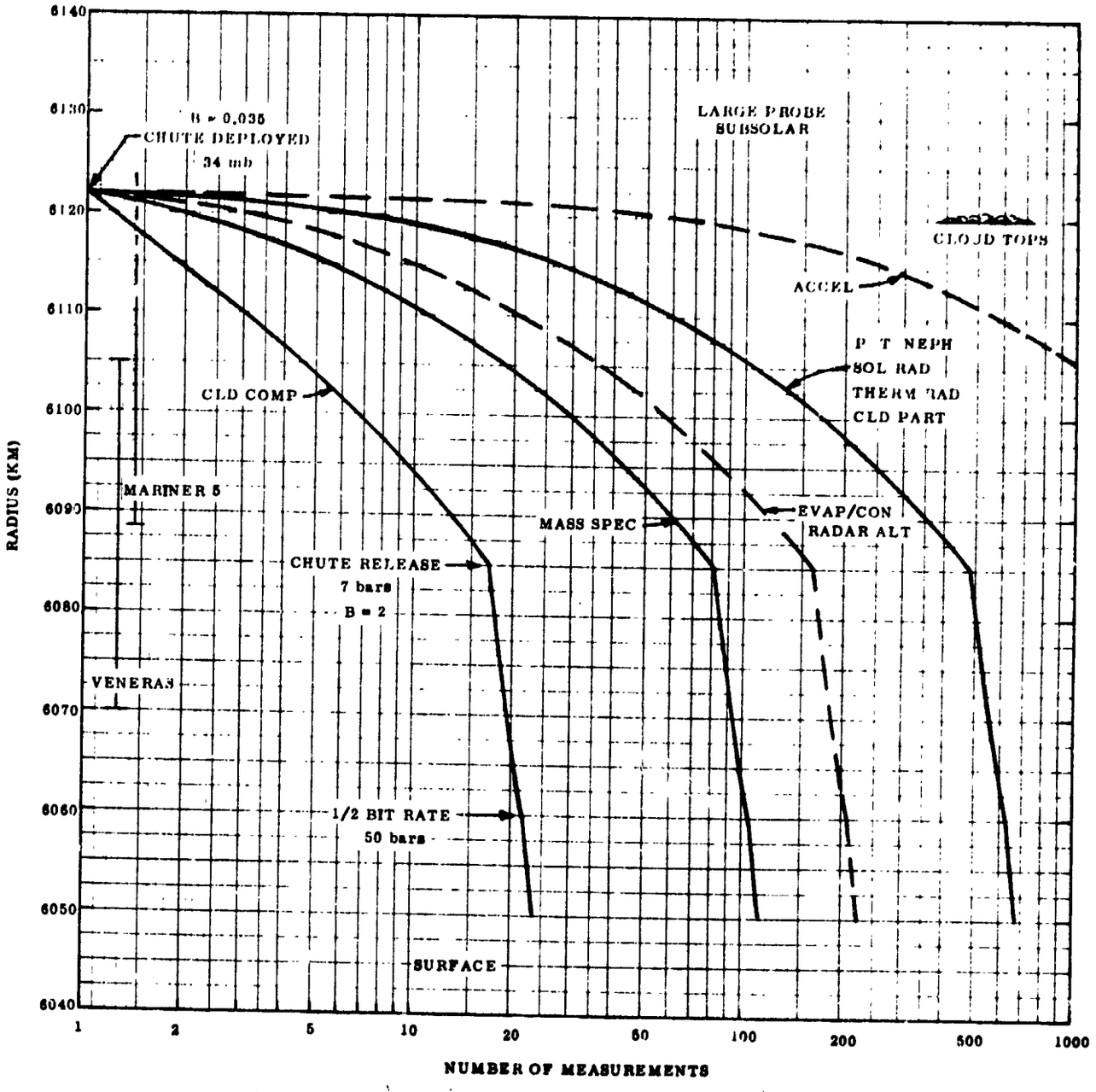


Fig. III-9 Number of Samples vs Altitude

2. Engineering Mechanics - Large Descent Probe

a. Requirements - Design of the structural and mechanical subsystems of the descent probes is influenced by several general requirements, including:

- Meeting quarantine restrictions;
- Achieving a stable entry and descent attitude;
- Holding entry heating and viscous forces to reasonable levels;
- Obtaining clean atmospheric samples;
- Survival to the surface.

Specific requirements for each descent probe are associated with the target and the descent profile needed for the particular instrument complement carried. For the large probe these requirements are given below:

Entry angle, -50°;

Science instrument weight, 69.5 lb;

Communications system weight, 54.8 lb;

Power dissipated by science instruments and communications equipment, 274 W;

Altitude (radius) at deployment of science instruments, 6122 km;

Ballistic coefficient required for descent rate control at instrument deployment altitude, 0.035 slugs/ft^2

Altitude (radius) at release of rate control decelerator, 6085 km;

Ballistic coefficient of descent capsule after decelerator release, 2.0 slugs/ft^2.

The ambient temperature history for the descent profile resulting from the above conditions is shown in Fig. III-10. The V5M atmosphere is used to establish temperature and pressure histories, but science instrument deployment altitude and deceleration design and staging altitude are based on the lower density atmosphere.

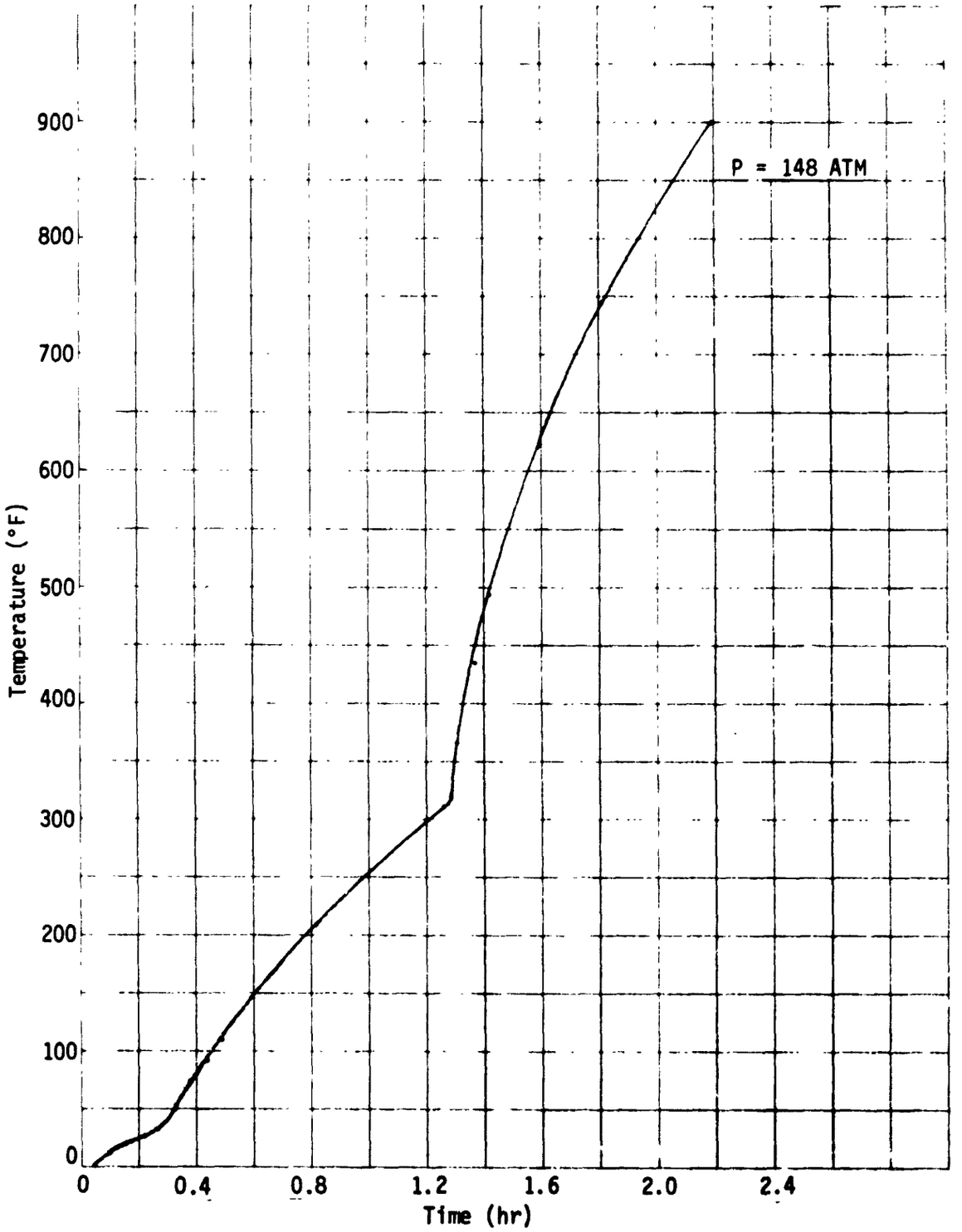


Fig. III-10 Ambient Temperature History, Large Descent Probe

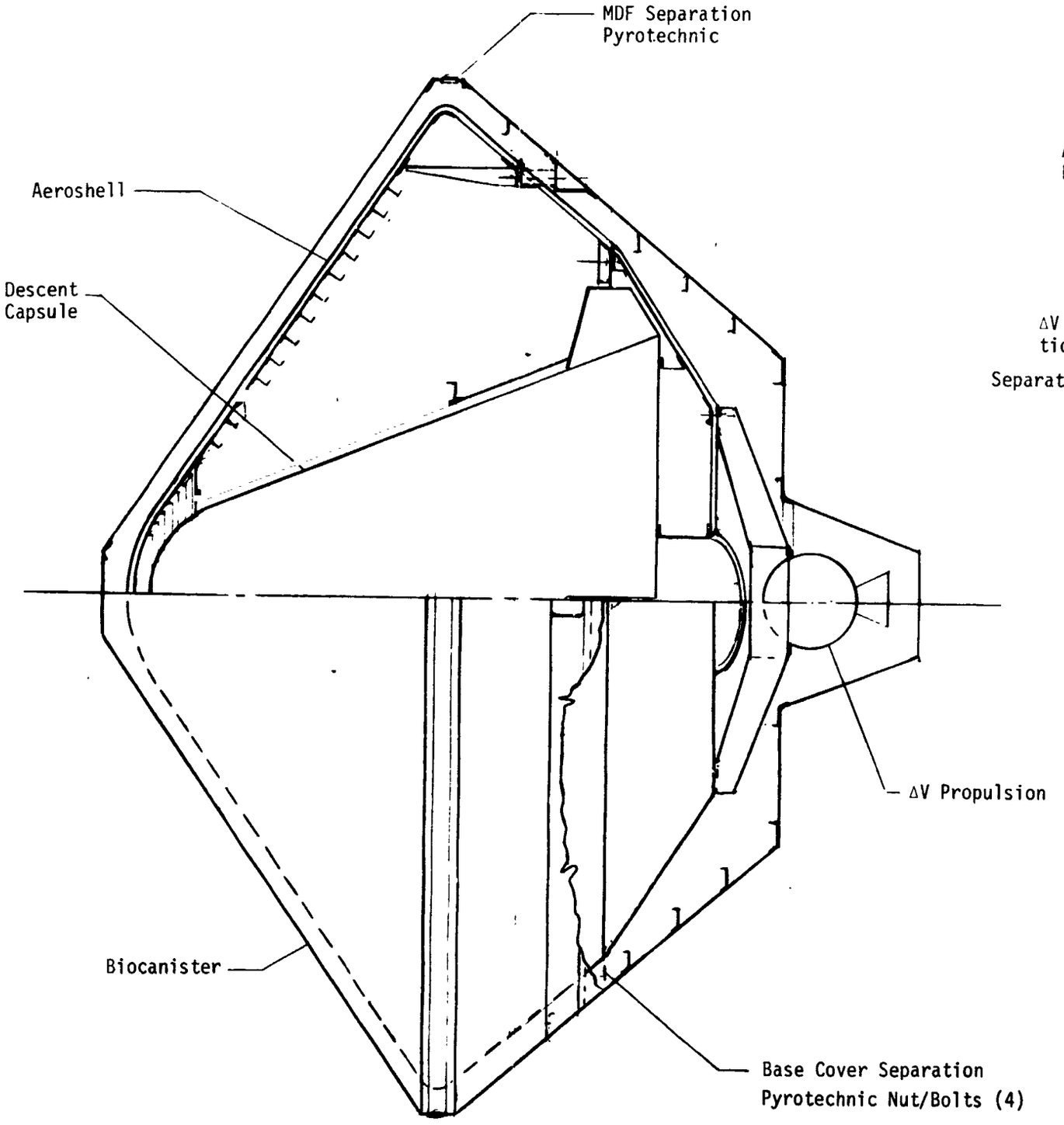
b. Configuration Definition and Weight Summary - The inboard profile of the large descent probe is shown in Fig. III-11 and the inboard profile of the large descent capsule in Fig. III-12. A weight summary is presented in Table III-3.

Functional Description - The large probe system includes the terminal descent capsule, capsule deployment and decelerator system, the deflection propulsion system, the spin-up/despin system, the Entry Vehicle, and the biocanister/adapter structural and mechanical system. The complete system is shown in the inboard profile drawing, Fig. III-11. The major assemblies and interfaces are defined with separation planes.

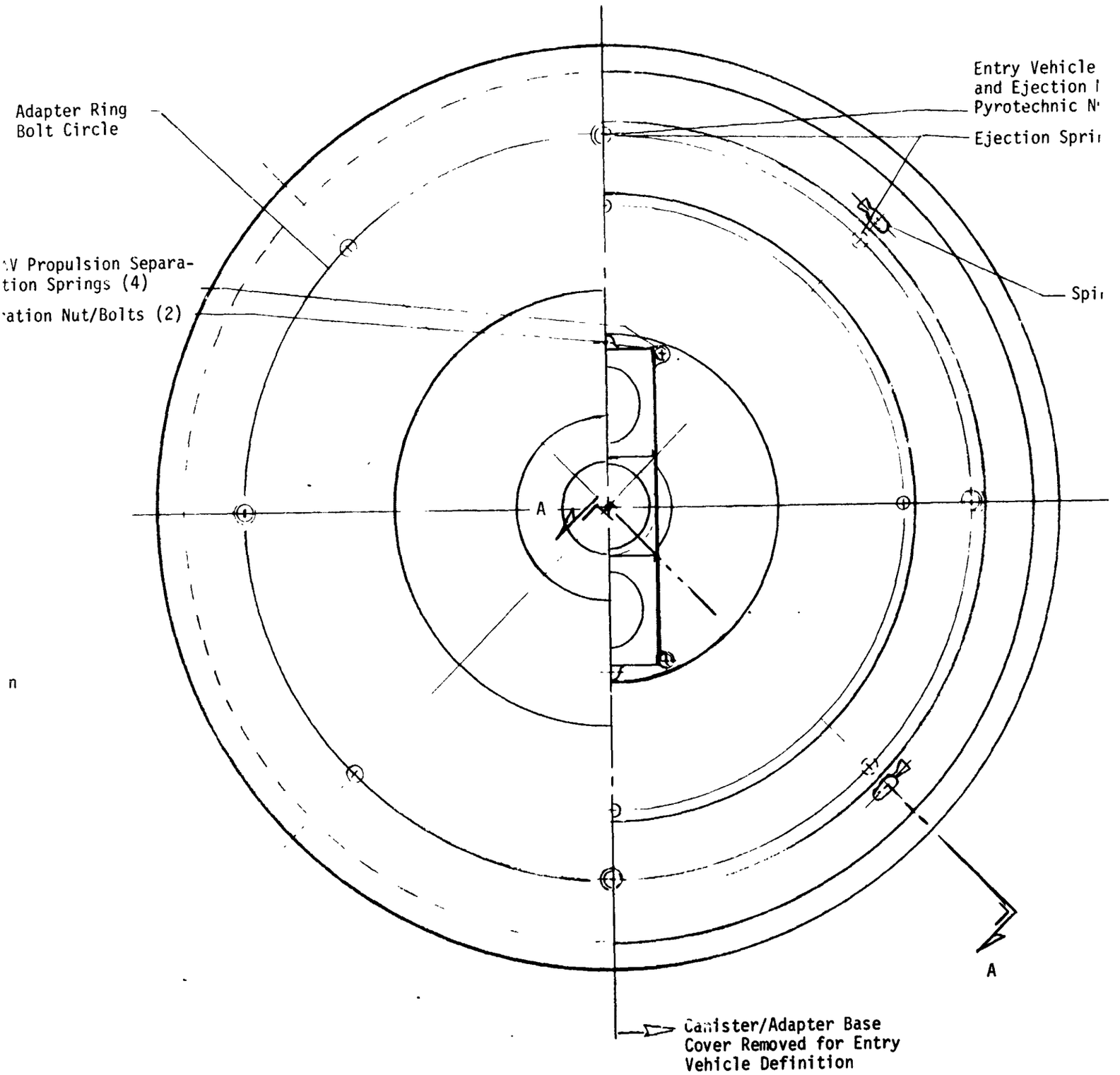
The Entry Vehicle system is encapsulated in a biocanister/adapter structural shell before sterilization. The system is maintained sterile during boost and trans-Venus cruise to encounter. The biocanister cover separation is achieved by ignition of an encapsulated linear charge [Mild Detonating Fuse (MDF)] encircling the maximum diameter of the canister shell. The MDF impulse breaks the structural connection and imparts a separation velocity to the cover.

The biocanister base shell includes an adapter ring that mounts the Entry Vehicle with four pyrotechnic nut/bolts equally spaced. It provides the stiffness and strength to the assembly required for handling and shipping of the probes. The canister adapter ring mates with a support ring that is an integral part of the adapter truss system of the Planetary Vehicle for support for booster loads and Planetary Vehicle maneuvering.

Entry Vehicle ejection impulse is supplied by eight compression springs equally spaced. Four are located concentric with the mounting bolts and four are alternately centered between the mounting bolts.



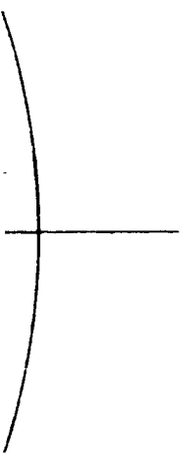
FOLDOUT FRAME

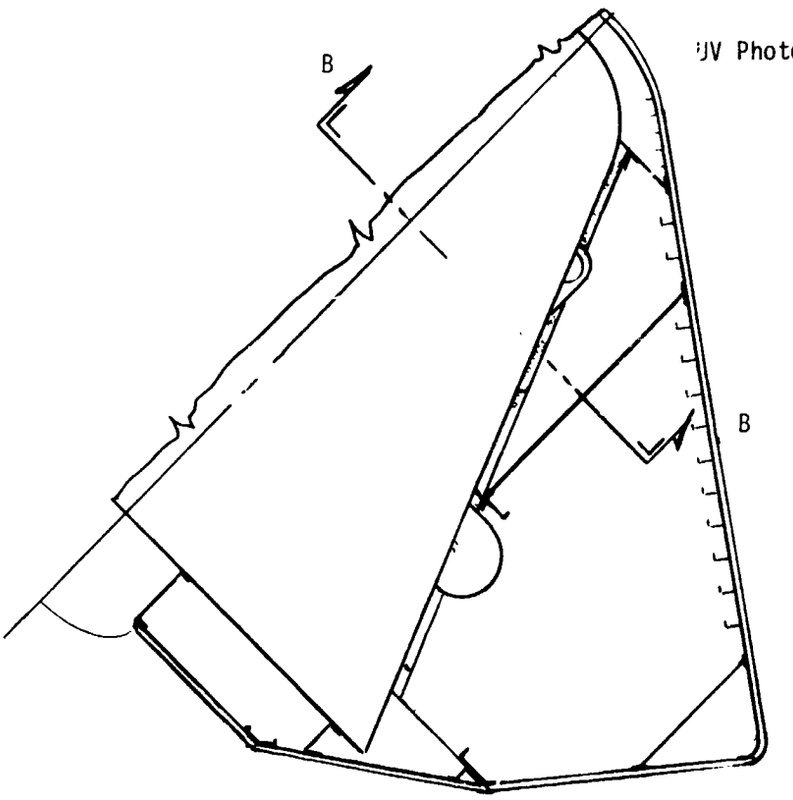


FOLDOUT FRAME 2

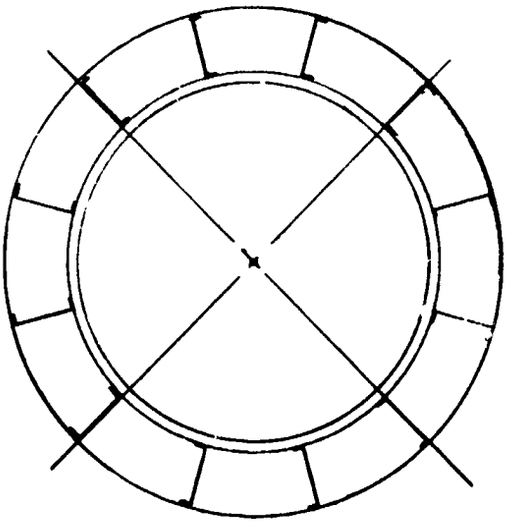
Vehicle Separation
ection Mechanism
chnic Nut/Bolts (4)
on Springs (8)

Spin-Up Rockets (4)

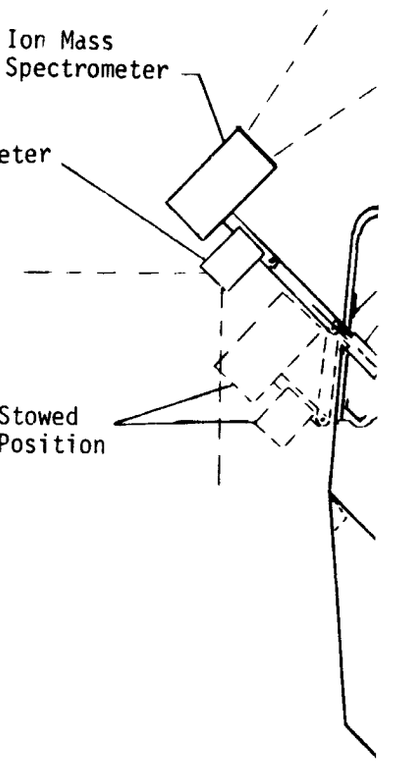




Section A-A

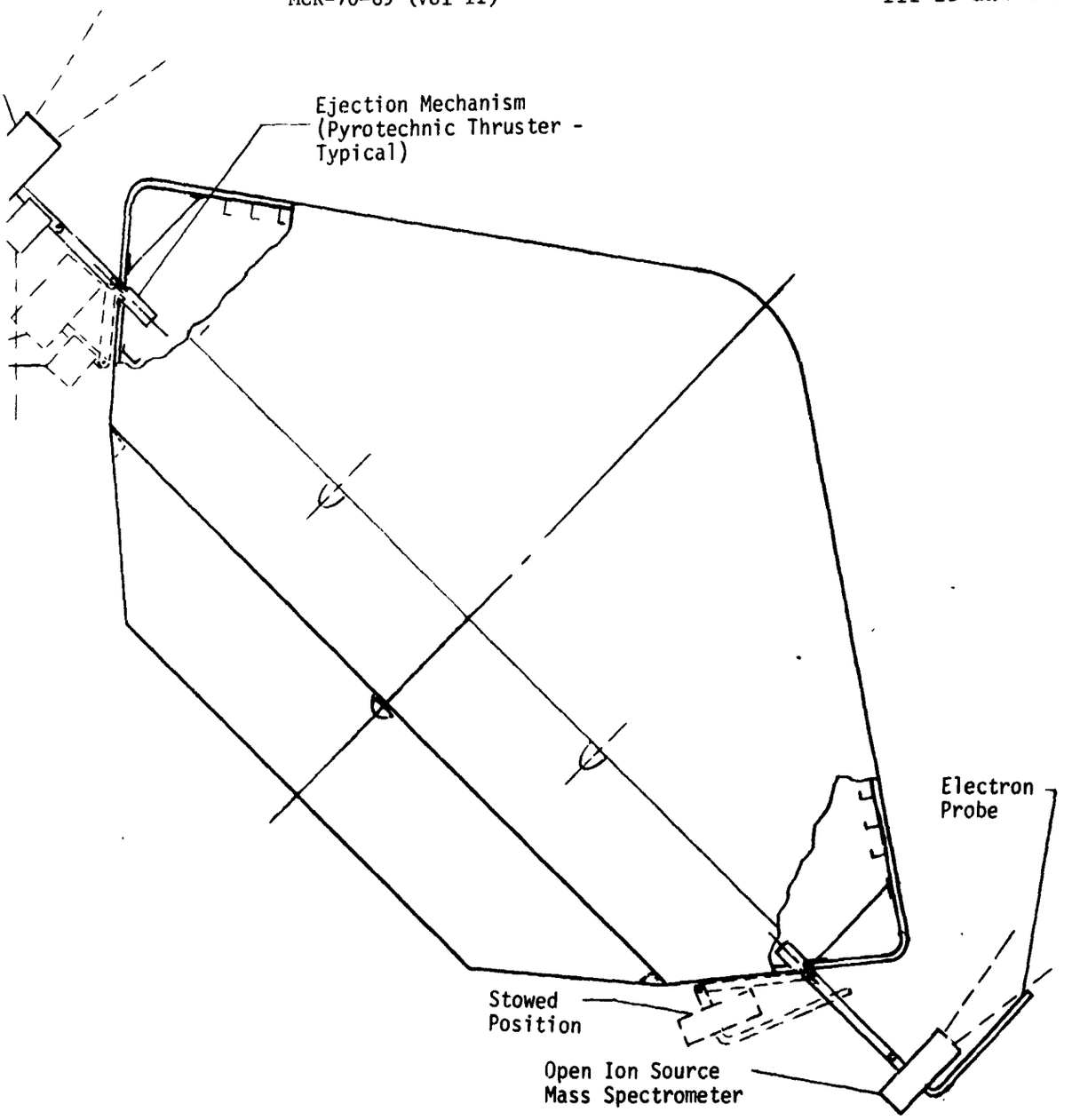


Section B-B



Scale: 1/10

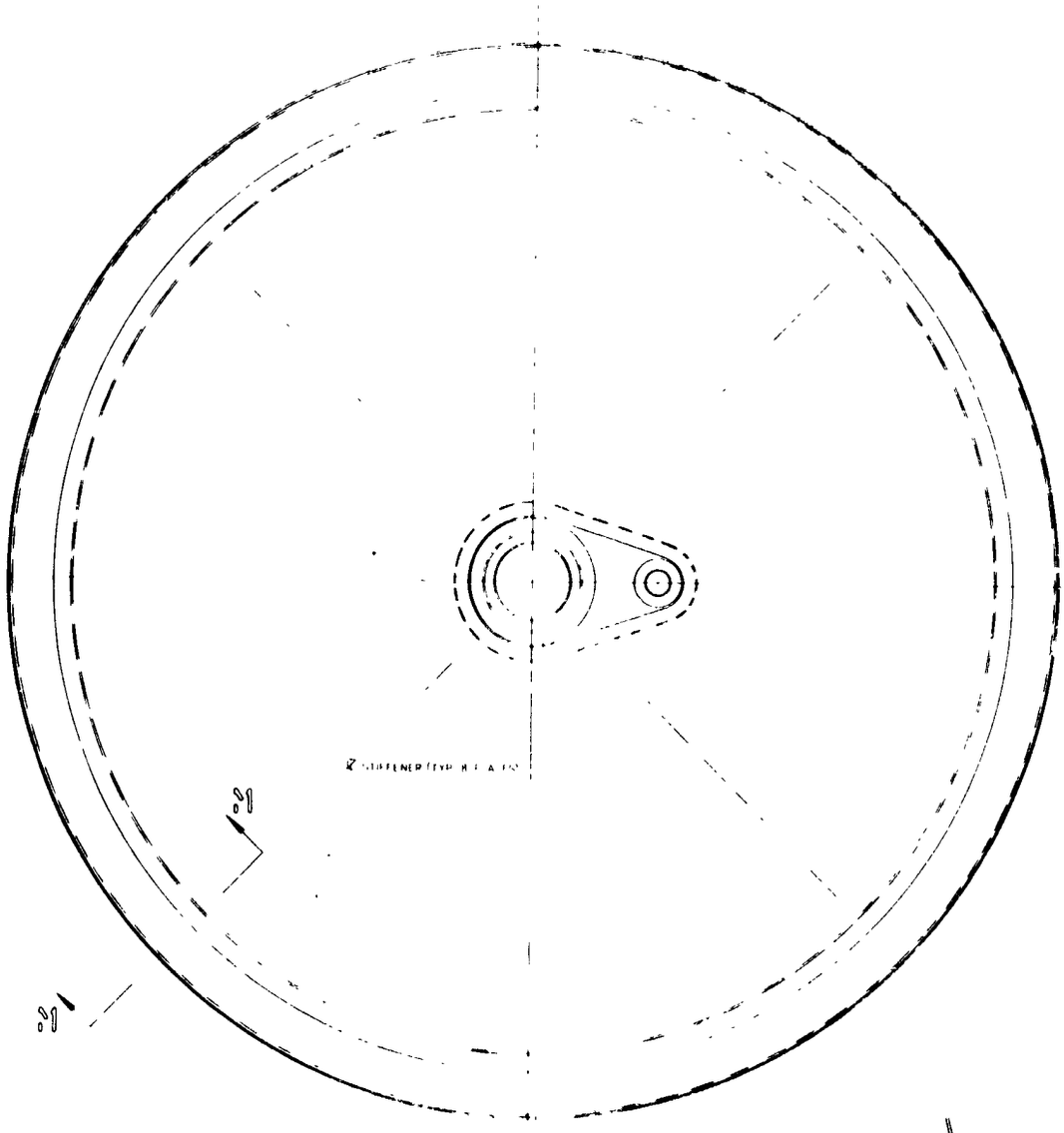
FOLDOUT FRAME 3

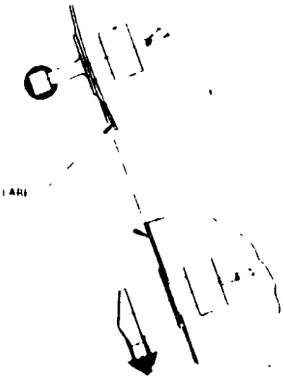


Upper Atmosphere Science for Flyby
Mission Alternative Configuration

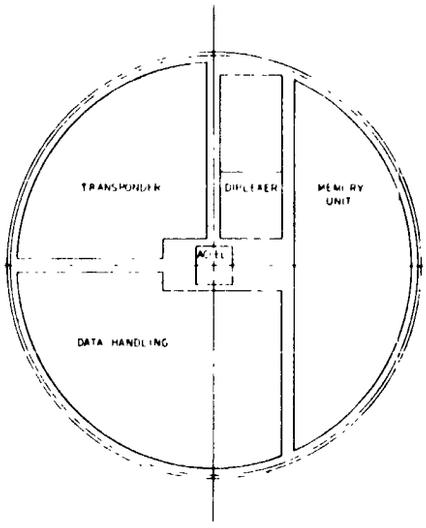
Fig. III-11 Inboard Profile, Large Ballistic Descent Probe System

FOLDOUT FRAME 4

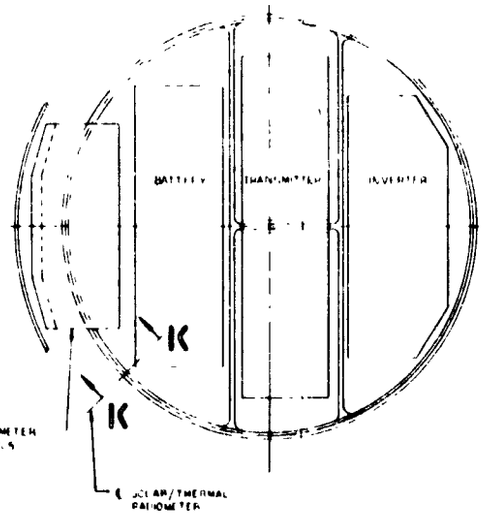




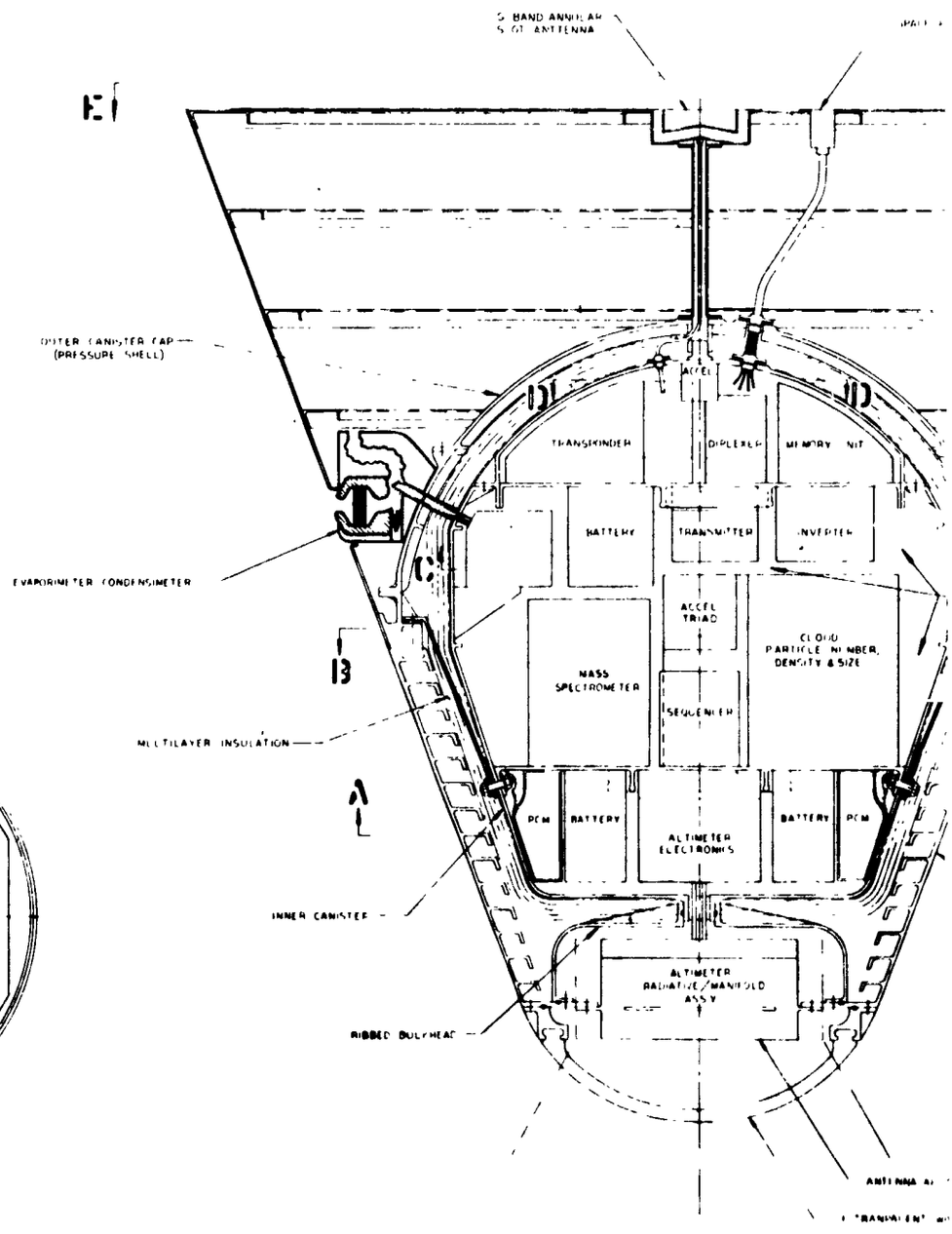
FOLDOUT FRAME



D-D

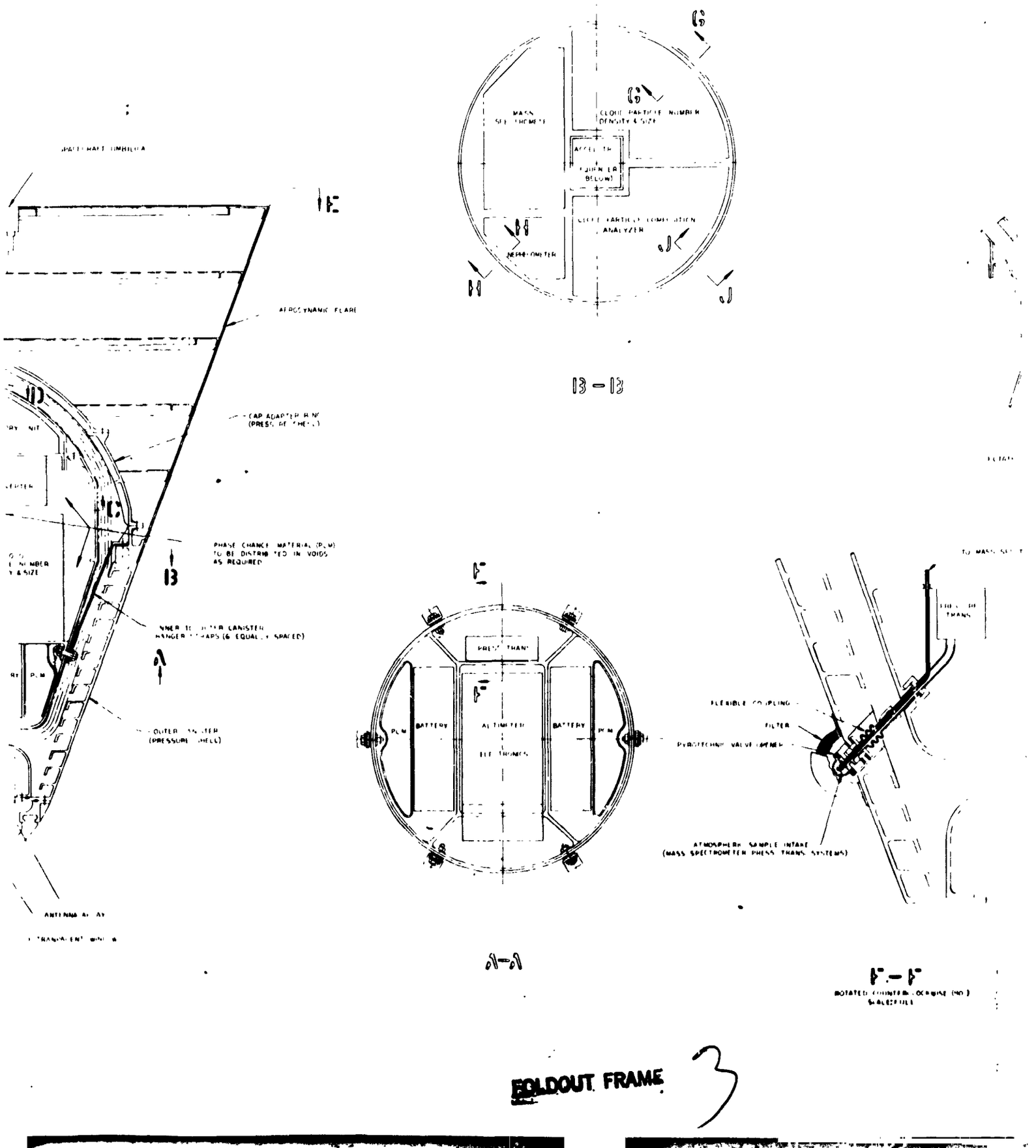


C-C



MAIN VIEW

FOLDOUT FRAME



B – B

D – D

F – F
ROTATED COUNTERCLOCKWISE (NO.)
SCALE FULL

FOLDOUT FRAME 3

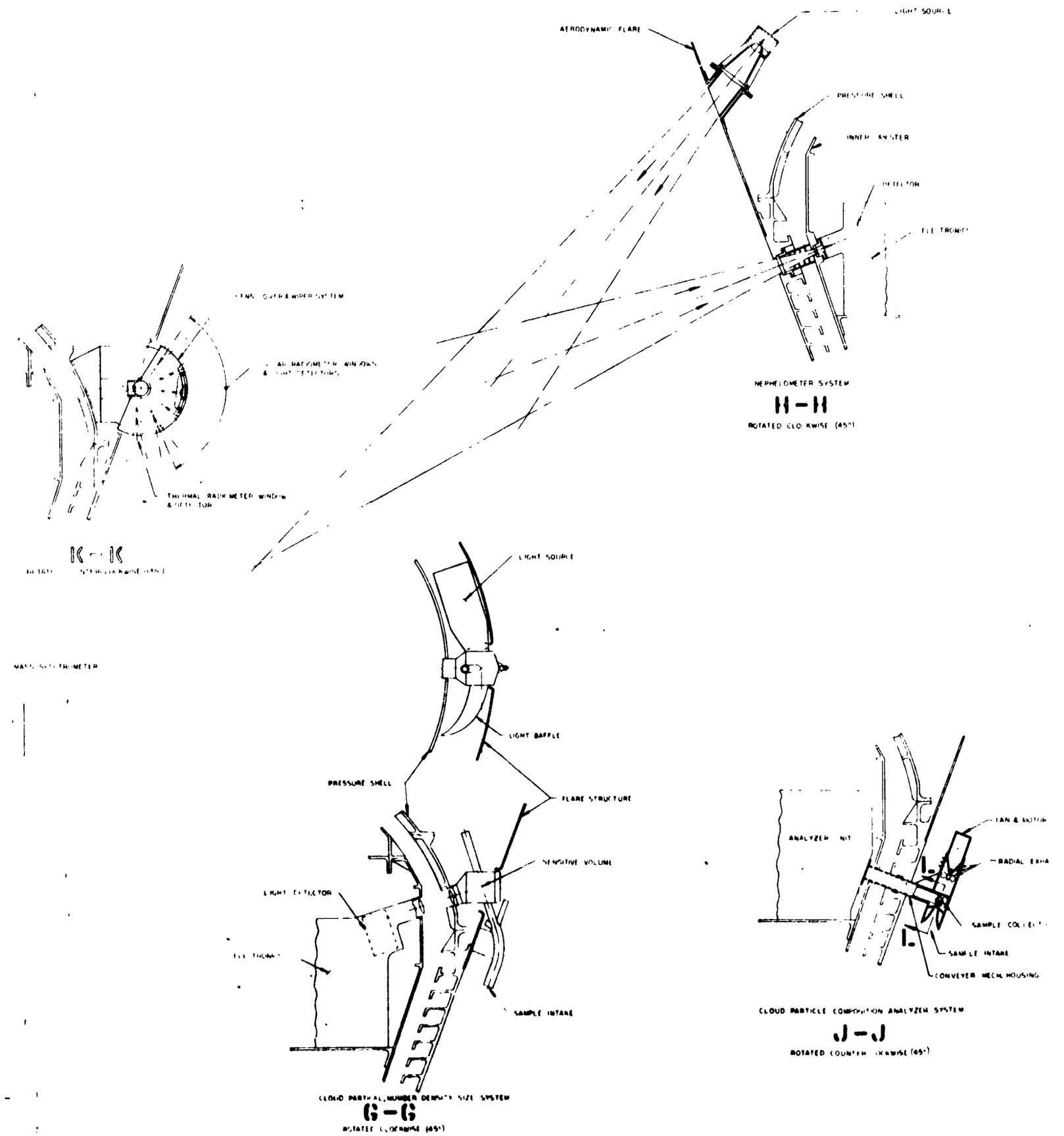


Fig. III-12 I

FOLDOUT FRAME 4

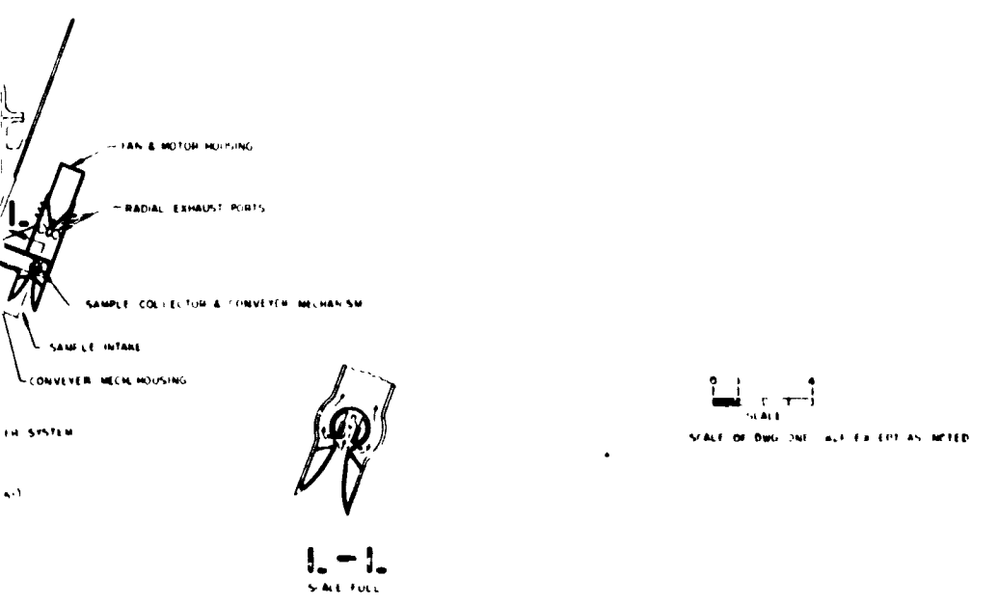


Fig. III-12 Internal Arrangement, Large Ballistic Descent Capsule

FOLDOUT FRAME 5

Table III-3 Large Ballistic Probe Weight Summary
(Impacting S/C Mode)

Element	Weight (lb)	
Descent Capsule		(274.5)
Science	69.5	
Electronics	54.8	
Pressure Vessel	87.0	
Internal Structural Shell	18.0	
Internal Equipment Support and Science Integration	12.0	
Aerodynamic Flare and Fins	12.0	
RF Nose Cap Window	4.0	
Internal Insulation	7.9	
Phase Change Material	6.3	
Antenna and Umbilicals	3.0	
Decelerator System		(21.7)
Main Parachute	16.7	
Drogue and Chute Cans	5.0	
Aeroshell		(196.0)
Aeroshell Structure Weight	106.0	
Heatshield		
Forward Cone	71.0	
Base	19.0	
Separation Hardware		(2.0)
Spin-Up/Despin (Fixed)		(4.0)
Entry Weight		498.2
Spin/Despin/Separation (Spent)		9.0
Biocanister/Adapter		55.0
ΔV Propulsion		7.0*
Total System		569.2†

*18 lb for flyby mode.

†608.8 lb for flyby mode (includes 28.6 lb for upper atmosphere science instruments and supporting electronics).

Four spin-up rockets are mounted to the Entry Vehicle base cover near the major diameter. These are jettisoned after spin-up by timed pyrotechnic pin pullers. The deflection propulsion module is mounted to the base through a structural box. The box-like structure permits using four separation springs and alignment screws at the corners while requiring two pyrotechnic separation nut/bolts.

The yo-yo despin system includes a pair of yo-yo weights on the base cover, their cables circumscribing the Entry Vehicle support and ejection bolt/spring circle adapter ring. The yo-yos are released by a pyrotechnic pin-puller at each weight. The capsule deployment and decelerator chute is packaged in an annular compartment below the Entry Vehicle base cover at the base of the capsule.

The umbilical connector for the probe system to spacecraft is a rigid multipin-type socket that requires a low axial force for disconnect.

The aeroshell structure is a ring-stiffened aluminum monocoque shell frontal body covered with a carbon phenolic heat shield. A fabricated ring at the major diameter provides the primary support of the cone shell for the entry pressure loads. Intermediate rings at 2.0-in. spacing provide the support of the shell for local instability. The nose cover is an integrally stiffened spherical cap.

The base cover is a ring-stiffened thin shell. It is covered with ESA 5500 lightweight ablator. The cover separates at an intermediate diameter on the base cone to minimize the size of the removable cover, but large enough to allow extraction of the descent capsule without interference. Base cover separation is provided by four pyrotechnic nut/bolts and removed with a drogue chute.

The descent capsule is supported within the Entry Vehicle in a sphere/cone receptacle that is backed up with radial ribs outward to a cylindrical shell. The cylindrical shell ties to the aeroshell along its circumference to uniformly react the high deceleration loads of entry. The rigid capsule shell bears directly on an interposing medium in the sphere/cone receptacle. The pressure distribution medium is a high density insulation material such as Min-K.

The descent capsule is an aerodynamically stable sphere/cone/flare body to achieve the desired descent time for science sampling. The internal arrangement is shown in Fig. III-12. The 21° cone/flare half angle and 42.0-in.-diameter base result in a ballistic coefficient of 2.0 slugs/ft^2 after release from the chute. Capsule roll control during descent is effected through four small fins fixed in an inclined position with respect to the roll axis.

To provide protection from the high temperature and pressure to impact, the major portion of the science instruments and the supporting equipment are encapsulated in a double-walled canister. The concept is a pressure sustaining hermetically sealed outer shell structure encapsulating a hermetically sealed inner canister. An evacuated annular cavity between the two canisters is lined with multilayered insulation. The inner canister contains one atmosphere of sulfur hexafluoride gas. The inner canister is structurally attached to the outer canister for high g entry loads by six equally spaced slender titanium straps. It is supported for lateral loads on the center at each end by a concentric pin and bushing arrangement. The bushing is phenolic to effect a low conduction heat path.

A small cavity that houses the radar altimeter antenna in the nose of the canister is isolated from the main compartment within a single-walled canister design. An RF transparent nose cap is required for forward view.

The pressure sustaining outer shell of the nose is fused silica (quartz) glass or pyroceram mounted in a metal frame. The cone frustum shell is an integrally machined and welded ring stiffened titanium shell. The aft closure spherical bulkhead is a waffle stiffened titanium shell. The titanium alloy 6Al-4V is selected for all titanium structures.

The inner canister is a pure monocoque welded titanium shell structure. The equipment is mounted to beryllium shelves to provide a heat sink. Numerous penetrations through both walls and the insulation require local built-in adapters in the pressure shells that are installed primarily by welding.

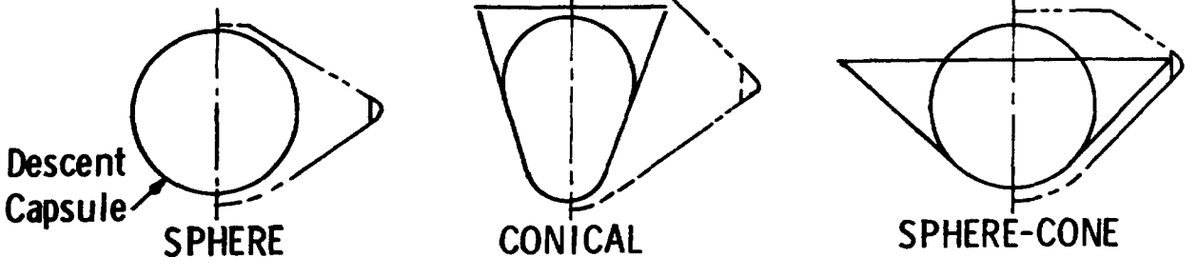
The assembly joint at the major diameter of the base bulkhead is required for installation of the inner canister with the tension straps and the multilayer insulation. The second assembly joint of the cap within the base bulkhead facilitates installation of science instruments that penetrate both walls.

The penetration designs shown can feasibly be made to accommodate seals. Definition of the seals for all penetrations was not within the scope of this study.

c. Descent Capsule Design - Large Descent Probe

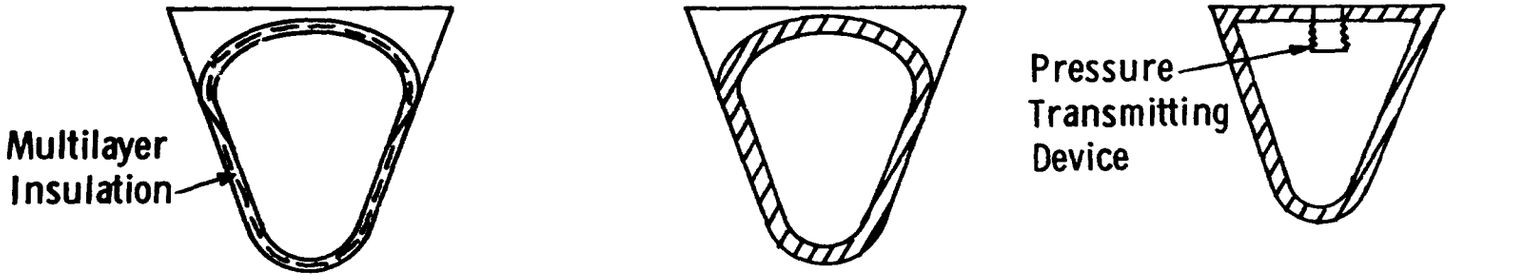
Configuration Selection - The primary factors controlling the shape of the descent capsule of the large probe are achieving the descent rate and time needed for the science instruments and the requirement for a stable descent to avoid loss of signal due to antenna pointing deviations. Several possible shapes considered are shown in Fig. III-13, including the selected shape in the center. The first of these, the sphere, is structurally more efficient, smaller in size, and results in lower system weights. However, its high ballistic coefficient, $\sim$10 slugs/ft^2, results in exceeding the desired measurement interval by a factor of 2. Also, little data are available pertinent to the stability of this configuration and predictions of antenna pointing angle and instrument sample port orientation are thus subject to large uncertainties.

DESCENT CAPSULE SHAPE



	SPHERE	CONICAL	SPHERE-CONE
Descent Time (hrs)	0.4	0.9	1.8
Relative System Weight	0.8	1.0	1.0

THERMAL/STRUCTURAL DESIGN



DOUBLE-WALLED CANISTER
Used in Study

OUTSIDE INSULATION
Potentially Lighter

PRESSURE EQUALIZED
Lightest - Avoids Sealing Problems

Fig. III-13 Descent Probe Tradeoffs

The last shape shown, a conical, 45° half angle, skirted sphere retains the structural efficiency of the sphere and provides more certain stability. This shape has a long descent time and thus has about the same weight as the selected system. Stability of the selected 21° conical capsule is the best of the three, e.g., the gust magnitude required to pitch the more slender (21°) cone 30° is twice the magnitude that is required for the 45° skirted sphere (at an altitude of 6080 km).

Thermal/Structural Design - A passive thermal control system is capable of providing instrument protection to the surface for the descent times required in this study. The insulated, double-wall design concept evolved in Ref III-1 was used to take advantage of the existing subsystem design data. This approach provides an evacuated space between an outer and an inner wall for the multilayer insulation in order to achieve as low a thermal conductivity as possible. However the many penetrations of these layers for cabling, structural attachment, etc, significantly degrade the multilayer performance. Also, the outer shell must resist the 150 bar pressure at temperatures of over 900°F. Thus an alternative design using external insulation and a single pressure resistant wall is potentially lighter and less complex. The performance of the external insulation in the presence of the high pressure, high temperature CO_2, however, is not well defined at this point. This concept, shown in Fig. III-13, is discussed in Chapter VIII, Section A, in detail.

A third concept, equalizing the pressure within the instrument container with that of the outside atmosphere, is also attractive because it eliminates the pressure vessel entirely and thus avoids many of the sealing problems. It is also discussed in Chapter VIII.

For the double-walled design used in this study, a program for calculating the pressure vessel volume and wall thickness, insulation thickness, and amount of phase change material required is described in Chapter VIII. This program has been used to optimize the relative amounts of structure, insulation, and phase change material.

In addition to the descent profile and payload weight and power dissipated, the value used for packaging density is also significant in establishing the design because pressure vessel weight is directly proportional to the internal volume. A value of 40 lb/ft^3 has been used, which represents a 60 to 70% volumetric efficiency. This is not believed to be a particularly conservative value in view of values experienced in previous hardware programs. The sensitivity of capsule weights to packaging density and other design parameters is shown in Chapter VIII.

A titanium alloy was selected for the pressure vessel based on trade studies conducted in Ref III-1.

The specific input quantities for sizing both the large and small descent capsule thermal and structural systems are given in Table III-3 and the resulting capsule dimensions and weights are given in Fig. III-11 and Table III-4.

d. Entry Vehicle Design - Large Descent Probe

Configuration Considerations - The size and shape of the descent capsule that must be contained, and the altitude at which its science instruments have to start gathering data, are the major factors determining the Entry Vehicle shape and ballistic coefficient. Other considerations are entry heating, entry dynamic stability, and attitude control system design considerations.

Table III-4 Design Information for Descent Probes

Model Atmosphere	Large Probe V5M	Small Probe V5M
Radius at Beginning of Subsonic Descent (km)	6122.0	6122.0
Radius at Chute Release (km)	6090.0*	6103.5†
Ballistic Coefficient before Chute Release (slugs/ft^2)	0.035	0.015
Ballistic Coefficient after Chute Release (slugs/ft^2)	2.0	2.0
Mass of Science and Communication Equipment (lb_m)	125.6	62.8
Packaging Density of Payload (lb_m/ft^3)	40.0	40.0
Allowable Temperature Rise of Instruments (°F)	60.0	60.0
Initial Instrument Temperature (°F)	70.0	70.0
Average Specific Heat of Instrument $\left(Btu/(lb_m\text{-}°F)\right)$	0.2	0.2
Electrical Power Dissipation (W)	274.0	110.7
Pressure on Planet Surface, R = 6050 km (psia)	2210.0	2210.0
Initial Pressure Shell Temperature (°F)	70.0	70.0
Density of Structural Material ($lb_m/in.^3$)	0.16	0.16
Modulus of Elasticity of Structural Material (psi)	9.6×10^6	9.6×10^6
Poisson's Ratio of Structural Material	0.31	0.31
Safety Factor	1.1	1.1
Allowable Stress	7.0×10^4	7.0×10^4
Conductivity of Structural Material [Btu/(hr-ft-°F)]	5.86	5.86
Specific Heat of Structural Material $\left(Btu/(lb_m\text{-}°F)\right)$	0.154	0.154
Absorptivity of Probe Surface	0.69	0.69
Emissivity of Probe Surface	0.24	0.24
View Factor between Probe and Sky, Probe and Clouds	0.5	0.5
View Factor between Sun and Probe	0.5	0.5
Conductivity of Insulation [Btu/(hr-ft-°F)]	0.0004	0.0004
Conductance of Penetrations [Btu/(hr-°F)]	0.76	0.3
Density of Insulation (lb_m/ft^3)	10.0	10.0
Enthalpy of PCM (Btu/lb_m)	100.0	100.0
Density of PCM (lb_m/ft^3)	50.0	50.0
Specific Heat of Insulation ($Btu/lb_m\text{-}°F$)	0.2	0.2

*Radius in V5M atmosphere at pressure corresponding to 6185 km in lower density atmosphere model.

†Radius in V5M atmosphere at pressure corresponding to 6100 km in lower density atmosphere model.

From the entry heating and stability standpoint, and from compatibility with a spin-stabilized attitude control system, it has been found in past studies (Ref III-1 and III-2) that the desirable range of aeroshell half cone angles is 45° to 60°. This range, in conjunction with nose radii of 4 to 12 in., and the ballistic coefficients of 0.6 slugs/ft^2 or less, results in acceptable peak convective and radiative heating levels. This range of cone half angles also gives ratios of roll inertia to pitch inertia greater than 1.0, which is a requirement for spin stabilization.

Within this range of aeroshell cone angles, the shape of the descent capsule and the ballistic coefficient required to achieve subsonic (staging) velocities with the Entry Vehicle at a given altitude establish the specific aeroshell design. A curve of altitude vs m/C_DA for Mach 0.9 is shown in Fig. III-14. Generally, lighter design is achieved with the highest ballistic coefficient that meets the altitude/Mach number criteria because it requires the smallest aeroshell. Thus, from Fig. III-14, a value of 0.37 slugs/ft^2 is seen to be desirable for the large probe. The shallower aeroshells, 60° half angle, generally yield lower aeroshell weights because their surface area is smaller; however, the relatively long axial dimension of the descent capsule of the large probe makes it necessary to limit cone half angle to a value of 55°.

Aeroshell Structure - The selected ballistic coefficient of 0.37 slugs/ft^2, entry angle of -50°, and entry velocity of 37,400 fps result in a peak dynamic pressure of 4073 psf, a peak stagnation pressure of 57 psi, and a peak deceleration of 342 g. Ring stiffened aluminum aeroshell design data described in Chapter VIII and shown in Fig. III-15 as a function of stagnation pressure was used to establish the weight of the large probe aeroshell.

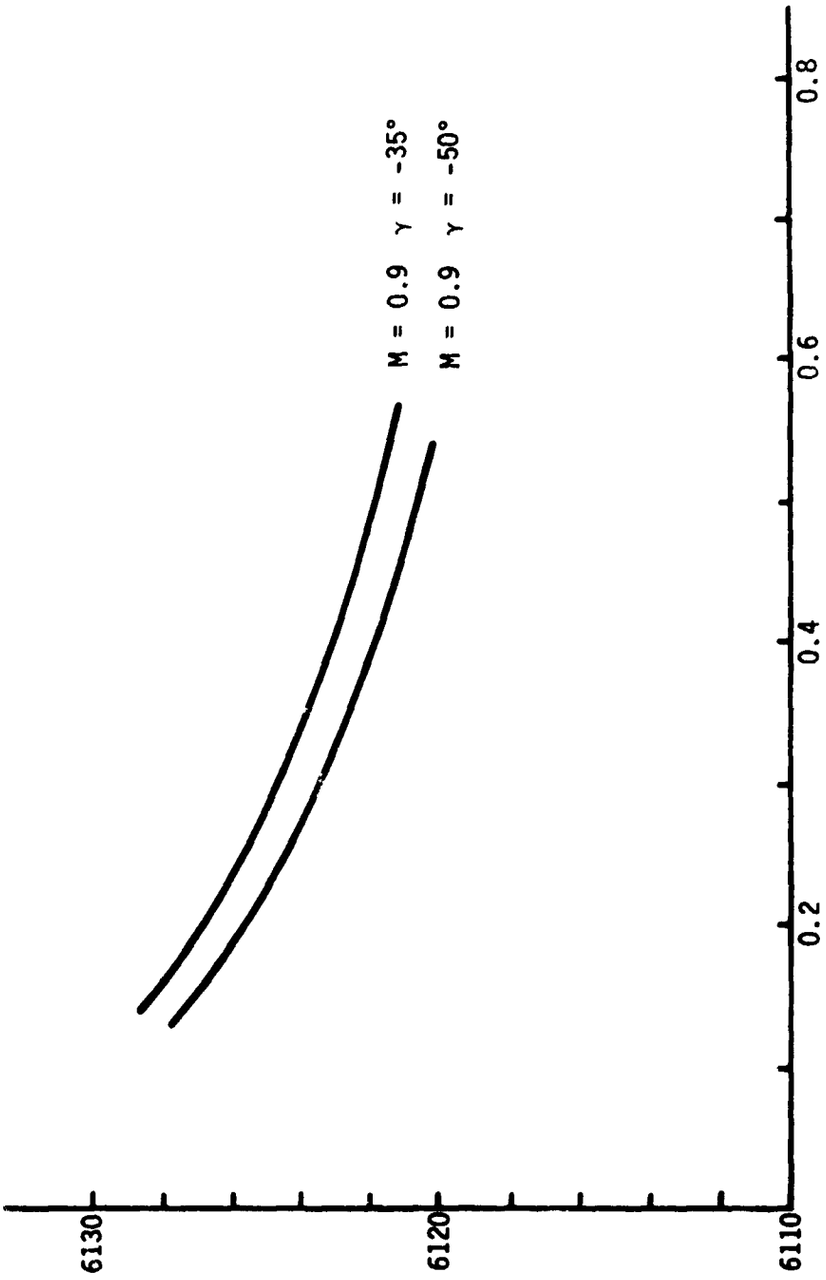


Fig. III-14 Sensitivity of Altitude for Reaching Subsonic Velocity to Ballistic Coefficient

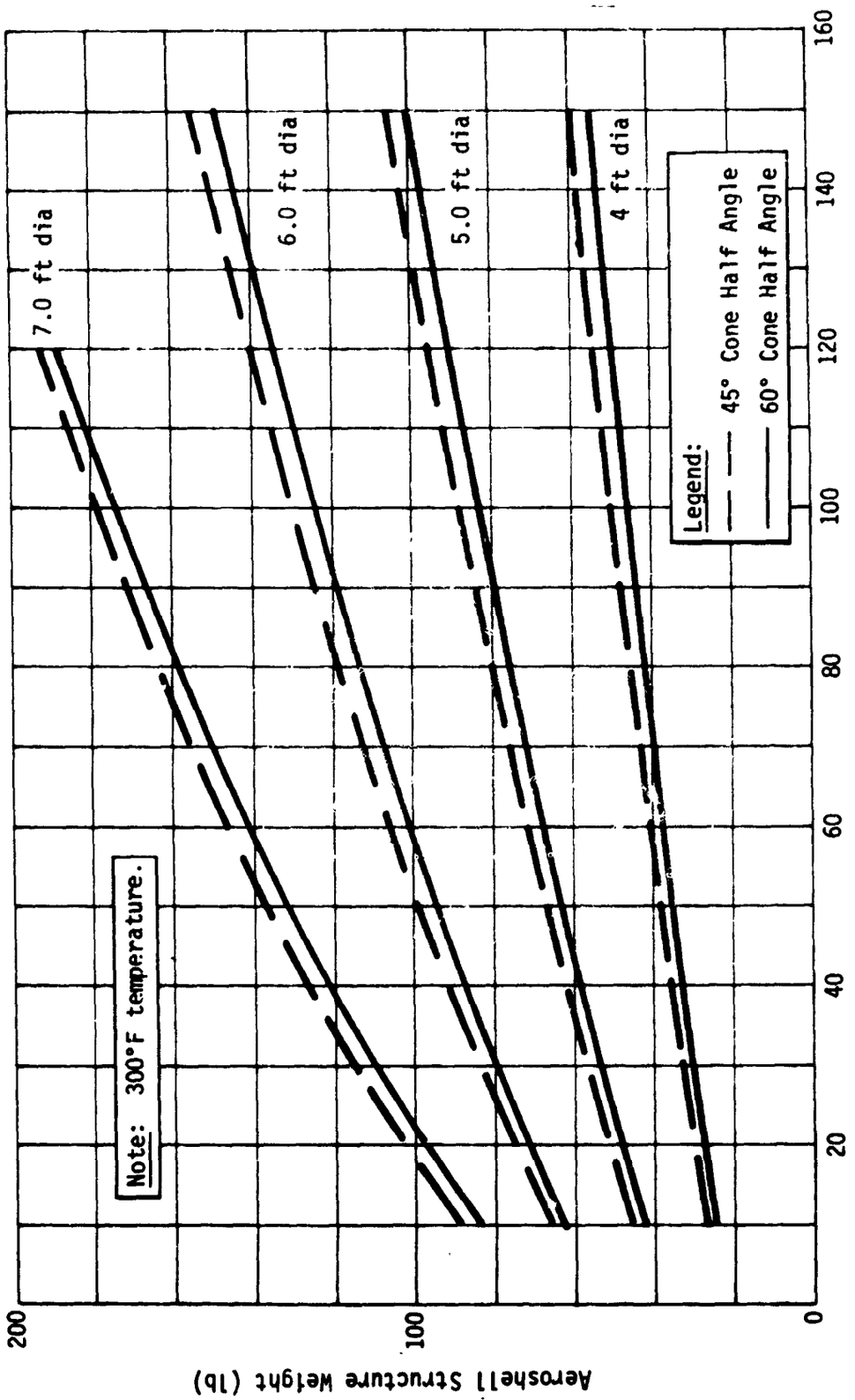


Fig. III-15 Aeroshell Parametric Weight Data

The use of the aluminum design data which is based on 300°F peak temperature at maximum load is compatible with the heat shield design. The heat shield data provided by JPL is designed to limit peak structural temperatures to 600°F any time, and peak pressure loads occur well before 300°F is reached as is seen in Fig. III-16. The only loads occurring at higher temperatures than 300°F are those incurred at staging. These are minor and also occur before the peak temperature is reached as staging is accomplished at Mach 0.9.

The aeroshell structural design data were derived in previous Martin Marietta studies and a comparison is made with Ref III-1 data in Chapter VIII. Ring stiffened designs were found in Martin Marietta studies to be about the same weight as aluminum sandwich structure in the pressure range of interest. For the large probe a weight of 106 lb is required.

Increasing the aeroshell ballistic coefficient for a constant weight descent capsule will result in a reduced aeroshell weight since aeroshell size decreases faster than the unit structural and heat shield weight increase. However, as mentioned previously, higher ballistic coefficients cause the altitude at which subsonic velocity is reached to exceed that established by the vertical targeting requirements of the instruments.

A possible tradeoff is the weight of a supersonic decelerator against the aeroshell weight saved by going to a higher ballistic coefficient design. The disadvantages of supersonic decelerator development, however, appear to outweigh the slight weight advantage of that approach.

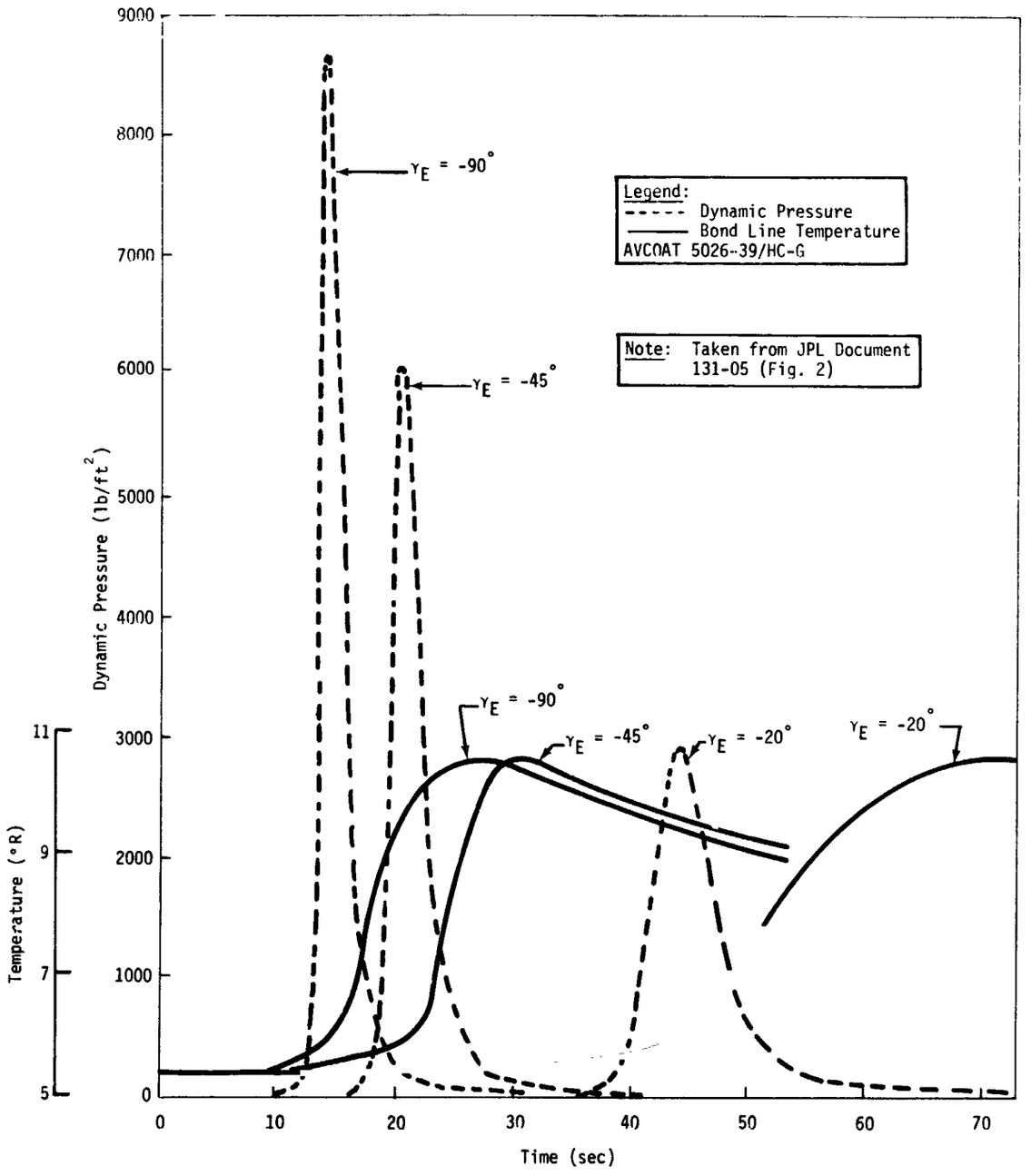


Fig. III-16 Dynamic Pressure and Bond Line Temperature (V_E = 36,000 ft/sec; M/C_DA = 0.6 slugs/ft²)

Heat Shield - Design data for heat shield weight and thickness have been provided by JPL for this study in JPL Document 131-05, which is included as Appendix E to this report (Volume III). Data are provided for two materials that exemplify two possible extremes in material types, i.e., a dense, high-conductivity erosion-resistant material, carbon phenolic, and a low-density low-conductivity material that is susceptible to pressure gradient and viscous shear-induced mechanical erosion, AVCOAT 5026. The unit weights differ by a factor of 2½ to 3.0 as seen in Fig. III-17, but limitations on allowable pressure gradient and shear force as defined in Ref III-1 limit the application of the lower density material to large bluntness ratio aeroshells. The large radius required, 2 to 3 ft, to achieve the bluntness ratio R_N/R_B of 1.0 utilized in Ref III-1, result in quite large aeroshells whose additional surface area offsets the advantage of the lighter material. An exception is the special case where a large, low-ballistic coefficient probe is required for high-altitude deceleration, such as in the case for the high-cloud probe discussed in Section D of this chapter.

For the large descent probe a nose radius of 6.0 in. gives the best descent capsule packaging, and hence carbon phenolic was selected. For the entry conditions of $\gamma = -50°$ and $m/C_DA = 0.37$ slugs/ft^2, the unit weight of the heat shield is 1.9 lb/ft^2. The 6.25-ft-diameter aeroshell forebody thus requires a total weight of 71 lb, which is 14% of the 498-lb entry weight. Peak entry heating rates and pressures fall within the test capability envelope defined in Fig. III-18.

[From Fig. 345&6 (JPL Document No. 131-05 Revised)]

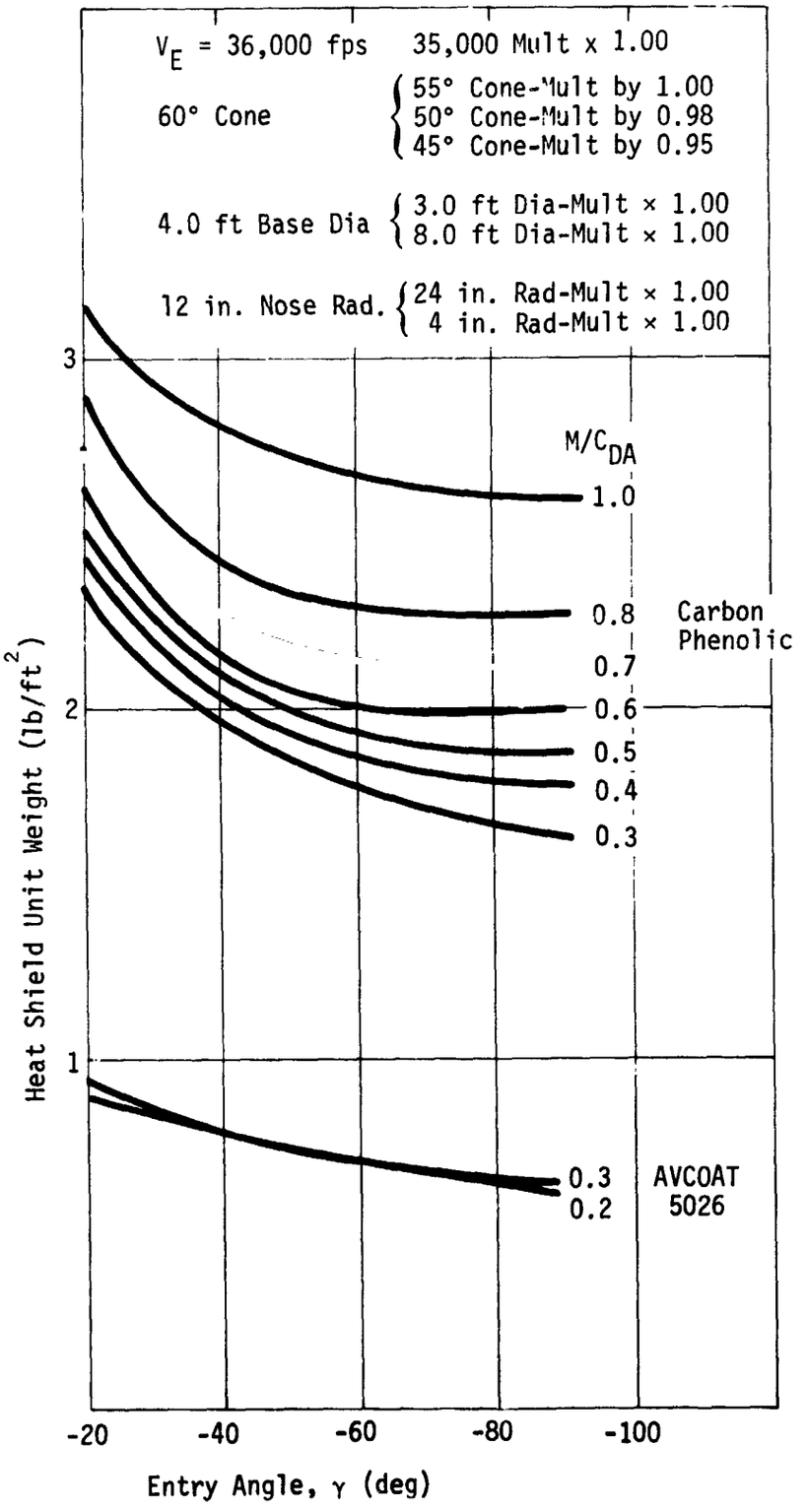


Fig. III-17 Summary of Heat Shield Unit Weights

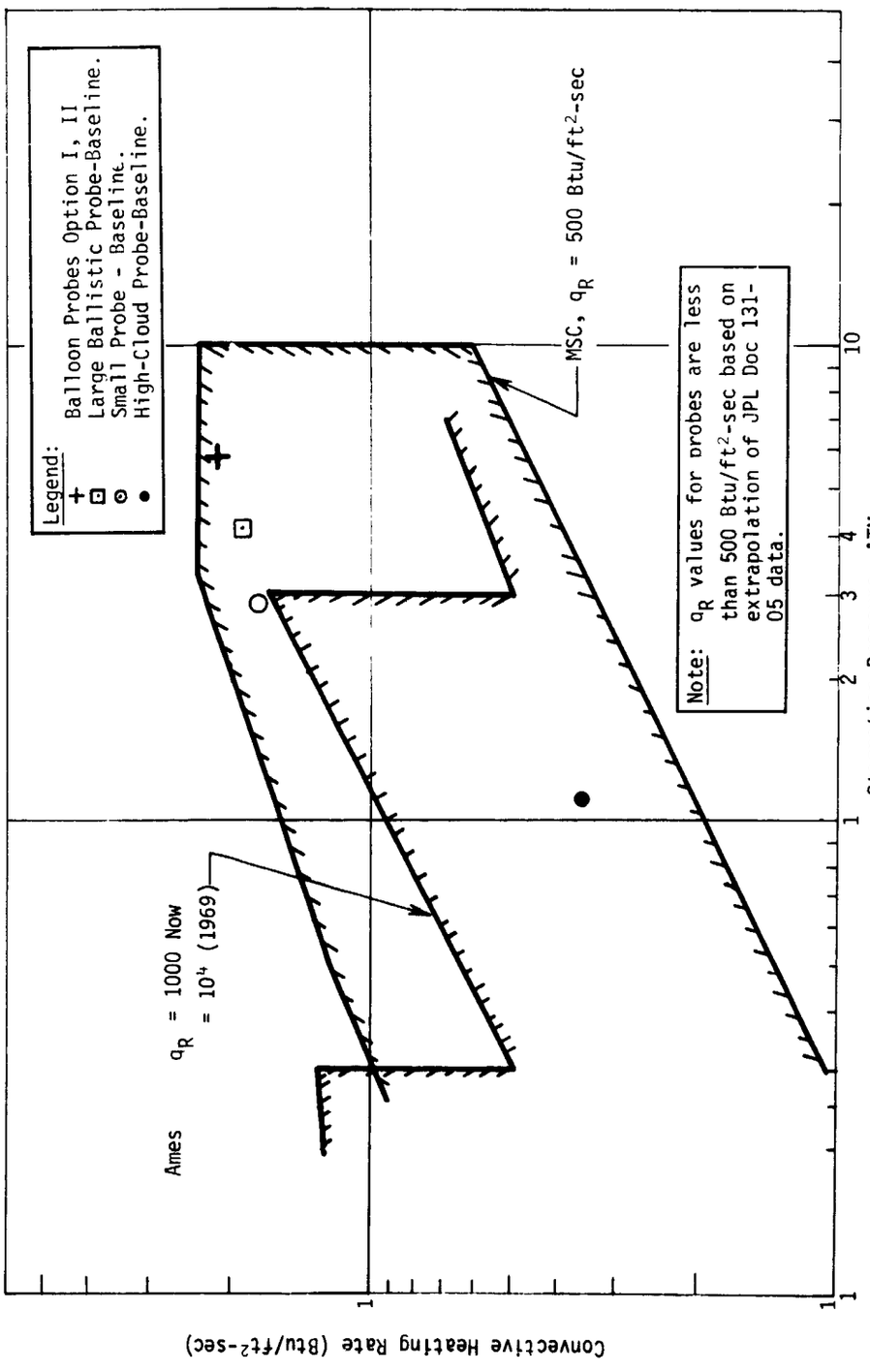


Fig. III-18 NASA Ground Test Simulation Capability and Baseline Mission Entry Conditions

For the aft cover, heat protection is also required because of radiation heating from the high enthalpy wake neck. Estimates of heat flux levels and heat shield requirements for the base were not provided by JPL for this study so a unit weight of 0.5 lb/ft^2 has been used, based on previous Martin Marietta studies (Ref III-2), which used a reinforced elastomeric silicone material, ESA 5500 M, developed by Martin Marietta for both forebody and aft cover applications.

Thermal Control - Temperatures during the period after probe ejection from the spacecraft through start of entry are controlled passively by coatings. The coating α/ε properties are selected to cool the probes, which are on the high side of the allowable temperature range, $\sim$120°F, at the time of probe ejection, to approximately 50°F during the 300-hr approach phase (see Chapter VIII, Section A).

Entry heating is of brief duration, $\sim$12 sec, and the probe heat shield is jettisoned before heat shield soak-through affects probe internal temperatures.

Attitude Control - Spin stabilization is used to maintain probe attitude for the deflection impulse thrust application and the subsequent 12-day coast period to the planet. Four small solid rocket motors are used for spinning up the probe to 3 rad/sec. Despin to 0.5 rad/sec is necessary to allow the probe to converge from its initially high angle of attack, 34°, to a value of less than 5° at peak heating. Despin can be accomplished either by solid rocket motors or by a yo-yo system.

The large descent probe roll inertia is 62 $slug/ft^2$ and four Atlantic Research Corporation MARC 18A1* rocket motors of 17.6 lb/sec total impulse each will provide the required 3 rad/sec spin rate. Average thrust is 40.9 lb, burn time is 0.41 sec, and loaded weight is 0.49 lb/motor.

*This rocket motor is defined in detail on pg 3-475 of Ref III-1.

Providing a three-axis system for reorienting the probe to zero angle of attack at entry would result in more positively limiting the angle of attack at time of peak heating. In addition, it would provide a alignment of the upper atmosphere instruments with the velocity vector of the probe (for the flyby spacecraft mode). However these benefits do not appear to warrant the added complexity and weight of such an approach.

Deflection Propulsion - Solid rocket motors provide the probe deflection impulse for the lowest system weight and are compatible with deflection accuracy requirements provided a sufficiently long burn time, ∿15 sec, is used.

For the impacting spacecraft mode, the deflection impulse imparted by the ejection spring system which produces a velocity of ∿1 fps may be adequate, but an addition of 5 m/sec is provided by a small rocket motor. For the flyby mode, however, the probe requires a ΔV of 40 m/sec and a total impulse of 1950 lb-sec. This is about twice the maximum value considered in Ref III-1, but the system weight and size requirements can be established by looking at an existing motor that has approximately the performance needed. Aerojet-General Corporation's ullage orientation control motor has the following characteristics:

Length, 20.5 in.;	Impulse, I_T, 1820 lb-sec;
Diameter, 4.6 in.;	Average Sea Level Thrust, 97 lb;
Weight Loaded, 16.7 lb;	
Weight Expended, 7.6 lb;	Burn Time, 17.7 sec.

e. Decelerator Design - Large Descent Probe - The decelerator design for the large descent probe is based on the requirement for a ballistic coefficient of 0.035 slugs/ft^2. This ballistic coefficient results from instrument sampling rate and terminal descent velocity requirements at 6122-km radius.

It is desirable to deploy the science instruments as high as possible; however, the system design penalties become prohibitive above about 6125 km. For the large probe an overall system design compromise resulted in an initial deployment radius of 6122 km. With an entry angle, γ_E, of -50° and a ballistic coefficient of 0.37 slugs/ft^2 the parachute deployment conditions at 6122 km are Mach 0.95 and a dynamic pressure of 40 psf. A small pilot chute is used to extract the reefed main chute. To be consistent in design, the main chute weight was increased to account for dynamic pressures greater than 25 psf.

Design curves and weight estimation data are presented in Chapter VIII, Section C for the disk-gap-band-type parachute chosen for this application.

The resultant parachute design required to support a probe weight of 275 lb at a ballistic coefficient of 0.035 slugs/ft^2 is as follows:

Type	Disk-Gap-Band
Drag Coefficient	0.53
Parachute Diameter	25 ft
Parachute Weight	16.7 lb

f. Integration of Instruments - The double-walled canister concept to achieve a suitable structural/thermal design poses problems of design complexity especially where penetrations are required to mechanize and integrate instruments. The large descent capsule exhibits the most critical case for any instrument in this matter since its science complement includes all types.

The front most position is most desirable for mounting all instruments that require a vertical view down toward the surface. It is also desirable to locate the heavier components forward to lower the center of gravity for stability purposes. The design effort in packaging and integration of science instruments involved compromises in achieving these desired goals.

Radar Altimeter - The radar altimeter was given top priority for the forward position because of its large size and weight and it requires a direct vertical downward view. Its large size and the requirement of an RF transparent medium between the radar antenna and the Venus surface necessitated deviating from a strict compliance with the double-walled concept, otherwise the packaging would begin appreciably aft of a double RF transparent window. The result is a single-walled cavity in the nose to contain the radar antenna so as to minimize the weight penalty due to the quartz glass window. Isolating the antenna and locating the electronics in the inner canister resulted in a single seal joint at the inner canister for this instrument.

Optical Windows - Certain science instruments such as the cloud particle counter, the thermal radiometer, and the nephelometer require an optical view to the outside from within the inner canister. A double optical window requires a seal around the glass to maintain an atmosphere in the inner canister for the cruise mode as one critical requirement, and a vacuum in the annular cavity during final descent as another. The design of seals with a high degree of reliability was not within the scope of this study however, the designs shown do have the potential solution exhibited. The thermal short potential of an optical port across the multilayered insulation is minimized by proper material selection for the baffled duct spanning the distance, such as a low density ceramic or a phenolic.

Sample Inlet Ducts - The acquisition and transport of an atmospheric sample for the mass spectrometer or the cloud composition analyzer instrument require semirigid connections into both the inner and outer canisters. The leak potential of this type of connection is high because the structure gets worked in a lightweight design by relative deflections of the inner canister with

respect to the outer. A structural/mechanical bellows is a suitable design to allow deflections with minimum stressing. Mechanical seals must be developed for each specific application where working parts are involved.

Solar Radiometer - Isolating the numerous optical windows required in a solar radiometer system into a single head and mounting it outside the double-walled canister reduced the potential hazard that many seals may pose to the total system reliability. The head is a single-walled evacuated pressure vessel that contains the sensors and is packed with a phase change material for thermal control. A power actuated window/cover mechanism rotates the clear glass cover as an adjacent open segment of the cover is aligned over the inner window. After a sequence of scanning at the consecutive angles of inclination, the cover is allowed to return to its initial position.

3. Mission Analysis

The targeting, deflection, and entry probe design data are presented in Table III-5 for the large probe at the subsolar point. Data are presented for both flyby and impacting spacecraft trajectories and for both the lower density atmosphere model and the V5M. Main chute deployment can be achieved by a "g" sensor at -2.7 g as noted. The impacting spacecraft will exhibit the same targeting, deflection, and entry parameters as the large probe. However, it will cease operation at entry because of atmospheric loads, and therefore will not have a working descent profile.

Table III-5 Venus Large Ballistic Probe Design Data

* * * ENTRY PROBE DESIGN DATA * * *

TARGET (NEAR SIDE ENTRY)		SUB SOLAR	
APPROACH TRAJECTORY TYPE		IMPACT	FLYBY
PERIAPSIS RADIUS OF BUS	KM	2800.	12600.
DEFLECTION RADIUS	KM	4.000.000	4.000.000.
DEFLECTION VELOCITY	METERS/SEC	0 - 5	40.
DEFLECTION ANGLE	DEGREES	20.	20.
CAPSULE COAST TIME	HOURS	292.9	290.4
MAXIMUM ANGLE OF ATTACK	DEGREES	21.2	6.
ENTRY VELOCITY	FT/SEC	35367.	
ENTRY ANGLE	DEGREES	-50.	
ENTRY ALTITUDE	FEET	815000.	
ENTRY RADIUS	KM	6298.412	
ENTRY LATITUDE	DEG	-1.0956	
ENTRY LONGITUDE	DEG	24.3831	
EARTH ZENITH ANGLE (MASK)	DEG	69.6959	
SOLAR ZENITH ANGLE	DEG	24.4062	
AEROSHELL BALLISTIC COEF.	SLUGS/FT2	0.37	
TIME OF MACH 1 OCCURRENCE	SEC	31.5	
MAXIMUM DYNAMIC PRESSURE	LBS/FT2	4061.(V5M)	4073. (MMCL) (20 S)
MAXIMUM DECELERATION	G	341 (V5M)	342 (MMCL) AT 20 S
TIME FROM ENTRY TO MAIN CHUTE DEPLOYMENT	SECONDS	32.0	
MAIN CHUTE BALLISTIC COEF.	SLUGS/FT2	.035	
MACH NUMBER AT MCD		.945	
DECELERATION AT MCD	G	2.7	
DYNAMIC PRESSUPE AT MCD	LB/FT2	39.5	
ALTITUDE MAIN CHUTE DEPLOY	FT	248443.5 (V5M)	D=-2.7 G
ALTITUDE MAIN CHUTE DEPLOY	FT	237175.0 (MMCL)	D=-2.7 G
RADIUS MAIN CHUTE DEPLOYED	KM	6125.7257 (V5M)	6122.2910 (MMCL)
TIME FROM ENTRY TO MAIN CHUTE RELEASE	HOURS	1.30 (V5M)	1.35 (MMCL)
TERMINAL BALLISTIC COEF.	SLUGS/FT2	2.0	
CHUTE RELEASE PRESSURE	BARS	7.0	
RADIUS MAIN CHUTE RELEASE	KM	6089.8225 (V5M)	6084.8934 (MMCL)
TIME TO 50.0 BARS	HOURS	1.67 (V5M)	(6012 SEC) R=6066.87
TIME TO 50.0 BARS	HOURS	1.75 (MMCL)	(6292 SEC) R=6060.0
INITIAL BIT RATE	BITS/SEC	120.	
FINAL BIT RATE	BITS/SEC	60.	
RADIUS TO CHANGE BIT RATE	KM	6060.	
TIME FROM ENTRY TO IMPACT	HOURS	2.18 (V5M)	2.01 (MMCL)

The large probe descent profile is presented in Fig. III-19 and III-20. In the sequence of events the large probe is separated from the spacecraft last. Therefore, the pointing dispersion is 0.64°. No deflection impulse is required for targeting in the impacting spacecraft case and separation between the spacecraft and large probe will be accomplished by springs. For the impacting case the entry dispersions will result from final spacecraft position accuracy which is estimated to yield an error in periapsis radius of 120 km. The resulting downrange entry error is ±1.67° and the path angle error is ±1.09°. The crossrange errors are much smaller than the downrange error.

For the flyby spacecraft the downrange and entry path errors become ±3.26° and ±2.12° respectively. The crossrange error is about ±0.75°. Since the angle of attack at entry for the flyby case is about 6°, the accuracy could be improved by increasing the application angle from 20° and reducing the ΔV_{EJ}. Of course the staggered entry conditions would be affected to some degree and would require investigation. Improved accuracy also could be achieved by decreasing the periapsis radius. At a periapsis radius of 7700 km the downrange error would be 2°.

The atmosphere models cause about 10 minutes difference in descent time and the initial entry time can be off by about 6 minutes.

4. Telecommunications and Data System - Large Probe

a. Telecommunications System - The large probe enters at a communication angle of 70° from subearth. Consider first the impacting spacecraft option. The selected antenna, as discussed in Chapter VII, Section E is a vertically polarized 0.6 λ diameter annular slot, flush mounted in the top of the probe. The radiation pattern is shown in Chapter VII, Section F. Gain is 6 db.

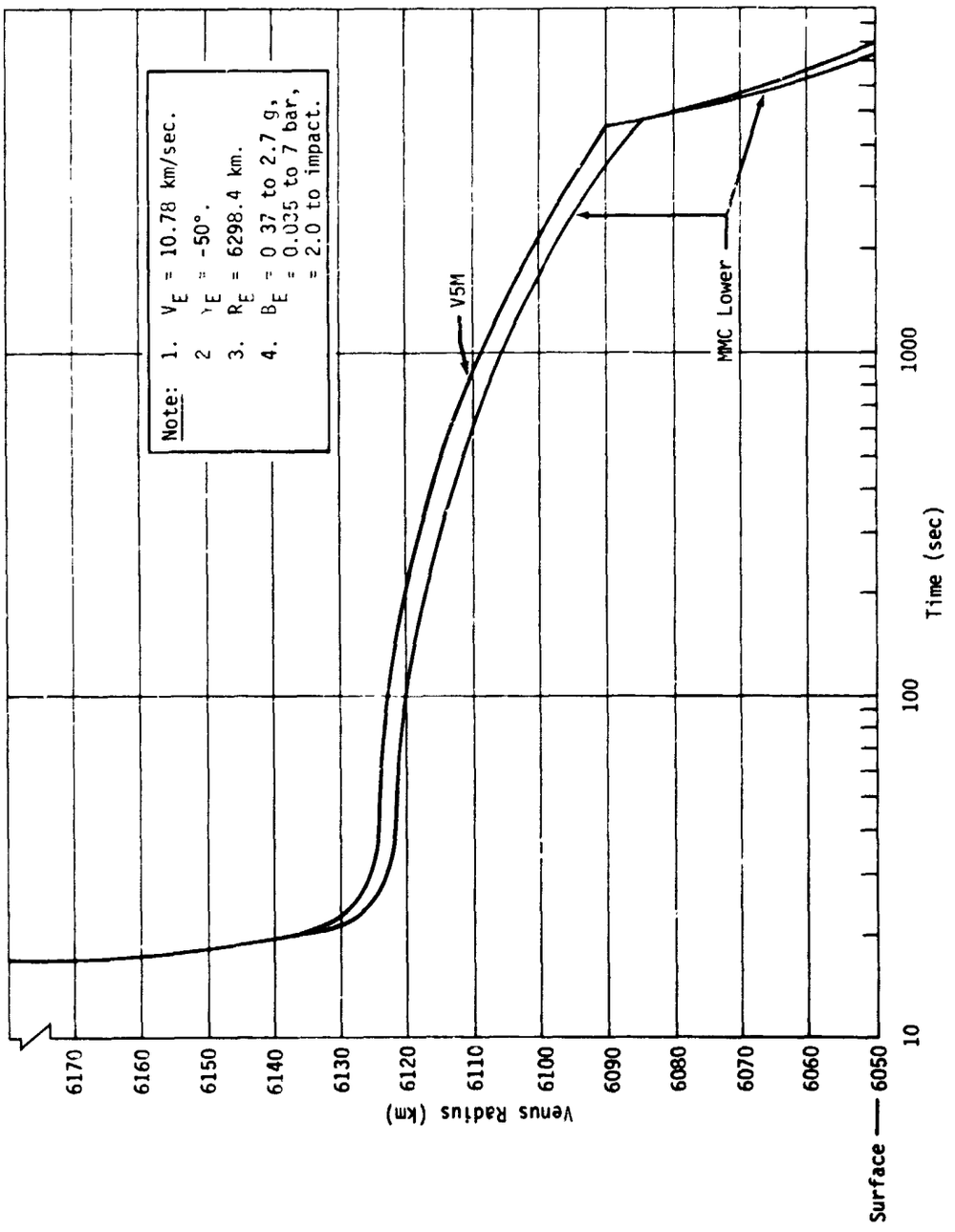


Fig. III-19 Large Probe Descent Profile

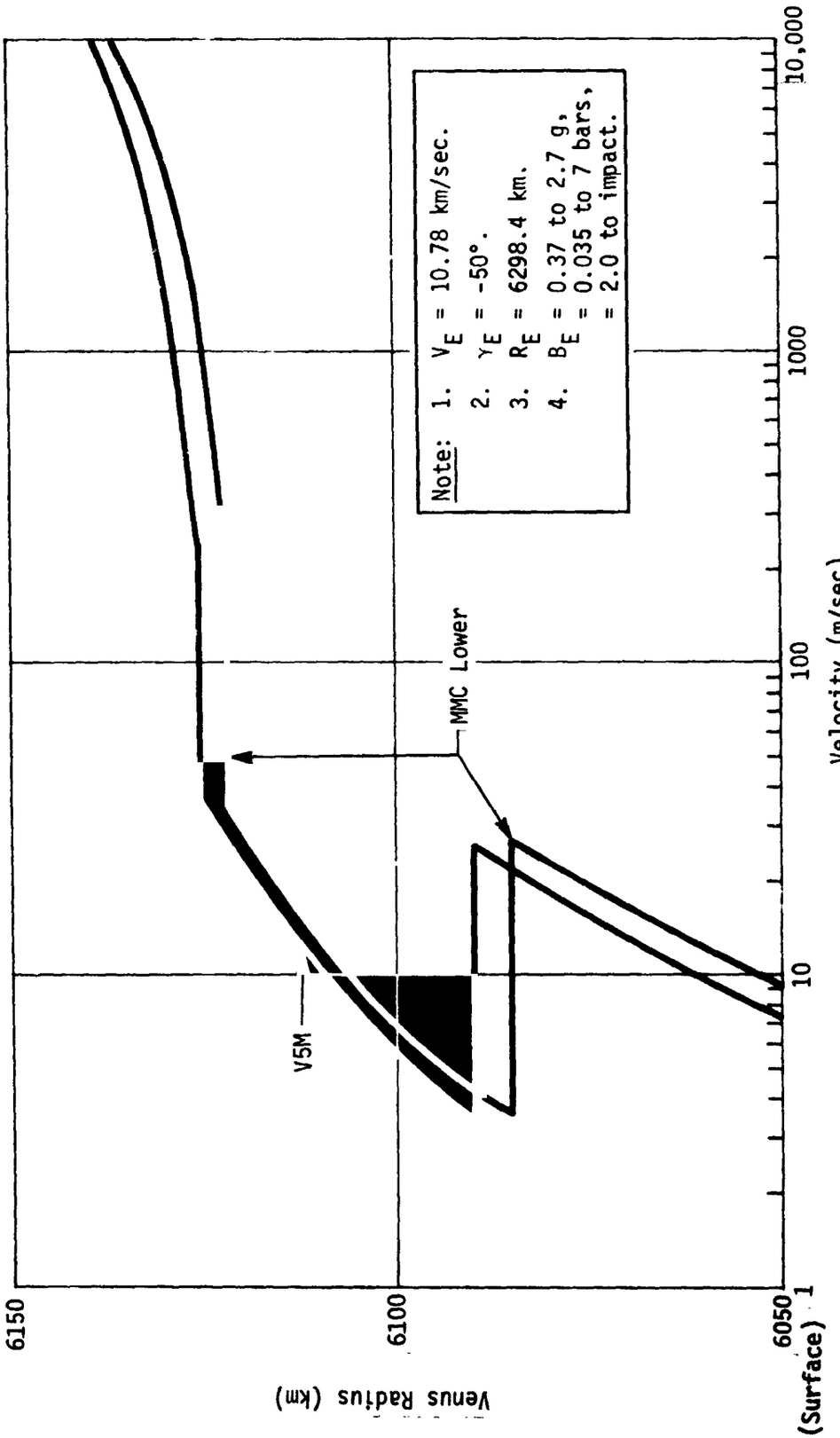


Fig. III-20 Large Probe Descent Profile, Subsolar

Transmitter power requirement has been set at 20 W. This is based on the required instrument sampling rates and is justified in the link calculation given in Table III-7 later in this discussion. Solid-state transmitters have been selected for all probes in preference to TWT transmitters. Although their efficiency is slightly lower than a TWT, their lighter weight, greater reliability, and markedly lower voltage requirement more than offset this disadvantage.

A transponder for two-way Doppler is specified for all probes. It will be used to infer wind turbulence by measuring earth-directed accelerations. Ranging will not be done by the descent probes, but is specified for the balloon probes.

Accuracy of the Doppler readout depends on the integration or cycle-counting time. Fractional cycles can be resolved. Accuracy is limited by the phase noise in the PLL. At our design loop SNR of 9 db, the 1-σ phase noise is 0.632 radians or 0.101 cycle (Ref III-3). Since it occurs on both ends of the count, uncertainty is 0.142 cycles. This is the 1-σ uncertainty in cycle count regardless of integration time. It corresponds to 0.97 cm/sec velocity for a 1-sec integration time, or $0.97/T_i$ cm/sec for integration time T_i. Thus, for a 10-sec integration time, for example, the 1-σ uncertainty in the earth-directed velocity would be 0.097 cm/sec. Uncertainty can be reduced to an arbitrarily low value by increasing T_i, assuming no cycle-slipping occurs in the PLL. However, increasing T_i beyond a few tens of seconds would smooth out the fine structure in the turbulences, and 1-σ accuracies in excess of 0.1 cm/sec are probably not warranted in view of targeting and other uncertainties. Accordingly, a 10-sec averaging time is recommended.

Weight and power consumption estimates for the RF components of the system are based on work currently being done by Motorola under NASA contract to develop deep-space RF hardware. These data are given in Table III-6.

Table III-6 RF Components, 1972 Technology, DSN Frequencies

Component	Volume (cu in.)	Weight (lb)	Power (W)
Receiver	55	2.0	0.5
Ranging	--	1.5	1.0
Command Decoder	20	0.8	0.5
Transmitter, 5 W	18	0.9	27.5% efficiency
Transmitter, 20 W		4.0	27.5% efficiency

Data rate is cut from 120 to 60 bps during the terminal part of the descent to gain more margin to cover the increased atmospheric losses in the lower atmosphere. This is justified for science sampling by the lower probe velocity in the lower atmosphere.

The problem of locking up the two-way Doppler link must be considered. It is important to begin collection and transmission of the science data as early as possible. This requires that transmission begin at the same time as instrument sampling is begun, immediately after parachute deployment. This will be done using a fixed frequency source, without waiting for the up-link acquisition to be completed. Predetection recording would be used for these initial data. This could be on an adjacent channel to avoid the possibility of the ground station acquiring this signal and then having to jump to another frequency after probe lock-on has occurred.

It is assumed that the ground station would begin up-link transmission a short time before the expected entry. Just after parachute deployment, the probe transmitter would be turned on, using the fixed frequency reference, and the probe receiver would begin a search for the up-link signal. After acquisition, the probe transmitter would be switched to the locked frequency reference. The ground station would then search for and acquire this signal, and would begin real-time demodulation. Predetection recording could be continued, as a backup, if desired.

The transmitter will use coherent PSK-PM modulation with a single square-wave subcarrier to minimize intermodulation loss. Our tentative assumption is that this same modulation format can be used both before and after up-link acquisition. However it is our understanding* that the recording currently done at the DSIF is subcarrier recording (which requires carrier lock), not predetection recording. Further, although a predetection recording capability is planned for the near future, there is some question about its performance with coherent modulation due to tape jitter problems. Noncoherent modulation is preferred. Therefore, it may be necessary to use noncoherent MFSK modulation for the preacquisition mode, switching to coherent modulation after lock. Link calculations for the two modes are shown in Tables III-7 and III-8. The decision on which modulation format to use hinges on several contingencies related to the future capabilities of the DSIF. First, if it develops that predetection recording of coherent signalling can be used, then, as stated earlier, the same coherent modulation format would be used before and after acquisition. If noncoherent signalling must be used with predetection recording, the capabilities of the MFSK receiving system (which

*Telecon with Messrs. Joe Buffington and Carl Johnson of JPL, November, 1969.

does not exist at this time) must be examined. If it is limited to very low bit rates as presently planned, the best approach would be to eliminate the predetection recording and simply lose the early data. If a higher data rate capability (120 bps) is available, then, in view of the high priority assigned to this data, it is recommended that noncoherent MFSK be used initially, switching to coherent signalling after up-link acquisition. This would be recommended only for the large and high-cloud probes, where the early data are of more importance.

Our link calculation for the noncoherent link, Table III-8, assumes that additional coding is superimposed on the M'ary coding used to select the MFSK symbols. If the requisite decoding capability is not available in the DSIF, the data rate in the noncoherent case would have to be reduced to about 80 bps. This would require switching of the data system clock from this lower rate before acquisition to the higher rate after acquisition.

As stated earlier, the all-coherent approach is our baseline system. The above discussion on noncoherent signalling, together with Table III-8, are included as backup material for an alternative in case the baseline system proves to be incompatible with DSIF capabilities. If the all-coherent approach is used, the margins shown in Table III-7 would have to be reduced during the predetection recording phase by whatever signal degradation is introduced by the recording-playback operation. This loss is unknown at this time because of the unresolved tape jitter problem cited earlier. A loss of up to 2.6 db could be tolerated by the link, since the atmospheric loss would be zero at this high altitude. It seems likely that if the system is used at all it will be better than this.

Table III-7 Link Calculations, Downlink, Large Probe, Impacting Spacecraft Option

Item	Parameter	Postentry, 120 bps 70° Comm Angle		Lower Atmosphere, 60 bps 70° Comm Angle	
		Nominal (db)	Adverse Tolerance (db)	Nominal (db)	Adverse Tolerance (db)
1.	Total Transmitter Power, 20 W	+43.0 dbm	0.4	+43.0 dbm	0.4
2.	Transmitter Circuit Loss	-0.4	0.2	-0.4	0.2
3.	Transmitter Antenna Gain	+6.0	0	+6.0	0
4.	Transmitter Antenna Pointing Loss	0	3.0	0	3.0
5.	Space Loss, 2297 MHz, 95 × 10^6 km	-259.2	0	-259.2	0
6.	Atmospheric Losses	0	1.0	-1.0	2.0
7.	Polarization Loss	0	0.5	0	0.5
8.	Receiver Antenna Gain, 210-ft Dish	+61.4	0.3	+61.4	0.3
9.	Receiver Pointing Loss	0	0	0	0
10.	Receiver Circuit Loss	-0.1	0	-0.1	0
11.	Net Circuit Loss	-192.3	5.0	-193.3	6.0
12.	Total Received Power	-149.3 dbm	5.4	-150.3 dbm	6.4
13.	Received Noise Spectral Density, 35°K	-183.1 dbm	0.6	-183.1 dbm	0.6
Carrier Performance, Data Demodulation					
14.	Carrier Power to Total Power	-6.0	0.4	-4.0	0.4
15.	Received Carrier Power	-155.3 dbm	5.8	-154.3 dbm	6.8
16.	Carrier Threshold Bandwidth, 12 Hz	+10.3	0.5	+10.3	0.5
17.	Threshold S/N in 2 B_{LO}	+9.0	0	+9.0	0
18.	Threshold Carrier Power	-163.8 dbm	1.1	-163.8 dbm	1.1
19.	Margin, Carrier	+8.5	6.9	+9.5	7.9
Data Channel Performance					
20.	Receiver Loss	-1.5	0.2	-1.5	0.2
21.	Data Channel Power/Total	-1.0	0.2	-1.3	0.2
22.	Total Data Power	-151.8 dbm	5.8	-153.1 dbm	6.8
23.	Data Threshold E/NO	+2.5	0	+2.5	0
24.	Data Rate	+20.8	0	+17.8	0
25.	Data Channel Threshold	-159.8 dbm	0.6	-162.8 dbm	0.6
26.	Data Channel Margin	+8.0	6.4	+9.7	7.4

Table III-8 Link Calculations, Downlink, Large Probe, Noncoherent Signalling

Item	Parameter	Postentry, 120 bps 70° Comm Angle	
		Nominal (db)	Adverse Tolerance (db)
1.	Total Transmitter Power, 20 W	+43.0 dbm	0.4
2.	Transmitter Circuit Loss	-0.4	0.2
3.	Transmitter Antenna Gain	+6.0	0
4.	Transmitter Antenna Pointing Loss	0	3.0
5.	Space Loss, 2297 MHz, 95×10^6 km	-259.2	0
6.	Atmospheric Losses	0	0
7.	Polarization Loss	0	0.5
8.	Receiver Antenna Gain, 210-ft Dish	+61.4	0.3
9.	Receiver Pointing Loss	0	0
10.	Receiver Circuit Loss	-0.1	0
11.	Net Circuit Loss	-192.3	4.0
12.	Total Received Power	-149.3 dbm	4.4
13.	Received Noise Spectral Density, 35°K	-183.1 dbm	0.6
Data Channel Performance			
14.	Recorder Loss	0.5	0
15.	Data Channel Power/Total	0	0
16.	Total Data Power	-149.8	4.4
17.	Data Threshold E/NO	+3.5	0
18.	Data Rate	+20.8	0
19.	Data Channel Threshold	-158.8 dbm	0.6
20.	Data Channel Margin	9.0	5.4

Frequency uncertainties at the probe receiver would consist of probe oscillator frequency uncertainty and Doppler uncertainty. If we assume high-quality crystal-controlled oscillators for both sources, and further assume that their free-running frequency is monitored just before probe release, then it is reasonable to assume a preentry uncertainty of $1:10^7$. Postentry uncertainty would be increased by the high-g entry shock. An uncertainty of $1:10^6$ can be assumed. This gives an uncertainty of 2.1 kHz on the up-link. Initial postdeployment velocity is around 30 m/sec. The earth-directed component of this is 30 cos 70° $\tilde{=}$ 10 m/sec, which corresponds to a Doppler frequency of 72 Hz. Given a strong SNR, a loop can search at a rate of 0.1 B_N^2, where B_N is the loop noise bandwidth. We have assumed a 50 Hz loop, giving a search rate of 250 Hz/sec. Assuming a total uncertainty of 2.2 kHz, this search should take less than 10 sec. However, even if it takes somewhat longer it is not crucial because the only data lost are the turbulence data given by the Doppler measurement.

Uncertainty at the ground station would be confined to the two-way Doppler value of about 150 Hz. Assuming the 12 Hz loop and a 14 Hz/sec search rate, this should take around 11 sec to complete. This is confirmed by extrapolation of a curve in the DSIF criteria document (Ref III-4), which gives an acquisition time of 9 sec. However, note that this 150 Hz is the estimated Doppler, not the uncertainty in this estimate, which is much smaller. If a Doppler prediction is used, lock-on should be almost instantaneous, less than 1 sec.

The probe will undergo a brief but high acceleration just after probe release from the parachute. This will be a maximum of about 10 m/sec^2, and last for a few seconds. The one-way Doppler rate due to this, seen by the probe, will be 24 Hz/sec.

The 50 Hz loop will be able to track this. However, the two-way Doppler rate seen by the ground station will be 50 Hz/sec, which is more than the 12 Hz loop can track. One possibility would be to simply accept a brief loss of lock and data during this period. The data could possibly be recovered if backup predetection recording were used. It would also be possible to send a warning signal from the spacecraft a few seconds before the parachute release event. This would be used to trigger a predicted Doppler trajectory program in the ground station for the immediate post-release period. Loop stress would then be limited to that due to the error in this prediction, which should be small enough to maintain loop lock. This would permit reconstruction of the actual Doppler trajectory during this period, which would be of some scientific and engineering value. However, our baseline design does not include this capability, but simply assumes that a brief period of data might be lost at this time.

Annotations, Table III-7 - In all items computed by combining other items, the adverse tolerances associated with the input items are added to give the adverse tolerance associated with the computed item.

For Item 6, Atmospheric Losses, it is desired to switch to the lower bit rate when atmospheric losses reach 1 db. Atmospheric loss curves are given in Chapter VII, Section A. Assuming a 5° targeting error, $\psi = 75°$, and the worst-case (V5M) atmosphere, this will occur at a radius of 6066 km. A pressure switch will be used to initiate the switchover to the lower bit rate. At r = 6066 km in the V5M, pressure is 53 bars. This same pressure occurs at 6059 km in the Lower and 6060 km in the Lower-Iso. At $\psi = 75°$, these radii correspond to atmospheric losses of 0.8 db and 1.0 db, respectively. Switching will actually be done at 50 bars to give some safety margin.

The worst-case atmospheric loss at the surface, shown as 3 db, assumes a 5° pointing error and the worst-case atmosphere (Lower-Iso, 6045 km surface).

Item 11 is the sum of items 2 thru 10.

Item 12 is item 1 plus item 11.

Item 14 and 21. Note that each time the data rate is switched, the partitioning of power between carrier and data is also changed, by changing the modulation index. Since a single square-wave subcarrier is assumed, there will be no intermodulation loss.

Item 15 is item 12 plus item 14.

Item 17 could have been optimized as a function of bit rate. However, it was arbitrarily set at 9 db. Over the bit rates of interest, the difference in performance between this and the optimum is negligible.

Item 18 is the sum of items 13, 16, and 17.

Item 19 is 15 minus 18.

Item 20 is given by the loop S/N. The threshold value, +9 db, was used instead of the higher value given by adding the margin minus the sum of the adverse tolerances to this value. This is conservative. The receiver loss was taken from a curve due to Lindsey (Ref III-3) which gives a loss of 1.5 db for a loop SNR of 9 db. The up-link noise reference loss must be added to this. For the worst-case loop SNR of 20 db (see Table III-10), this loss is 0.1 db. The adverse tolerance was arbitrarily increased an additional 0.1 db.

Item 22 is the sum of items 12, 20, and 21.

Item 23 assumes convolutional coding with advanced decoding techniques. It is supported by JPL interoffice memo No. 3300-68-819 (Ref III-5), which says in part "Coded telemetry transmission such that the required E/N_o is 1.5 to 3.0 db for telemetry sideband energy." We have selected 2.5 db arbitrarily from this range. This is supported by recent work due to the Heller (Ref III-6), which shows a coding-decoding system giving a 10^{-3} bit error rate at E/N_o = 2.5 db. It is expected that further developments within the next few years will give significant improvement over this performance.

Item 25 is the sum of items 13, 23, and 24.

Item 26 is item 22 minus item 25.

Annotations, Table III-8 - In item 17, Data Threshold E/N_o, Noncoherent Signaling, the somewhat lower performance of noncoherent detection must be accounted for by increasing the required E/N_o above the +2.5 db used for coded coherent signalling. Lindsey (Ref III-7) has shown that for sufficiently complicated codes the Shannon limit can be approached with either coherent or noncoherent signalling, and that for moderately long orthogonal codes the difference between them is quite small. For example, for n = 5 (32-ary FSK) and a word error probability of 10^{-3}, the advantage of coherent over noncoherent signalling is less than 1 db. We assume 32-ary FSK, with further coding superimposed on this. The exact comparison between this and a coherent system with coding of the same constraint length nas not been made. It is conservative to assume that this same disadvantage remains. Therefore, we assume E/N_o = +3.5 db.

For other items, see the annotations for Table III-7.

Next, consider the flyby spacecraft option. In this case the preentry science is placed on the large probe, and the resulting data are communicated in real time. The communications angle during this period is 20°, so the 70° antenna used for the postentry mission cannot be used. The recommended antenna, as described in Chapter VII, Section E is the four-arm equiangular spiral on a cone, which gives an axial beam in one feed mode for preentry communications and a conical beam in the other feed mode for postentry communications. The radiation patterns are shown in Chapter VII, Section E. Both modes give right-hand circular polarization. An RF switch, activated by the entry event (0.1 g deceleration), would select the proper feed mode. This switch will have an insertion loss of 0.7 db, which would be present in both modes. For the flyby spacecraft option the margins shown in the link calculations in Table III-7 must be reduced by this amount. Peak antenna gain is lower than that in Table III-7, but this is offset by a lower pointing loss for a 15° pointing error.

The preentry link calculation is shown in Table III-9. As stated above, the transmitter was sized at 20 W based on a postentry bit rate requirement of 120 bps. In the preentry mode the link will support 180 bps, which is adequate for the preentry science. The preentry transmission period is estimated at 22 minutes.

The up-link for all descent probes will consist of unmodulated carrier. No commands or ranging will be sent. Generally, there will be two probes operating simultaneously. Table III-10 shows the link calculation. It is designed to cover all descent probes, with atmospheric losses, circuit losses, receiver antenna gains, and pointing losses reflecting worst-case conditions.

Table III-9 Link Calculations, Downlink, Large Probe, Flyby Spacecraft Option

Item	Parameter	Preentry, 180 bps 20° Comm Angle	
		Nominal (db)	Adverse Tolerance (db)
1.	Total Transmitter Power, 20 W	+43.0 dbm	0.4
2.	Transmitter Circuit Loss	-1.1	0.2
3.	Transmitter Antenna Gain	+5.9	0
4.	Transmitter Antenna Pointing Loss	0	0.5
5.	Space Loss, 2297 MHz, 95 × 10^6 km	-259.2	0
6.	Atmospheric Losses	0	0
7.	Polarization Loss	0	0.5
8.	Receiver Antenna Gain, 210-ft Dish	+61.4	0.3
9.	Receiver Pointing Loss	0	0
10.	Receiver Circuit Loss	-0.1	0
11.	Net Circuit Loss	-193.1	1.5
12.	Total Received Power	-150.1 dbm	1.9
13.	Received Noise Spectral Density, 35°K	-183.1 dbm	0.6
Carrier Performance, Data Demodulation			
14.	Carrier Power to Total Power	-9.0	0.4
15.	Received Carrier Power	-159.1 dbm	2.3
16.	Carrier Threshold Bandwidth, 12 Hz	+10.3	0.5
17.	Threshold S/N in 2 B_{LO}	+9.0	0
18.	Threshold Carrier Power	-163.8 dbm	1.1
19.	Margin, Carrier	4.7	3.4
Data Channel Performance			
20.	Receiver Loss	-1.5	0.2
21.	Data Channel Power/Total	-0.6	0.1
22.	Total Data Power	-152.2 dbm	2.2
23.	Data Threshold E/N_o	+2.5	0
24.	Data Rate	+22.5	0
25.	Data Channel Threshold	-158.1 dbm	0
26.	Data Channel Margin	5.9	2.8

Table III-10 Link Calculations, Uplink, Descent Probes, Data Transmission Mode, Two-Way Doppler Channels

Item	Parameter	Large, Small, High Cloud, Two Simultaneous Channels	
		Nominal (db)	Adverse Tolerance (db)
1.	Total Transmitter Power/Channel, 40 kW	+76.0 dbm	0.3
2.	Transmitter Circuit Loss	-0.4	0.1
3.	Transmitter Antenna Gain, 210-ft Dish	+59.2	0.5
4.	Transmitter Antenna Pointing Loss	0	0
5.	Space Loss 2116 MHz, 95×10^6 km	-258.2	0
6.	Multipath and Atmospheric Losses	-1.0	2.0
7.	Polarization Loss	0	0.5
8.	Receiver Antenna Gain	+6.0	0
9.	Receiver Pointing Loss	0	3.0
10.	Receiver Circuit Loss	-1.1	0.2
11.	Net Circuit Loss	-195.5	6.3
12.	Total Received Power	-119.5 dbm	6.7
13.	Received Noise Spectral Density, 3000°K	-163.8 dbm	0
Carrier Performance			
14.	Carrier Power to Total Power	0	0
15.	Received Carrier Power	-119.5 dbm	6.7
16.	Carrier Threshold Bandwidth, 50 Hz	+17.0	0.5
17.	Threshold S/N in 2 B_{LO}	+20.0	0
18.	Threshold Carrier Power	-126.8 dbm	0.5
19.	Margin, Carrier	7.3	7.2

Annotations, Table III-10 - In item 1 the single channel transmitter power for the 210-ft dish is 400 kW. Two-channel power is nominally specified as 100 kW each. However, experience to date* has shown that the two-channel power must be limited to 40 kW each to suppress intermodulation effects. If these difficulties are subsequently overcome, an additional 4 db of margin can be added to this link.

For item 13 a receiver noise temperature of 3000°K is assumed. This corresponds to a receiver that does not have a RF preamplifier but does have a high-quality preselector-mixer front end.

In item 17 the threshold loop SNR is set at 20 db. As discussed in the annotations for Table III-7, item 20, this gives a negligible carrier suppression loss of 0.1 db.

For explanation of other items, see the annotations for Table III-7.

b. Data System - Large Probe (Baseline) - The data system for the large probe will perform the multiplexing, analog-to-digital conversion, formatting, and data storage for science and engineering data. For the impacting spacecraft case these systems are operational beginning just before entry in a data storage mode and in a real time mode beginning at aeroshell separation. The instrument sampling rates, and consequently the frame and data rates, are reduced by ½ at an atmospheric pressure of 50 bars (6066 to 6060 km radius) to compensate for atmospheric defocusing and attenuation losses (communication) as the probe descends deeper into the atmosphere.

*Information furnished by Mr. J. R. Hall of JPL, 15 December 1969.

Portions of the system are used during cruise (capsule attached to spacecraft) to supply engineering data to be relayed by the spacecraft to earth, as described in Chapter IV, Section B.

Diagrams, Measurement Lists, and Data Formats - Tables III-11 and III-12 show the measurement lists, sampling intervals, and resulting bit rates for the various instruments including engineering, frame count, and identification and sync functions. The measurement lists reflect the required sampling intervals and frame rates to satisfy the science requirements. The engineering measurements were restricted so as not to exceed the available total bit rate.

A third list, Table III-13 shows preentry sampling rates for additional large probe preentry instrumentation that is required (when an impacting spacecraft is not used) to obtain ionospheric and other above-the-atmosphere data.

A block diagram of the data system and the data formats for all data modes are shown in Fig. III-21 and III-22. The data storage block indicated on Fig. III-21 is used for storing data (from the four accelerometers) that are being accumulated at a rate of 240 bps during the 17-sec time interval between 0.1 g increasing and aeroshell separation. This amounts to about 4080 bits of entry data and suggests a storage capacity of 5120 bits to allow for time variation in entry profile.

Main data storage readout occurs "first in first out" at a rate of 16 bps for an estimated 5980 sec in the V5M atmosphere (6260 sec in the MMC Lower) and 8 bps thereafter for the next 1832 sec (948 sec in the MMC Lower), giving a total of approximately 110,000 bits read from storage for the V5M atmosphere and 107,700 bits for the MMC Lower atmosphere. This quantity is sufficient to give at least 20 repeat transmissions, which may be excessive, but it has the advantage of accomplishing a complete memory read in the first 3.2 minutes after beginning real-time data transmissions.

Table III-11 Telemetry Measurement List 1, Large Probe (Baseline)

Parameter	Bits per Sample	Bits per 10 sec Frame (bits)	Sample Interval (sec)	Bit Rate (bps)*
Accelerometer (3)	30	300	1	30.0
Cloud Particle Number	80	80	10	8.0
Memory Read Out†	40	160	Note	16.0
Events (On-Off)	6	6	10	0.6
Nephelometer	16	16	10	1.6
Mass Spectrometer	600	100	60	10.0
Cloud Composition	1800	60	300	6.0
Solar Radiometer	1200	200	60	20.0
Evaporimeter/Condensimeter	456	152	30	15.2
Radar (Altitude and Drift)	60	20	30	2.0
Static Phase Error	8	8	10	0.8
Probe Internal Pressure	8	8	10	0.8
Probe Internal Temperature	8	8	10	0.8
Thermal Radiometer	16	16	10	1.6
Atmospheric Pressure	8	8	10	0.8
Atmospheric Temperature	8	8	10	0.8
Subcommutated Channel†	8	8	10	0.8
Sub Frame Count	5	5	10	0.5
Frame Count	10	10	10	1.0
Format Identification	6	6	10	0.6
Frame Sync Code	21	21	10	2.1
Total		1200		120.0

*Bit rate reduced to ½ value at atmospheric pressure of 50 bars.

†See Table III-12 for stored measurement list and subcommutator channels.

Table III-12 Telemetry Measurement List 2, Large Probe (Baseline)

Parameter	Bits per Sample	Bits per 2 sec Frame (stored)	Sample Interval (sec)	(Stored) Bit Rate (bps)
Input to Memory (0.1 g Increasing to Aeroshell Staging)				
Accelerometers (4)	40	440	2/11	220.0
Events (5)	5	5	2	2.5
Frame Count	10	10	2	5.0
Format Identification	4	4	2	2.0
Frame Sync Code	21	21	2	10.5
Total		480		240.0 (Stored)

Subcommutator Channels for Real-Time Preentry and Postentry Telemetry*	Bits per Sample	Sample Interval Preentry (20 min)	Sample Interval above 50 bars Pressure	Sample Interval below 50 bars Pressure
Calibrate	8	10	100	200
Exciter Power Out	8	10	100	200
VCO Temperature (Transponder)	8	10	100	200
Battery Voltage	8	10	100	200
Battery Temperature	8	10	100	200
Battery Current	8	10	100	200
Clock Temperature	8	10	100	200
Transmitter RF Power	8	10	100	200
Probe Internal Temperature	8	10	100	200
Probe Internal Pressure	8	10	100	200

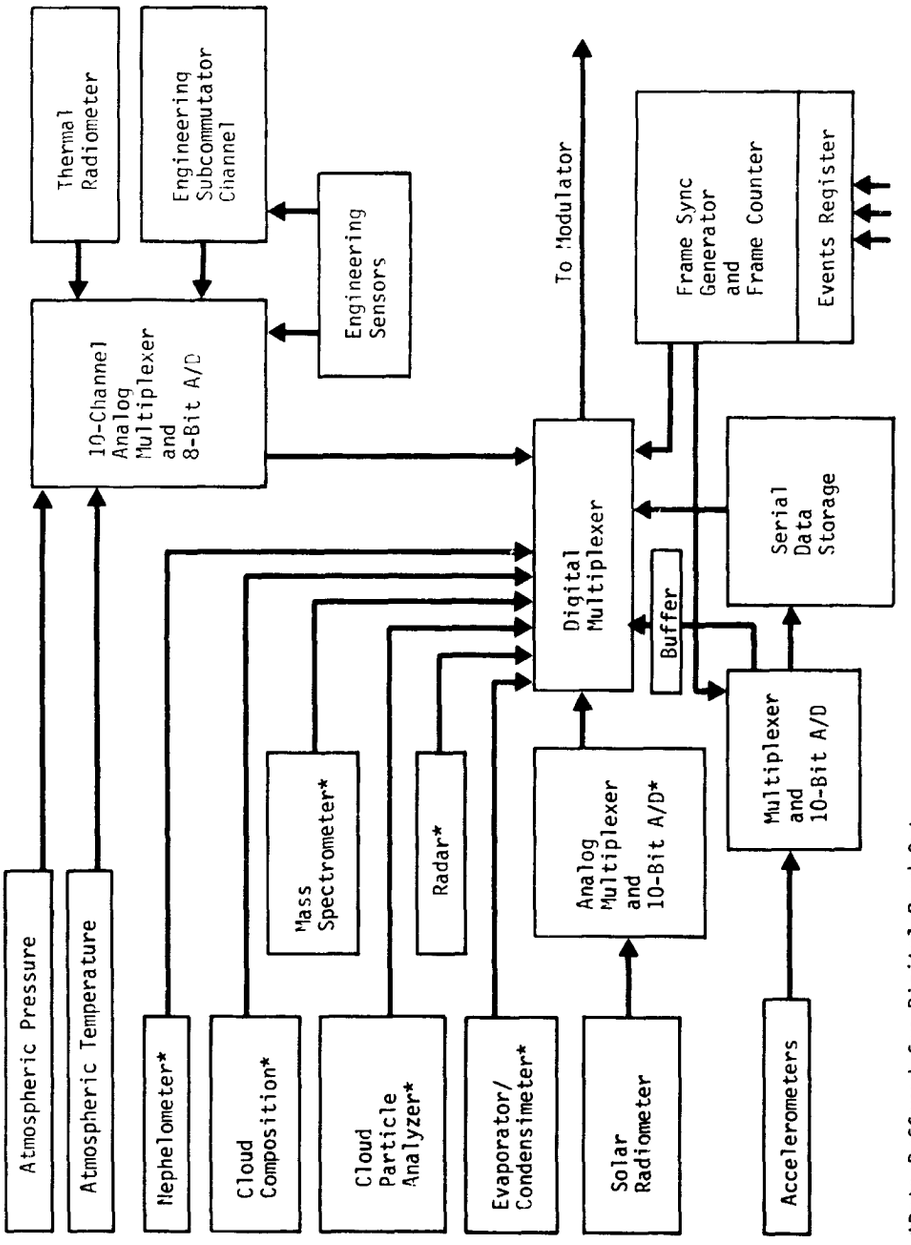
*Preentry transmissions are used only for the nonimpacting spacecraft case. Sample intervals are in seconds.

Table III-13 Telemetry Measurement List 3, Large Probe (Baseline)*

Parameter	Bits per Sample	Bits per 10 sec Frame (bits)	Sample Interval (sec)	Bit Rate (bps)
Ion Mass Spectrometer	200	200	10	20.0
Neutral Particle Spectrometer	600	600	10	60.0
Electron Density and Temperature	30	600	0.5	60.0
Ultraviolet Photometer	10	100	1	10.0
Calibrate	1[illegible]	100	1	10.0
Static Phase Error	[illegible]	80	1	8.0
Subcommutated Channel†	[illegible]	80	1	8.0
Events	5	5	10	0.5
Frame Count	10	10	10	1.0
Format Identification	4	4	10	0.4
Frame Sync Code	21	21	10	2.1
Total		1800		180.0

*This is a pre-entry measurement list large probe - (Baseline) (Used only when spacecraft does not impact planet).

†Subcommutated channel assignments are shown on measurement list 2 (Table III-12).



*Data Buffered for Digital Read Out

Fig. III-21 Telemetry Data Handling, Large Probe (Baseline with Impacting Spacecraft)

Real Time Main Telemetry Format - Post Entry (see Note 1)

Sync	ID	Frame Count	Sub-frame Count	Subcommutator Channel	Atmosphere Temperature	Atmosphere Pressure	Thermal Radiation	Probe Internal Temperature	Probe Internal Pressure	Static Phase Error
21	6	10	5	8	8	8	16	8	8	8
				Note 6						

Cont. →

Cont. →

Radar	Evap/ Cond.	Solar Rad.	Accel 1,2,3 3x10x5	Cloud Comp.	Mass Spect	Neph	Events	Memory Read	Cloud Part	Accel 1,2,3
20	152	200	150	60	100	16	6	160	80	150
Note 4	Note 4	Note 2		Note 3	Note 2					

Subcommutator Format (Note 6)

Calibrate	Exciter Pwr Out	VCO Temp (X-Pond)	Batt Volt	Batt Temp	Batt Current	Clock Temp	Xmit Pwr Out	Probe Temp.	Probe Press
8	8	8	8	8	8	8	8	8	8

Stored Entry Data Format (Note 5)

Sync	ID	Frame Count	Events	Accelerometers 1,2,3,4 Eleven Samples Each
21	4	10	5	440

Real Time Preentry Data Format (Notes 7 & 8)

Sync	ID	Frame Count	Events	Sub-Comm Chan	Static Phase Error	Cal	UV	Electron Temp & Density	Neutron Particle	Ion Mass Spec.
21	4	10	5	8	8	10	10	60	60	20
				Note 8						

Repeat for Total of 10 times/frame

1800 bits/frame

Note:
1. Main frame length is 1200 bits; Main frame period is 10 sec(Note 9).
2. Six main frames to complete.
3. Thirty main frames to complete.
4. Three main frames to complete.
5. Stored at 240 bps 0.1 g to aeroshell staging.
6. Ten frames to complete cycle.
7. Used only when spacecraft will not impact.
8. Same subcommutator as for postentry.
9. Bit rates:
   Post-entry - 120 or 60;
   Preentry - 180 bps.

Fig. III-22 Telemetry Data Formats, Large Probe (Baseline)

A change of mode to eliminate memory read after a fixed time period is worth consideration, but for the sake of simplicity in the baseline the data mode is not changed after staging except for the change of bit rate at 50 bars, which can easily be accomplished by a clock rate change.

Analog-to-digital conversion and individual buffer storage is required for cloud composition, cloud particle analyzer, evaporimeter/condensimeter, solar radiometer, and accelerometers because of the need to sample multiple detectors in a short period or to analyze in a longer period than allowable for real-time conversion or because of a digital counting operation. Capacity and other buffer characteristics for instrumentation buffers are indicated in Table III-14. Where dual buffers are indicated in the table for the various instruments one buffer is being used alternately to store data being acquired by the instrument while the other is freed to output data to the data system for transmission. This concept gives an upper bound on the data storage capacity required per instrument, minimizes timing problems, provides flexibility in interfacing the instruments with data systems for the various types of descent capsules and creates a firm interface base for the balance of the system where (as in this case) no detail interface was provided other than the instrument output in bits/word and bits per sample or words per sample as shown in Appendix B-1.

The data formats are based on the same interface data and include the necessary time reference (frame number) and subcommutated channel sync.

Table III-14 Buffering Requirements for Large Probe Data System

Instrument	Number and Capacity of Buffers			
	Part of Instrument		External to Instrument	
	No. of Buffers	No. of Bits Each	No. of Buffers	No. of Bits Each
Accelerometers (4), Initial Entry			1	5120
Accelerometers (3), Postdeploy			2	150
Cloud Particle No.	2	80		
Nephelometer	1	16		
Mass Spectrometer	2	600		
Cloud Composition	2	1800		
Solar Radiometer			1	200
Evaporimeter	2	456		
Radar	1	60		
Ion Mass Spectrometer*	2	200		
Neutral Particle Spectrometer*	2	600		

*Used for nonimpacting spacecraft case only.

Note: 1. All external buffers are solid state flip flops except the main memory which is core.
2. Where two buffers are indicated, one is used alternately to store data being generated by the instrument while the other is free to output data for transmission.

Hardware Considerations - The electronic components necessary to meet the requirements of the data handling system are now available. The digital control logic can be implemented with the N54L00 series of low power TTL logic to minimize power consumption. This line of digital logic has been in production for some time and a few MSI functions are now available. The analog data multiplexer can be implemented with present day MOS integrated circuits such as the Siliconex SDG 2100 which is a three-channel differential multiplexer with an integral switch driver for each channel. The driver includes a translator for direct compatibility with TTL logic levels (0-5 v). This three channel multiplexer and driver combination is housed in a single 14 lead flatpak.

Martin Marietta has recently delivered to NASA-MSFC an Addressable Remote Multiplexer Unit that uses much of the technology discussed above (Contract NAS8-25066). This unit was designed to sample 30 analog channels of 0-5 v data and convert the data to a 10-bit binary word. Also included was a 20-bit binary multiplexer. The system included its own power conditioner and required approximately 8.5 W of power with a weight of about 12 lb.

Present technology is adequate to meet the requirements for the data handling system but it is anticipated that some of the semiconductor technology now in development will be proven and available when hardware design is initiated. Thus MOS-LSI technology with the advantages of low power and hardware minimization (weight and volume) can be used to advantage.

Alternative Approaches - The data system described above is not necessarily optimum but is a reasonable approach to obtaining the desired sampling rates. The system is representative of present practice in data handling systems for space applications. The method minimizes the hardware required for digitizing analog data from multiple sources. The system illustrated may be simplified by further sharing of analog-to-digital converters through

use of additional analog multiplexing. This remains to be investigated in later mission phases when detail instrument interfaces can be resolved. Formats for the data sampling system must also be revised when the interfaces become better defined. At that time optimizing the formats to minimize hardware (buffers and buffer capacity for example), and minimize error rate or deletion rate for the selected error correction and detection decoding algorithm will be beneficial.

5. Power System - Large Ballistic Probe

All of the descent probes have a power system based wholly on battery storage. (The balloon probes, discussed in Section E of this chapter, have solar panels.) These batteries must support the probes from spacecraft separation to the end of their descent missions. Before spacecraft separation, battery condition is maintained by trickle charging from the spacecraft power system.

A nominal battery voltage of 28 v is assumed. Battery derating and sizing procedures are described in Chapter VII, Section F. These are based on silver-zinc batteries. Nonsterilizable batteries are assumed for the large and small probes, and sterilizable batteries are assumed for the balloon and high-cloud probes. For the large probe, the result is 21.6 lb (impacting spacecraft) and 22.. lb (flyby spacecraft). These are based on the descent times given by the V5M atmosphere, which gives the longest descent time of the atmosphere models used on this program.

It is assumed that each of the electronic components of the probe (listed in Tables III-15 and III-16) have their own internal power conditioning equipment, and that its efficiency is included in the power usage assigned to each component. However, this was not assumed for the science instruments, and a power conditioner (Listed in Table III-15 and III-16 as "inverter") having an efficiency of 85% was assigned to this load.

Table III-15 Weight and Power Summary, Large Ballistic Probe, Impacting Spacecraft Option

Component	Weight (lb)	Descent Power for 2.175 hr (W)	Cruise Power for 264 hr (W)
Antenna	0.8		
Diplexer	1.4		
Transponder			
Receiver	2.0	0.5	
RF Exciter	0.9	1.5	
Modulator	0.9	0.5	
Transmitter (20 W)	5.0	73.0	
Sequencer	4.0	3.0	0.1 + 1.75 W-hr
Data Handling	7.0	7.0	
Memory	2.2	0.2	
Inverter	4.3	18.8	
Cabling	4.2		
Battery	21.6		
Subtotal	54.3	104.5	
Instruments		125.3	
Instrument Heater	0.5	5	
Total	54.8	234.8	

Note: 1. Average battery power dissipation during descent is 60.2 W.
2. Total power dissipation during descent is 274 W.
3. Total energy converted to heat during descent is 596 W-hr.

Table III-16 Weight and Power Summary, Large Ballistic Probe, Flyby Spacecraft Option

Component	Weight (lb)	Descent Power for 2.175 hr (W)	Approach Power for 0.368 hr (W)	Cruise Power for 263.6 hr (W-hr)
Antenna	1.6			
RF Switch	1.4			
Diplexer	1.4			
Transponder				
Receiver	2.0	0.5	0.5	
RF Exciter	0.9	1.5	1.5	
Modulator	0.9	0.5	0.5	
Transmitter (20 W)	5.0	73.0	73.0	
Sequencer	4.0	3.0	3.0	0.1
Data Handling	7.0	7.0	7.0	
Memory	2.2	0.2	0.2	
Inverter	4.3	18.8	3.3	
Cabling	4.6			
Battery	22.6			
Subtotal	57.9	104.8	89.0	
Approach Instrument			22	
Descent Instrument		125.3		
Instrument Heater	0.5	5		
Total	58.4	234.8	111.0	0.1

Note:
1. Average battery power dissipation during approach and descent is 51 W.
2. Total power dissipation during approach is 142 W and during descent is 266 W.
3. Total energy converted to heat during approach and descent is 630 W-hr.

Power dissipated within the probe during descent was computed and used as an input to the thermal control analysis described in Chapter VIII, Section A. A minimum battery temperature of 0°F during storage and +40°F during use was specified. A maximum temperature for a brief period at the end of the mission of +140°F was also specified.

The EMI problem must be considered as an overall system design, with low-noise regulators, differential inputs in the telemetry system to reject common-mode noise, and the latest practices in the routing, shielding, and bundling of cables used. Each probe should have its own single-point ground system. However, this raises the possibility of incompatibility with the Mariner grounding system during interplanetary cruise when the probe batteries are being charged from the Mariner power system. This could be solved with an isolating inverter for the Mariner power system input into each probe if it is considered necessary.

a. Weight and Power Summary - The weight and power summaries for the impacting spacecraft option and the flyby spacecraft option are shown in Tables III-15 and III-16. Data for these tables are taken from a number of sources. In-house estimates were used for components where design experience exists within the company. This includes antennas, diplexers, RF switches, sequencers, data handling, inverters, cabling, and batteries. The balance of the data came from vendor sources, Motorola for the transmitter and transponder (Table III-15), and EMI for the memory. Instrument power consumption was given in the RFP.

b. Sequencer for Large Probe (Baseline) - Each of the probes requires a sequencing subsystem to control functions following separation from the parent spacecraft. These sequence functions are detailed in Chapter V, Section C for each of the probes. Certain of these functions are common for all of the probes, and therefore commonality of design can be considered, especially for the functions occurring immediately after probe separation from the spacecraft through the period when 0.1 g increasing is first detected at entry. General commonality of discrete functions following entry also exist for all of the ballistic probes.

In general the postentry discrete events are triggered by acceleration or pressure sensing rather than time. The balloon probes are the exception, which, because of functions related to balloon inflation and multiple data transmissions, require several additional timed discretes and operation of a timing cycle for several days after deployment.

Description - The large probe sequencing subsystem is made up of two units, a coast sequencer and an entry sequencer. The coast sequencer is a battery-driven mechanical timer (tuning fork) and clock mechanism that initiates capsule spin and deflection burn soon after separation from the spacecraft and transfer to entry sequencer near the end of the coast phase. Deflection engine vernier shutdown, if required, is provided by an electronic countdown clock that can be set before launch and started by the mechanical timer 20 minutes after separation from the spacecraft. Trimming of the total capsule coast time can be done by the postentry sequencer by counting down from the end of the preentry sequencer run for a preset count. In this manner the mechanical timers can be identical for all probes and the capsule coast time variations up to a few hours can easily be preset into the system giving an overall accuracy essentially equal to the tuning fork timer accuracy for 11 days.

The entry sequencer controls all events subsequent to run out of the coast timer. The sequence is essentially based on either g or pressure after release of the despin mechanism. These references are obtained from the data system in digital form in synchronism with the data system commutation cycle.

Digital comparators are used for detecting the two acceleration and two pressure referenced events. Solid-state switching is used throughout for arm, fire, safe switching, and power control. The master clock for all timing pulses is included in the data system because that subsystem is the major user. The sequencer subsystem obtains countdown timing for adjustments of deflection burn and coast from the master clock during those periods. Otherwise the master clock is not running until entry.

Timing precision for the various types of events is shown in Table III-17.

Table III-17 Timing Precision, Large Probe Sequencing

Type of Function*	Sequencer		Number of Occurrences		Precision (sec)		Remarks
	Coast	Entry	Coast	Entry	Coast	Entry	
Spin-in (Pyro)†	X		1		±0.1		
Fire Propulsion (Pyro)	X		1		±60		
Stop Propulsion (Burn Interval)	X		1		±0.01		
Transfer to Entry Timer	X		1		±20		
Despin Pyro		X		1		±10	Transfer to entry timer is the reference.
Jettison Weights		X		1		±10	Same
Begin g Sensing		X		1		±10	Same
Staging (Pyro)		X		1		+0.4 -0	g reference.
Start Data Record		X		1		+0.4 -0	g reference.
Release Main Chute Pyro		X		1		+20 -0	Pressure reference.
Reduce Data Rate to ½		X		1		+20 -0	Pressure reference.
Start And Stop High-Altitude Data Mode Transmission§	X			1		±10	Transfer to entry timer is the reference.

*Functions are not in order of occurrence.

†All pyro functions require arm, fire and safe.

§High altitude transmission is only for case where spacecraft does not impact.

C. BASELINE MISSION - SMALL BALLISTIC PROBES

The baseline mission studies identified the need for atmospheric entry data to augment the data obtained by the large probe at the subsolar target. Two probes, with more modest instrument complements and targeted at the polar and antisolar regions, respectively, fulfill this requirement. Except as modified by the reduced instrumentation, the design philosophy for these probes is essentially the same as for the large probe. Both probes provide data from entry to impact.

1. Small Probe Science Capabilities

The small probe systems were defined to provide information on the horizontal variations of the atmospheric structure and composition, the cloud structure and composition, and the atmospheric dynamics between the subsolar region and the antisolar and polar regions. The instrument complement (Table III-18) is physically the same for both the polar and the antisolar probes. The "solar" radiometer on the antisolar probe measures infrared radiation while that on the polar probe measures visible radiation. These instruments have only three vertical view fields rather than five as on the large probe.

Accelerometer sampling is initiated at 0.1 g increasing and continues until parachute deployment is complete. Deceleration profiles for the two probes are shown in Fig. III-23 and III-24. Parachute deployment is initiated at 1.5 g decreasing and is complete by 6124.5 km (21 mb) for the polar probe and by 6122.5 (31 mb) for the antisolar probe. All instruments are sampled as shown in Table III-18, resulting in the number of measurements and altitude resolution shown in Fig. III-25 and III-26.

Table III-18 Baseline Small Probes Instrument Complement

Instrument	Bits per Sample	Sample Time Interval (sec)	Altitude Sample Interval at 6120 km (m)	Total Number of Measurements
Pressure	8	10	191	607
Temperature	8	10	191	607
Mass Spectrometer	60C	60	1100	101
Solar Radiometer	120	15	285	404
Nephelometer	16	10	191	607
Evaporimeter/Condensimeter	456	60	1100	101
Accelerometers (3)	3 × 10	1	19	3 × 6074
Transponder	--	continuous	--	--
Impact Indicator	--	10	--	3 minimum
Accelerometers (4) Entry	4 × 10	<0.2	--	4 × 130

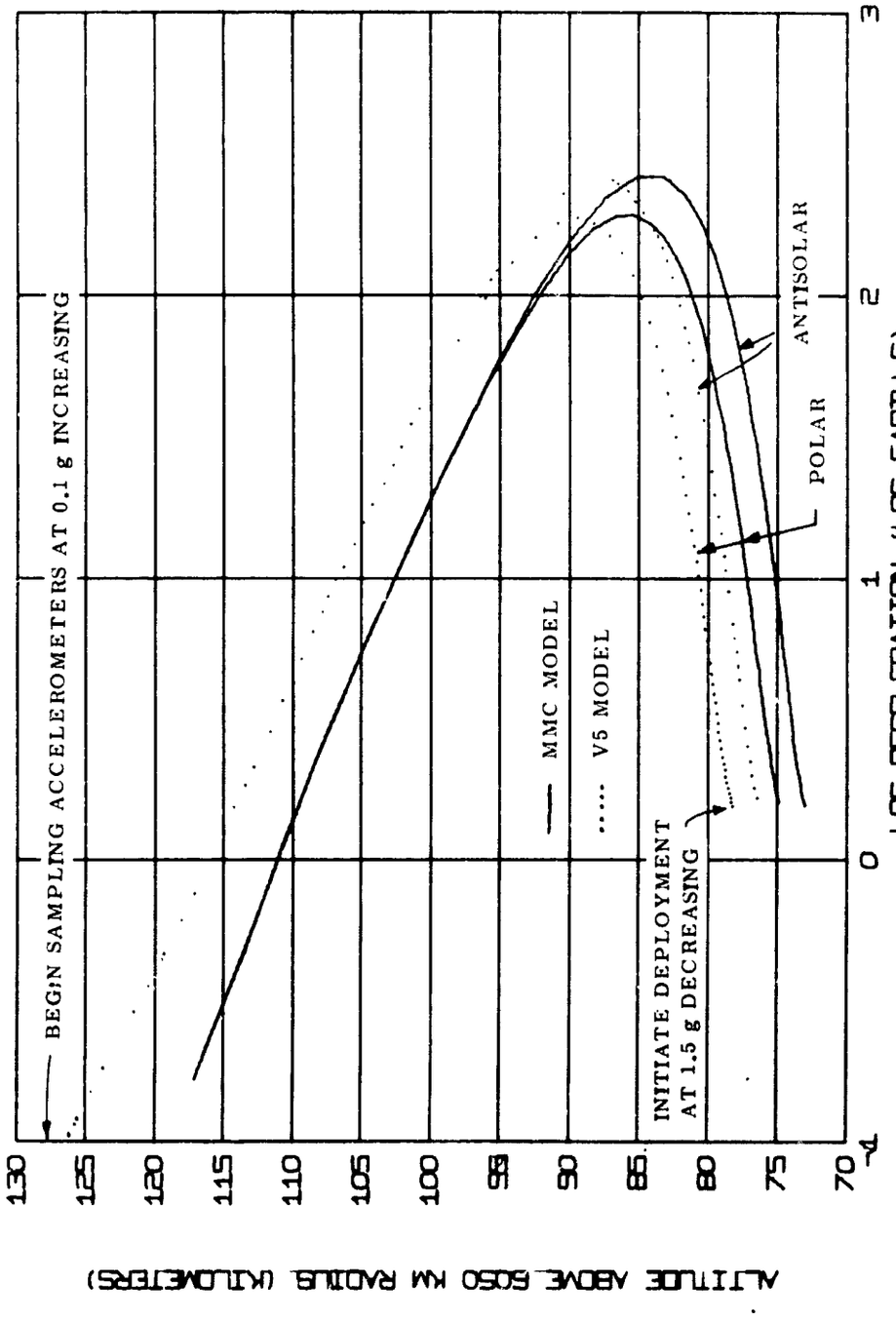


Fig. III-23 Deceleration vs Altitude for Small Probes

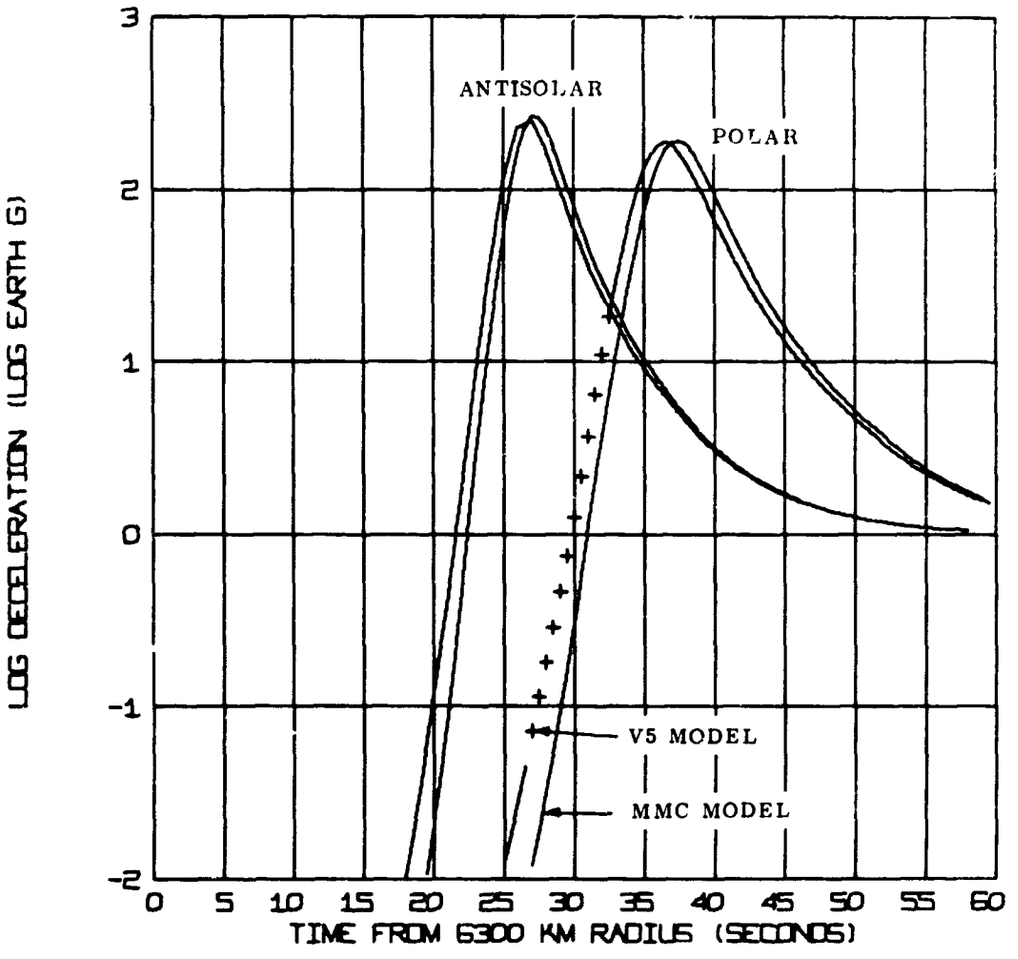


Fig. III-24 Deceleration vs Time for Small Probes

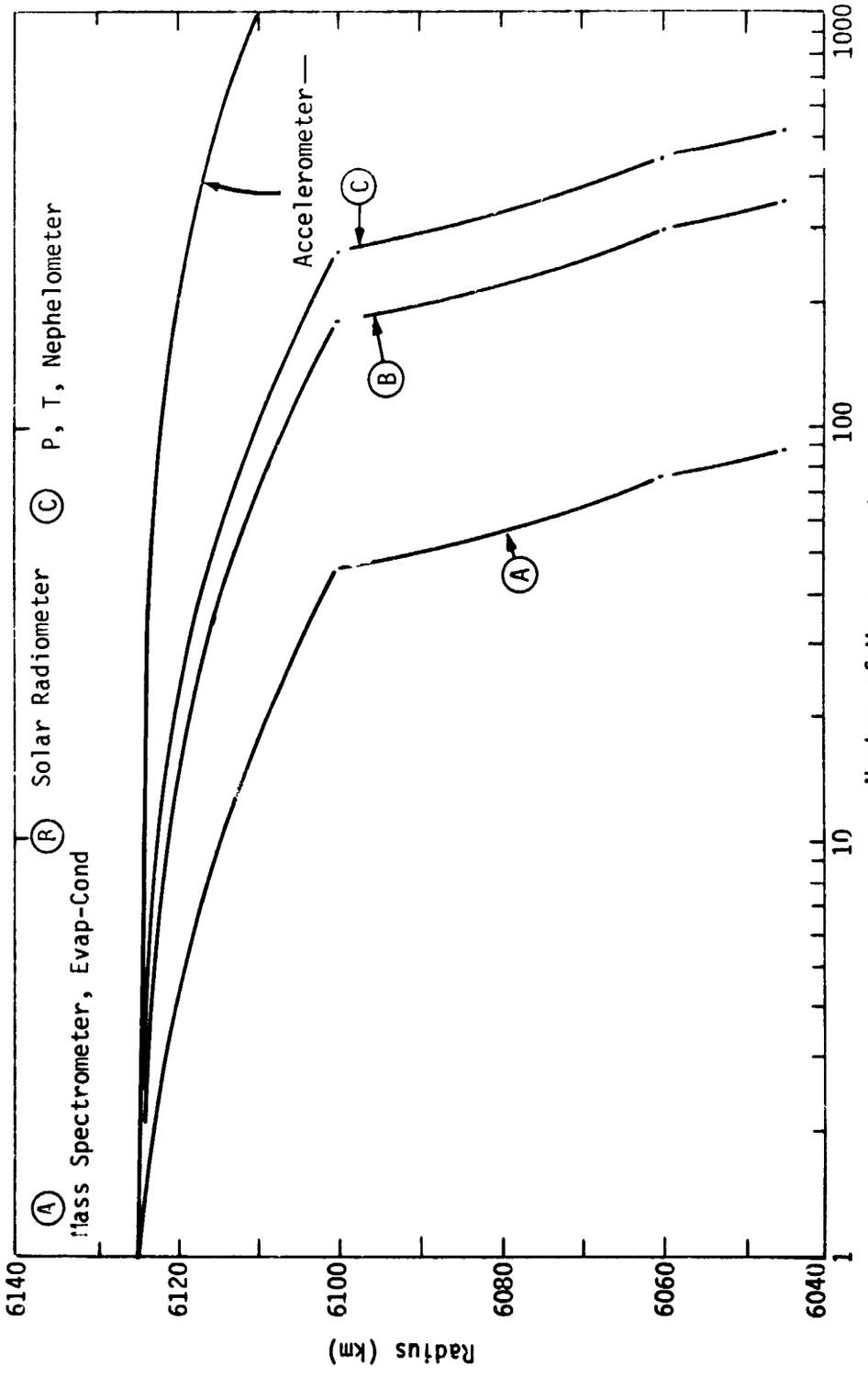


Fig. III-25 Number of Measurements vs Altitude, Small Probe

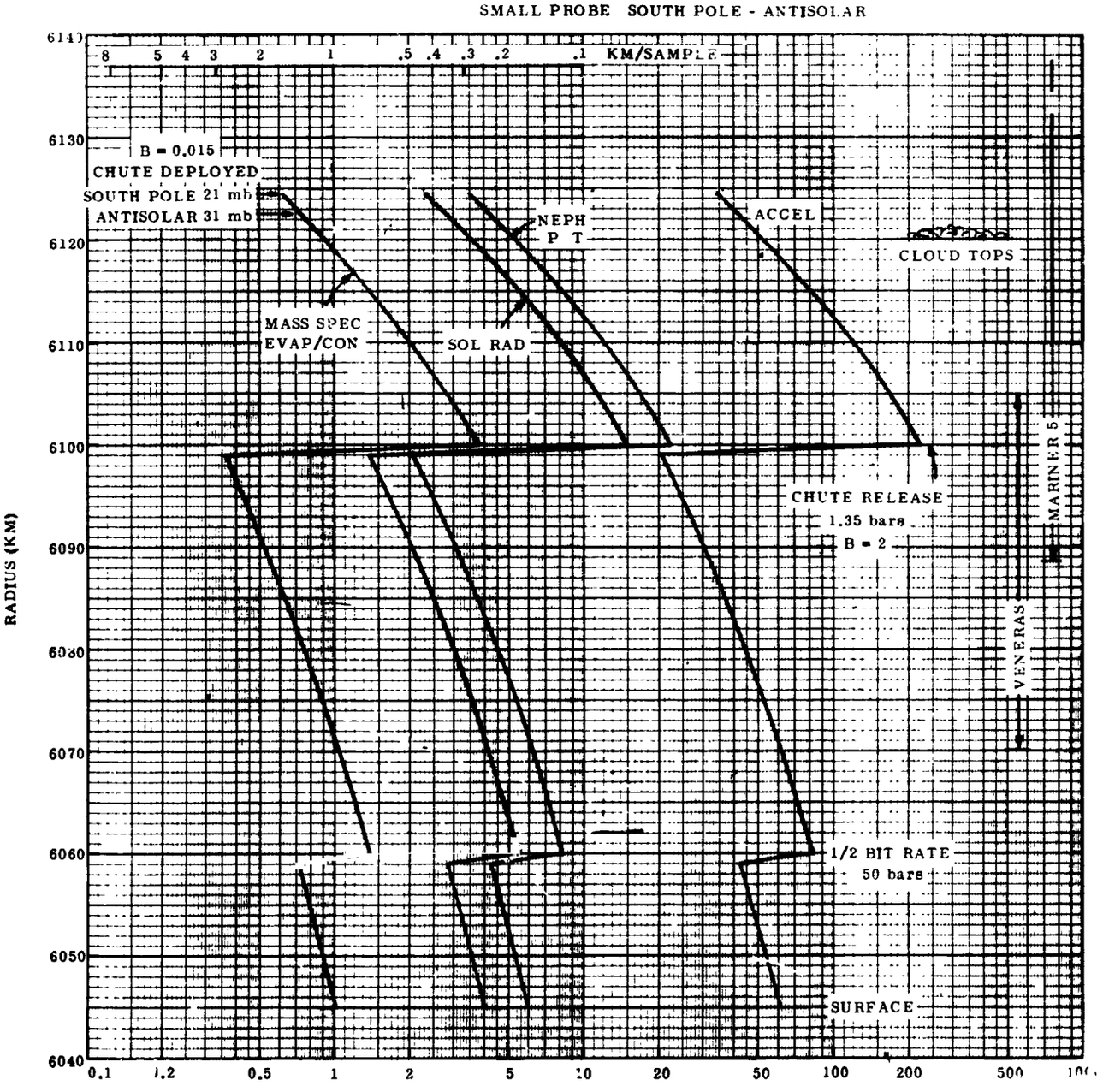


Fig. III-26 Number of Samples vs Altitude, Small Probe

The parachute is released at 1.35 bars (6100 km) after passing through the tropopause and the region where H_2O clouds are possible. Sample intervals are larger than nominal only between about 6100 and 6085 km where the large probe resolution is best. Below this, the sample intervals remain better than nominal even after the sample rate is halved at 50 bars (6060 km). At 50 bars, the impact indicator is armed. After its threshold range of 300 m is reached, a code word indicating surface approach replaces one of the accelerometer words every 10 sec. This gives an indication every 80 to 100 m for a total of at least three readings before impact. Impact velocity is between 8 and 10 m/sec.

2. Engineering Mechanics - Small Descent Probe

a. Requirements - In addition to the general requirements defined in Section III.B.2, the specific requirements for the small probe are:

Item	Anti-solar	South Pole
Entry Angle (deg)	-35	-25
Science Instrument Weight (lb)	26.5	26.5
Communications System Weight (lb)	36.3	36.3
Power Dissipated (w)	110.7	110.7
Radius at Deployment of Science Instruments (km)	6122.5	6122.5
Ballistic Coefficient Required for Descent Rate Control at Instrument Deployment Altitude (slug/ft^2)	0.015	0.015
Radius at Release of Rate Control Decelerator (km)	6100	6100
Ballistic Coefficient of Descent Capsule after Decelerator Release (slug/ft^2)	2.0	2.0

The ambient temperature history for the descent profile resulting from the above conditions is shown in Fig. III-27. The V5M atmosphere is used to establish temperature and pressure histories, but science instrument deployment altitude and decelerator design and staging altitude are based on the lower density atmosphere.

b. Configuration Definition and Weight Summary - The inboard profile of the small descent probe is shown in Fig. III-28, and the internal arrangement of the small descent capsule is shown in Fig. III-29. A weight summary is given in Table III-19.

Functional Description - The small probe system is similar to the large probe and includes the terminal descent capsule, capsule deployment and decelerator system, the velocity deflection system, the spin-up/despin system, the Entry Vehicle, and the biocanister/adapter structural system. A complete system is shown in Fig. III-28. The major assemblies and interfaces are defined with separation planes.

The descent capsule is an aerodynamically stable sphere/cone/flare body with a 21° cone/flare half angle and 29.0-in.-diameter base.

Two versions of the small descent capsule are required. One that is designed for the South Pole target requires a solar radiometer, while the other design for the antisolar point requires a thermal radiometer. The remaining instrument and electronic equipment requirements are the same. Both configurations are defined with noted exceptions on the capsule internal arrangement drawing (Fig. III-29).

The pressure-sustaining structure of the outer shell is an integrally machined and welded ring shell of 6Al-4V titanium alloy. The inner canister shell is a welded titanium pure monocoque shell. The interfacing rings are machined to provide good seal configuration and seating. Locally built-up and machined sections are welded into the canister shell at penetrations.

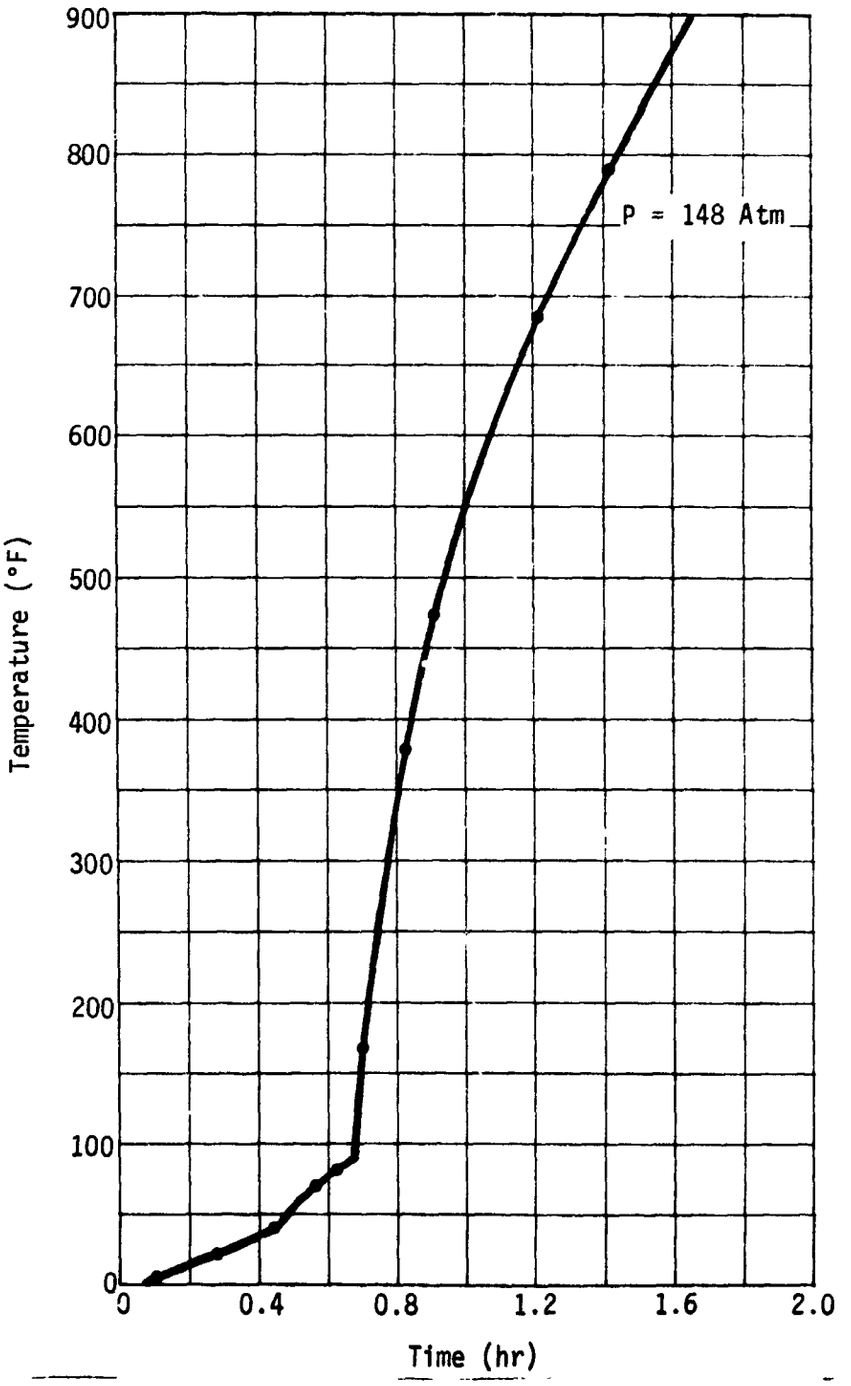


Fig. III-27 Ambient Temperature History, Small Descent Probe

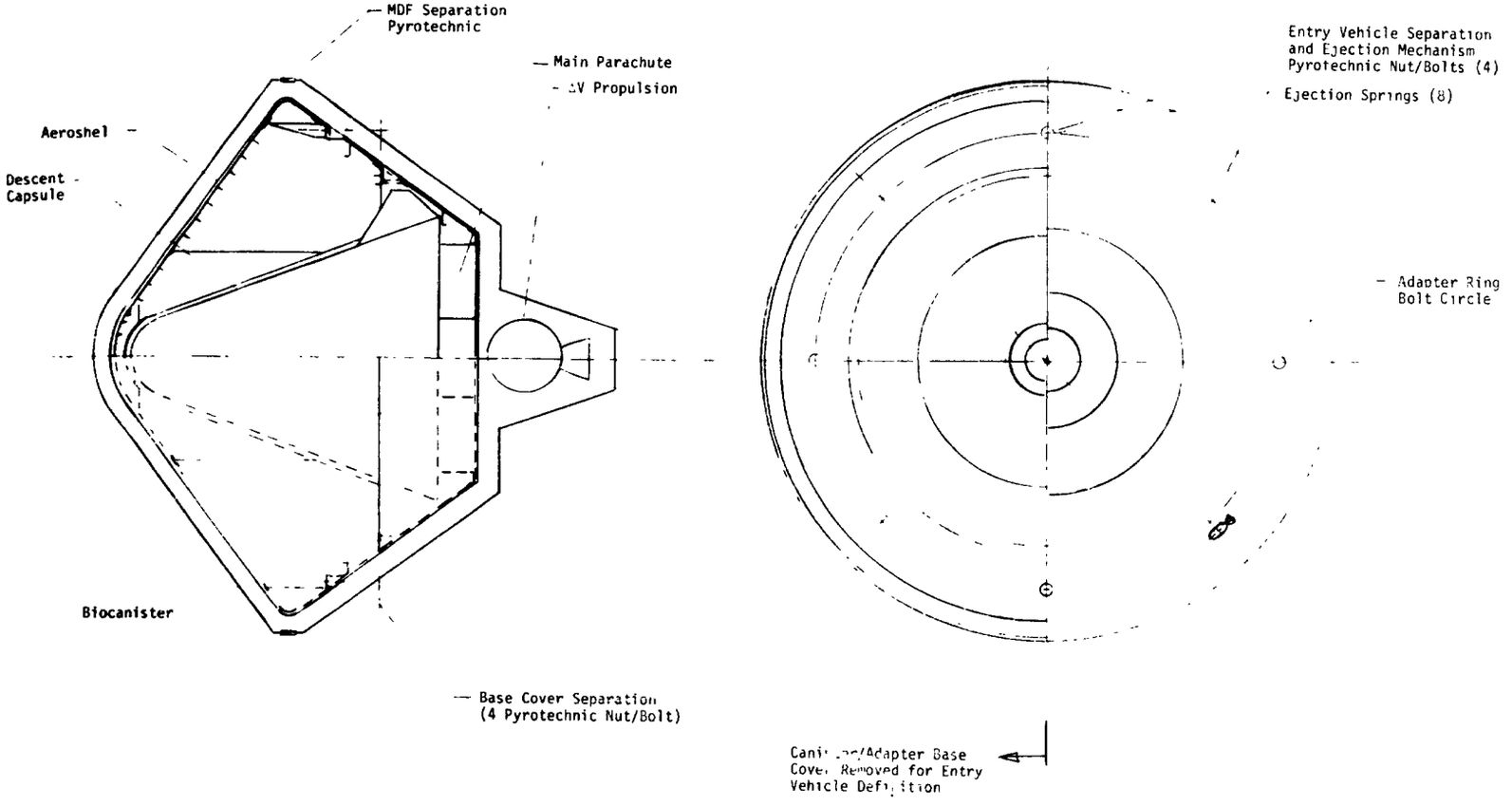
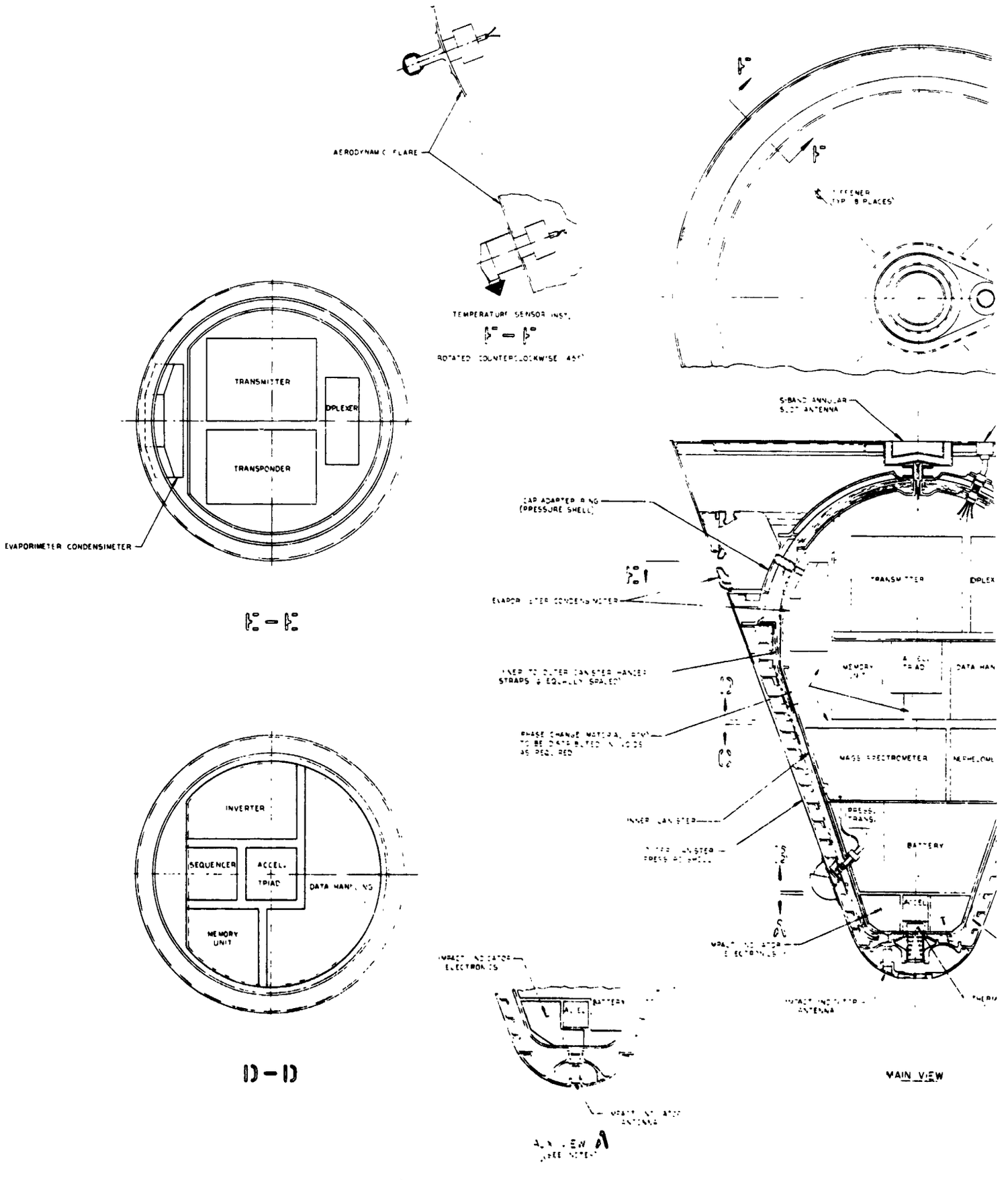
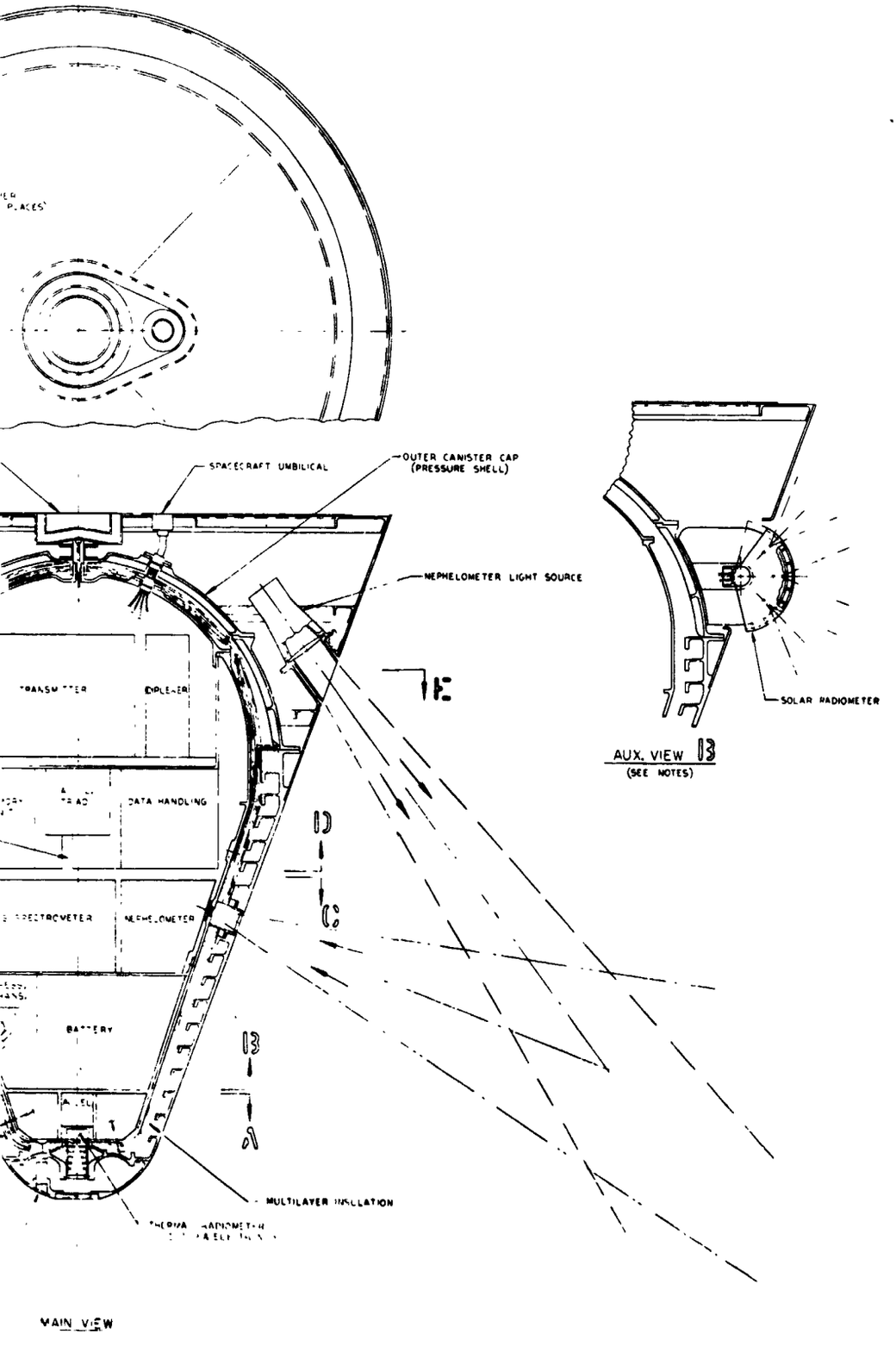


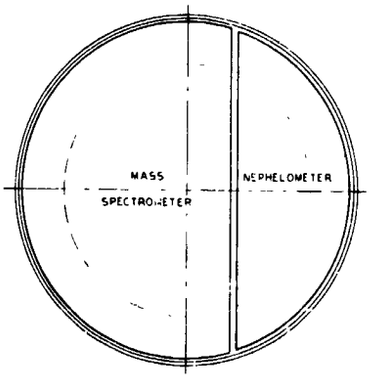
Fig III-28 Inboard Profile, Small Ballistic Descent Probe

PRECEDING PAGE BLANK NOT FILMED.

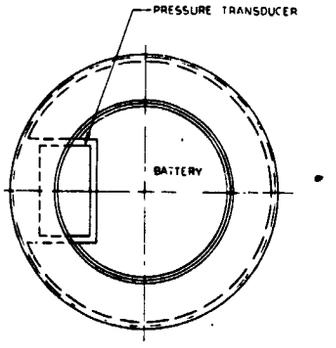


FOLDOUT FRAME

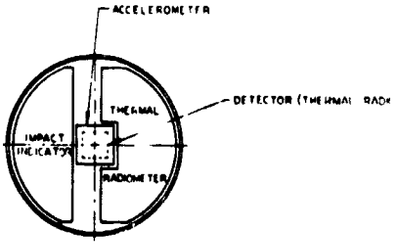




C – C



B – B



A – A

Fig. III-29 Internal Arrangement, S

FOLDOUT FRAME 2

II)

ELOMETER

RANSDUCER

TER

DETECTOR (THERMAL RADIOMETER)

NOTES.
1. THIS DRAWING DEFINES THE INSTRUMENTS FOR TWO CAPSULE DESIGNS BOTH HAVE THE SAME EQUIPMENT EXCEPT AS FOLLOWS
   1. CAPSULE FOR PROBE TO SUB SOLAR TARGET-HAS THE COMPLEMENT OF INSTRUMENTS AS SHOWN IN MAIN VIEW
   2. CAPSULE FOR PROBE TO SOUTH POLE TARGET-HAS INSTRUMENT OPTIONS AS DEPICTED IN AUXILIARY VIEW A & B

SCALE

ALL OF DWG ONE HALF

rrangement, Small Ballistic Descent Capsule

2 FOLDOUT FRAME 3

Table III-19 Small Ballistic Probe Weight Summary
(Impacting Spacecraft Case)

System	Weight (lb)	
Descent Capsule		(131.9)
Science	26.5*	
Electronics	35.9	
Pressure Vessel	38.6	
Internal Shell and Mounting Structure	15.6	
Science Integration	2.5	
Aerodynamic Flare	6.0	
Internal Insulation	2.3	
Phase Change Material	2.5	
Antenna and Umbilicals	2.0	
Decelerator System		(21.2)
Main Parachute	16.7	
Drogue and Chute Cans	4.5	
Aeroshell (4.33 ft dia, 55° Half Angle)		(93.0)
Aeroshell Structure Weight	43.0	
Heatshield		
Forward Cone	40.0	
Base	10.0	
Separation Hardware		(2.0)
Spin-Up/Despin (Fixed)		(4.0)
Entry Weight		252.1
Spin/Despin/Separation (Spent)		6.0
Biocanister		35.0
ΔV Propulsion		11.0†
Total System		304.1

*Includes transponder.

†16 lb for flyby spacecraft case.

c. Descent Capsule Design - Small Descent Probe - The configuration selection considerations and thermal/structural design concept selection are the same for the small descent probe as those defined in Chapter III.B for the large probe. The specific input quantities for the small probe descent capsule design are included in Table III-4. Resulting capsule dimensions and weights are given in Fig. III-29 and Table III-19.

d. Entry Vehicle Design - Small Descent Probe - Since the small probes go to two target sizes, two entry angles are involved. The steeper of the two, the -35° for the antisolar point, is used to establish the ballistic coefficient as a common probe design is desirable. From Fig. III-14 and the 6122.8 km radius required (including 0.3 km for deployment), it is seen that a ballistic coefficient of 0.4 is indicated. A 55° cone half-angle aeroshell is again found to provide the best fit for the relatively deep descent capsule.

The peak stagnation pressure for aeroshell design for the -35° angle and a 0.4 slug/ft^2 ballistic coefficient entry is 41 psi. Peak deceleration is 232 g. Resulting aeroshell weight is 43.0 lb (Table III-19).

Carbon phenolic is selected for the heat shield and is sized for the shallower of the two entry angles, γ = -25°, because total heat is greater for that case. A unit weight of 2.3 lb is required (Fig. III-17), or a total weight of 40 lb, which is 16% of the entry weight. Aft cover heat protection is taken as the same unit weight as that for the large probe, 0.5 lb/ft^2.

Thermal control during postseparation is provided by coatings, and attitude control is provided by spin stabilization. Two of the small solid rocket motors defined for spin-up of the large probe are required. The initial angle of attack for the small probe to the South Pole is 51°, which is higher than desirable, but still within the range found in Ref III-1 to converge

to low values, <5°, at peak heating. This initial angle could be improved by adjustment of ejection angle, ejection radius, and deflection velocity, but the existing value is deemed acceptable.

Deflection impulse requirements are 1140 lb-sec and 1780 lb-sec, respectively, at the polar and antisolar target probes. For the case of an impacting spacecraft, ΔV's are 45 m/sec and 70 m/sec. Solid rocket motor requirements thus fall in the range of the 889 lb-sec impulse, 7.3-lb motor defined in Ref III-1 and the 1820 lb-sec impulse, 16.7-lb motor defined in the large probe section (Section B). For the flyby case, the ΔV's required are 70 m/sec and 112 m/sec for polar and antisolar probes, respectively. This results in a maximum impulse requirement for the small probe of 2850 lb-sec, thus a correspondingly larger solid rocket motor, ∿20 lb, would be required.

e. Decelerator Design - Small Descent Probe - The decelerator design for the small descent probe is based on the requirement for a ballistic coefficient of 0.015 slug/ft^2.

The mission constraints dictated the following deployment conditions:

Parameter	γ_E = -25°	γ_E = -35°
Aeroshell M/C_DA (slug/ft^2)	0.4	0.4
Deployment Radius (km)	6124.5	6122.5
Deployment Mach Number	0.92	0.79
Deployment Dynamic Pressure (psf)	24	25

A parachute of the disk-gap-band type described in Chapter VIII was designed with the following characteristics:

M/C_DA	0.015 slug/ft^2
Drag Coefficient	0.53
Parachute Diameter	30 ft
Parachute Weight	19 lb (same for both cases)

3. Mission Analysis

The targeting, deflection, and entry probe design data are presented in Table III-20 for the small probe at the South Pole and Table III-21 for the small probe at the antisolar point. Main chute deployment for this probe would occur at -1.5 g if the system were based on "g" sensing.

Descent profiles at the South Pole are presented in Fig. III-30 and III-31. Descent profiles at the antisolar point are shown in Fig. III-32 and III-33. The two atmosphere models exhibit descent times that differ by about 12.8 minutes. The different entry angles at the two sites produce no substantial difference in total descent time, and about 1.3 minutes in time to main chute release.

The probe targeted to the South Pole is the first probe released, and the maximum pointing error is 0.55°. The entry error dispersions for the impacting case from all sources are ±3.35° downrange, ±1.65° crossrange, and ±2.06° in entry path angle. The entry angle of attack is about 51°, which is near the maximum desirable value. For a flyby spacecraft, the entry dispersions become ±4.16° downrange, ±1.0° crossrange, and ±2.6° in entry path angle. These dispersions can be reduced by increasing the deflection angle and decreasing ΔV_{EJ}, or by reducing the flyby periapsis radius.

Table III-20

VENUS SMALL PROBE (SOUTH POLE)

* * * ENTRY PROBE DESIGN DATA * * *

TARGET (NEAR SIDE ENTRY)		SOUTH POLE	
APPROACH TRAJECTORY TYPE		IMPACT	FLYBY
PERIAPSIS RADIUS OF BUS	KM	2800.	12600.
DEFLECTION RADIUS	KM	4,000,000	4,000,000.
DEFLECTION VELOCITY	METERS/SEC	45.	70.
DEFLECTION ANGLE	DEGREES	20.	20.
CAPSULE COAST TIME	HOURS	290.6	288.5
MAXIMUM ANGLE OF ATTACK	DEGREES	50.5	42.
ENTRY VELOCITY	FT/SEC	35367.	
ENTRY ANGLE	DEGREES	-25.	
ENTRY ALTITUDE	FEET	815000.	
ENTRY RADIUS	KM	6298.412	
ENTRY LATITUDE	DEG	-62.0176	
ENTRY LONGITUDE	DEG	83.1456	
SOLAR ZENITH ANGLE	DEG	86.7899	
EARTH ZENITH ANGLE (MASK)	DEG	65.9179	
AEROSHELL BALLISTIC COEF.	SLUGS/FT2	0.4	
TIME OF MACH 1 OCCURRANCE	SEC	57.5	
MAXIMUM DYNAMIC PRESSURE	LBS/FT2	2307. (V5M)	2364 (MMCL) AT 38 SEC
MAXIMUM DECELERATION	G	180 (V5M)	184 (MMCL) AT 38 SEC
TIME FROM ENTRY TO MAIN CHUTE DEPLOYMENT	SECONDS	60.0	
MAIN CHUTE BALLISTIC COEF.	SLUGS/FT2	.015	
MACH NUMBER AT MCD		.918	
DECELERATION AT MCD	G	1.5	
DYNAMIC PRESSURE AT MCD	LB/FT2	24.	
ALTITUDE MAIN CHUTE DEPLOY	FT	256238.1 (V5M)	244586. (MMCL)
RADIUS MAIN CHUTE DEPLOYED	KM	6128.1015 (V5M)	6124.5499 (MMCL)
TIME FROM ENTRY TO MAIN CHUTE RELEASE	HOURS	0.7477 (V5M)	.761 (MMCL)
TERMINAL BALLISTIC COEF.	SLUGS/FT2	2.0	
CHUTE RELEASE PRESSURE	BARS	1.35	
RADIUS MAIN CHUTE RELEASE	KM	6103.3655 (V5M)	6099.9914 (MMCL)
TIME TO 50.0 BARS	HOURS	1.24 (V5M)	(4460 SEC) R=6066.83
TIME TO 50.0 BARS	HOURS	1.27 (MMCL)	(4590 SEC) R=6060.0
INITIAL BIT RATE	BITS/SEC	70	
FINAL BIT RATE	BITS/SEC	35.	
RADIUS TO CHANGE BIT RATE	KM	6060.	
TIME FROM ENTRY TO IMPACT	HOURS	1.745(V57)	1.535 (MMCL)

Table III-21

VENUS SMALL PROBE (ANTI SOLAR)
* * * ENTRY PROBE DESIGN DATA * * *

TARGET (FAR SIDE ENTRY)		ANTI SOLAR	
APPROACH TRAJECTORY TYPE		IMPACT	FLYBY
PERIAPSIS RADIUS OF BUS	KM	2800.	12600.
DEFLECTION RADIUS	KM	4.000.000	4.000.000.
DEFLECTION VELOCITY (DEL V)	METERS/SEC	70.	112
DEFLECTION ANGLE	DEGREES	20.	20.
CAPSULE COAST TIME	HOURS	289.12	286.4
MAXIMUM ANGLE OF ATTACK	DEGREES	46.5	44.6
ENTRY VELOCITY	FT/SEC	35367.	
ENTRY ANGLE	DEGREES	-35.	
ENTRY ALTITUDE	FEET	815000.	
ENTRY RADIUS	KM	6298.412	
ENTRY LATITUDE	DEG	0.4186	
ENTRY LONGITUDE	DEG	157.7547	
EARTH ZENITH ANGLE (MASK)	DEG	63.8075	
SOLAR ZENITH ANGLE	DEG	157.7509	
AEROSHELL BALLISTIC COEF.	SLUGS/FT2	0.4	
TIME OF MACH 1 OCCURRENCE	SEC	42	
MAXIMUM DYNAMIC PRESSURE	LBS/FT2	2955 (V5M)	2981 (MMCL) AT 28 S
MAXIMUM DECELERATION	G	230 (V5M)	232 (MMCL) AT 28 SEC
TIME FROM ENTRY TO MAIN CHUTE DEPLOYMENT	SECONDS	46.6	
MAIN CHUTE BALLISTIC COEF.	SLUGS/FT2	.015	
MACH NUMBER AT MCD		.785	
DECELERATION AT MCD	G	1.5	
DYNAMIC PRESSURE AT MCD	LB/FT2	25.16	
ALTITUDE MAIN CHUTE DEPLOY	FT	249985.8 (V5M)	D=-1.5 G
ALTITUDE MAIN CHUTE DEPLOY	FT	238580.1 (MMCL)	D=-1.5 G
RADIUS MAIN CHUTE DEPLOYED	KM	6126.1653 (V5M)	6122.7193 (MMCL)
TIME FROM ENTRY TO MAIN CHUTE RELEASE	HOURS	0.725(V5M)	.737 (MMCL)
TERMINAL BALLISTIC COEF.	SLUGS/FT2	2.0	
CHUTE RELEASE PRESSURE	BARS	1.35	
RADIUS MAIN CHUTE RELEASE	KM	6103.3655 (V5M)	6099.9914 (MMCL)
TIME TO 49.5 BARS	HOURS	1.21 (V5M)	(4367 SEC) R=6066.83
TIME TO 49.5 BARS	HOURS	1.25 (MMCL)	(4507 SEC) R=6060.0
INITIAL BIT RATE	BITS/SEC	70.	
FINAL BIT RATE	BITS/SEC	35	
RADIUS TO CHANGE BIT RATE	KM	6060.	
TIME FROM ENTRY TO IMPACT	HOURS	1.725 (V5M)	1.512 (MMCL)

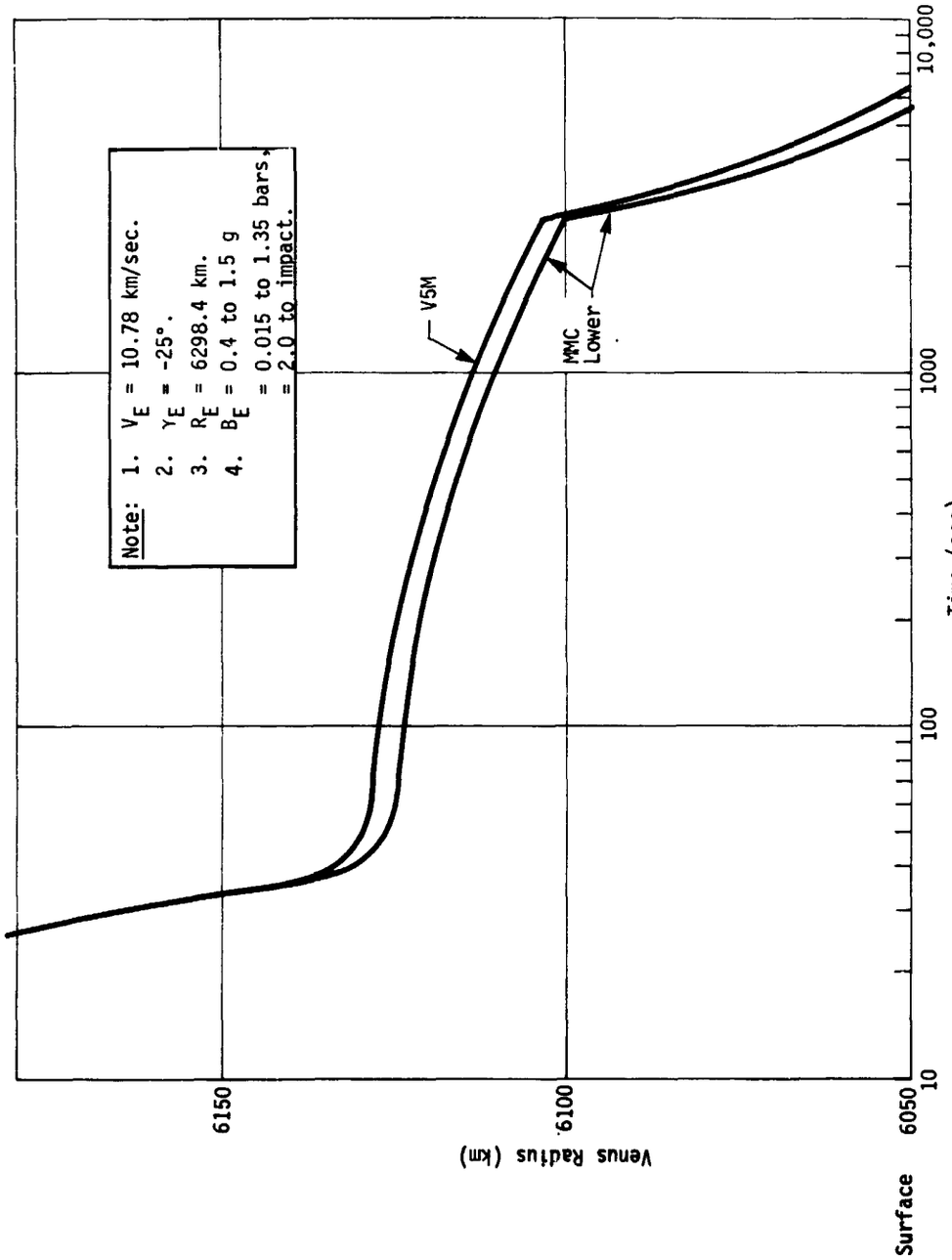


Fig. III-30 Small Probe Descent Profile, South Pole

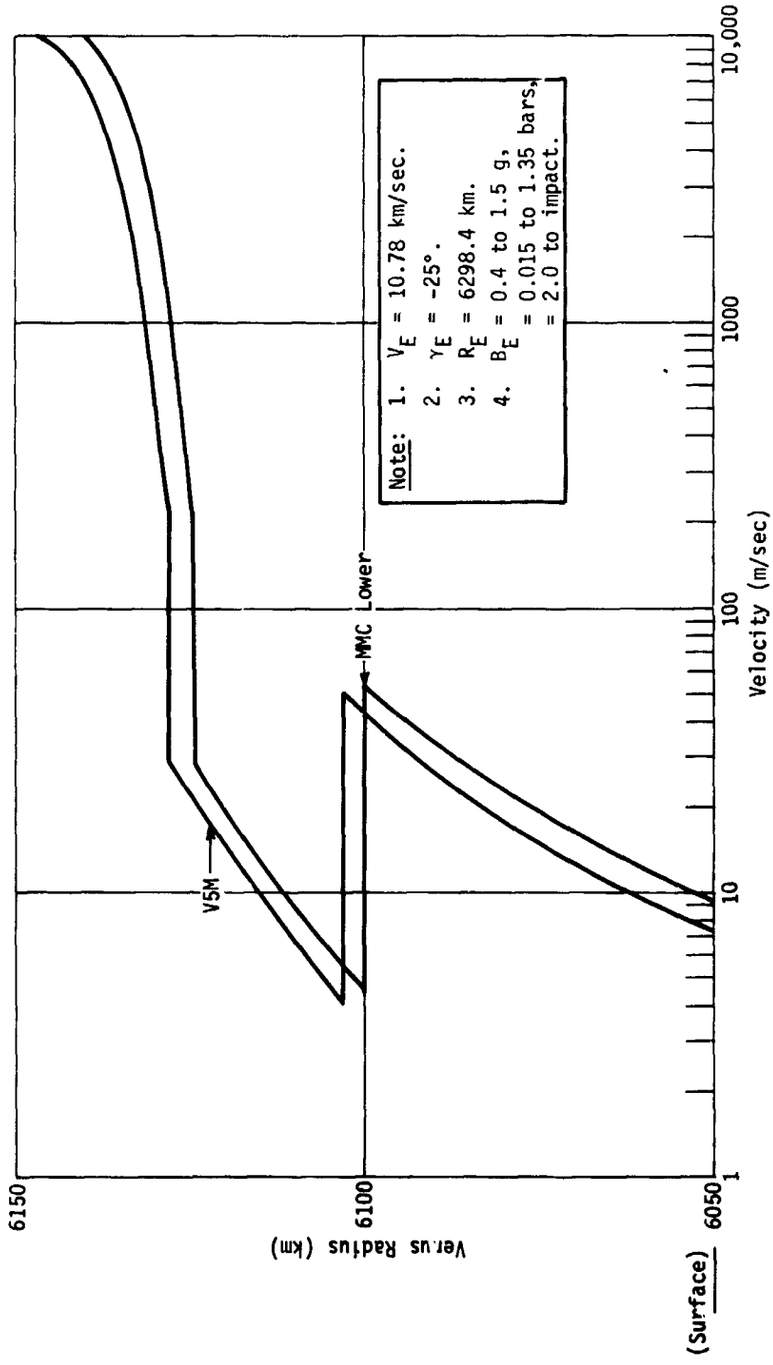


Fig. III-31 Small Probe Descent Profile, South Pole

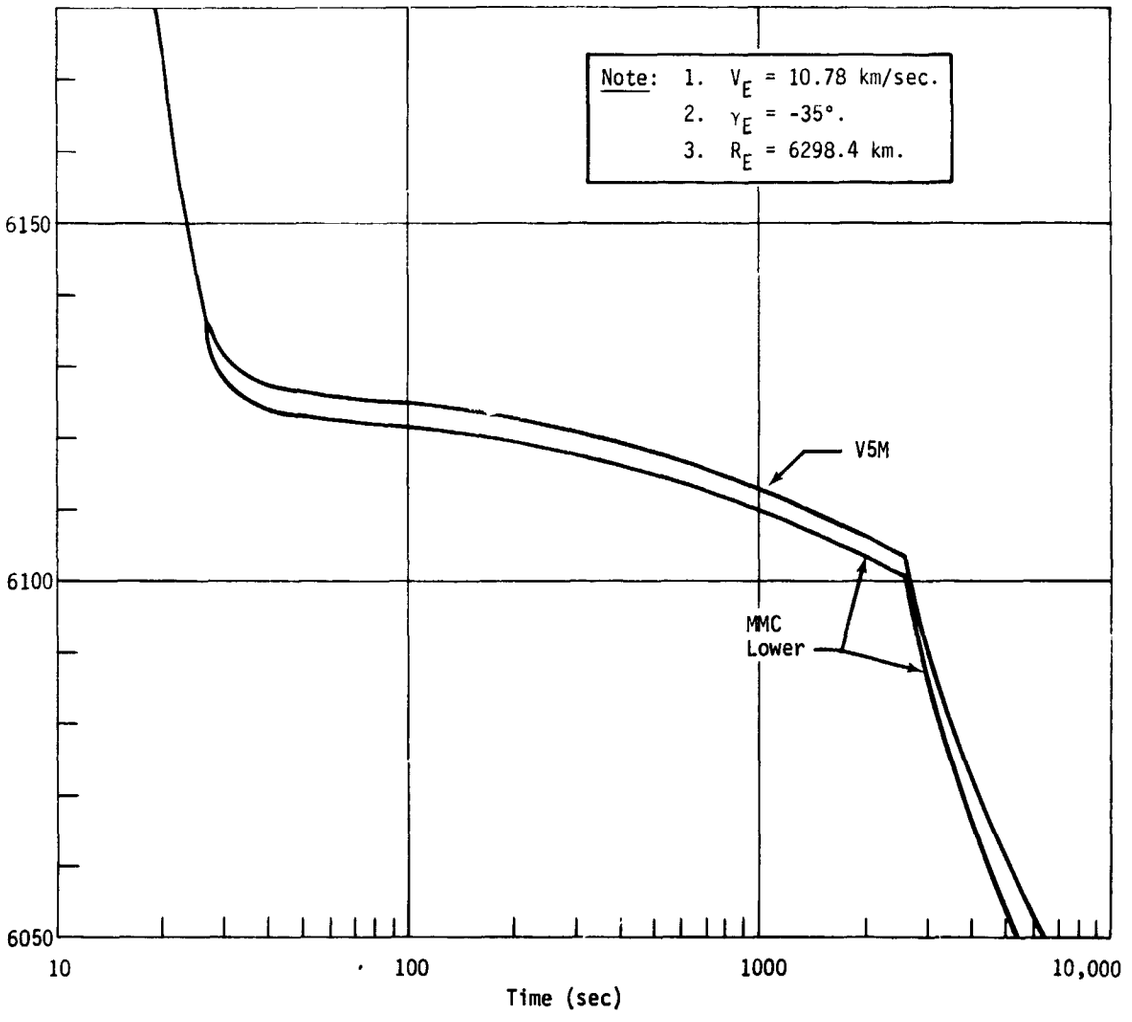


Fig. III-32 Small Probe Descent Profile, Antisolar

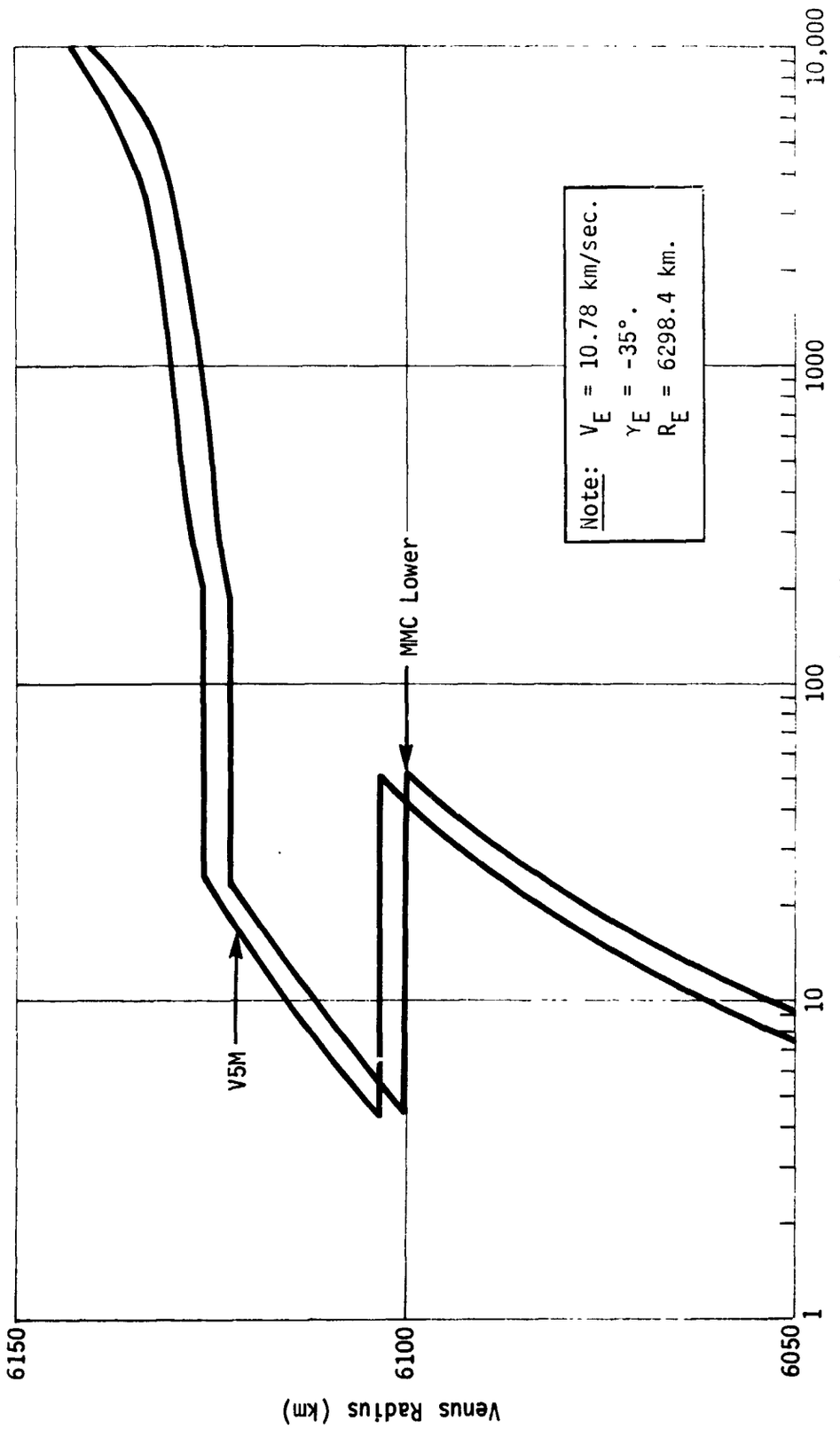


Fig. III-33 Small Probe Descent Profile, Antisolar

The probe targeted to the antisolar point is the third probe released and exhibits a maximum pointing error of 0.59°. The deflection of this probe is the greatest of all those studied and yields a farside entry. This condition is defined as an entry that occurs on the farside of a plane through the V_{HE} point and the center of the planet from the spacecraft path. Because the deflection velocity is large and the deflection angle is small, the entry dispersions are somewhat larger than the nearside entry. In this particular case, the impacting spacecraft mission yields downrange dispersions of ±5.78° and crossrange dispersions of ±2.63°. The entry path angle dispersion is ±3.66°.

For a flyby spacecraft mission, the dispersions become ±10.6° in downrange, ±1.62° in crossrange, and ±6.68° in entry path angle. The sensitivity to deflection angle is a major contribution to entry dispersions for flyby missions. These sensitivities can be reduced by nearly 30% by increasing the deflection angle to 25°. Of course, the ΔV_{EJ} will be reduced to achieve the desired targeting and this will, in turn, affect the interval between probe operating times. The angle of attack will be increased to approximately 50°, which is comparable to the direct impact mission. Table III-22 presents the sensitivities for farside entries and a 25° deflection angle. Although data are shown for the impacting case also, the entry angle of attack exceeds 50° and is considered to be unsatisfactory in this study. Another approach is to decrease the radius of periapsis. At 7700 km the sensitivities have been reduced 15% for the 20° deflection angle and 20 to 25% for 25° deflection angles. Still another means of improving the accuracy is to retarget the flyby path so that all deflection maneuvers result in nearside entries. The orientation of the flyby plane in the trial mission achieves this goal.

Table III-22 Sensitivities for Far Side Entries

	γ_E = -35°, ι = -25°				
	ΔR (deg)	T (hr)	V_E (m/sec)	γ_E (deg)	
$\frac{\partial(\ )}{\partial R_{EJ}}$ km	58.41 × 10^{-6}	74.3 × 10^{-6}	0	56.93 × 10^{-6}	R_p = 2,800 km
$\frac{\partial(\ )}{\partial V_{HE}}$ km/sec	-10.25	-73.7	346	-3.346	
$\frac{\partial(\ )}{\partial R_p}$ km	-1.896 × 10^{-2}	-0.9 × 10^{-4}	0	-1.202 × 10^{-2}	
$\frac{\partial(\ )}{\partial \iota}$ deg	-8.771	-0.08	+0.10	-5.5487	
$\frac{\partial(\ )}{\partial \Delta V}$ m/sec	4.0193	-0.047	0.32	2.54	
$\frac{\partial(\ )}{\partial R_{EJ}}$ km	93.03 × 10^{-6}	73.9 × 10^{-6}	0	58.743 × 10^{-6}	R_p = 12,600 km
$\frac{\partial(\ )}{\partial V_{HE}}$ km/sec	-21.18	-72.6	348	-10.520	
$\frac{\partial(\ )}{\partial R_p}$ km	-1.14 × 10^{-2}	-0.5 × 10^{-4}	0	-0.72502 × 10^{-2}	
$\frac{\partial(\ )}{\partial \iota}$ deg	-14.024	-0.13	+0.3	-8.8659	
$\frac{\partial(\ )}{\partial \Delta V}$ m/sec	3.97	-0.046	-0.32	2.513	

4. Telecommunication and Data Systems

a. Telecommunications Sytem, Small Ballistic Probe - Much of the discussion in Section B on the large probe can be applied to the small probe. It will have no preentry science in either spacecraft option. Its instrument complement is smaller, giving an initial bit rate of 70 bps. It is a limb probe (communications angle, 70°), so it uses the same 0.6 λ annular slot antenna as the large probe, and it reduces its bit rate to 35 bps at the same elevation as the large probe to compensate for increasing atmospheric losses.

Less importance is given to transmitting the few seconds of early data generated before transponder uplink lock-on. It is recommended that transmission simply be deferred until the lock-on is completed.

The link calculations in Table III-23 show that a 15-W transmitter is required. Except for this and the lower data rates, it is identical to the large probe link calculation, as given in Table III-7. The uplink is shown in Table III-10.

The Doppler rate transient generated by probe parachute release will be somewhat less severe than that generated by the large probe, and will be handled in the same way.

b. Data System - Small Probes (Baseline) - The data systems for each of the two small probes for the baseline mission are identical, except the solar radiometer is replaced with a thermal radiometer for the antisolar probe. Functionally, they operate in the same modes as the large probe (impacting scacecraft case). That is, entry data are stored until aeroshell staging, then the stored data are interleaved in the real-time telemetry train. Likewise, the transmission bit rate is reduced to 1/2 rate at 50 bars (6066 to 6060 km). The major difference between the data system for the small probes and the large probe is the reduction in instrumentation and data rate.

Table III-23 Link Calculations, Downlink, Small Probes

Item	Paramater	Postentry, 70 bps 70° Comm Angle		Lower Atmosphere, 35 bps 70° Comm Angle	
		Nominal (db)	Adverse Tolerance (db)	Nominal (db)	Adverse Tolerance (db)
1.	Total Transmitter Power, 15 W	+41.8 dbm	0.4	+41.8 dbm	0.4
2.	Transmitter Circuit Loss	-0.4	0.2	-0.4	0.2
3.	Transmitter Antenna Gain	+6.0	0	+6.0	0
4.	Transmitter Antenna Pointing Loss	0	3.0	0	3.0
5.	Space Loss, 2297 MHz, 95 × 10^6km	-259.2	0	-259.2	0
6.	Atmospheric Losses	0	1.0	-1.0	2.0
7.	Polarization Loss	0	0.5	0	0.5
8.	Receiver Antenna Gain, 210-ft Dish	+61.4	0.3	+61.4	0.3
9.	Receiver Pointing Loss	0	0	0	0
10.	Receiver Circuit Loss	-0.1	0	-0.1	0
11.	Net Circuit Loss	-192.3	5.0	-193.3	6.0
12.	Total Received Power	-150.5 dbm	5.4	-151.5 dbm	6.4
13.	Received Noise Spectral Density, 35°K	-183.1 dbm	0.6	-183.1 dbm	0.6
Carrier Performance, Data Demodulation					
14.	Carrier Power to Total Power	-5.0	0.3	-3.0	0.2
15.	Received Carrier Power	-155.5 dbm	5.7	-154.5 dbm	6.8
16.	Carrier Threshold Bandwidth, 12 Hz	+10.3	0.5	+10.3	0.5
17.	Threshold, S/N in 2 B_{LO}	+9.0	0	+9.0	0
18.	Threshold Carrier Power	-163.8 dbm	1.1	-163.8 dbm	1.1
19.	Margin, Carrier	+8.3	6.8	+9.3	7.9
Data Channel Performance					
20.	Receiver Loss	-1.5	0.2	-1.5	0.2
21.	Data Channel Power/Total	-1.7	0.2	-3.0	0.2
22.	Total Data Power	-153.5 dbm	5.8	-156.0 dbm	6.8
23.	Data Threshold E/NO	+2.5	0	+2.5	0
24.	Data Rate	+18.5	0	+18.5	0
25.	Data Channel Threshold	-162.1 dbm	0.6	-165.1 dbm	0.6
26.	Data Channel Margin	+8.6	6.4	+9.1	7.4

Diagrams, Measurement Lists, and Formats - The measurement list for the small probes is shown in Table III-24. The sampling intervals and resulting bit rates for the various instruments including engineering, frame count, format identification and frame sync are also shown. The system block diagram and data formats are given in Fig. III-34 and III-35.

The stored entry data (accelerometer and events) are accumulated at the same rate as for the large probe (240 bps) for a period of approximately 32 sec for entry resulting in an accumulation of 7680 bits, which suggests a memory capacity of 8 kbits.

Stored entry data readout occurs at 4 bps above 49.5 bars atmosphere and 2 bps below 49.5 bars. The period available for readout at 4 bps varies with entry conditions (targeting) and atmosphere model and is different for each of the two small probes as shown in Table III-25. At the rates shown at least two readouts of the memory will occur for both probes for either atmosphere before the data transmission rate is reduced by 1/2 at 49.5 bars.

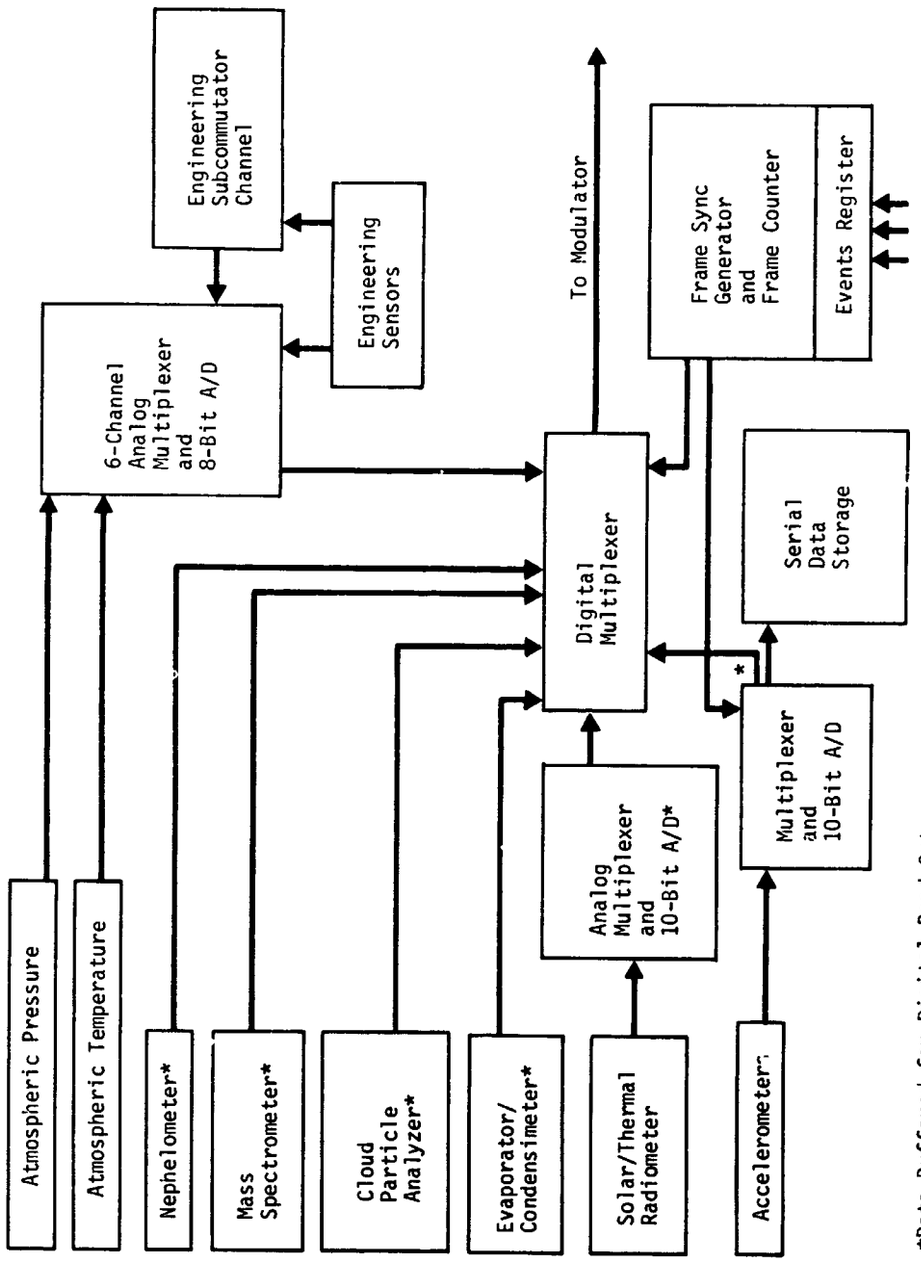
Buffering of data for the nephelometer, accelerometers, radiometers, mass spectrometer, and evaporimeter/condensimeter are required for the small probe system for reasons similar to those detailed for the large probe. Table III-26 gives the buffering requirements for a typical approach.

At an altitude of approximately 300 m the impact detector will sense the surface and will cause all event registers to go "0" state and, further, will substitute all "ones" for the γ accelerometer output.

Table III-24 Telemetry Measurement List, Small Probes (Baseline)

Parameter	Bits per Sample	Bits per 10 sec Frame (bits)	Sample Interval (sec)	Bit Rate (bps)
Accelerometers (3)*	30	300	1	30.0
Mass Spectrometer	600	100	60	10.0
Stored Memory Readout	40	40	--	4.0
Accelerometers (4)	40	--	0.18	--
Events	8	--	2	--
Frame Count	11	--	2	--
Frame Sync	21	--	2	--
Radiometer	480	80	60	8.0
Nephelometer	16	16	10	1.6
Evaporimeter/Condensimeter	480	80	60	8.0
Static Phase Error (SPE)	8	8	10	0.8
Atmospheric Temperature	8	8	10	0.8
Atmospheric Pressure	8	8	10	0.8
Subcommutated Channel	8	8	10	0.8
Probe Internal Temperature	8	--	60	--
Probe Internal Pressure	8	--	60	--
Battery Temperature	8	--	60	--
Battery Current	8	--	60	--
Battery Voltage	8	--	60	--
Transmitter Power Out	8	--	60	--
Subframe Count	3	3	10	0.3
Frame Count	11	11	10	1.1
Events*	13	13	10	1.3
Format Identification	4	4	10	0.4
Frame Sync Code	21	21	10	2.1
Total		700		70.0

*At approximately 300 m altitude the impactometer will sense the surface. At that time all event registers will "zero" and all "ones" will be substituted for accelerometer on the X axis.



*Data Buffered for Digital Read Out

Fig. III-34 Telemetry Data Handling, Small Probes (Baseline)

Real Time Main Telemetry Format (Notes 1 & 4)

Sync	ID	Events	Frame Count	Sub-frame Count	Subcomm Channel	ATM Press	ATM Temp	Static Phase Error	Evap/ Cond	NEPH	Accelerometers 1, 2, 3 5 Samples (Buffered)
21	4	13	11	3	8	8	8	8	80	16	150
									Note 2		

cont →

cont →

Radiometer	Memory Read	Mass Spec	Accelerometer 1, 2, 3 5 Samples Each
80	40	100	150
Note 2		Note 2	

Note:
1. Main frame length, 700 bits; main frame period, 10 sec.
2. Six frames to complete.
3. Stored at 240 bps (0.1 g to aeroshell staging).
4. Data transmission rate of 70 bps reduced to 35 bps at 49.5 bars atmospheric pressure.

Subcommutated Channel Format (Note 2)

→

Probe Interval Temp	Probe Interval Pressure	Batt Temp	Batt Current	Batt Volts	Xmit Power
8	8	8	8	8	8

Stored Data Format (Note 3)

→

Sync	Frame Count	Events	Accelerometers 1, 2, 3, 4	Accelerometers 1, 2, 3, 4 10 Samples Each
21	11	8	40	400

Fig. III-35 Telemetry Data Format, Small Probes (Baseline)

Table III-25 Entry Data Store and Read Times for Small Probes

Targeting Area	South Pole		Antisolar	
	V5M	MMC Lower	V5M	MMC Lower
Time 0.1 g to Aeroshell Staging (sec)	32	31	27	26
Time Aeroshell Staging to Pressure of 49.5 bars (sec)	4,400	4,530	4,320	4,460
Time 49.5 bars to Impact (sec)	1,833	945	1,843	946
Bits Stored 0.1 g to Aeroshell Staging @ 240 bps (bits)	7,680	7,440	6,480	6,240
Bits Transmitted from Storage @ 4 bps (bits)	17,600	18,120	17,280	17,840
Bits Transmitted from Storage @ 2 bps (bits)	3,666	1,890	3,686	1,892
Total Bits Transmitted from Storage (bits) (Aeroshell Staging to Impact)	21,266	20,010	10,966	19,732

Note: Telemetry data rate changes from 120 bps to 60 bps at an atmospheric pressure of 49.5 bars. This results in a reduction of entry storage data read rate from 4 bps average to 2 bps at that time.

Table III-26 Buffering Requirements for Small Probe Data System

Instrument	Number and Capacity of Buffers			
	Part of Instrument		External to Instrument	
	No. of Buffers	No. of Bits Each	No. of Buffers	No. of Bits Each
Accelerometers (3), Postdeploy			2	150
Mass Spectrometer	2	600		
Radiometer			2	120
Nephelometer	1	16		
Evaporimeter/ Condensimeter	2	480		
Accelerometers (4) Stored, Predeploy			1	8000

Note: All external buffers are solid state flip flop (MOS) except main memory which is core.

5. Power System - Small Ballistic Probe

The discussion in Section B on the large probe power system and weight estimates applies generally to the small probe also. Battery weight is computed to be 10.6 lb. This is unaffected by the spacecraft option (impacting or flyby). An unsterilizable battery is assumed. The power system weight and power is summarized in Table III-27.

6. Sequencer for Small Probes (Baseline)

The sequencer for both small probes for the baseline system are identical in design to those for the large probe except for the difference in g and pressure references for decelerator and parachute release. The small probe impactometer is powered at the time of switching the bit rate to 1/2 value.

Table III-27 Weight and Power Summary, Small Ballistic Probe

Item	Weight (lb)	Descent Power for 1.7 hr (W)	Cruise Power for 264 hr (W)
Antenna	0.8		
Diplexer	1.4		
Transponder			
Receiver	2.0	0.5	
RF Exciter	0.9	1.5	
Modulator	0.9	0.5	
Transmitter (15 W)	4.0	54.6	
Sequencer	4.0	3.0	0.1 + 1.75 W-hr
Data Handling	6.0	3.0	
Memory	2.2	0.2	
Inverter	3.0	4.6	
Cabling	4.1		
Battery	10.6		
Subtotal	39.9	67.9	
Instrumentation		30.8	
Instrument Heat	0.2	2.0	
Total	40.1	100.7	

Note: 1. Average battery power dissipation during descent is 23 W.

2. Total power dissipation during descent is 108.7 W.

3. Total energy converted to heat during descent is 184.8 W-hr.

D. BASELINE MISSION - HIGH-CLOUD PROBE

The high-cloud probe has been designed to provide the upper cloud data at as high an altitude as can be reasonably achieved. For this reason, the probe carries only those instruments used for high-cloud measurements. A low ballistic coefficient is provided to allow decelerator deployment at a high altitude. A large parachute combined with minimum system weight produces the descent velocity required for sample acquisition and processing. The instrument canister is not protected against the thermal and pressure environment encountered below 6100 km radius. This is to minimize system weight.

1. High-Cloud Probe Science Capabilities

The high-cloud probe system was defined specifically to investigate the cloud composition and structure and the winds in the regions from above the cloud tops down through the tropopause. This is the region to which most earth-based measurements refer. The large and small probes are deployed above the nominal cloud tops, but below their upper uncertainty limit and the region of the UV scattering haze. The high-cloud probe parachute is deployed by 6127.5 km (11.5 mb). Terminal velocity at this point is 22.4 m/sec. The instrument complement is given in Table III-28 and the number of measurements and altitude resolution for each of the instruments are shown in Fig. III-36 and III-37. The high-cloud probe will survive to at least 1.35 bars (6100 km, 350°K).

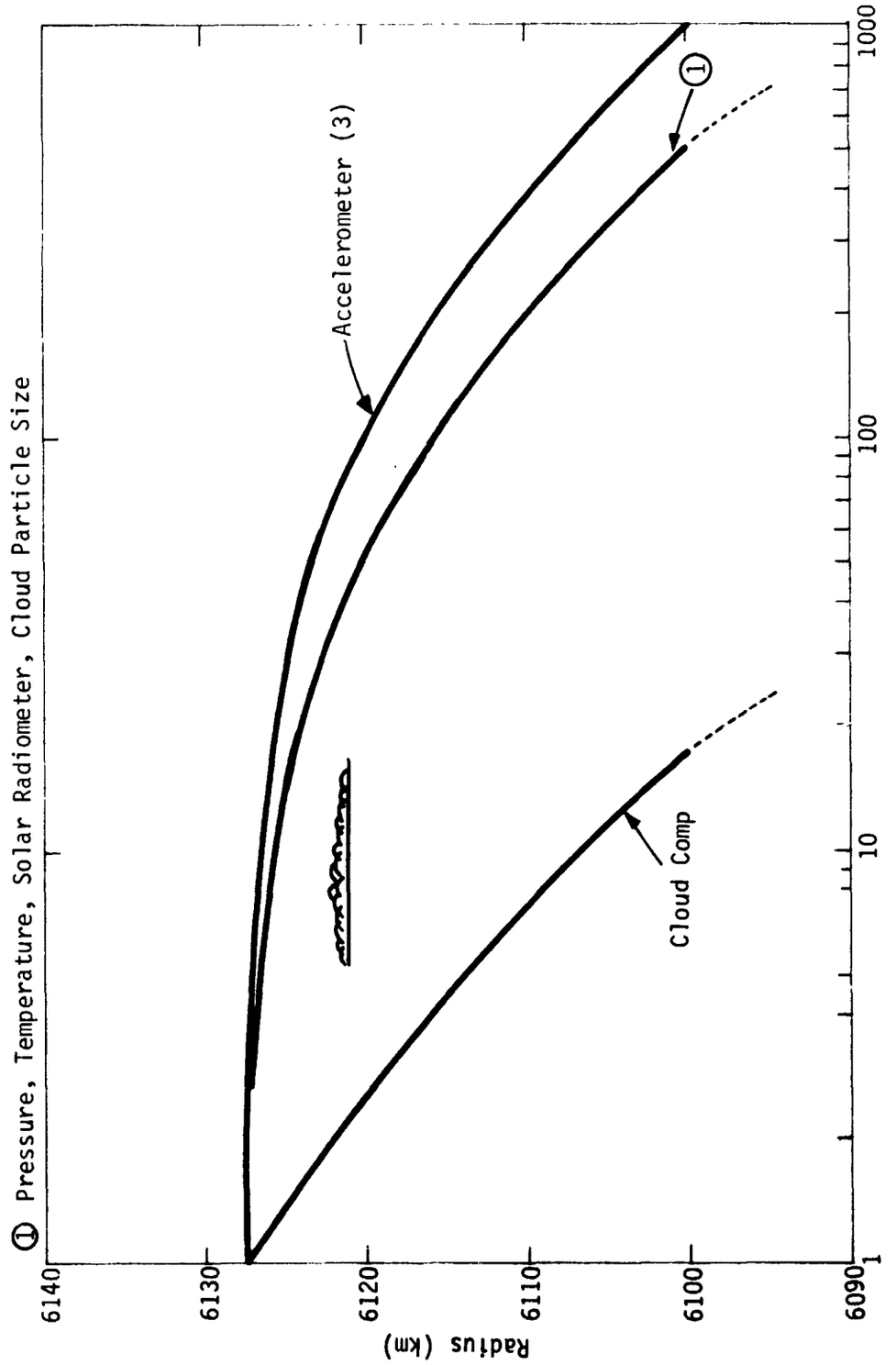


Fig. III-36 Number of Measurements vs Altitude, High-Cloud Probe

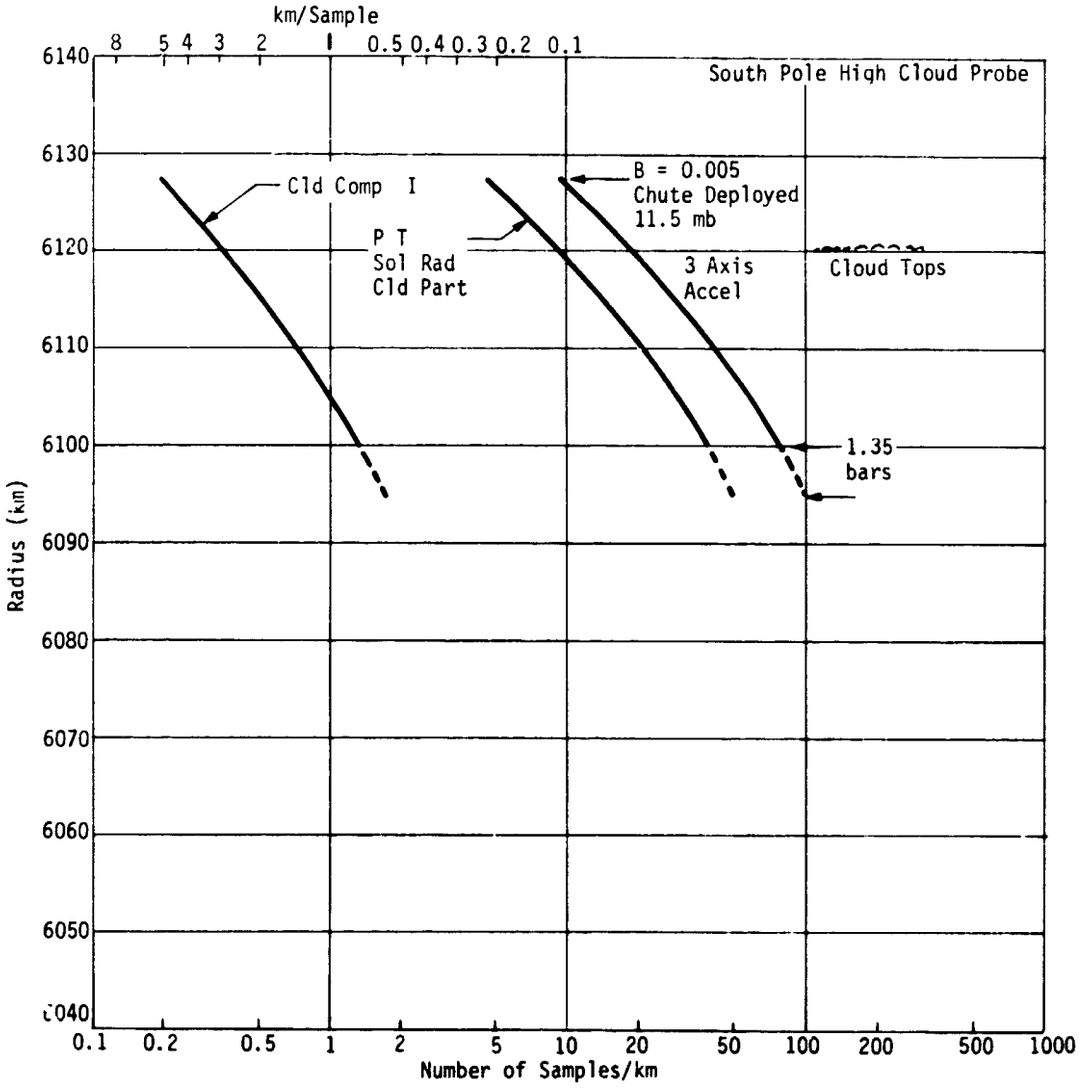


Fig. III-37 Number of Samples vs Altitude, High-Cloud Probe

Table III-28 Baseline High-Cloud Probe Instrument Complement

Instrument	Bits Per Sample	Sample Time Interval (sec)	Altitude Sample Interval at 6120 km (m)	Total Number of Measurements
Pressure	8	10	110	483
Temperature	8	10	110	483
Solar Radiometer	200	10	110	483
Cloud Particle Size and Number	80	10	110	483
Cloud Composition	1800	300	2920	16
Accelerometers (3)	3 × 10	5	55	3 × 966
Transponder	--	Continuous	--	--

2. Engineering Mechanics - High-Cloud Probe

a. Requirements - The general requirements concerning the deflection and entry phases are the same for the high-cloud probe as for the other probe types, however no requirement exists for survival to the surface. Also, no inherent stability is required of the instrument capsule because it remains suspended from a parachute throughout its operating life. Because this probe does not require a sealed capsule for survival, the quarantine requirements dictate that the capsule interior and equipment be sterilized.

The specific requirements for the high-cloud probe are the following:

Science instrument weight, 39.5 lb;

Communications system weight, 30.5 lb;

Power dissipated by science instruments and communications equipment, 123 W;

Radius at deployment of science instruments, 6127.5 km;

Ballistic coefficient required for descent rate control at instrument deployment altitude, 0.005 slugs/ft^2.

The ambient temperature history resulting from the above conditions is shown in Fig. III-38 based on the V5M atmosphere. Deployment altitude and deceleration design is based on the lower density atmosphere.

b. Configuration Definition - The inboard profile of the high-cloud probe configuration is shown in Fig. III-39. The internal arrangement of the instrumentation canister is shown in Fig. III-40. A weight summary is presented in Table III-29.

Functional Description - The high-cloud probe system includes the instrumentation canister, its deployment and decelerator system, the velocity deflection propulsion, the spin-up/despin system, the Entry Vehicle, and the biocanister/adapter structural and mechanical system. The inboard profile drawing, Fig. III-39, shows the systems and their interfaces and separations.

The Entry Vehicle system is similar to that described for the large probe in Section B of this chapter.

The instrumentation canister is supported within the aeroshell by cylindrical stiffened shell beam to transmit the loads uniformly to the aeroshell at their juncture where the beam ties in through a continuous integral flange.

The instrumentation canister is supported by the ring beam and attaches by means of a continuous V-ring band and clamp arrangement. A pyrotechnic nut in the band provides the disconnect at canister separation and deployment.

The main shute compartment skirt mates with the top of the instrumentation canister. It is attached to the base cover to separate with it. Four shear/alignment pins locate the skirt on the canister. A nometallic (RF transparent) shell attached to the canister top ring lines the chute skirt to contain the chute after base cover separation before the chute is deployed.

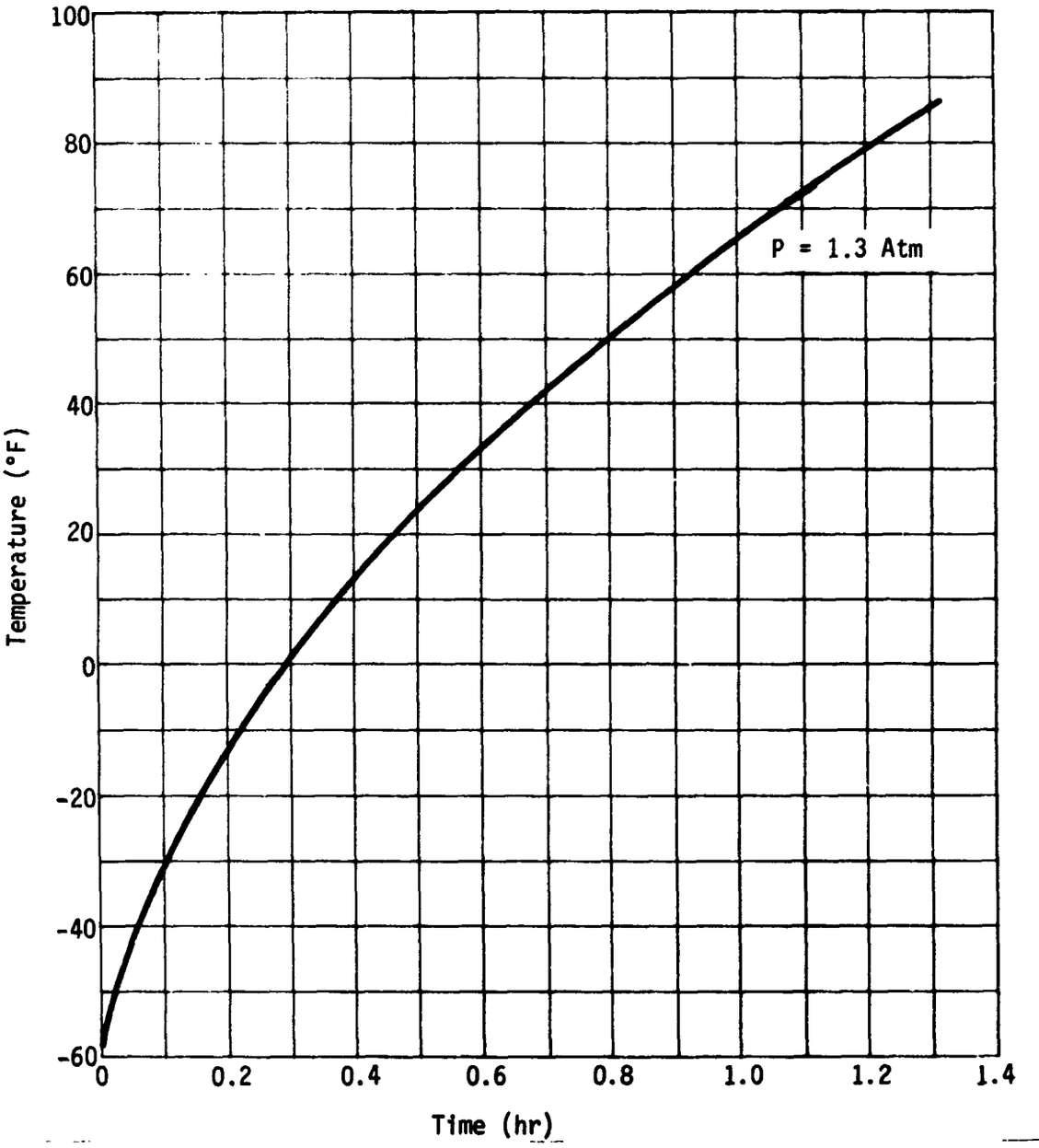
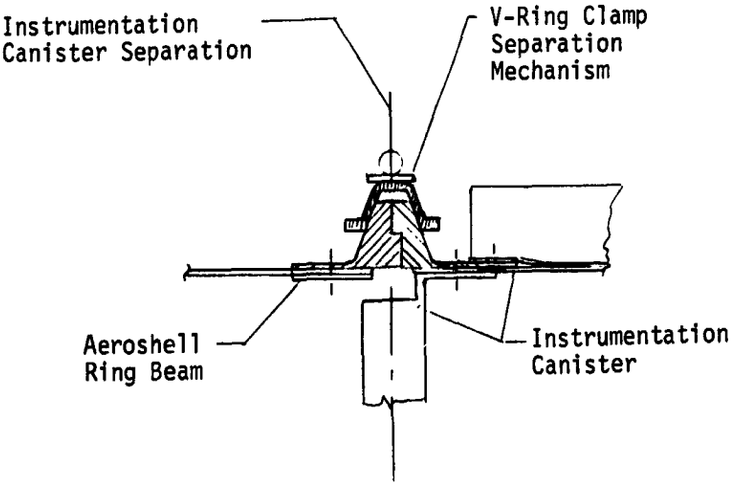


Fig. III-38 Ambient Temperature History, High-Cloud Probe

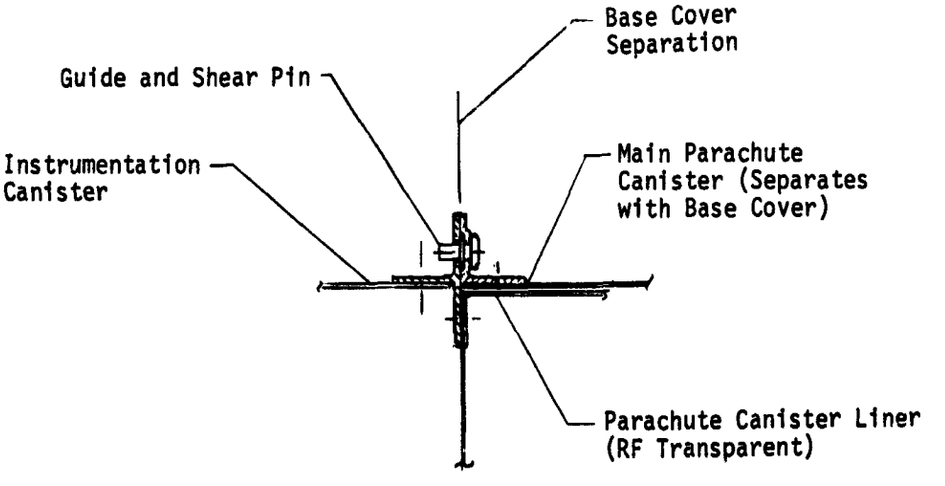
Table III-29 High-Cloud Probe Weight Summary
(Impacting Spacecraft Case)

Item	Weight (lb)	
Instrumentation Canister		(85.0)
Science	39.5*	
Electronics	30.5	
Structure and Mechanics	15.0	
Decelerator System		(51.0)
Main Chute	44.0	
Drogue and Canister	7.0	
Aeroshell		(113.0)
Aeroshell Structure Weight	68.0	
Heatshield		
Forward Cone	30.0	
Base	15.0	
Separation Hardware		(2.0)
Spin-Up/Despin (Fixed)		(4.0)
Entry Weight		255.0
Spin/Despin/Separation (Spent)		6.0
ΔV Propulsion		9.0†
Biocanister/Adapter		46.0
Total System		316.0

*Including transponder.
†16 lb for flyby spacecraft case.

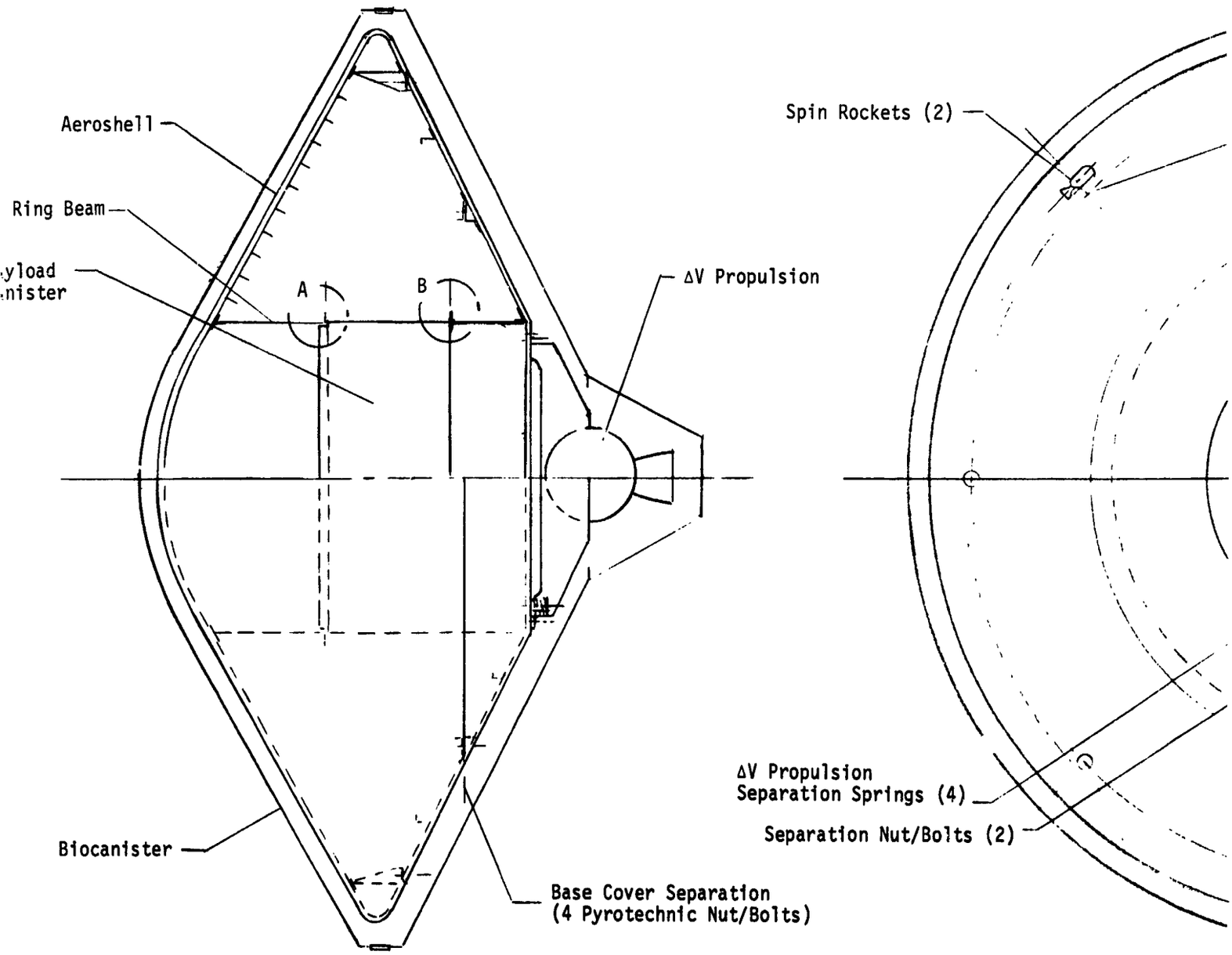


Detail A



Detail B

FOLDOUT FRAME



Canister/Adapter
Cover Removed for
Vehicle Definiti

FOLDOUT FRAME 2

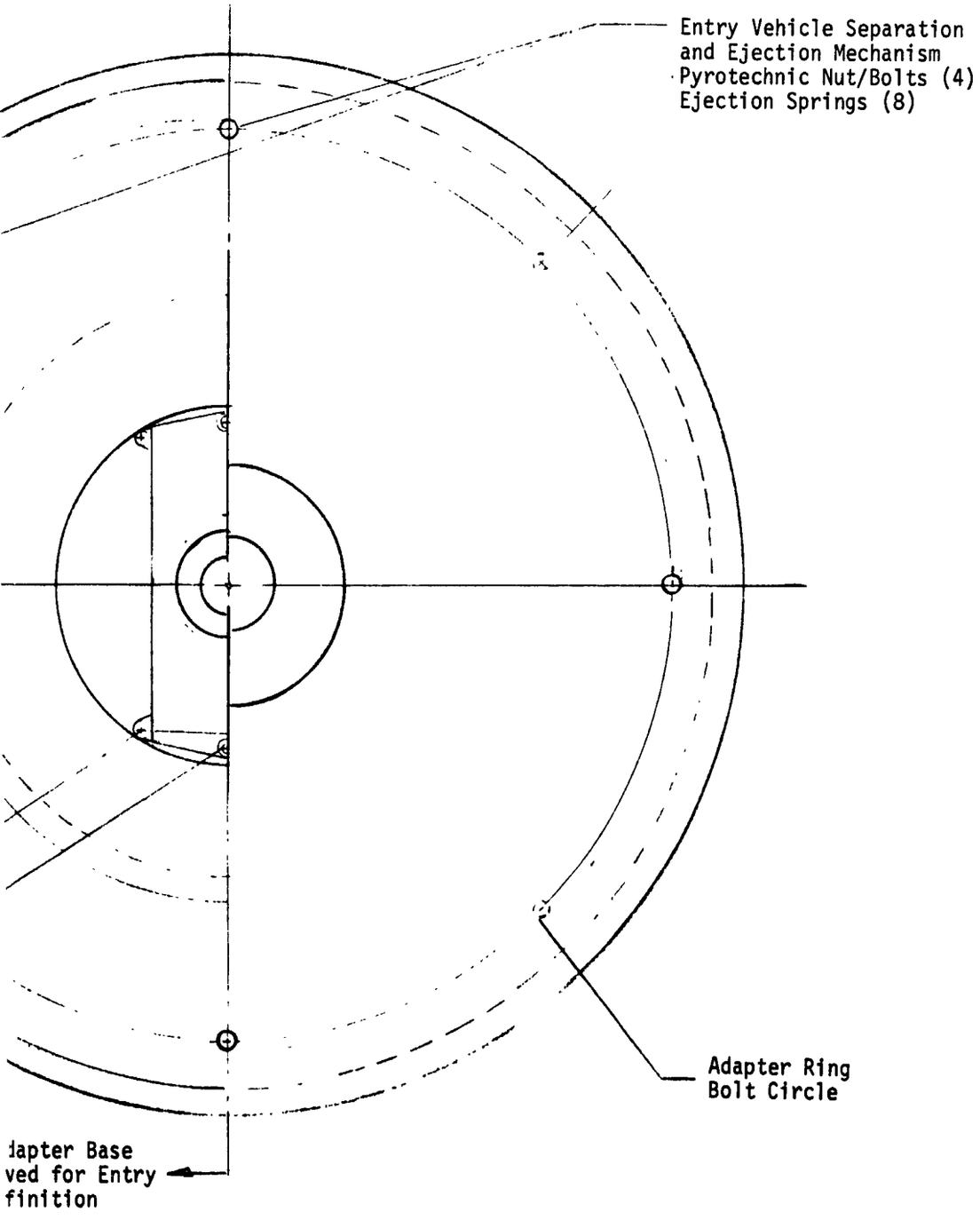
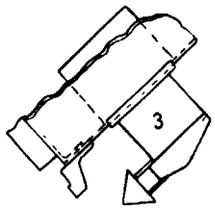


Fig. III-39 Inboard Profile.High-Cloud Probe

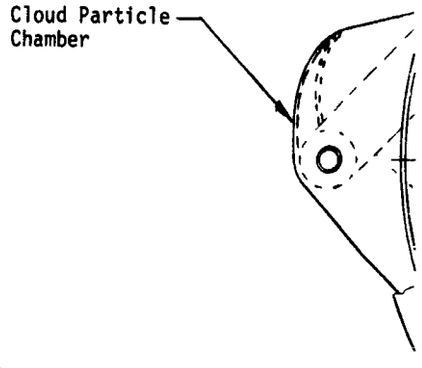
FOLDOUT FRAME 2

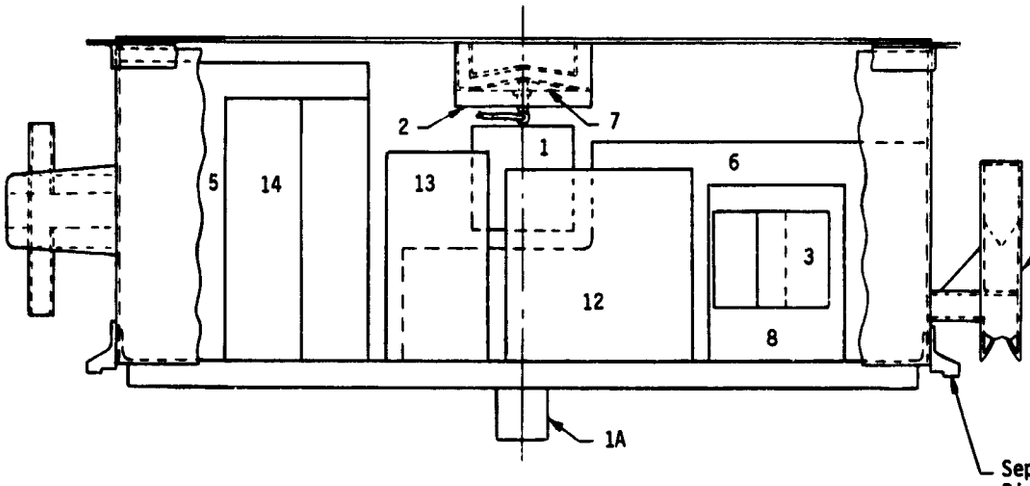
Parachute Attach Poin
(4 Places)



Alignment & Shear Pin —
Receptacle (4 Equally
Spaced)

B - B





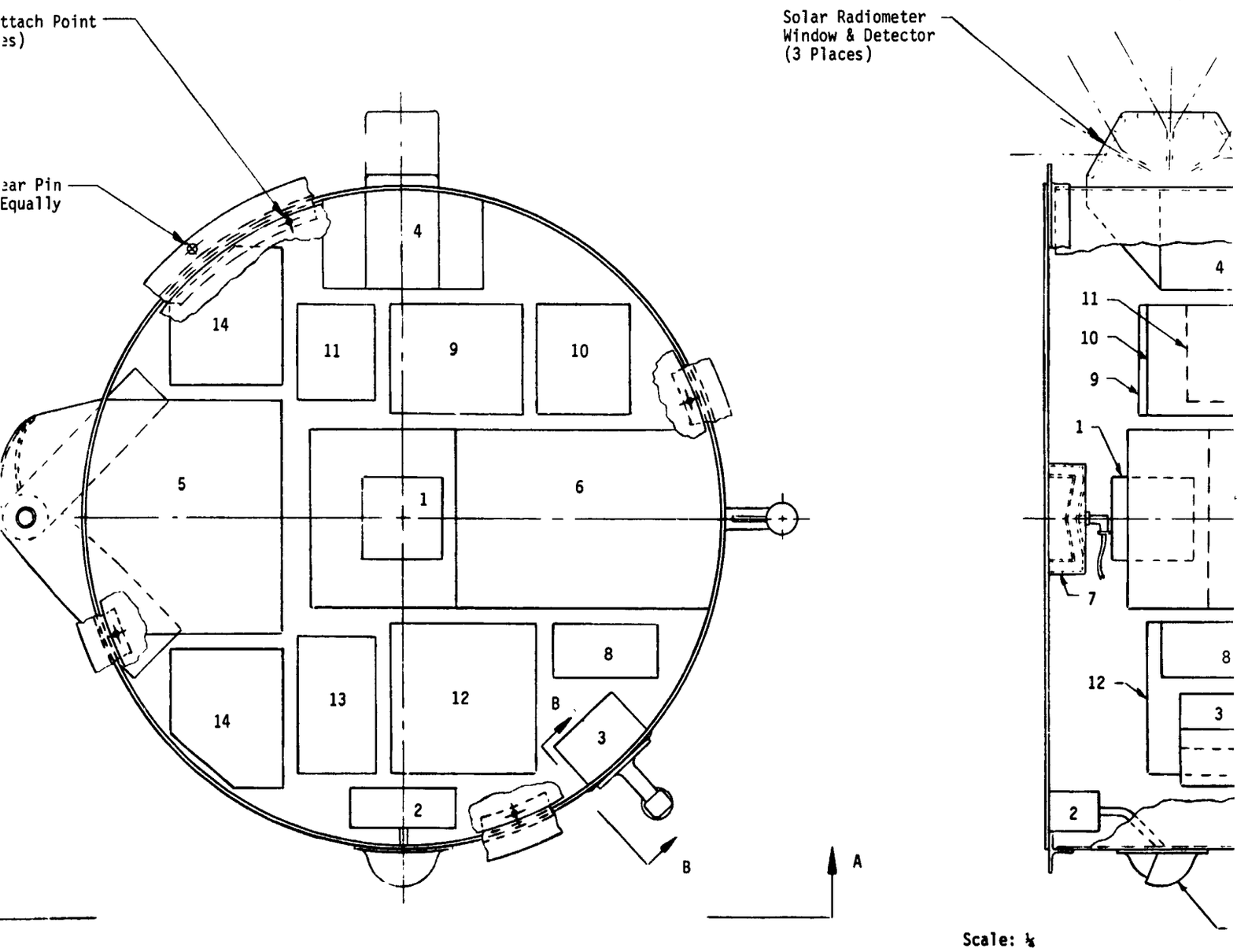
Cloud Analyzer
Sample Collector

A

Separation
Ring

A-A

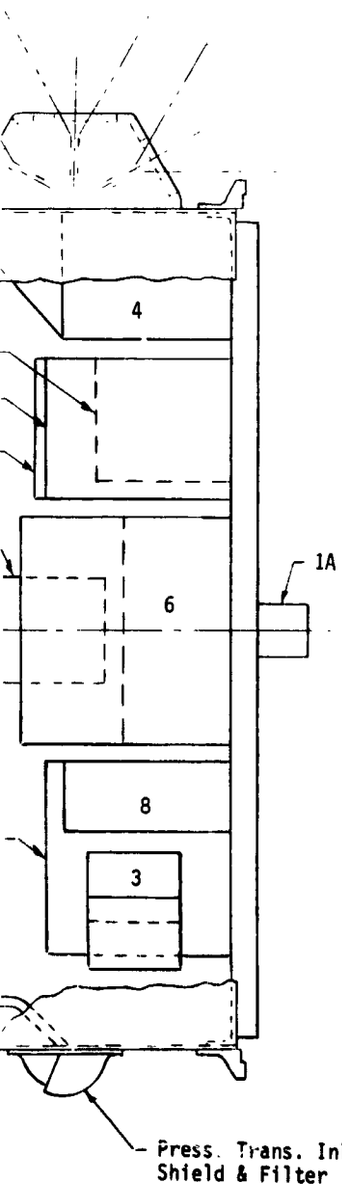
FOLDOUT FRAME



Scale: ½

Fig. III-4

FOLDOUT FRAME 2



Legend:

1	Accelerometer (Triad)
1A	Accelerometer (Single)
2	Pressure Transducer
3	Temperature Sensor
4	Solar Radiometer
5	Cloud Particle Number Density & Size
6	Cloud Composition Analyzer
7	S-Band Annular Slot Antenna
8	Diplexer
9	Transponder (Receiver, RF Exciter, Modulator)
10	Transmitter
11	Sequencer
12	Data Handling
13	Inverter
14	Battery

Note: For Science Instrument Definition see Fig. III-12

Fig. III-40 Internal Arrangement, High-Cloud Probe Instrumentation Canister

FOLDOUT FRAME

The instrument and electronic canister is a stiffened cylindrical aluminum shell. The equipment mounting platform is an aluminum sandwich to provide the strength at a minimum weight for the high entry g loads.

The top closure is a thin metal cover that mounts the cavity helix-annular slot antenna. The internal arrangement of instrumentation and electronic equipment and the science mechanization is shown in Fig. III-40.

c. Descent Capsule Design - In this case, the descent capsule only descends to an altitude where the ambient pressure is 1 atmosphere and the temperature 70°F. Thus capsule configuration and thermal/structural design problems are avoided. The resulting payload temperature history is shown in Chapter VIII. No insulation or phase change material is required. The analysis is described in Chapter VIII.

d. Entry Vehicle Design - The Entry Vehicle design is dominated by the requirement to deploy instruments at 6127.5 km radius. From Fig. III-41 it is seen that even at the low entry angle of the polar target a very low ballistic coefficient, 0.2 slugs/ft^2, is needed to achieve subsonic velocities at this deployment altitude. Because of the large size (45 ft diameter) of the parachute required to meet the 0.005 slugs/ft^2 ballistic coefficient after deployment, it is especially desirable to achieve subsonic velocities and low dynamic pressures before the parachute is deployed. It is possible to accomplish this with a supersonic ballute instead of going to the 0.2 slugs/ft^2 ballistic coefficient aeroshell. If the 0.4 slug/ft^2 aeroshell is used, the ballute would have to be deployed at Mach 4.0 and would weigh approximately 70 lb (see Chapter VIII). The entry weight for this approach would thus be comparable to the 0.2 slugs/ft^2 aeroshell approach.

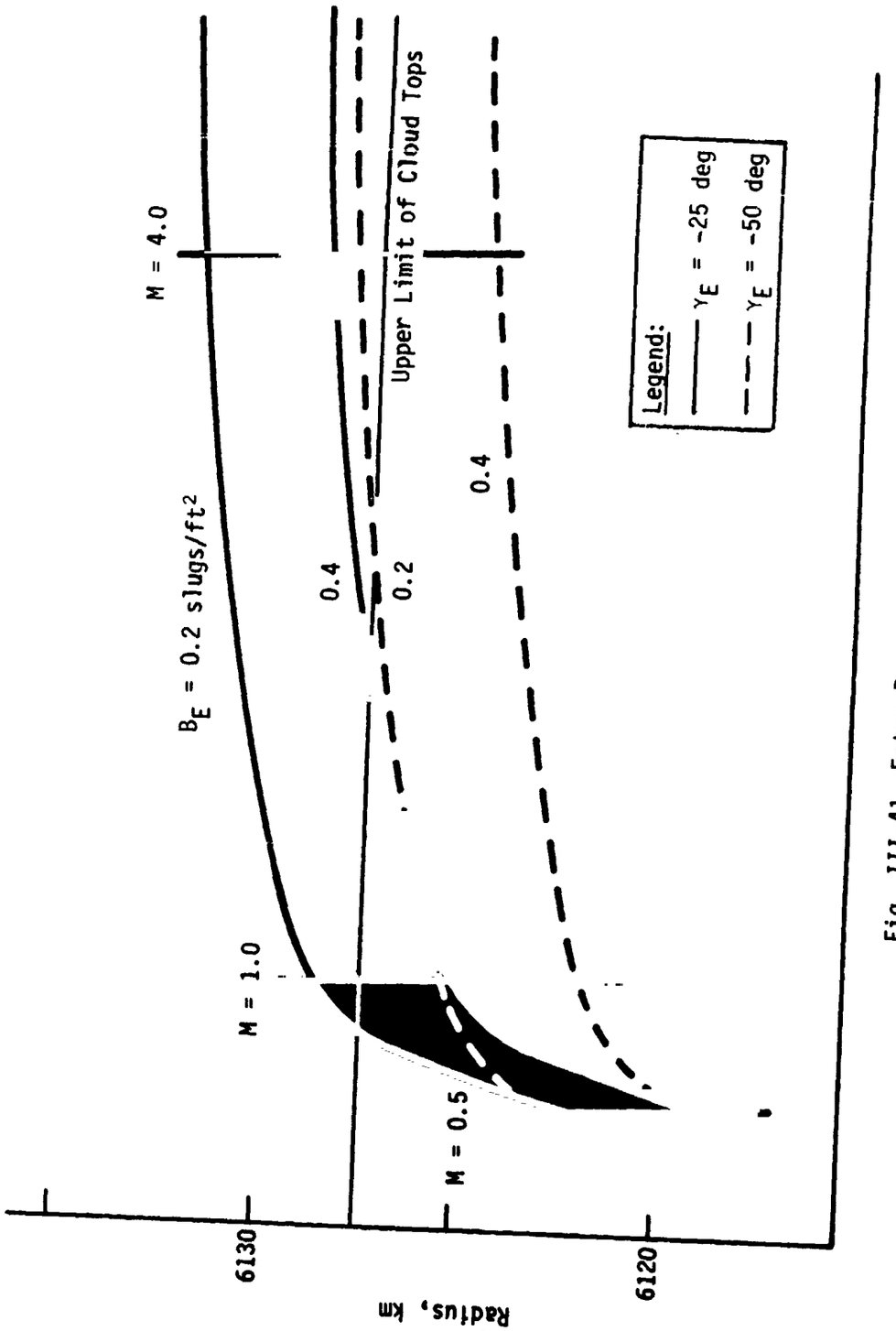


Fig. III-41 Entry Parameters Selection

The 0.2 slugs/ft^2 aeroshell design was selected to avoid the added complexity design risk and development costs associated with the ballute design. Aeroshell and heat shield weights are determined from the design curves described earlier (Fig. III-15 and III-17). A large nose radius, 2.0 ft, is possible due to the low $M/C_D A$ and the shallow shape of the descent capsule; therefore, the low density AVCOAT 5026 heat shield material was selected. Peak heating and pressure conditions for this probe are well within the test capability as depicted in Fig. III-18.

Thermal control, altitude control, and deflection propulsion are accomplished as discussed for the small descent probe, i.e., passive α/ε coatings, spin stabilization and solid rocket motor deflection. The deflection velocity and total impulse for the impacting and flyby spacecraft modes are respectively: 45 m/sec and 1150 lb-sec, and 70 m/sec and 1800 lb-sec.

Cloud Probe Tradeoffs - The effect of targeting the high-cloud probe to the steeper entry subsolar target instead of to the pole is shown in Fig. III-42. The -50°γ of the subsolar target dictates the use of a ballute even with a 0.2 slugs/ft^2 aeroshell, and therefore increases the entry weight from 255 to 380 lb and the aeroshell diameter from 5.75 ft to 7.0 ft. Also shown in the figure is the effect on entry weight of designing the probe to survive to the surface. This also increases the weight to about 380 lb. The cost of carrying a full complement of instruments, 73 lb, through the descent profile described for the cloud instruments is also depicted in Fig. III-42. The ~800 lb entry weight that results is accompanied by an unacceptably large 10.0-ft-diameter aeroshell design.

Target Influence

	B (slugs/ft^2)	Dia (ft)	Weight (lb)
Pole	0.2	5.75	250
Subsolar	0.2	7.0	380

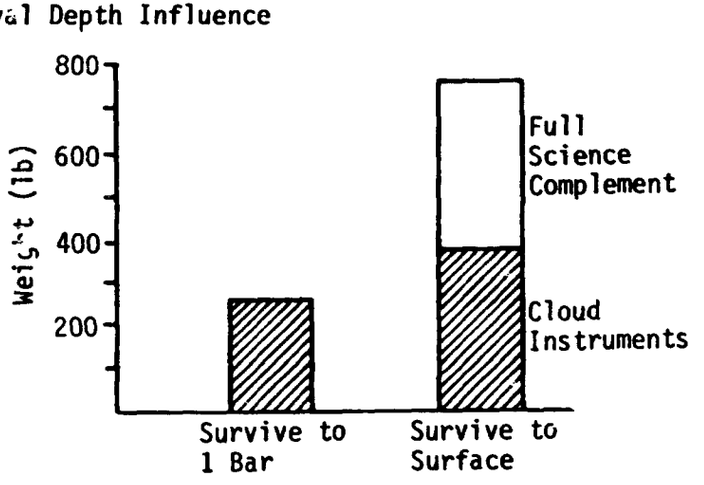


Fig. III-42 Influence of Targeting and Survival Depth on Cloud Probe Design

e. Decelerator Design - High-Cloud Probe - The decelerator design for the baseline high cloud probe is based on the requirement for a ballistic coefficient, M/C_DA of 0.005 slugs/ft^2. This requires a large, lightweight parachute design.

The mission constraints dictated the following deployment conditions:

Entry angle, γ_E, -25°;

Entry M/C_DA, 0.2 slugs/ft^2;

Deployment radius, 6127.5 km;

Deployment Mach number, 0.92;

Deployment dynamic pressure, 12 psf.

The very low dynamic pressure allows use of a disk-gap-band-type parachute with minimum gage material (1.3 oz/yd^2). The chute is deployed in the reefed condition using a pilot chute just before the above conditions occur.

A parachute was designed to the above criteria using the design data of Chapter VIII.C, and the resultant characteristics are as follows:

M/C_DA, 0.005 slugs/ft^2;

Drag coefficient, 0.53;

Parachute diameter, 45 ft;

Parachute weight, 44 lb.

For a possible targeting option, a ballute designed for Mach 4.0 deployment was required. Chapter VIII.C.2 describes some applicable test experience for similar ballutes and Chapter VIII. C.4 describes supersonic decelerator design as applied to this high cloud probe ballute.

The resultant ballute design was as follows:

Ballute plus aeroshell M/C_DA, 0.077 slugs/ft^2;

Average drag coefficient, 0.9;

Ballute diameter, 10 ft;

Ballute weight, 64 lb;

Deployment Mach number, 4.0;

Deployment dynamic pressure, 205 psf.

3. Mission Analysis

The targeting, deflection, and entry probe design data are presented in Table III-30 for the high-cloud probe at the South Pole. The descent profiles for the high-cloud probe are presented in Fig. III-43 and III-44. The entry dispersions for the high-cloud probe are essentially the same as those presented for the small probe targeted to the South Pole.

4. Telecommunications and Data System, High-Cloud Probe

a. Telecommunications System - The high-cloud probe does not pentrate deeply enough into the atmosphere to require any margin for atmospheric losses, and therefore it can retain its initial bit rate throughout its descent. Except for this, its telecommunications system is similar to that on the large ballistic probe. Its bit rate is sized by the science requirements at 50 bps. The link calculations, Table III-31, show that an 8 W transmitter is required.

The initial few seconds of data generated after parachute deployment and before transponder uplink lock-on are very important on this probe, so the discussion on how to handle these data given in Section B of this chapter for the large probe would also be applied to the high-cloud probe.

The probe is never released from its parachute, so the Doppler rate transient associated with this event does not occur.

b. Data System - The baseline high-cloud probe data system differs from the large and small probe systems in number of instruments, data rate, and storage requirements. This system contains

Table III-30

VENUS HIGH CLOUD PROBE (SOUTH POLE)
* * * ENTRY PROBE DESIGN DATA * * *

TARGET (NEAR SIDE ENTRY)		SOUTH POLE	
APPROACH TRAJECTORY TYPE		IMPACT	FLYBY
PERIAPSIS RADIUS OF BUS	KM	2800.	12600.
DEFLECTION RADIUS	KM	4.000.000	4.000.000.
DEFLECTION VELOCITY (DEL V)	METERS/SEC	45.	70.
DEFLECTION ANGLE	DEGREES	20.	20.
CAPSULE COAST TIME	HOURS	290.6	288.5
MAXIMUM ANGLE OF ATTACK	DEGREES	50.5	42.
ENTRY VELOCITY	FT/SEC	35367.	
ENTRY ANGLE	DEGREES	-25.	
ENTRY ALTITUDE	FEET	815000.	
ENTRY RADIUS	KM	6298.412	
ENTRY LATITUDE	DEG	-62.0176	
ENTRY LONGITUDE	DEG	83.1456	
EARTH ZENITH ANGLE (MASK)	DEG	65.9179	
SOLAR ZENITH ANGLE	DEG	86.7899	
AEROSHELL BALLISTIC COEF.	SLUGS/FT2	0.2	
TIME OF MACH 1 OCCURRENCE	SEC	56	
MAXIMUM DYNAMIC PRESSURE	LBS/FT2	1208 (VSM)	1202 (MMCL) AT 36 SEC
MAXIMUM DECELERATION	G	188 (VSM)	187 (MMCL) AT 36 SEC
TIME FROM ENTRY TO MAIN CHUTE DEPLOYMENT	SECONDS	58.6	
MAIN CHUTE BALLISTIC COEF.	SLUGS/FT2	.005	
MACH NUMBER AT MCD		.915	
DECELERATION AT MCD	G	1.5	
DYNAMIC PRESSURE AT MCD	LB/FT2	12.	
ALTITUDE MAIN CHUTE DEPLOY	FT	268074.4 (VSM)	D=-1.5 G
ALTITUDE MAIN CHUTE DEPLOY	FT	255745.3 (MMCL)	D=-1.5 G
RADIUS MAIN CHUTE DEPLOYED	KM	6131.7092	(VSM)
RADIUS MAIN CHUTE DEPLOYED	KM	6127.9513	(MMCL)
TIME FROM ENTRY TO MAIN CHUTE RELEASE	HOURS	1.33 (VSM)	1.352 (MMCL)
CHUTE RELEASE PRESSURE	BARS	1.35	
RADIUS MAIN CHUTE RELEASE	KM	6103.3655 (VSM)	6099.9914 (MMCL)
BIT RATE	BITS/SEC	50.	

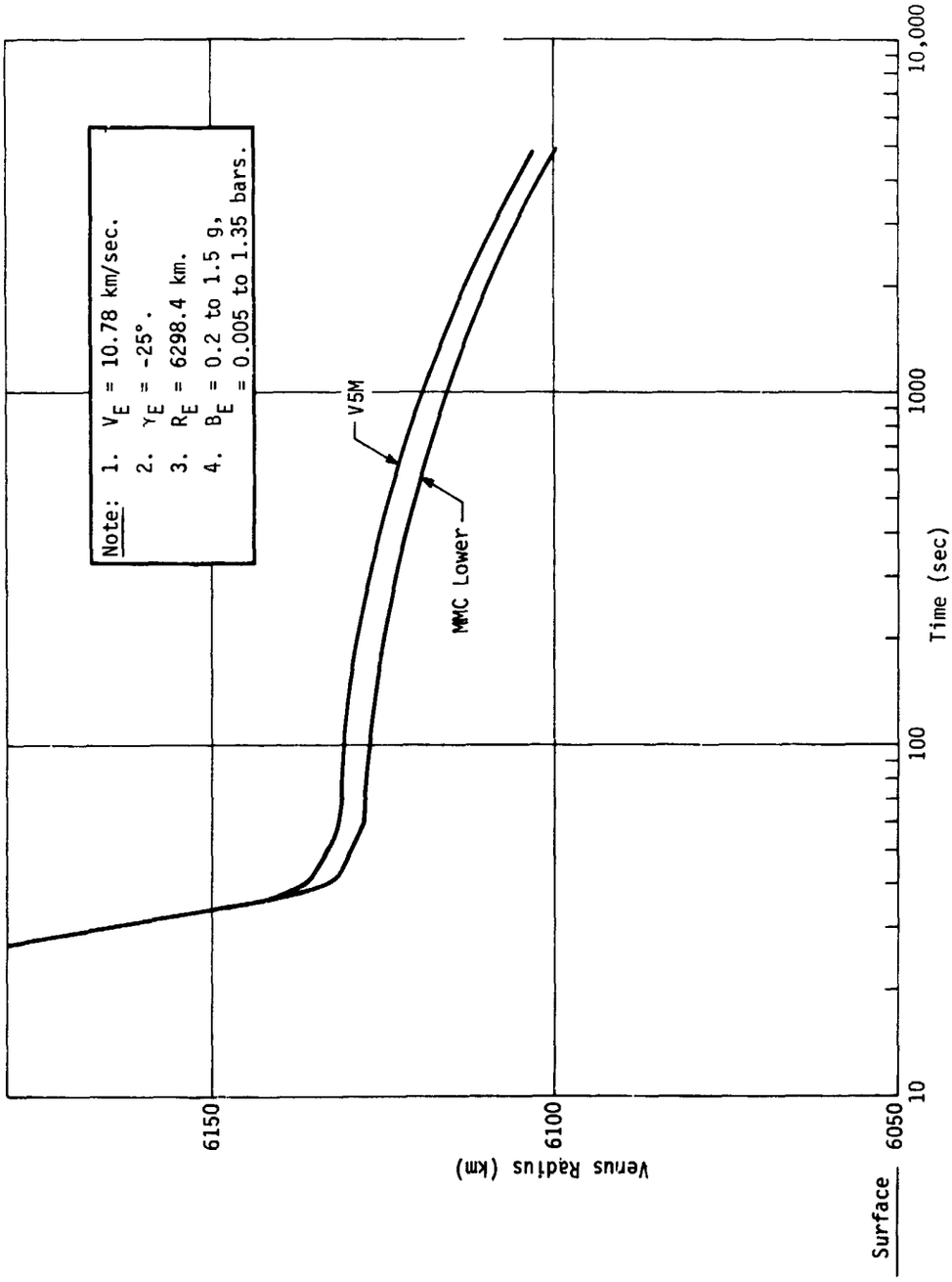


Fig. III-43 High-Cloud Probe Descent Profile, South Pole

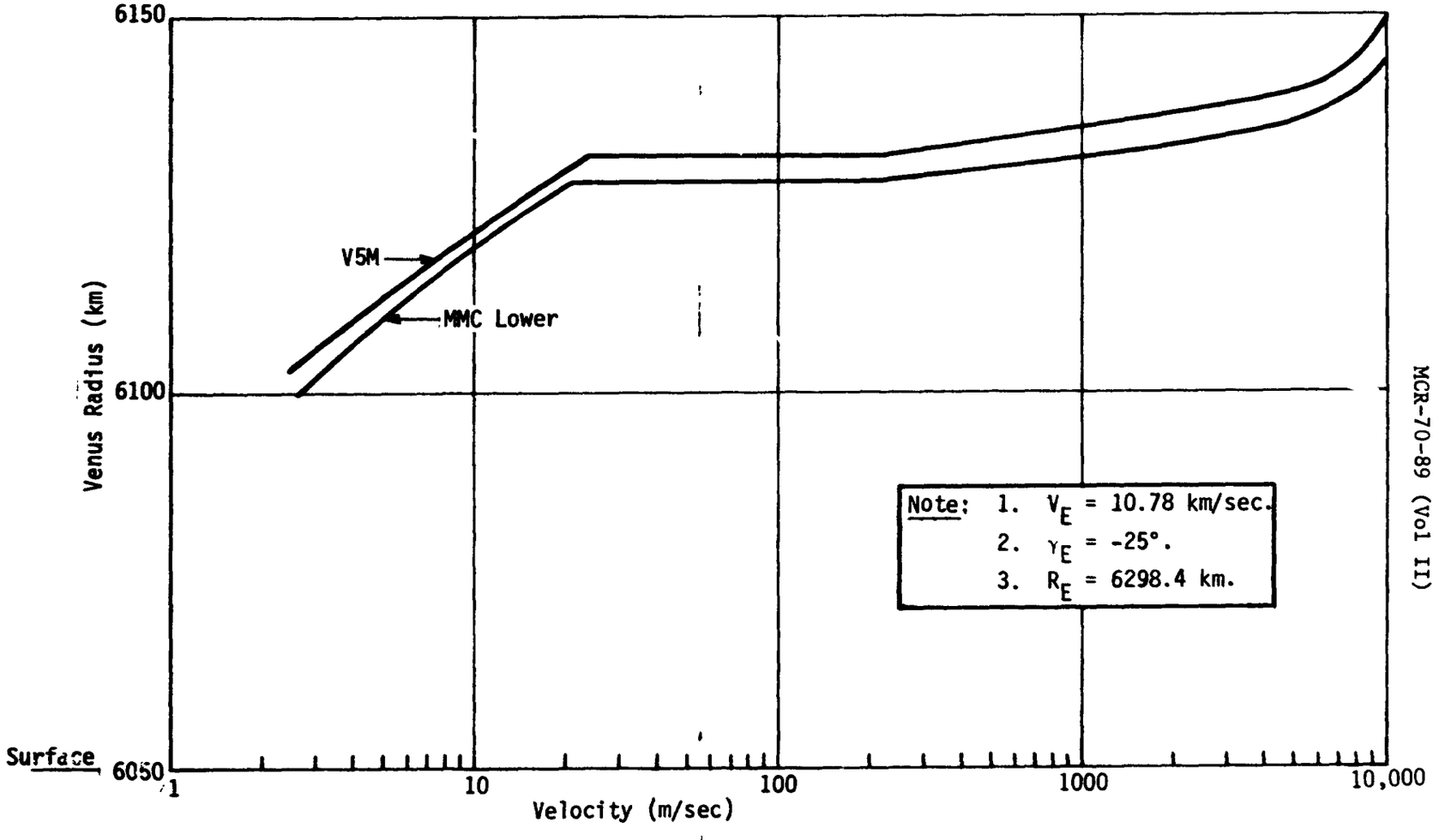


Fig. III-44 High-Cloud Probe Descent Profile, South Pole

Table III-31 Link Calculation, Downlink, High-Cloud Probes

Item	Parameter	Post Entry, 50 bps Comm Angle, 70°	
		Nominal (db)	Adverse Tolerance (db)
1.	Total Transmitter Power, 8 w	+39.0 dbm	0.4
2.	Transmitter Circuit Loss	-0.4	0.2
3.	Transmitter Antenna Gain	+6.0	0
4.	Transmitter Antenna Pointing Loss	0	3.0
5.	Space Loss, 2297 MHz, 95×10^6 km	-259.2	0
6.	Atmospheric Losses	0	0
7.	Polarization Loss	0	0.5
8.	Receiver Antenna Gain, 210-ft Dish	+61.4	0.3
9.	Receiver Pointing Loss	0	0
10.	Receiver Circuit Loss	-0.1	0
11.	Net Circuit Loss	-192.3	4.0
12.	Total Received Power	-153.3 dbm	4.4
13.	Received Noise Spectral Density, 35°K	-183.1 dbm	0.6
Carrier Performance, Data Demodulation			
14.	Carrier Power to Total Power	-4.2	0.3
15.	Received Carrier Power	-157.5 dbm	4.7
16.	Carrier Threshold Bandwidth, 12 Hz	+10.3	0.5
17.	Threshold S/N in 2 B_{LO}	+9.0	0
18.	Threshold Carrier Power	-163.8 dbm	1.1
19.	Margin, Carrier	+6.3	5.8
Data Channel Performance			
20.	Receiver Loss	-1.5	0.2
21.	Data Channel Power/Total	-2.1	0.2
22.	Total Data Power	-156.9 dbm	4.8
23.	Data Threshold E/NO	+2.5	0
24.	Data Rate	+17.0	0
25.	Data Channel Threshold	-163.6 dbm	0.6
26.	Data Channel Margin	+6.7	5.4

no entry data storage capability and the bit rate remains constant at 50 bsp from aeroshell staging until impact on the surface.

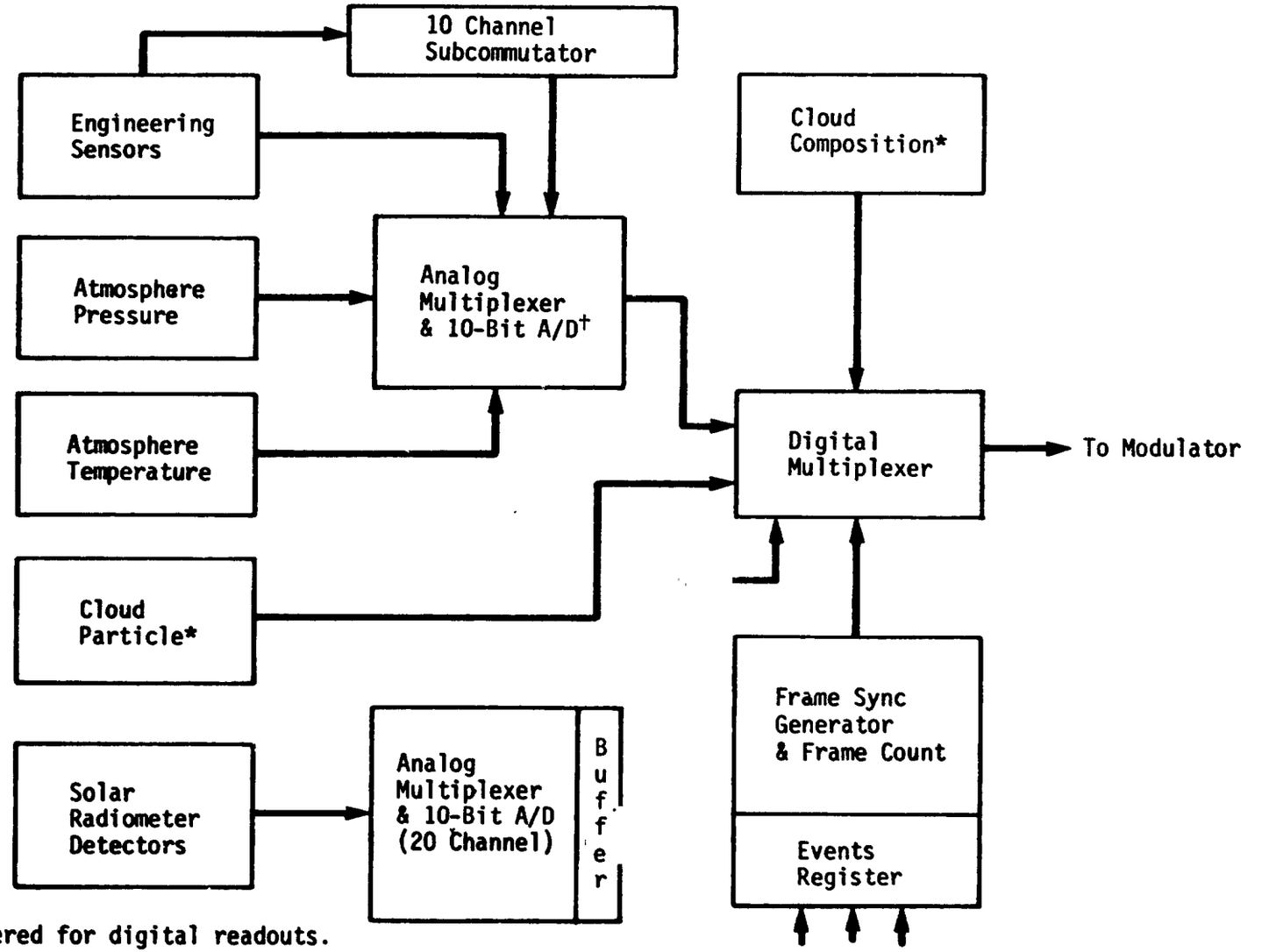
Both the baseline high-cloud probe and the option 2 high-cloud probe are identical in functional operation. For antisolar targeting the solar radiometer becomes a thermal radiometer with identical interface and format.

Diagrams, Measurement List, and Format - The data measurement list, block diagram, and data format are shown in Table III-32 and Fig. III-45 and III-46, respectively. Buffering for the cloud particle, cloud compositon, & solar radiometer are required as for the large and small probes. Table III-33 gives buffer requirements and characteristics.

The accelerometers in this case are sampled by the engineering analog multiplexer and analog-to-digital converter, which is a 10-bit converter; however, the two least significant bits are dropped on all measurements by acceleration. Buffering for the accelerometers is dispensed with in this case and accelerometers are sampled once each 5 sec by supercommutation. The interval over which the three are sampled is 60 bps divided by 30 bits or 1/2 sec as opposed to a few milliseconds (<5) for the large and small probes where buffering is used.

Table III-32 Measurement List, High-Cloud Probe (Baseline or Option 2)

Parameter	Bits per Sample	Bits per 10 sec Frame (bits)	Sample Interval (sec)	Bit Rate (bps)
Solar Radiometer	200	200	10	20.0
Cloud Composition	1800	60	300	6.0
Cloud Particle No.	80	80	10	8.0
Accelerometers (3)	30	60	5	6.0
Atmospheric Pressure	8	8	10	0.8
Atmospheric Temperature	8	8	10	0.8
Probe Temperature	8	8	10	0.8
Probe Pressure	8	8	10	0.8
Static Phase Error	8	8	10	0.8
Subcommutated Channel	8	8	10	0.8
Calibrate	8	--	80	--
RF Power Out	8	--	80	--
Transmit OSC Temperature	8	--	80	--
Battery Voltage	8	--	80	--
Battery Current	8	--	80	--
Battery Temperature	8	--	80	--
Clock Temperature	8	--	80	--
Science Instrument Temperature	8	--	80	--
Transmitter P.A. Temperature	8	--	80	--
Regulated Bus Voltage	8	--	80	--
Events	12	12	10	1.2
Subframe Count	5	5	10	0.5
Frame Count	10	10	10	1.0
Format Identification	4	4	10	0.4
Frame Sync Code	21	21	10	2.1
Total		500		50.0



*Data buffered for digital readouts.

†8 bits for all but accelerometers.

Fig. III-45 Telemetry Data Handling, High-Cloud Probe (Baseline and Option 2)

Main Telemetry Frame Format (Note 1)

Sync	ID	Frame Count	Subframe Count	Events	Subcomm Channel	Atm Temp	Atm Press.	Accel 1, 2, 3	Solar Rad	Probe Temp	Probe Press.
21	4	10	5	12	8	8	8	30	200	8	8
					(Note 3)				(Note 2)		

Cont →

cont →

Accel 1, 2, 3	Static Phase Error	Cloud Part No.	Cloud Composition
30	10	80	60

Note:
1. Frame length 500 bits; frame period 10 sec; bit rate 50 bits/sec.
2. Six frames required to complete.
3. Ten frames to complete.
4. Thirty frames to complete.

Subcommutated Channel Format (Note 3)

Calibrate	RF Pwr Out	Xmit OSC Temp	Batt Volt	Battery Current	Battery Temp	Clock Temp	Sicence Inst Temp	Xmtr Pwr Amp Temp	Regulated Bus Volt
8	8	8	8	8	8	8	8	8	8

Fig. III-46 Telemetry Data Formats, High-Cloud Probe (Baseline and Option)

Table III-33 Buffering Requirements for Cloud Probe Data System

Instrument	Number & Capacity of Buffers			
	Part of Instrument		External to Instrument	
	No. of Buffers	No. of Bits Each	No. of Buffers	No. of Bits Each
Solar Radiometer			1	200
Cloud Composition	2	1800		
Cloud Particle No.	2	80		
Note: All external buffers are solid state flip flop.				

5. Power System, High-Cloud Probe

The discussion in Section B on the large probe power system and weight estimates also applies to the high-cloud probe, except that a sterilizable battery must be used on the high-cloud probe, while a nonsterilizable battery is used on the large and small probes. As discussed in Chapter VII, this increases the battery weight somewhat. This weight, calculated using the procedure described in Chapter VII, is 10.4 lb. The weight and power summary is tabulated in Table III-34.

6. Sequencer for Cloud Probe

The sequencer requirements for the cloud probe are essentially identical to those for the large and small probes. The differencs are in g and pressure level reference and lack of requirement to initiate store of entry and change of data rate; therefore, from a design standpoint, the sequencers are identical.

Table III-34 Weight and Power Summary, High-Cloud Probe

Item	Weight (lb)	Descent Power for 1.13 hr (W)	Cruise Power for 264 hr (W)
Antenna	0.8		
Diplexer	1.4		
Transponder			
Receiver	2.0	0.5	
RF Exciter	0.9	1.5	
Modulator	0.9	0.5	
Transmitter (8 W)	1.4	29.2	
Sequencer	4.0	3.0	0.1
Data Handling	5.0	3.0	
Inverter	3.0	9.2	
Cabling	4.4		
Battery	10.4		
Subtotal	34.2	46.9	
Instrumentation		61.3	
Instrument Heat	0.2	2.0	
Total	34.4	110.2	

Note: 1. Average power dissipation in the battery during descent is 25.0 W.

2. Total power dissipation during descent is 123.2 W.

3. Total energy converted to heat is 139.7 W-hr.

E. OPTIONAL MISSIONS PROBE CONFIGURATIONS

Two optional missions were studied in addition to the baseline mission. The first option required the addition of a new design specifically directed at obtaining science data on the wind circulation patterns of Venus. A balloon floating at an ambient pressure of 500 mb was defined to meet this requirement. The second option considered was an extension of the first and at the same time was directed toward obtaining more data from the high clouds. The total probe complement of Option 2 consists of the four probes of the baseline mission plus

1) The balloon at 500 mb of Option 1, plus
2) Another Balloon at 50 mb, plus
3) Another high-cloud probe directed at an antisolar target.

The system design philosophy for the optional missions was directed at establishing feasibility of the concepts and pursuing new designs to the extent required for assessment of impact and expected gains. Commonality of design was exercised where practicable. As might be expected, the 50 mb balloon required most of the special consideration and was responsible for the most significant increases in weight. The main data supplied by the balloons are their position as they drift with the winds. This is supplemented by temperature, pressure, and solar radiometer.

1. Optional Probes Science Capabilities

The baseline mission probes give profiles of localized wind conditions (transponder and accelerometers) at several points on the planet. However, the circulation patterns cannot be determined unambiguously from this information alone. Therefore, the first option on the baseline mission consists of adding a 500 mb balloon targeted to the lightside of the morning terminator. This target was selected because it gives the maximum time in view of Earth for any drift pattern. The instrument complement is listed in Table III-35.

The second option improves the determination of the circulation pattern by targeting two balloons (50 and 500 mb) to the lightside of the morning terminator and adds a high-cloud probe targeted to the antisolar region. The latter, in conjunction with the large probe near subsolar and the high-cloud probe near the pole, provides information on the cloud structure and composition at the three most different points on the planet. The instrument complements for the 50 mb balloon and the antisolar cloud probe are the same as those for their counterparts with the exception of the "solar" radiometer on the cloud probe. This instrument would have detectors sensitive to IR for the antisolar target, but the configuration would remain the same as for lightside targets.

Table III-35 Ballon Probes Instrument Complement

Instrument	Objectives
Pressure	Atmospheric conditions
Temperature	(Balloon floats at constant density level)
Solar radiometer	Cloud cover, solar flux.
Transponder	Circulation. Tracking by line of sight velocity and range.

2. Engineering Mechanics - Optional Balloon Probes

a. Requirements - The general requirements for the deflection and entry phases are the same for the balloon probe as for the descent probes. Since a sealed capsule is not required, because no survival to the surface is required, the interior and equipment of the capsule must be sterilized. Specific requirements for the 500 mb balloon are given:

Entry angle, -65°;
Science instrument weight, 10.9 lb;
Communications system weight, 31.0 lb;
Duty cycle, transmit 7 minutes every 8 hr;
Power dissipated during transmission, 2.8 W;
Lifetime independent of sun, 7 days;
Temperature at float altitude -
V5M Atm Model, 26°F;
Lower Atm Model 64°F.

b. Configuration Definition - The inboard profile of the balloon probe is shown in Fig. III-47 and the internal arrangement of the gondola is shown in Fig. III-48. A weight summary is tabulated in Table III-36.

Functional Description - The balloon probe system includes the Buoyant Station, its deployment and decelerator system, the balloon inflation system, the velocity deflection propulsion, the spin-up/despin system, the Entry Vehicle, and the biocanister/adapter structural and mechanical system. The inboard profile drawing, Fig. III-47, shows the systems and their interfaces and separations.

The philosophy of using biocanisters for sterilization and concepts of providing structural integrity of support for all modes, mechanization for assembly, installation, and separation is the same for the balloon probe as it is for the large ballistic descent probe. Spin-up and despin are achieved in the same manner.

The deflection propulsion requirements are for a retrovelocity to be imparted to retard the time of arrival. The propulsion module to satisfy this requirement is shown as a cluster of three small solid rockets attached to a symmetrical cone frustum saddle that nests over the nose of the aeroshell cone. Three rigging straps are extended along the meridians of the cone body over the

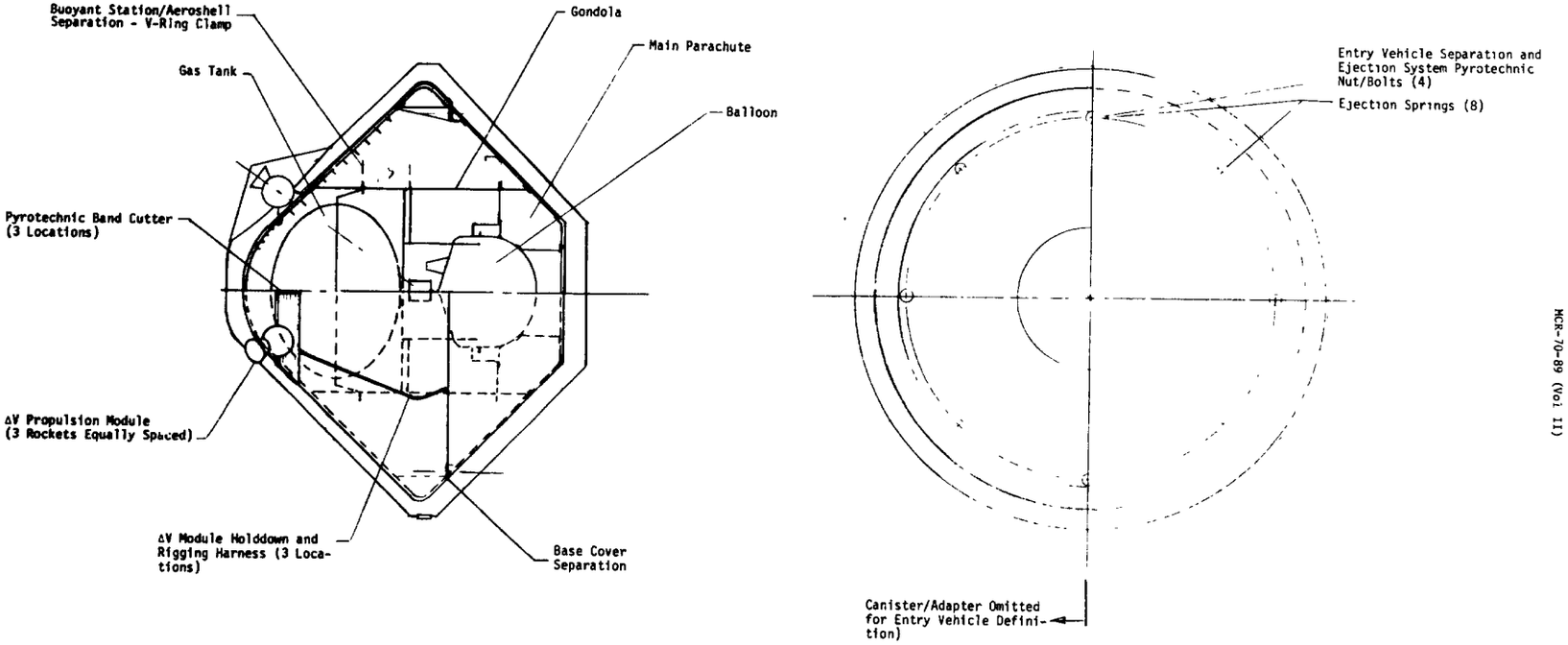
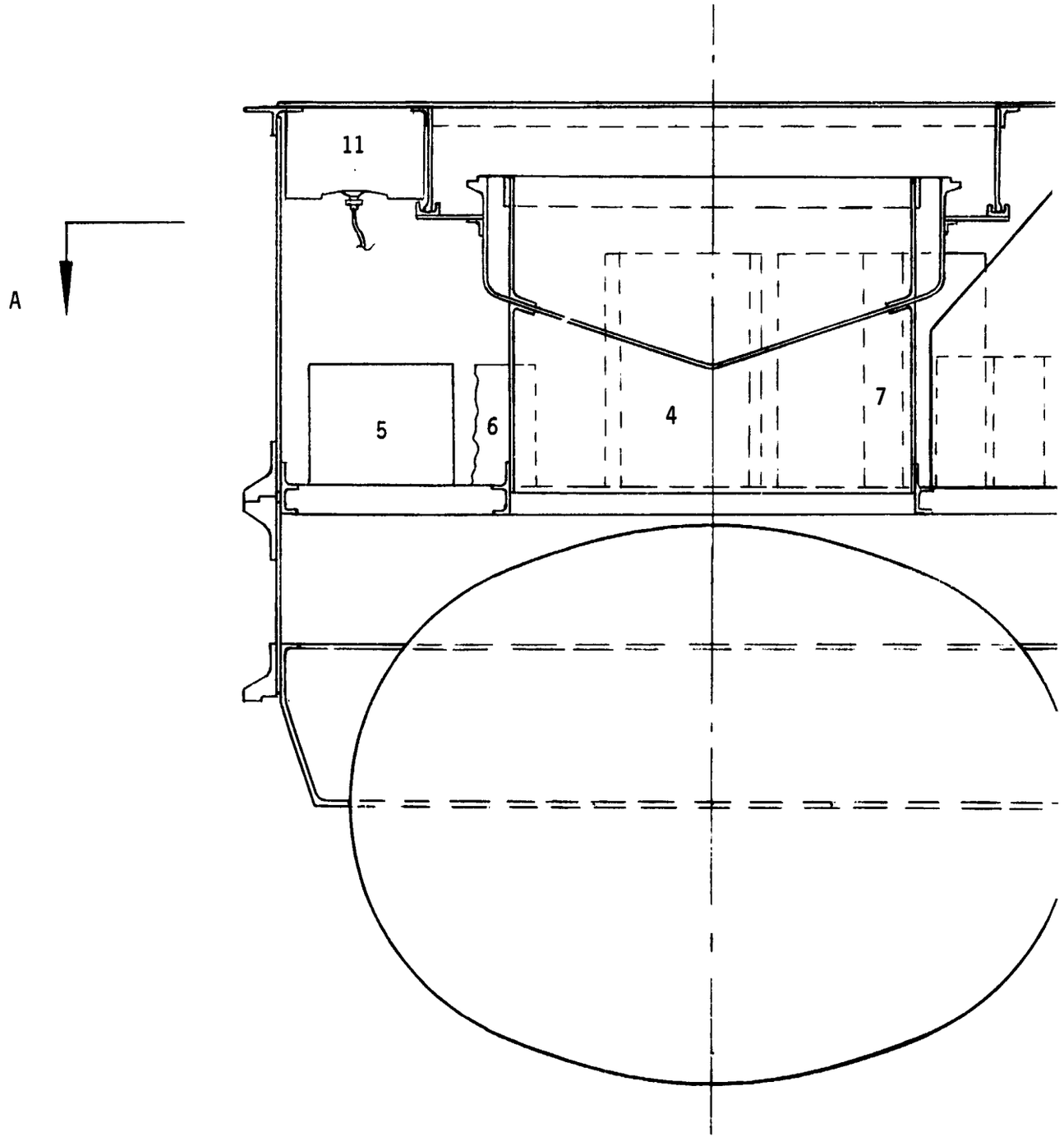
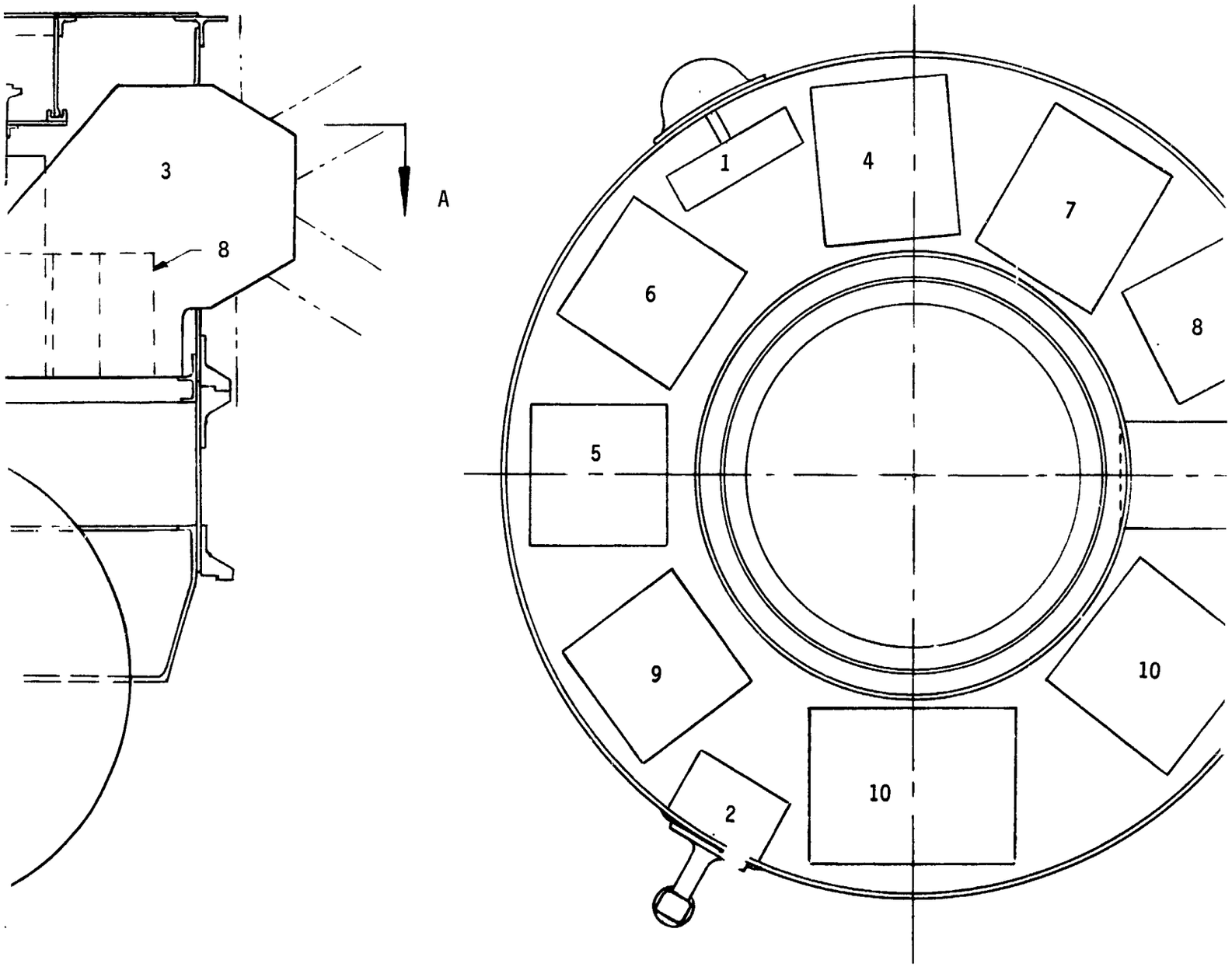


Fig. III-47 Inboard Profile, Balloon Probe System



FOLDOUT FRAME 1



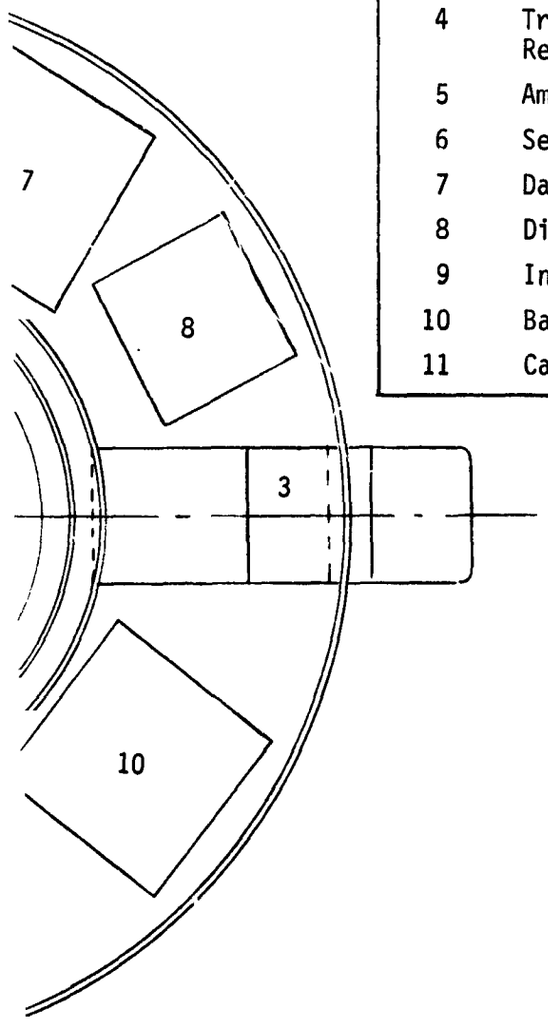
A-A

Scale: ½

FOLDOUT FRAME 2

Fig. I

Legend:	
1	Pressure Transducer
2	Temperature Sensor
3	Solar Radiometer
4	Transponder (RF Exciter, Modulator, Receiver, Ranging)
5	Amplifier
6	Sequencer
7	Data Handling
8	Diplexer
9	Inverter
10	Battery
11	Cavity Helix-Annular Slot Antenna



Note: For Science Instrument Definition see Fig. III-12 and III-40.

Fig. III-48 Internal Arrangement, Buoyant Station Balloon Probe

FOLDOUT FRAME 5

Table III-36 Balloon Probe Weight Summary, 500 mb Configuration

Item	Weight (lb)	
Buoyant Station (Floated Weight)		(70.0)
Science	11.0*	
Electronics (7-day life time, min)	31.0	
Structure	12.0	
Inflation Hardware	2.5	
Balloon (13.0 ft dia)	10.5	
Hydrogen in Balloon	3.0	
Staged Items		(62.0)
Inflation Tanks	45.7	
Residual Hydrogen	0.3	
Structure and Separation Hardware	6.5	
Parachute	7.0	
Parachute Canister/Hardware	2.5	
Aeroshell		(90.0)
Aeroshell Structure	48.0	
Heat Shield		
Forward	33.0	
Base	9.0	
Separation Hardware		(3.5)
Spin-Up/Despin (Fixed)		(4.5)
Drogue and Canister		(4.0)
Entry Weight		234.0
Spin/Despin/Separation (Spent)		6.0
ΔV Propulsion		5.0
Biocanister/Adapter		35.0
Total System		280.0

*Includes transponder.

aeroshell major diameter and looped over an open hook anchored at the adapter ring. To jettison, three pyrotechnic cutters equally spaced to sever the saddle at three places will allow the centrifugal force being generated by the spinning rocket motors about the roll axis to thrust outward. As they approach the extent of travel defined by the length of the rigging harness, the harness will slip out of the open hook. Actuating two of the three cutters will achieve jettison, however, three will assure no perturbation to the spinning entry body.

The aeroshell structure for the front cone body is similar to that of the large probe.

The base cover is a ring-stiffened shell covered with ESA 5500 ablator. The cover separates at the major ring frame that mounts the Entry Vehicle attachment and separation bolts. The parachutes are packaged inside the base cover above the gondola.

The Buoyant Station system is supported within the aeroshell by a cylindrical stiffened shell beam. The beam is tied into the aeroshell through a continuous integral flange. The high g entry loads are applied at the top of the beam uniformly and are transmitted through it in the same manner to be reacted by the aerodynamic pressures.

The Buoyant Station, as it is drawn out ot the aeroshell by the parachute is made up of the gondola, which contains the mission science and electronics, the balloon in a hermetically sealed canister, and the balloon inflation system.

Separation from the aeroshell is achieved by pyrotechnically cutting a V-band ring clamp. A V-band ring clamp is used to secure and detach the balloon canister cover. After the balloon is deployed and inflated, the inflation system is jettisoned by breaking a V-band ring clamp pyrotechnically.

The gondola is a stiffened aluminum shell with an annular bottom platform of aluminum sandwich material. It is vented with respect to the ambient pressure. The type of construction facilitates direct paths for uniform load distribution. The internal arrangement is shown in Fig. III-48.

c. Balloon System Design - 500 mb - The balloon system was designed to meet the following criteria:

1) Use spherical, superpressure balloon;
2) Use hydrogen for inflation, stored at 4500 psi in the gaseous state;
3) Use filament-wound tank design;
4) Float altitude at ambient pressure to 500 mb (a density altitude of 0.0555 lb/ft^3);
5) Solar cells and battery will provide indefinite data link lifetime while in sun and batteries will provide 7-day data link lifetime on dark side;
6) All systems will be sterilizable.

The operational sequence is as follows:

1) Entry Vehicle enters, decelerates to subsonic velocity (M = 0.5, q $\simeq$ 30 psf), and pilot chute removes rear cover and extracts main parachute;
2) Timer sequences deployment of balloon and starts blow-down of inflation gas to balloon;
3) Timer seals lines and releases inflation tank and main chute;
4) Gas heats up, inflates balloon, and probe seeks equilibrium float altitude;
5) Pressure control and vent system protects balloon from overpressure;

6) Solar cells maintain battery charge and mission proceeds until either loss of battery on dark side or destruction of balloon through turbulence or leak.

Balloon sphere design is discussed in Chapter VIII, including discussion of those factors affecting the design supertemperature and superpressure. The resulting balloon design is summarized below:

Conditions:

Float radius,	6107 km;
Float altitude,	57 km;
ΔP, superpressure,	85 mb;
ΔT, supertemperature,	90°F;
P_A, ambient pressure,	500 mb;
T_A, ambient temperature,	64°F;
Balloon skin temperature,	154°F;
Sterilization temperature,	275°F;
Float density,	0.0555 lb/ft^3.

Configuration:

Balloon diameter,	13 ft;
Balloon volume,	1150 ft^3;
Construction,	Laminated Kapton film/ nomex fabric;
Main parachute diameter,	17 ft;
Parachute weight	7 lb;
Parachute m/C_DA,	0.032 slugs/ft^2;
Balloon weight,	10.5 lb;
Hydrogen in balloon,	3.0 lb;
Total floated weight,	70.0 lb.

A balloon probe tradeoff was done to investigate the sensitivity of balloon probe and entry weight to survival time on the dark side.

The balloon probes have been designed with solar cells and batteries to provide a data link with prolonged operating time while on the sun side of the planet, given at least 20% solar effectiveness to 500 mb. Adequate power is provided for 7 days operation independent of the sun. The sensitivity of entry weight to minimum survival time on the dark side is shown in Fig. III-49. At 500 mb ambient pressure, the variation in weight is due to battery weight required for the data link only. Also shown on this figure is the curve for a 50 mb balloon design. At 50 mb ambient pressure, an additional battery plus a heater and insulated structure are required to maintain survivable temperatures within the probe.

Figure III-50 shows the sensitivity of entry weight to balloon superpressure. The design superpressure values shown are based on balloon temperatures resulting from a maximum variable Venus environment radiation model including clouds as described in Chapter VIII. Again, the 50 mb balloon design includes additional weights for thermal control of the instruments and data system.

d. Entry Vehicle Design - 500 mb Balloon Probe - Since there is no requirement for decelerating at a high altitude, the balloon probe aeroshell design is controlled primarily by the volume required to house the balloon, gondola, hydrogen tank, and deployment parachute. The smallest aeroshell consistent with these requirements is a 4-ft-diameter, 45° half angle cone. The resulting 0.55 slug/ft^2 ballistic coefficient and -65° entry angle result in peak deceleration and stagnation pressures of 332 g and 80 psi, respectively. Weights for the carbon phenolic heat shield and ring stiffened aluminum aeroshell are obtained from the design curves discussed previously, Fig. III-15 and III-17.

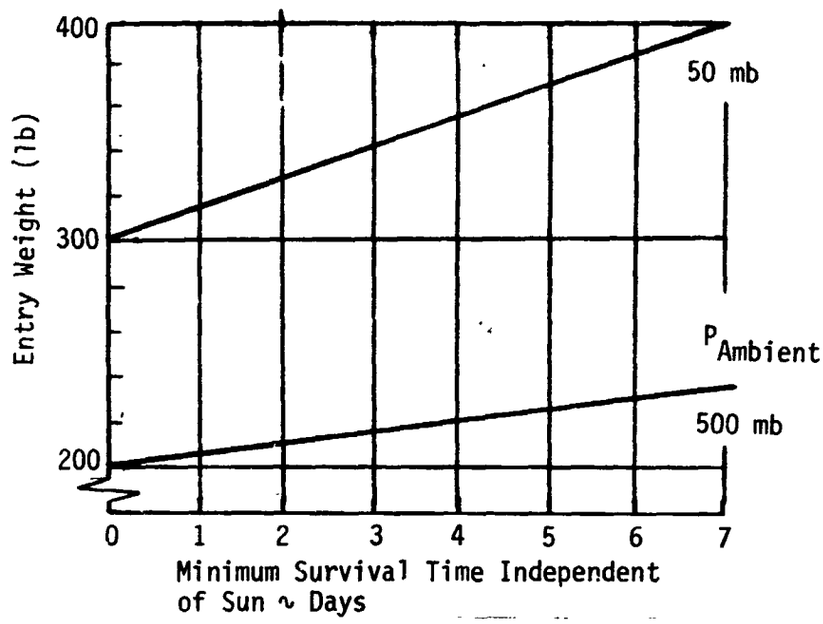


Fig. III-49 Balloon Probe Entry Weight vs Survival Time

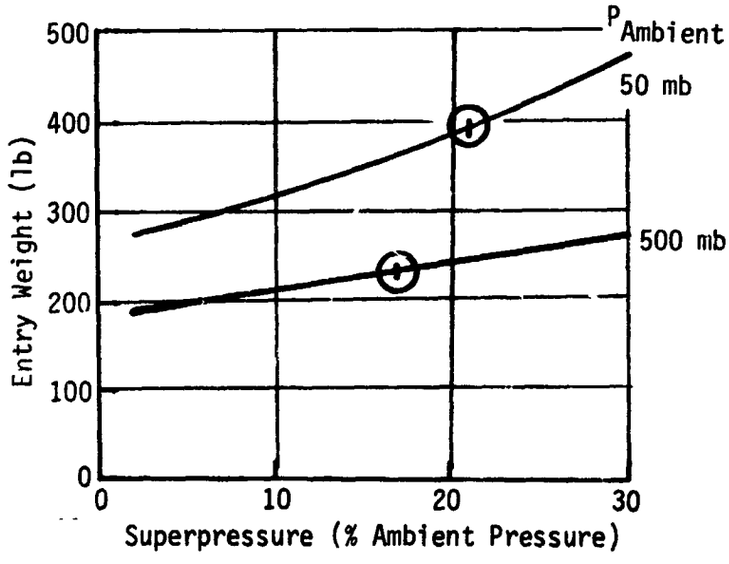


Fig. III-50 Balloon Probe Entry Weight vs Superpressure

Attitude control, thermal control, and deflection propulsion systems are similar to those for the baseline mission probes. The maximum deflection impulse for the flyby spacecraft case, is ∿2200 lb-sec. For purposes of staggering the arrival time of the probes, the deflection impulse can be retrodirected by mounting the solid rocket motor on the forward side of the probe. Reference III-1 defines a method of attaching the motor through the heat shield. The approach described earlier, i.e., strapping a system of three motors on the outside of the heat shield and letting the centrifugal force separate them from the probe after burnout and strap tiedown release, is preferred.

e. Balloon System Design - 50 mb (Option 2) - The 50 mb balloon weight summary is given in Table III-37. Primary changes to the design for the 500 mb balloon are those dictated by the larger balloon size and by the additional requirement for thermal control at the -30°F float altitude. The gondola structural weight is increased to provide a double wall canister to utilize evacuated multilayer insulation. A battery-powered heater is also required, as discussed later in this section.

3. Mission Analysis

The mission options include the use of balloon probes at the light side of the morning terminator and a high-cloud probe at the antisolar point. Balloon targeting, deflection, and entry probe design data are presented in Table III-38 and III-39. The high-cloud probe data are presented in Table III-40. Descent profiles for the balloons are presented in Fig. III-51 and III-52. High-cloud probe descent profiles are presented in Fig. III-53 and III-54. Entry dispersions for the high-cloud probe at the antisolar point will be similar to those presented in Section C of this chapter.

Table III-37 Balloon Probe Weight Summary, 50 mb Configuration

Item	Weight (lb)	
Buoyant Station (Floated Weight)		(119.6)
Science	11.0*	
Electronics (7-day lifetime)	43.6	
Structure and Thermal Insulation	25.5	
Inflation Hardware	2.5	
Balloon	31.5	
Hydrogen in Balloon	5.5	
Staged Items		(107.0)
Inflation Tank	84.0	
Excess Hydrogen	0.5	
Support Structure/Hardware	7.5	
Parachute	12.0	
Parachute Canister/Hardware	3.0	
Aeroshell		(154.0)
Aeroshell Structure	76.0	
Heatshield		
Forward Cone	62.0	
Base	16.0	
Separation Hardware		(3.0)
Spin-Up/Despin (Fixed)		(5.5)
Drogue and Canister		(6.0)
Entry Weight		395.1
Spin/Despin/Separation (Spent)		7.0
ΔV Propulsion		8.0
Biocanister/Adapter		45.0
Total System		455.1

*Including Transponder.

Table III-38

VENUS BALLOON 50 MB
* * * ENTRY PROBE DESIGN DATA * * *

TARGET (NEAR SIDE ENTRY)		LSMT	
APPROACH TRAJECTORY TYPE		IMPACT	FLYBY
PERIAPSIS RADIUS OF BUS	KM	2800.	12600.
DEFLECTION RADIUS	KM	4,000,000	4,000,000.
DEFLECTION VELOCITY (DEL V)	METERS/SEC	22.	62
DEFLECTION ANGLE (TAU)	DEGREES	160.	160.
CAPSULE COAST TIME	HOURS	294.75	297.533
MAXIMUM ANGLE OF ATTACK	DEGREES	155.4	151.02
* * * * * * * * * * * *	* * * * * * * *	* * * * * * * * * * * * * * * *	
ENTRY VELOCITY	FT/SEC	35367.	
ENTRY ANGLE	DEGREES	-65.	
ENTRY ALTITUDE	FEET	815000.	
ENTRY RADIUS	KM	6298.417	
ENTRY LATITUDE	DEG	0.7628	
ENTRY LONGITUDE	DEG	69.8569	
EARTH ZENITH ANGLE (MASK)	DEG	24.2356	
SOLAR ZENITH ANGLE	DEG	69.8588	
* * * * * * * * * * * *	* * * * * * * *	* * * * * * * * * * * * * * * *	
AEROSHELL BALLISTIC COEF.	SLUGS/FT2	0.6	
TIME OF MACH 1 OCCURRENCE	SEC	27	
MAXIMUM DYNAMIC PRESSURE	LBS/FT2	4921 (V5M)	6.27 (MMCL) AT 18 SEC
MAXIMUM DECELERATION	G	255 (V5M)	343 (MMCL) AT 18 SEC
* * * * * * * * * * * *	* * * * * * * *	* * * * * * * * * * * * * * * *	
TIME TO MAIN CHUTE DEPLOY	SECONDS	44.0	
MAIN CHUTE BALLISTIC COEF.	SLUGS/FT2	.032	
RADIUS MAIN CHUTE DEPLOYED	KM	6116.5	
MACH NUMBER AT MCD		.348 (V5M)	.481 (MMCL)
DYNAMIC PRESSURE AT MCD		27.6 (V5M)	30.7 (MMCL)
DECELERATION AT MCD	G	.96 (V5M)	1.07 (MMCL)
* * * * * * * * * * * *	* * * * * * * *	* * * * * * * * * * * * * * * *	
TIME TO REACH 6116.5 KM FROM 1.5 G LEVEL	SECONDS	40.0 (V5M)	10.0 (MMCL)
BIT RATE	BITS/SEC	20.	

Table III-39

VENUS BALLOON 500 MB
ENTRY PROBE DESIGN DATA

TARGET (NEAR SIDE ENTRY)		LSMT		
APPROACH TRAJECTORY TYPE		IMPACT		FLYBY
PERIAPSIS RADIUS OF BUS	KM	2800.		12600.
DEFLECTION RADIUS	KM	4,000,000		4,000,000.
DEFLECTION VELOCITY (DEL V)	METERS/SEC	22.		62
DEFLECTION ANGLE (TAU)	DEGREES	160.		160.
CAPSULE COAST TIME	HOURS	294.75		297.533
MAXIMUM ANGLE OF ATTACK	DEGREES	155.4		151.02
ENTRY VELOCITY	FT/SEC	35367.		
ENTRY ANGLE	DEGREES	-65.		
ENTRY ALTITUDE	FEET	815000.		
ENTRY RADIUS	KM	6298.412		
ENTRY LATITUDE	DEG	0.7628		
ENTRY LONGITUDE	DEG	69.8569		
EARTH ZENITH ANGLE (MASK)	DEG	24.2356		
SOLAR ZENITH ANGLE	DEG	69.8588		
AEROSHELL BALLISTIC COEF.	SLUGS/FT2	0.54		
TIME OF MACH 1 OCCURRENCE	SEC	27		
MAXIMUM DYNAMIC PRESSURE	LBS/FT2	4246 (V5M)	5776 (MMCL)	AT 18 SEC
MAXIMUM DECELERATION	G	245 (V5M)	332 (MMCL)	AT 18 SEC
TIME TO MAIN CHUTE DEPLOY	SECONDS	74.5 (V5M)		
TIME TO MAIN CHUTE DEPLOY	SECONDS	74.0 (MMCL)		
MAIN CHUTE BALLISTIC COEF.	SLUGS/FT2	.032		
RADIUS MAIN CHUTE DEPLOYED	KM	6117.0		
MACH NUMBER AT MCD		.346 (V5M)	.479 (MMCL)	
DECELERATION AT MCD	G	.96 (V5M)		
DECELERATION AT MCD	G	1.07 (MMCL)		
DYNAMIC PRESSURE AT MCD		24.8 (V5M)		
DYNAMIC PRESSURE AT MCD		27.6 (MMCL)		
TIME TO REACH 6117 KM FROM 1.5 G LEVEL	SECONDS	40.5 (V5M)		
TIME TO REACH 6117 KM FROM 1.5 G LEVEL	SECONDS	10.0 (MMCL)		
BIT RATE	BITS/SEC	20.		

Table III-40

VENUS HIGH CLOUD PROBE (ANTI SOLAR)
* * * ENTRY PROBE DESIGN DATA * * *

TARGET (FAR SIDE ENTRY)		ANTI SOLAR	
APPROACH TRAJECTORY TYPE		IMPACT	FLYBY
PERIAPSIS RADIUS OF BUS	KM	2800.	12600.
DEFLECTION RADIUS	KM	4,000,000	4,000,000.
DEFLECTION VELOCITY	METERS/SEC	70.	112.
DEFLECTION ANGLE	DEGREES	20.	20.
CAPSULE COAST TIME	HOURS	289.12	286.4
MAXIMUM ANGLE OF ATTACK	DEGREES	46.5	44.6
ENTRY VELOCITY	FT/SEC	35367.	
ENTRY ANGLE	DEGREES	-35.	
ENTRY ALTITUDE	FEET	815000.	
ENTRY RADIUS	KM	6298.412	
ENTRY LATITUDE	DEG	0.4186	
ENTRY LONGITUDE	DEG	157.7547	
EARTH ZENITH ANGLE (MASK)	DEG	63.8075	
SOLAR ZENITH ANGLE	DEG	157.7509	
AEROSHELL BALLISTIC COEF.	SLUGS/FT2	0.2	
TIME OF MACH 1 OCCURRENCE	SEC	40.5	
MAXIMUM DYNAMIC PRESSURE	LBS/FT2	1703 (VSM)	1488 (MMCL) AT 26 SEC
MAXIMUM DECELERATION	G	265 (VSM)	231 (MMCL) AT 26 SEC
TIME FROM ENTRY TO MAIN CHUTE DEPLOYMENT	SECONDS	45.7	
MACH NUMBER AT MCD		.783	
DECELERATION AT MCD	G	1.5	
DYNAMIC PRESSURE AT MCD	LB/FT2	12.6	
ALTITUDE MAIN CHUTE DEPLOY	FT	261917.1 (VSM)	249979.8 (MMCL)
RADIUS MAIN CHUTE DEPLOYED	KM	6129.83 (VSM)	6126.19 (MMCL)
TIME FROM ENTRY TO MAIN CHUTE RELEASE	HOURS	1.30 (VSM)	1.327 (MMCL)
MAIN CHUTE BALLISTIC COEF.	SLUGS/FT2	.005	
CHUTE RELEASE PRESSURE	BARS	1.35	
RADIUS MAIN CHUTE RELEASE	KM	6103.3655 (VSM)	6099.9914 (MMCL)
BIT RATE	BITS/SEC	50.	

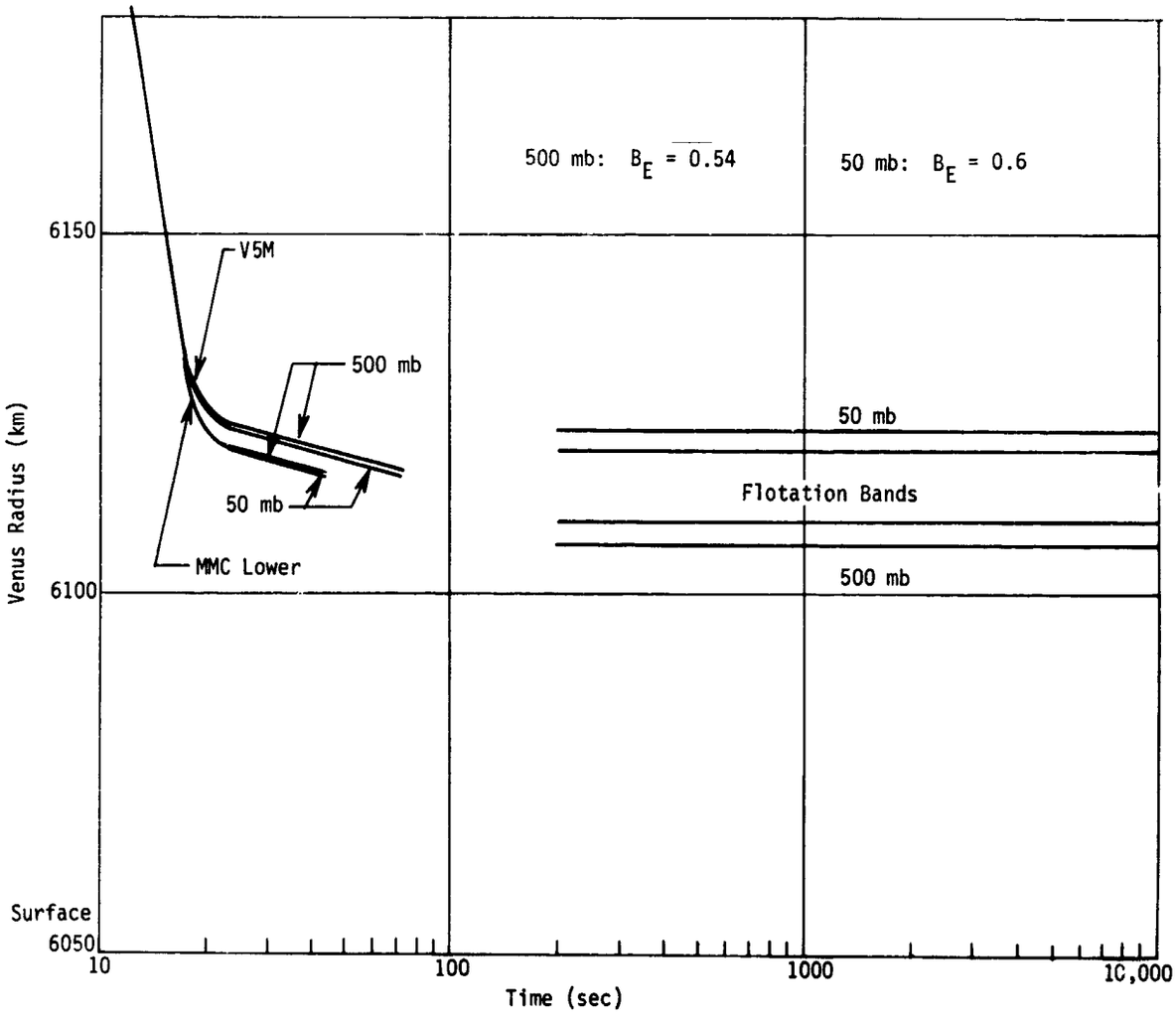


Fig. III-51 Balloon Probes (LSMT) Descent Profile

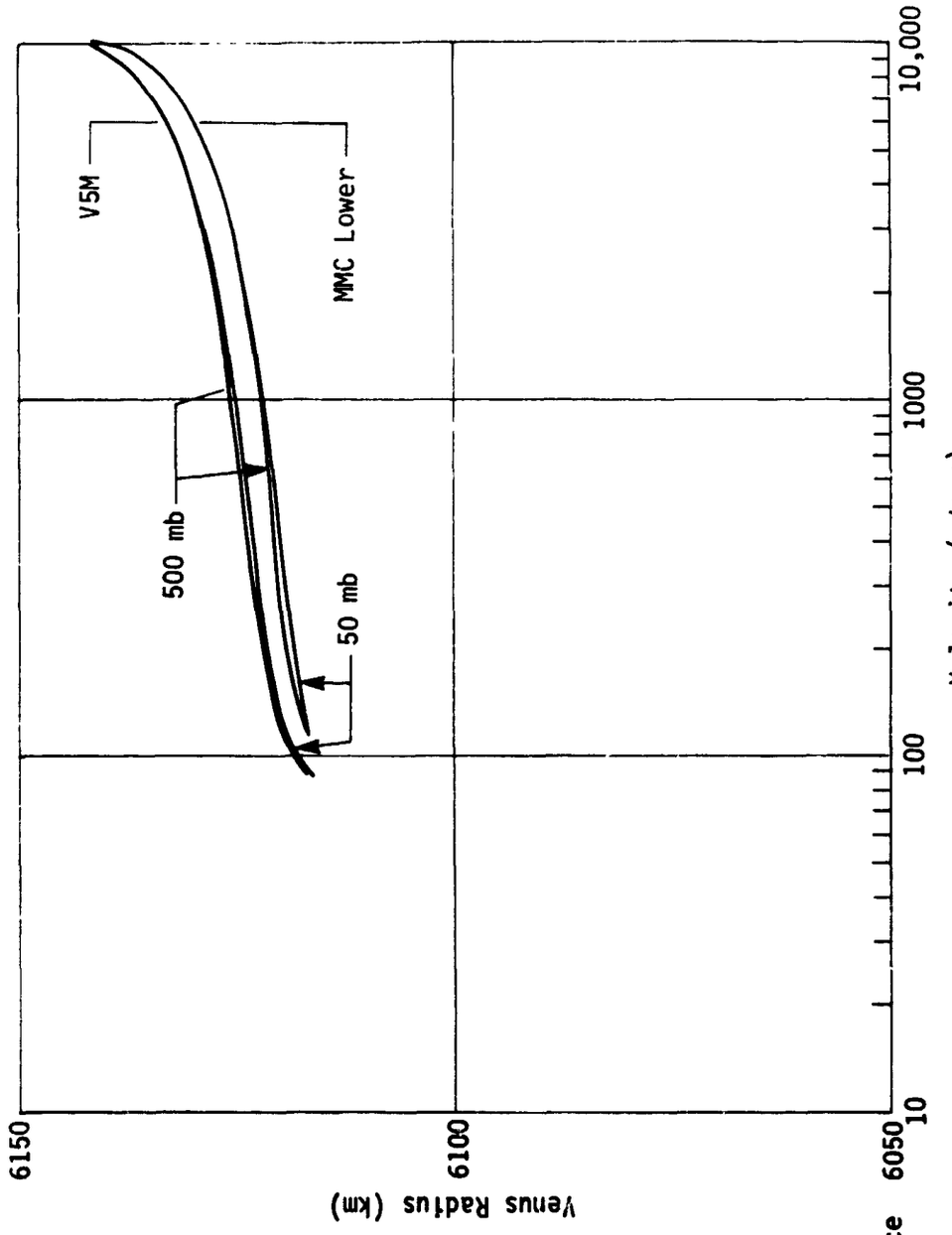


Fig. III-52 Balloon Probes (LSMT) Descent Profile

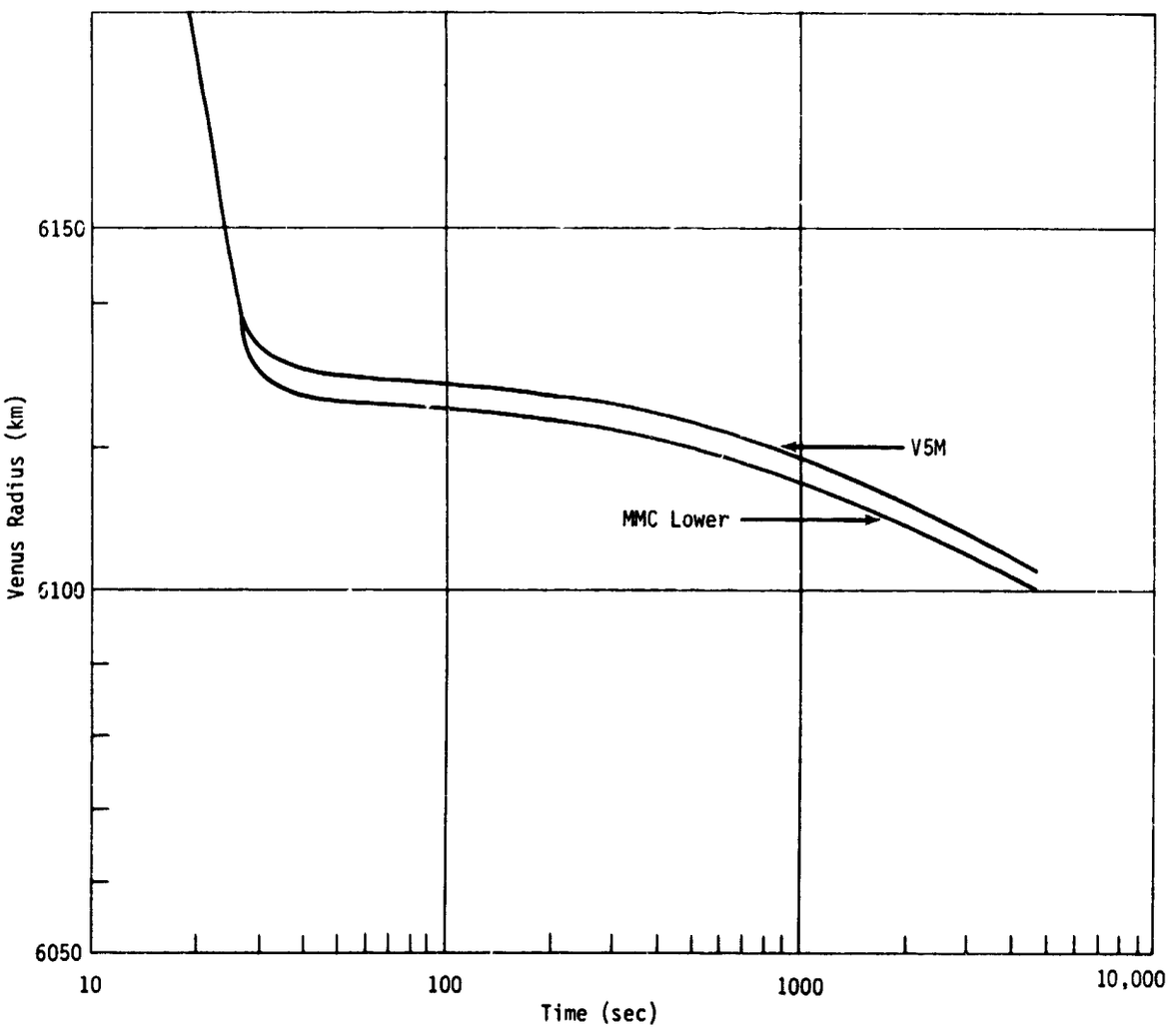


Fig. III-53 High-Cloud Probe Descent Profile, Antisolar

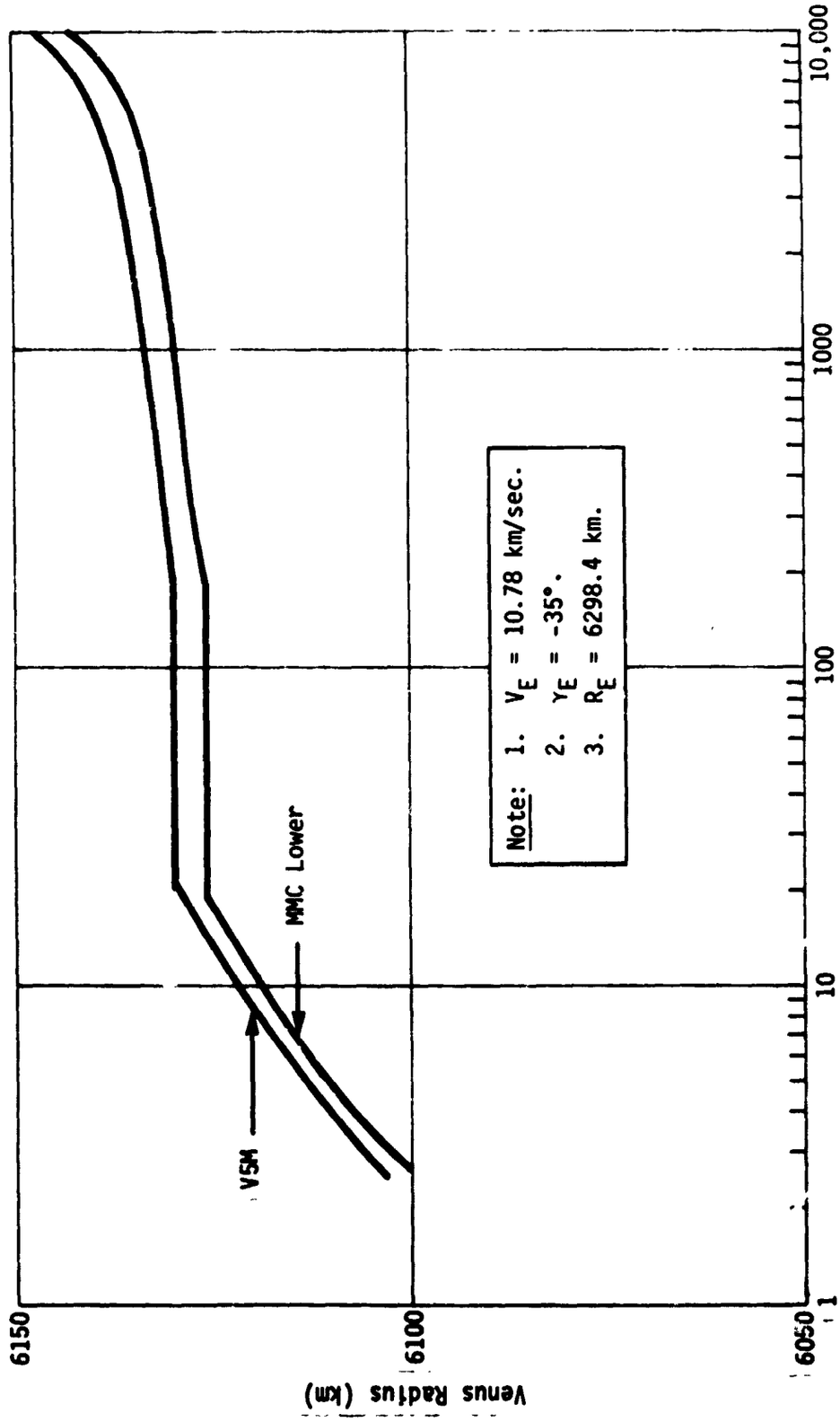


Fig. III-54 High-Cloud Probe Descent Profile, Antisolar

The balloon probes are targeted to a new area (LSMT) and exhibit different entry dispersions. The error in deflection angle is assumed to be 0.75°. The error in periapsis radius is assumed to be 120 km and the deflection velocity increment error is 0.22 m/sec for the impacting case and 0.62 m/sec for the flyby case. For the impacting case the entry dispersions are ±1.53° downrange, ±0.113° crossrange, and ±1.015° in entry path angle. For the flyby case these dispersions become ±3.95° downrange, ± 0.284° crossrange, and ±2.64° in entry path angle.

4. Telecommunications Systems - Optional Probe Configuration

Options 1 and 2 add a second high-cloud probe and two balloon probes. The telecommunications system in the added high-cloud probe is the same as is in the one in the baseline option, which was discussed earlier. The two balloons have identical telecommunications systems.

Both balloons are targeted to the same point, the light side of the morning terminator, 24° from the subearth point. They will float at different elevations, 50 and 500 mb.

The primary purpose of the balloon probes is to furnish wind circulation information. This is done by making periodic position fixes on them throughout their lifetime, nominally 7 days. During this period they drift over the planet surface, and may drift out of sight. As long as their darkside lifetime is not exceeded (see Subsection 6 following), they may drift back into sight later, and resume contact with the ground stations. This possibility should be periodically monitored by the DSIF for several weeks after the last successful contact.

Contact with the balloon is not continuous. There will be an initial contact immediately after deployment, followed by periodic brief contacts thereafter until it goes out of sight. These brief contacts are nominally once each 8 hr, but provisions are made to vary this if desired. The sequence for contacts after the first one (which is a special case, to be discussed below) is outlined.

1) Once each hour, controlled by the on-board sequencer, the probe receiver will come on and look for an uplink signal. If none is found, it will go off until the next hour. If the ground station wishes to make a contact, it will have its transmitter on at this time, transmitting carrier plus ranging. In this case, the receiver will find a signal, lock onto it, and the sequence will continue;
2) The transmitter will be turned on in the coherent transponder mode. It will transmit ½ minute of unmodulated carrier, 2 minutes of instrument and engineering data, and 2½ minutes of ranging. It will then be turned off;
3) 30 minutes later, the transmitter will be turned on, in the open loop mode (no uplink lock-on), unmodulated carrier, for 2 minutes, for the antenna polarization experiment.

Some discussion is required for each of these items. As discussed in the antenna selection discussion (Chapter VII.E), the coverage requirements for the balloon probe, which can drift to any point on the planet, are best met by a two-antenna system. A circularly polarized 0.5λ cavity helix antenna is recommended for angular distance from subearth, ϕ, less than 45°, and a linearly polarized 0.6λ annular slot is recommended for $\phi > 45°$. The probe receiver must measure the signal strength received over both of these antennas and select the one having the strongest signal for the subsequent ranging and data transmissions. Its choice will be identified in the data transmission. This selection will require an RF switch. Since the antenna whose polarization matches that of the upcoming signal will have a 3 db advantage, it will usually be selected. Therefore, the ground station must select its polarization based on previous position fix information. (The initial position will be known. It is well inside the $\phi > 45°$ region, at $\phi = 24°$).

The initial ½ minute of unmodulated carrier is used to assure ground station receiver lock. Since signalling is coherent, the only uncertainty is Doppler. As discussed in Section B of this chapter, lock-on for an unpredicted earth-directed velocity of 10 m/sec takes only 9 sec. The earth-directed component of the probe velocity can only be large near the limbs, and by the time it reaches this region there will have been sufficient position fixes to give a reasonably good prediction of its velocity, so the ½ minute is considered to be sufficient for lock-on. If it does take somewhat longer than this, some of the 2-minute data period may be lost. However, this consists of multiple repeats of the same data, so little would be lost.

Link calculations for ranging and data are shown in Tables III-41 thru III-45. They show that the 2.5 minutes of ranging and the 20 bps data rate can be handled with some margin using an 8 W transmitter. A receiver having a low noise (1200°K) RF amplifier front end has been assumed. This substantially reduces the required ranging time. It should be well within the state of the art by 1972.

As discussed in Chapter VII.D, position determination will be by ranging and measurement of the polarization direction of the vertically polarized signal from the annular slot antenna. The polarization experiment is delayed for 30 minutes to allow time to switch the DSN antenna to the polarization tracking feed. This feed has a very limited power handling capability,* so it will be used in a receive-only mode, with the probe transmitter operating open-loop. Assuming a loop stress signal is sent during the coherent portion of the contact, frequency uncertainty should be quite small and acquisition by the ground station should take only a few seconds. The 2-minute period is specified to allow some time to average out angle variations from swinging of the gondola caused by wind turbulence. It is assumed that this averaging will give a reading accurate to 3° or better.

*J. R. Hall, personal communication.

Table III-41 Link Calculation, Uplink, Balloon Probes, Two-Way Doppler Channel

Item	Parameter	Comm Angle, 0 To 80° One Channel Only	
		Nominal (db)	Adverse Tolerance (db)
1.	Total Transmitter Power, 400 kw	+86.0 dbm	0.3
2.	Transmitter Circuit Loss	-0.4	0.1
3.	Transmitter Antenna Gain, 210-ft Dish	+59.2	0.5
4.	Transmitter Antenna Pointing Loss	0	0
5.	Space Loss, 2116 MHz, 95 × 10^6 km	-258.2	0
6.	Multipath Losses	0	0.5
7.	Polarization Loss	0	0.5
8.	Receiver Antenna Gain	+8.0	0
9.	Receiver Pointing Loss	0	6.0
10.	Receiver Circuit Loss	-1.1	0.2
11.	Net Circuit Loss	-192.5	7.8
12.	Total Received Power	-106.5 dbm	8.1
13.	Received Noise Spectral Density, 1200°K	-167.8 dbm	0.5
Carrier Performance, Data Demodulation			
14.	Carrier Power to Total Power	0	0
15.	Received Carrier Power	-106.5 dbm	8.1
16.	Carrier Threshold Bandwidth, 50 Hz	+17.0	0.5
17.	Threshold, S/N in 2 B_{LO}	+20.0	0
18.	Threshold Carrier Power	-130.8 dbm	1.0
19.	Margin, Carrier	+24.3	9.1

Table III-42 Link Calculation, Downlink, Balloon Probes, Data Transmission Mode

Item	Parameter	Initial Postentry Contact, 20 bps 24° Comm Angle		Later Contacts, 20 bps Comm Angle 0 to 80°	
		Nominal (db)	Adverse Tolerance (db)	Nominal (db)	Adverse Tolerance (db)
1.	Total Transmitter Power, 8W	+39.0 dbm	0.4	+39.0 dbm	0.4
2.	Transmitter Circuit Loss	-1.1	0.2	-1.1	0.2
3.	Transmitter Antenna Gain	+7.5	0	+8.0	0
4.	Transmitter Antenna Pointing Loss	0	2.0	0	6
5.	Space Loss, 2297 MHz, 95 × 10^6km	-259.2	0	-259.2	0
6.	Multipath Losses	0	0	0	0.5
7.	Polarization Loss	-3.0	0	0	0.5
8.	Receiver Antenna Gain, 210-ft Dish	+61.4	0.3	+61.4	0.3
9.	Receiver Pointing Loss	0	0	0	0
10.	Receiver Circuit Loss	-0.1	0	-0.1	0
11.	Net Circuit Loss	-194.5	2.5	-191.0	7.5
12.	Total Received Power	-155.5 dbm	2.9	-152.0 dbm	7.9
13.	Received Noise Spectral Density, 35°K	-183.1 dbm	0.6	-183.1 dbm	0.6
Carrier Performance, Data Demodulation					
14.	Carrier Power to Total Power	-2.4	0.2	-2.4	0.2
15.	Received Carrier Power	-157.9 dbm	3.1	-154.4 dbm	8.1
16.	Carrier Threshold Bandwidth, 12 Hz	+10.3	0.5	+10.3	0.5
17.	Threshold S/N in 2 B_{LO}	+9.0	0	+9.0	0
18.	Threshold Carrier Power	-163.8 dbm	1.1	-163.8 dbm	1.1
19.	Margin, Carrier	5.9	4.2	9.4	9.2
Data Channel Performance					
20.	Receiver Loss	-1.5	0.2	-1.5	0.2
21.	Data Channel Power/Total	-3.7	0.2	-3.7	0.2
22.	Total Data Power	-160.7 dbm	3.3	-157.2 dbm	8.3
23.	Data Threshold E/NO	+2.5	0	+2.5	0
24.	Data Rate	+13.0	0	+13.0	0
25.	Data Channel Threshold	-167.6 dbm	0.6	-167.6 dbm	0.6
26.	Data Channel Margin	+6.9	3.9	+10.4	8.9

Table III-43 Link Calculation, Uplink, Balloon Probes, Ranging

Item	Parameter	Single Channel Comm Angle, 0 to 80°	
		Nominal (db)	Adverse Tolerance (db)
1.	Total Transmitter Power, 400 kw	+86.0 dbm	0.3
2.	Transmitter Circuit Loss	-0.4	0.1
3.	Transmitter Antenna Gain, 210-ft Dish	+59.2	0.5
4.	Transmitter Antenna Pointing Loss	0	0
5.	Space Loss, 2116 MHz, 95×10^6 km	-258.2	0
6.	Multipath Losses	0	0.5
7.	Polarization Loss	0	0.5
8.	Receiver Antenna Gain	+8.0	0
9.	Receiver Pointing Loss	0	6.0
10.	Receiver Circuit Loss	-1.1	0.2
11.	Net Circuit Loss	-192.5	7.8
12.	Total Received Power	-106.5 dbm	8.1
13.	Received Noise Spectral Density, 1200°K	-167.8 dbm	0.5
Carrier Performance, Ranging Demodulation			
14.	Carrier Power to Total Power	-13.0	1.0
15.	Received Carrier Power	-119.5 dbm	9.1
16.	Carrier Threshold Bandwidth, 50 Hz	+17.0	0.5
17.	Threshold S/N in 2 B_{LO}	20.0	0
18.	Threshold Carrier Power	-130.8 dbm	1.0
19.	Margin, Carrier	11.3	10.1
Ranging Channel Performance			
20.	Receiver Loss	-0.1	0.1
21.	Ranging Channel Power/Total	-0.2	0.1
22.	Total Ranging Power	-106.8 dbm	8.3
23.	Filter Loss, 15 kHz Bandwidth	-0.3	0
24.	Ranging Signal Power	-107.1	8.3
25.	Noise Bandwidth, 15 kHz	+41.8	0
26.	Ranging Noise Power	-126.0 dbm	0.5
27.	S/N at Limiter	+18.9	8.8
28.	Limiter Suppression	+23.0	10.0
29.	S/N at Modulator	+41.9	18.8
30.	S/(S + N) at Modulator (Ranging Suppression)	0	0.1

Table III-44 Link Calculation, Downlink, Balloon Probes, Ranging

Item	Parameter	Clock Rate, 5 KHz Comm Angle , 0 to 80°	
		Nominal (db)	Adverse Tolerance (db)
1.	Total Transmitter Power, 8 W	+39.0 dbm	0.4
2.	Transmitter Circuit Loss	-1.1	0.2
3.	Transmitter Antenna Gain	+8.0	0
4.	Transmitter Antenna Pointing Loss	0	6.0
5.	Space Loss, 2297 MHz, 95 × 10^6 km	-259.2	0
6.	Multipath Losses	0	0.5
7.	Polarization Loss	0	0.5
8.	Receiver Antenna Gain, 210-ft Dish	+61.4	0.3
9.	Receiver Pointing Loss	0	0
10.	Receiver Circuit Loss	-0.1	0
11.	Net Circuit Loss	-191.0	7.5
12.	Total Received Power	-152.0 dbm	7.9
13.	Received Noise Spectral Density, 35°K	-183.1 dbm	0.6
Carrier Performance, Ranging Demodulation			
14.	Carrier Power to Total Power	-2.4	0.2
15.	Received Carrier Power	-154.4	8.1
16.	Carrier Threshold Bandwidth, 12 Hz	+10.3	0.5
17.	Threshold S/N in 2 B_{LO}	+9.0	0
18.	Threshold Carrier Power	-163.8 dbm	1.1
19.	Margin, Carrier	9.4	9.2
Ranging Channel Performance			
20.	Receiver Loss	-1.5	0.2
21.	Ranging Channel Power/Total	-3.7	0.2
22.	Total Ranging Power	-157.2 dbm	8.3
23.	Ranging Suppression	0	0.1
24.	Receiver and Correlator Loss	0	0.1
25.	Ranging Signal Level	-157.2 dbm	8.5
26.	Threshold S/N_o for 2.5 min Acquisition	+13.9	0
27.	Threshold Ranging Power	-169.2 dbm	0.6
28.	Margin, Ranging Channel	+12.0	9.1

Table III-45 Link Calculation, Downlink, Balloon Probes, Polarization Experiment Mode

Item	Parameter	Unmodulated Carrier Comm Angle, 5 to 80°	
		Nominal (db)	Adverse Tolerance (db)
1.	Total Transmitter Power, 8 w	+39.0 dbm	0.4
2.	Transmitter Circuit Loss	-1.1	0.2
3.	Transmitter Antenna Gain	+5.5	0
4.	Transmitter Antenna Pointing Loss	0	7.5
5.	Space Loss, 2297 MHz, 95×10^6 km	-259.2	0
6.	Multipath Losses	0	1.4
7.	Polarization Loss	0	0.5
8.	Receiver Antenna Gain, 210-ft Dish	+61.4	0.3
9.	Receiver Pointing Loss	0	0
10.	Receiver Circuit Loss	-0.1	0
11.	Net Circuit Loss	-193.5	9.9
12.	Total Received Power	-154.5 dbm	10.3
13.	Received Noise Spectral Density, 35°K	-183.1 dbm	0.6
Carrier Performance			
14.	Carrier Power to Total Power	0	0
15.	Received Carrier Power	-154.5 dbm	10.3
16.	Carrier Threshold Bandwidth, 12 Hz	+10.3	0.5
17.	Threshold S/N in 2 B_{LO}	+6.0	0
18.	Threshold Carrier Power	-166.8 dbm	1.1
19.	Margin, Carrier	+12.3	11.4

It has been decided to use a 10^4 bps ranging code instead of the conventional 10^6 bps code in order to save transmitter power. This will give a range accuracy of 1.5 km, which is more than adequate for the wind circulation experiment. A multicomponent 2, 11, 47 = 1034 code is proposed. This gives an ambiguity distance of 17,230 km, which should be more than adequate because it is about three times the planet radius. Using the technique described by Easterling (Ref III-8), acquisition time for this code is found to be

$$\frac{S}{N_o} = \frac{3640}{T}$$

This is used to compute item 26 in Table III-44, the link calculation for ranging. This calculation indicates that an acquisition time of 2.5 minutes will give a 2.9 db margin over the adverse tolerances. The ranging will be relayed for a 2.5-minute period immediately following the data (and preceded by a warning code), and then stopped without waiting for a command confirming acquisition. This avoids transmission while waiting for the round-trip propagation time of about 10 minutes. This is an accepted technique that has been used on previous programs.

Table III-42 has a column entitled "Initial Postentry Contact," and one entitled "Later Contacts." The "Initial Postentry Contact" column is applicable only to the impacting spacecraft option. The sequence of events chart in Chapter II.B shows that in the impacting spacecraft case the two balloons are deployed right in the middle of the large probe's communication period. In this case a brief initial data transmission will be made by the balloons. However, it will be done in the open-loop mode, with no ranging, Doppler, or antenna experiment. These will be deferred until later contacts, after all of the probe descents are completed. This is required by the limitations of the DSN. This has two consequences

in the link calculation. First, since the DSN antenna will be linearly polarized for the large probe and the balloons will be using circularly polarized antennas, they will suffer a 3 db polarization loss (item 7). This more than offset (compared to the "Later Contacts" column) by the smaller pointing loss, a consequence of the known location of the initial contact. Later contacts may be from any point on the visible side of the planet, and the pointing loss must be sized accordingly.

The sequence of events chart for the flyby spacecraft option shows that the balloons are deployed well after all of the other probe descents are completed. In this case the initial contact can be just like all the subsequent ones, and the "Later Contacts" column of Table III-42 can be used for all of them.

The specified angular coverage for this mode is 0 to 80° from subearth. This is a consequence of the pointing loss, which rises rapidly beyond this point, which in turn is a consequence of the annular slot antenna radiation pattern. This was selected to have a narrow null in the vicinity of zenith, so that the polarization experiment could be carried out as closely as possible to the subearth point. Relaxing this requirement would permit increasing the gain beyond $\phi = 80°$, and extending the coverage in the near-limb region. However, it is expected that all of the worst-case tolerances would not generally occur simultaneously, so communications could probably be carried out some distance beyond $\phi = 80°$.

The multipath losses shown in Tables III-41 thru III-45 are taken from Chapter VII.B.

Tables III-43 and III-44 cover the ranging. They reflect the analysis in Chapter VII.C, where explanations of items 23 thru 30 in Table III-43 and items 23 thru 28 of Table III-44 can be found. The use of a 10^4 bps code rate puts the transponder received SNR into the strong signal domain, so a transponder bandwidth of 15 kHz is used.

Finally, Table III-45 covers the polarization experiment, which transmits unmodulated carrier and uses the annular slot antenna regardless of probe position. Since the receiver phase-locked reference is not used to demodulate data, the threshold SNR was set at 6 db. Assuming the antenna pattern shown in Chapter VII.E, this link will operate to within 5° of the subearth point.

5. Data System - Optional Probe Configuration

Option 1 mission has, in addition to the baseline probes, a 500 mb balloon probe. Option 2 has, in addition to the baseline and option 1 balloon probe, a 50 mb balloon probe and a high-cloud probe.

The balloon probe data systems are identical to each other and since the high-cloud data system is identical to the baseline high-cloud probe described previously, only the balloon probe data systems will be discussed further.

The balloon probes of Option 1 and Option 2 have data systems somewhat simpler than the probes described previously because no entry data storage is required and there are only three relatively simple science instruments involved.

Diagrams, Measurement List, and Format - A data system measurement list, block diagram, and data format for the balloon probes are given in Table III-46 and Fig. III-55 and III-56, respectively. A bit rate of 20 bps is used for all PCM telemetry transmissions. Each data transmission is scheduled to last 120 sec, which is sufficient to complete one major frame of data including the subcommutated data. Entry to the system via interrogation from the DSIF once every 8 hr or on an hourly basis is discussed in the following subsection on sequencers.

Table III-46 Measurement List, Balloon Probe (Baseline Option 1 or 2)

Parameter	Bits per Sample	Bits per 10 sec Frame (bits)	Sample Interval (sec)	Bit Rate (bps)
Solar Radiometer	120	120	10	12.0
Atmospheric Pressure	8	8	10	0.8
Atmospheric Temperature	8	8	10	0.8
Static Phase Error (Transponder)	8	8	10	0.8
Subcommutated Channel	8	8	10	0.8
Calibrate	8	--	90	--
Battery Voltage	8	--	90	--
Battery Current	8	--	90	--
Balloon Temperature 1	8	--	90	--
Balloon Temperature 2	8	--	90	--
Balloon Differential Pressure	8	--	90	--
Transmitter Power Out	8	--	90	--
Battery Temperature	8	--	90	--
Events (On-Off)	8	--	90	--
Subcommutator Position	4	4	10	0.4
Time (Recycles Hourly)	6	6	10	0.6
Events (On-Off)	3	3	10	0.3
Frame Count	10	10	10	1.0
Frame Identification	4	4	10	0.4
Frame Sync Code	21	21	10	2.1
Total		200		20.0

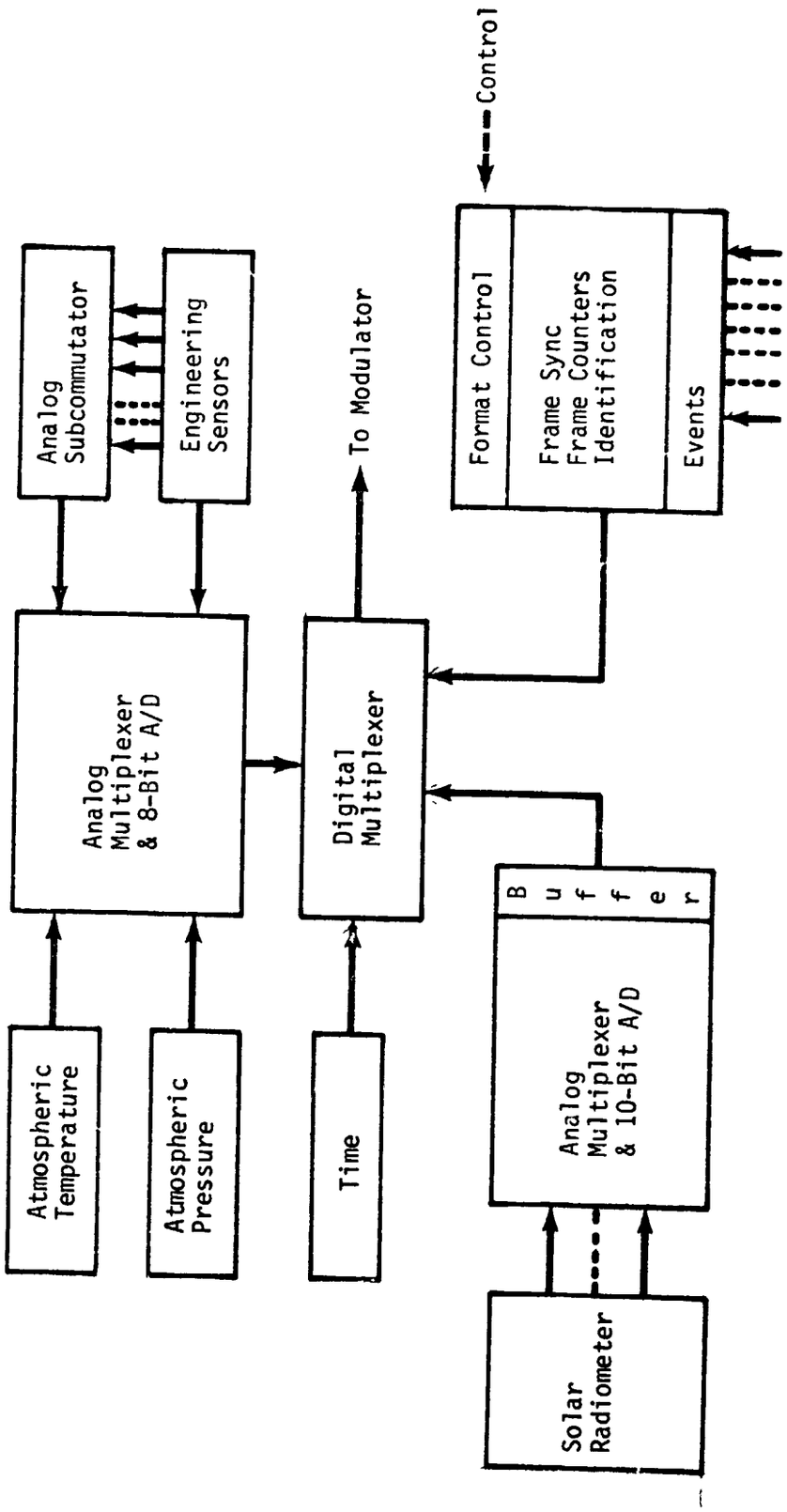


Fig. III-55 Telemetry Data Handling, Balloon Probe (Baseline Option)

Main Frame Format 200 bits/10 sec = 20 bps

Sync	ID	Frame Count	Events	Time	Subcomm Count	Subcomm Channel	Static Phase Error	Atm Temp	Atm Press	Solar Rad
21	4	10	3	6	4	8	8	8	8	120

See Below

Frame Length
200 bits

Subcommutated Channel Format - 1 Meas/90 sec

Calibrate	Batt Volt	Batt Current	Batt Temp	Balloon Temp 1	Balloon Temp 2	Balloon Diff Pressure	Xmtr Power	Events
8	8	8	8	8	8	8	8	8

Fig. III-56 Telemetry Data Formats, Balloon Probe (Baseline Option)

A buffer capacity of 120 bits is required for the solar radiometer so that the detectors can be sampled nearly simultaneously; otherwise, no buffering or storage is required.

6. Power System, Balloon Probes

Much of the discussion in Section B of this chapter on power system and weight estimates for the large ballistic probe also applies to the balloon probes. However, there are some important differences.

The balloons are designed with solar panels and batteries to survive for an extended period after deployment. The nominal design has solar panel capacity for sustained operation on the planet light side, and batteries sufficient for a 7-day life on the dark side of the planet. It will continue to operate indefinitely so long as it always returns to the light side within this 7-day period. This 7-day period can be extended or reduced, as desired, with a weight penalty associated with its darkside lifetime. The battery weight penalty is computed in Chapter VII.F, and the total weight penalty is discussed previously in this section. Sterilizable batteries are assumed.

Design of the solar panels is considered in Chapter VII.F. This design is, of course, strongly affected by the ambient conditions. According to current models, the 500 mb balloon will be below the clouds and the 50 mb balloon may be either in or above the clouds. The design covers both possibilities. The weight and power estimates for 500 mb and 50 mb balloons are given in Tables III-47 and III-48, respectively.

Table III-47 Weight and Power Estimate, 500 mb Balloon Probe

Item	Weight (lb)	Float Active Power (Watts) (7 min each 8 hr)	Float Inactive Power (Watts) (Constant during Balance of Float)
Antenna			
Circular	0.8		
Linear	0.7		
Switch	1.0		
Diplexer	1.4		
Transponder			
RF Exciter	0.9	1.5	
Modulator	0.9	0.5	
Receiver	2.0	0.5	
Ranging	1.5	1.0	
Amplifier (8 Watt)	1.4	29.2	
Sequencer	5.0	3.0	0.1
Data Handling	3.0	3.0	
Inverter	0.5	0.3	
Cabling	5.0		
Battery			
5-Day Dark	7.5		
7-Day Dark	9.1		
10-Day Dark	12.3		
Instrumentation		2.0	
Solar Array Panel	0.9		
Power Conditioning and Distribution	0.3	1.0* (When light only)	1.0* (When light only)
Totals			
5 Day	32.8	Light 42.0	Light 1.1
7 Day	34.4		
10 Day	37.8		
Dark		Dark 41.0	Dark 0.1

*Charge-discharge and line losses included.

Note: Average total array power during light = $\frac{1.1 \times 473 + 42 \times 7}{480}$ = 1.7 Watts

Table III-48 Weight and Power Estimate, 50 mb Balloon Probe

Item	Weight (lb)	Float Active Power (W) (7 min each 8 hr)	Float Inactive Power (W) (Constant during Balance of Float)
Antenna			
Circular	0.8		
Linear	0.7		
Switch	1.0		
Diplexer	1.4		
Transponder			
RF Exciter	0.9	1.5	
Modulator	0.9	0.5	
Receiver	2.0	0.5	
Ranging	1.5	1.0	
Amplifier (8 Watt)	1.4	29.2	
Sequencer	5.0	3.0	0.1
Data Handling	3.0	3.0	
Inverter	0.5	0.3	
Cabling	5.0		
Battery			
5-Day Dark	16.4		
7-Day Dark	21.6		
10-Day Dark	25.7		
Thermal Control	0.5		Variable
Power Conditioning & Dist.	0.6	1.6* (When light only	1.6* (When light only
Instrumentation		2.0	
Solar Array Panel	0.5		
Solar Array Mounting Structure	1.3		
Totals			
5 Day	43.4	Light 42.6	1.7
7 Day	48.6		
10 Day	52.7		
Dark		Dark 41.0	

*Charge-discharge and line losses included.

Note: Average total array power during light = $\frac{1.7 \times 473 + 42.6 \times 7}{480} = 2.30$ W.

The principal difference between the 50 and 500 mb balloons is that the latter is in an acceptable ambient temperature and does not need any thermal control, while the former is in a cold environment and does require an active thermal control system. A vacuum bottle system similar to the one on the descent probes (except that it is designed for lower external pressure) is used to provide insulation. Heating would be thermostatically controlled. Heat dissipated by the electronics (which includes all power used in the probe except the radiated RF signal) is as useful for this purpose as is that generated by the heaters, so the heating load would change as a function of the electronics usage. One consequence of this is that increasing the transmitter power up to the point where it supplies all needed heat during its low duty cycle on-times can be done with little penalty. Insulation has been sized to maintain temperature with about 2.2 W average power. As shown in Table III-49, all of this is generated by the electronics when the probe is on the light side and is periodically communicating with Earth. As the probe goes on the dark side and/or out of sight of Earth, increasing portions of this load are assumed by the thermal control system. It is assumed that the heating requirements do not vary significantly between the light and the dark side.

7. Sequencers for Balloon Probes

The uniqueness of the balloon probe sequencer requirements as compared to the other types of probes is confined to the entry sequencer and results essentially from the requirement for additional discretes to handle the balloon inflation sequence and to cycle the communications and data system over a period of several days following entry. Noted also that no atmospheric pressure referenced events are required and that a g-switch must be added to detect the time for initial aeroshell staging because accelerometers are not included in the data system.

Table III-49 Heating Power Sources, 50 mb Balloon

Item	Light Side		Dark Side	
	Earth Contacts	Earth Not Visible	Earth Contacts	Earth Not Visible
Sequencer Power	0.1	0.1	0.1	0.1
Active Power (Averaged)	0.5	0	0.5	0
Power Conditioning Power	1.6	1.6	0	0
Heater Power	0	0.5	1.6	2.1
Totals (W)	2.2	2.2	2.2	2.2

Since the communications receive system must be cycled on an hourly basis after station deployment as described previously, with data transmissions occurring every 8 hr or less, a clock cycling on an 8-hr basis is required. In the interest of low power consumption to conserve battery life, a low power sequencer similar to the tuning fork and clock mechanism of the coast sequencer can be used to generate the hourly and once per 8-hr time signals. Cycling through the antenna search, carrier transmit, ranging, PCM data transmit and carrier transmit cycles in turn can be controlled electrically by portions of the entry sequencer, which is activated by the tuning fork and clock mechanism. The 8-hr clock mechanism must be designed to withstand the entry environment, whereas the coast sequencer with its common design for all probes does not require it.

Table III-50 gives estimates of time precision for the various types of discretes required in the balloon probe entry and post-deploy operations. For the impacting spacecraft case, the transmitter will be activated at aeroshell staging time in a PCM data mode and the search, ranging, and antenna experiment will be dispensed with until 1 hr later when the system will be available for access by the DSN. This differs from the flyby mission because of an overlap in arrival times of the probes resulting in nonavailability of a DSN uplink channel for the balloon probes.

Table III-50 Timing Precisic.., Balloon Probe Sequencing

Type of Function*	Sequencer		Number of Occurrences		Precision (sec)		Remarks
	Coast	Entry	Coast	Entry	Coast	Entry	
Spinup (Pyro)	X		1		±0.1		
Fire Propulsion Pyro	X		1		±60		
Stop Propulsion (Burn Interval)	X		1		±0.01		Burn interval precision
Transfer to Entry Timer	X		1		±120		
Despin Pyro		X		1		±10	Transfer of timers is time reference for precision
Jettison Weights		x		1		±10	Same
Begin g Sensing		X		1		±10	Same
Release Afterbody (Pyro)		X		1		±0.1g	g reference
Extract Balloon (Pyro)		X		1		±0.1	Timed from g reference
Inflate Balloon (Pyro)		X		1		±0.1	Same
Release Chute(Pyro)		X		1		±0.1	Same
Terminate Inflation (Pyro)						±0.1	Same
Release Inflation System (Pyro)						±0.1	Same
Begin Search for DSN Signals		X		†		†	
Turn on Xmtr Section		X		†		±0.1	
Open Ranging Channel		X		†		±0.1	
Close Ranging Channel		X		†		±0.1	
Begin PCM Data Transmission		X		†		±0.001	
End Data Transmission		X		†		±0.001	
Switch to Linear Antenna		X		†		±0.1	
Turn Off Data System		X		†		±0.1	

*Functions not necessarily in sequence.

†Begins at extract balloon during entry for flyby case and continues through cycle for total of 7½ minutes. During flotation period of several days, search for signal begins once every hour with precision of ±5 sec. If DSN signal is sensed, the cycle is continued and runs for 7½ minutes, otherwise receiver is shut down until the next hour.

§For impacting spacecraft case only PCM data transmission is enabled during entry. There is an arrival time overlap with other probes for the impacting spacecraft case which results in a nonavailability of an uplink channel.

F. REFERENCES

III-1 *1972 Study of a Flyby/Entry Probe Mission Study.* AVCO/JPL Report.

III-2 *Buoyant Venus Station Mission Feasibility Study.* NASA CR-66725-3, January 1968.

III-3 William C. Lindsey: *A Theory for the Design of One-Way and Two-Way Phase-Coherent Communications Systems.* JPL Technical Report 32-986, July 15, 1969, p 20.

III-4 *Criteria to Establish RF Compatibility between DSIF and Spacecraft Projects.* JPL Document 831-1, Rev A, October 1, 1968, p 3-64.

III-5 R. Stevens and J. F. Koukel to F. E. Goddard and H. J. Stewart: "Outer Planet Mission Telecommunications System Characteristics." JPL Interoffice Memo 3300-68-819, August 5, 1968.

III-6 J. A. Heller: *Sequential Decoding: Short Constraint Length Convolutional Codes.* JPL Space Program Summary 37-54 (Vol III).

III-7 William C. Lindsey: "Coded Noncoherent Communications." *IEEE Transactions on Space Electronics and Telemetry,* March 1965.

III-8 M. Easterling: *Digital Communications with Space Applications.* (S. W. Golomb, Ed.) Prentice-Hall, 1964, Chapter 6.

IV. PLANETARY VEHICLE SYNTHESIS

A. BASELINE FLYBY MISSION

The requirements of the Planetary Vehicle were defined as those operations and functions necessary to support, orient, provide services such as thermal control, power conditioning, separation, and biological protection for the entry vehicles. Another important function was to provide a single clean interface between the multiple entry probes and the Mariner spacecraft. These criteria have served to avoid duplication of items required by each probe while on the Planetary Vehicle, and to allow use of the Mariner spacecraft as the core member with as few modifications as possible.

The basic components of the Planetary Vehicle are the Mariner spacecraft, the capsule adapter, (and its subsystems), and the entry capsule systems. The Launch Vehicle adapter is considered a part of the Planetary Vehicle only from a build and supplier standpoint; however, in operation it stays with the Launch Vehicle at staging.

The Planetary Vehicle uses the Mariner communications, attitude control system (ACS), and propulsion as its main operating systems during interplanetary cruise, midcourse maneuvers, and separation orientation. The orientation maneuvers will be accomplished using the Mariner ACS (with resized thrusters) in the same mode it was designed for. After a gyro warm up command and the change to inertial reference, all vehicle attitudes will be controlled by automatically programing the ACS system. Eight maneuvers are required as defined in Chapter V.C to position and separate all probes and return to the sun-Canopus reference. This operation

will require slightly over 2 hr off-sun time using the normal turn rate (both pitch and roll) of 3.1416 mrad/sec. Additional power is provided on the capsule adapter for this period, however it may be deleted if further spacecraft system operational and design data permits. Attitude error build up during the separation sequence is contributed to by the initial reference error (sun-Canopus), the time dependent gyro drift, and time dependent calibration errors. The effect of these errors is discussed in Chapter VIII.D. However they can be reduced if required, by increasing vehicle turn rates, and by subtracting out predefined gyro drift errors. The system shall be automatic so that the sequence needs no additional earth commands subsequent to the initial r orient signal. Interlocks that open when the proper separation attitude has been achieved, as well as when probe separation has occurred, are required to allow the sequence to proceed. Command access is also required to continue the sequence in the event of a separation failure, and the system could be stepped to the next probe to be separated.

After all probe separations are complete, the Planetary Vehicle returns to its sun-Canopus reference in preparation for the encounter.

1. Engineering Mechanics

The Planetary Vehicle structural assembly includes the modified Mariner spacecraft, the adapter truss assembly, and the payload adapter. The probe assemblies are not considered a part of the adapter structure required to support the loads.

The total Planetary Vehicle is supported above the Titan IIIC transtage interface by the payload adapter. It attaches and separates from the booster through pyrotechnic nut/bolts at four equally spaced longerons. The adapter truss assembly provides the integrated attachment of all probe systems to the spacecraft

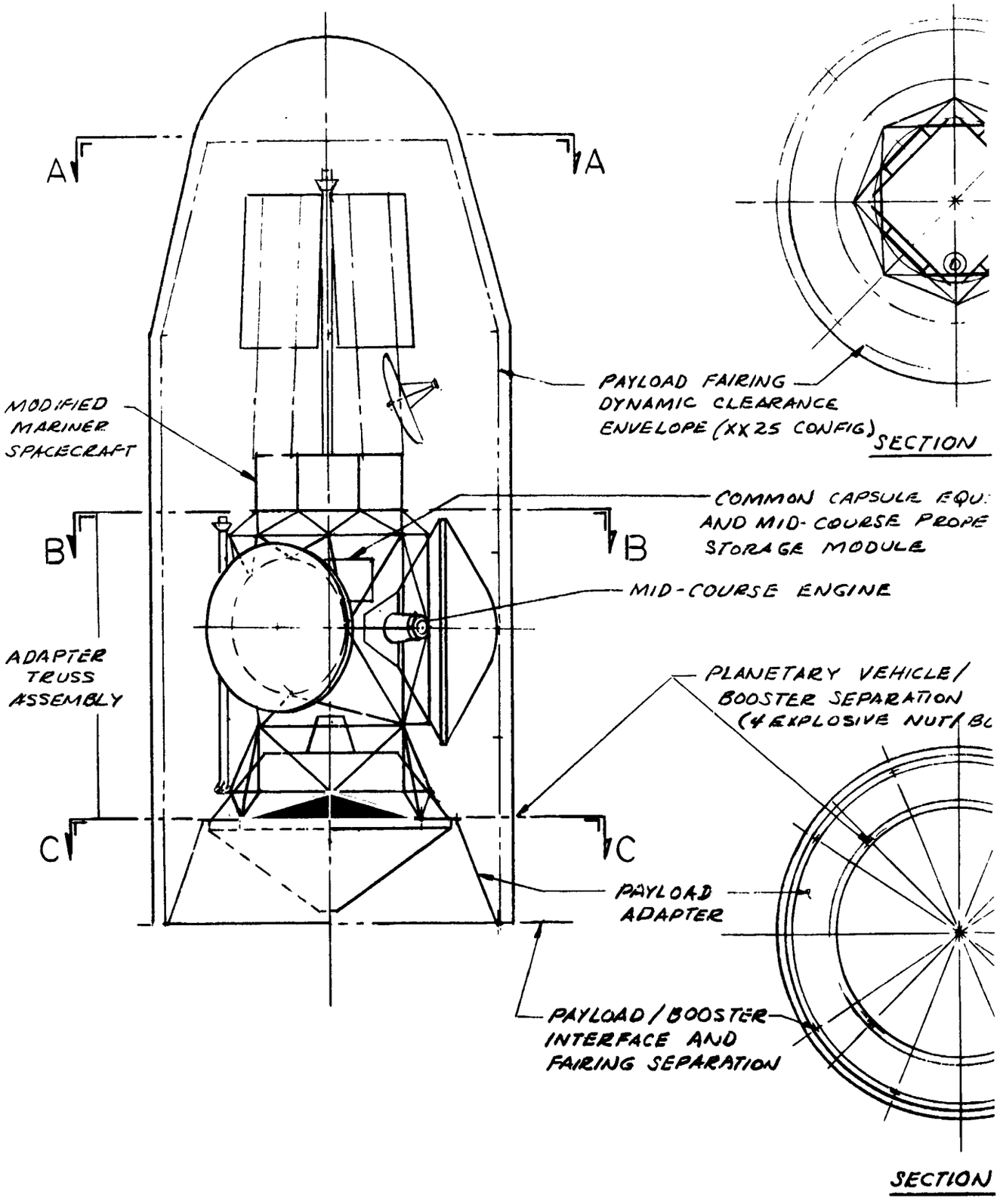
during the trans-Venus cruise mode, as well as support on the booster to transmit the launch and acceleration loads. It provides the facility of attaching each probe system independently to the truss and the support for all equipment necessary to integrate the capsule systems into the Planetary Vehicle system. This is characteristic of the baseline and the optional mission probe complements as well. The general arrangement for the baseline is shown in Figure IV-1 and weights are summarized in Table IV-1.

a. Functional Description - The probes are arranged and spaced apart in the assembly so that the reaction to the separation impulses imparted to each probe is directed through the center of gravity (cg) of the remaining mass. The cg of the planetary system is on the vertical centerline when all probes are attached and when only the Mariner spacecraft and the large probe remain. The small probes are shown located in a diametrical plane with their centerlines normal to the centerline of the Planetary Vehicle at its cg. This arrangement allows the probes to be located at varied angles within the adapter assembly if advantages can be gained in separation and deflection toward their respective targets. These aspects have not been investigated in this study.

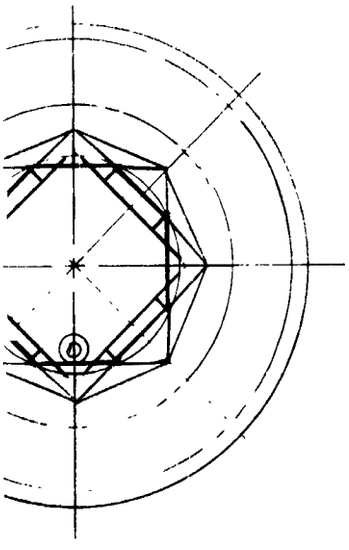
The arrangement of locating the spacecraft at the upper end of the payload is typical for the baseline and Options 1 and 2. The large probe is located symmetrically on the centerline because it offsets the spacecraft mass so that a constant cg can be maintained during probe separation providing it is the last probe separated.

Table IV-1 Planetary Vehicle Weight Summary
(for Flyby Spacecraft)

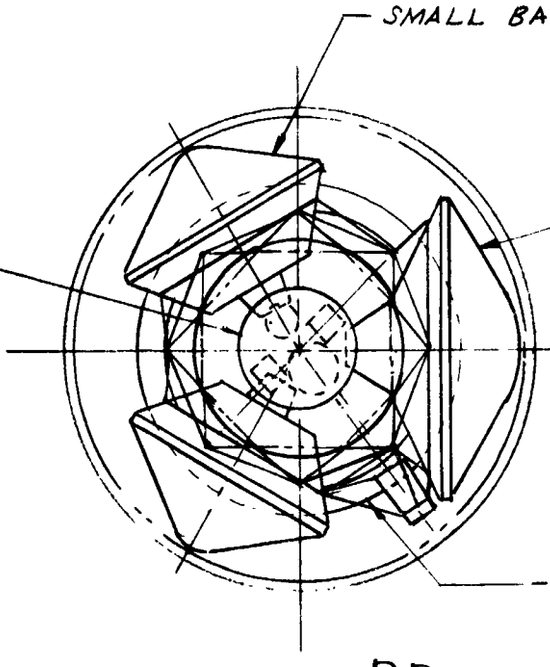
Baseline		Weight (lb)
Probes Separated (4)		1381.6
Biocanisters/Adapters		171.0
Upper Atmosphere Science and Electronics		0*
Adapter Truss Assembly, Umbilicals, and Cabling		292.0
Payload Adapter		98.0
Spacecraft		819.5
		2762.1
Contingency		386
		3148.1
*Included in probe weights.		
†Breakdown as follows:		
Structure (less 49 lb for Launch Vehicle adapter)		156
Radio		49
Command		9.5
Power		94
Central Computer and Sequencer		18
Telemetry		23.8
ACS		62
Pyro		130
Cabling		68.5
Propulsion (midcourse)		50
Thermal		29.0
Mechanical Devices		27.3
Data Storage		22.0
Data Automation		23.0
Scan Control		24.2
Microwave Imager		36.0
Additional ACS (Increased Thrust Levels)		12.0
Common Capsule Adapter Module		102.2
Structure/Thermal Control	18.0	
Power and Electronics	44.2	
Additional Midcourse Propulsion System	40.0	
		819.5



FOLDOUT FRAME



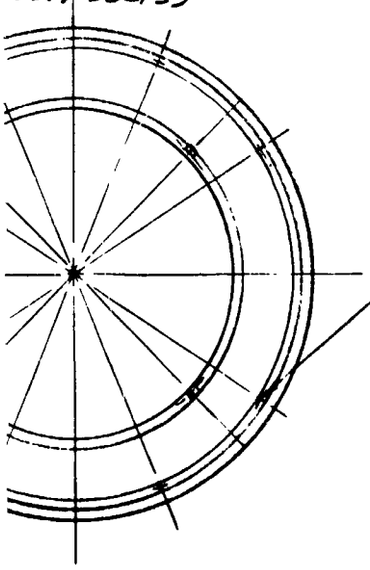
CTION A-A



SECTION B-B

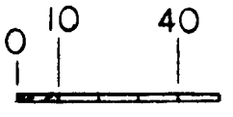
E EQUIPMENT
PROPELLANT
E

ICLE/
TION
NUT/BOLTS)



STANDARD BOLT LOCATIONS AT BOOSTER INTERFACE (111.77 B.C. DIA. - BASIC) LIGHT PAYLOAD STRUCTURAL INTERFACE

ECTION C-C



(BASELINE)

Fig. IV-1 Planetary Vehicle/Booster Integration, Baseline

FOLDOUT FRAME 2

b. Structure-Payload Adapter Configuration - The payload adapter is a cone frustum longeron-stiffened shell structure with a major ring frame at each end. The Planetary Vehicle system is mounted above the upper frame through pyrotechnic nut/bolt attachments at four equally spaced longerons. These pyrotechnics separate the Planetary Vehicle from the booster. The longerons provide the primary axial load-carrying members in transmitting the booster acceleration to the payload. The booster side of the payload interface is made up of eight longeron attachment points that are not equally spaced. All points need not be used for payload attachment. The stiffened shell provides the transition due to mismatch between the longerons as well as side shear and torsional load stability.

This configuration results from a cursory investigation of the total adapter structure problem. A design study and analysis may find it more economically from a weight standpoint to align the payload separation points with four of the booster attachments.

c. Structure-Adapter Truss Assembly Configuration - The structural adapter truss assembly is a welded aluminum tube truss that provides the longitudinal load carrythrough between the booster separation plane and the Mariner spacecraft and all probes systems between. It attaches or separates from the payload adapter through pyrotechnic nut/bolt assemblies at four equally spaced longeron pads. The truss assembly extends the four longeron members through the lower large probe standoff truss. A major ring frame is built in at the lower end of the standoff to provide lateral support for the A-frame braces and the longerons that extend outward and down to the load pads that mate with the adapter longerons. The large probe canister/adapter is supported within the envelope provided by the longerons/A-frames/ring by means of tension attachments to

the ring frame. The four pyrotechnic nut/bolts that support the large probe internally within its canister are located coincident with the four main truss support points at the lower end of the standoff truss. The large probe is supported during launch through tension of these bolts. A major ring arrangement is provided at the upper end of the standoff truss to provide a lateral support for the diagonal truss members that make the standoff segment rigid, as well as the adapters and the bracing to support the small probes.

Each probe, independently canistered before final installation is supported off the primary longitudinal truss members within a ring adapter. Since the three smaller probes are equally spaced within this structural segment, only two of the four equally spaced lower longitudinal truss members can be extended directly upward. The other two are extended diagonally upward to meet at an upper ring. The ring adapters are built into the truss framework to provide mutual interconnection and bracing to effect the longitudinal structure continuity to the spacecraft and the stability for lateral loads. A cone frustum upper ring is made up of a network of regular diagonally patterned trusses between an interface ring at the base of the Mariner spacecraft and a larger ring that is integrated into the lower structure.

Diagonals primarily in the diametral plane will be incorporated between opposite corners and at the probe adapter rings to make the truss assembly rigid for overall torsional stability, as well as to react the kick loads due to the eccentricity of the small probes with their respective mounting interface ring and the primary structure.

2. Telecommunications System

Overall design of the Planetary Vehicle telecommunications system is outside the scope of this program, which is limited to consideration of modifications to the AVCO Configuration 20a Mariner. For the flyby option, no modifications are required.

3. Data System - Common Capsule Adapter (CCA)

The Common Capsule Adapter data system for the baseline Planetary Vehicle must process all capsule status monitoring data for transfer to the spacecraft flight telemetry system (FTS). The type of data to be sampled for the various entry capsule and common adapter instrumentation are shown in Table IV-2.

Table IV-2 Typical Measurement List for CCA Cruise Telemetry

For All Capsules
Structural Temperature 1, 2
Battery Voltage
Battery Current (Charge)
Battery Temperature
Sequencer Temperature
General Instrumentation & Events (CCA Mounted Sensors)
Capsule Separation Indicators (Switches)
Common Capsule Sequencer Status (Discretes)
CCA Temperature 1
CCA Temperature 2
CCA Temperature 3
CCA Temperature 4
Note: Sampling intervals are not critical for the measurements during cruise. Intervals of 10 to 15 minutes should be adequate except for the discretes that may require monitoring at intervals of a minute or less during capsule separation sequencing.

Provisions for accepting these data by the spacecraft FTS must be accomplished. One approach is to use the subcommutators already existing in the capsules along with their sensors to provide capsule monitor data to a CCA main commutator. In some cases this will require gating of the channels to change inputs and eliminate others. Further, these subcommutators and sensors must be designed so that sources external to the capsule can supply power, control, and clocking for the monitoring function.

There are several approaches to providing output to the FTS. The output can be digital (7 bits) to feed to a "spare" digital status channel or it can be subcommutated analog to a spare channel of the main FTS analog deck with digital discretes to the FTS digital multiplexer. Decisions of this nature are deferred to a later study when the overall engineering and DAS channel assignments for the spacecraft can be defined.

In general, the central spacecraft subsystems will supply the power, timing, and control for the CCA data system as indicated in Chapter V.F.

4. Power System

Functions carried out during interplanetary cruise by the common capsule to spacecraft adapter (CCA) include trickle charging to maintain battery condition within the probes, periodic monitoring of engineering measurements within the probes, and probe heating power. It is estimated that probe heating will not be required. However, heaters and thermostats will be installed for protection against unanticipated low temperatures. Power required to do the monitoring will be negligible. Power for trickle charging is also negligible, less than 1 W for the whole system including the batteries to be mounted on the truss (discussed below). This total load of about 1 or 2 W can be placed on the regular spacecraft power system without noticeable effect.

The probe ejection maneuvers will place a burden on the spacecraft power system because of loss of power from the solar panels while they are off the sun during these maneuvers. The maneuver time duration will be about 2.1 hr for the baseline mission, rising to 2.5 hr if Option 1 is added. Option 2 does not add any maneuver time.

The Mariner specifications give a spacecraft battery capacity of 900 W-hr (M69-4-2004B, p 11) and a power usage rate during maneuvers of 430 W (M69-3-250B, p 23). This is increased to 432 W by the probe load. This will exhaust the spacecraft battery capacity in 2.08 hr. However, it has been decided that the spacecraft battery reserve should not be used during maneuvers for probe launch. An additional battery will be placed on the adapter truss. It will have sufficient capacity to carry the spacecraft through the probe ejection period. This battery will be placed on the same bus as the spacecraft battery, thus enlarging its capability.

Additional capacity needed is 965 W-hr for a 2.1-hr period and 1150 W-hr for a 2.5-hr period. Using the derating and weight calculation procedure described in Chapter VII.F, the following weights are calculated:

2.1-hr maneuver, 34.5 lb;

2.5-hr maneuver, 39.4 lb.

An unsterilized battery can be used for the flyby option.

After completion of the probe ejection maneuvers, the spacecraft could return to sun orientation. It would then have about 11 days for the batteries to recover before the flyby or impacting portion of the mission. Sizing of the spacecraft solar panels is beyond the scope of this program, but they could be substantially smaller than the 83 sq ft panels used on the Mars 1969 mission, which would deliver an estimated 1500 W in the vicinity

of Venus. A solar cell area of 27 sq ft would deliver around 500 W, which should be sufficient. A weight and power summary is presented in Table IV-3.

Table IV-3 Weight and Power Summary, Electronics and Power System, Planetary Vehicle CCA, Baseline Flyby Mission

Item	Weight (lb)	Power (W)
Battery	34.5	
Cabling	6.5	
Battery Charging		1.0
Probe Heating	1.0	1.0
CCA Multiplexer Converter	0.5	0.4
Engineering Instrumentation	1.5	0.3
CCA Sequencer	0.2	0.5
Total	44.2	3.2

5. Common Capsule Adapter Sequencer

a. Requirements - The function of the Common Capsule Adapter Sequencer (CCAS) is to provide the common sequencing discretes for separation of all capsules from the spacecraft on command from the spacecraft CC&S and report back to the CC&S when separation has occurred.

The required output discretes are:

a) Arm, fire, and safe - all biocanisters pyro;
b) Report above accomplished to spacecraft CC&S;
c) Start coast sequencer - first capsule;
d) Arm, fire, and safe - first separation;
e) Report above accomplished to spacecraft CC&S;
f) Repeat c), d), and e) in turn for each capsule on command from the spacecraft CC&S.

b. Description - The CCAS for the flyby mission is a rather simple device. It consists of a counter with three separate outputs occurring 2 sec apart in sequence plus logic to detect occurrence of separation events for each of the biocanisters and capsules. The three timed outputs are reset and switched in a stepped fashion to the next pyro function or event each time a command is received from the CC&S. The confirmation of events having taken place is the presence of a voltage that can be detected by the spacecraft CC&S. The sequencer is an all solid-state device that interfaces with the spacecraft subsystems to obtain power, countdown clock pulses, and command signals.

B. BASELINE DIRECT IMPACT MISSION

The Planetary Vehicle for the impacting mission is similar in almost all respects to the flyby Planetary Vehicle. The major difference is the addition of the high altitude instruments to the capsule adapter truss, and the positioning of the scan platform. Additional support equipment for the science instruments is also required.

System operation is identical except for separation altitudes and times.

1. Engineering Mechanics

The impacting configuration is similar to the flyby and spacecraft except that the upper atmosphere instruments are mounted on the truss (Fig. IV-2). The sun-Canopus reference is maintained during upper atmosphere measurements and sampling ports of the instruments are aligned with the spacecraft velocity vector.

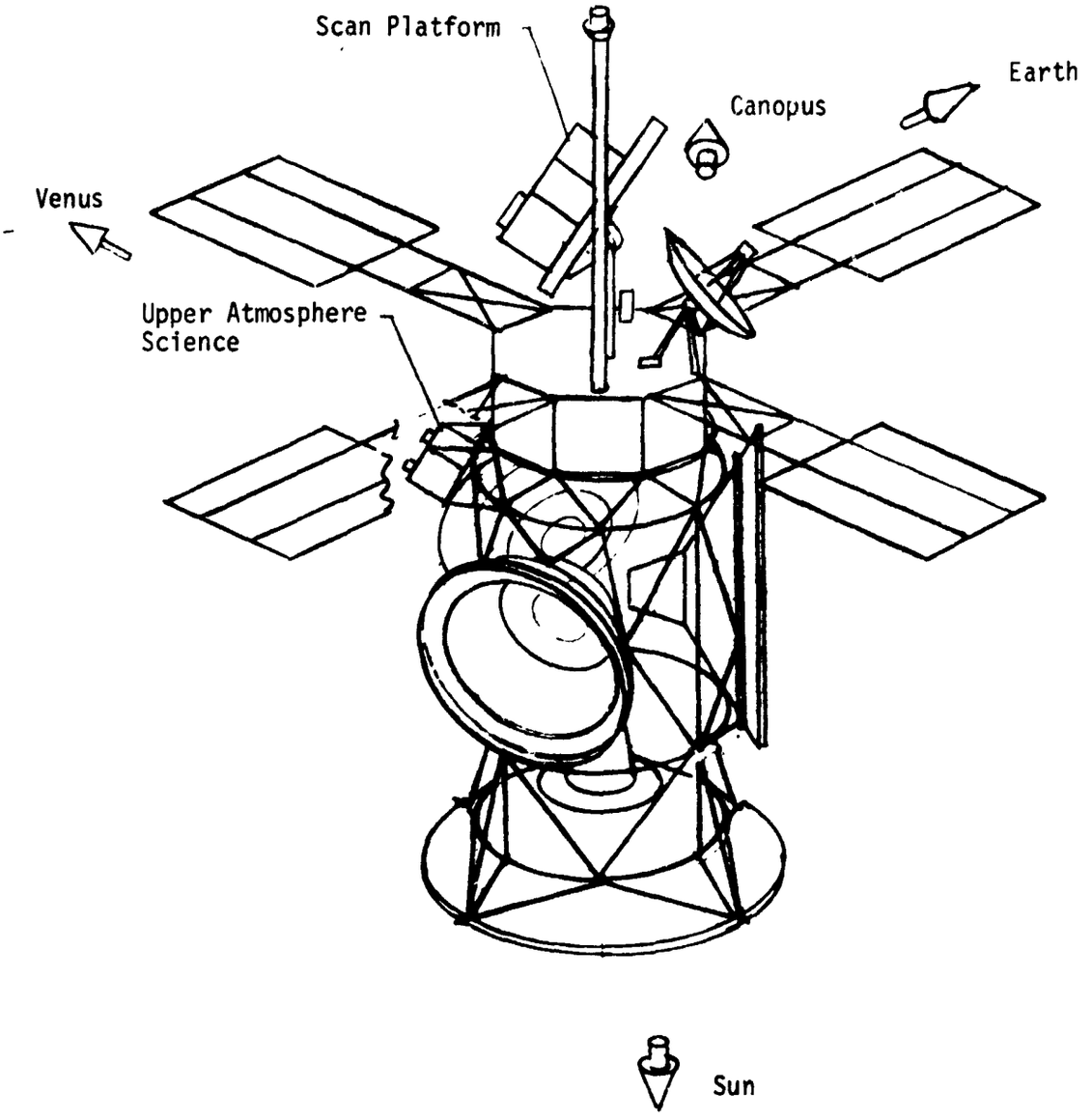


Fig. IV-2 Impacting Spacecraft Configuration

Weights are the same as the flyby Planetary Vehicle, Table IV-1, except as influenced by deflection propulsion requirements and the location of the upper atmosphere instruments on the spacecraft instead of on the large descent probe, i.e., "probes separated" now weigh 1325 lb and total Planetary Vehicle weight is 3118.6 lb. The spacecraft weight is 824 lb including an increase of 4.5 lb in battery weight for operation of the upper atmosphere instruments.

2. Telecommunications System

The impacting spacecraft option will require a number of changes from the 20a configuration, because the 20a configuration was designed for a flyby mission. The relatively low data rate of the 20a configuration requires storage of the flyby science data, with subsequent low-rate playback and transmission after encounter is completed. This option is not open to an impacting spacecraft. Also, the impacting spacecraft has a high-altitude science mission from 5 radii to 0.1 g in addition to the science mission specified by AVCO. The data generation rate of the latter mission is 4640 bps. (See table 5.14, AVCO report.) This is increased by 180 bps, to 4820 bps by the high-altitude science mission at the end of the flight. Since no storage can be used, this must all be transmitted in real time. AVCO's mission has the spacecraft communication into an 85-ft dish. Using the 210-ft dish will permit the necessary data rate, with a substantial margin. This is demonstrated in the link calculation, Table IV-4. This calculation allows a small amount of power for a second low rate (8 1/3 bps) subcarrier for engineering data.

Table IV-4 Link Calculation, Downlink, Spacecraft

Item	Parameter	Nominal (db)	Adverse Tolerance (db)
1.	Total Transmitter Power, 20 W	+43.0 dbm	0.4
2.	Transmitter Circuit Loss	-1.3	0.3
3.	Transmitter Antenna Gain	+23.5	0
4.	Transmitter Antenna Pointing Loss	0	0.5
5.	Space Loss, 2297 MHz, 95 x 10^6 km	-259.2	0
6.	Multipath and Atmospheric Losses	0	0
7.	Polarization Loss	-3.0	0.5
8.	Receiver Antenna Gain, 210-ft Dish	+61.4	0.3
9.	Receiver Pointing Loss	0	0
10.	Receiver Circuit Loss	-0.1	0
11.	Net Circuit Loss	-178.7	1.6
12.	Total Received Power	-135.7 dbm	2.0
13.	Received Noise Spectral Density, 35°K	-183.1 dbm	0.6
Carrier Performance, Data Demodulation			
14.	Carrier Power to Total Power	-17.0	0.5
15.	Received Carrier Power	-152.7 dbm	2.5
16.	Carrier Threshold Bandwidth, 12 Hz	+10.3	0.5
17.	Threshold S/N in 2 B_{LO}	+15.0	0
18.	Threshold Carrier Power	-157.8 dbm	1.1
19.	Margin, Carrier	+5.1	3.6
Data Channel Performance			
20.	Receiver Loss	-0.5	0.1
21.	Data Channel Power/Total	-0.1	0.1
22.	Total Data Power	-135.1 dbm	2.2
23.	Data Threshold E/NO	+2.5	0
24.	Data Rate, 4820 bps	+36.8	0
25.	Data Channel Threshold	-143.8 dbm	0.6
26.	Data Channel Margin	+8.7	2.8

Accordingly, it is recommended that the spacecraft use this higher rate for real time readout of all its science, and that it be allocated a channel in the 210-ft dish receiver. As shown in the sequence of events chart, Chapter II.B, there will be other probes communicating during part of this period. This will use the full two-way Doppler capability of the network, so during this portion of the mission, the spacecraft will be required to use a one-way link (no Doppler). These probes use linearly polarized antennas and the DSN antenna will be configured for linear polarization also. Therefore, a 3 db polarization loss is shown in Table IV-4.

3. Data System - Common Capsule Adapter (CCA)

The data system for the CCA for the impacting spacecraft mission performs the same functions as for the flyby spacecraft mission plus the added function of processing data for the following encounter instruments located on the CCA truss:

Ion mass spectrometer;

UV radiometer;

Neutral particle spectrometer;

Electron temperature and density instrument.

The desired sampling rates, bits per sample, and resulting desired bit rates for the above science instrumentation are assumed to be the same as if they were included in the large probe, and therefore are the same as shown in Chapter III.B.

For purposes of estimating power and weight, it is assumed that the instruments are buffered as for the large probe for the flyby case and present a digital interface with the spacecraft DAS, which is undefined for this study,

Power, control, and clocking for this data system are assumed supplied by the spacecraft subsystems.

4. Power System

The power system differs little from the system described for the baseline flyby missions. Since sterilizable batteries must be used, the battery weight for the 2.1 hr maneuver load will be 37.5 lb instead of 34.5 lb.

The entry science power load that will occur during encounter is estimated at 38 W in addition to the normal spacecraft load. This can be delivered by the regular spacecraft system without modification. The weight and power summary for the direct impact mission is presented in Table IV-5.

Table IV-5 Weight and Power Summary, Electronics and Power System, Planetary Vehicle CCA, Baseline Direct Impact Mission

Item	Weight (lb)	Power (W)
Battery	37.5	
Cabling	6.5	
Battery Charging		1.0
Probe Heating	1.0	1.0
CCA Multiplexer Converter	0.5	0.4
Engineering Instrumentation	2.0	0.3
CCA Sequencer	0.2	0.5
Science Data Processor	1.0	0.3
Total	48.7	3.5

5. Common Capsule Adapter Sequencer

The Common Capsule Adapter for the baseline impacting spacecraft mission is the same as for the baseline flyby spacecraft mission because it does not perform any data system control functions associated with the encounter science.

C. OPTIONAL MISSION PLANETARY VEHICLE CONFIGURATION

Optional mission Planetary Vehicle for Option 1 mission is identical in all respects to the baseline excepting the provisions for one additional probe.

The Option 2 Planetary Vehicle places two additional entry probes in a second plane (between the first plane and the spacecraft). These probes are equipped with reaction jet separation and spin systems, since spring reaction forces for separation could not be directed through the vehicle center of gravity, and disturbing torques would be produced.

The attitude sequence for Option 1 requires one additional attitude (two maneuvers) because a new target site has been identified -- light side morning terminator. The Option 2 sequence can be completed with no additional maneuvers above the Option 1 by properly clocking the probes going to identical target zones.

1. Engineering Mechanics

a. Option 1 Structure Description - The structural adapter truss assembly for the Option 1 mission (Fig. IV-3) is different than the baseline in that more weight is boosted and four smaller probes are accommodated in the diametrical plane instead of three. The four probes allow symmetry in the spacing of the probes and are compatible with the four primary longitudinal members to be maintained at equal spacing, which carries through from the booster separation. The Option 1 weight summary is shown in Table IV-6.

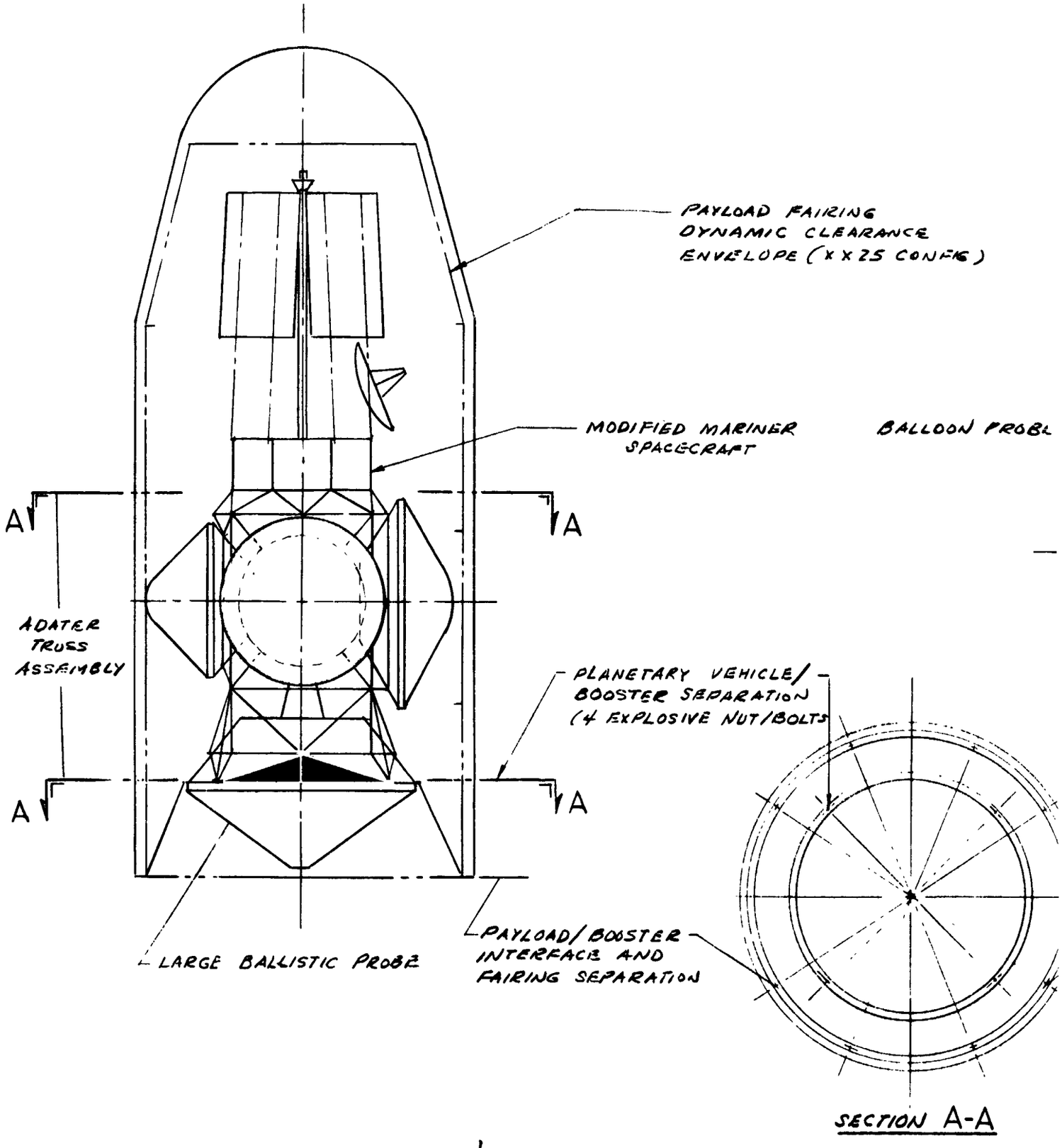
Table IV-6 Planetary Vehicle Weight Summary, Option 1

Item	Weight (lb)
Probes Separated (5)	1570
Biocanisters/Adapters	206
High Altitude Science and Electronics	25
Adapter Truss Assembly Umbilicals and Cabling	313
Payload Adapter	100
Spacecraft	824
	3038
Contingency	443
Total	3481

b. Option 2 Structure Description - The structural adapter truss assembly for the Option 2 mission is basically same as the baseline in regards to the general arrangement and the functional performance of the major structural systems. Two diametrical tiers of probe systems are required to accommodate the six smaller probes. By locating four in one tier and two in the other, the four primary longitudinal member structural arrangement is retained. The packaging arrangement shown is not optimized and poses problems of control and maneuver. The main advantage of this arrangement is that all probes installed in this position require no deployment for cruise mode and are in a position that each can be separated independently without mutual interference. The Option 2 weight summary is shown in Table IV-7.

Table IV-7 Planetary Vehicle Weight Summary, Option 2

Item	Weight (lb)
Probes Separated (7)	2247
Biocanisters/Adapters	292
High Altitude Science and Electronics	25
Adapter Truss Assembly Umbilicals and Cabling	429
Payload Adapter	105
Spacecraft	824
	3922
Contingency	78
Total	4000



FOLDOUT FRAME 1

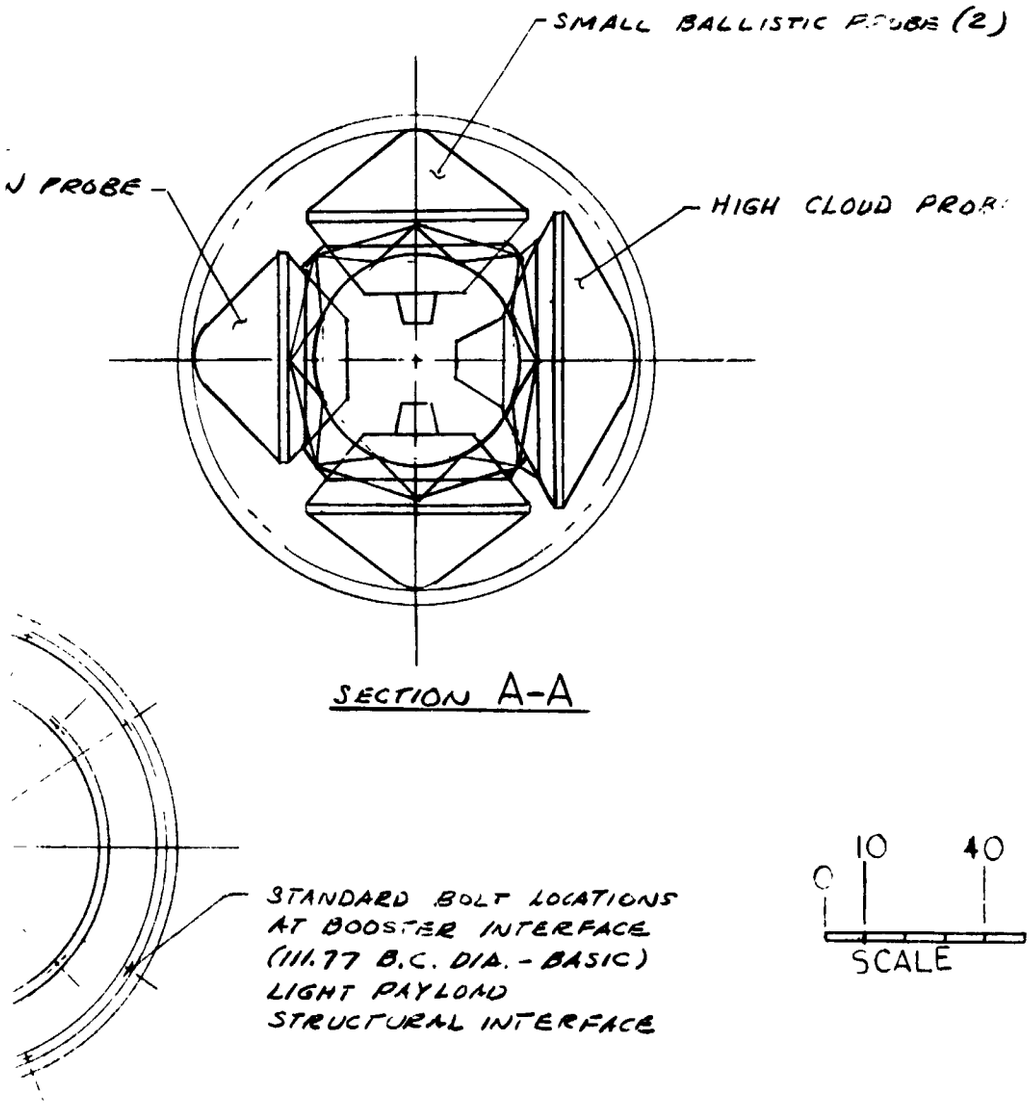


Fig. IV-3 Planetary Vehicle/Booster Integration, Option 1

FOLDOUT FRAME 2

2. Telecommunications System

The optional add-on missions have no effect on the Planetary Vehicle telecommunications system. The descriptions of the flyby and impacting vehicles apply here.

3. Power System

The maneuver time for probe separation is increased from 2.1 to 2.5 hr by the addition of Option 1. This increases the battery size to 39.4 lb (flyby mission, unsterilized batteries) or 42.4 lb (impacting mission, sterilized batteries). Except for this change, the power system is identical to that for the baseline missions. The weight and power summary for the optional missions is presented in Table IV-8.

Table IV-8 Weight and Power Summary, Electronics and Power System, Planetary Vehicle CCA, Optional Missions

Item	Flyby		Direct Impact	
	Weight (lb)	Power (W)	Weight (lb)	Power (W)
Battery	39.4		42.4	
Cabling	6.5		6.5	
Battery Charging		1.0		1.0
Probe Heating	1.0	1.0	1.0	1.0
CCA Multiplexer Converter	0.5	0.4	0.5	0.4
Engineering Instrumentation	1.5	0.3	2.0	0.3
CCA Sequencer	0.2	0.5	0.2	0.5
Science Data Processor			1.0	0.3
Total	49.1	3.2	53.6	3.5

4. Common Capsule Adapter Sequencer

For the optional missions the CCAS must accommodate an additional stepping sequence to handle one additional capsule for Option 1 and three additional capsules for Option 2. The effect on size, weight, power, and interface is negligible.

D. MODIFICATIONS TO THE SPACECRAFT

1. Systems Engineering Requirements

The task of Planetary Vehicle synthesis was approached with a philosophy of using existing designs. The operational capabilities of AVCO configuration 20a were retained where possible, and were departed from only where requirements for modification were identified. As a particular example, the capsule separation philosophy, together with the design of separation mechanisms and the separation sequence are aimed at minimum disturbance to the spacecraft and its normal operating modes. The modifications that are summarized in the following paragraphs are compatible with existing spacecraft design practices. The modifications will require review as the designs are developed to evaluate the interactions between subsystems and also to detail the interfaces of the Planetary Vehicle.

2. Structural Modifications (Refer to Fig. IV-1)

a. Relocation of Equipment - The spacecraft is mounted above the adapter truss assembly in the booster fairing, thus avoiding loads on spacecraft structure during launch and boost that are imposed by other than the spacecraft subsystems. The scan platform and the enlarged ACS gas supply tanks are mounted above the spacecraft octagon body in the same manner as the reference 20a configuration. The view angle requirements for the antennas, scan platform, and other equipment will necessitate relocation of the equipment on the top side of the octagon structure. Since adequate space is available, the equipment need not be cantilevered laterally with respect to the body structure. The inertia loads induced on spacecraft structure by the mass of this equipment should not exceed those for the 20a configuration because ACS gas supply weight increases are more than offset by scan platform weight decreases.

The total mass of equipment supported through the spacecraft/adapter truss interface, is less than in configuration 20a because no probe system equipment is supported by the Mariner body.

b. Relocation of Midcourse Engine - The midcourse propulsion unit will be relocated to a position on the adapter truss in the diametrical plane of the Planetary Vehicle center of gravity. It will be supported off the main adapter truss by an auxiliary truss mount that would position it so that the engine exit plane is outside the extremity of any probe biocanister (reference section B-B of Fig. IV-1). The 90° clock angle location of the 20a configuration will be achieved by rotating the probe package and the adapter truss with respect to the spacecraft.

c. Propellants and Pressurants - The midcourse propellant supply and pressurant tanks, probe systems control and sequencing equipment, and battery pack are contained in an equipment module added for the 1975 multiprobe mission. The module is located below the spacecraft, body centered, and supported by the adapter truss. The propellant supply is located near the midcourse engine to facilitate engine feed and thermal control.

d. Low-Gain Antenna - It will be necessary to relocate the deployable low-gain antenna of AVCO configuration 20a to provide an unobstructed field. The antenna will be mounted on the lower end of the probe support truss.

e. Solar Panel Hinges - As presently defined, the solar panel hinge locations are the same as in configuration 20a. If required they can be set out or lowered to be coincident with the lower face of the body. This change would be made by extending the hinge mounts and bracing externally to the body to avoid changes to the inner octagon structure.

3. Midcourse Propulsion Modifications

a. Total Impulse Requirements - The spacecraft configuration 20a has a total Planetary Vehicle weight of 1350 lb and uses the Mariner '69 propulsion system. That system has 21.5 lb of propellant. Total impulse requirements for the baseline mission will be greater than configuration 20a by the weight ratio of 2762 lb or, 2.05. Thus, approximately an additional 22 lb of propellant would be required to provide the same capability, and the burn time would increase from approximately 80 sec to 160 sec. An allowance of 40 lb of system weight has been included in the spacecraft weight (Table IV-1) to account for the extra propellant load and resulting propulsion system weight increases, including pressurant and tankage.

b. Moment Arm Requirements - Since the cg of the Planetary Vehicle is now located at the center of the small probe cluster, the propulsion system will be relocated on the adapter truss in the plane normal to the roll axis containing the new cg. The changed moment arm for the jet vanes, in addition to vehicle inertia changes by factors of 3 in roll and 10 in pitch, will undoubtedly necessitate changes in the autopilot gains.

c. Increased Burn Time Requirements - The increased burn time required, ∿160 seconds, will necessitate modifications to the hydrazine catalytic bed since it is currently limited to about 100 sec of operation. Other components of the propulsion unit may also require revisions due to the longer burn time, e.g., exhaust products may tend to collect on the jet vanes presenting the possibility of binding in the mechanism, also valve operation vibration limits may be exceeded, and valve damage could occur from heat soak back.

d. Plume Impingement - The exit plane of the rocket exhaust will be located outboard of any other systems to minimize the effect of plume impingement. However, the heating and contamination influence on surfaces of the insulation layers on the probe biocanisters and on the probe separation pyrotechnics in the vicinity must be evaluated before final location of the engine is established.

4. Thermal Control Modifications

The louvers, as discussed in Chapter VIII.A may require modifications due to either the reversal of the solar panels or the solar exposure incurred during the deflection maneuver. The thermal interface between the payload and the Planetary Vehicle in the 20a configuration was essentially adiabatic, and this concept would be retained by minimizing thermal conductance through the payload adapter. Moving the midcourse engine and the hydrazine and pressurant tanks from the interior of the spacecraft to the adapter truss and the common capsule adapter, respectively, simplifies the thermal control requirements of the Planetary Vehicle. However, provisions must be made to accommodate them at their new location. The common capsule adapter would be protected with multilayer insulation and a thermal control coating just as the probes are. The engine and connecting feed lines will be maintained within the 35°F to 90°F allowable operating temperature. This will be accomplished by insulation and coating provisions similar to those employed for probe thermal control plus a heater system, if found to be necessary on the basis of detailed analysis.

5. Attitude Control System Modifications

The moment of inertia of the Planetary Vehicle with the four probes mounted is much greater than that for configuration 20a. This is indicated in Table IV-9.

Table IV-9 Moment of Inertia Summary, Baseline Planetary Vehicle

Principal Moment of Inertia	Configuration 20a Baseline, One Probe, Total Weight 1350 lb (slug-ft^2)	Baseline Current Study, Four Probes, Total Weight 2762 lb (slug-ft^2)	Baseline Current Study, All After Probes Ejected (slug-ft^2)
Roll	160	570	208
Pitch	100	1030	415

Also, additional maneuvers are required to orient for the probe ejections. Consequently a study was conducted to determine how the ACS gas requirement would be affected if the accelerations of the 20a configuration were retained at $\sim$0.8 mrad/sec^2 by increasing the thrust levels proportionately and if the existing π mrad/sec turn rate was also retained. For an upper bound, it was assumed that the spacecraft would be reoriented to sun-Canopus after each probe ejection. The results of the study indicate that 3.12 lb of gas would be required for the entire mission including: tip-off, stabilization, midcourse correction (normally accomplished by jet vanes), probe orientation and ejection, and final return to sun-Canopus, assuming only one set of valves is operating. This would mean carrying 9.36 lb of gas, to permit the depletion of one of the two gas tanks at launch, which is the standard criterion. This would require an increase of 3.36 lb over the 6.0 lb current capacity. The corresponding thrust levels would be 0.043 lb in pitch and in yaw and 0.025 lb in roll.

Subsequent to the above study, a probe separation sequence was developed based on not returning to sun-Canopus after each probe ejection. For this case propellant usage would be slightly less because of the fewer number of turns, and hence, acceleration cycles. However, a time-off-the-sun of 2.08 hr results. This raises the question of whether the ACS turn rate should be increased to shorten turn time, thereby reducing the time-dependent

error build-up (gyro drift), and also the battery weight required. In this investigation, lower thrust levels were also established to prevent the acceleration of the reduced inertia spacecraft (after final probe ejection) from exceeding the 0.8 mrad/sec^2 considered to be the maximum allowable for the Mariner. These thrust levels are 0.018 lb in pitch/yaw and 0.009 lb in roll. Corresponding accelerations before the first probe ejection are 0.33 mrad/sec^2 in pitch and 0.30 mrad/sec^2 in roll.

The results of this analysis are shown in Fig. IV-4. The propellant weights shown are only for the probe orientation maneuvers themselves, and are seen not to be a controlling factor. Time-off-sun can be reduced to 1.2 hr and battery weight can be reduced by about 20 lb if peak turn rates are increased to a value constrained by the 0.8 mrad/sec^2 acceleration rate, i.e., the turns would consist of an acceleration and deceleration cycle with zero coast time.

The need for operating in the above mode is primarily dependent on error build-up considerations because the battery weight is not critical. If the error build-up rate of the JPL/AVCO study is used (0.24°/hr, which is believed to be conservative) an acceptable situation exists with the normal turn rate (nominal time-off-sun of 2.08 hr) with the possible exception of the antisolar probe in the flyby/spacecraft case for which a slightly greater range error than desired results. Probe deflection errors are discussed further in Chapters VIII.D and II.E.

It is concluded that for the baseline mission the thrust levels should be increased to 0.018 lb and 0.00[illegible] lb in pitch and yaw, respectively, and the turn rate retained at π mrad/sec.

Modifications to the ACS are also brought about by the physical relocation of the propulsion system to a different location and its increased impulse requirements.

Acceleration Limits (mrad/sec²)	Thrust Levels Pitch/Roll	
	Min Required (lb) (All Probes in Place)	Max Allowable (lb) (All Probes Ejected)
0.8 (Max)	N/A	0.018/0.009
0.2 (Min)	0.011/0.006	N/A

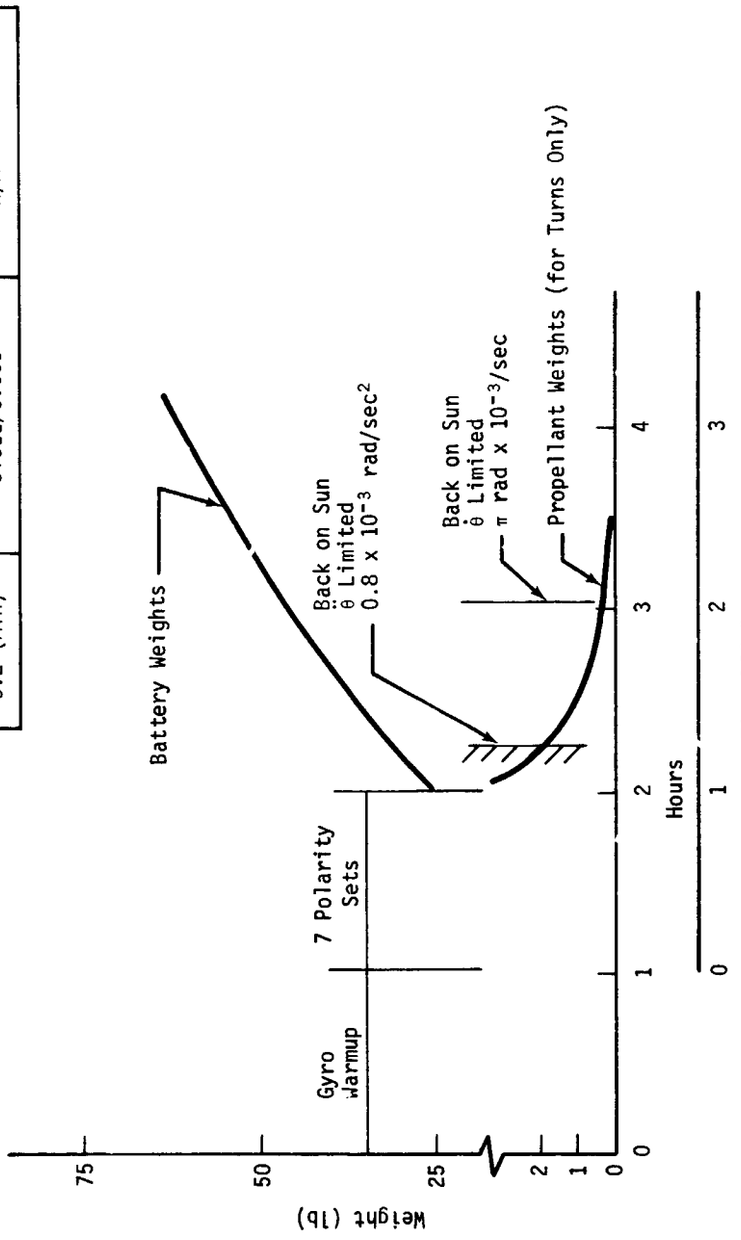


Fig. IV-4 Sensitivity of ACS Gas Weight and Spacecraft Battery Weight to Maneuver Time

6. Telecommunications Modifications

One of the two low-gain antennas of configuration 20a has been relocated to the probe support truss. Cabling and junctions necessary to connect this antenna to the spacecraft RF system must be supplied.

7. Power Modifications

The capsule will require power from the spacecraft, battery trickle charging, and operation of the CCA data system. Power consumption is estimated to be less than 3 W. Solar panel sizing would have to be designed for this mission (27 sq ft is estimated).

8. Sequencer

The sequencing discretes for capsule separation will be generated by the Common Capsule Adapter Sequencer (CCAS). The sequences will be initiated by the spacecraft CC&S, and operations of the CCAS will be reported back to the CC&S.

V. SYSTEMS ENGINEERING SUPPORTING STUDIES

A. BASELINE MISSION PROFILE

The baseline mission, consisting of three ballistic probes descending to the surface of Venus and one probe to investigate the region of high clouds, is described in this section. A top level diagram of Multiple Probe Systems is shown in Fig. V-1. Relationships between probe subsystems are shown in Fig. V-2. This section summarizes the mission profile following the sequence of the functional flow diagrams contained in Section B of this chapter.

1. Prelaunch Operations

The Entry Capsule systems will be weighed, balanced, and built up sequentially in all configurations in which they must later be dynamically stable to assure that separation and jettison functions do not cause instability. Operations involving exposed equipment that will enter the Venus atmosphere will be done in sterile facilities meeting the requirements of planetary quarantine. The individual capsules and the spacecraft will be installed on adapter structure as checked out systems and interface wiring will be verified. For the impacting spacecraft mission, a biocanister covering the entire planetary vehicle will be provided. Adapter structure includes the capability to mate with the Titan IIIC Launch Vehicle, including the XX25 Payload Fairing. The payload assembly will be covered with a protective shroud or dummy fairing. Following transport to the launch pad, and hoisting into the Universal Environmental Shelter of the Mobile Service Tower, the spacecraft will be mated to the Launch Vehicle and the flight fairing installed. Final checks will include powering up of all subsystems for verification. Entry Capsule checkout capability will be provided through the Common Capsule Adapter.

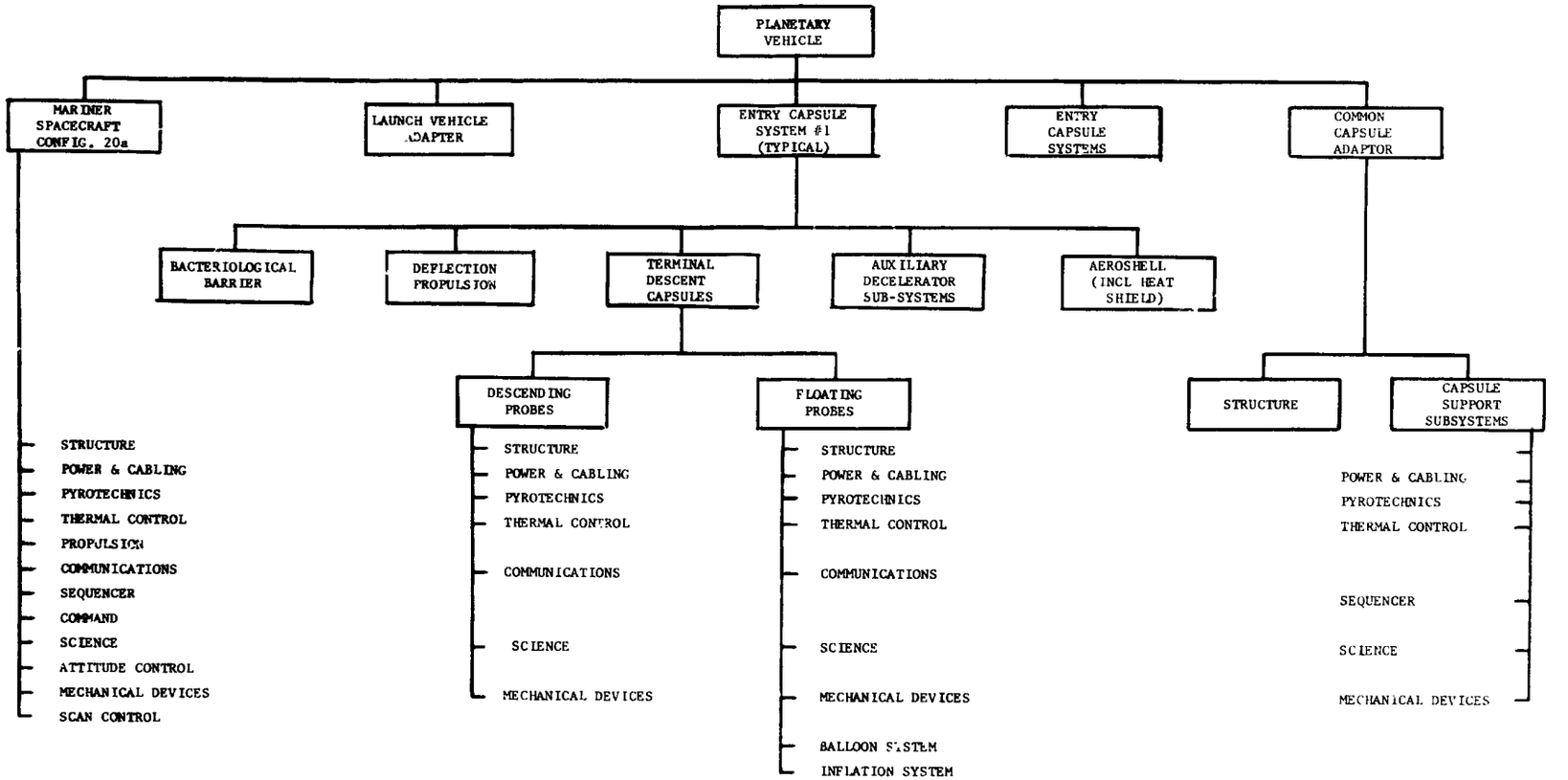


Fig. V-1 Multiple Probe Syste s Top Level Diagram

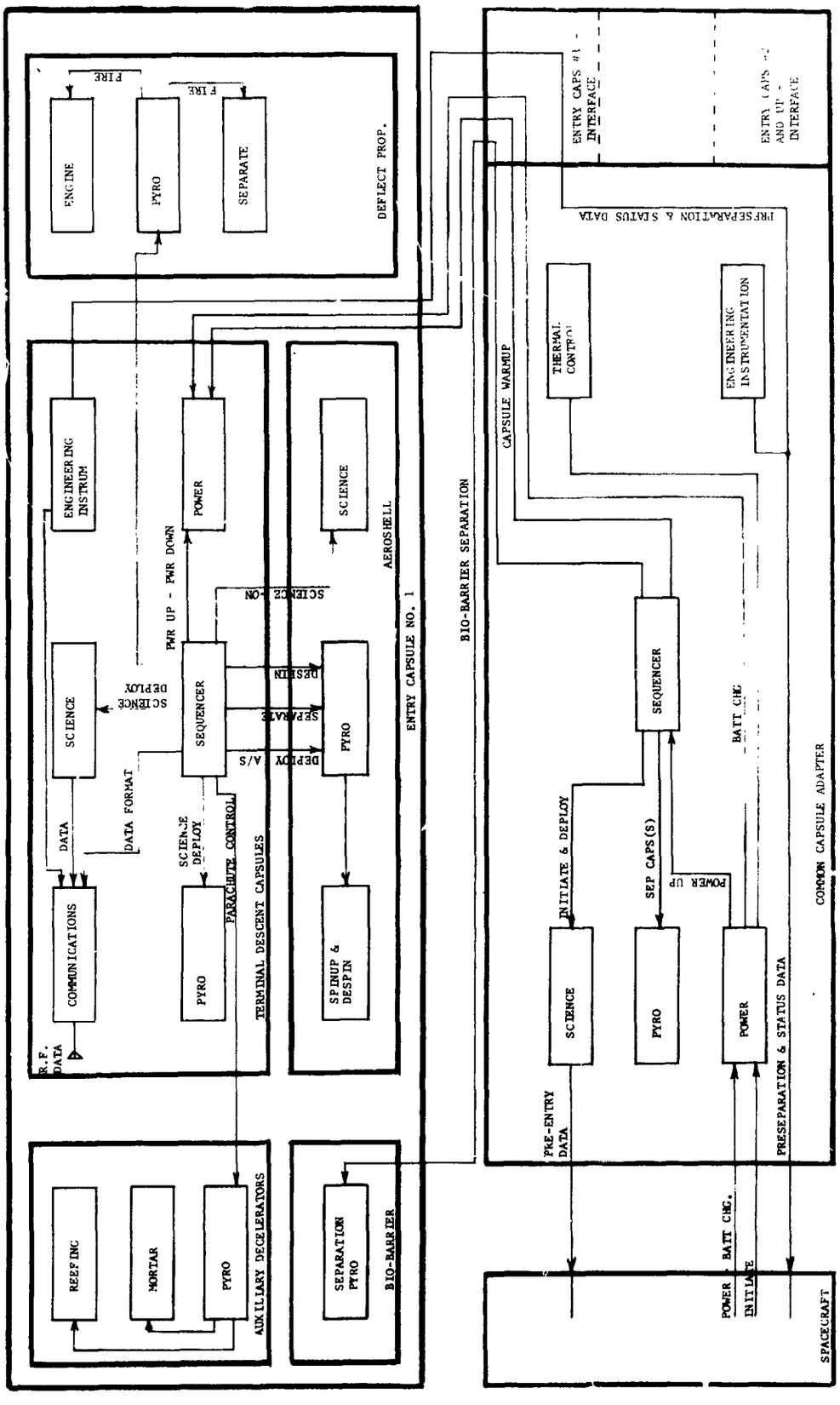


Fig. V-2 Composite Diagram of Systems

Probe Systems Interfaces - Interfacing systems of the probes that will later be active during the mission will be checked out in the interfacing configurations. This will include verifying and maintaining the charge of the flight batteries.

2. Launch

The Titan IIIC with Planetary Vehicle payload will be available for the launch period of May 15, 1975 to June 4, 1975. Final on-pad checks will include readiness monitoring of Entry Capsule systems. The countdown will proceed according to normal Titan IIIC procedures with respect to the Launch Vehicle and according to normal Mariner procedures for the payload. The Launch Vehicle will boost the payload out of the Earth's atmosphere and Payload Fairing separation will occur at launch plus 280 sec. If the mission is for an impacting spacecraft rather than a Venus flyby, the main biocanister will also be separated at this time.

Entry Capsule System Interfaces - The Entry Capsule Systems are inactive during launch.

3. Planetary Vehicle Separation

The Planetary Vehicle will separate from the Titan IIIC Transtage, which will remain on a noninterplanetary trajectory. The Mariner spacecraft will place the Planetary Vehicle on the trajectory for Venus encounter. Mariner solar panels will be deployed and the spacecraft systems will be activated. Trickle charging power for the Entry Capsule batteries will be provided by the spacecraft, and Entry Capsule monitoring data will be transmitted over the spacecraft communications link.

Entry Capsule Systems Interfaces - The Common Capsule Adapter will distribute battery charging power to the Entry Capsules and will accept and format status monitoring data for delivery to the spacecraft telemetry system.

4. Interplanetary Cruise

During the period of interplanetary cruise the Planetary Vehicle will be under the control of the Mariner systems. Orientation of the +Z axis, on which the Entry Capsule systems will be mounted, will be toward the sun. Thermal control of the Entry Capsule systems will be exercised through the selection of surface coatings and internal arrangements that will retain temperature limits within specified values. Attitude control will be provided by Mariner navigation and control systems, which will be modified from the AVCO configuration 20a to compensate for the larger moments of inertia. Midcourse maneuvers will be performed according to normal Mariner procedures.

Entry Capsule Systems Interfaces - These interfaces will be the same as for the preceding phase.

5. Preseparation

As the deflection radius (4×10^6 km from the center of Venus) is approached, preparations will be made for capsule separation from the Planetary Vehicle. These will include a final survey by flight controllers of capsule systems data, verification of spacecraft systems, the actual trajectory, and orientation. The spacecraft gyros will be activated and allowed to warm up for a period of 64 minutes followed by separation of the biocanister from all capsules. The spacecraft will then transfer to inertial reference and execute a pitch maneuver of 20° followed by the roll maneuver required for the first capsule. The attitude control system will then be locked and the sequencer of the common capsule adapter will be initiated. Separation of the first capsule will follow as described in the following subsection.

Preseparation preparations for the second and following capsules will be the same as for the first, beginning with the Planetary Vehicle maneuver.

Entry Capsule Systems Interfaces - Interfaces between the systems of the Entry Capsules consist of requirements on the communications (data) system for the collection of status information.

6. Capsule Separation and Spin Up

Capsule orientation in space and separation from the Planetary Vehicle will be controlled by the Mariner spacecraft. The sequencer of the common capsule adapter will be initiated via the Mariner command link and will control the sequence of release of the individual capsules.

Upon receipt of the ground initiated command the biocanisters of all capsules will be separated and separation verified. The spacecraft will then maneuver to the attitude for first capsule release. The maneuver will be accomplished on inertial reference from the spacecraft gyros and will consist of a pitch turn followed by a roll turn. Turning will be accomplished at a constant rate of 3.1416 mrad/sec with impulse forces supplied by the cold gas jets of the spacecraft attitude control system.

For the baseline mission, capsule separation forces will be supplied by springs restrained by an ordnance-operated mechanism. The first capsule to be released will be the small ballistic probe to the South Pole. The capsule separation reaction force will be directed through the center of gravity of the remaining Planetary Vehicle. This will permit a separation velocity of 1 fps to have little effect on orientation of either the released capsule or the Planetary Vehicle.

One second after separation the capsule will be spun up about the longitudinal axis to an angular velocity of about 3 rad/sec. The spin up impulse will be delivered by Jets, will last for approximately 0.5 sec, and will not affect the spacecraft.

Capsule System Interfaces - Capsule interfaces in the separation and spin-up phase consist of:

1) Power requirements on the sequencer for signal impulses;
2) Pyro requirements on power and the sequencer for arming, firing, and safing functions;
3) Sequencer requirements on power for electronic timer operation;
4) Propulsion requirements on structure for release and on pyro and sequencer for initiation.

7. Probe Deflection

Each spinning probe will drift away from the spacecraft with its postseparation velocity until the deflection propulsion impulse.

Each probe sequencer will have been referenced by the spacecraft to a deflection time that is preselected for each probe.

Deflection impulse, to be supplied by solid rocket motors, will occur 20 minutes after separation with each probe given the velocity increments shown in Table V-1.

Table V-1 Probe Separation and Deflection

No.	Probe	Target	Planetary Vehicle Attitude		Probe Deflection (mps) / (lb-sec)
			Pitch (deg)	Roll (deg)	
1	Small Ballistic	South Pole	+17	0	45 / 1160
2	Hi-Cloud	South Pole	+17	-120	45 / 1240
3	Small Ballistic	Anti-solar	+9	-240	70 / 1810
4	Large Ballistic	Sub-solar	+105	-120	0.3 / 53

The deflection velocity will cause the probes to disperse to their respective targets. Following deflection the deflection modules will be jettisoned.

Probe System Interfaces - Probe system interfaces during this phase consist of:

1) Pyro requirements on power for firing;
2) Pyro requirements on sequencer for arming, firing, and safing;
3) Sequencer requirements on power for operation of the electronic timer;
4) Propulsion requirements on structure (mechanisms) for orientation of the thrust vector and on pyro for initiation.

8. Probe Coast and Despin

Probe systems will be dormant during coast to conserve battery power. The dormant period will occur upon switching control to a mechanical timer and shutdown of the electronic timer. The electronic timer will be reactivated for system warmup 20 minutes before entry. Five minutes before entry despin weights will be deployed to reduce the angular velocity to approximately .5 rad/sec and the weights will be jettisoned. The nutation half angle after despin will be retained below 2.5°.

Probe System Interfaces - Probe system interfaces during this period consist of:

1) Structural (mechanism) on pyro for deployment and jettison of despin weights;
2) Power requirements on the sequencer for initiation and termination of the dormant period;
3) Pyro requirements on power and sequencer for arming, firing and safing;
4) Sequencer requirements on power for preentry warmup.

9. Probe Entry and Aeroshell Deceleration

For the baseline mission the three ballistic probes and the high cloud probe will enter the atmosphere (considered to start at an altitude of 815,000 ft above the reference radius of 6050 km) at the conditions shown in Table V-2.

Table V-2 Baseline Mission Entry Parameters

Probe	Target	Entry Latitude (deg)	Entry Longitude (deg)	Entry Angle, γ_E (deg)
Large Ballistic	Subsolar	-1.0	24.38	-50
Small Ballistic	South Polar	-62.0	83.14	-25
Small Ballistic	Antisolar	0.42	157.75	-35
High Cloud	South Polar	-62.0	83.14	-25

Aeroshells will provide stability and aerodynamic drag and will contribute to thermal protection through use of a heat shield. The entry heat pulse will last for approximately 12 sec, resulting in a structural maximum temperature of 600°F. Maximum temperatures at peak dynamic pressures will not exceed 300°F. Ballistic coefficients and entry load factors for the baseline mission are shown in Table V-3.

Table V-3 Aeroshell Loads

Probe	Target	Ballistic Coefficient	Maximum Loading (g)
Large Ballistic	Subsolar	0.37	342
Small Ballistic	South Polar	0.4	184
Small Ballistic	Antisolar	0.4	232
High Cloud	South Polar	0.2	187

For the ballistic probes entry will be sensed by an accelerometer at 0.1 g when the deceleration curve has a positive slope. This will be used to activate recording of entry data for later transmission.

Probe System Interfaces - Probe systems interfaces during aeroshell deceleration consist of:

1) Requirements of all systems on the structure to withstand entry loads and heating;
2) Requirements of communications (data) and science for power;
3) Requirements of sequencer on science for sensing entry.

10. Probe Parachute Deceleration

Parachute deployment will be accomplished by means of a mortar-deployed drogue which extracts the main parachute. The systems will be designed for deployment at Mach numbers and dynamic pressures as shown in Table V-4. Actual values and deployment altitude will be referenced to acceleration levels also shown in the table. Parachute deployment will be followed by aeroshell staging and deployment of science instruments.

For the ballistic probes, the data stored entry will then be transmitted on a "first in-first out" basis interleaved with real-time data. Parachute release will be initiated by pressure sensing at the altitudes shown in the table.

Probe Systems Interfaces - Probe systems interfaces during parachute deceleration consist of:

1) Structural requirements on pyro for parachute deployment;
2) Pyro requirements on power and sequencer for operation;
3) Communications requirements on power and sequencer;
4) Sequencer requirements on science for sensing accelerations and pressures;
5) Science requirements on power and on structure and pyro for deployment;
6) Decelerator requirements on pyro for deployment and release.

Table V-4 Parachute Deceleration Phase

Probe	Target	Ballistic Coefficient	Deployment				Release	
			Mach No.	q	Altitude (km)	g (ref)	Altitude (km)	Pressure (bars)
Large Ballistic	Subsolar	0.035	0.95	39.6	6122.25	2.7	6084.99	7.0
Small Ballistic	South Polar	0.015	0.92	24	6124.5	1.5	6099.99	1.35
Small Ballistic	Antisolar	0.015	0.79	25	6122.72	1.5	6099.99	1.35
High Cloud	South Polar	0.005	0.92	12	6127.95	1.5	6099.99	1.35

Note: Altitudes are referenced to the MMC lower atmosphere.

11. Probe Terminal Descent

This phase begins with parachute release after which the ballistic probes will continue to collect data to the surface (6050 km). The high-cloud probe will not be designed for operation below 1.0 bar. The ballistic probes will be switched to one-half their previous data rates at an altitude of 6060 km, as sensed by a pressure of 50.0 bars in the MMC lower atmosphere.

Probe Systems Interfaces - The probe system interfaces during terminal descent consist of:

1) The requirements of communications and science, each on the other, and of both on power, thermal control, and sequencer;
2) The requirements of sequencer on science for sensing the data rate switching pressure.

12. Spacecraft and Common Capsule Adapter

Impacting Spacecraft - Following capsule separation the Planetary Vehicle will consist of the spacecraft and the components of the Common Capsule Adapter (CCA). Among the latter will be four instruments for gathering encounter science data beginning at a

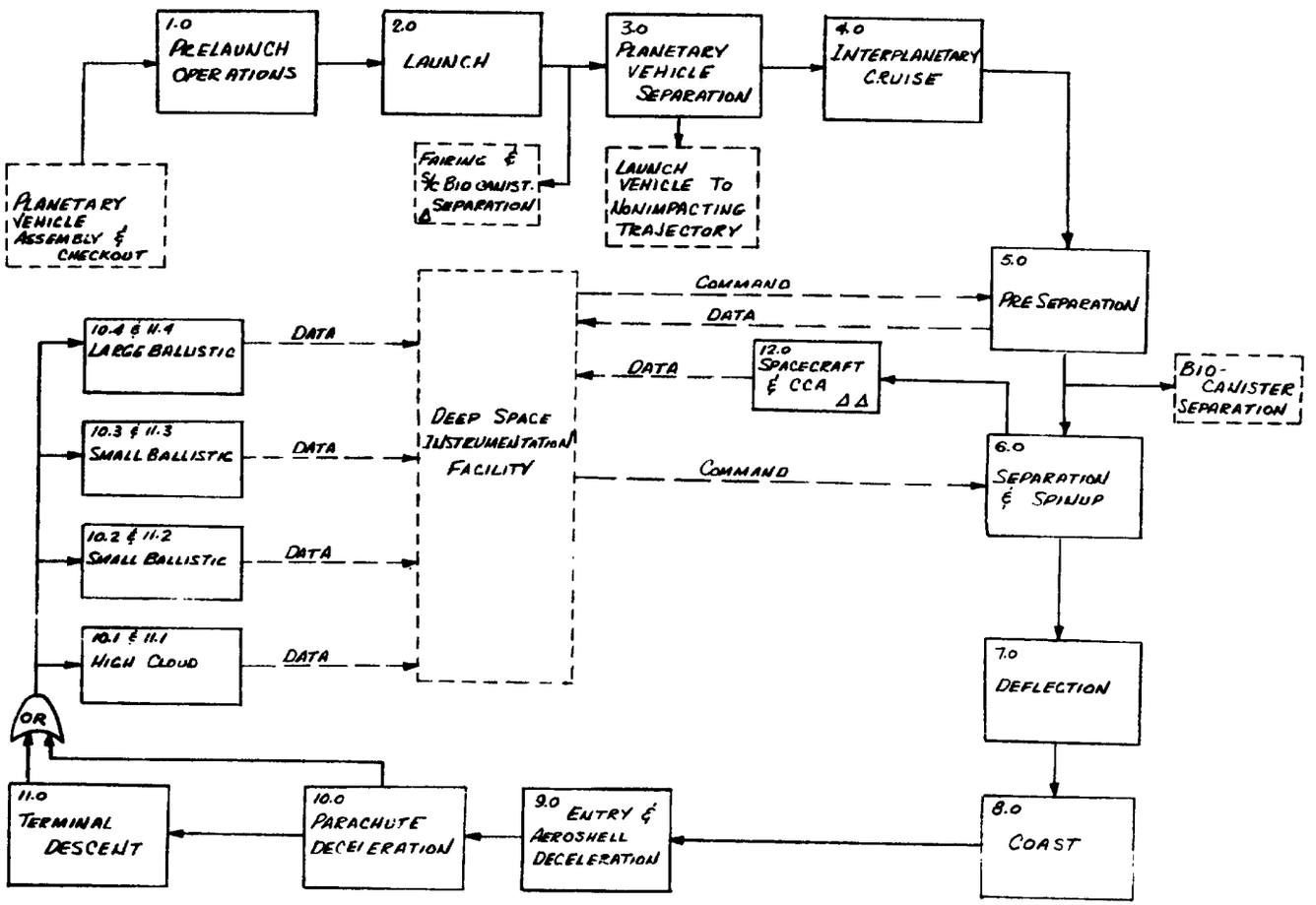
distance of 5 planet radii from Venus. Data will be processed by the Common Capsule Adapter data system and routed to the spacecraft for transmission to Earth. No protection will be provided against the entry environment and the spacecraft will be destroyed.

Common Capsule Adapter Interfaces - Interfaces consist of the requirements of:

1) Science and data on power (CCA battery) for operation;
2) Science and data on sequencer for activation signals to be issued 1 hr before entry.

B. MISSION FUNCTIONAL FLOW DIAGRAM

Flow diagrams showing the functional sequence from launch to mission completion are shown in Fig. V-3 thru V-9. The major phases of Fig. V-3 are keyed to the Baseline Mission Profile Summary of Section A of this chapter for reference, and are backed up with lower functions in the figures following.



PHASES 5.0 THROUGH 12.0 ARE AMPLIFIED IN SHEETS FOLLOWING.

Fig. V-3 Functional Flow Diagram Baseline Mission Phase

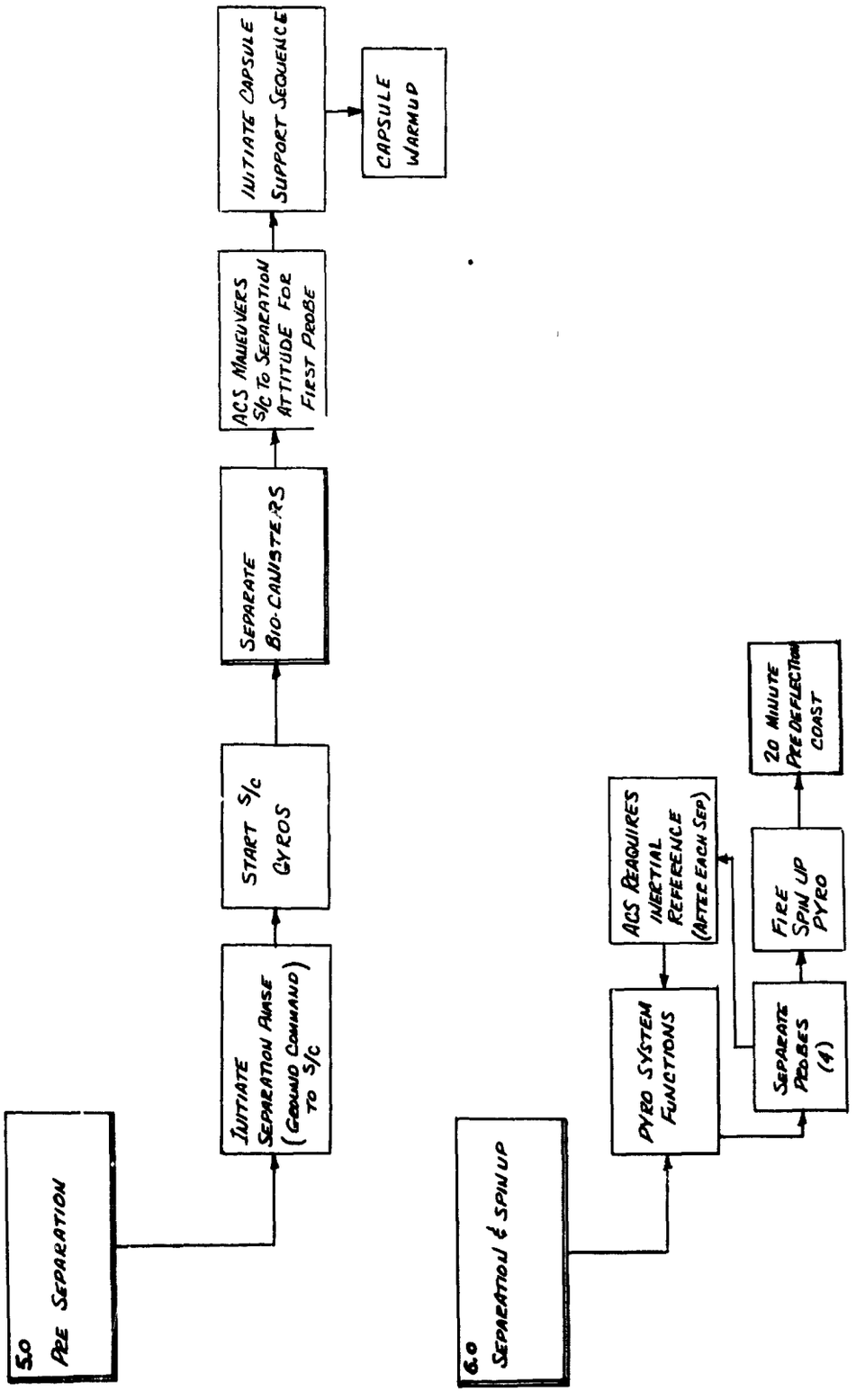
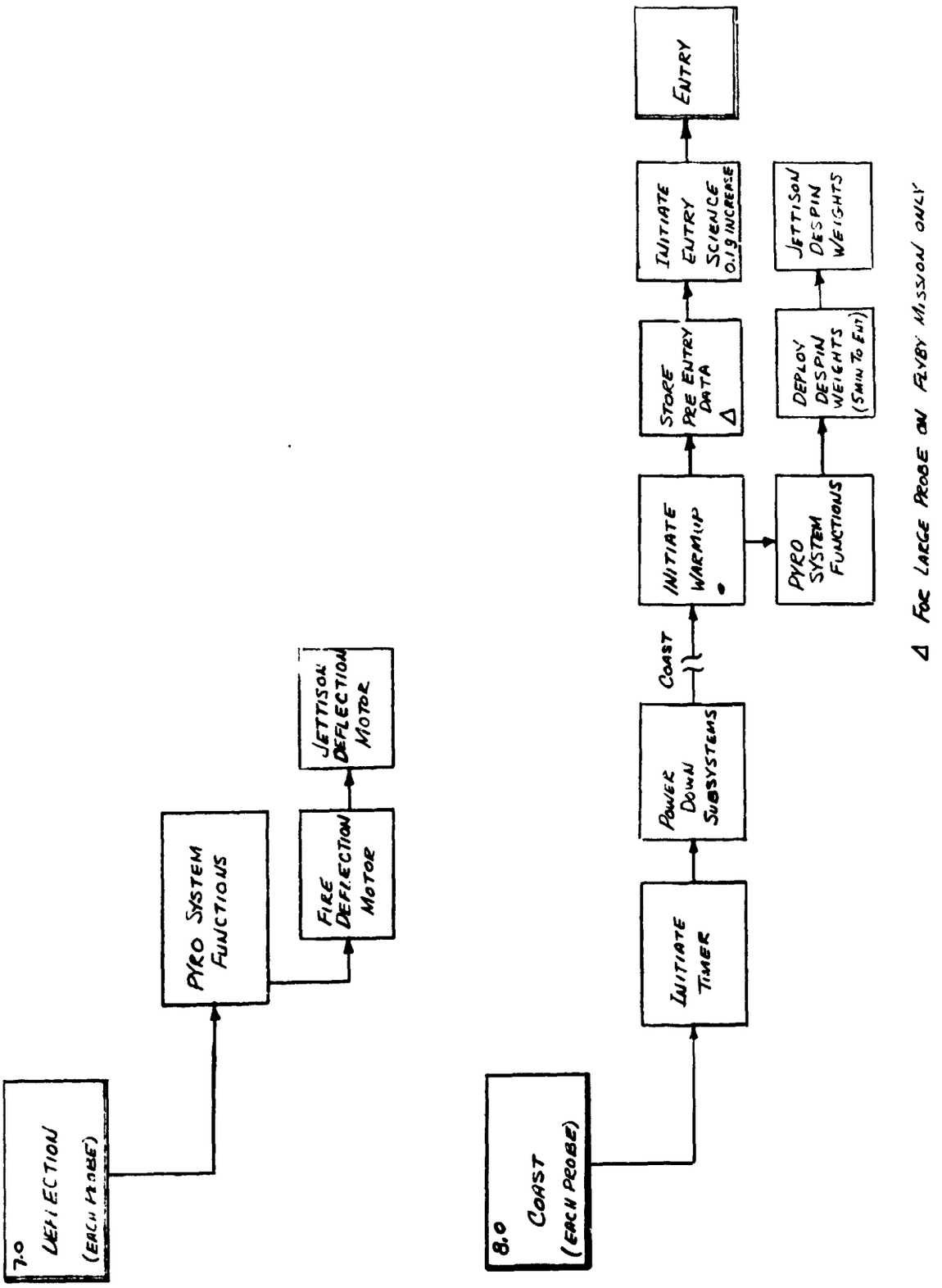


Fig. V-4 Phases 5.0 and 6.0



Δ FOR LARGE PROBE ON FLYBY MISSION ONLY

Fig. V-5 Phases 7.0 and 8.0

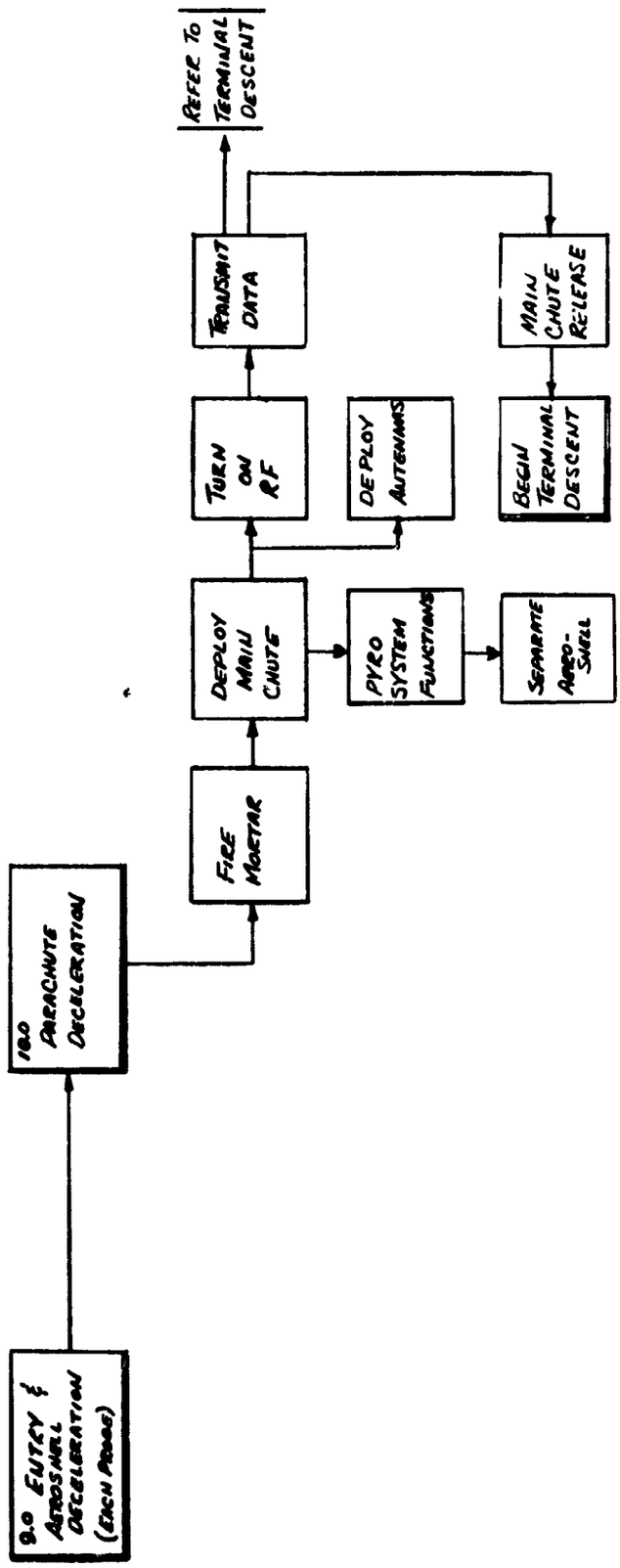


Fig. V-6 Phase 9.0

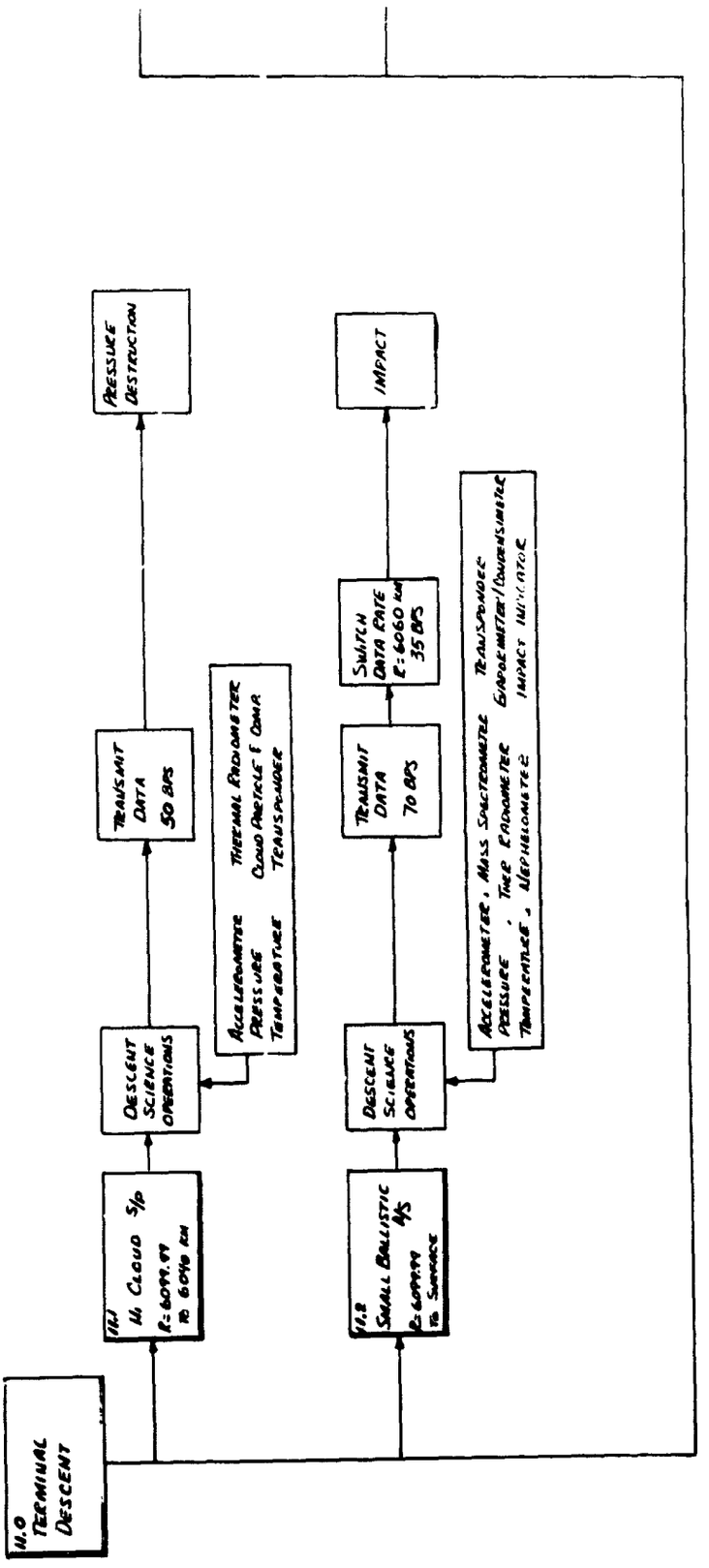


Fig. V-7 Phase 11.0

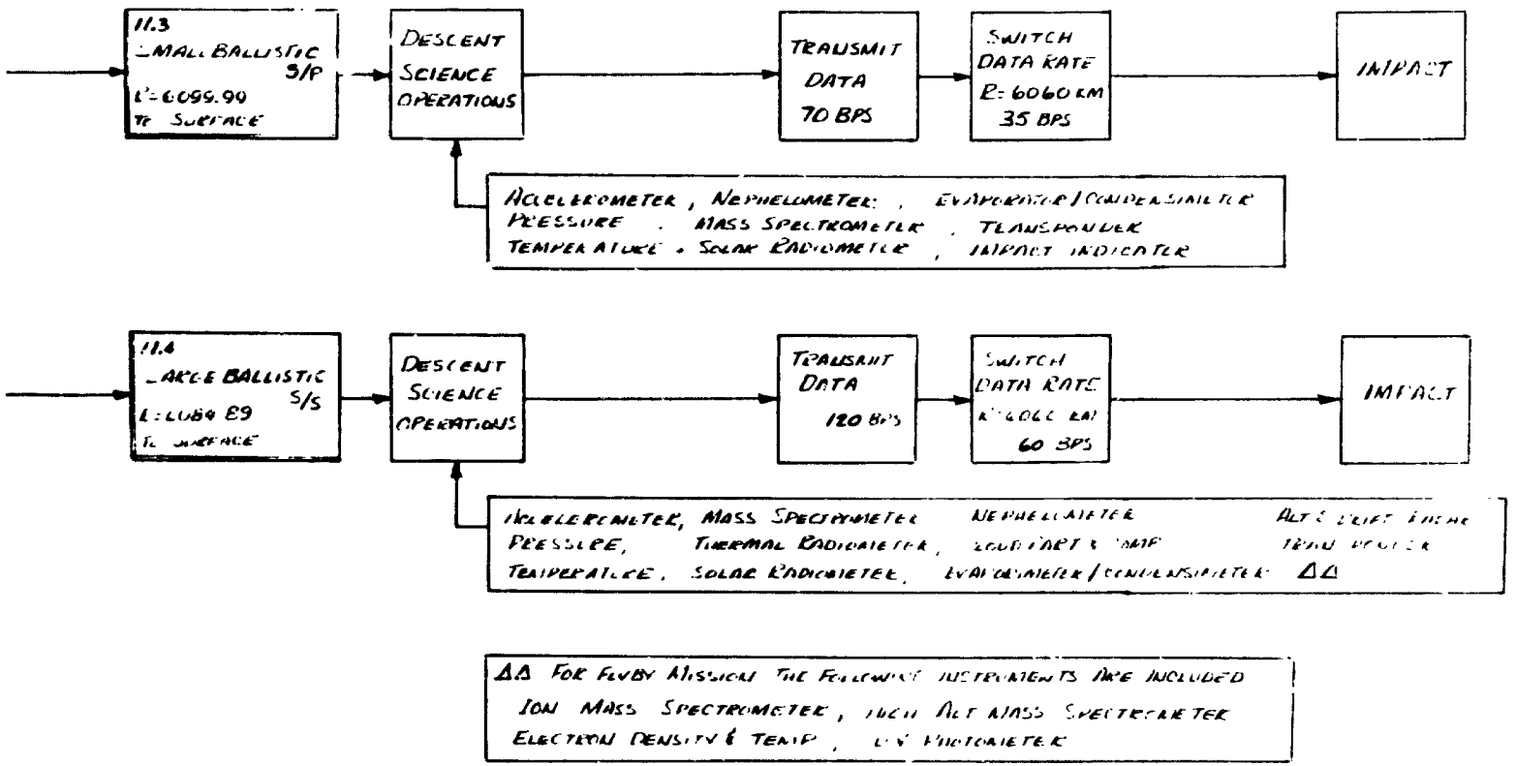
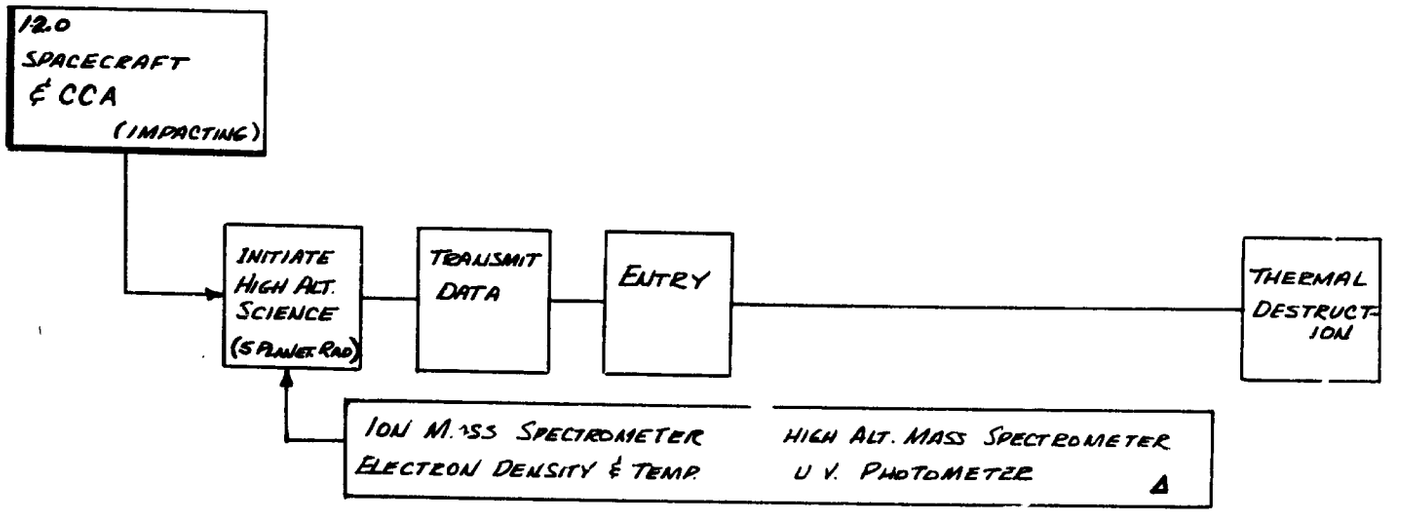


Fig. V-8 Phases 11.3 and 11.4



Δ THESE INSTRUMENTS ARE CARRIED IN THE LARGE PROBE FOR THE FLYBY MISSION.

Fig. V-9 Phase 12.0

C. MISSION SEQUENCE OF EVENTS

1. Planetary Vehicle Sequence of Events

The Planetary Vehicle sequence of events leading to separation of the capsules for the baseline mission and for the impacting spacecraft is shown in Table V-5. The sequence is constructed so that the large ballistic probe, to be placed on essentially the same trajectory as the Planetary Vehicle, is in position for its small (less than 5 m/sec) deflection impulse to be delivered 20 minutes after separation. The sequence also accounts for the time of spacecraft maneuvering through the various angles at a constant rate of 3.1416 mrad/sec. In addition, a period of 8 minutes 32 seconds is allowed before each turn during each maneuver in accordance with Mariner procedures. The sequence would be essentially unchanged for the flyby mission, with the same capsule complement, except that the large probe would be separated approximately 2.5 hr later.

2. Entry Capsule Sequence of Events

After separation, the various capsules are sequenced as shown in Table V-6. During coast to entry, commonality exists for all probes. During entry and terminal descent, similarity exists for probes of the same general types. Descent functions are actuated by sensing accelerations and pressures related to the descent profile. In the case of the balloon probes used on the optional missions, a 10-sec delay, from an easily sensed time of occurrence of 1.5 g, is used to extract the balloon. All aerodynamic parameters are referredcto the MMC Lower Atmosphere.

Table V-5 Planetary Vehicle/Capsule Separation Sequence of Events

Spacecraft Time to Entry	Capsule Time	Event	To	Source
E-294:45:00		Receive Separation Sequencer Initiate Command Mariner Maneuver Enable	S/C CCS S/C ACS	S/C CMMD S/C CCS
E-294:40:40		Start Spacecraft Gyros	S/C ACS	S/C CCS
		Arm Biocanister No. 1 Separation Pyros	CCA Seq	S/C CCS
		Fire Biocanister No. 1 Separation Pyros	CCA Seq	S/C CCS
		Safe Biocanister No. 1 Separation Pyros (Repeat for No. 2, No. 3, and No. 4)	CCA Seq	S/C CCS
E-294:40:39		Complete Biocanister Separation Switch to Inertial Reference	CCA Seq S/C ACS	S/C CCS S/C CCS
E-294:39:36		Initiate Planetary Vehicle Maneuver (Pitch Turn, +17°)	S/C ACS	S/C CCS
E-294:29:29	S_1 - 8 sec	Complete Planetary Vehicle Maneuver	S/C CCS	S/C ACS
	S_1 - 6 sec	Effect Planetary Vehicle Attitude Lock	S/C ACS	S/C CCS
	S_1 - 4 sec	Enable Capsule Release (Initiates CCA Sequencer)	CCA Seq	S/C CCS
	S_1 - 2 sec	Arm Capsule No. 1 Separation Pyro	Pyro	CCA Seq
E-294:30:21	S_1 = 0	Fire Capsule No. 1 Separation Pyro (Small Ballistic, SP)	Pyro	CCA Seq
		(Initiates Capsule No. 1 Timer)	Capsule No. 1 Seq Seq	CCA Seq
	S_1 + 2 sec	Safe Capsule No. 1 Separation Pyro Capsule No. 1 Functions - (See Table V-6)	Pyro	CCA Seq
	S_1 + 4 sec	Confirm Capsule Release	S/C CCS	CCA Seq
	S_1 + 6 sec	Mariner Maneuver Enable	S/C ACS	S/C CCS
E-294:30:15		Initiate Planetary Vehicle Attitude Maneuvers (Roll Turn, -120°)	S/C ACS	S/C CCS
E-294:10:33	S_2 - 8 sec	Complete Planetary Vehicle Attitude Maneuvers	S/C CCS	S/C ACS
	S_2 - 6 sec	Effect Planetary Vehicle Attitude Lock	S/C ACS	S/C CCS
	S_2 - 4 sec	Enable Capsule Release (Reinitiates CCA Sequencer)	CCA Seq	S/C CCS
	S_2 - 2 sec	Arm Capsule No. 2 Separation Pyro	Pyro	CCA Seq
E-294:10:25	S_2 = 0	Fire Capsule No. 2 Separation Pyro (Hi-Cloud, SP) (Initiates Capsule No. 2 Timer)	Pyro Capsule No. 2 Seq	CCA Seq CCA Seq
	S_2 + 2 sec	Safe Capsule No. 2 Separation Pyro Capsule No. 2 Functions (See Table V-6)	Pyro	CCA Seq
	S_2 + 4 sec	Confirm Capsule Release	S/C CCS	CCA Seq
	S_2 + 6 sec	Mariner Maneuver Enable	S/C ACS	S/C CCS

Table V-5 (concl)

Spacecraft Time to Entry	Capsule Time	Event	To	Source
E-294:10:19		Initiate Planetary Vehicle Attitude Maneuvers (Pitch Turn, +10°; Roll, -120°)	S/C ACS	S/C CCS
E-293:40:09	S_3 - 8 sec	Complete Planetary Vehicle Attitude Maneuvers	S/C CCS	S/C ACS
	S_3 - 6 sec	Effect Planetary Vehicle Attitude Lock	S/C ACS	S/C CCS
	S_3 - 4 sec	Enable Capsule Release (Reinitiates CCA Sequencer)	CCA Seq	S/C CCS
	S_3 - 2 sec	Arm Capsule No. 3 Separation Pyro	Pyro	CCA Seq
E-293:41:01	S_3 = 0	Fire Capsule 3 Separation Pyro (Small Ballistic A/S) (Initiates Capsule No. 3 Timer)	Pyro Capsule No. 3 Seq	CCA Seq CCA Seq
	S_3 + 2 sec	Safe Capsule No. 3 Separation Pyro Capsule No. 3 Functions (See Table V-6)	Pyro	CCA Seq
	S_3 + 4 sec	Confirm Capsule Release	S/C CCS	CCA Seq
	S_3 + 6 sec	Mariner Maneuver Enable	S/C ACS	S/C CCS
E-293:40:55		Initiate Planetary Vehicle Attitude Maneuvers (Roll Turn, +15°; Pitch, +90°)	S/C ACS	S/C CCS
E-293:14:08	S_4 - 8 sec	Complete Planetary Vehicle Attitude Maneuvers	S/C CCS	S/C ACS
	S_4 - 6 sec	Effect Planetary Vehicle Attitude Lock	S/C ACS	S/C CCS
	S_4 - 4 sec	Enable Capsule Release (Reinitiates CCA Sequencer)	CCA Seq	S/C CCS
	S_4 - 2 sec	Arm Capsule No. 4 Separation Pyro	Pyro	CCA Seq
E-293:14:00	S_4 = 0	Fire Capsule 4 Separation Pyro (Large Ballistic SS) (Initiates Capsule No. 4 Timer)	Pyro Capsule No. 4 Seq	CCA Seq CCA Seq
	S_4 + 2 sec	Safe Capsule No. 4 Separation Pyro Capsule No. 4 Functions (See Table V-6)		
	S_4 + 4 sec	Confirm Capsule Release	S/C CCS	CCA Seq
	S_4 + 6 sec	Mariner Maneuver Enable	S/C ACS	S/C CCS
E-293:14:06		Start Celestial Reacquisition Phase (Roll Turn +185°; Pitch, -105°)	S/C ACS	S/C CCS
E-292:30:07*		Complete Celestial Reacquisition Phase Planetary Vehicle Coast	S/C CCS	S/C ACS
E-1:30:05		Initiate CCA Sequencer	CCA Seq	S/C CMMD
E-1:30:00	E -1:30:00	Turn on All CCA Science (≈5 Planet Radii)	CCA Science	CCA Seq
E = 0	E = 0	Planetary Vehicle Entry		

*This is the minimum maneuver required to reestablish celestial reference. This maneuver provides a basis for minimum additional roll search for Canopus acquisition.

Table V-6 Capsule Sequence Functions

Function	To	Source
Preentry - All Probes		
Arm Spin-up Pyro	Pyro	Seq
Fire Spin-up Pyro (Separation plus 1 sec)		
Safe Spin-up Pyro		
Arm Deflection Propulsion Start		
Fire Deflection Propulsion Start (Separation plus 20 minutes minimum)		
(Arms Deflection Propulsion Stop)		
Fire Deflection Propulsion Stop		
(Safes Deflection Propulsion Start)		
(Arms Deflection Propulsion Separate)		
Fire Deflection Propulsion Separate		
(Safes Deflection Propulsion Stop)		
Safe Deflection Propulsion Separate	Pyro	Seq
Transfer to Low Power Mode	Seq	Power
(Capsule Coast 298 hr)		
Power up for Entry (Entry minus 10 minutes)	Mech. Timer	Power and Seq
(Initiates Electronic Timer)		
Arm Despin Pyro	Pyro	Seq
Fire Despin Pyro (Entry minus 5 minutes)	Pyro	Seq
Safe Despin Pyro		
(Arms Despin Weight Jettison)	Pyro	Seq
Jettison Despin Weights	Pyro	Seq
Safe Despin Weight Jettison	Pyro	Seq
Postentry - Ballistic Probes		
Sense $g(t) = 0.1$ g, $[\dot{g}(t) > 0]$ $(E_1 = 0)$	Seq	Accel
Record Entry Data	Data	Seq
Sense $g(t) = x$, $[\dot{g}(t) < 0]$ $(E_2 = 0)$	Seq	Accel
$[(X_{Large} = 2.7\ g)]$		
$[(X_{Small} = 1.5\ g)]$		
Arm Decelerator Mortar	Pyro	Seq
Fire Decelerator Mortar	Pyro	Seq
Safe Decelerator Mortar	Pyro	Seq
Turn On RF; Start Data Transmission	Data	Seq
(Stage Aeroshell/Deploy Science)	--	--
Fire Chute Release	Pyro	Seq
Safe Chute Release		
(Arms Inflation Terminate)		
Fire Inflation Terminate		
Safe Inflation Terminate		
(Arms Inflation System Release)		
Fire Inflation System Release		
Safe Inflation System Release	Pyro	Seq
Begin Normal Operation	Data	Seq
Sense P	Seq	Press.
$[(P_{Large} = 7.0\ bar)]$		
$[(P_{Small} = 1.35\ bar)]$		
Arm Main Chute Release	Pyro	Seq
Fire Main Chute Release	Pyro	Seq
Sense P = 50.0 bar	Seq	Press.
Switch Data Rate	Data	Seq
Postentry Hi Cloud Probes		
Sense $g(t) = 1.5\ \dot{g}$, $g(t) < 0$	Seq	Accel
Arm Decelerator Mortar	Pyro	Seq
Fire Decelerator Mortar	Pyro	Seq
Turn on RF; Start Data Transmission	Data	Seq
(Stage Aeroshell/Deploy Science)	--	--
Safe Decelerator Mortar	Pyro	Seq
Sense P = 1.35 bars	Seq	Press.
Arm Main Chute Release	Pyro	Seq
Fire Main Chute Release	Pyro	Seq
Safe Main Chute Release	Pyro	Seq
Postentry - Balloon Probes		
Sense $g(t) = 1.5$ g, $\dot{g}(t) < 0$ $(E_2 = 0)$	Seq	Accel
Activate Data System	Data	Seq
Arm Afterbody Parachute Deploy	Pyro	Seq
Fire Afterbody Parachute Deploy	Pyro	Seq
Safe Afterbody Parachute Deploy	Pyro	Seq
(Arms Afterbody Separate)		
Fire Afterbody Separate	Pyro	Seq
(Extends Main Chute)		
Sense E_2 + 10 sec (6117 500 mb; 6116.5 50 mb)	Seq	--
Arm Balloon Extract	Pyro	Seq
Fire Balloon Extract	Pyro	Seq
Safe Balloon Extract	Pyro	Seq
(Arms Balloon Inflate)		
Fire Balloon Inflate	Pyro	Seq
Safe Balloon Inflate	Pyro	Seq
(Arms Chute Release)		

D. FLYBY MISSIONS VERSUS DIRECT IMPACTING MISSIONS

1. Configuration Effects

The configuration of most probe and planetary vehicle systems is not influenced by the flyby or direct impact mission mode selection. The major configuration differences are the biocanister design, the location of upper altitude instruments, and the deflection propulsion total impulse.

The direct impacting spacecraft creates a requirement to maintain the entire Planetary Vehicle in a sterile atmosphere after terminal sterilization. This is accomplished by a large biocanister, essentially the shape of the payload fairing, which is split and pulled off by the Launch Vehicle final stage at separation. This large biocanister is required in addition to individual containers for each entry probe.

The upper altitude instruments are located on the capsule adapter truss for the impacting case and their data are transmitted via the spacecraft telemetry link. Power and control is provided by capsule adapter subsystems. For the flyby case the instruments must be located in an entry vehicle, and the large probe has been selected since their impact will be less than if located on other probes. Additional power and data handling capacity must also be provided for on the large probe.

The deflection impulse velocity increment for the flyby mission mode is approximately 40 m/sec for all probes over that for the impacting mission. The increase is greater for the large probe since it is targeted near the spacecraft on the impacting mission and no propulsive force other than spring separation (0.5 m/sec) is provided.

These configuration changes result in a total mission weight increase for the flyby mission of 34 lb, and an increase of large probe entry weight of 28.6 lb. These changes in weight are considered minimal in view of the Titan IIIC payload capability.

2. Mission Operation

Mission operation for entry probes is not appreciably different in either case. The large biocanister must be stripped off the Planetary Vehicle for the impacting mission, and thereby presents an additional function to be performed.

The initial targeting will be different in that the flyby spacecraft will never be allowed on an impacting trajectory. All biocanisters will also be separated so that an inadvertent entry cannot occur. The periapsis radius will be adjusted at the midcourse burn to a minimum of 12,600 km. The impacting spacecraft will be targeted directly for the planet and the biocanister covers will be allowed to enter the atmosphere since they will be sterile both inside and out. The Planetary Vehicle attitude maneuvers will be essentially the same for deflection impulse attitude orientation, although the final separation attitudes will differ. The entry conditions for each probe (flight path angle and angle of attack) will also differ, however no intolerable cases are experienced with either.

The flyby mission will be capable of certain scientific measurements that the impacting mission will not be capable of. These are longer television and imaging experiments and occultation. Also, these measurements may be started farther from the planet. The flyby spacecraft may also store the data for playback at a later time when probe entry and descent activities are complete.

3. Implementation Effects

Although this study is to determine a configuration and operational sequence for each mode, a much more important factor in selecting the proper mode than the above has been identified. If the existing criterion, which states that the atmosphere conducive to life shall not be contaminated, is still in effect for this mission, all entry items must be sterile. While all new items, probes, and capsule adapter can be designed compatible with sterilization

with minimal effect, the requirement of sterilization on the Mariner spacecraft appears formidable. Redesign, testing, and qualification of all Mariner systems would appear to be a costly exercise especially when all other factors in the decision are of minimal consequence or advantage.

E. STERILIZATION AND DECONTAMINATION

1. Sterilization Criteria and Requirements

The mission shall be consistent with NASA planetary quarantine policy specified in NASA Management Manual 4-4-1 (Ref V-1), which for this mission is interpreted to mean that the region of the atmosphere that might be conducive to life forms shall not be contaminated.

For purposes of this study:

1) The system shall be assembled in "clean rooms" at specified levels of assembly;
2) All hardware entering the planet's atsmophere must be capable of withstanding ETO exposure in accordance with JPL Specification No. VOL-50503-ETS (Ref V-2);
3) Selected probe equipment (e.g., heat shield and other elements that might outgas or vent to the atmosphere) must be capable of withstanding heat sterilization as defined in Ref V-2;
4) The planetary entry systems shall be enclosed in a bacteriological barrier to maintain cleanliness and sterility. After decontamination, the enclosure shall not be opened within any portion of the Earth's atmosphere that might recontaminate the entry system;
5) Adherence to the four items cited above shall apply only to the entry probes. (Note: Exclusion of the spacecraft at this time is for purposes of this study only.)

The significant planetary quarantine and sterilization requirements summarized from the above criteria are as follows:

1) Contamination probability level of 10^{-3} for all potential sources of contamination while biological studies of the planet are being carried out;
2) The Probe/Entry Vehicles will be heat sterilized so that the probability that a live microorganism remains is as shown in Table on page V-32.
3) The probability of impact of the planet Venus by an unsterilized orbiter shall not exceed 3×10^{-5} in an orbit not to decay within 50 years;
4) The probability of accidental planetary entry by an unsterilized flyby spacecraft shall not exceed 3×10^{-5};
5) Design of the canister shall be such that no contaminated surface shall be in line-of-sight of a sterile surface during canister separation;
6) The trajectory of the separated canister shall be such that it does not violate the planetary quarantine requirement;
7) Each flight capsule shall be manufactured, assembled, tested, and encapsulated in such a manner as to enter the terminal sterilization cycle with less than 1×10^{-5} viable spores;
8) The terminal sterilization process shall subject the capsule to a time-temperature cycle equivalent in lethality to 125°C for 24.5 hr;
9) The Probe/Entry Vehicles shall be biologically sealed in a sterilization canister following terminal sterilization and remain sealed until separation for entry.

2. System Assembly and Test Sequence

The general system assembly and test sequences and clean room requirements are as follows:

Class 100,000 Clean Room

1) Initial subsystem accumulation and storage;
2) Capsule system assembly and Level 1 tests;
3) Flight article environmental tests;
4) Disassemble to subsystem level and inspection;

Class 100 Clean Room

5) Clean subsystems to class 100 level;
6) ETO decontaminate all subsystems;
7) Reassemble capsule system and Level 2 test;
8) Install live propulsion and pyro;
9) Install into biocanister and Level 3 test;
10) Terminal heat sterilization;

Class 100,000 Clean Room

11) Level 4 tests;
12) Certification and buyoff.

3. General Operational Approach

The general operational approach required to conform to the sterilization and decontamination criteria is discussed in the following paragraphs.

a. Launch Vehicle - (Nonimpacting) - No Launch Vehicle equipment will be placed on an impacting trajectory.

b. Planetary Vehicle Sterilization - The requirements for Planetary Vehicle sterilization depend on whether the mission uses a flyby spacecraft or an impacting spacecraft.

The flyby mode presents no particular problem since all entry articles will be sterilized and contained in sealed biological canisters. Before Planetary Vehicle reorientation for each capsule's separation, the biocanister will be separated in such a manner that an inadvertent entry into the planet's atmosphere will not occur. This will be accomplished in sequence for each Entry Capsule.

The direct impacting spacecraft mission presents a requirement considerably different from the above approach. Because the study constraints require that the portion of the atmosphere conducive to life not be contaminated, the capsules, capsule adapter, and spacecraft must be sterilized items. The method integrated into the baseline mission configuration studies will assemble sterilized capsules, spacecraft, and capsule adapter under clean room conditions. This payload may then be attached to the Launch Vehicle above a biologically secure barrier. A lightweight container will then enclose all entry items inside the payload fairing. Ethylene oxide will then be introduced into the container for an appropriate time to resterilize the exterior of the items that were exposed to contamination after sterilization. This container will remain intact until the Launch Vehicle is out of the Earth's atmosphere and may remain either with the Payload Fairing or the Launch Vehicle final stage. The biocanisters will then be used primarily to provide thermal control surfaces, since they will be sterilized inside and out. They will remain with the Entry Capsules until just prior to capsule separation; however, they need not be deflected to a nonimpacting trajectory.

c. Entry Capsules - Two operational modes are required for the four types of Entry Capsules. The four types of Entry Capsules are large and small probes, high-cloud probe, and balloon probes.

The first approach considers the probes that pass rapidly through the altitude zone that is conducive to life forms. This includes the large and small probes. These probes must be sterilized externally, including heat shield, decelerators, ordnance items, and all exposed surfaces. The equipment inside the pressure vessel need not be sterilized because the probability of failure of the structural pressure vessel can be made to satisfy mission requirements.

The high-cloud probe must follow a second approach because it will not be built with the equipment packaged in a high strength, sealed, pressure vessel. Since a structural breakup could occur while the probe is still in a moderate temperature zone in the atmosphere, the internal parts of the system must be sterilized.

The balloon probes must also follow the second approach because they will be floating for extended periods at altitudes conducive to life. Both the balloon and the payload package will be sterilized because balloon failure will expose the interior and encapsulated microbes and the payload will rapidly descend to higher pressures and rupture.

A general philosophy is being developed in the current Viking program which is resulting in reduced sterilization heating times for some portions of the capsule. The method involves detailed bookkeeping of the microbial count for each part and decontamination of each part before mating. The end result is virtual elimination of mated surface or encapsulated microbes and the assembly can be treated for the more easily killed surface microbes. Every subassembly or part is treated as a separate case and its history is recorded throughout the assembly and test procedure.

Well insulated items such as parachutes and balloons will be sterilized and biologically sealed before the terminal heat sterilization cycle. Otherwise, providing sufficient heat to the center of these insulated items would result in extended heating to those subassemblies toward the outside of the capsule.

The equipment contained within the sealed pressure shells for the probes that descend to the surface does not require sterilization. However, the internal equipment for the high-cloud probe and the balloon probes does require decontamination and sterilization because these probes are not designed to withstand high pressure. Although the sealed pressure vessel on the descent probe

does not require sterilization, it may receive a significant heat pulse while the external assemblies are being sterilized. Therefore, the internal pressure vessel assemblies must be designed to take a portion of the terminal heat for a brief period. Analyses are required to determine the blocking effect of probe insulation on the amount of heat that soaks into the probe.

4. Planetary Contamination Allocation

To determine the effect of the planetary quarantine requirements on the program planning, engineering, and scheduling, a sample allocation of the permissible probe contamination probabilities is given in the following paragraphs.

a. Allocation to the Mission Level - The international goal of preserving the biological integrity of the planet over the anticipated 50 years required for the biological investigation with a failure probability of 0.001 is allocated to the level of a single mission with the assumption that there will be at least one mission launched per launch opportunity. This assumption allocates a probability of contaminating the planet on a single opportunity of 3.2×10^{-5}.

b. Allocation to the Probe Level - The mission contamination probability is further allocated to the individual probe level by taking into account the inherent differences of the probe types. The large and small probe design, featuring a container capable of surviving intact to the surface, requires only a sterile outer surface. Similarly the flyby spacecraft only needs to miss the planet with an acceptable probability. The high-cloud probes that crush during their descent need a larger allocation. The balloon probes that must stay for a protracted length of time in the hospitable portion of the Venus atmosphere, and the impacting spacecraft that presents special sterilization problems, require a greater allocation. Probe allocations in the following tabulation were established.

Mission	No. Required	Worst Case	Total Allocation
Descent Probes (pressurized)	1×10^{-6}	3	3×10^{-6}
High Cloud Probes	3×10^{-6}	2	6×10^{-6}
Balloon Probes	8×10^{-6}	2	1.6×10^{-5}
Flyby Spacecraft	1×10^{-6}	0	
Impacting Spacecraft	7×10^{-6}	1	7×10^{-6}
Total (Option 2, Impacting Spacecraft)			3.2×10^{-5}

c. Probability of Biota Surviving - The probability of a biota transported to the upper atmosphere of Venus and successfully replicating itself is assumed to be 1×10^{-3}. It is felt that this probability is conservative. The effect is to increase the permissible chance of the probes' contaminating the atmosphere by a factor of 10^3.

d. Resulting Contamination Probabilities - The results in the following tabulation indicate that active sterilization of the various probes will be required even for the inhospitable Venus atmosphere. The total contamination probability for any given level of treatment is a function of the mission option actually chosen. The tabulation illustrates the difference the option makes.

Mission	Baseline	Option 1	Option 2
	3 descent	3 descent	3 descent
	1 cloud	1 cloud	2 cloud
	0 balloons	1 balloon	2 balloon.
Flyby	7×10^{-6}	1.5×10^{-5}	2.6×10^{-5}
Impacting	1.3×10^{-5}	2.1×10^{-5}	3.2×10^{-5}

5. Sterilizable Equipment Survey Results

During the performance of the contract "Buoyant Venus Station Mission Feasibility Study for 1972 and 1973 Launch Opportunities," by Martin-Marietta for NASA-LRC (NAS1-7590) a survey of sterilizable equipment was made. The sterilization and decontamination criteria were the same as those established for this study and were based on Ref V-2. The results of this survey are generally applicable to the present probe study and are shown in Table V-7.

Table V-7 Venus Probe(s) Sterilizable Hardware

Probe(s) Equipment List	Sterilization Status: Acceptable	Under Investigation	To be Investigated	Reference/Remarks
Electronic				
Central Data Multiplexer/ Encoder	x			
Data Storage	x	x		Plated wire memory. CSAD Librascope
Low Gain Antenna	x			CSAD omni antenna system
Data Handling Subsystem Program	x			
Command Receiver	x			CSAD (S-band)
Command Detector	x			CSAD (S-band)
Command Decoder	x			CSAD (S-band)
Transmitter	x			CSAD (S-band)
Diplexer	x			CSAD (S-band)
Main Antenna	x			CSAD (S-band)
Radar Alt (Electronics)	x			
Radar Alt (Array)	x			
Sequencer	x			CSAD
Electrical				
Main Batteries	x			
Aux Batteries	x			
Instrument Power Supply	x			CSAD
Power Pack	x			CSAD
Solar Cells	x			
Cable and Connectors	x			
Science				
Bioscience			x	
Triax Accelerometer	x			
Pressure Experiment	x			CSAD
Temperature Experiment	x			CSAD
Light Backscatter			x	
Solar Aspect	x			1964 Mariner image dissector; CBS Labs
Water Vapor	x			CSAD
Visual Photometer			x	
Mechanical/Electromechanical				
Structure	x			
Balloon Controls			x	
Ordnance Valves	x			
Pressure Switch	x			
Solenoid Valves	x			
Parachute	x			PEPP
Balloon	x			Martin/LRC Contract NAS1-7590 "Venus Mission Feasibility" Addendum "Balloon Materials Feasibility Tests."

The information shown in the table is based, in part, on work done at Martin Marietta with sterilizable electronic hardware and electrical power sources. The information came from a variety of reports, but the one most frequently used was a JPL report in which they reported their work with the Capsule System Advanced Development (CSAD) program (Ref V-3). A Martin Marietta report (Ref V-4) was another source in which information was obtained.

The equipment shown as acceptable in Table V-7 indicates that there are acceptable parts available (heat sterilizable) for the general classification of electronic equipment using common parts (integrated circuits, resistors, capacitors, etc). JPL has tested and reported on the successful temperature cycling of wet-foil tantalum capacitors at temperatures up to 140°C.

An investigation has recently been completed at Martin Marietta on sterilization compatibility of balloon materials and processing under NASA contract NAS1-7590 (Ref V-5). Test data indicate that the balloon material (singular or composite), can be heat sterilized. Manufacturing techniques have not, as yet, been developed.

F. PLANETARY VEHICLE SYSTEM INTERFACES

A key element of the Planetary Vehicle is the Common Capsule Adapter, which presents a single set of interfaces from the Entry Capsule to the spacecraft and also serves to interface the Planetary Vehicle with the launch vehicle.

The degree of integration of systems at the interfaces depends on the phase of the mission under consideration as discussed below:

1) During prelaunch assembly and checkout the interfaces between the spacecraft and the capsule systems exist from the time of mating. The capability for checkout

of the separate systems, and also of the interfaces, will be provided through the Planetary Vehicle-to-Launch Vehicle adapter portion of the Common Capsule Adapter;

2) During launch all Planetary Vehicle systems are dormant. The Planetary Vehicle-to-Launch Vehicle adapter bears the launch loads and retains the Planetary Vehicle within the dynamic envelope limits of the Payload Fairing and within the control authority limits of the Launch Vehicle;

3) At Planetary Vehicle separation the major interface becomes that of the spacecraft with the DSIF. This interface will be handled according to normal Mariner procedures and the only modification is that capsule systems data are included in the spacecraft data streams. An interface exists within the Planetary Vehicle in that up to 2 watts of solar panel power will be required for monitoring and charging capsule batteries;

4) Preparatory to separation of the Entry Capsules, the interfaces between the spacecraft and the Common Capsule Adapter sequentially activate and release the capsules after they have been given entry orientation through spacecraft maneuvers.

1. Capsule Systems to Spacecraft Interfaces

Requirements on the spacecraft to support capsule systems in the baseline mission and reciprocal requirements on capsule systems are described in this subsection.

a. Requirements of Capsule Systems on the Spacecraft

Structural Requirements - It will be required that the spacecraft structural subsystem mate with the structure of the Common Capsule Adapter and provide mounting for the science instruments of the Planetary Vehicle.

Radio Frequency Requirements - It will be required that the movable low-gain antenna of the AVCO Configuration 20a operate with the radio frequency system after having been relocated on the Common Capsule Adapter.

Flight Command Requirements - It will be required that the flight command subsystem accept commands for initiation of capsule systems prior to release. Planetary Vehicle maneuvers before capsule release will be performed in accordance with normal Mariner procedures.

Power Requirements - The spacecraft is required to provide approximately 2 watts of power for engineering measurements, heating of the capsules, and charging capsule batteries. The solar panel orientation of AVCO Configuration 20a will be retained.

Central Computer and Sequencer Requirements - It will be required that the central computer and sequencer provide a signal to initiate the CCA sequencer. It will be required that the central computer and sequencer initiate attitude maneuvers and signal that the maneuver is complete. It will be required that the central computer and sequencer accept verification signals that capsule release has occurred.

Flight Telemetry Requirements - The spacecraft flight telemetry subsystem will be required to accept data streams from the Common Capsule Adapter concerning capsule systems status before separation, capsule initiation during separation, and verification that release has been accomplished. Data formatting will be accomplished by the Common Capsule Adapter to be compatible with the spacecraft requirements.

Attitude Control Requirements - The spacecraft attitude control subsystem will be required to maintain orientation of the +Z axis toward the sun during interplanetary cruise and maneuver to the attitude for capsule release. Cold gas supply and thrust

of the attitude control jets are subject to tradeoffs of moments of inertia of the selected configuration, time to reach the design turning rate (3.1416 mrad/sec) and possible capability for longer off-sun orientation.

Cabling Requirements - The cabling subsystem will be required to interface with the Common Capsule Adapter. Requirements for cable routing and redundancy of wiring are subject to tradeoff studies. This interface will not be broken during the mission.

Propulsion Requirements - The midcourse propulsion engine will be required to be oriented to provide thrust through the center of gravity of the Planetary Vehicle. This interface also affects the attitude control interface cited above. Methods of augmenting the propellant supply are also subjects for study.

Temperature Control Requirements - Because the louvers of the thermal control subsystem of AVCO Configuration 20a are inverted from the Mariner '69 orientation, verification of operability will be required.

Mechanical Device Requirements - It will be required that the mechanisms for deploying the movable low-gain antenna and the solar panels (because of reduced weight) be verified in the selected configuration. Operation of the scan control platform in the new configuration is also to be studied.

b. Requirements of the Spacecraft on Capsule Systems

Structural Requirements - The structure of the Common Capsule Adapter will be required to support the spacecraft during launch and be so arranged that the dynamic properties of the Planetary Vehicle are within the control limits of the spacecraft after Planetary Vehicle separation. The capsule release forces must not cause the spacecraft to lose inertial reference.

Power and Cabling Requirements - It will be required that the Common Capsule Adapter accept up to 2 watts of power from the solar panels and distribute this for monitoring and battery charging.

Thermal Control Requirements - The spacecraft will be required to maintain sun orientation in accordance with normal Mariner procedures.

Communications (Data) Requirements - The Common Capsule Adapter will be required to provide data formats compatible with the spacecraft flight telemetry subsystem for transmission.

Sequencer Requirements - The sequencer of the Common Capsule Adapter will be required to perform the following functions:

Accept a signal from the spacecraft that the release orientation has been achieved for each capsule;

Control all functions of capsule release and verify to the spacecraft that release has been accomplished;

Accept a command override from the flight commmand subsystem in the event of failure of a capsule to release.

2. Planetary Vehicle to Launch Vehicle Interfaces

Requirements of prelaunch and launch are described in this section.

a. Requirements of the Planetary Vehicle on the Launch Vehicle

Structural Requirements - It will be required that prelaunch systems monitoring capability for the Planetary Vehicle be provided through structural cutouts in the payload fairing. If an impacting Planetary Vehicle is to be flown, the XX25 Payload Fairing will be required to interface with the biocanister of the Planetary Vehicle. The Launch Vehicle will separate the biocanister simultaneously with Payload Fairing separation.

Planetary Vehicle Separation Requirements - At Planetary Vehicle separation it will be required tnat tip off rates be less than 50 mrad/sec about any axis. Separation forces will be provided by the Launch Vehicle.

b. Requirements of the Launch Vehicle on the Planetary Vehicle Structural Requirements - The Planetary Vehicle will be required not to violate the dynamic envelope of the XX25 fairing. Mass properties distribution and structural rigidity of the Planetary Vehicle (Common Capsule adapter) must not violate the control authority limits of the Launch Vehicle. The center of gravity of the Planetary Vehicle will be within the variations of the actual centerline from the theoretical centerline of the Launch Vehicle.

G. POTENTIAL PROBLEM AREAS AND UNCERTAINTIES

Some areas of uncertainty were identified during the study. None of these were considered to lie beyond the state of the art for July 1972 or to require new technology development. The areas are summarized in this section.

1. Descent Probes

a. Engineering Mechanics - Implementation of the subsystems described for the baseline mission generally appears quite feasible. One area of some uncertainty however is the double-wall pressure vessel instrument container design. Ensuring integrity of the many seals at joints and penetrations will be difficult. Also, predictions of the performance of the multilayer insulation as installed in the vacuum jacket and as affected by the heat flow through the penetrations are subject to considerable uncertainty. However, alternative designs appear possible, as discussed in Chapter VIII. The alternative designs present fewer problems of this nature and are compatible with the current system weights.

In either of the design concepts involving use of a pressure vessel, development of seals, feedthroughs, and connectors will be required. Likewise, development is required in the area of protection for external surfaces of optical windows.

b. Telecommunications and Power - Most of the design of the telecommunications and power system assumes present state-of-the-art with no problems anticipated. However, there are a number of uncertainties, listed below. These are discussed in more detail in the appropriate section of the report.

Atmospheric Attenuation - The assumed zenith RF attenuation is based on radar measurements and is believed to be reasonable. There is some uncertainty in this value, and if it is substantially in error the impact on mission design could be significant. This can only be resolved with certainty by a descent probe.

Signal Margins - The link calculations assume a coding-decoding system that will give an adequate error performance with an E/N_o of +2.5 db. While this is theoretically possible, it has not yet been realized in practice. If the decoders actually installed and operational in the DSN at mission time cannot achieve this performance, this would result in a reduction of the effective margin in the communication links unless transmitter power were increased.

c. Data Subsystem - There is no indication that a major technical development is required in the data handling area. Once the method of obtaining the physical sample and the analog voltage, or count representative of the desired measurement, is established for the instrument design there is no significant problem in implementing a data handling system using today's technology. Uncertainties, of course, exist in that some of the science instruments do not presently exist and it can be anticipated that the interface specifications will change.

2. Balloon Probes

a. Balloon Probe Design - For the balloon probe design, the general concepts have been shown to be feasible in both study and hardware test programs under contract with NASA, Langley Research

Center. However, in detail design there are potential problem areas and uncertainties that must be more fully resolved before final design. The potential problem areas include:

1) Lightweight, high-pressure tank development;
2) Balloon material quality control and development of fabrication techniques;
3) Large diameter (D = 20 ft) balloon deployment techniques.

The uncertainties in the criteria for the present designs are reflected primarily in the system weight penalties. Hopefully, with additional Venus atmospheric data from ballistic probes, and results of study and hardware testing, the uncertainties will be reduced before final design proceeds. The main uncertainties at this time are in the following areas:

1) Venus atmosphere radiation and cloud model;
2) Balloon thermal model with updated materials properties;
3) Establishment of appropriate balloon system design margins to account for the variations in expected environment, such as changes in temperature and atmospheric turbulence, as well as changes in material characteristics due to environment.

b. Telecommunications and Power - Balloon position determination by ranging and polarization is an untried technique. Although no serious problems are anticipated, there are some uncertainties. Perhaps the greatest of these is the use of ground-based ionospheric soundings to infer the polarization rotation due to the Earth's ionosphere.

The balloon solar panels are based on sunlight levels derived from a specific cloud model. Although this model is in good agreement with all available knowledge, it has not been verified by a descent probe, so uncertainties exist that cannot be resolved without a descent probe.

Assumed stored energy-to-weight ratios for both sterilizable and unsterilizable batteries are well within the limits of performance generally predicted for 1972, but they have not yet been realized in quantity production, so some uncertainty exists here also. This could have a significant effect on probe weight.

3. Planetary Vehicle

a. Engineering Mechanics - The major problem in adapting the Mariner spacecraft to serve as a bus for the probes of the current study is the relocation and increased impulse required on the midcourse propulsion system. Structurally, space is available on the probe support truss and in the common adapter module to relocate the motor and tankage respectively, but significant changes will be required in the mechanical, thermal, and electronic designs of this system. Less significant potential problems are those associated with ACS thrust level increases, thermal control louver and insulation blanket design modifications, and in the dynamic load magnification aspects of the added length of the Planetary Vehicle.

b. Telecommunications and Power - No areas of uncertainty with respect to the spacecraft and its interfaces with the probe systems were identified.

H. TECHNOLOGY DEVELOPMENT REQUIRED

No major technology development requirements have been identified to accomplish this mission. Certainly the progress required to reach the ground rule 1972 state of the art must be achieved. These areas include sterilizable batteries, lightweight transmitters, the programed capability of the deep space network, and production of science instruments as defined, with provisions for integration into probe systems, as indicated in Volume II, Chapter VI.

I. REFERENCES

V-1 *NASA Unmanned Spacecraft Decontamination Policy.* NASA Management Manual 4-4-1, September 1963.

V-2 *Environmental Specification Voyager Capsule Flight Equipment Type Approval and Flight Acceptance Test Procedures for the Heat Sterilization and Ethylene Oxide Decontamination and Environments.* JPL Specification VOL-50503 ETS, January 12, 1966.

V-3 *Capsule System Advanced Development Program.* JPL Summary 37-49 (Vol III), February 29, 1968.

V-4 "Investigation of the Feasibility of Sterile Assembly of Silver-Zinc Batteries." (NASA Contract NAS1-7656), Martin Marietta Corporation, September 1968.

V-5 *Materials Feasibility Tests for a Buoyant Venue Station Concept.* PR-22-69-17 (Vol 1). Martin Marietta Corporation, June 1969.

VI. SCIENCE SUPPORTING STUDIES

A. SCIENCE MISSION TRADES

The scientific mission requirements were discussed in Chapter I. This chapter considers some of the effects of the required altitude coverage, altitude sampling intervals, and targeting in the mission design and selection of probe types.

Figures VI-1 and VI-2 show the descent velocity and descent time from 6130 km vs ballistic coefficient ($B = m/C_D A$) at various levels in the MMC Lower Density Model Atmosphere. The lower density model is used because it represents a worst case for the instrument sampling intervals and required data rates. While the instruments generally require low velocities, and hence long descent times, considerations of the power and thermal control subsystems indicate a feasible upper limit of about 2 to 3 hr for the descent time. Thus, a ballistic coefficient of 0.005 slug/sq ft (parachute) required for the cloud composition instrument near the cloud tops is impractical if it is also desired to reach the surface. (Descent time for $B = 0.005$ is in excess of 24 hr.) The obvious solution is to release the parachute to a high ballistic coefficient configuration. For example, releasing the 0.005 chute at 6100 km to a ballistic coefficient of 2 results in a total descent time of 2.3 hr, as seen from Fig. VI-2 (83 min from 6130 to 6100 km and 56 min from 6100 to 6045 km with $B = 2$). Because of the extreme thickness of the Venus atmosphere, there is no single ballistic coefficient that will both satisfy the instrument sampling requirements at all altitudes and remain within the limits of feasibility. Satisfying the requirements near the cloud tops dictates a low ballistic coefficient, but results in excessive descent times. Keeping the descent time for a single ballistic coefficient within reason results in extremely poor resolution near the cloud tops.

For example, a ballistic coefficient of 0.5 gives a 2-hr descent time (Fig. VI-2), but the descent velocity at 6125 km is 175 m/sec (Fig. VI-1). This gives an altitude resolution of 24 km for the cloud composition instrument; that is, if a sample were taken at 6125 km, the probe would fall to 6101 km before the instrument could process another sample.

Thus, meeting the scientific objectives from above the cloud tops to the surface with the available instrumentation requires either a single vehicle with two (or more) ballistic coefficient stages or several vehicles with different (fixed) ballistic coefficients chosen to provide the desired altitude resolution.

The instrument sample time intervals required to obtain a given altitude resolution at various levels in the MMC Lower Model Atmosphere are plotted in Fig. VI-3 thru VI-8 as a function of ballistic coefficient. These data were used to select the descent ballistic coefficients and sample times (bit rates) for the baseline mission probes. The altitude resolution and number of measurements that result for the baseline mission are shown in Fig. VI-9 thru VI-14.

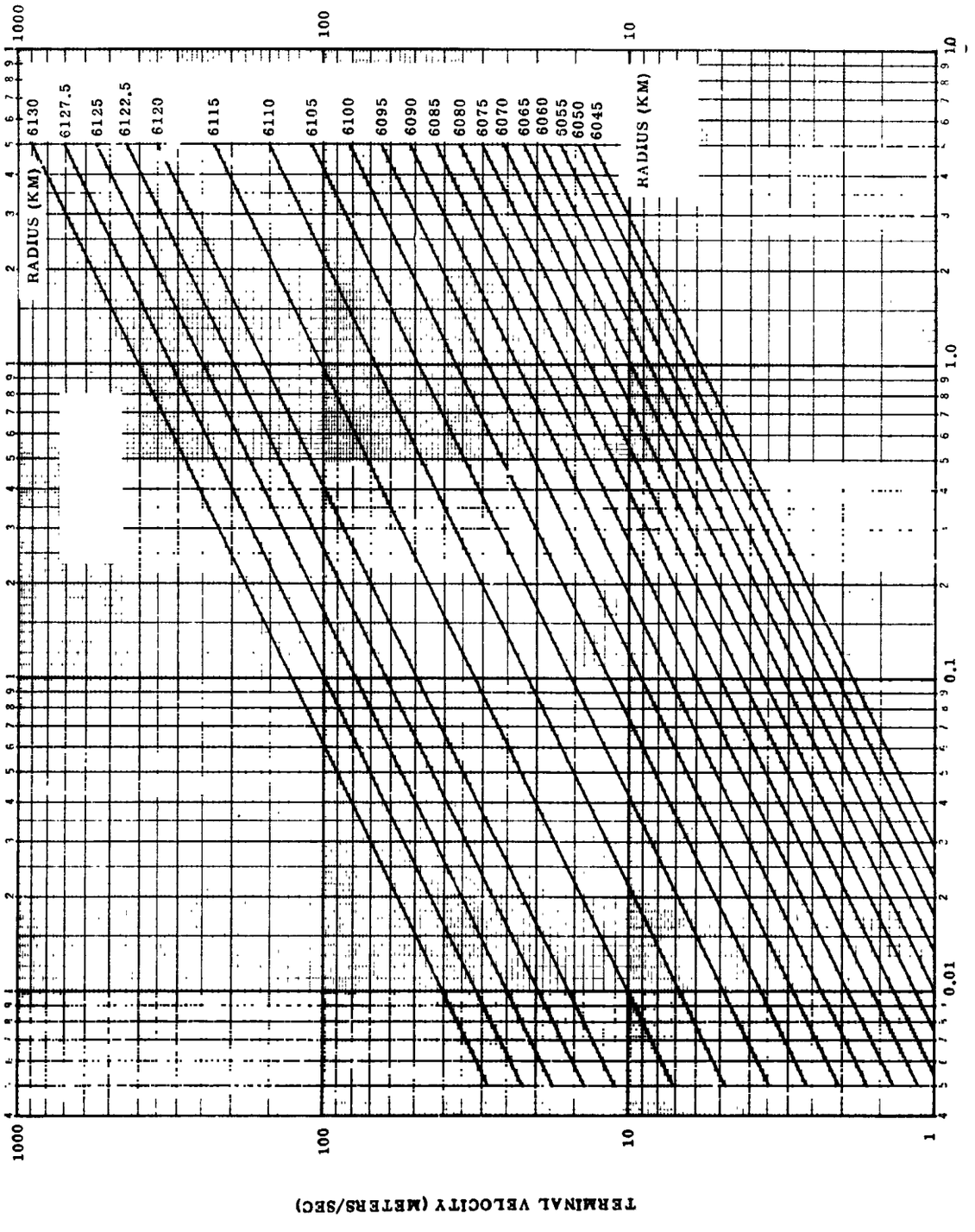


Fig. VI-1 Terminal Velocity in MMC Lower Density Model Atmosphere

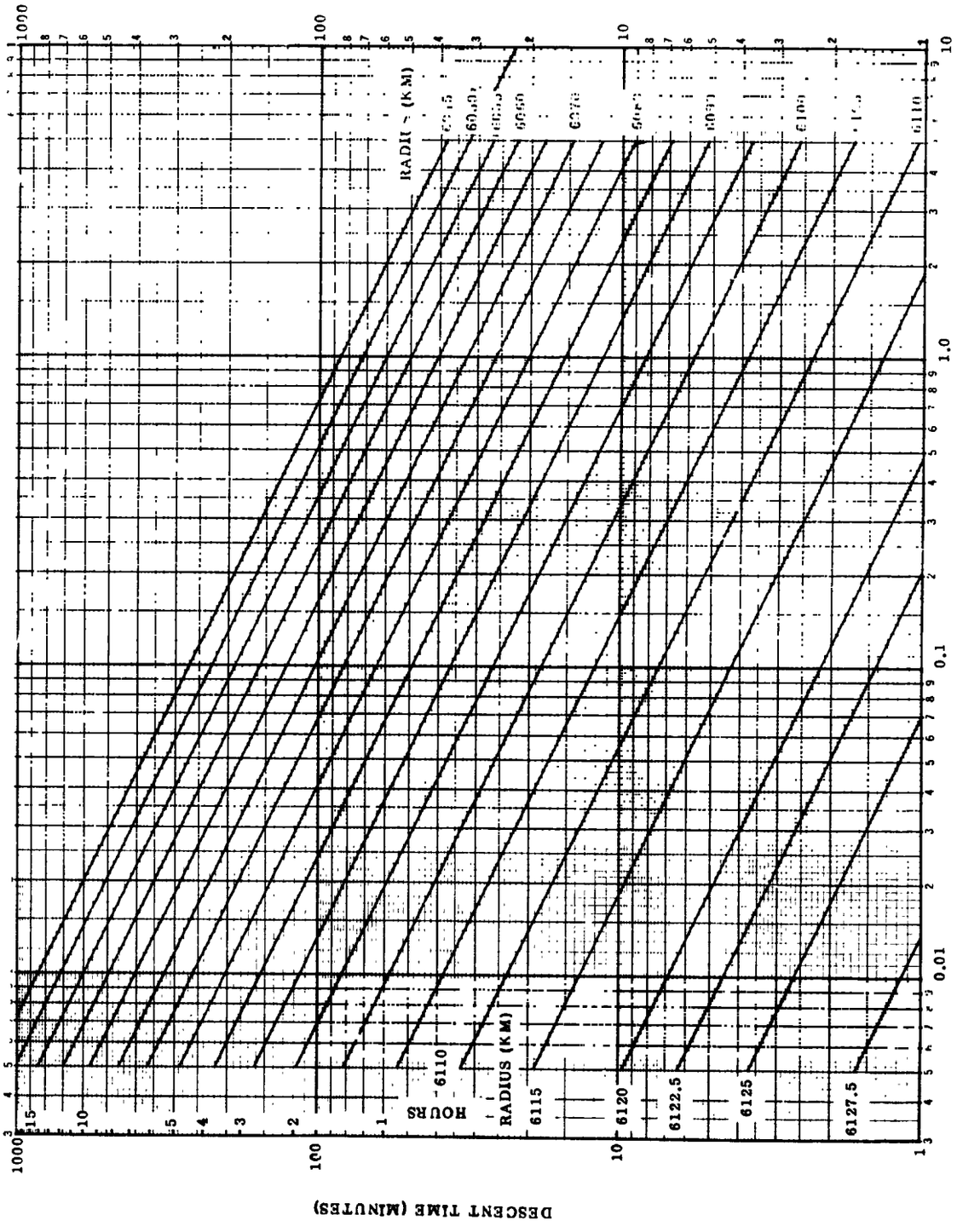


Fig. VI-2 Descent Time from 6130-km Radius in MMC Lower Density Model Atmosphere

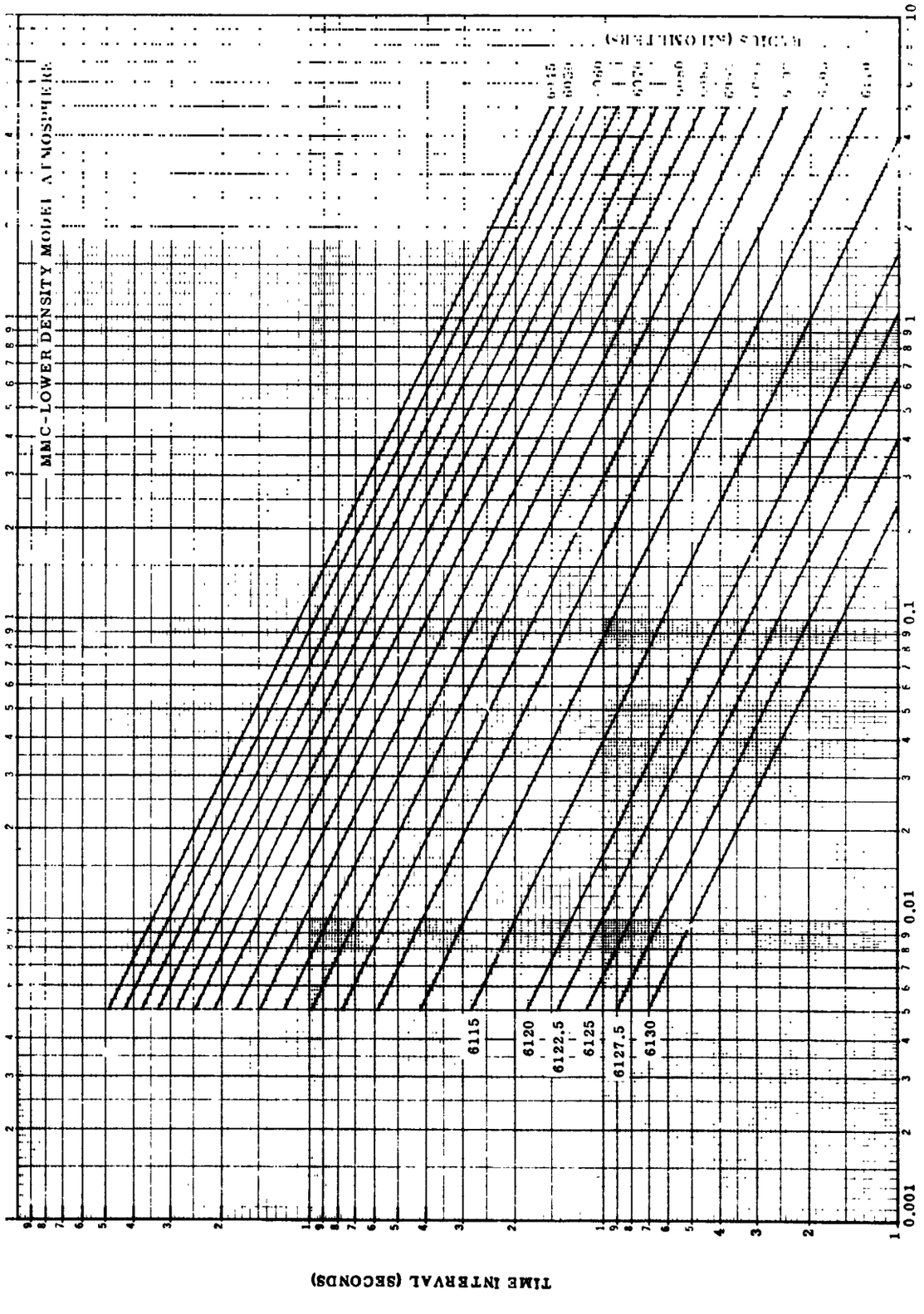


Fig. VI-3 Sample Time Intervals Required to Obtain 200-m Altitude Interval

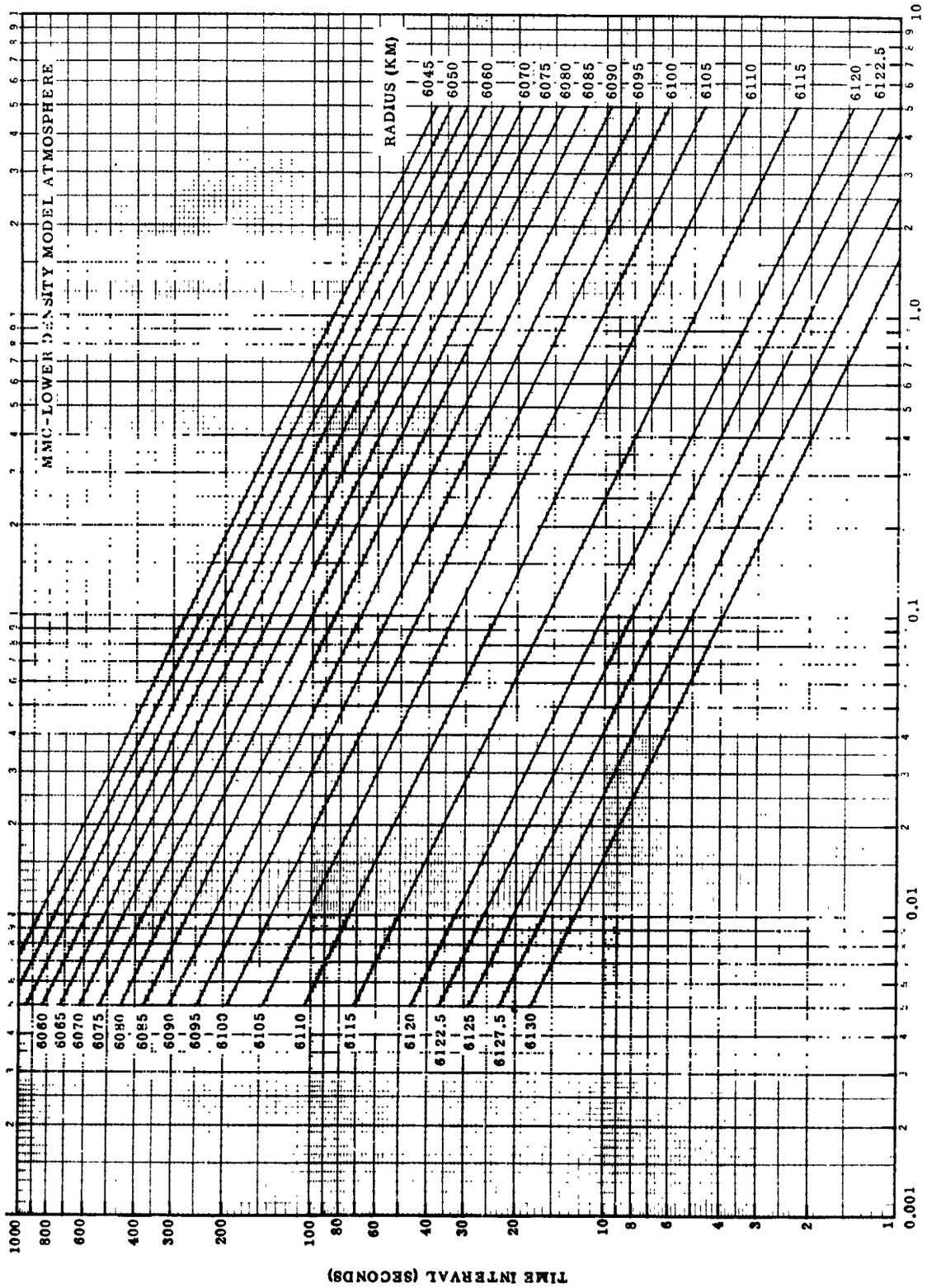


Fig. VI-4 Sample Time Intervals Required to Obtain 500-m Altitude Interval

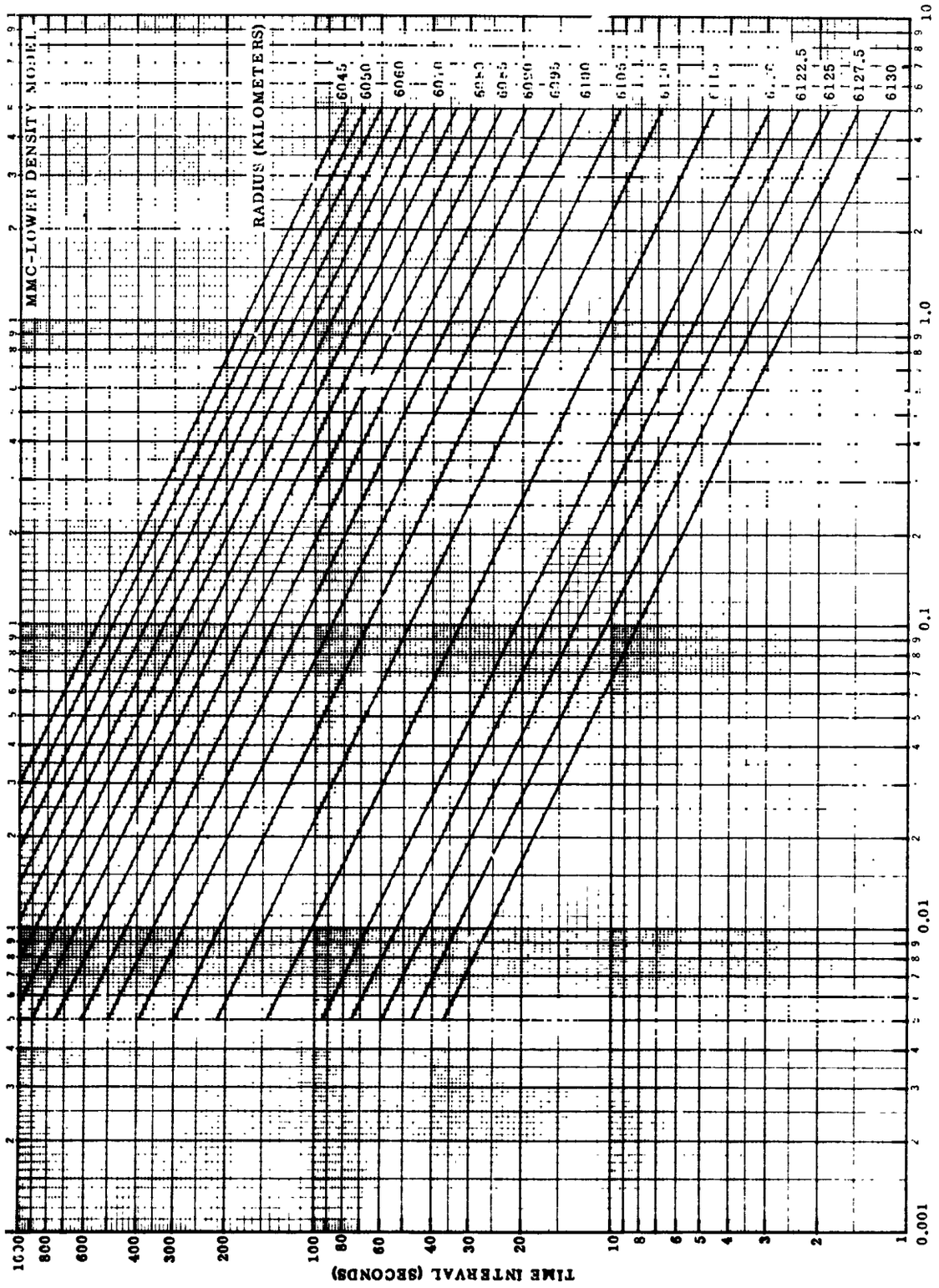


Fig. VI-5 Sample Time Intervals Required to Obtain 1000-m Altitude Interval

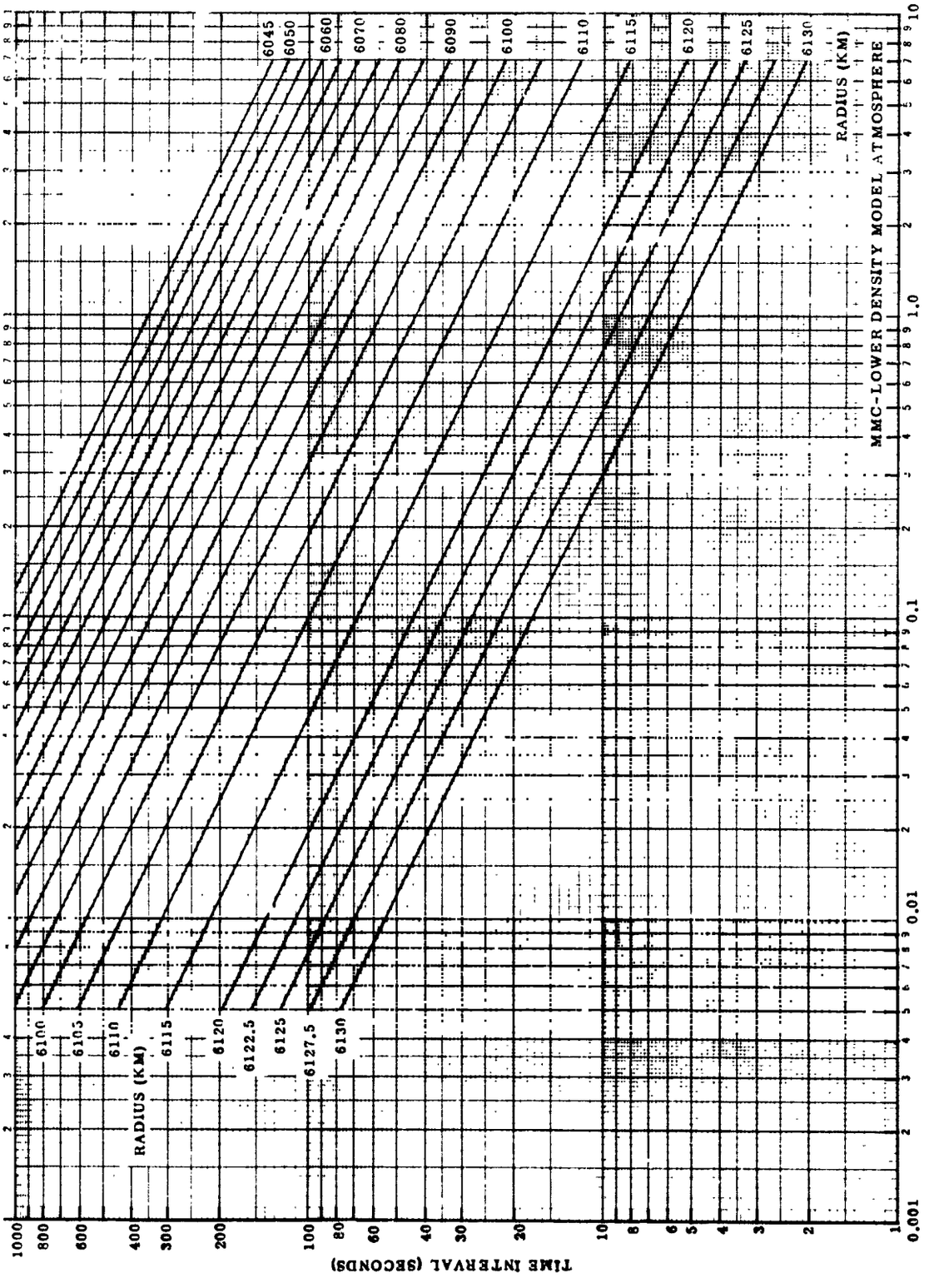


Fig. VI-6 Sample Time Intervals Required to Obtain 2000-m Altitude Interval

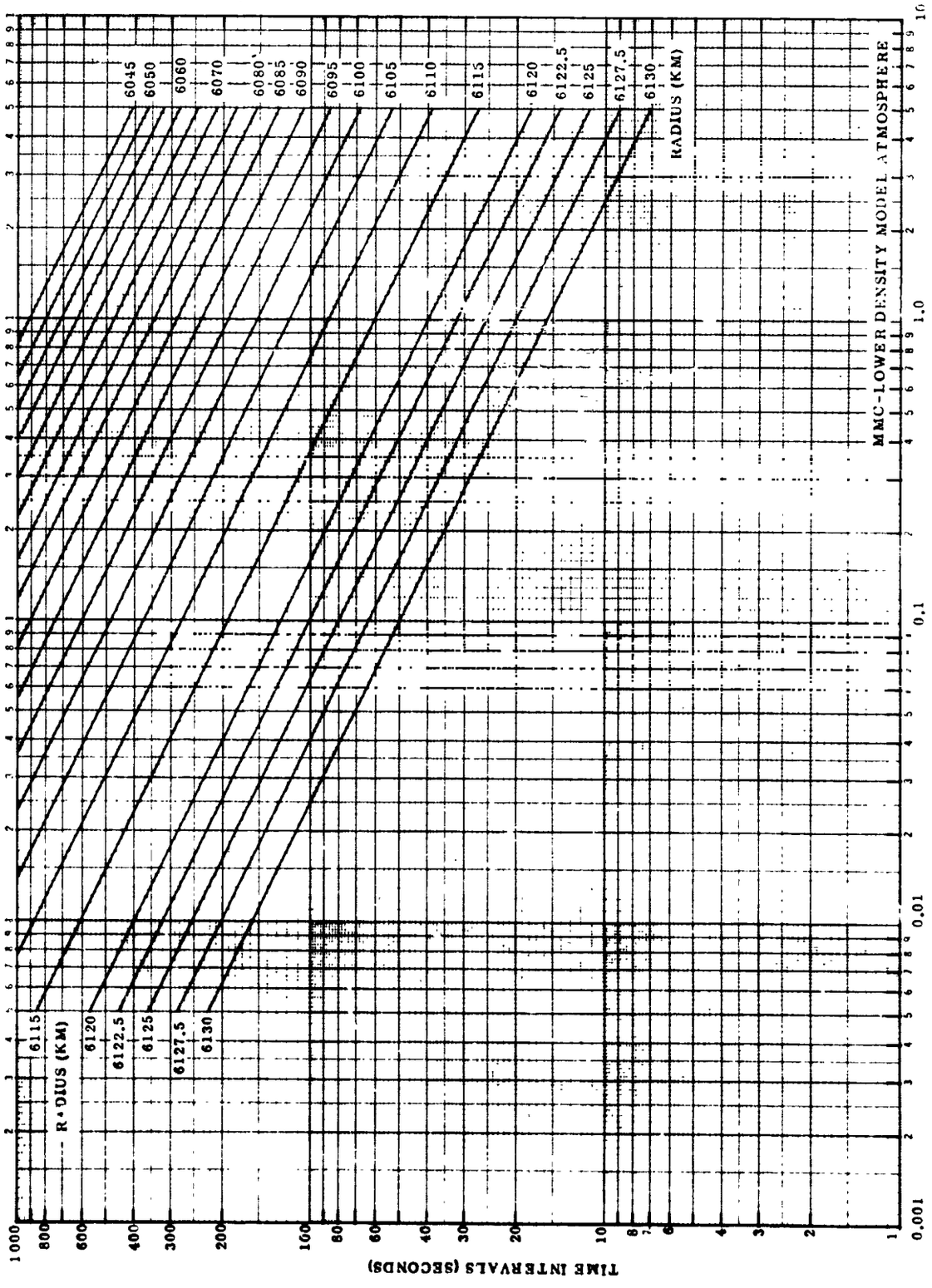


Fig. VI-7 Sample Time Intervals Required to Obtain 5000-m Altitude Interval

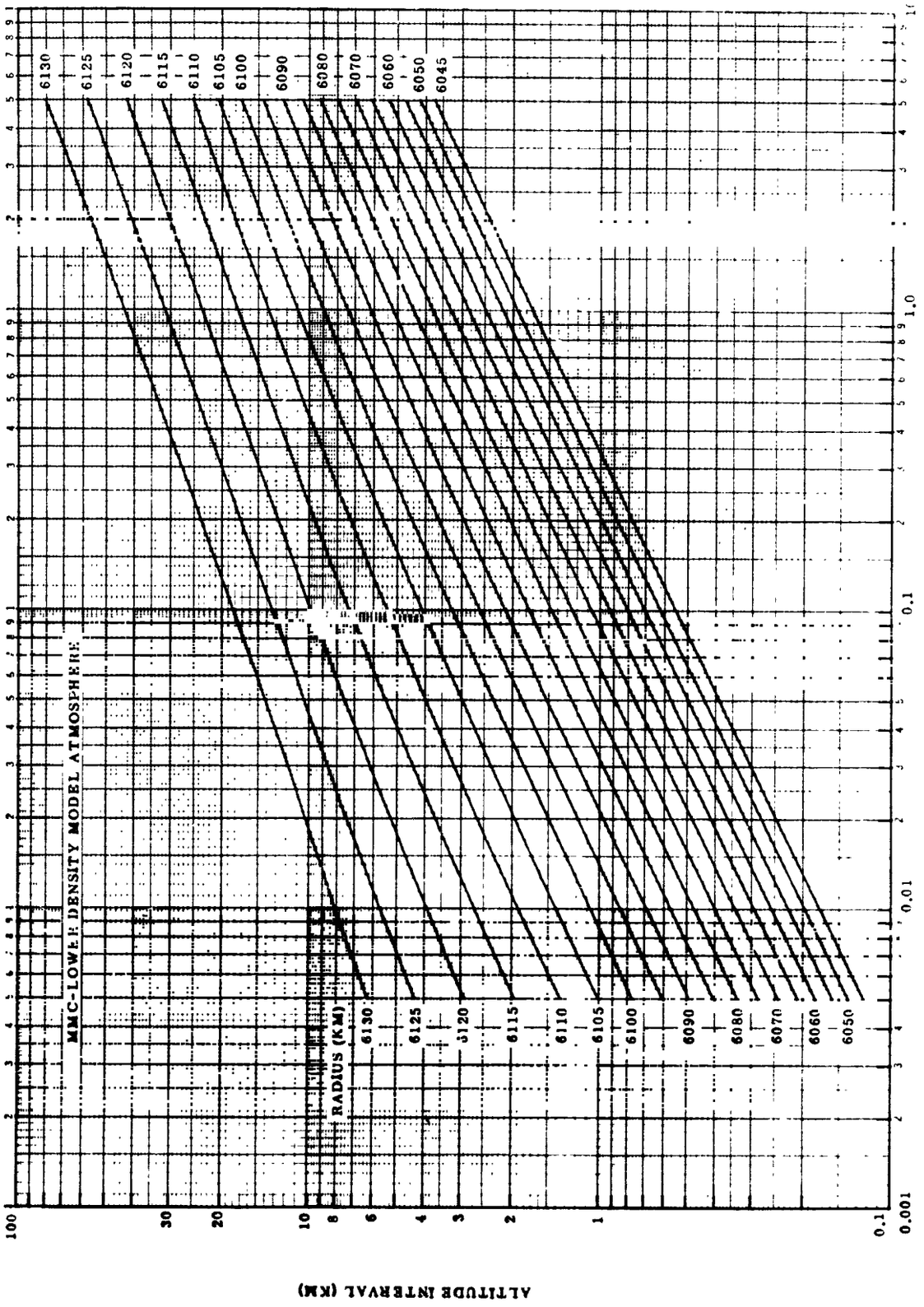


Fig. VI-8 Altitude Intervals Obtained with 300-sec Sample Time

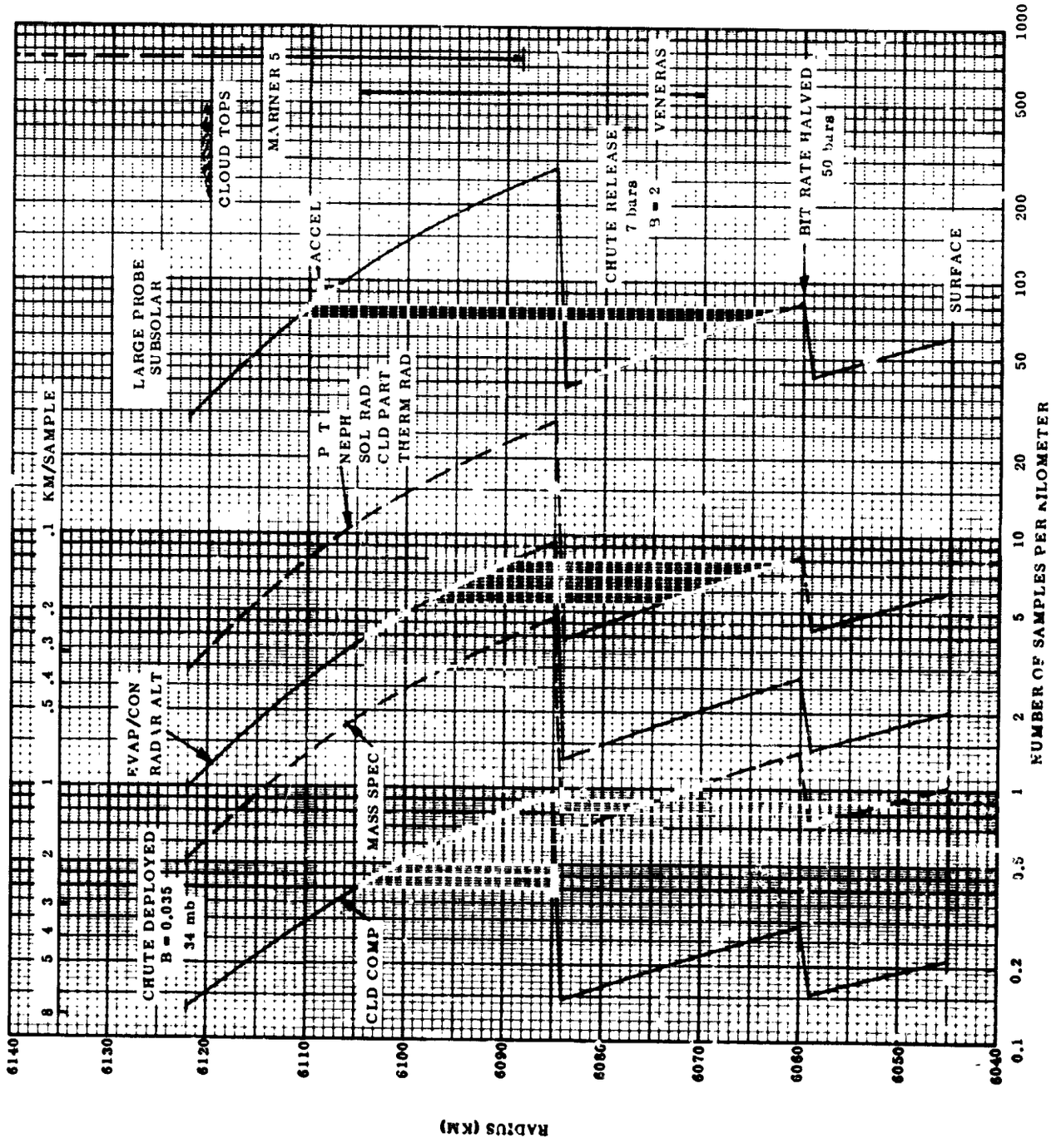


Fig. VI-9 Altitude Resolution for Large Probe

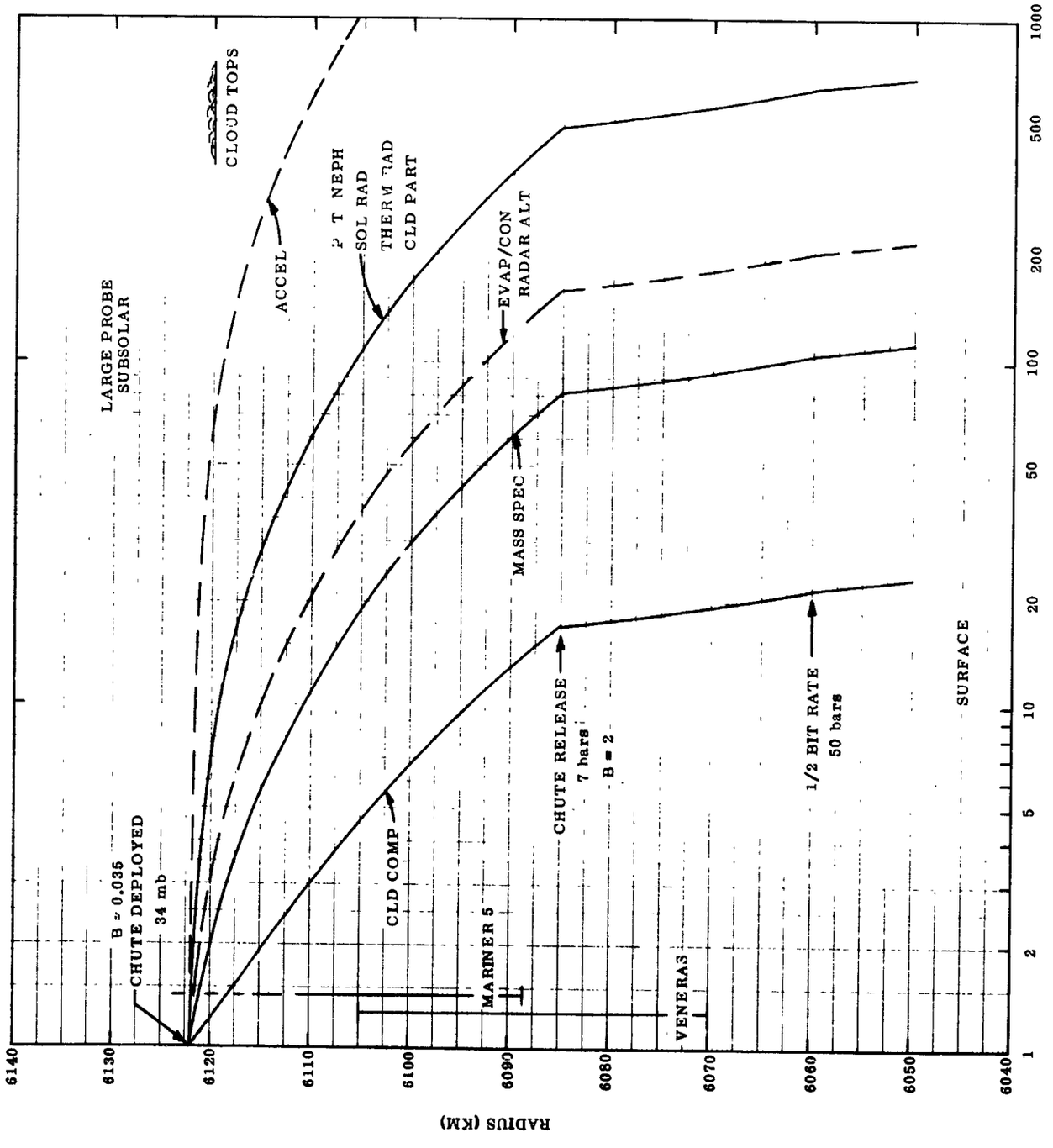


Fig. VI-10 Number of Measurements vs Altitude for Large Probe

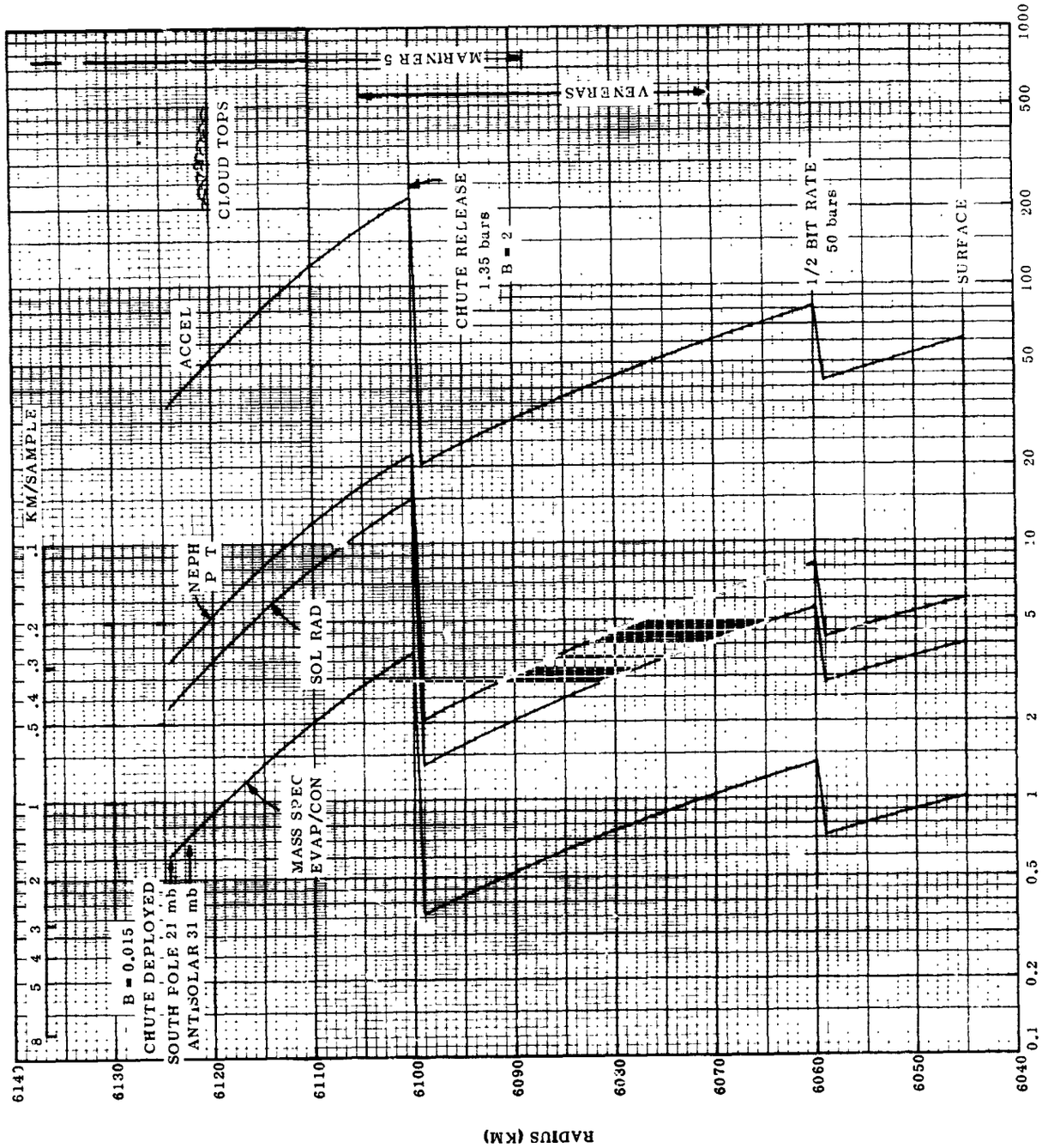


Fig. VI-11 Altitude Resolution for Small Probes

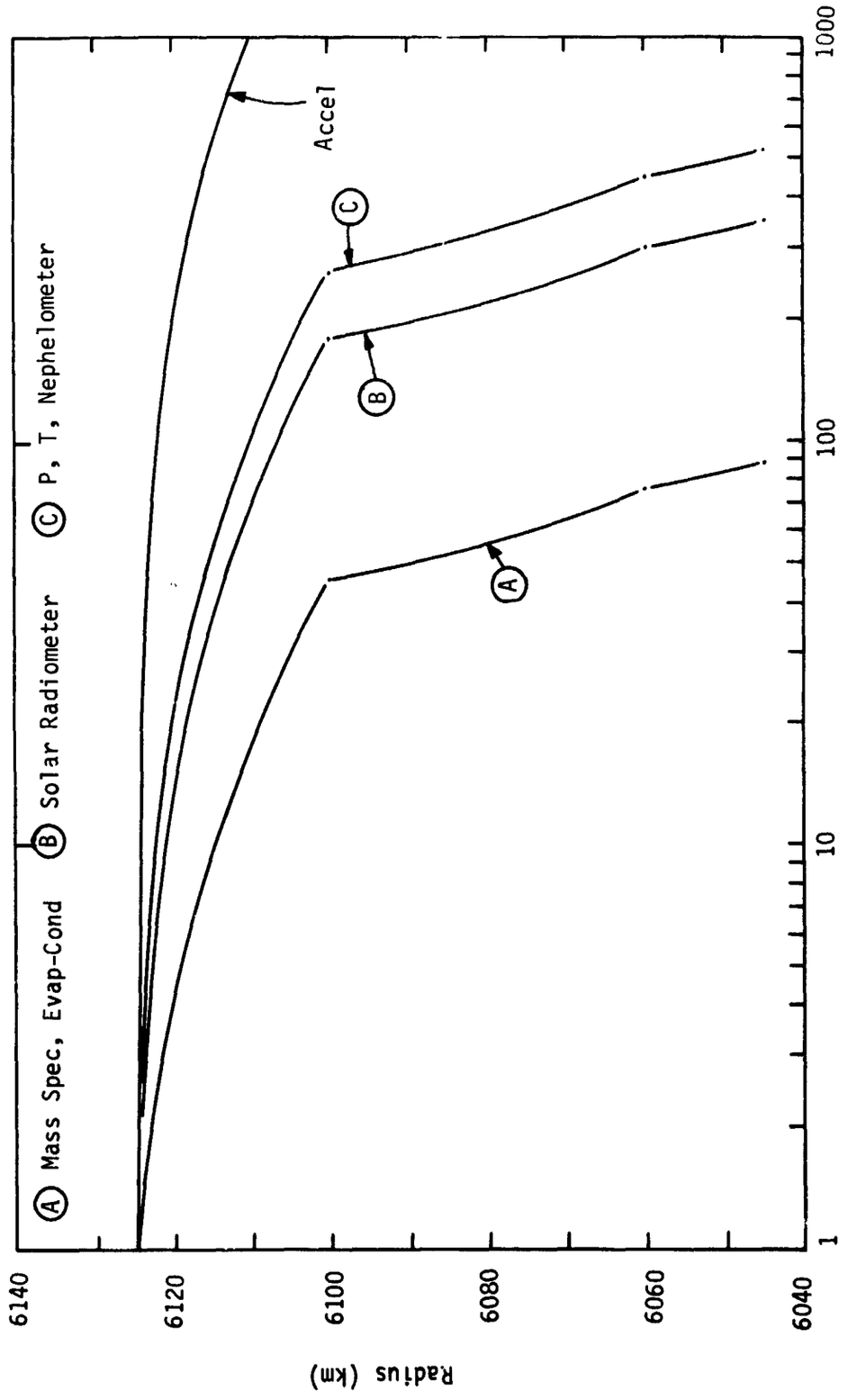


Fig. VI-12 Number of Measurements for Small Probes

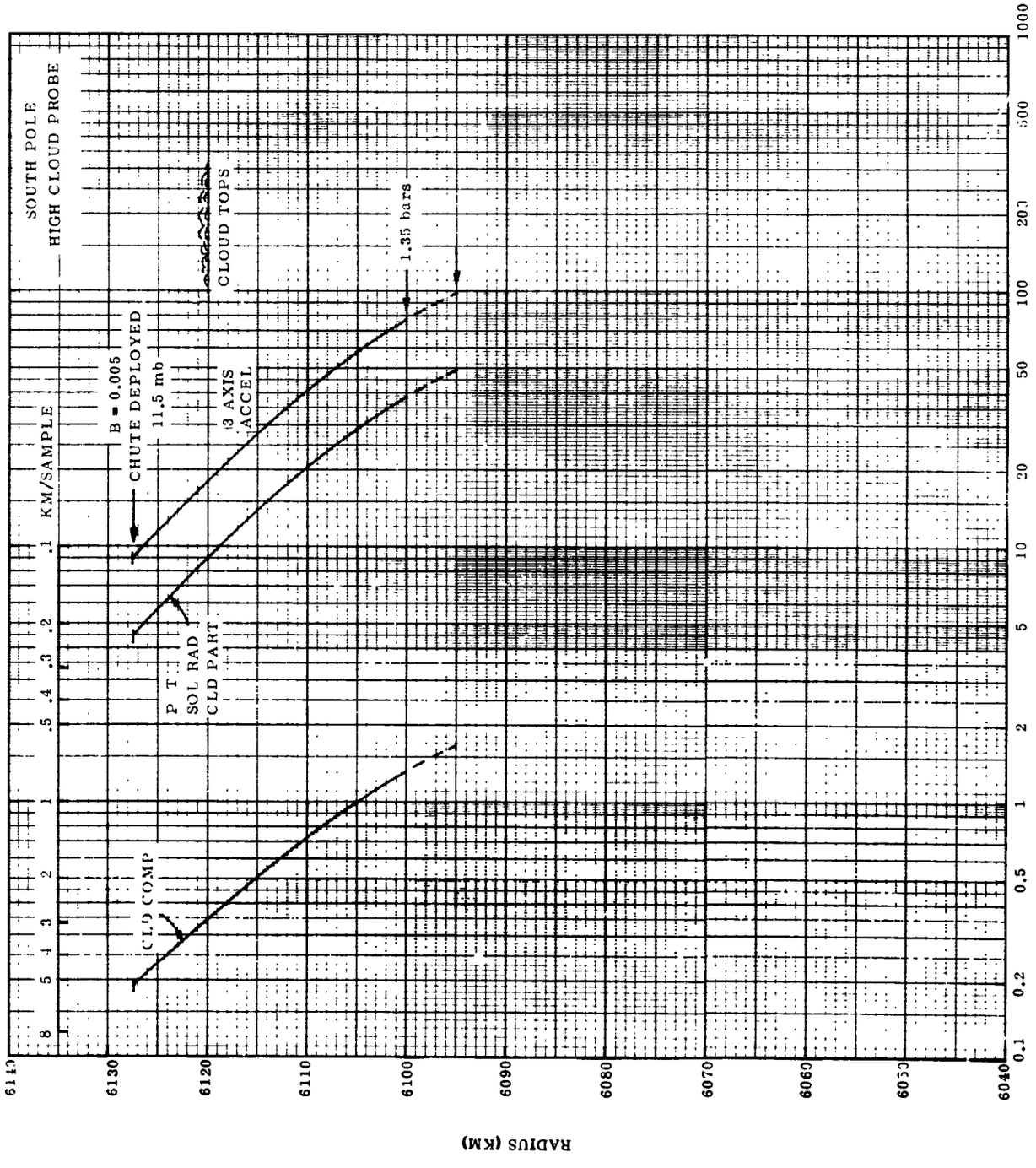


Fig. VI-13 Altitude Resolution for Small Probes

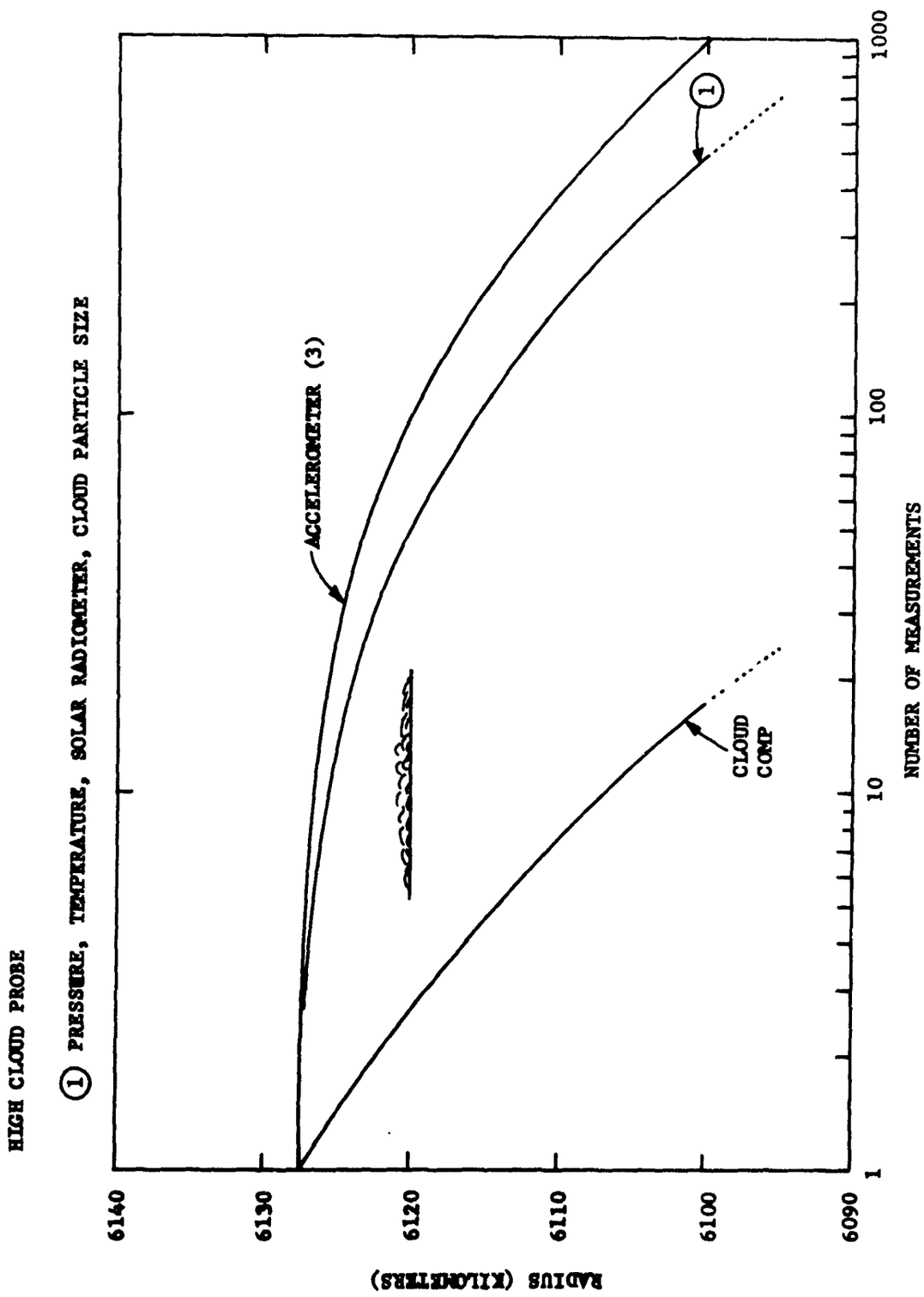


Fig. VI-14 Number of Measurements for High-Cloud Probes

B. SCIENCE MECHANIZATION

1. General Objectives

This section discusses design mechanization of science instrument sampling and/or data gathering, including physical arrangement of instruments, ducting, and sensor exposure required to obtain meaningful measurements of the Venus environment. Analysis of instrument design is not within the scope of this study; however, assumptions about the instrument designs were made, when required for design mechanization of science instrument sampling and/or data gathering. Our assumptions are based on the descriptions of the Venus entry probes' instrumentation provided in the RFP and listed in Table I-3 (Chapter I of this volume).

Because these descriptions are brief and do not provide detailed design data about each instrument, the mechanization concepts should be revised when more information about the science instruments becomes available. A major objective of this discussion is to point out mechanization problems for the science instruments and to show concepts to overcome the difficulties. It is recognized that the mechanization concepts presented require further analysis, design, and developmental testing that may result in significant changes when flight hardware is designed.

These science mechanization objectives must be achieved in spite of interferences by atmospheric conditions, restraints of weight, power, and size, and competing requirements of thermal control, probe structure, and aerodynamics. The fundamental tradeoff factors are weight and cost. Major difficulties are caused by the wide range of possible environmental disturbances and the requirements of low heat transfer and low power consumption.

Table VI-1 is a summary of instrument specifications, sample intervals, bits per sample, and a tabulation of probe types for which each instrument is used. The large ballistic probe measures in the subsolar zone below a planet radius of 6122 km. The small ballistic probes measure below 6124 km radius in the antisolar and polar target zones. The measurement range of the high-cloud probe is between 6128 and 6090 km of planetocentric radius. Balloon probes float at about 6122 or 6108 km of planetocentric radius.

2. General Considerations for Science Mechanization

Mechanization of sample acquisition and processing is strongly influenced by the requirements of thermal control, aerodynamic probe stability, resistance to high pressures and temperatures, and general compatibility with the environment.

The high-cloud probe and the 500 mb balloon probe require little if any thermal insulation. The ballistic probes and the 50 mb balloon probe have an external pressure shell with multilayer thermal insulation in an evacuated annular cavity between the pressure shell and the temperature controlled instrument and electronic compartment inside the probe. To minimize thermal conduction between the inner and outer canister by provisions for science instrument sampling, penetrations through the thermal insulation are in most cases limited to light signals (radiometers, nephelometer, particle counter, condensimeter/evaporimeter) and electrical signals (temperature gage, nephelometer, particle counter, condensimeter/evaporimeter). When feasible, all or a large part of each instrument is mounted outside the pressure shell. This is especially important when instrument sampling requires a large atmospheric flow. Heating of flow channels is necessary to avoid condensation of the sample gas along the walls of the tubes. All electronics and light detectors are mounted inside the probe. Light sources and simple mechanisms are mounted on the outside.

Table VI-1 Summary of Information About Instruments

Instrument and Row No. in Table VI-2	Weight (lb)	Power (w)	Actual Sampling Time (sec)	Desired Interval (m)	Nominal Radius for Sampling Interval (km)	Bits per Sample	Probe Type* of Instrument Use	Remarks
Accelerometers (4), Row 8	1.9	4.0	0.2		6130<R<6180	40	L, S, H	Entry phase 0.1 g to staging
	1.9	4.0	1		6130>R>6045	10	L, S	After staging
			5			30	H	After staging
Pressure Gages (5), Row 6	0.8	0.1	10	200-500	6045-6070	8	L, S	Range switched
	0.5	0.1	10			8	H	
	0.2	0.1	10			8	B	
Temperature Gage (Range Switched), Row 7	0.8	0.2	10	200-500	6100-6130	8	L, H, S	L, S 200-900°K; H 200-500°K B, 250-350°K or 200-300°K
	0.8	0.2	~8 hr					
Neutral Particle Mass Spectrometer, Row 14	10.0	10-20	60	1000-2000	6110-6130	600	L, S	
Thermal Radiometer, Row 2	3	3	10	200-500	6120	16	L	
			15			120	S	
Solar Radiometer, Row 1	4	3	10	1000	6110-6130	200	L, H	
			15			120	S	3 45°/Viewing cones
Nephelometer, Row 3	4	3	10	200-500	6120	16	L, S	
Cloud Particle (No.-Density, Size), Row 4	8	10	10	200-500	6120	80	L, H	
Cloud Particle Composition, Row 14	20	50-60	300	~5000	6115-6130	1800	L, H	
				~2000	<6115			
Evaporimeter-Condensimeter, Row 5	2	10	30	1000-2000	6110-6130	456	L	
	2	10	60			456	S	
70 km Radar, Row 10	15	35	30	1000	~6120	60	L	
Transponder, Row 9	2	0.5	Continuous				L, S, H	Measures velocity only
	3.5	1.5					B	Measures velocity & range
Impact Indicator, Row 11	0.2	0.5	Continuous			See Remarks	S	Signal inserted near ground
Ion Mass Spectrometer, Row 12	3	1	7	8800	6150-7000	320	L	Instrument separated at 0.1 g
Open Ion Source Spectrometer, Row 12	10	10	10	8800	6150-7000	560	L	Separated at 0.1 g
Electron Probe, Row 12	3	3	0.5	8800	6150-7000		L	Separated at 0.1 g
UV Photometer, Row 12	2	1	1		6150-7000		L	Separated at 0.1 g

*L = large ballistic probe, S - small ballistic probes.
H = high-cloud probe, B = balloon probe

Particles suspended in the atmosphere are deflected by shields to avoid impingement upon sensors or windows. Windows are kept clean with protective covers that can be combined with a window wiping device if required. The cover is opened only during measurements and therefore the window is exposed for about 1% of the descent time.

When sample flow to instruments is caused by the dynamic pressure, the mass flow increases with ambient density, and varies with changes in ballistic coefficient. Simple flow controls can be used to generate an approximately constant mass flow to the instruments.

The inlet leak for the mass spectrometer will be heated to avoid condensation and blockage. The sampler for the cloud particle analyzer collects particles outside the probe wall and transports the collected samples by means of a transport rod and a tube through the probe walls to the analyzer.

3. Experiment Mechanization

Each experiment requires evaluation of specific tradeoff factors. Table VI-2 is a summary of mechanization concepts and tradeoff factors. A discussion of each science instrument's mechanization and integration follows. Additional information about sample acquisition and integration into the probe design is presented in Chapter III.

a. Solar Radiometers

1) Requirements - The solar radiometers measure radiation in four optical wavelength ranges ($\lambda<0.5\mu$, $0.5<\lambda<1.5\mu$, $1.5<\lambda<2.5\mu$, and $\lambda>2.5\mu$). Several radiometer units are contiguously arranged. The large ballistic probe and the high-cloud probe have five radiometer units with contiguous fields of view. Each field of view has a 30° cone angle. The small ballistic probe for the polar target zone has three radiometer units with a 45° cone angle for each unit.

TABLE VI-2 SCIENCE MECHANIZATION

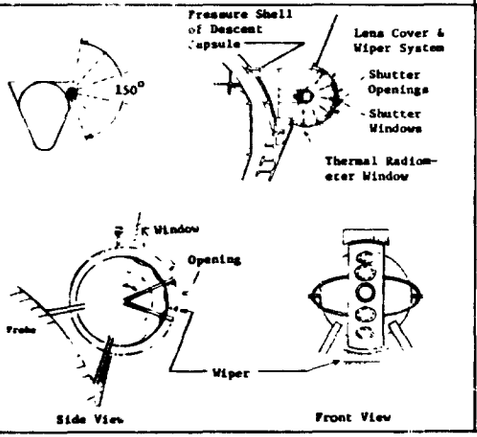
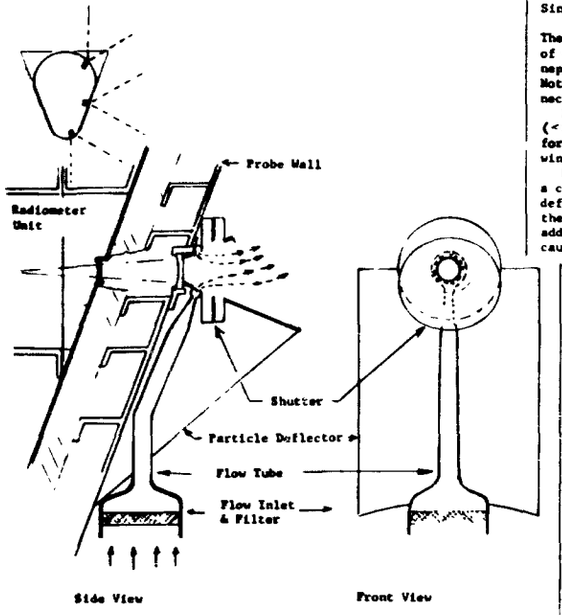
SCN NUMBER	MEASUREMENT OBJECTIVE	ALTERNATE MECHANIZATION APPROACHES		EVALUATION OF MECHANIZATION APPROACH
		SKETCH OF CONCEPT	DESCRIPTION	
1	**Solar Radiometer** **Measure solar radiation in 4 wavelength ranges (λ<0.5 μ, 0.5<λ<1.5 μ, 1.5<λ<2.5 μ, λ> 2.5 μ). Coverage of roughly 4 π steradian is desired, the field of view for each radiometer unit has a cone angle of 30 to 90° depending on number of radiometers and probe configuration.**		Solar Radiometer with 5 Contiguous Beams The radiometer windows are installed on a semisphere as shown in the figure. The independent radiometer unit is attached to the pressure shell. Normally the radiometer windows are covered by the shutter windows. For measurements the shutter rotates 15°, a wiper attached to the shutter cleans the radiometer windows and the measurements are conducted through the shutter openings. Should the shutter drive fail, degraded measurements are conducted through the shutter windows. Referring to the sketch at the left: separate sphere with all solar radiometer units and one oscillating or rotating ring to protect lenses against contamination. The lens protection ring has 4 windows and one opening. Only during measurement is the opening positioned in front of the respective lens. During movement of lens protection ring wipers clean the lenses and the lens protective ring.	Preferred in Modified Form Thermal and solar radiometers can be combined in one unit which is attached to pressure shell. Single shutter moves 15 degrees to open all radiometers. Only one shutter mechanism required. Windows in shutter provide degraded performance if mechanism fails. Window leakage would not interfere with probe thermal insulation. Simple integration into probe. Disadvantages: Rotating drive mechanism required. Relatively high surface area and high heat transfer.
			Single Radiometer Unit with Shutter The figure to the left shows a combination of various means to protect radiometer or nephelometer windows against contamination. Not all these protective features are necessary in each application. Because of the short radiometer response (< 0.1 sec), the shutter exposes the window for less than 1% of the descent period. A window wiper can be combined with the shutter. For view angles within $\pm 30^{\circ}$ off horizontal a conical shield combined with a particle deflector and/or dry, filtered flow toward the outside of the conical shield provide additional protection. The flow can be caused by the probe's dynamic pressure.	Not Preferred for Solar Radiometers With a shutter the total window exposure period of descent probe is in the order of one minute. Development of a solenoid operated, high temperature shutter which functions in spite of ice and other condensibles is considered feasible. Danger of window contamination can be further reduced by conical shield, particle deflector and/or filtered dry gas flow. Low cooling requirements, location not critical, one design applicable to protect all windows Disadvantages: Several radiometer units, therefore more electronics and housing weight; accurate alignment of openings in probe walls required; thermal control of radiation detectors cannot be combined, probe integration is difficult.

TABLE VI-2 (cont)

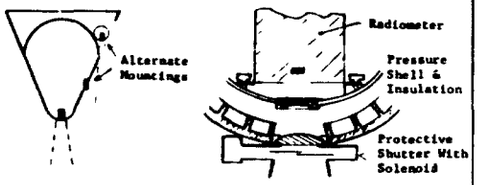
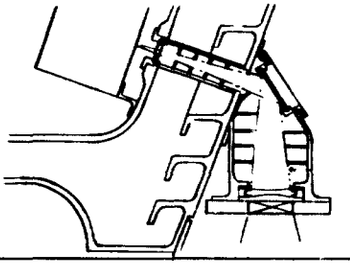
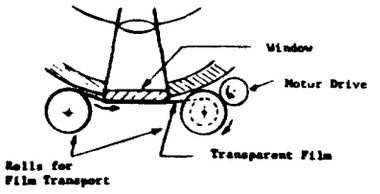
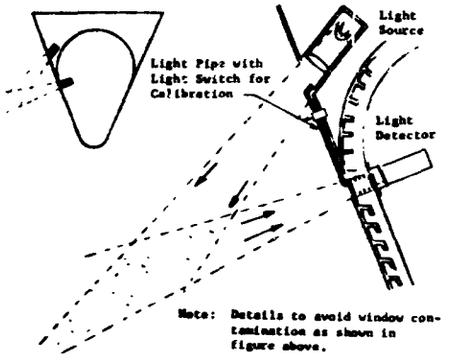
ROW NUMBER	MEASUREMENT OBJECTIVE	ALTERNATE MECHANIZATION APPROACHES SKETCH OF CONCEPT	DESCRIPTION	EVALUATION OF MECHANIZATION APPROACH
2	**Thermal Radiometer** Has a vertical, downward looking, and narrow field of view. Measures radiation in 6.5 to 8.5 μ and 9.2 to 10.8 μ bands.	 	Thermal Radiometer with Shutter Protection Similar to the approach described in column 1 above a protective shutter exposes the radiometer window only during the short measurement periods. A window wiping device can be combined with the shutter drive. Atmospheric flow with condensible vapors to the window is reduced by the short baffle in front of the window. Alternate window protections are shown in columns 3 and 1 above.	Preferred in Nose of Probe The protective shutter is simple and reliable. It exposes the window for only 1% of the time and window wiping can be combined with the shutter. Atmospheric flow with condensible vapors and particles can be reduced near the window by the short baffle. Alternate concepts are discussed in columns 1 and 3. The side mounted thermal radiometer was not preferred because of aerodynamic interference.
			Window Protection by Periodically Replaced Film Window contamination is avoided by replacement of transparent film before each measurement. Step-wise film movement is preferred, but continuous film movement is acceptable if it simplifies drive mechanization. Other approaches to film transport are possible.	Not Selected Mechanization of film drive outside of probe shell is complicated and availability of high temperature film which is transparent for all required spectra is doubtful. Thick layers of particles and ice, etc., cause severe problems for transport mechanism. Advantages: Complete replacement of window surface shortly before measurement.
3	**Nephelometer** Emits light beam and measures light scattered by aerosol at selected distance.		Nephelometer with Only One Probe Window Only one window (about 1.0 in. dia.) through the pressure shell is necessary because the light source can be designed to withstand the ambient environment. Light modulation discriminates ambient light. A light baffle reduces the effect of light which is not scattered by the aerosol sample. A calibration device controls the detector gain to eliminate the influence of light source variations and window contamination.	Preferred Only one window through pressure shell is required. In flight calibration includes transparency of window; light baffle increases signal to noise ratio. Window protection similar to that listed in 2. above is possible if required.

Table VI-2 (cont)

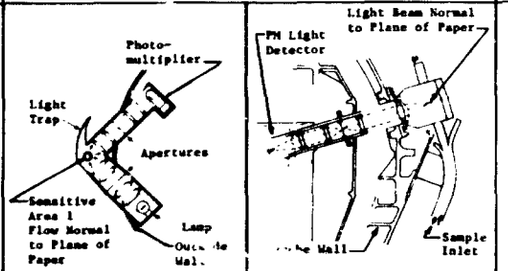
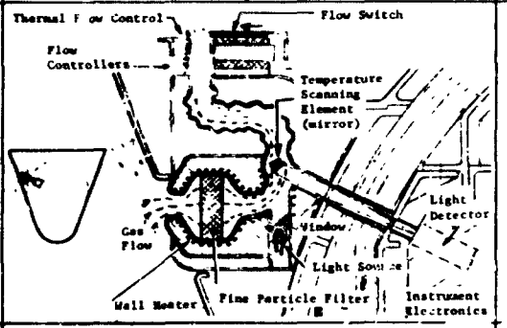
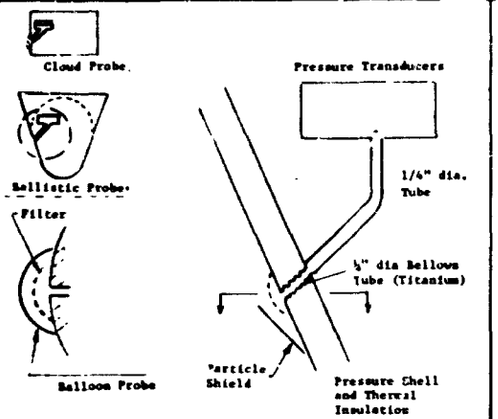
ROW NUMBER	MEASUREMENT OBJECTIVE	ALTERNATE MECHANIZATION APPROACHES SKETCH OF CONCEPT	DESCRIPTION	
4	**Cloud Particle Number - Density and Size Sensor** This instrument distinguishes between different groups of particle size and counts the particles in each group. Estimated range of particle sizes is 0.5 to 20μ diameter.	 High Cloud Probe Installation Ballistic Probe Installation	Only Light Detector of Particle Sensor is Inside Probe The tube sampling the particles and the light source are outside the pressure shell. The particles in the sample flow are distinguished from stationary particles by electronic signal handling (differentiation). A device for window wiping could be incorporated, but an arrangement to calibrate all variations of the optical system is preferred.	Preferred This approach causes only a small amount of heat transfer through the probe shell (one small window 0.5 in. dia.). Little or no window heating is required. No cooling of sampling channels needed.
5	**Evaporimeter-Condensimeter** Measures temperature at which atmospheric constituent, condense.		Evaporimeter-Condensimeter (Detector Outside of Probe) The channel walls ahead of the condensation/evaporation mirror are heated slightly above the ambient temperature. Therefore, part of the instrument is mounted outside the pressure shell. Large particles fly by the inlet because of their inertia and small particles are filtered out. The mirror is heated and cooled thermoelectrically. The light signal is sensed inside the pressure shell. The light source is mounted outside the pressure shell. If required, light chopper and resonance filter for electrical signal reduce ambient light interference. Electrically and thermally controlled flow regulators optimize heat transfer conditions.	Preferred This approach was chosen because of low heating and cooling requirements for channel walls and instrument respectively. Other advantages are short flow channels and design simplicity. Disadvantages: Pump required for higher sensitivity. Window through pressure shell needed. Some interference by ambient light possible.
6	**Pressure Transducers** Measures the ambient atmospheric pressure.		Pressure Gauges in Probe & Protection Against Flow Blockage The particle shield deflects particles away from the pressure inlet and an in-situ filter provides a large area of inlet ports and reduces circulation of condensible vapors into the pressure connections. Because of gravity, liquid condensed in the pressure connection flows to the outside. A small diameter, thin wall bellows tube minimizes the heat transfer through the thermal insulation. About 0.4 pound additional weight is required for pressure proof transducer housing.	Preferred for descent probes This concept of pressure inlet and connection avoids blockage of pressure connections and minimizes heat conduction to inside of probe. Temperature of transducers is within narrow range (±10°C).

TABLE VI-2 (cont)

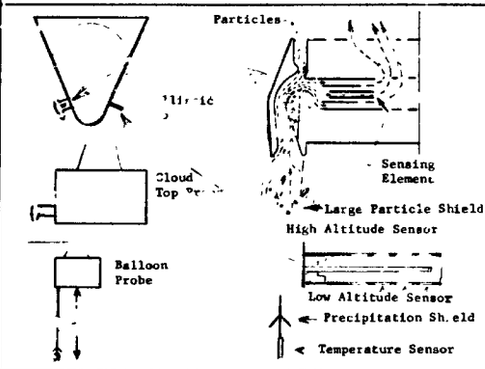
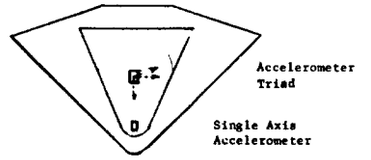
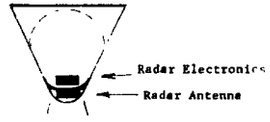
ROW NUMBER	MEASUREMENT OBJECTIVE	ALTERNATE MECHANIZATION APPROACHES SKETCH OF CONCEPT	DESCRIPTION	EVALUATION OF MECHANIZATION APPROACH
7	**Temperature Gauge** Measures from 200 to 900°K. Temperature ranges are 200-300, 300-400, 400-600, and 600-900°K. Range switching is temperature actuated. Accuracy ± 0.5% of temperature interval.		Temperature Gauge with Particle Separator To avoid damage to the sensing element or temperature errors, large particles and droplets are deflected by the large particle shield, smaller particles are separated when the flow makes a right angle turn. The boundary layer growth is controlled by small holes along the flow channel. The flow inlet is at least 2 inches away from the probe wall. To avoid condensation, the temperature probe has good heat transfer to ambient, low thermal inertia and is thermally insulated from the supporting structure. For ballistic probes two temperature sensors are recommended. One sensor can be optimized for low atmospheric density and fast response, the second sensor is primarily designed for the dense atmosphere and ruggedness. The balloon probe temperature gauge is deployed about 40 feet below the probe and has a precipitation shield.	Preferred Avoids boundary layer interference, provides protection against particles and drops combined with satisfactory sensor response time. Interference of balloon and probe during down drafts is avoided by sensor deployment. The sensor is shielded against precipitation. The mounting requirements are necessary to achieve accurate data for atmosphere reconstruction.
8	**Accelerometers** Measure acceleration along 3 orthogonal axes in aeroshell cg and fourth measurement along roll axis.		Accelerometer Mounting The accelerometer triad is mounted in the aeroshell cg and is accurately aligned relative to the roll axis. A single axis accelerometer which is mounted away from the cg is sensitive along roll axis. Automatic range switching increases measurement sensitivity.	Preferred The mounting requirements are necessary to achieve accurate data for atmosphere reconstruction.
9	**Transponder** Measures probe range and drift speed.		The transponder is connected to the transmitter and antenna. Its ambient temperature is between -20 and 70°C. Any mounting orientation is acceptable.	Preferred There are no difficult integration requirements.
10	**70 KM Radar** Measures altitude and drift velocity		Pressure and Temperature Controlled Radar An assembly of phased array radar and associated electronics are mounted in the probe nose. The radar assembly is temperature controlled by PCM and radiates through an RF transparent and pressure resistant cover.	Preferred To avoid a large number of coaxial cables between about 100 elements of the phased array radar and the electronics, atenna and electronic elements are combined and temperature controlled.
11	**Impact Indicator** Measures proximity of surface with small short range (300 m) radar ($\lambda \approx 4$ cm).		Slot Antenna in Probe Nose The probe nose is the preferred location for the slot antenna. No conducting parts are in front of it. The radar electronics are mounted inside the pressure shell. The antenna with RF transparent window is outside pressure shell.	Preferred Mounting of the impact indicator antenna in the probe nose causes no aerodynamic disturbances and is compatible with other requirements.

TABLE VI-2 (cont)

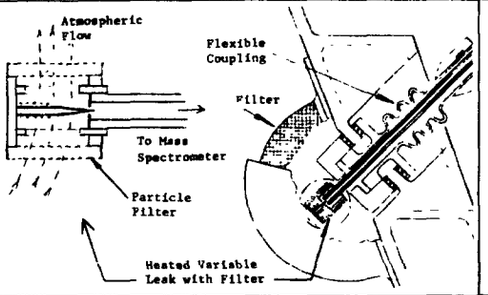
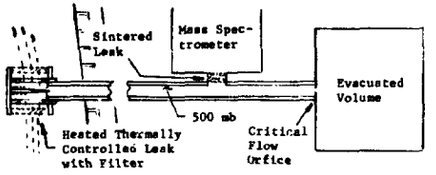
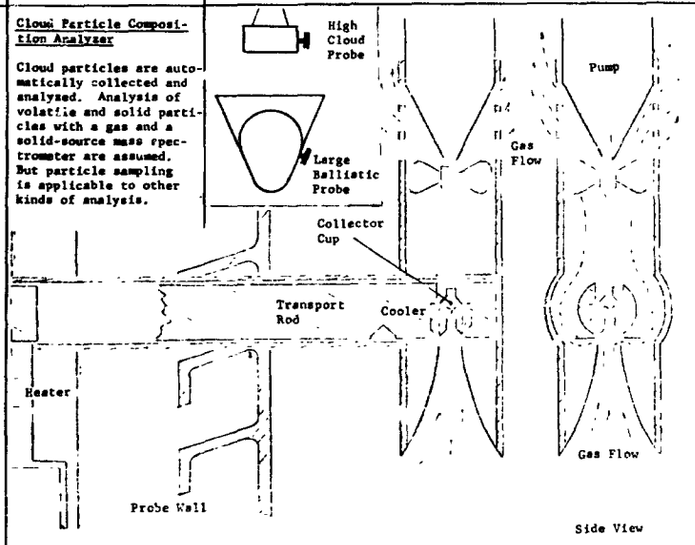
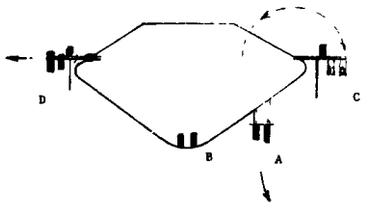
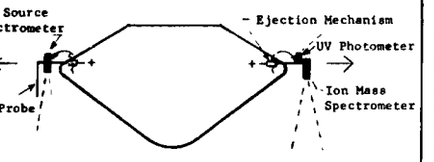
ROW NUMBER	MEASUREMENT OBJECTIVE	ALTERNATE MECHANIZATION APPROACHES SKETCH OF CONCEPT	DESCRIPTION	EVALUATION OF MECHANIZATION APPROACH
12	**Neutral Specie Mass Spectrometer** Measures atmospheric composition (1-90 AMU) from probe deployment to surface.		Mass Spectrometer with One Variable Inlet Leak. The pressure is reduced by one inlet leak which is automatically adjusted for constant MS pressure. Large and small particles are removed by particle shield and heated filter respectively. The small variable leak is heated about 20°C above ambient. The short pressure connection to MS is designed for small delay (volume) but sufficient molecular conductance.	Preferred if reliable Variable Leak can be developed Similar variable leaks for laboratory use have been built. However the feasibility of a small variable leak for Venus environment remains to be demonstrated. Development is required. Disadvantage: Further development of leak required.
			Mass Spectrometer with Two Pressure Reduction Stages Variable leak of relatively high conductance regulates flow to an evacuated volume which is connected through a critical flow orfice. The pressure near the sintered leak is controlled near 0.5 bars and supplies sample to molecular leak for MS. Dust particle filtering as described above.	Preferred if reliable Low Flow leak outlined above is not available. This approach is feasible with a minimum inlet leak flow which is several orders of magnitude higher than the variable leak outlined above. Disadvantages: Evacuated volume required, more instrument parts.
13	**Cloud Particle Composition Analyzer** Cloud particles are automatically collected and analyzed. Analysis of volatile and solid particles with a gas and a solid-source mass spectrometer are assumed. But particle sampling is applicable to other kinds of analysis.		Particle Collection Outside Probe To avoid hot gas flow through the probe, the cloud particles are inertially separated and deposited in a small sample collector-cup which is deployed outside the probe. For sample analysis a transport rod retracts the cup into the probe. Volatile constituents are evaporated and analyzed in the gas-source mass spectrometer. The remaining particles are analyzed in the solid-source mass spectrometer. The analyzer volume is pressure sealed from other probe subsystems.	Preferred This concept permits high sample flow without much heat transfer to probe interior. A preliminary concept of the challenging design for sample transport and processing is shown in Figure VI-23. To avoid a more complicated design, only one sample collector cup was assumed for all particles. Disadvantages: Compared with other science instruments, this analyzer requires complicated mechanisms and an early start development effort is anticipated.

TABLE VI-2 (concl)

ROW NUMBER	MEASUREMENT OBJECTIVE	ALTERNATE MECHANIZATION APPROACHES		EVALUATION OF MECHANIZATION APPROACH
		SKETCH OF CONCEPT	DESCRIPTION	
14	Open Ionsource Mass Spectrometer, Ion Mass Spectrometer, Electron Probe, UV Photometer (These instruments measure before heat pulse) Open Ion Source Mass Spectrometer Neutral particle Measurement (1 to 90 amu; pressure 10^{-9} to 10^{-4} torr) Ion Mass Spectrometer Free Ions (1 to 45 amu, 5 to 10^{5} ions/cm^{3}) Electron Probe Measures electron temperature and density (0 to 10^{6} el/cc) UV Photometer	Alternate approaches to Instrument Mounting  	Four alternative concepts of instrument mounting are considered. The table on the left shows for what instruments the alternate mounting concepts are feasible. The basic problem is instrument sampling before aeroshell heating without causing interference during aeroshell heating. Following is a description of the alternate mounting concepts. A. The instruments are mounted ahead of the aeroshell and ejected near 0.1g deceleration. B. Instruments are mounted behind a metallic (beryllium) or ceramic shield with sampling holes. Flow through can be avoided by application of ion pump for mass spectrometer. C. The instruments are retracted behind aeroshell shortly before heat pulse. D. The instruments are mounted to sample beyond the aeroshell rim. They are ejected to the side at 0.1g deceleration.	A. Compatibility of mounting with heat shield is questionable. Ejected instruments might impact on heat shield. B. Heat shield near apex is heavy (many pounds). Only feasible for mass spectrometers. C. Requires mechanism for retraction and covering to avoid overheating. D. Preferred approach, see details below.
		 	Instruments Ejected Normal to Roll Axis After spacecraft separation both arms supporting the instruments are deployed on opposite sides of the aeroshell rim. Each instrument package is supported in its cg. The instruments are ejected about normal to the roll axis. The aeroshell is spinning and the instrument temperature is determined by their thermal control coatings. The accelerometer sensitive along the roll axis triggers the ejection.	Preferred This mounting concept is preferred because instrument separation is simple and causes no danger to the spacecraft. All high altitude instruments can be mounted with this concept.

The temperature of the detector unit should be controlled within ±1°K below 300°K. Otherwise, it must at least be measured with an accuracy of ±1°K. Occasional dark readings and calibration readings from a standard light source are suggested.

2) Major Mechanization Problem Areas - The major problems are:

Clear radiometer field of view without window contamination;

Change of instrument characteristics because temperature of detector and optics changes.

3) Experiment Mechanization

Clear Radiometer Windows - The response time of the radiometers is a fraction of a second. Measurements are conducted in intervals of 10 or 15 sec. Therefore, the radiometer windows must be exposed for only about 1% of the descent period, and the windows can be covered most of the time.

The window cover can be transparent to provide at least degraded viewing if the shutter mechanism fails. A window wiping device is combined with the shutter. Filtered gas flow past the outside of the windows and particle deflection shields around the radiometer windows would provide additional protection. However, these features are not considered necessary. Rows 1 and 2 of Table VI-2 show mechanization concepts that apply using the protective features outlined above.

Temperature Effects - The radiometer is temperature controlled within approximately ±20°C by phase change material. The detector units of the radiometers are cooled to the lowest instrument temperature by thermoelectric cooling. The estimated average power consumption for thermoelectric cooling is 2 W. The temperature of any thermal radiometer window on the outside of the probe will be measured.

4) Conclusions and Mechanization Concept - Rows 1 and 2 of Table VI-2 show various radiometer mechanization concepts for instruments with one or several combined radiometer units. We have preferred to combine all solar radiometer units in one instrument as shown in Row 1 of Table VI-2. This concept has the advantages of a single shutter drive, independence from the probe, and combined thermal control of the detectors. Pressure leakage through any window of the radiometer unit would not interfere with the thermal control of the main canister.

b. Thermal Radiometer

1) Requirements - The thermal radiometer looks downward, has a view cone angle of approximately 30°, and measures radiation in the 6.5 to 8.5μ and 9.2 to 10.8μ regions. We assume one radiometer window and automatic change of broad band interference filters.

2) Major Mechanization Problem Areas - The major problems are:

Window contamination similar to that of the solar radiometer;

Requirements of temperature control for the radiation detector are similar to those of the solar radiometer; however the temperature of the windows and baffles has a higher influence on the thermal radiometer measurements.

3) Experiment Mechanization

Clear Windows - The considerations for clear radiometer viewing are very similar to those discussed in the preceding discussion for the solar radiometer. Unless the thermal radiometer is combined with the solar radiometer (large ballistic probe), a single window with protective shutter is proposed. This shutter can be actuated by a high temperature solenoid.

Thermal Radiation from Windows and Baffles - The windows will be selected for environmental compatibility, high transmittance, and low emissivity. The temperature of the windows and the light baffle will be determined.

4) Conclusions and Mechanization Concept - In the large ballistic probe the thermal radiometer is combined with the solar radiometer. The thermal radiometer looks downward and is contained in the same auxiliary compartment as the solar radiometer. However, the temperatures of the windows' light baffle and light chopper must be determined.

Row 2 of Table VI-2 shows a concept with the thermal radiometer in the nose of the probe. The temperature of optical parts radiating to the detector must also be determined.

c. Mechanization of Nephelometer

1) Requirements - The nephelometer unit periodically emits light pulses. Particles outside the canister reflect a small part of the emitted light. The instrument light detector senses the light scattered by atmospheric particles and provides a measure of the particle or cloud concentration. The nephelometer is carried by the large and small ballistic probes.

2) Major Mechanization Problems - The major problems are:

Measurement accuracy is influenced by changes of light source intensity, window transmittances, and detector sensitivity;

Heat transfer through probe insulation by nephelometer;

Interference by ambient light.

3) Experiment Mechanization

Measurement Accuracy - The nephelometer windows could be protected by shutters similar to the radiometer windows. However, because the light source and light detector are also subject

to drift, we assumed a fine light pipe (quartz) conducting light from outside the light source window to the outside of the light detector window. This light flow is normally interrupted and the increase of light through the fine light pipe provides a calibration of the complete instrument.

Heat Transfer by Instrument through Probe Insulation - The light source and the light detector of the nephelometer must be several inches apart. The light detector cannot operate at ambient temperature and must be inside the canister. Therefore one window with about a 1-in. diameter is needed. The light source can be heated to 900°F and is mounted outside the pressure shell and behind the aerodynamic skirt.

Interference by Ambient Light - Ambient light is discriminated by electronically filtering out the light signals that have the pulse rate of the light source.

4) Conclusions and Mechanization Concept - Row 3 of Table VI-2 shows the preferred mechanization concept. No light baffles are applied outside the aeroshell to avoid aerodynamic disturbances. The light source is outside the canister shell but inside the aerodynamic skirt. The window through the pressure shell has a diameter of about 1 in. Low thermoconductivity baffles are provided to filter out undesirable light.

d. Cloud Particle Number, Density, and Size Sensor

1) Requirements - This instrument detects, measures, and counts particles by optical means. We have assumed a method that counts light flashes due to 90° scattering by particles traversing the sensitive area of the sampling tube. At the present state of development, this instrumentation concept is not frequently used for measurement of particles with a diameter of 0.5 to 20 μ. However, the requirements for the second instrumentation method, which observes the shadows of the particles against a fiber-optic detecting mosaic, are similar.

2) Major Mechanization Problem Areas - The major problem areas are:

Particle evaporation and heat transfer into the probe;

Instrument calibration drift;

Aerodynamic interference with probe stability.

3) Experiment Mechanization

Particle Evaporation and Heat Transfer into the Probe - Above a planetocentric radius of 6100 km the canister is warmer than ambient and tends to heat ambient particles. At lower altitudes, ducting of the ambient particles into the canister would cause significant heat transfer into the probe. To overcome these problems, the sampling tube, the light source, and associated optics are mounted outside the pressure shell.

Instrument Calibration - The light detector (photomultiplier), the light source (filament lamp), and the exposed windows can change their optical characteristics. One concept to calibrate the instrument is to use a light pipe that conducts the light from the sensitive volume toward the light detector. By interrupting this light beam by a chopper with selected openings, traversing particles of specific size are simulated. Another approach for calibration is to inject calibration particles into the flow, while the ambient particles are temporarily filtered out.

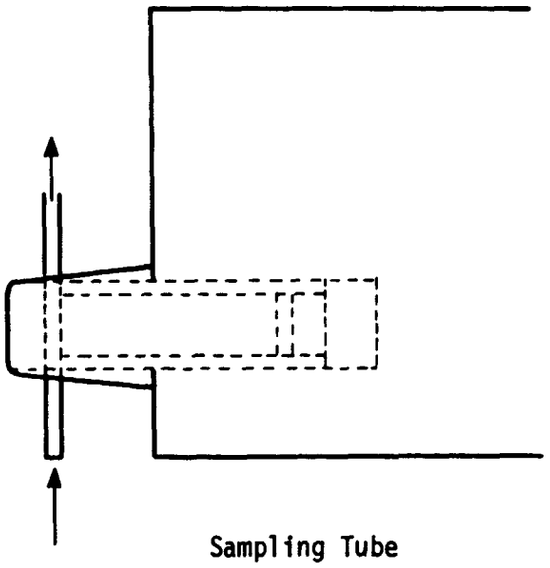
Aerodynamic Interference - The best arrangement for the particle counter is to mount the sampling tube in front of the probe's nose or to align it with the flow vector outside the boundary layer of the probe. However, size constraints and the aerodynamic disturbances caused by the light source (~1.5 in. diameter) and the sensitive volume require compromises. The large ballistic probe collects the particles about 1.5 in. off the probe wall. Then, a slightly bent channel with a 0.5x0.5 in. cross section conducts the particles toward the detector. The influence of inertial forces on larger (5 to 30 μ diameter) particles can be overcome by sensing only the flow near the center of

the sampling tube. For this reason, the flow near the inner and outer walls of the bent sampling channel was separated just ahead of the particle detector.

The high-cloud probe is suspended on a parachute and no aerodynamic instabilities are caused by protruding instruments. However, the best orientation of the sampling tube requires aerodynamic testing. A small fan for the sampling flow would diminish the influence of flow field and descent velocity. In all cases the flow velocity in the sampling tubes has to be evaluated because it depends on descent velocity, flow channel impedance, aerodynamic conditions, and sampling pump, if a pump is used. Figure VI-15 shows the mounting of the particle counter for the cloud probe.

4) Conclusions and Mechanization Concept - The preferred mechanization concepts are shown in Row 4 of Table VI-2 and Fig. VI-16. The high-cloud probe is suspended on a parachute and is not disturbed by protrusions from the probe. Therefore, the straight sampling tube and the particle detector are mounted 2 in. away from the wall of the probe.

The large ballistic probe samples the particles with a slightly bent tube to avoid aerodynamic disturbances. The light source with associated optics is mounted outside the pressure shell, but behind the aerodynamic skirt. Inertial particle separation in the bent tube is overcome by measuring only the particles near the center of the flow channel.



Sampling Tube

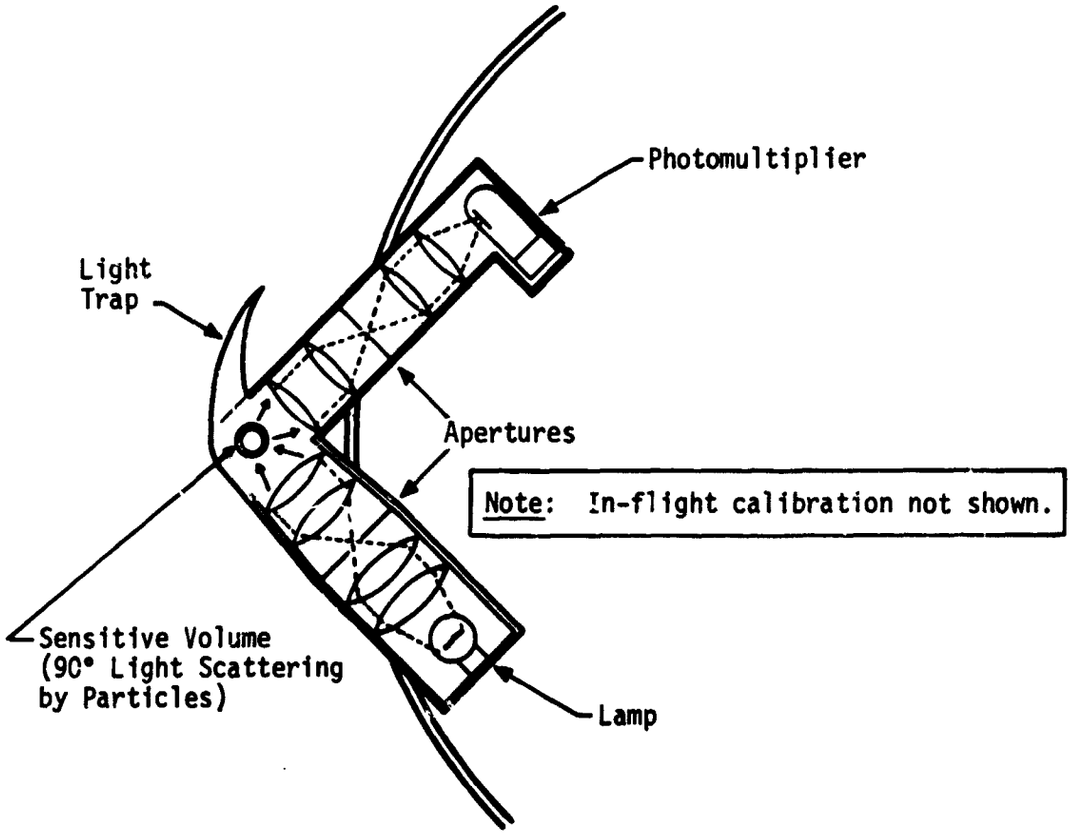


Fig. VI-15 Mounting of Cloud Particle Counter on High-Cloud Probe

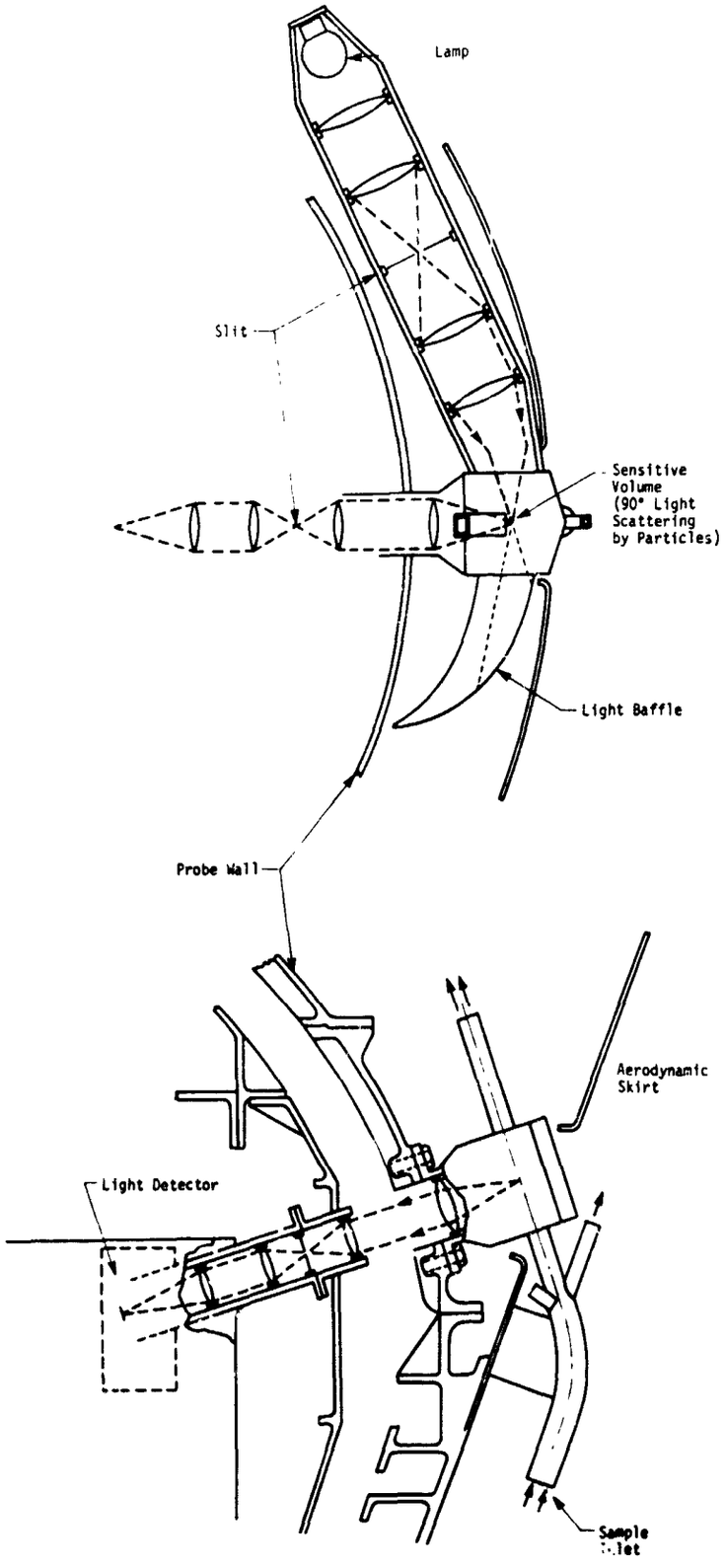


Fig. VI-16 Cloud Particle Counter in Ballistic Probe

e. Mechanization of Evaporimeter/Condensimeter

1) Requirements - This instrument measures the temperature at which atmospheric constituents condense or evaporate. The condensation temperatures depend on composition and partial pressure of the constituents. The instrument is based on a detector element (mirror) that assumes various temperatures and is bathed in atmospheric flow. When the temperature controlled element is at or below the evaporation/condensation temperature, then a condensation layer is formed. This layer is detected by sensing the change of optical reflectivity on the mirror. The flow channels to the evaporation/condensation detector and the optical windows must be heated about 20°C above the ambient temperature to prevent condensation on the optical components and the channel walls. The gas sprayed on the evaporation/condensation detector must be dust free to avoid erroneous indications. For the sample flowrate a compromise between response time, power requirements for the condensation detector, and instrument sensitivity is necessary. We assumed that the detector temperature changes between +20°C and -30°C relative to ambient temperature.

2) Major Mechanization Problems - The major problems are:

Heat transfer into the probe and electrical power requirements must be minimized;

The atmospheric flow to the detector must be free from dust particles and/or droplets, so that no interference with the condensation detection occurs;

Flow control to minimize heat transfer to detector (mirror).

3) Experiment Mechanization

Heat Conduction and Power Requirements - The flow channels and optical windows ahead of the condensation detector are heated about 20°C above the ambient temperature. As a minimum, the light detector sensing the condensation layer on the

mirror and the instrument electronics must be mounted inside the pressure shell. The other instrument components can be designed to withstand the ambient environment. If the sample flow is conducted to the inside of the probe, many watts of electrical power are required to heat the channel walls and to control the mirror temperature. Therefore, all parts of the evaporimeter/condensimeter except the light detector and the electronics are mounted outside the pressure shell. A 1-in.-diameter window through the probe wall is sufficient. To avoid aerodynamic instabilities the instrument is located behind the aerodynamic skirt (see Fig. VI-17). The inlet channel to the detector can be short, and about 3 W are required for channel heating.

Separation of Dust from Sampled Flow - Large particles (>10μ diameter) are separated because of the difference in inertial forces of particles and gas in a curved flow. Fine particles are removed by a heated filter. If this filter restricts the flow too much, then a compromise between a detector cleaning mechanism, a flow pump, and the probability of detector contamination is required.

Flow Control and Heat Transfer to Condensation Detector - For a constant ballistic coefficient, mass flow and heat transfer to the detector are roughly proportional to ambient density. A louver-type flow restrictor controlled with bimetallic strips appears to be a simple device to stabilize the mass flow. Another electrically released reduction in flow conductance will adjust for the change in ballistic coefficient at parachute separation. A compromise between power requirements, flowrate, and sensitivity is necessary.

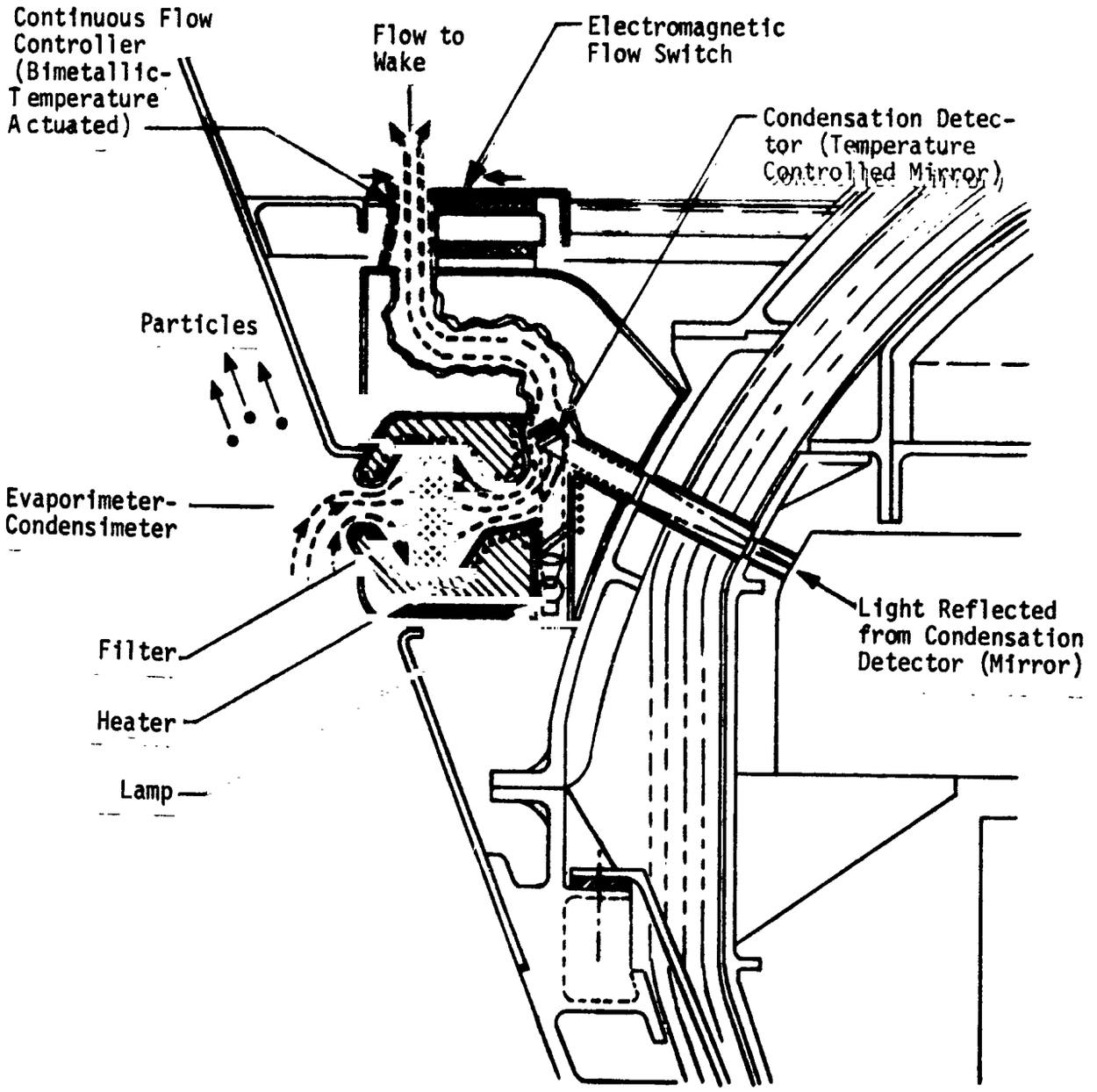


Fig. VI-17 Installation of Evaporimeter-Condensimeter

4) Conclusions and Mechanization Concept - Power requirements and measurement errors caused by dust, droplets, or condensation are the biggest concerns for the mechanization of the condensimeter/evaporimeter. Figure VI-17 shows the mechanization concept. Because the wake pressure of the probe is below ambient atmospheric pressure, gas is sucked into the evaporimeter/condensimeter normal to the probe skirt and large particles fly by. Fine particles are filtered out. The heated channel to the thermoelectrically cooled mirror is only about 2 in. long. The instrument's light source is mounted outside the pressure shell. A thermally controlled and an electrically controlled flow restrictor are shown near the flow exit.

f. Mechanization of Atmospheric Pressure Measurement

1) Requirements - The atmospheric pressure between 0.01 and 170 bars will be determined. The measurements will be conducted in time intervals of 10 sec. The measurement range depends on the probe configuration. The balloon, high-cloud, and ballistic probes measure 25 to 100 or 250 to 1000, 10 to 2000, and 20 to 200,000 mb, and have one, three, and five pressure ranges, respectively. The pressure ranges are automatically switched.

2) Major Mechanization Problem Areas - Major problem areas are:

Blockage of pressure inlets and/or connections by solidifications of atmospheric constituents or particle/droplet accumulation;

Heat transfer by pressure connections;

Deviations of sampled pressure from ambient pressure because of probe velocity, probe tumbling, and sampling port configuration;

Bursting of the pressure transducer's diaphragm.

3) Experiment Mechanization

Blockage of Pressure Connections - In all probes the pressure transducers and pressure connections will be oriented so that any condensed or collected liquids will flow out due to gravity. On the dropsondes, pressure inlet shields and location of inlet ports will reduce the number of particles or drops that might enter the pressure port. Some form of filter near the inlet is desirable. To avoid localized condensation there will be no sudden temperature changes of the pressure connections. For our conceptual design a spherical cover of 4 sq in. with many 0.05-in.-diameter holes is assumed. This cover will be close to ambient temperature to avoid condensation.

Heat Transfer by Pressure Connections - Weight and thermoconductivity of the pressure tubing are proportional to the square of the tube diameter. A 1/16-in. inside tube diameter is sufficient for short transducer response, but a larger diameter is desirable because of possible condensation and/or solidification of vapors. For a constant volume of the transducers, the layer of condensible material is inversely proportional to the tube diameter. A titanium or stainless steel tube of 1/8- or 1/4-in. inside diameter and 0.01- or 0.02-in. wall thickness, respectively, can withstand 200 bars of pressure. Shock and vibration effects require somewhat higher wall thickness. The strength of titanium is similar to that of stainless steel, but titanium has only about 60% of the stainless steel thermoconductivity. The thermoconductivity of a 1/4-in.-diameter bellows-type titanium tube with 0.04-in. wall thickness is equivalent to the heat transfer through about 5 sq in. of probe surface area (0.02 Btu/hr ft°F). This appears to be a good compromise between heat conduction losses and danger of tube blockage. Therefore, such a pressure connection through the thermal insulation of the ballistic probes was selected for the conceptual design.

Aerodynamic Effects - The dynamic pressure at velocities of 100, 50, and 30 m/sec is respectively about 10, 2.5, and 1% of the static pressure. For most of the measurements (>80%), the probe velocities are less than 30 m/sec and the difference between sampled and ambient pressure is only about 1/4 of the dynamic pressure. With preflight aerodynamic calibration and velocity measurements (radar, transponder), the aerodynamic effects should cause errors of less than 2, 1, and 0.4% at 100, 50, and 30 m/sec velocity. The aerodynamic errors for the cloud top probe and the Buoyant Venus Station are negligible (<0.2%) unless wind velocities of more than 50 m/sec occur.

Bursting of Transducer Diaphragm - The diaphragms or Bourdon tubes of pressure transducers are expected to burst when the pressure exceeds 10 times the full range pressure. Therefore, the transducer must be in a pressureproof housing or it must be mounted outside the pressure shell. The pressure transducer on Venera 4 could operate over a temperature range of 430°C, but its rms measurement error was ±2.74% of full scale. The estimated temperature range for accurate (±0.5%) state-of-the-art pressure transducers is 25 to 75°C. Therefore special thermal control is required for accurate pressure transducers mounted on the outside of the canister. Internal mounting requires a pressureproof housing. The weight of such a housing increases proportional to the third power of the diameter. The weight for a 1.5-in.-diameter pressure housing is approximately 0.1 lb. This weight penalty is acceptable. We assume pressureproof housings for two transducers in the ballistic probes and a weight penalty of 0.2 lb.

4) Conclusions and Mechanization Concept - The major concern in regard to mechanization of the pressure measurement is blockage of the pressure connections because of condensation/solidification of atmospheric constituents, or by cloud particles and

drops. The pressure connections can be designed for acceptable heat losses and the aerodynamic disturbances are small. A pressureproof housing for the transducers requires about 0.2 lb of additional weight.

Row 6 of Table VI-2 shows the mechanization concepts for the probe configurations. No active heating is anticipated for balloon probes. Because of the probe's thermal lag, some condensation in the pressure connections may occur. To minimize the thickness of any condensation layer, filters such as wire mesh near the entrance port reduce gas circulation between gas in the transducer and ambient. Because the channels have a diameter of approximately 0.25 in., a thin layer of condensed material cannot cause blockage.

The conceptual designs for the cloud probe and the ballistic probes are similar. A particle shield deflects large particles (>10μ diameter). The filter provides additional particle protection and reduces gas circulation to the pressure connection. A 1/4-in.-diameter titanium tube conducts the pressure. Any condensed liquids flow outside due to gravity and all pressure gages are assembled in one unit.

g. Mechanization of Temperature Measurements

1) Requirements - The ballistic, high-cloud, or balloon probes measure the ambient temperature over a range of 200 to 900°K, 200 to 500°K, and 250 to 350°K (500 mb) or 200 to 300°K (50 mb), respectively. Measurement errors before telemetry of ±0.5°K, ±1°K, and ±1.5°K are requested for the ranges of 200 to 400°K, 400 to 600°K, and 600 to 900°K, respectively. The rms temperature error of Venera 4 was ±17°K after telemetry. All descent probe measurements are sampled every 10 sec.

2) Major Mechanization Problem Areas - Major problem areas are:

Low heat transfer by low density gas at high altitudes (<0.1 bar of pressure);
Temperature errors because of evaporating or condensing particles on sensing element;
Mechanical damage caused by large particles impacting on sensing element or high deceleration during entry;
Heat transfer from the atmospheric probe to the sensed gas.

3) Experiment Mechanization

Low Heat Transfer to Sensing Element at Low Atmospheric Densities - To avoid measurement errors caused by heat conduction from the supports of the sensing wire or radiation from the surrounding area, a length-to-diameter ratio on the order of 100 is required for the sensing wire when the ambient pressure is between 0.01 and 0.1 bar. Radiation errors are reduced by a highly reflective surface of the temperature sensing element.

Temperature Errors Caused by Condensing or Evaporating Drops and Particles - Drops or particles on the sensing element tend to stabilize the temperature when they change their liquid or solid phase. This is best avoided by separating inertially at least the larger particles (>10μ diameter). Therefore the high altitude temperature sensor has a curved flow as shown in Fig. VI-18 and Table VI-2, Row 7. The temperature sensor for the balloon probe has a precipitation shield and is very small and highly reflective. By periodic heating, ice and other condensibles are evaporated. The temperature change rate during heating can be used to indicate the mass of condensation layers. A similar process of heating can be applied to the small but rugged temperature sensor for low altitude measurements.

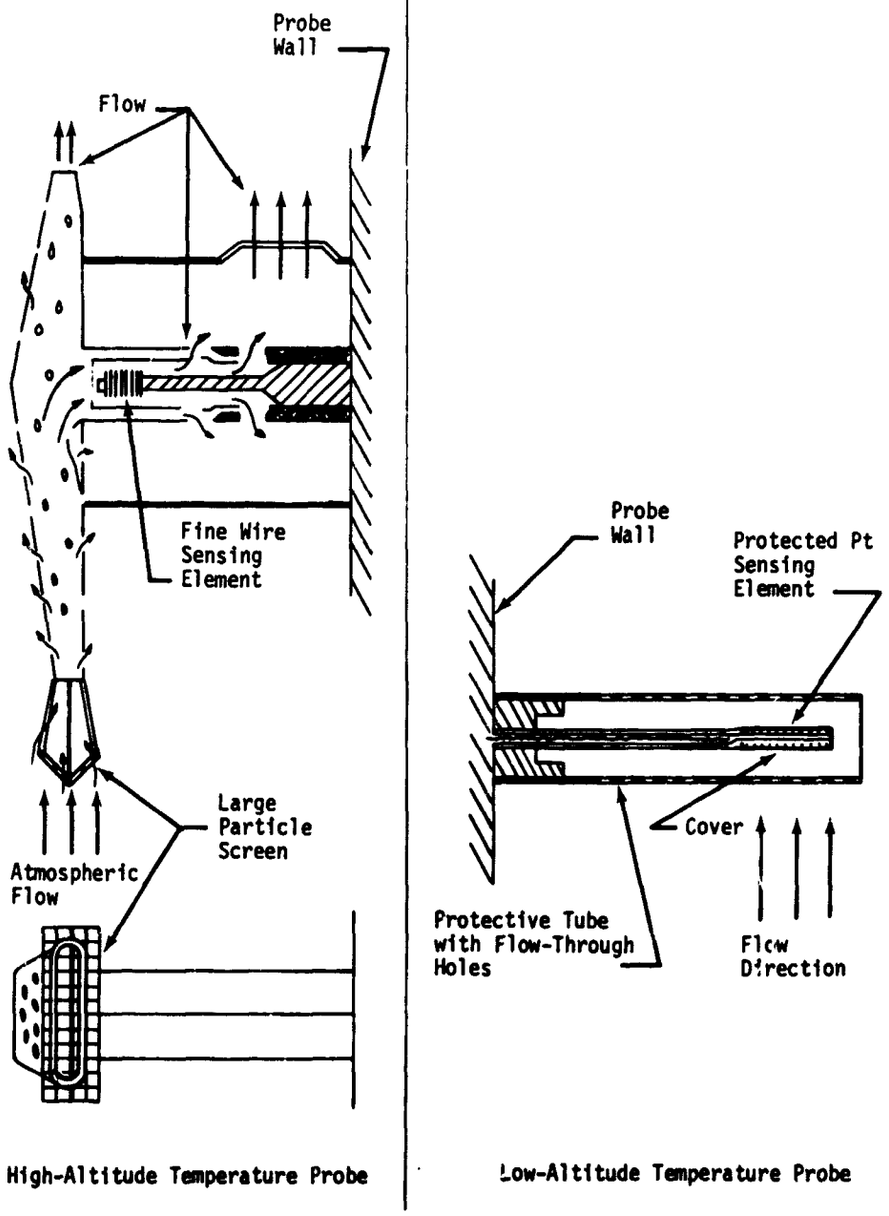


Fig. VI-18 Temperature Probes Optimized for Low and High Atmospheric Densities

Damage to Sensing Element by Particles - The high-altitude temperature sensor must have a delicate sensing element (large surface to mass ratio). Large particles (30 to 3000 μ diameter) will be separated inertially because of curved flow. Larger particles that might block the flow to the temperature sensor are stopped by a screen ahead of the flow inlet to the high altitude temperature sensor.

During deceleration, high stress on the fine platinum wire can be avoided by supporting the wire at many points. If the wire supporting structure is very close to the gas temperature, the length to diameter ratio of the platinum wire can be much less than 100 between the support points.

Thermal Probe Interference on Temperature Measurement - To avoid thermal influence from the descent probes, all temperature sensors sample outside the probe's boundary layer. The balloon probe temperature sensor is deployed approximately 40 ft below the balloon because downdrafts can otherwise transfer enough heat from the balloon to cause measurement errors.

For the high-altitude sensor, the temperature probe's design must also take into consideration the boundary layer influence of the temperature probe itself. We assumed a sensor design similar to Rosemount Engineering Model 102 non-deiced total temperature probe. These instruments are generally used at velocities above 30 m/sec and evaluation at lower velocities is suggested.

4) Conclusions and Mechanization Concept - In general, the technology required for the temperature measurements is within the state of the art. However, attention to various design details is necessary to assure very accurate and also reliable measurements in the new environment.

The ballistic probe has two temperature probes (Fig. VI-18). One sensor is rugged and optimized for low altitudes. The other sensor is optimized for high altitude (low atmospheric density) measurements. This temperature sensor has a delicate sensing element and particles are inertially separated from the flow to the platinum wire. The high-altitude temperature sensor is also used for the high-cloud probe. Below a planetocentric radius of 6110 km the ballistic probe's temperature sensors are sampled alternately to check each sensor against the other.

The small, highly reflective balloon temperature sensor has a reflective precipitation shield and is deployed about 40 ft below the balloon. Short heating periods (0.5 W, 5 min) before measurement evaporate ice or other condensibles from the temperature sensor.

h. Mechanization of Accelerometer Measurements

1) Requirements - The accelerometer triad is mounted in the entry capsule's center of gravity. For redundancy and also to obtain information about probe oscillations, a fourth accelerometer sensitive along the roll axis is mounted on the roll axis as far away from the cg as possible, but within the pressure canister. The accelerometers must be turned on at a planet radius greater than 6250 km. The data must be transmitted when any acceleration exceeds 0.01 g. After aeroshell separation the accelerometers will be used to measure the turbulence during descent. The mode of data sampling will then depend on the specific mission and probe configuration.

2) Mechanization Concept - The accelerometers are accurately aligned relative to the aeroshell. The accelerometer triad and the associated preamplifiers are mounted in the aeroshell's center of gravity. A change of the capsule's center of gravity due to ablation has to be considered. Most of the instrument electronics can be mounted in any convenient location.

i. Mechanization of Transponder - The carrier transponder receives a signal from earth and returns an accurately phased transmitter signal to measure probe departure speeds to within ±2 cm/sec from earth. The transponder for the balloon probe also provides range measurements with an accuracy of ±150 m.

Short connections between antenna and transmitter are desirable. Along the roll axis the instrument must withstand about 500 g deceleration. The electronics can be packaged in any desirable shape. There are no requirements for science sampling, but some engineering measurements (loop stress, transmitter power, temperature) are required.

j. 70-km Radar

1) Requirements - This instrument measures altitude and horizontal probe velocities below 70 km altitude. The antenna consists of approximately 100 phased array antenna elements. Each element must be connected t. its transmitter module. A downward field of view of ±45° off the roll axis is required. The temperature environment of the associated electronics may not exceed 100°C.

2) Major Mechanization Problems - The major problems are:
The antenna field of view must be RF transparent;
Thermal control of radar electronics.

3) Experiment Mechanization

Thermal Control of Radar Electronics - The phased array antenna can be designed to withstand the ambient environment. The temperature of the associated electronic modules must be controlled between 0 and 100°C. Coaxial cable connections between each temperature controlled electronic module and the antenna elements were considered. However, thermal control of the complete radar assembly was preferred because of the high heat conduction by the approximately 100 coaxial cables and additional integration difficulties.

RF Transparent Antenna Window - Because of the thermal control requirement for the complete radar unit, the radar is mounted inside the pressure shell. The best location is in the nose of the ballistic probe. A pressure-resistant dome of RF transparent material such as pyroceram or quartz glass protects the radar in front. The space between antenna and pressure dome is evacuated or filled with RF transparent and thermally insulating foam. On the other side, the radar unit is surrounded by phase change material.

4) Conclusions and Mechanization Concept - The size of the antenna for the altitude and drift radar in the ballistic probe is an important tradeoff factor. To avoid aerodynamic instabilities the probe antenna should not extend beyond the probe shell. Short wavelengths are required to generate a narrow beam with a small antenna, but solid-state technology and atmospheric absorption set a lower limit for the wavelength. We assumed a radar similar to the MERA (Molecular Electronics for Radar Applications) radar proposed by Texas Instruments in NASA CR-66383. This radar would have about 100 antenna elements for the phased array and dimensions of approximately 8x8x4 in. for the antenna with the associated RF modules that operate at a wavelength of about 4 cm. Other associated electronics are connected by cable to the MERA array assembly. The design concept is shown in Fig. VI-19 and in Row 10 of Table VI-2. The design concept applies the conclusions discussed in the preceding Experiment Mechanization discussion.

k. Mechanization of Impact Indicator - The impact indicator senses the proximity of the ground over a distance of about 300 m. The instruments have a 2x1/2-in. slot antenna with a cavity length of 1 in. Frequency is around 3 GHz. The associated electronics (10 $in.^3$, 0.2 lb, 0.5 W) are connected to the antenna by coax cable. A downward field of view of about $\pm 20^\circ$ is required. Except for the integration of the antenna into the ballistic probe structure, no major mechanization problems are foreseen.

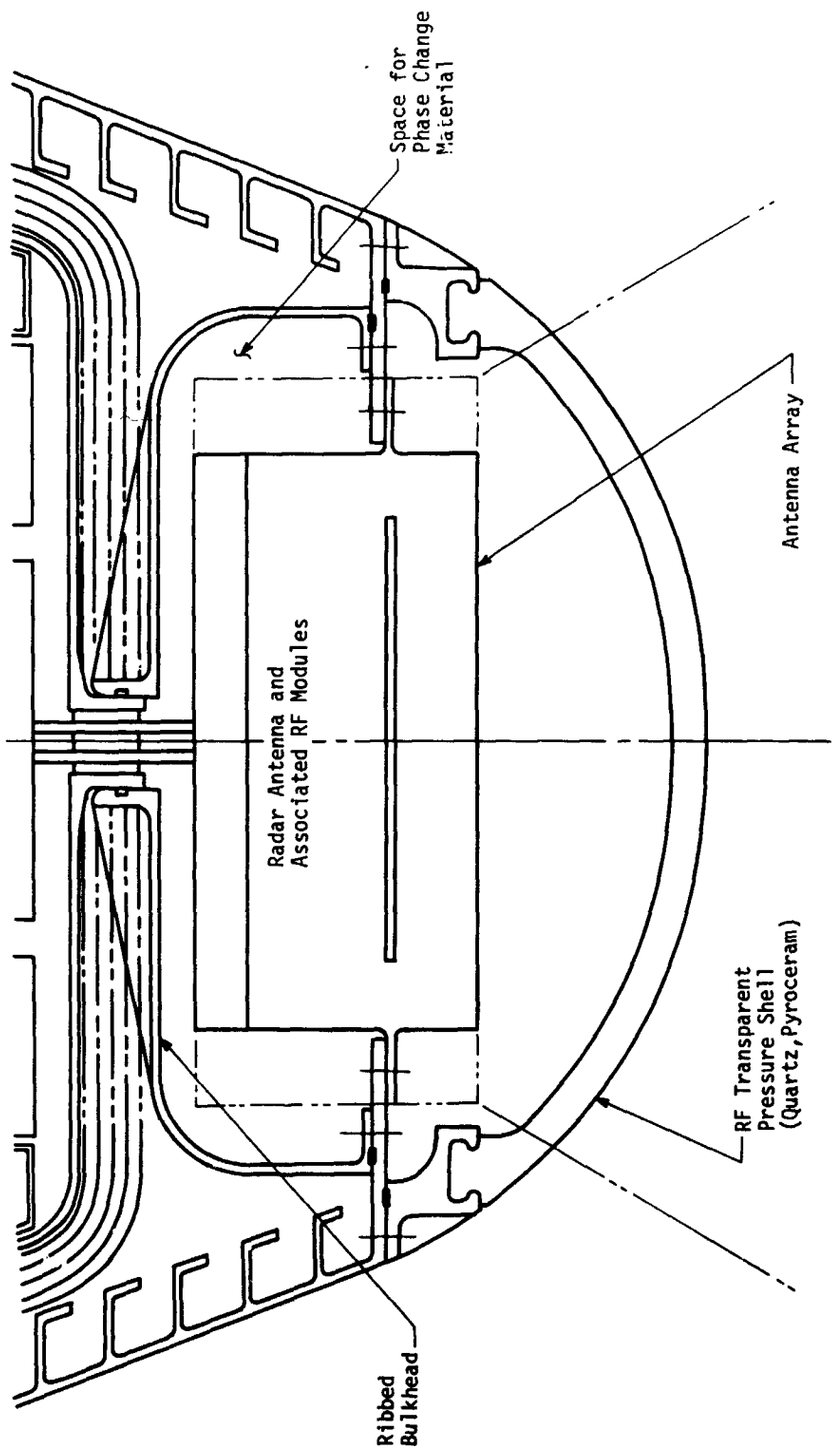


Fig. VI-19 Integration of Radar in Ballistic Probe

1. Mechanization of Neutral Particle Mass Spectrometer

1) Requirements - This instrument measures atmospheric composition from probe deployment down to the surface of Venus. For analysis in the mass spectrometer, the gas pressure must be reduced to 10^{-8} to 10^{-5} mb. Inlet leaks with openings in the order of 1μ diameter are required and blockage of these leaks by particles or condensation must be avoided.

2) Major Mechanization Problems - The major problems are:

Pressure reduction from ambient (0.05 to 170 bars) to less than 10^{-8} bar;

Atmospheric sampling without blockage of inlet leaks by particles or condensation;

Change of atmospheric sample because of condensation, chemical reactions, or outgassing.

3) Experiment Mechanization

Pressure Reduction - In spite of the minute sample required for the mass spectrometer analysis, reliable pressure reduction of the high atmospheric pressure is difficult and requires further development. Small mechanical pumps are not practical. Mass spectrometer pumping with evacuated volumes is promising if volumes on the order of 10^{-2} cm^3 can be periodically opened and closed without leakage through the small valves. Figure VI-20 shows a block diagram for this concept.

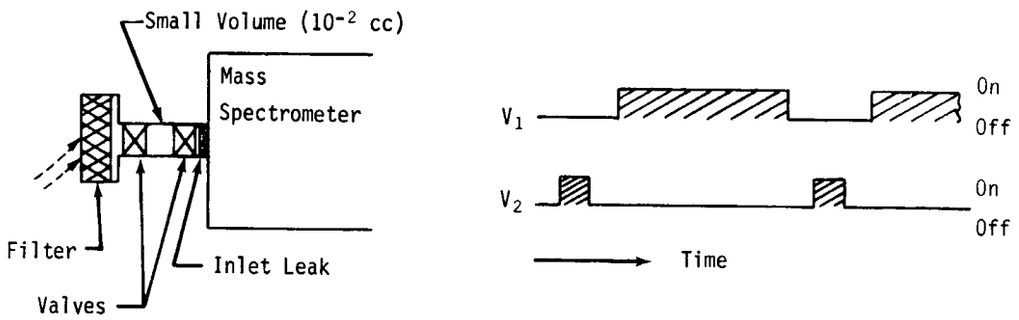


Fig. VI-20 High Pressure Sampling with Two Valves

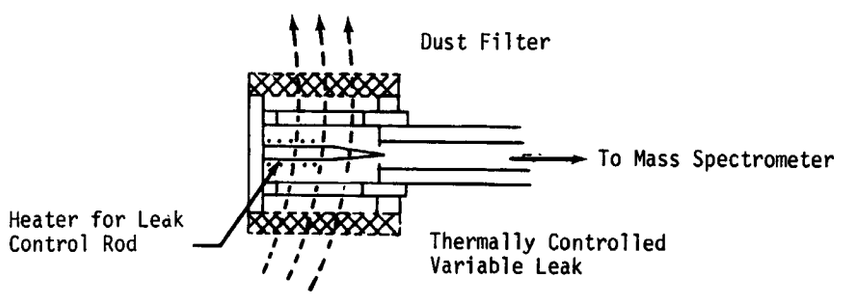


Fig. VI-21 Single Mass Spectrometer Leak

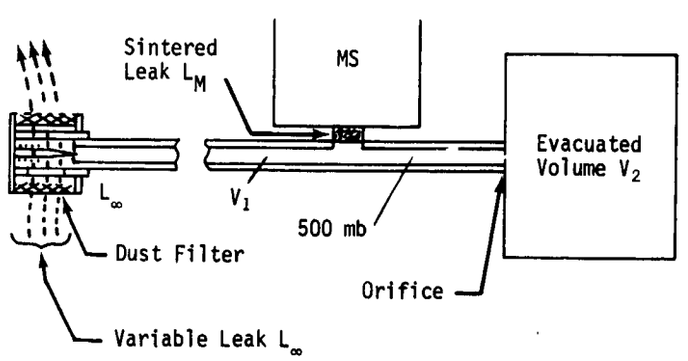


Fig. VI-22 Dual-Stage Pressure Reduction for Mass Spectrometer

The simplest pressure reduction method is a variable leak that controls the leak flow into the mass spectrometer so that the mass spectrometer pressure does not exceed 10^{-5} mb (Fig. VI-21). For a 1-ℓ/sec ion pump, the leak flow must not exceed 10^{-5} std cc/sec. This corresponds to about 0.5×10^{-7} cc/sec at 170 atmospheres. Large (30 $in.^3$) variable leaks that have approximately the required characteristics have been built, but additional development and miniaturization is needed to provide a leak which meets all Venus probe requirements. An application with a variable leak would sense the controlled pressure and adjust the leak flow. The conductance of the tube for molecular flow between variable leak and mass spectrometer must be large enough to prevent large pressure gradients, but the tube volume may not cause delay of many seconds. Blockage of the adjustable leak by a small particle can cause a problem. The leak valve opens and the flow into the analyzer may be too high for the ion pump after the dust particle has passed the leak. An additional getter pump will help to overcome such a problem.

An alternative approach that requires a minimum leak flow of only about 10^{-4} cc/sec is shown in Fig. VI-22. The sintered molecular leak, L_M, for the neutral particle mass spectrometer is designed for a maximum pressure of 500 mb. At probe staging the ambient pressure is about 50 mb and the adjustable leak L_∞ is open. As the ballistic probe descends, the adjustable leak controls the pressure in V_1 at 500 mb. The volume of V_1 is on the order of 0.1 cc and the volume V_2 (~1000 cc) causes a continuous constant flow (0.05 cc/sec) through the orifice between V_1 and V_2. Change of relative concentrations because of the molecular leaks must be considered. CO_2 filtering would enhance the sensitivity and accuracy of the minor constituent measurements.

Blockage of Inlet Leaks - Blockage of the inlet leak by particles or condensation must be prevented. Condensation is avoided by heating the inlet leak about 20°C above the ambient temperature. Small inlet leaks are required to limit the heater power to about 2 W. Because the inlet leak causes a large pressure drop, only heating of the high-pressure leak is anticipated. To avoid blockage by particles one might pump a small flow through a fine (0.5μ) filter. However, this power consuming process is not considered necessary. Large particles (>20μ) can be inertially separated with a particle shield. The dynamic pressure and turbulence near a descent probe are considered sufficient to cause enough flow through a filter to the inlet leak.

Change of Sample Composition because of Condensation - During descent in the hot atmosphere, the instrument compartment must be colder than the ambient. Any sampling tube through the probe would require heating of the tube walls to avoid possible condensation. At 170 bars, even carbon dioxide will condense near room temperature. Electrical heating of these tube walls would require many watts. Therefore the inlet leak will be mounted on the outside of the probe. The pressure in the tube to the analyzer has less than 1/10 of the ambient pressure.

4) Conclusions and Mechanization Concept - Development of a small variable leak for the ballistic probes is recommended. Depending on the minimum flowrate that can be achieved reliably, one- or two-stage pressure reduction is required. Functional diagrams of both concepts are shown in Fig. VI-21 and VI-22. The pressure shell feedthroughs for the mass spectrometer and the pressure transducer are combined (Row 12, Table VI-2). A particle shield deflects large particles and small (<5μ dia) particles cannot fly through the filter that surrounds the variable leak. The variable leak is mounted outside the pressure shell and is heated about 20°C above the ambient temperature to avoid

condensation. The variable leak is controlled by the ion pressure gage in the mass spectrometer and regulates the pressure in the analyzer.

m. Cloud Particle Composition Analyzer

1) Requirements - This instrument collects cloud particles, transports them to the analyzer, and performs particle analysis. Each analysis cycle requires 5 minutes.

2) Major Mechanization Problem Areas - The cloud particle composition analyzer requires an extensive development effort. Early start of critical development tasks is recommended. Following are major problems for design mechanization of science instruments:

Low heat transfer into probe in spite of large sample flow;

High sample flowrate to collect sufficient particles in small collector cup;

Prevent particle evaporation before analysis;

Sample transport to analyzer(s).

3) Experiment Mechanization

Large Sample Flow but Low Heat Transfer into the Probe - Sample flow into the probe or to particle collectors which are carried outside the descent probe by a rotating disk is practical for the high-cloud probe. However, for the large ballistic probe the concept shown in Fig. VI-23 was preferred. The particles are collected in small cups that are deployed for approximately 4 minutes outside the probe wall. Then the low thermoconductivity rod retracts them to the analyzer. No flow of the ambient hot gas into the probe is necessary.

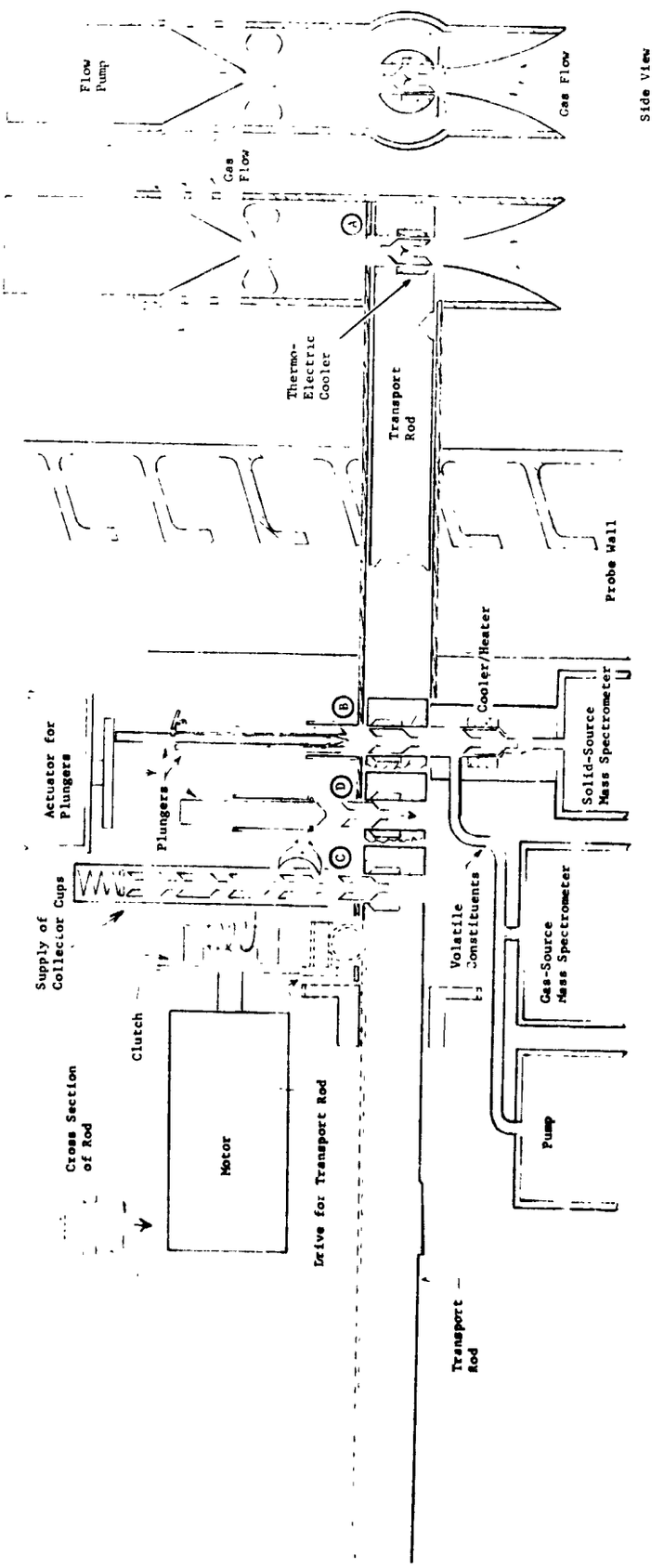


Fig. VI-23 Concept for Cloud Particle Transport with Collector Outside Probe Wall

High Sample Flow to Collect Sufficient Particles - A high flow impedance is necessary for the inertial particle separator. Particles with more than 0.5μ diameter are collected. Therefore a flow pump or fan is required (see Fig. VI-23). Development of an electrical high temperature motor (3 W) is considered feasible. Another possibility is to use a small turbine driven by the ambient flow to provide the energy for the flow pump.

Prevent Particle Evaporation before Analysis - To avoid particle evaporation the collector cup is thermoelectrically cooled approximately 30°C below ambient temperature. The electrical power (~3 W) for the cooler is conducted along the transport rod.

Sample Transport - The sample transport mechanism requires extensive study and development efforts. To indicate basic feasibility, an initial concept is illustrated in Fig. VI-23 and the operation is outlined below.

Station A - Atmospheric flow through the particle collector tube is caused by the probe's descent velocity and the fan near the tube exit. Because of inertial separation, the particles exceeding a diameter of about 0.5μ fly into the collector cup. If the labyrinth-type channels in the cup cannot retain the particles, then a filter is added. The cup's characteristics can be adjusted to the altitude range for each cup. The collector cup is thermoelectrically cooled about 30°C below ambient to avoid evaporation of collected particles. After approximately 4 minutes of particle collection, the drive motor turns the transport rod 180° and retracts it to Station B.

Station B - The outside plunger pushes the cup from the transport rod into the oven and the transport rod closes the oven. In the oven the particles are heated and the volatile constituents flow to the gas mass spectrometer. After analysis of the volatile constituents the transport rod is retracted a step backward and the center rod of the plunger pushes the solid particles into the solid source mass spectrometer. Then the transport rod moves to Station C.

Station C - When the cup opening is at Station C a new cup is released and drops into the cup opening and the transport rod moves to Station D.

Station D - The plunger pushes the collector cup into the transport rod. Then the rod with the new cup is pushed to its deployed position and rotates 180°. Now a new sequence of particle collection starts.

4) Conclusions and Mechanization Concept - An extensive study and development effort is required to provide a reliable cloud particle analyzer and collector. Early start of work to solve critical instrumentation problems is recommended. An initial concept for the particle collector and particle transport is shown in Fig. VI-23. To avoid hot gas flow through the probe, the cloud particles are inertially separated and deposited in a small sample collector-cup deployed outside the probe. For sample analysis a transport rod retracts the cup into the probe. Volatile constituents are evaporated and analyzed in the gas-source mass spectrometer. The remaining particles are analyzed in the solid-source mass spectrometer. The analyzer volume is pressure sealed from other probe subsystems.

n. Mechanization of Open Ion Source Mass Spectrometer, Ion Mass Spectrometer, Electron Probe, and UV Photometer

1) Requirements - These instruments measure respectively from atmospheric entry (7000 km of planetocentric radius) to 0.1 g deceleration:

Neutral specie (1 to 90 amu) at pressures from 10^{-9} to 10^{-14} torr;

Free positive ions (1 to 45 amu) from 5 to 10^{5} ions/cm^{3};

Electron temperature and density;

UV radiation in several wave bands.

2) Major Mechanization Problem Areas - Major problem areas are:

Damage to heat shield during entry heat pulse or at instrument separation;

Interference of entry vehicle with sensed atmosphere.

3) Experiment Mechanization

Damage to Heat Shield during Entry Heat Pulse or at Instrument Separation - Alternate mounting concepts are shown in Table VI-2, Row 14. After capsule separation, the instruments will be deployed by rotating the support arm 150°. At 0.1 g deceleration the arm with the instruments is pyrotechnically ejected normal to the probe axis.

Interference of Entry Vehicle with Sensed Atmosphere - During the mass spectrometer measurements, gaseous molecules can interact with the aeroshell and change their composition or ionization. Analysis of these particles is avoided by a wide field of view for the mass spectrometers and discrimination of low velocity particles along the instrument's axis.

4) Conclusions and Mechanization Concept - The major mechanization difficulties are to avoid interference of the entry capsule during measurement and damage to the capsule during

the entry heat pulse. The instrument temperatures must be between 0 and 70°C. The instrument mounting concept is shown in Table VI-2, Row 14. The instruments are deployed after separation from the spacecraft. At 0.1 g deceleration the arm supporting the instruments is ejected normal to the capsule's axis.

VII. ELECTRONICS SYSTEMS SUPPORTING STUDIES

A. PROPAGATION LOSSES IN THE VENUS ATMOSPHERE

There are two loss mechanisms that occur for communications origination or terminating within the dense Venus atmosphere. These are attenuation loss and defocusing loss. For communications from a probe to Earth, both of these increase markedly as the communicating probe moves away from the subearth point toward the planet limbs. This section describes our determination of these losses and presents the results of these calculations.

Atmospheres considered were the JPL model V5M for an upper bound on a thick atmosphere, a Martin Marietta model, hereinafter referred to as "Lower," for a lower bound, and a lower model with an isothermal extrapolation from 6069 km down. The latter two were taken to a radius of 6045 km and the first was taken to 6050 km. These atmospheres are defined in the Appendix (Volume III) of this report and their definition will not be repeated here. Using these as input data, profiles of refractivity, index of refraction, and dielectric constant versus radius, r, were computed.

The refractivity, N, was computed from an empirical relationship due to Stratton (Ref VII-1).

$$N(r) = \frac{P(r)}{T(r)} \cdot \left(0.1367 A_{CO_2} + 0.0813\ A_{N_2}\right) \qquad [1a]$$

where P is the pressure in atmospheres, T is the temperature in degrees kelvin, and A_{CO_2}, A_{N_2} are the abundances of CO_2 and N_2 in the atmosphere. For the V5M, 90%-10% composition this reduces to

$$N(r) = 0.1311\ \frac{P(r)}{T(r)}, \qquad [1b]$$

and for the Lower, 95%-5% composition it is

$$N(r) = 0.1340 \frac{P(r)}{T(r)}. \qquad [1c]$$

The refractivity profiles are plotted in Fig. VII-1.

Index of refraction, n, and dielectric constant, ε, were computed from:

$$n = 1.0 + N(r), \qquad [2]$$

$$\varepsilon = n^2. \qquad [3]$$

The initial radius of curvature of a horizontal ray, r_c, depends only on the local gradient of temperature and pressure at the given radius, r. This is given in Ref VII-1 as

$$r_c = \frac{nT}{(n - 1)\left(\frac{gM}{R} + \frac{dT}{dr}\right)}, \qquad [4]$$

where:

g = planetary gravity,

M = mean molecular weight of the atmosphere,

R = Universal gas constant.

For $r_c < r$ a horizontal ray is trapped, and will be turned into the surface of the planet. The maximum trapping radius, r_t, where $r_c = r$, was used in the calculation of some other results, to be discussed below, and for a check on agreement with the Mariner 5 results. Trapping radii were found to be 6090.0 km in the V5M and 6083.1 for the Lower.

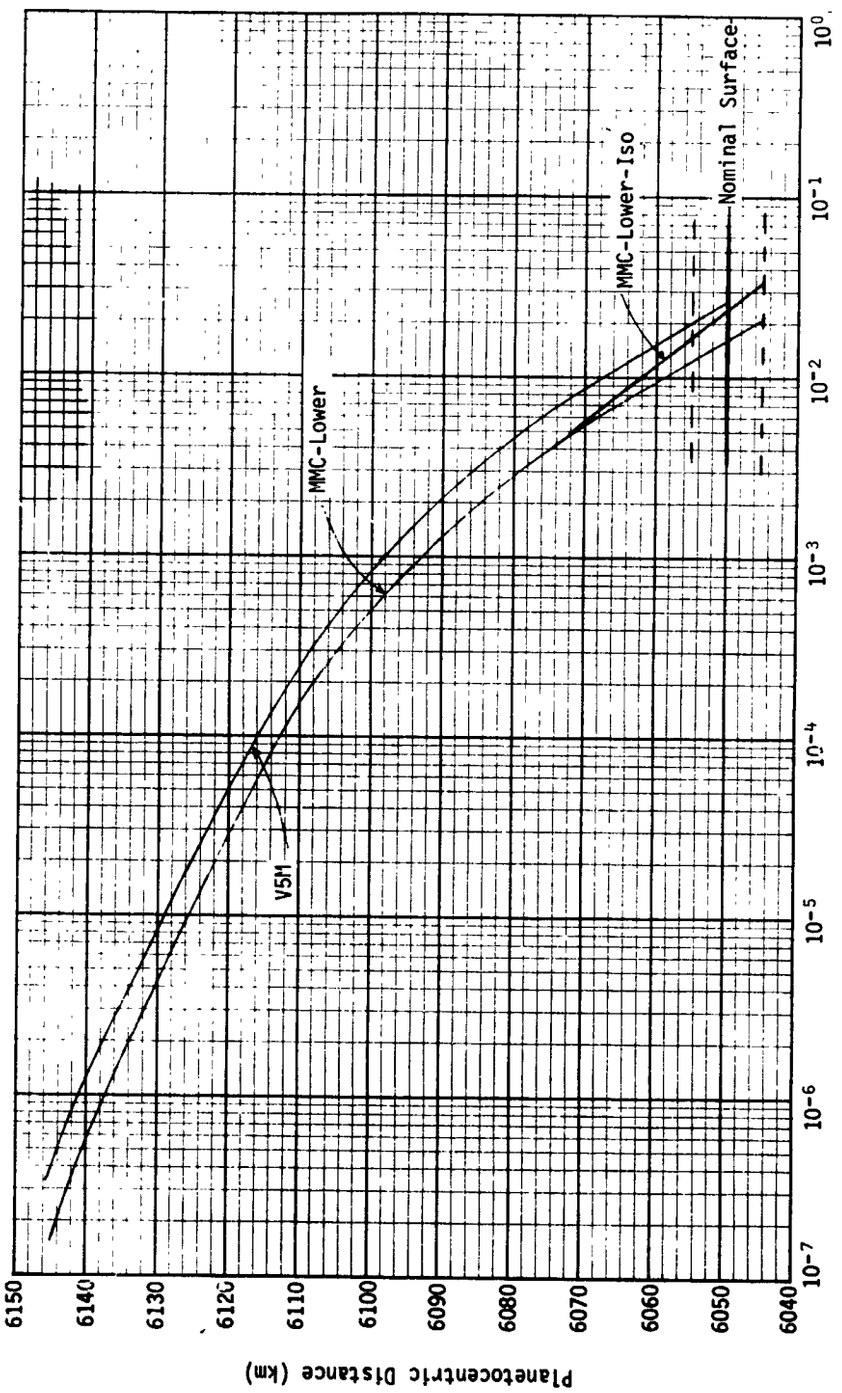


Fig. VII-1 Refractibility of Neutral Venus Atmosphere

Signal propagation times were also calculated. These are of interest for ranging and tracking. Over each altitude increment, Δr, the propagation time,

$$\Delta t = \frac{\Delta r\ (n)}{c}, \qquad [5]$$

(c = free space propagation velocity) was computed and accumulated, together with the difference between this propagation time and that of free space. At the 6050 km surface this difference was found to be 5.467 μsec for the V5M and 0.939 μsec for the Lower. This time uncertainty of about 4.5 μsec would represent a ranging uncertainty of about 675 m. This corresponds to communications from the subearth point. This uncertainty would increase as the limbs were approached to around 2 km at 70° from subearth. However, it should be noted that the multiprobe mission should return sufficient data to markedly reduce these uncertainties.

The refractivity profiles contain all the data necessary to do ray-tracing in the Venus atmosphere, which in turn generates data necessary to the accurate computation of both the defocusing and the attenuation loss for the various model atmospheres. However, because of limited time and manpower, plus the uncertainty in the models themselves, it was decided to complete the effort using approximate solutions.

Ray tracing is simplified by the fact that in a medium with spherical symmetry the rays are plane curves (Ref VII-2). Therefore, the investigation can be limited to rays in a plane without error. Ray tracing is based on Fermat's principle, which says that in a continuous but variable medium a ray between two points always takes the path giving minimum time delay. Fortuitously, in problems such as ours, this is also the path giving minimum attenuation.

It is first necessary to approximate the refractivity profile in the lower atmosphere with an exponential model of the form

$$N(h) = N_o \exp(-\beta h) \qquad [6]$$

where h is an elevation above the surface, not a radius. In each case, N_o was taken as the computed N at the surface. Two approaches were used to select β. In the first approach, β was selected to give a trapping radius r_t equal to that found by Eq [4], using

$$h_t = \frac{1}{\beta} \ln \left(N_o \, r_s \, \beta \right) \quad \text{(from Ref VII-3).} \qquad [7]$$

where r_s is the surface radius. The trapping radius r_t is equal to $r_s + h_t$.

The trap angle, ϕ_t, is the maximum angle above horizontal at which a ray, launched from the surface, is trapped. This ray will become horizontal at elevation h_t. The geometry is sketched in Fig. VII-2.

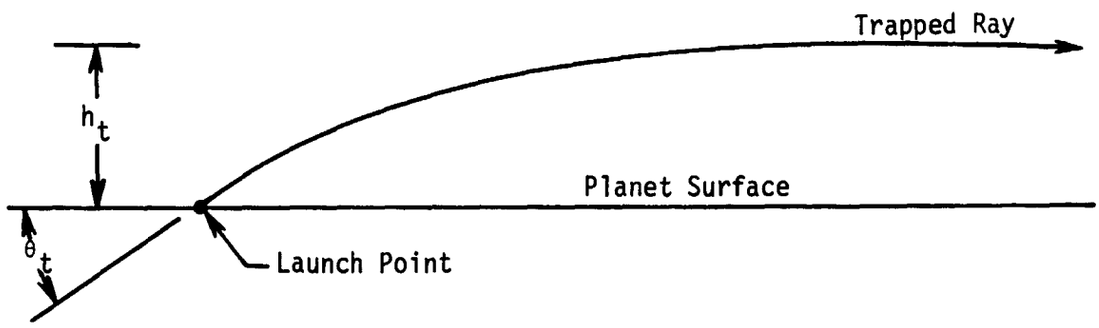


Fig. VII-2 Ray-Trapping Geometry

The trap angle, ϕ_t, can be calculated from

$$\phi_t = \sqrt{2 \left[N_o \left[1 - \exp \left(-\beta \, h_t \right) \right] - \frac{h_t}{r_s} \right]} \quad \text{(from Ref VII-3).} \qquad [8]$$

This can be modified for launch points other than the surface by substituting the desired value for r_s and using the N and h_t corresponding to the selected launch radius. The Russians (Ref VII-3), using their 20 atmosphere model, found $\theta_t = 3.3°$ and $h_t = 12$ km.

Their surface was at a radius of 6060 km, so this corresponds to a trap radius of 6072 km. Mariner 5 data indicates a trap radius of 6080 to 6090 km. Our first method data are summarized in Table VII-1.

Table VII-1 Ray Trapping Angles and Radii, First Method

Table VII-1 Ray Trapping Angles and Radii, First Method

Model	Surface Radius (km)	Pressure (atmospheres)	Trap Angle, ϕ_t (deg)	Trap Altitude, h_t (km)	Trap Radius (km)	N_o (x 10^{-2})	β km^{-1} (x 10^{-2})
V5M	6055	108.9	8.5	35.0	6090.0	1.989	5.31
V5M	6050	148.1	10.2	40.0	6090.0	2.572	5.25
Lower	6050	93.0	6.9	33.1	6083.1	1.629	4.56
Lower	6045	124.9	8.5	38.1	6083.1	2.083	4.63
Lower-Iso	6050	107.7	9.1	33.1	6083.1	2.335	6.86
Lower-Iso	6045	156.5	12.9	38.1	6083.1	3.392	7.03

The second approach consisted of selecting β to give a best fit over the lower part of the refractivity profile, with no attention paid to the consequences on h_t. The results of this approach are summarized in Table VII-2.

Table VII-2 Ray Trapping Angles and Radii, Second Method

Model	Surface Radius (km)	Trap Angle, ϕ_t (deg)	Trap Altitude h_t (km)	Trap Radius (km)	β km^{-1} (x 10^{-2})
V5M	6055	8.8	32.4	6087.4	6.22
V5M	6050	10.5	36.5	6086.5	6.25
Lower	6050	7.5	30.0	6080.0	5.88
Lower	6045	9.0	34.0	6079.0	5.91
Lower-Iso	6050	9.7	35.8	6085.8	5.94
Lower-Iso	6045	12.5	42.1	6087.1	5.96

The trap angle, ϕ_t, is the most important of these results, and there is reasonably good agreement between the two sets of results in this quantity. It was decided to use the values in Table VII-2 because they are more heavily influenced by the lower portion of the atmosphere where most of the ray bending and attenuation occurs. Also, the wide scatter in the β-values resulting from the first method suggests that it is less reliable than the second method.

Next, it was necessary to generate a curve of pointing error vs θ for each of the six models listed in Table VII-2, where θ is measured from vertical. At the trap angle, $\theta_t = 90° - \phi_t$, the pointing error is infinite, which gives an asymptote for these curves. A pointing error curve, $E(\theta)$ vs θ, for the Russian 20 atmosphere model is contained in Ref VII-3. It is repeated in Fig. VII-2.

This was computed for the other models using the refraction integral (Ref VII-3),

$$E(\theta) = N_o(1 + N_o) \sin\theta \int_o^\infty \frac{e^{-x}\,dx}{\left(1 + N_o e^{-x}\right)\sqrt{\left(1 + \frac{x}{\beta r_s}\right)^2 \left(1 + N_o e^{-x}\right)^2 - \left(1 + N_o\right)^2 \sin^3\theta}}. \qquad [9]$$

Two examples are shown in Fig. VII-3.

A plot of defocusing loss L_d vs θ is derivable from the pointing error curve using

$$L_d(\theta) = \frac{1}{1 + \frac{dE}{d\theta}} \qquad [10]$$

This will give a plot of L_d vs the ray launch angle θ. A more useful curve is one of L_d vs the angle at which the ray emerges from the atmosphere, $\psi = \theta + E(\theta)$. This is the angle of the ray directed toward Earth, equal to the probe location angle away from the subearth point. The geometry is sketched in Fig. VII-9.

Examples of this, converted to decibels, are shown in Fig. VII-4. These were made for the six models of Table VII-2. The curve for the Russian 20 atmosphere model was taken from Ref VII-3.

Using this last curve for both of our models at the elevation at which they reach 20 atmospheres pressure (6078.5 km in the V5M and 6072.5 km in the Lower) gives L_d vs ψ plots at three elevations for each model atmosphere. These three points, together with the zero asymptote for high elevations, can be used to plot L_d vs elevation at any fixed ψ. Plots were made at $\psi = 45°$ and 70°. The results are included in the combined curves of Fig. VII-8.

Next, the attenuation loss, L_a, must be considered. The most recent data on Venus attenuation is given in Ingalls and Evans (Ref VII-4). They estimate that the difference between the one-way zenith attenuation at 3.8 cm and 12.5 cm (7.9 GHz and 2.4 GHz) is 2.4 db. This appears to be the most reliable piece of data in this paper. The loss at 3.8 cm is found to be bounded by 2.5 and 4.5 db. This is later guessed at 4 ± ½ db, on rather tenuous grounds, but the two values 4 ± ½ db at 3.8 cm and 1.6 ± ½ db at 12.5 cm cannot be made to match an f^2 law, which they should, neglecting ionospheric effects. The 2.4 db difference can be made to fit well within the brackets of the data used in the AVCO report (Ref VII-5), using (for example) 0.3 db at 12.5 cm and 2.7 db at 3.8 cm, which also falls within Ingalls' bound of 2.5 to 4.5 at 3.8 cm. This tends to support the AVCO numbers, so we will use their nominal value, L_a (0) = 0.28 db at 2.298 GHz, for the MMC-lower atmosphere, 6050 km surface. For V5M, 6050 km surface, we will use the AVCO worst-case value, L_a (0) = 0.6 db. The attenuation for the Lower-Iso-6045 km surface was also set at 0.6 db so that either it or the V5M (whichever turned out to be the worst) could serve as a worst case.

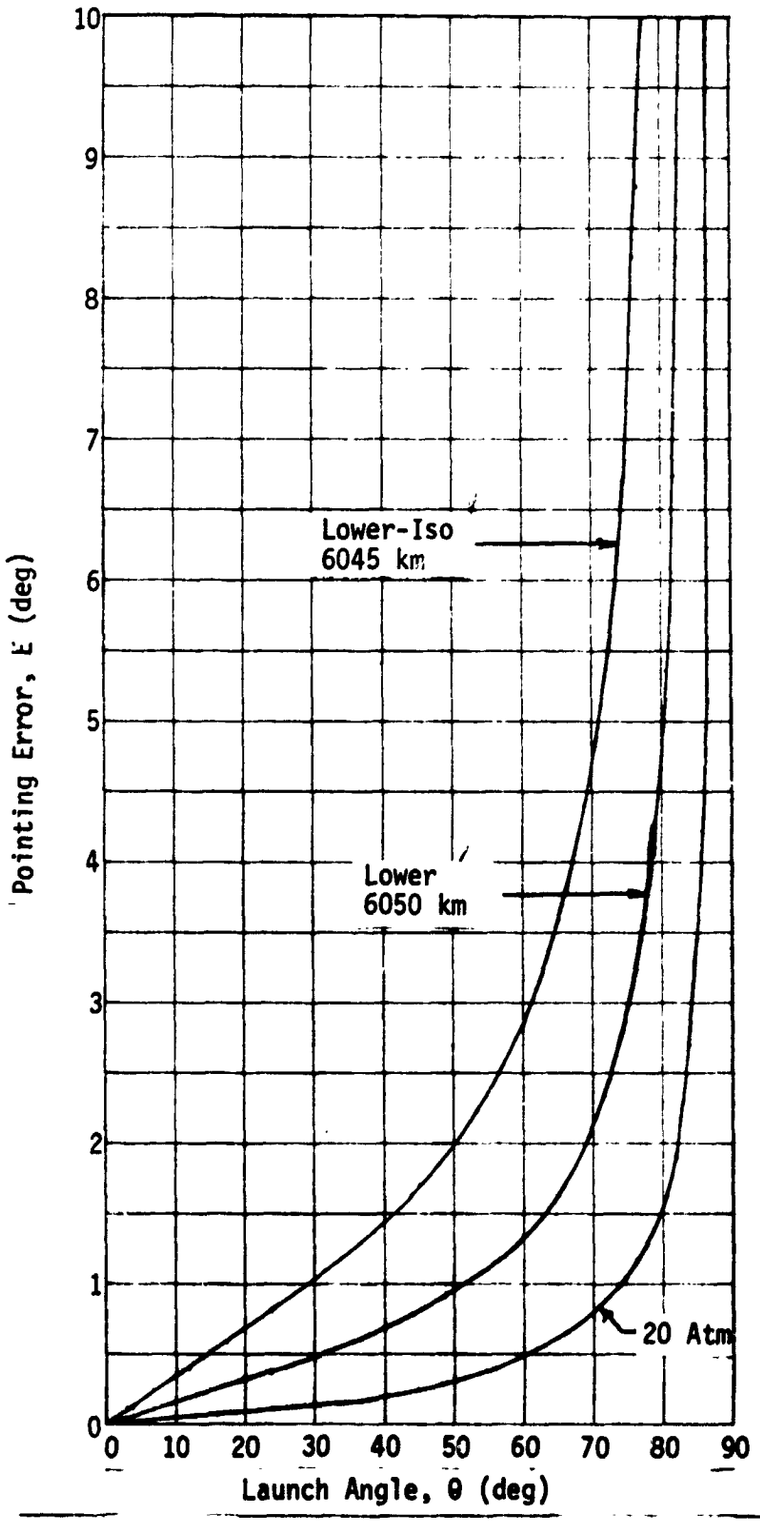


Fig. VII-3 Pointing Error for Several Model Atmospheres

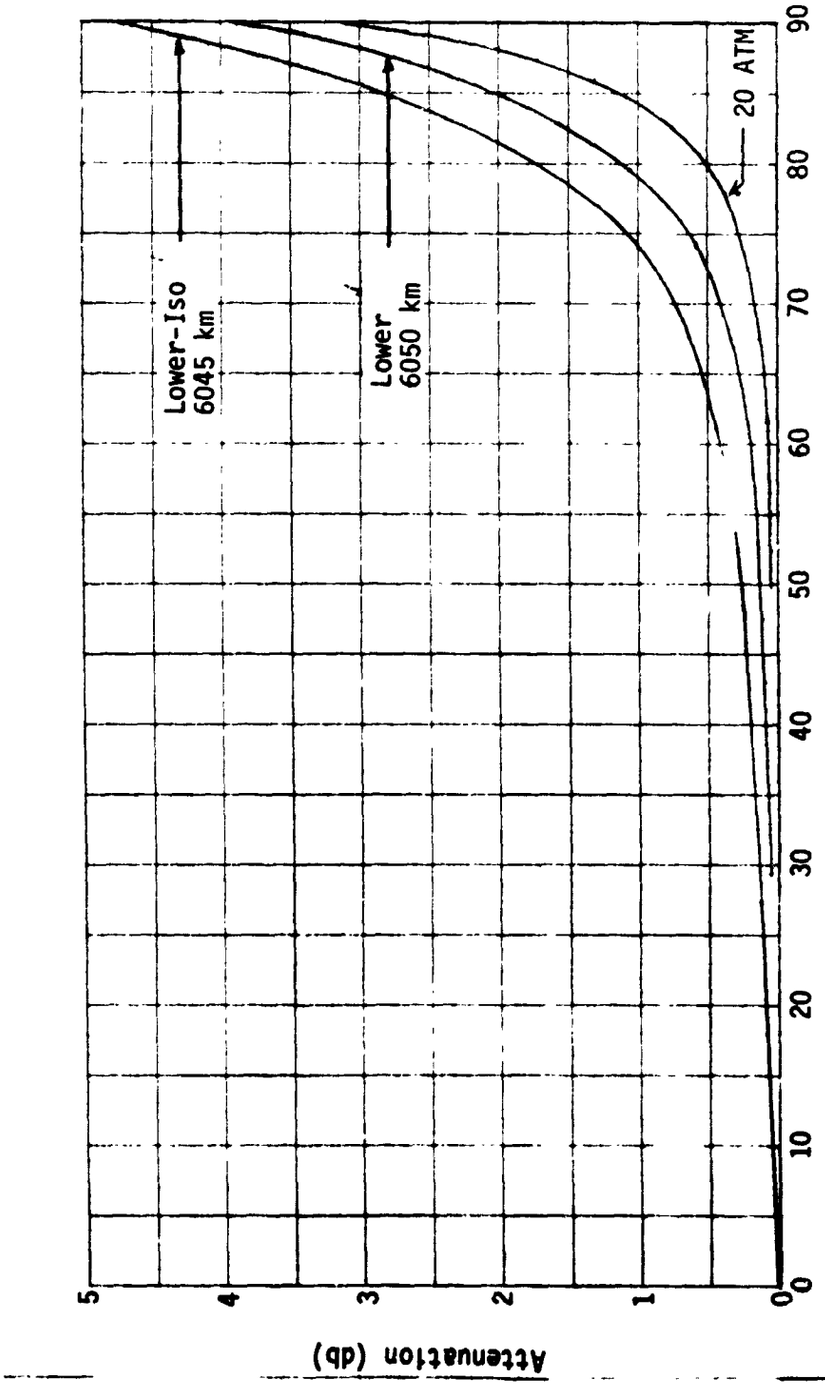


Fig. VII-4 Defocusing Loss for Several Model Atmospheres

The attenuation constant at any point in the atmosphere is related to pressure, temperature, and composition by (Ref VII-6)

$$\alpha = k \cdot \frac{p^2}{T^5} \cdot \left(15.7\ A^2_{CO_2} + 3.9 A_{CO_2} A_{N_2} + 0.085 A^2_{N_2}\right). \quad [11]$$

The bracketed term equals 13.1 for the 90% - 10% V5M composition and 14.3 for the 95% - 5% Lower composition. The tropospheric portion of the zenith attenuation from any point in the atmosphere is proportional to the integral of $\frac{p^2}{T^5}$ from that point upward. This was computed vs radius for the three atmospheres and then normalized by the appropriate multiplier so that the desired attenuation is given at the specified altitude.

As shown in Fig. VII-5, the V5M curve was normalized to 0.600 db (tropospheric portion, 0.560 db) at 6050 km. Adjusting this same normalizing constant for the different composition would give 0.246 db at 6050 km for the Lower atmosphere. This has been arbitrarily scaled upward to 0.280 db (tropospheric portion 0.260 db) to match the nominal AVCO value. This gives 0.402 db at 6045 km.

Using the same normalization on the Lower-Iso gives a sharply rising curve which reaches 1.232 db at 6045 km. This high loss is not consistent with observations and scaling it to 0.6 db at 6045 km would not be consistent with the Lower curve. Because there was no way to resolve these inconsistencies, a curve was drawn arbitrarily from 0.600 db at 6045 km, joining the Lower curve at 6069 km.

For small angles away from zenith, attenuation will follow a secant law. For larger angles, ray bending will cause a departure from the secant law. The L_a vs θ curve can be bounded in several ways. First, as θ approaches the trap angle, L_a becomes infinite, giving an asymptote. Two more bounds can be gotten by considering the sketch in Fig. VII-6 which shows a straight-line path at θ [whose loss would be given by L_a (0) sec (θ)], a straight-line path at ψ [whose loss would be given by L_a (0) sec (Ψ)], and the correct curved path. Note that the slope of the correct path is

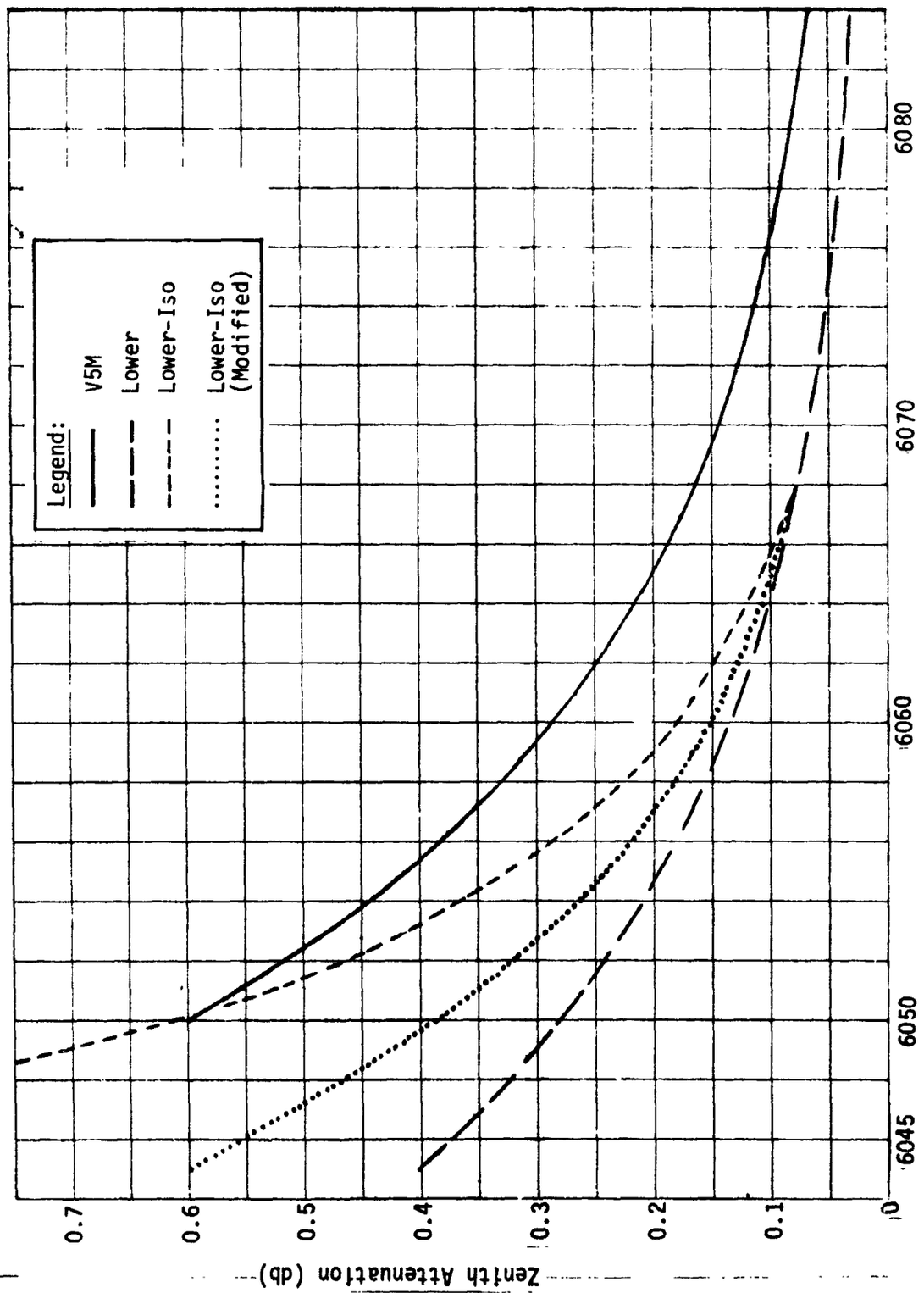


Fig. VII-5 Zenith Attenuation, 2.3 GHz

everywhere less than that of the θ-path and greater than that of the ψ-path, which implies that the correct path travels a greater distance (and thus has more attenuation) through any strata of the atmosphere than the θ-path, and less distance (less attenuation) than the ψ path. Therefore, plots of L_a (0) sec (θ) and L_a (0) sec (ψ) vs θ give a lower and upper bound on the L_a (θ) vs θ curve.

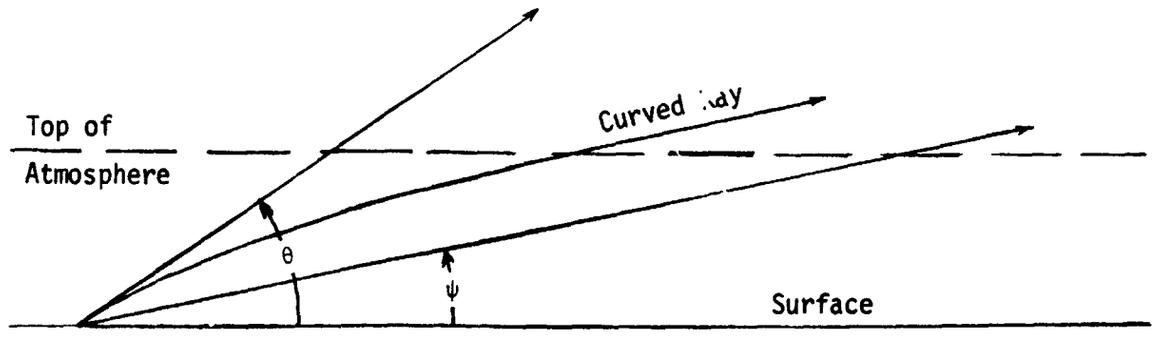


Fig. VII-6 Upper and Lower Bounds for Attenuation

These three bounds are plotted in Fig. VII-7 for the Lower-6050 km model, shown as an example. The spread between them becomes quite large for large values of θ, so some further calculation was necessary. A computation was made at a single point, θ = 70°. This consisted of first assuming many layers, partitioning the total zenith attenuation among these layers in proportion to $\frac{P^2}{T^5}$, partitioning the pointing error in proportion to $k \frac{P}{T} = N$ to get a ray angle in each layer, then using a secant law calculation for the attenuation in each layer, and then summing these attenuations. This single point, in conjunction with the bounds, allowed plotting of the L_a (θ) vs θ curve to adequate accuracy, at least out to θ = 70° (ψ $\simeq$ 75°). This was then converted to the more useful L_a (ψ) vs ψ plot, also shown in Fig. VII-7.

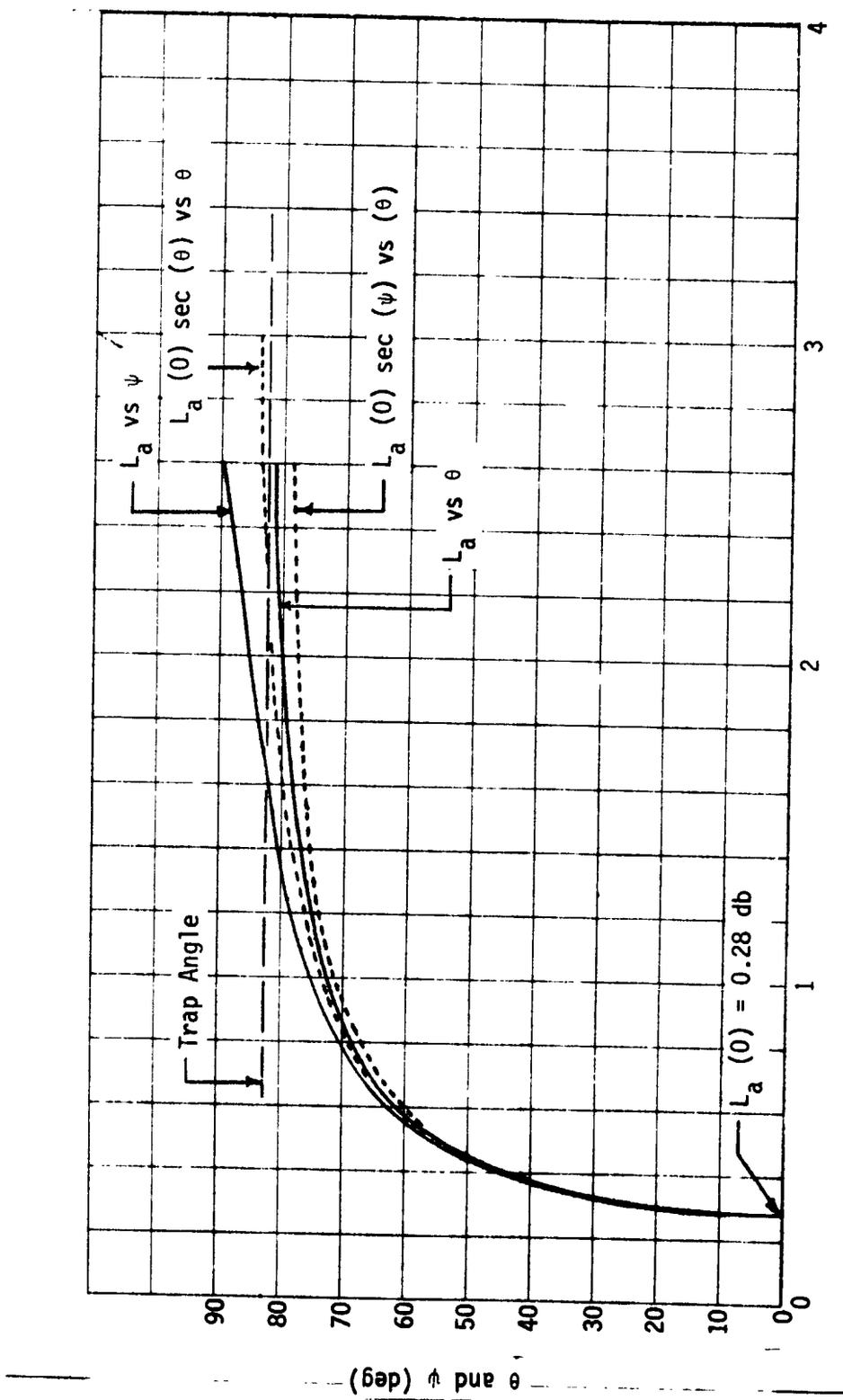


Fig. VII-7 Attenuation, Lower Atmosphere, 6050-km Surface

This should be quite accurate for $\psi < 75°$. Accuracy in the vicinity of $\psi = 90°$ is more questionable, but little use is made of this region of the curve. As mentioned earlier, Fermat's principle ensures that this last curve will be lower in attenuation than the curve given by a straight-line ray-path asymptote, L_a (0) sec θ vs θ. This is confirmed in Fig. VII-7.

The plots shown in Fig. VII-7 were repeated for all of the seven models used in the computation of L_d, permitting L_a vs elevation plots for the fixed ψ. Plots of the combined defocusing and attenuation loss for two values of ψ and all three model atmospheres are shown in Fig. VII-8.

Losses in the V5M-6050-km surface are almost the same as those in the Lower-Iso-6045-km surface, but the latter are slightly larger, so it has been selected to represent the worst case on our link calculations. The Lower-6050-km surface has been selected as the nominal atmosphere for link calculations. Plots of the combined losses from the surface for both of these vs ψ are shown in Fig. VII-9. Figure VII-10 shows ψ vs θ for these two atmospheres. These are derived from the pointing error curves.

In summary, the results presented here are based on a number of approximations. However, it is believed that their accuracy is at least as good as that of the atmosphere models. These are also approximations, based on rather tenuous data. For this reason, and also because of the limited scope of this program, these approximate results have been used in our communication system designs. It should be noted that the zenith attenuation is one of the principal uncertainties in this study The data used here are based conservatively on available radar data, and are believed to be reasonable. However, the data could be in error by an amount sufficient to have an impact on the mission.

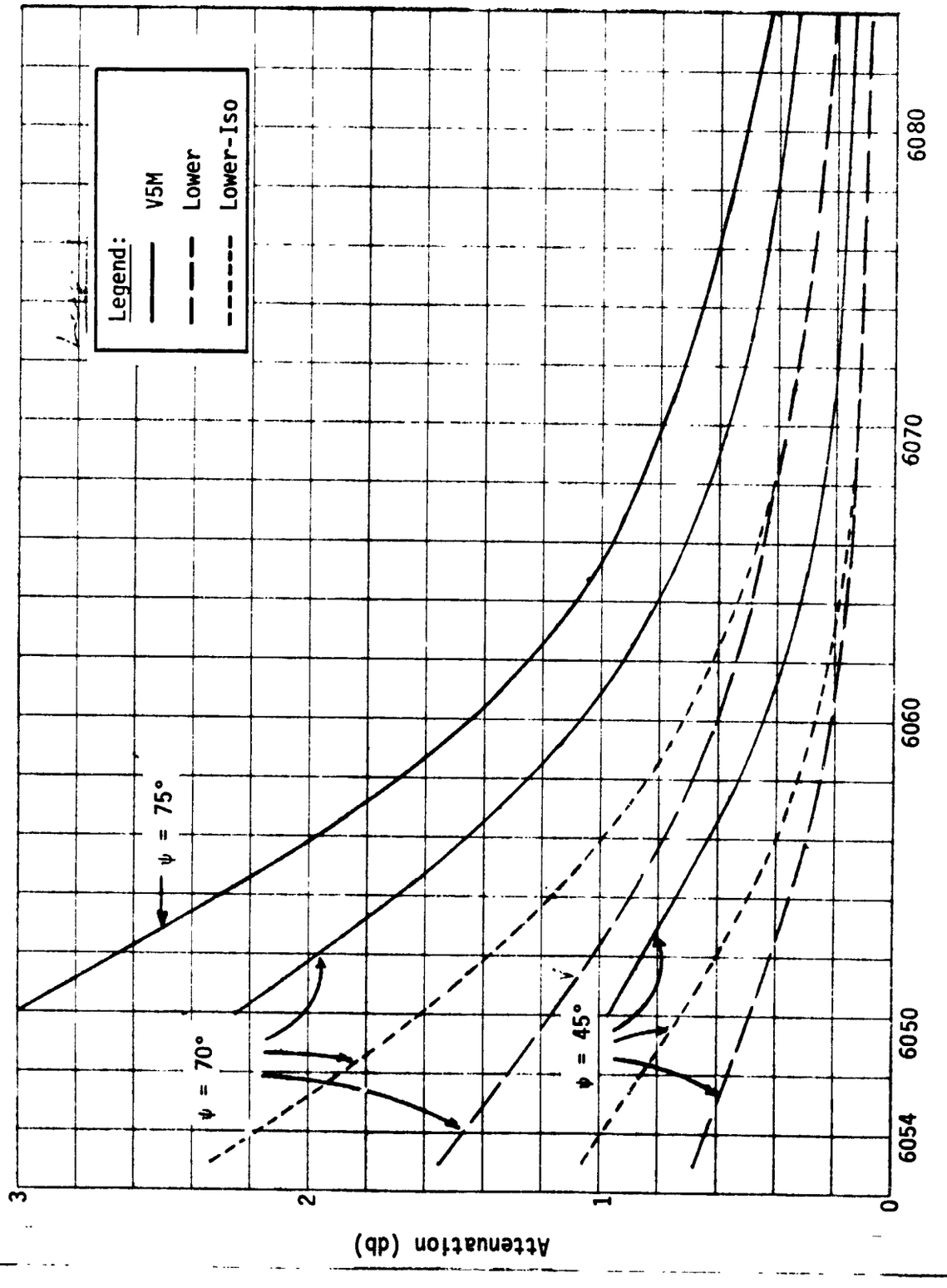


Fig. VII-8 Defocusing and Attenuation Loss vs Elevation for Several Departure Angles

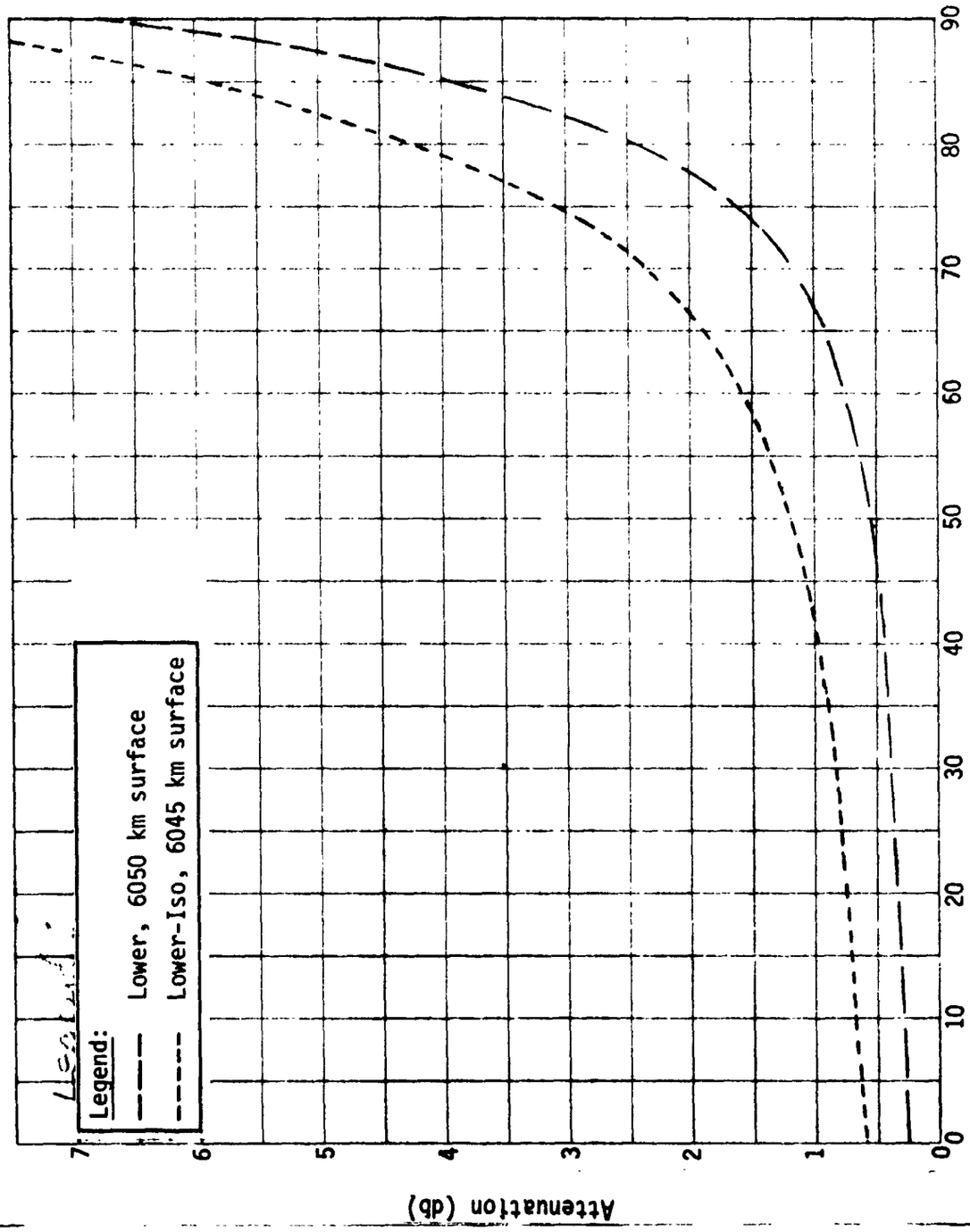


Fig. VII-9 Combined Attenuation and Defocusing Loss vs Departure Angle, Nominal and Worst-Case Atmospheres

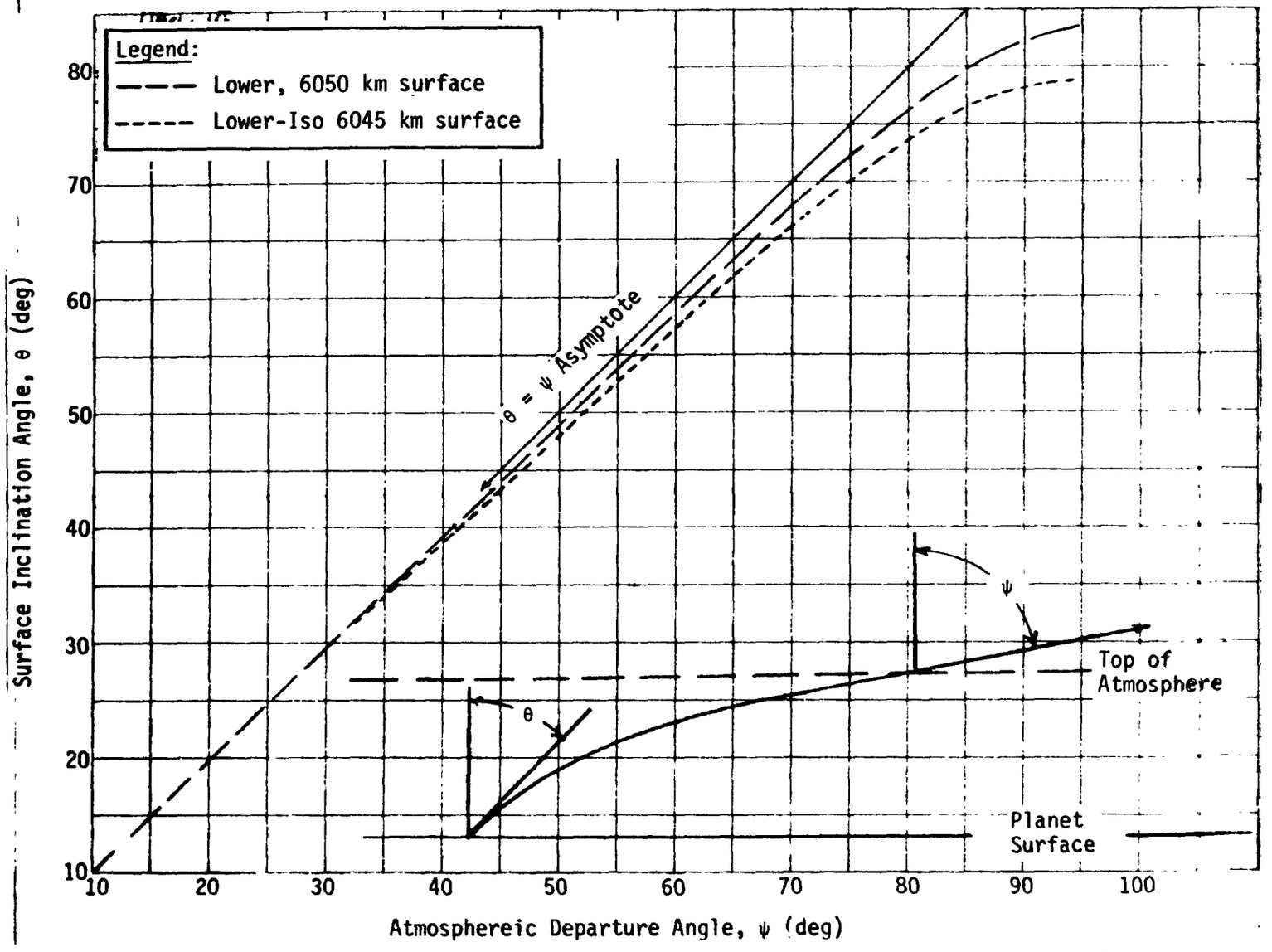


Fig. VII-10 Surface Angle vs Departure Angle, Nominal and Worst-Case Atmospheres

B. MULTIPATH ANALYSIS

Formulas and data used in the first part of this section are taken from Ref VII-7, and Ref VII-8 thru VII-10, which also borrow heavily from Ref VII-7.

First, consider an atmosphere-free planet. For entry angles out to about 80° away from subearth, and for elevations below about 150 km above the surface, the formulas given below, which do not consider curvature of the planet surface, will be sufficiently accurate. Results out to 90° would require consideration of planet surface curvature, at least for higher elevations. The geometry and the flat-planet approximate geometry are shown in Fig. VII-11 and VII-12.

One of the results in Ref VII-9 is that the power reflection coefficient of a rough surface, $|R|^2$, is approximately equal to that for a specular reflection from a smooth surface of the same dielectric constant, $|\Gamma|^2$, over most types of terrain. $|R|^2$ describes the average power in an incoherent, Rayleigh-distributed reflected signal, while $|\Gamma|^2$ describes the power in a clean specular signal.

Expressions for Γ_H (horizontal polarization) and Γ_V (vertical polarization) are from Ref VII-8:

$$\Gamma_H = \frac{\cos\theta - \sqrt{\varepsilon - \sin^2\theta}}{\cos\theta + \sqrt{\varepsilon - \sin^2\theta}} \qquad [12]$$

$$\Gamma_V = \frac{\varepsilon\cos\theta - \sqrt{\varepsilon - \sin^2\theta}}{\varepsilon\cos\theta + \sqrt{\varepsilon - \sin^2\theta}} \qquad [13]$$

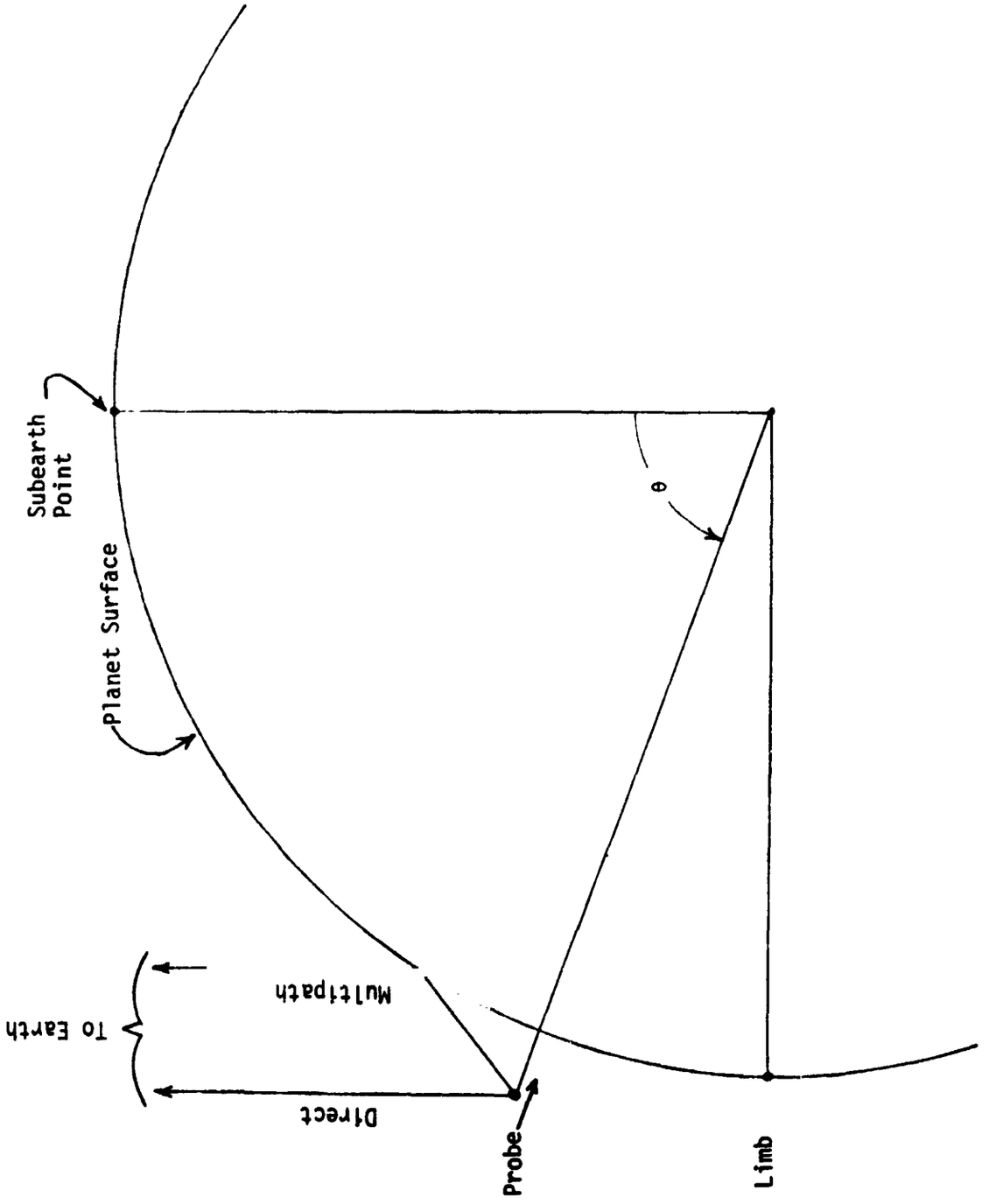


Fig. VII-11 Communications Geometry

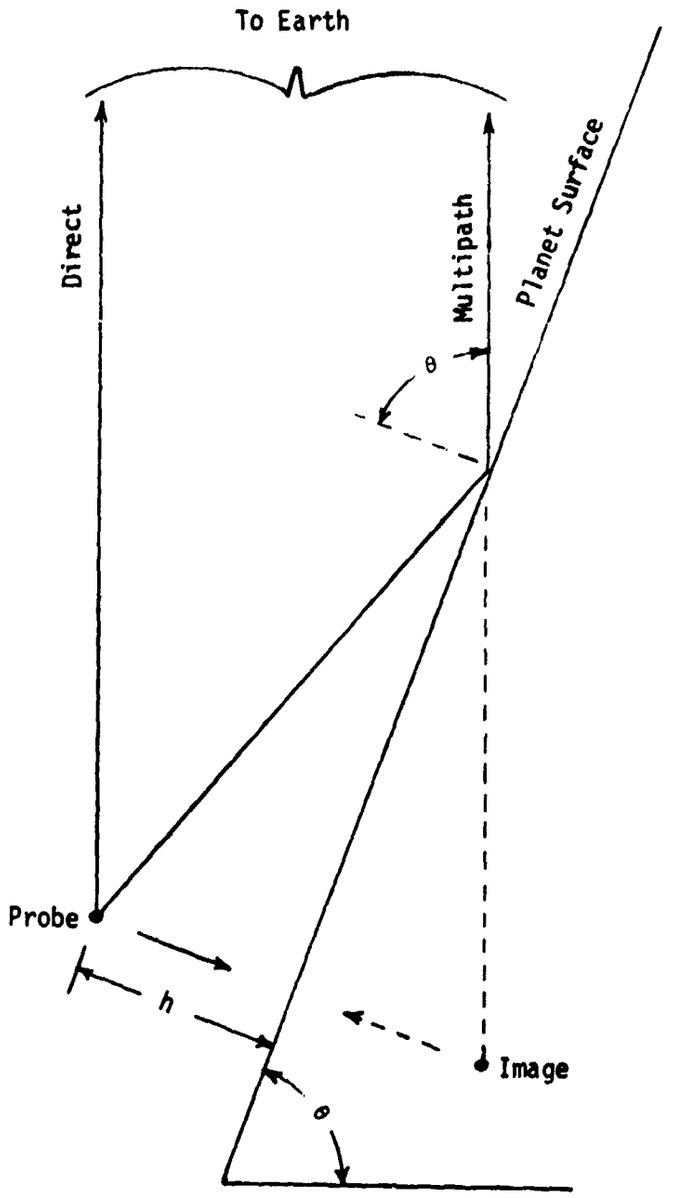


Fig. VII-12 "Flat Planet" Communications Geometry

ε has been estimated for Venus from radar data (Ref VII-11) as $\varepsilon \simeq 4$. Equations [12] and [13] are plotted in Fig. VII-13 using $\varepsilon = 4$. Note that E_V changes sign at $\theta = 63.5°$. This can be interpreted as follows: for $\theta < 63.5°$ an elliptically polarized wave will be reversed in sense, and for $\theta > 63.5°$ an elliptically polarized wave will not be reversed in sense. For θ near zero $\Gamma_V \simeq \Gamma_H$, which implies that a RHCP wave will reflect as a LHCP wave. In principle this means that if both the direct and reflected wave are circularly polarized, and if $\theta \simeq 0$ (probe near the subearth point), the reflected wave will be completely orthogonal in polarization to the direct wave, and thus can be completely eliminated in the receiver antenna. In practice this ideal is rarely realized because the down-looking part of the radiation pattern is usually only a very poor approximation to circularly polarized. However, it is reasonable to expect a 3 db advantage from this effect for probes near the subearth point providing circular polarization is used. For $\theta > 63.5°$ the effective R_C for circular polarization is the RMS average of R_V and R_H.

A more detailed analysis of rough surface scattering by Glenn (Ref VII-10) shows significant departures of $|R|$ from the $|\Gamma|$ curves for large θ. Data derived from his results are shown in Fig. VII-13 as dashed curves. Glenn also considers smooth surfaces, where "smooth" implies a ground roughness scale height, σ, much smaller than a wavelength. Since one wavelength is 13 cm it seems unlikely that these conditions will be found by any of the probes. We will assume that the dashed curves approximate the conditions on Venus.

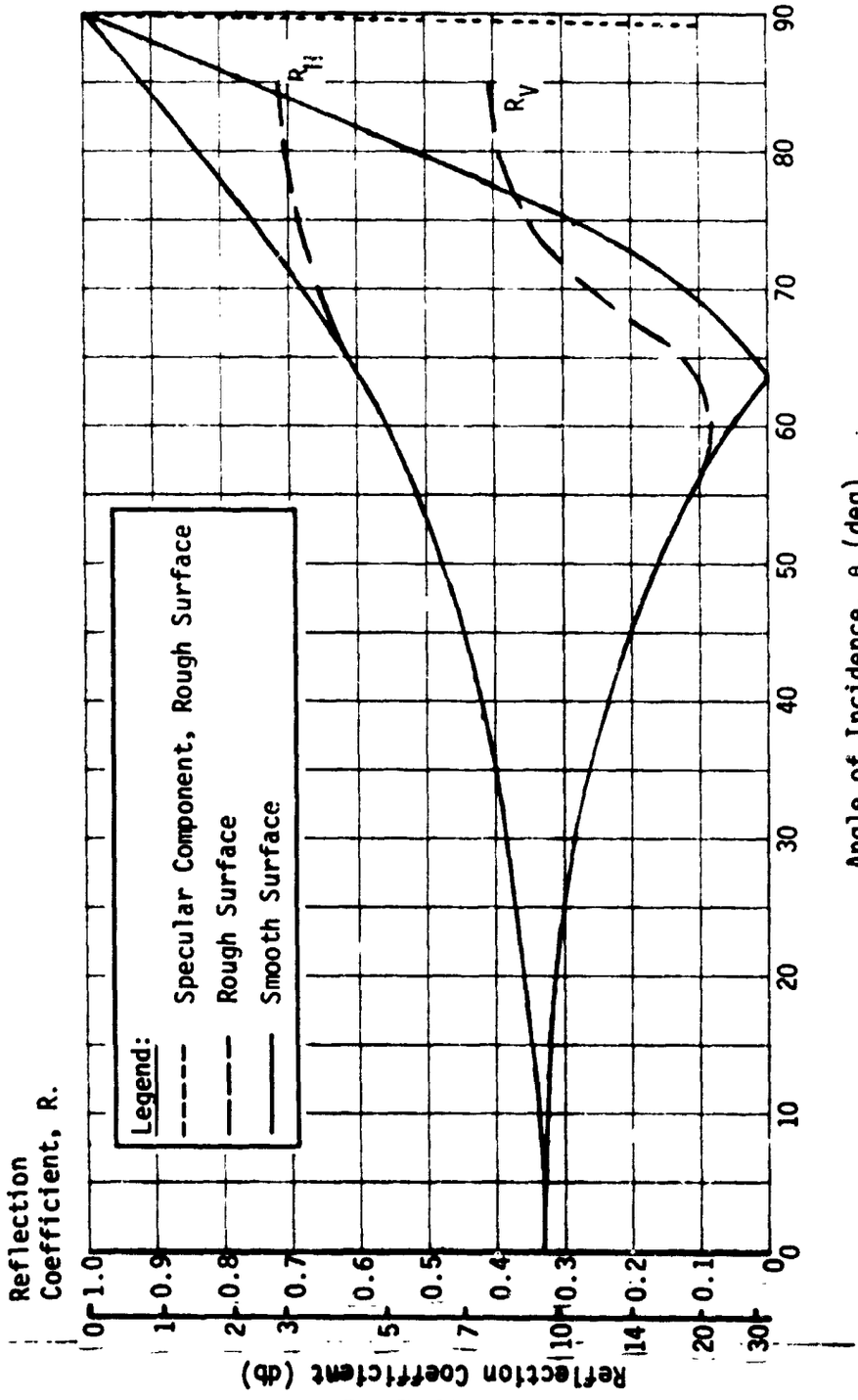


Fig. VII-13 Reflection Coefficients vs Incidence Angle

These curves cannot be valid all the way to $\theta = 90°$, because for near-grazing incidence any surface will become effectively a specular reflector. Glenn truncates his curves at $\theta = 85°$. An estimate of how far these curves may be extended can be gotten from an expression given by Beckmann (Ref VII-12) for the specular component.

$$|\Gamma|^2 = -670\left(\frac{\sigma \cos \theta}{\lambda}\right)^2 \text{ db} \qquad [14]$$

This is plotted for $\frac{\sigma}{\lambda} = 10$ in Fig. VII-13. From radar measurements $\frac{\sigma}{\lambda} > 10$ is the likely condition over most of the planet. The rough surface curves must become asymptotic to the specular component curve as $\theta \to 90°$. From Fig. VII-13 it is clear that the curves, as shown, are valid at least out to 85°, and probably for some distance beyond this point over typical Venusian terrain. Inasmuch as the critical angle below which rays are trapped in the Venus atmosphere ranges from 7.5° to 12.5° above grazing, depending on the model atmosphere used, the following very important result can be concluded: multipath signals from Venus are expected to be diffuse, regardless of the communication geometry, because rays close enough to grazing to give specular reflections would be trapped and would not emerge from the atmosphere. Therefore, we can conclude that in the near-limb region $|R_V| \leq -8$ db, $|R_H| \leq -3$ db, and $|R_C| \leq -4.5$ db.

As shown by Staras (Ref VII-9) most of the scattered power comes from the vicinity of the specular point. Accordingly, these coefficients must be multiplied by the antenna directivity, D, in the reflected path relative to the direct path. This depends on the anetnna design, but it generally will be quite good (0.1 or better) near $\theta = 0$ (probe near subearth), and will approach 1.0 (no directivity advantage) for $\theta \geq 70°$, at least for the low or

moderate gain (∿5 db) antennas that would be expected on most of the probes. Clearly, the multipath problem is most severe near the limbs, where the power in the multipath signal may not be much less than that in the direct signal.

Fortunately, Doppler offsets and fluctuations on the multipath signal will provide some assistance for moving probes, especially for the low data rates typical of these probes.

Consider first the case of a probe descending normal to the planet surface, as indicated in Fig. VII-12. If V is the descent velocity, then the direct link will have a Doppler offset of $\frac{-f_c V}{c} \cos \theta$ The multipath link will have the negative of this, giving a difference frequency

$$\Delta f = \frac{2 f_c V}{c} \cos \theta \qquad [15]$$

Picking some typical numbers, $f_c = 2.3 \times 10^9$ Hz, V = 10 m/sec, $c = 3 \times 10^8$ m/sec, $\theta = 70°$, gives $\Delta f = 52.5$ Hz. V = 10 m/sec is about the slowest descent speed expected for the ballistic probes.

In addition to this offset, the reflected arrival will have a fluctuation bandwidth given in Ref VII-10 as

$$B = \sqrt{8}\, \frac{2\pi}{\lambda}\, V\, \frac{\sigma}{L} \sin \theta \qquad [16]$$

$\frac{2\sigma}{L}$ is the mean slope of the planet. Earth-based radar measurements indicate that this ranges from 0.071 to 0.124. We will use $\frac{2\sigma}{L} = 0.10$, or $\frac{\sigma}{L} = 0.05$. At 2.3 GHz, $\lambda = 0.13$ m. Again using $\theta = 70°$ and V = 10 m/sec, Eq [16] gives B = 64 Hz. This fluctuation is a result of movement of the effective reflecting area across the rough terrain as the vehicle moves.

Equation [16] is really an order-of-magnitude relationship, and should be examined more closely. It is derived in Ref VII-9 from the autocorrelation function of the scattered signal, which was found (after some simplifying assumptions) to be gaussian-shaped,

$$R(\tau) = \exp\left\{-\left[\frac{\sqrt{8}\cdot 2\pi\cdot V\cdot \tau\cdot \sin\theta\cdot \sigma}{\lambda L}\right]^2\right\} = \exp\left[-\left(\frac{\tau}{\tau_o}\right)^2\right] \qquad [17]$$

where

$$\tau_o = \frac{\lambda L}{\sqrt{8}\cdot 2\pi\cdot V\cdot \sin\theta\cdot \sigma} = \frac{1}{B} \qquad [18]$$

The Fourier transform of $R(\tau)$ will give a gaussian-shaped spectrum

$$G(f) = \exp - \left[\frac{(\pi f)^2}{B}\right] \qquad [19]$$

This spectrum will be centered on the Doppler offset frequency, with sigma = $\frac{\sqrt{2}}{2\pi\tau_o}$. Thus B, as defined in Eq [16], is the $\sqrt{2}\ \pi$ = 4.45 sigma width of the spectrum. For the numerical example calculated above, the spectrum will be ±14.4 Hz to the one sigma points, centered on the offset Doppler frequency $f_o + \frac{\Delta f}{2}$. The spectrum is shown in Fig. VII-14. Clearly, if the signalling bandwidth is sufficiently narrow, most of the multipath signal can be filtered out.

For the descent probes, the bit rate will not exceed 120 bps. If this were sent using noncoherent MFSK, M = 32, 5 bits per symbol, each symbol integration time would be 0.042 sec, allowing a frequency resolution to a band 24 Hz wide. Assuming the spectrum of Fig. VII-14, a 24 Hz bandpath centered in f_o - 26.3 Hz would contain a negligible amount of the multipath signal. One could raise the signalling rate to 200 bps, and still have a managable interference level if MFSK signalling were used. However, it is unlikely that MFSK would be used for these higher bit rates, and MFSK does not provide Doppler information, so coherent signalling must also be considered.

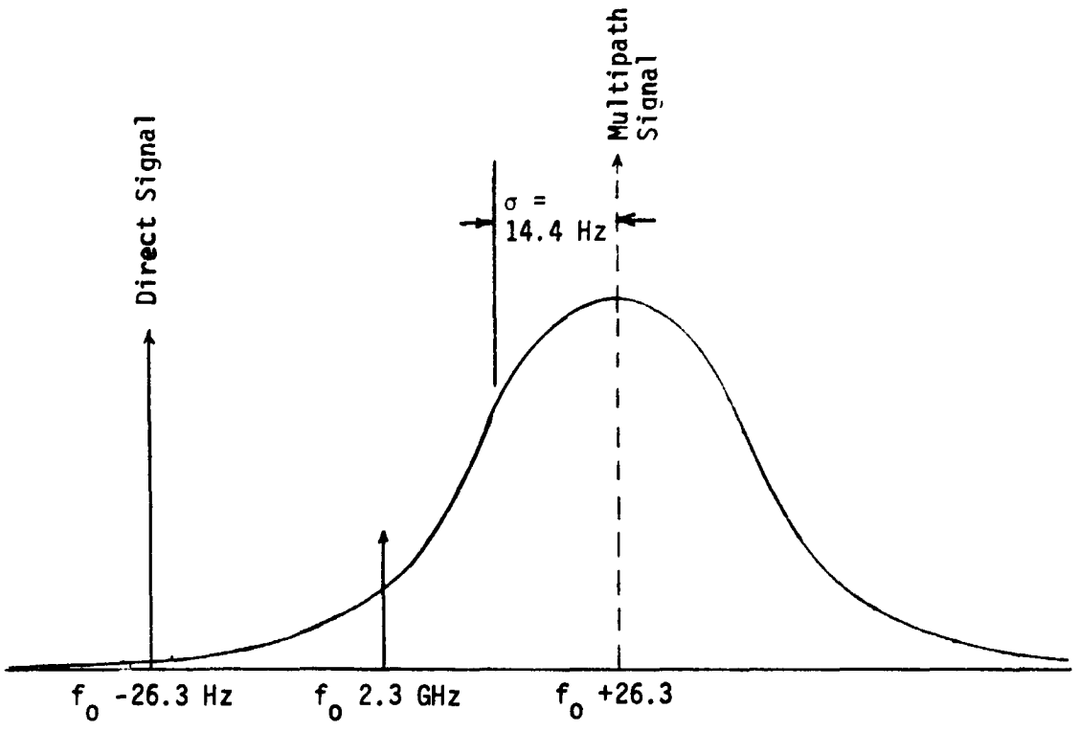


Fig. VII-14 Direct and Multipath Spectra, Descending Probe, 10 m/sec, $\theta = 70°$

First, consider the effects on a 12 Hz PLL. Using the spectrum of Fig. VII-14, this would put a negligible portion of the multipath energy into the loop bandwidth. Even if we assume that the direct and multipath powers are equal (which is very conservative) the multipath signal in the loop would be 32 db below the direct signal and about 23 db below the loop noise, so this can be neglected. This means that the phase reference generated by this loop will correspond to the phase of the carrier alone. It will not track the phase of the composite direct plus multipath signal.

It is important to note that bit-by-bit detection, which might be severely affected by the multipath for higher bit rates, need not be used. Any kind of error-control coding will have the effect illustrated above for the MFSK blocks, providing some degree of averaging over the highs and lows of the fading signal. The effectiveness of this averaging depends on the block or constraint length of the code used, and on the decoding method. It also depends on two external factors, multipath delay and multipath coherence bandwidth.

First, consider the multipath delay, or the time differential between the direct and the reflected paths. This is

$$\Delta t = \frac{h}{c}\left[\frac{1 + \cos(2\theta)}{\cos\theta}\right] \qquad [20]$$

where h is the probe elevation above the ground.

For $\theta = 70°$ this is $0.685\,\frac{h}{c}$. This will be small compared to the inverse of the RF bandwidth for all h of interest and all signalling except ranging.

The second factor is the coherence bandwidth. This is given in Ref VII-9 as

$$f_c \approx \frac{c\cos\theta}{\pi h}\left(\frac{L}{4\sigma}\right)^2 \qquad [21]$$

which is reasonably accurate except at small values of cos θ. f_c will be very large at low elevations. At h = 100 km and θ = 70°, f_c = 8.2 kHz, which is larger than any expected signalling bandwidth except for a ranging signal.

In the case where Δt is small compared to the inverse of the RF bandwidth and f_c is large compared to the RF bandwidth, the modulation on the multipath signal will track that on the direct signal, i.e., the multipath signal will look like a carrier of random amplitude and phase, phase modulated by the same signal as is on the direct carrier. The component of this that is orthogonal to the PLL phase reference will be rejected, leaving a sum signal of randomly varying amplitude (but nonvarying carrier phase) whose average power is somewhat greater than that of the direct signal alone. Therefore, a filter matched to this composite signal would give better performance than that given by the direct signal alone, providing it used the amplitude information (which can be measured) and providing it averaged over a period long compared to the average fluctuation period of the signal. This is $\sim$0.02 sec with the spectrum of Fig. VII-14, so a code that averaged over 0.1 sec or more would not require any multipath margin.

If convolutional coding is used, and if sufficiently well quantized (3 bits) amplitude information is preserved from the bit-by-bit detection, then the decoding operation can be designed to be in effect matched filter detection over the code constraint length. This is typically 20 information bits or more, allowing up to 200 bps to be collapsed to an effective bandwidth of 10 Hz or less, or an averaging period of 0.1 sec or more. This would give a negligible multipath problem. The decoding computation burden could be substantial if it were necessary to effectively use the whole constraint length of the code, but considering the

relatively low bit rate and the extremely high value of the information, this would be a minor consideration. Final decoding need not be done in real time but could be worked in detail after the mission was completed. Assuming a systematic code, preliminary decoding could be done in real time.

Next, we must consider a two-way ranging and Doppler link. This will have multipath problems on both the up and down link. For descent probes, ranging will probably not be done and only the Doppler will be required. The transponder PLL will typically have a bandwidth of 50 Hz. Again referring to Fig. VII-14, this will take in about 0.03 of the multipath signal, down about 15 db from the direct signal even assuming that the two signals are the same strength, so the loop should be able to handle this with only minor perturbations. If we assume vertical polarization, the multipath signal would drop an additional 10 db or more, to a completely negligible level.

The possibility that either loop would lock onto the multipath rather than the direct signal must also be considered. However, assuming diffuse reflection, this could only occur momentarily, and once the correct signal was acquired the multipath rejection given above would occur.

Next, consider a ranging signal. If we assume the conventional 10^6/sec bit rate, then over all but the last few hundred meters of the descent Δt will be greater than 1 μsec. Under these circumstances the multipath signal can be treated as a jamming signal. Ranging is complicated by the fact that the uplink signal is corrupted by the multipath signal, the corrupted signal is relayed, and then it is further corrupted by the downlink multipath arrival. One result of this is to divert some downlink power out of the desired signal and into amplification and retransmission of the uplink multipath signal. The other result is the jamming

effect mentioned above. The possibility of spurious correlations at a time delay corresponding to the multipath signal should be mentioned, but the Doppler offset $\Delta f \geq 50$ Hz, together with the coherence bandwidth when it is smaller than the signalling bandwidth, would convert this to an uncorrelated jamming signal for an averaging time greater than 1/50 sec, which will always be realized.

We have assumed vertically polarized antennas for the limb probes. Referring to Fig. VII-13, for entry angles between 60° and 70° the reflection coefficient is 10 db or better, so at most 1/10 of the power that should go into the ranging signal would be diverted into relaying of the multipath signal. This will require at most a 10% increase in the required ranging lock-on time, which should be tolerable. The jamming effect is completely negligible. Assuming a 0.1-sec integration time, a processing gain of 10^5 would occur, i.e., the multipath power would in effect be reduced by a factor of 10^5, to a completely negligible value. If a reduced rate ranging code, 10^5 bps, were used, suppression of the multipath power would be 10^4, which would still give a completely negligible amount.

Atmospheric effects are discussed in Section A of this chapter. These have two consequences on the multipath problem. First, the multipath signal will go through more atmosphere than the direct signal, and thus will receive more attenuation. This advantage vanishes as the probe approaches the surface, but is important for the balloon and high cloud probes. Second, ray-bending modifies the reflection coefficient chart (Fig. VII-13) by the amount of the pointing error. Thus, for example, for a probe at 70° from subearth, the surface incidence angle to use in Fig. VII-13 is about 65°, depending on the atmosphere model selected.

As discussed in Section E of this chapter, atmospheric effects impose a maximum communications angle of about 70° from subearth for probes that descend to the surface. We can now conclude that multipath effects do not further limit this. The multipath problem can be solved for descending probes over the range of bit rates of interest out to $\theta = 70°$, with no fading margin requirement, assuming proper encoding and decoding of the data. During the early part of the descent, when velocities are much higher than 10 m/sec, the problem vanishes completely.

Next, let us consider the effects of moving the high cloud probes all the way out to the limb, $\theta = 90°$. (Balloon probes will be considered later.) Using Eq [15] and [16], this will give a Doppler offset $\Delta f = 0$ and a slightly larger fluctuation bandwidth (sigma = 15.3 Hz for 10 m/sec descent velocity) than that shown in Fig. VII-14. For coherent communications, the PLL bandpass will be in the middle of the multipath spectrum, so most of the multipath power will be passed into the loop. This means that all coherent communications, including ranging and Doppler, will be affected. The multipath signal will introduce both phase and amplitude effects at the loop input. The former do little harm, and in fact permit constructive use of the multipath energy, but deep amplitude fades could cause loss of lock and cycle slipping in the loop.

Figure VII-15 shows the expected multipath signal strength as a function of angular distance from subearth θ. The multipath signal is reduced by three factors. These are two-way attenuation (Lower model assumed), antenna directivity (5 db antenna pointed at θ assumed), and surface reflectivity (vertical polarization assumed). The total of these drops rapidly as θ approaches 90° (the planet limb), to a minimum of about 13 db. Signal in the loops is further reduced by the filtering effects of the loop,

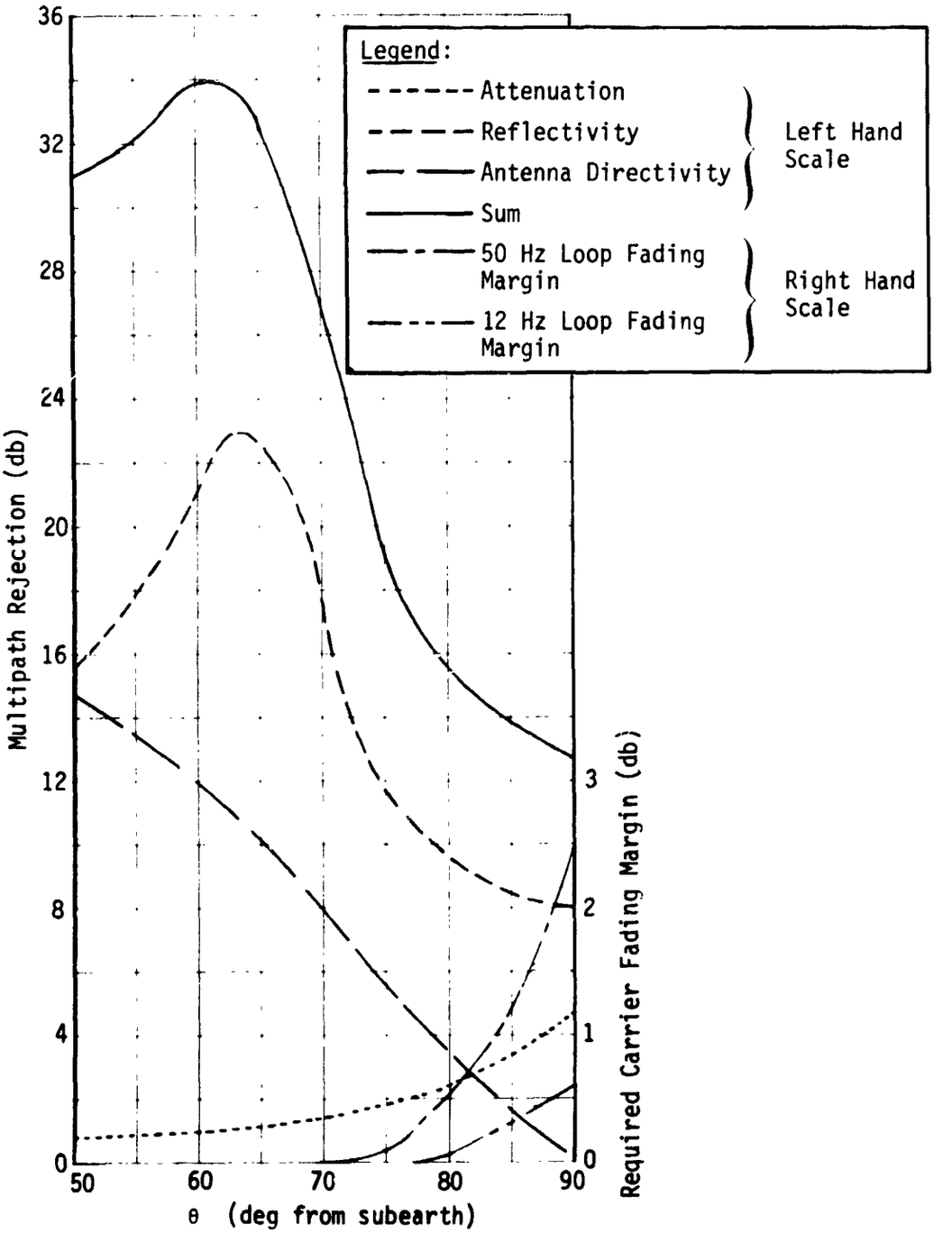


Fig. VII-15 Multipath Signal Strength and Required Carrier Fading Margin, Cloud Probes

which depends on the loop bandwidth, the Doppler offset, and the Doppler spreading. Again using a descent velocity of 10 m/sec to calculate these latter two values, required fading margins were calculated vs θ for a 50 Hz loop (on the probe) and a 12 Hz loop (in the ground station). These margins were calculated to maintain a ratio of signal to noise plus multipath, S/(N + M), of +9 db. These curves are also shown in Fig. VII-15. These are the required margins in the carrier only. The composite signal, ~~~en in the absence of a Doppler offset, will fade at about a 15 Hz rate due to the Doppler spreading. It is assumed that the information channel could be encoded to average over these fluctuations with no margin, as discussed earlier.

Low-rate noncoherent communications could also be carried out at $\theta = 90°$, with no margin, again assuming sufficient encoding. Coding could be superimposed on the MFSK signalling. This could be done by lumping groups of the M'ary symbols (together with the necessary parity symbols) into M'ary block or convolutional codes. As discussed earlier for coherent PSK signalling, if amplitude information resulting from the symbol detection is preserved and used, the decoding operation is similar to matched filter detection. The word "similar" is used here rather than "equivalent" because the noncoherent detection operation introduces nonlinearities that degrade performance, but this should be negligible in view of the relatively high signal-to-multipath ratio.

Next, let us consider the balloon probes. For these, we must assume zero vertical velocity and some horizontal velocity, V, in an unpredictable direction. V is measured with respect to the planet surface. In this case, the Doppler offset for the direct and multipath wave will be the same, so no advantage can be gained from it. The multipath fluctuation bandwidth for horizontal motion is

$$B = \sqrt{8}\,\frac{2\pi}{\lambda}\,V\,\frac{\sigma}{L}\cos\theta \qquad [22]$$

(from Ref VII-9), where B is again the 4.45 sigma bandwidth of a gaussian-shaped spectrum. B is independent of the direction of V. It is expected that the balloons will rarely go below a speed of 2 m/sec. With this velocity Eq [22] gives B = 7.05 Hz and σ_B = 1.58 Hz at θ = 70°. These go to zero at θ = 90°. While it might be practical to consider codes with constraint lengths of several seconds (at 20 bps or less) to handle the problem out to 70°, it is clearly not possible to take this approach out to or near 90° where the required constraint lengths approach infinity. Therefore, we are assuming that a multipath margin will be required for both the carrier and the information, and will also be required for noncoherent signalling. Figure VII-16 is similar to Fig. VII-15, but showing multipath signal strength and margin requirements for the balloon probes. There are several differences between the two figures. No filtering advantage is included in calculating the required margins. The antenna directivity curve is based on the annular slot antenna to be used on the balloon probe, shown in Section E of this chapter.

For data and ranging transmissions the annular slot is used only for $\phi > 45°$. For $\phi < 45°$ the cavity helix is used. Its very high front-to-back ratio (30 db or greater for $\theta < 45°$) reduces the multipath signal to a negligible level. Therefore, the fading margin shown in Fig. VII-16 should be used for data and ranging only for $\phi > 45°$, with zero margin required for $\phi < 45°$. The 9 db SNR curve should be used for these services. It is plotted only for $\phi > 45°$. The required margin is zero for $\phi < 70°$, rising to 2.5 db at $\phi = 90°$.

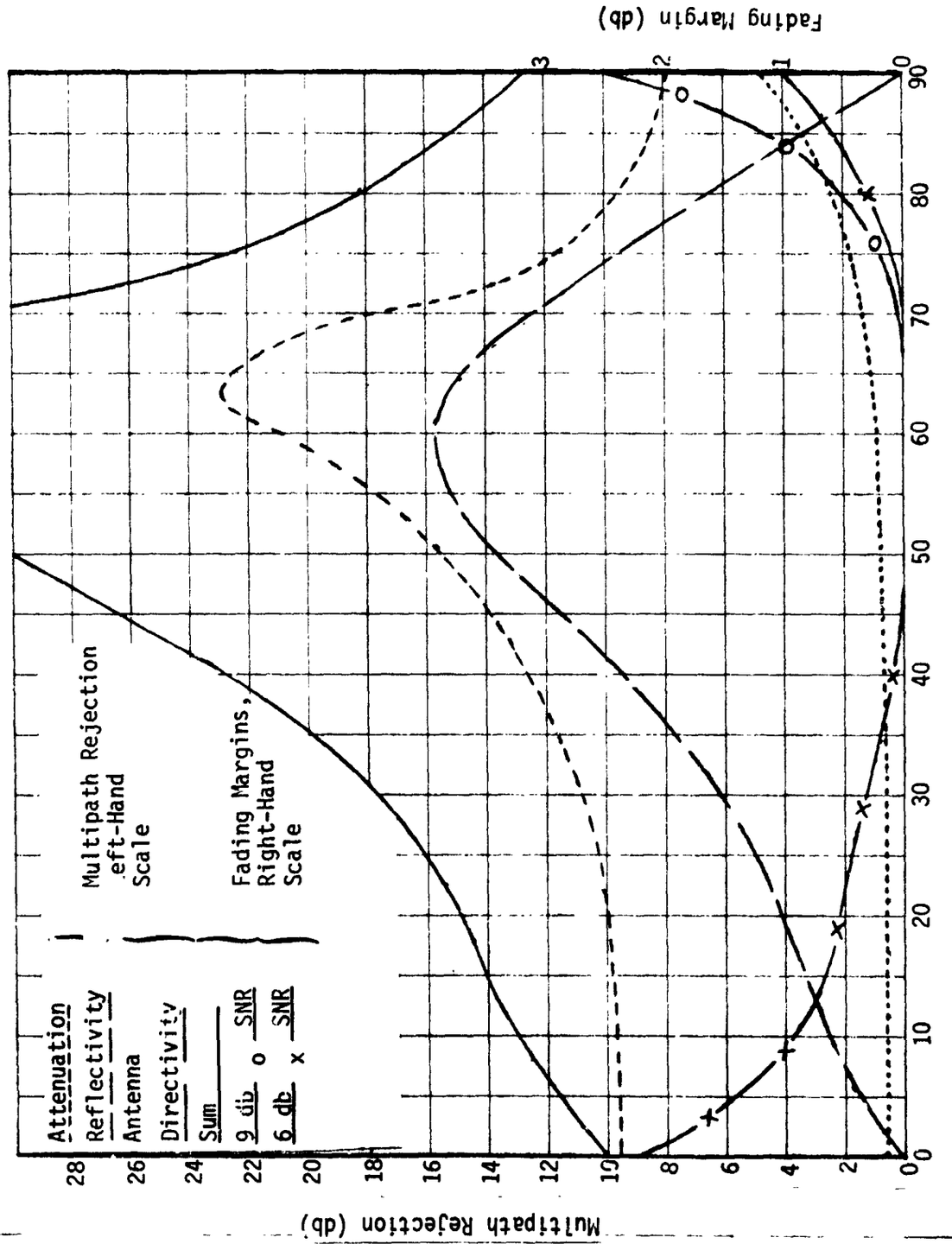


Fig. VII-16 Multipath Signal Strength and Required Fading Margin, Balloon Probes

The balloon is also required to carry out an antenna polarization experiment, described in Chapter V, Section D. The annular slot is used for this experiment for all ϕ. Carrier only is transmitted, and since it is not used for data demodulation a carrier loop SNR of +6 db will suffice for this experiment. A fading margin curve for +6 db SNR is given in Fig. VII-16, to be used for the polarization experiments. As shown on the figure, the required margin is zero for $45° < \phi < 70°$, rising outside this region to 2.3 db at $\phi = 0$ and 1.0 db at $\phi = 90°$. It will not be possible to carry out this experiment for $\phi < 5°$ because of a null in the antenna pattern at $\phi = 0$, so the worst-case fading margin, at $\phi = 5°$, is 1.4 db.

Next, consider the ranging signal. This is complicated by the fact that the uplink signal is corrupted by multipath, and then this corrupted signal is relayed and further corrupted by the downlink multipath signal. Another factor is the multipath time delay. For a balloon elevation of 60 km above the surface (this is about where the lower balloon will be) and $\theta = 70°$, the range difference between the two paths is 41.1 km and the time difference is 137 μsec. This is a negligible factor for the data transmission which has rates of perhaps 20 bps, but is quite significant for the wideband ranging sequence. At first glance it would suggest the possibility of a spurious correlation 137 μsec late and another one twice this late, but even assuming that they were strong enough, these delayed signals would not have enough coherence for this. From Eq [21] and assuming h = 60 km, the coherence bandwidth of the reflected signal is 25 kHz or less for $\theta > 50°$, which means that reflected signals with a bandwidth wider than this would experience frequency-selective fading. A 1 MHz signal (or even the 1/10 rate code, 100 kHz signal) such as the ranging code would become completely uncorrelated with its original form, and the multipath signal due to the ranging code would simply look like a weak, noncoherent wideband jamming signal. As such, it can be

averaged out like any other noise component in the ground receiver correlation procedure, with some negligible increase in the required integration time.

Diversion of the downlink power into retransmission of the uplink multipath must be considered. The multipath signal suppression shown in Fig. VII-16 (13 db or greater) will be enough to reduce the power diversion to a negligible level.

We can conclude from Fig. VII-16 that a negligible multipath margin of about 0.1 db will permit operation of the balloon probes for $\theta < 70°$. Going to $\theta = 90°$ will require a margin of 2.5 db.

In summary, our conclusions are:

1) Ballistic Probes Descending to the Surface - With proper coding, no margin requirements out to $\theta = 70°$. Beyond $\theta = 70°$ atmospheric losses rather than multipath effects will be the dominant problem, but multipath would also be significant;
2) High-Cloud Probes - With proper coding, no margin requirements out to $\theta = 70°$. For noncoherent signalling, no margin requirements out to $\theta = 90°$. For coherent signalling, margin in carrier only, rising to a maximum of 2.5 db for the uplink and 0.6 db for the downlink at $\theta = 90°$;
3) Balloon Probes - No margin requirements for data or ranging out to $\theta = 70°$. Margin requirement rising to a maximum of 2.5 db at 90°. For the antenna polarization experiment, no margin for $45° < \phi < 70°$. Margin rises on both ends, to 1.4 db at $\phi = 5°$ and 1.0 db at $\phi = 90°$.

There remains the possibility of fading due to multipath caused by irregularities in the atmosphere. Some fading was observed during the occultation of Mariner 5 (Ref VII-13 and VII-14). Fjeldbo (Ref VII-14) postulates spherical refractivity blobs as the cause for these fades. A more likely explanation, based on observations on Earth, is a horizontally stratified atmosphere. Fades due to this cause on Earth have been investigated by Watterson (Ref VII-15). This geometry will only cause fades at very low elevation angles. Watterson found no significant effects at angles greater than 2° above horizontal. These low angles cannot even be realized from the surface of Venus due to ray bending, except by trapped rays, but they could occur with a balloon or probe in the upper atmosphere providing it were very close to the limbs. For $\theta < 85°$ it is unlikely that any fades due to the atmosphere would occur unless the fades observed in the Mariner 5 occultation were due to absorptive rather than refractive irregularities. If absorptive irregularities exist they would have to be very localized because they have not been observed on Earth-based radar measurements.

C. OPTIMUM PROCESSING OF THE TURNAROUND RANGING SIGNAL

The switching rate of the conventional PN ranging signal is 1.0M bps. Although the spectrum of this sequence is conventionally shown as a sin x/x envelope, the actual spectrum of multi-component code (which includes a clock component) looks more like the sketch of Fig. VII-17, with spectral spikes at the clock frequency, 500 kHz, and at odd harmonics of this frequency.

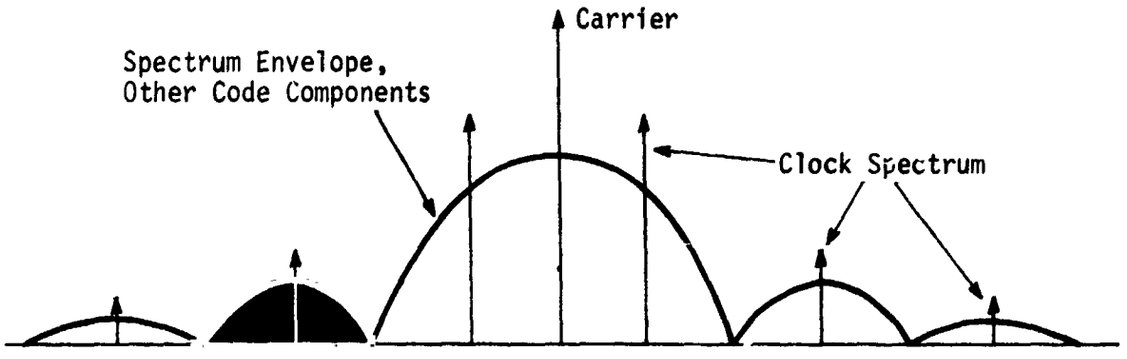


Fig. VII-17 Ranging Code Spectrum

The bandwidth of the low-pass filter used in the relay transponder on this signal prior to remodulating it onto the downlink carrier is specified to be quite wide -- 1.5 MHz is the minimum value (Ref VII-16). In the case of simple probes with low-gain antennas at planetary ranges the ranging signal received at the probe will generally be much smaller than the noise over this bandwidth. Using this bandwidth, a substantial part of the downlink carrier power is wasted by transmitting noise. This can be minimized by matching the filter bandwidth to the signal. Ideally, if the uplink signal were designed for minimum bandwidth, and if both the spaceborne and ground receivers were matched to the signal, the matched turnaround bandwidth would be given by the sampling theorem as 500 kHz. However, this ideal is not realized in the actual system.

It would be possible to analyze the signal format and the processing system, and determine a theoretically optimum filter for the turnaround signal, which would be a function of the SNR at the transponder receiver. However, this ideal would be virtually impossible to realize in a Venus probe, so we will simply determine what can be realized or approximated with simple filtering.

There are several effects that must be considered. These include signal loss due to filtering, losses in performance due to the ground receiver mismatch with the filtered signals (it is matched to ideal square-transition binary waveforms), and loss in resolution of the ranging waveform due to filtering of its high-frequency components.

Assuming for the moment a perfectly linear transponder with no intermodulation effects, if a fixed power P is allocated to the ranging channel, the output signal power S_o would be related to P and the input SNR, S_I/N_I, by

$$S_o = P \cdot \frac{S_I}{S_I + N_I} \quad \begin{cases} \longrightarrow P \dfrac{S_I}{N_I} \text{ for } N_I >> S_I \\ \longrightarrow P \text{ for } S_I >> N_I \end{cases} \qquad [23]$$

We will initially consider the weak-signal case, where S_o is proportional to the input $\frac{S}{N}$, and will then modify these results to include intermodulation effects and to include the cases where the weak-signal assumption is not valid. Baseband limiting will also be considered.

Consider first the clock component. Filtering it to just its fundamental will reduce its signal strength by a factor of $8/\pi^2 = 0.810$, or 0.92 db. If the ground receiver clock PLL were matched to a sinusoidal signal there would be no further loss, but because it is matched to a square wave, an additional 0.92 db of performance will be lost. If we assume an ideal rectangular bandpass filter, bandwidth F, 0.5 MHz < F < 1.5 MHz, then the signal and ground receiver mismatch losses in the clock channel will each be given by this 0.92 db and the noise will be proportional to F. Any filtering that was not flat out to 0.5 MHz would, of course, introduce a further signal loss in the clock component.

The signal power attenuation due to filtering of the rest of the sequence can be calculated from

$$S_z = \frac{\int_0^\infty \left(\frac{\sin(\pi f)}{f}\right)^2 \cdot |H(f)|^2 \, df}{\int_0^\infty \left(\frac{\sin(\pi f)}{\pi f}\right)^2 df} \qquad [24]$$

where f is in MHz and H is the filter transfer function. This was calculated vs the noise bandwidth F,

$$F = \int_0^\infty |H(f)|^2 \, df$$

for both an ideal rectangular filter and a gaussian filter. Again, this loss will be taken twice if the ground receiver is matched to the unfiltered waveform rather than to the filtered waveform.

A further loss results from the reduced resolution of the autocorrelation function of the filtered signal. A typical function is shown in Fig. VII-18. It was calculated for a sequence filtered by a rectangular bandpass 0.7 MHz wide. The ideal triangular autocorrelation function of the unfiltered sequence is also shown in Fig. VII-18 for comparison with the response of the filtered signal.

Assuming clock synchronization, the correlator must make a position decision based on the difference C(0)-C(1). This results in an effective signal power loss of $[1-C(1)]^2$, where C(0) is normalized to 1, compared to the unfiltered correlation function. Therefore, under the weak-signal assumptions described earlier, an index of performance for a filter is:

$$FOM_M = \frac{S_z \, [1-C(1)]^2}{F} \qquad \text{(Matched Ground Receiver)}$$

$$FOM_U = \frac{S_z^2 \, [1-C(1)]^2}{F} \qquad \text{(Unmatched Ground Receiver)} \qquad [25]$$

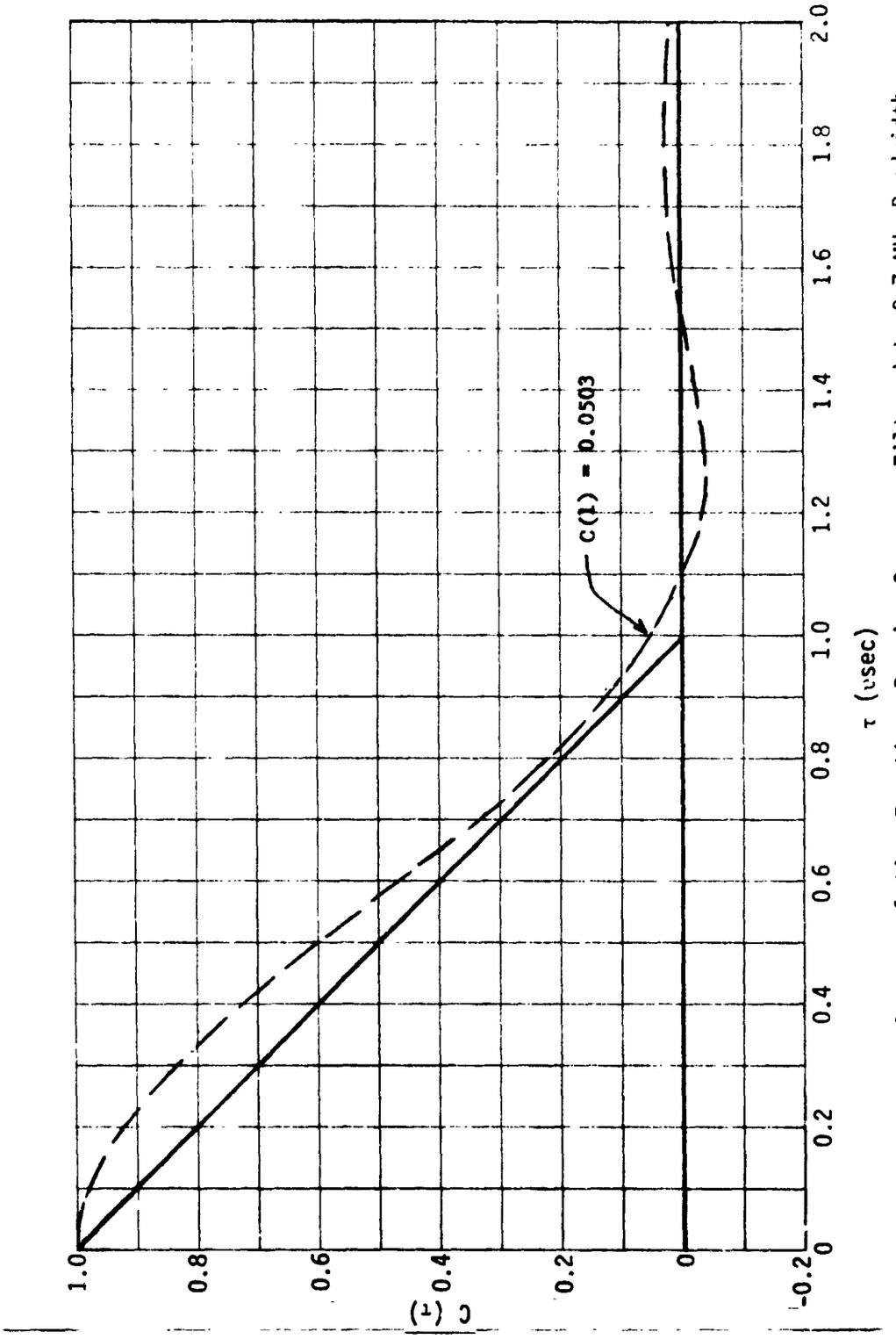


Fig. VII-18 Autocorrelation Function, Ranging Sequence Filtered to 0.7 MHz Bandwidth

These were computed vs F (F in MHz) for both the rectangular and the gaussian filter. Results for the rectangular filter are plotted in Fig. VII-19. Optimum F for the rectangular filter was found to be about 0.60 for the matched ground receiver and 0.65 for the unmatched ground receiver, with performance about 0.6 db poorer for the latter. Similar results were found for the gaussian filter, except that its performance was about 1.6 db poorer than the rectangular filter. Also, the gaussian filter would reduce the first harmonic of the clock which is unaffected by the rectangular filter for $F > 0.5$. Accordingly, we will assume an ideal rectangular filter for our calculations and further assume that the performance of a practical approximation to this filter will not differ greatly from this ideal.

Now for cases not near the weak signal limit, if we define S_I to be the power in the unfiltered received ranging signal, and N_o the noise power in a 1 MHz bandwidth, these performance indices must be modified by the factor

$$\frac{FN_o}{S_I S_z + FN_o},$$

which →1.0 in the weak signal limits, but will result in a larger optimum F as S_I/N_o is increased. For $S_I/N_o = 1$ for example, the optimum F occurs at 0.73 for the unmatched receiver case, compared to 0.65 at the weak signal limit, so the optimum F does not change very much up to this point. For $S_I/N_o > 1.0$ the change would be more rapid. For the cases of interest on the Venus probe application S_I/N_o will generally be less than 1, so we can simply assume a rectangular filter with $F = 0.7$, independent of S_I/N_o. The difference in performance between this and the actual optimum will be very small, less than 0.04 db at the weak signal limit. At this value of F, $S_z = 0.878$ and $[1-C(1)]^2 = 0.902$.

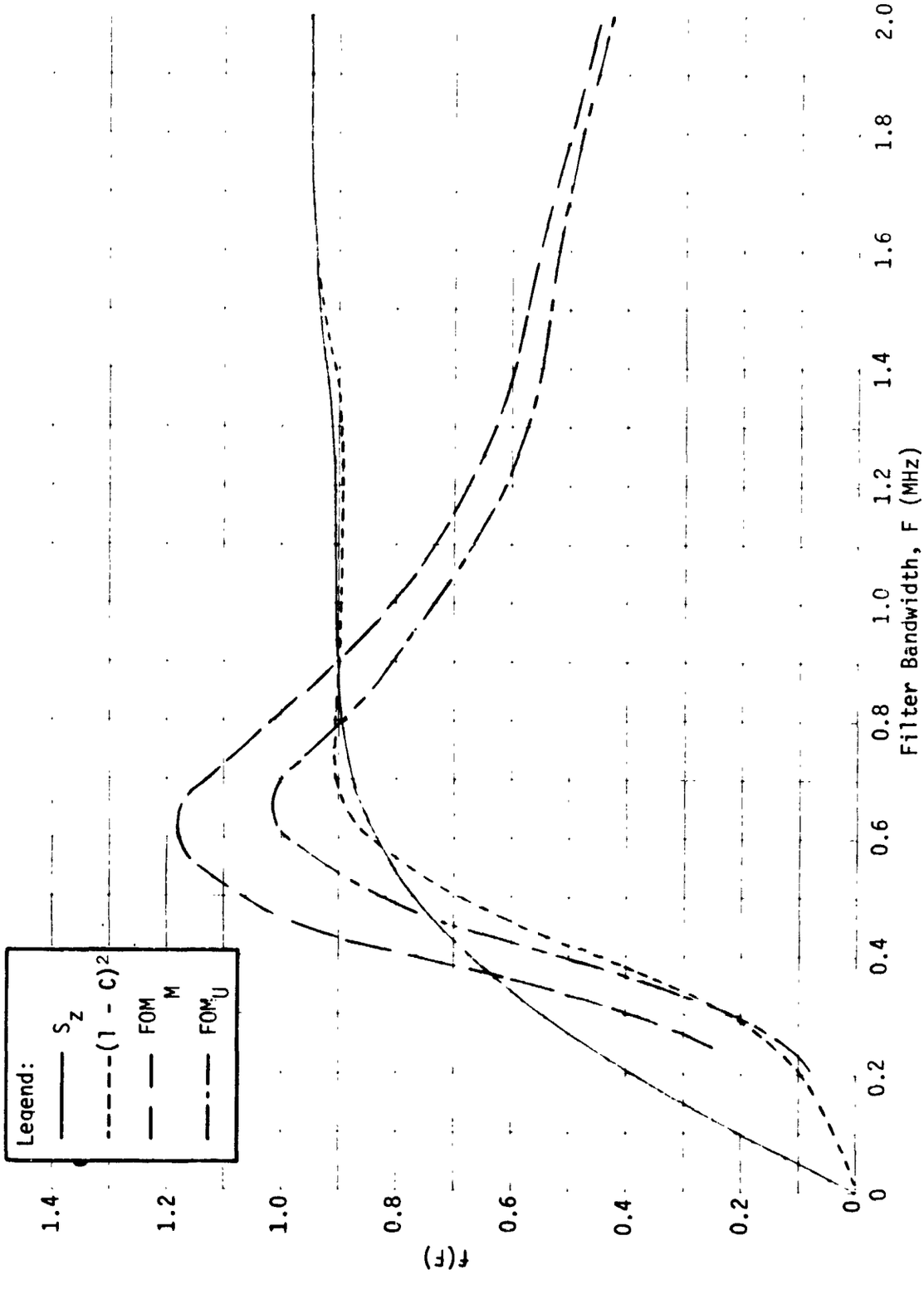


Fig. VII-19 Performance of a Rectangular Filter, Relayed Ranging Signal

With this assumption, the SNR into the modulator, $\frac{S_M}{N_M}$, will be given by

$$\frac{S_M}{N_M} = \frac{S_I}{N_o} \cdot \frac{S_z}{F} = \frac{S_I}{N_o} \cdot \frac{0.878}{0.7} = 1.254 \frac{S_I}{N_o} \quad [26]$$

and the mismatch and correlation losses at the receiver will be

$$[1-C(1)]^2 \cdot S_z = (0.950)^2 (0.878) = 0.791 = 1.01 \text{ db} \quad [27]$$

Next, let us consider intermodulation effects. We will initially assume that the downlink consists only of the carrier and the noisy ranging signal, and no other subcarriers, and further assume a linear or AGC receiver. Assume rms values of γ and σ_V for the signal and the noise, where $\left(\frac{\gamma}{\sigma_V}\right)^2$ is the SNR into the modulator $\frac{S_M}{N_M}$, and $\sigma = \left(\gamma^2 + \sigma_V^2\right)^{\frac{1}{2}}$ is the rms amplitude of the signal into the modulator. This can be selected to give the desired partitioning of power between the carrier and the ranging channel.

Under these circumstances the well-known equations describing the power partitioning are:

$$\frac{P_C}{P_T} = \cos^2(\gamma) \exp\left(-\sigma_V^2\right) \quad [28a]$$

$$\frac{P_S}{P_T} = \sin^2(\gamma) \exp\left(-\sigma_V^2\right) \quad [28b]$$

$$\frac{P_L}{P_T} = 1 - \frac{P_C}{P_T} - \frac{P_S}{P_T} \quad [28c]$$

(Square-wave signals), and

$$\frac{P_C}{P_T} = J_0^2(\sqrt{2}\gamma) \exp\left(-\sigma_v^2\right) \quad [29a]$$

$$\frac{P_S}{P_T} = 2J_1^2(\sqrt{2}\gamma) \exp\left(-\sigma_v^2\right) \quad [29b]$$

$$\frac{P_L}{P_T} = 1 - \frac{P_C}{P_T} - \frac{P_S}{P_T} \qquad [29c]$$

(Sinusoidal signals)

where

P_C = Carrier power,

P_S = Signal power,

P_L = Lost power,

P_T = Total power.

Our filtered signal is neither square nor sinusoidal, so these results cannot be used without some modification. Fortunately, for weak signals, we can invoke the central limit theorem and say that the signal plus noise has a gaussian distribution, with $\sigma = \left(\gamma^2 + \sigma_v^2\right)^{\frac{1}{2}}$. We now need some relationship similar to Eq [28] and [29] for modulation with a gaussian "signal." We have immediately (from Eq [28a]),

$$\frac{P_C}{P_T} = \exp\ (-\sigma^2) \qquad [30a]$$

To find $\frac{P_S}{P_T}$, assume that the gaussian signal is formed by a very large number, n, of uncorrelated, equal power sine-wave subcarriers, modulation index = β. Then $\sigma^2 = n\beta^2$ or $\beta = \sigma/\sqrt{n}$. Post-modulator signal power in the sum of these would be

$$\frac{P_S}{P_T} = n \cdot \sin^2\left(\frac{J}{\sqrt{n}}\right) \cdot \left[\cos^2\left(\frac{\sigma}{\sqrt{n}}\right)\right]^{n-1} .$$

For large n this gives

$$\lim_{n\to\infty} \frac{P_S}{P_T} = \sigma^2 \left(1 - \frac{\sigma^2}{2_n}\right)^{2n} = \sigma^2 \exp\ (-\sigma^2).$$

This gives

$$\frac{P_S}{P_T} = \sigma^2 \exp(-\sigma^2) \quad [30b]$$

$$\frac{P_L}{P_T} = 1 - (1 + \sigma^2) \exp(-\sigma^2), \quad [30c]$$

(gaussian signals).

Our desired signal is $\frac{\gamma^2}{\sigma_v^2 + \gamma^2}$ of this "signal," which gives:

$$\frac{P_C}{P_T} = \exp\left[-\left(\sigma_v^2 + \gamma^2\right)\right] \quad [31a]$$

$$\frac{P_S}{P_T} = \gamma^2 \exp\left[-\left(\sigma_v^2 + \gamma^2\right)\right] \quad [31b]$$

$$\frac{P_L}{P_T} = 1-(1 + \gamma^2) \exp\left[-\left(\sigma_v^2 + \gamma^2\right)\right] \quad [31c]$$

Assuming $\frac{P_C}{P_T}$ is given by the requirements of the link, Eq [31b] can be reduced to:

$$\frac{P_S}{P_T} = \frac{S_M}{S_M + N_M} \cdot \frac{P_C}{P_T} \ln\left(\frac{P_T}{P_C}\right) \quad [32]$$

Note that Eq [31] and [32] do not require that $S_M << N_M$, but only that their sum be approximately gaussian, a somewhat weaker requirement.

One conclusion that can be drawn from Eq [32] is that the optimization of F carried out earlier is not affected by intermodulation effects. Although intermodulation does result in lost power, it is "linear," i.e., $\frac{P_S}{P_T}$ is proportional to $\frac{S_M}{S_M + N_M}$, so the assumptions under which F was optimized are not violated over the range of validity of Eq [32].

If IF limiting is used in lieu of AGC, the results cited above will not change except by the limiter loss, which will be $\pi/4$ or 1.05 db at low SNR (Ref VII-17). Baseband limiting is another matter, and it will be examined next. Baseband limiting will cause some signal suppression. On the other hand, it reduces the statistics of the modulation signal to those of a square wave, permitting a PSK modulation that is free of intermodulation loss. Therefore, for circumstances under which the intermodulation loss given by a nonlimited modulating signal is greater than the limiter loss, baseband limiting would be advantageous.

The intermodulation loss L_{IM} can be derived from Eq [32]. It is defined by:

$$\frac{P_S}{P_T} = \left(1 - \frac{P_C}{P_T}\right) \frac{S_M}{S_M + N_M} \cdot L_{IM}.$$

Substituting this into Eq [32] gives:

$$L_{IM} = \frac{P_C}{P_T - P_C} \ln\left(\frac{P_T}{P_C}\right) \qquad [33]$$

This is plotted vs $\frac{P_C}{P_T}$ in Fig. VII-20. The loss with IF limiting, 1.05 db greater, is also plotted in Fig. VII-20. Again, this is strictly valid only if the signal plus noise at the modulator input has a gaussian distribution.

Next, consider baseband limiting, again at the weak signal limit. For square-transition binary signals in gaussian noise, the limiter loss, L_L, is the well-known 1.96 db or $2/\pi$ in the weak-signal limit, and less than this for SNRs > -10 db (Ref VII-17). However, we have assumed substantial prelimiter filtering. We will assume that in the weak signal limit, where the limiter loss is independent of signal strength, the 1.96 db figure is valid, and will retain the filter, mismatch, and correlator losses used

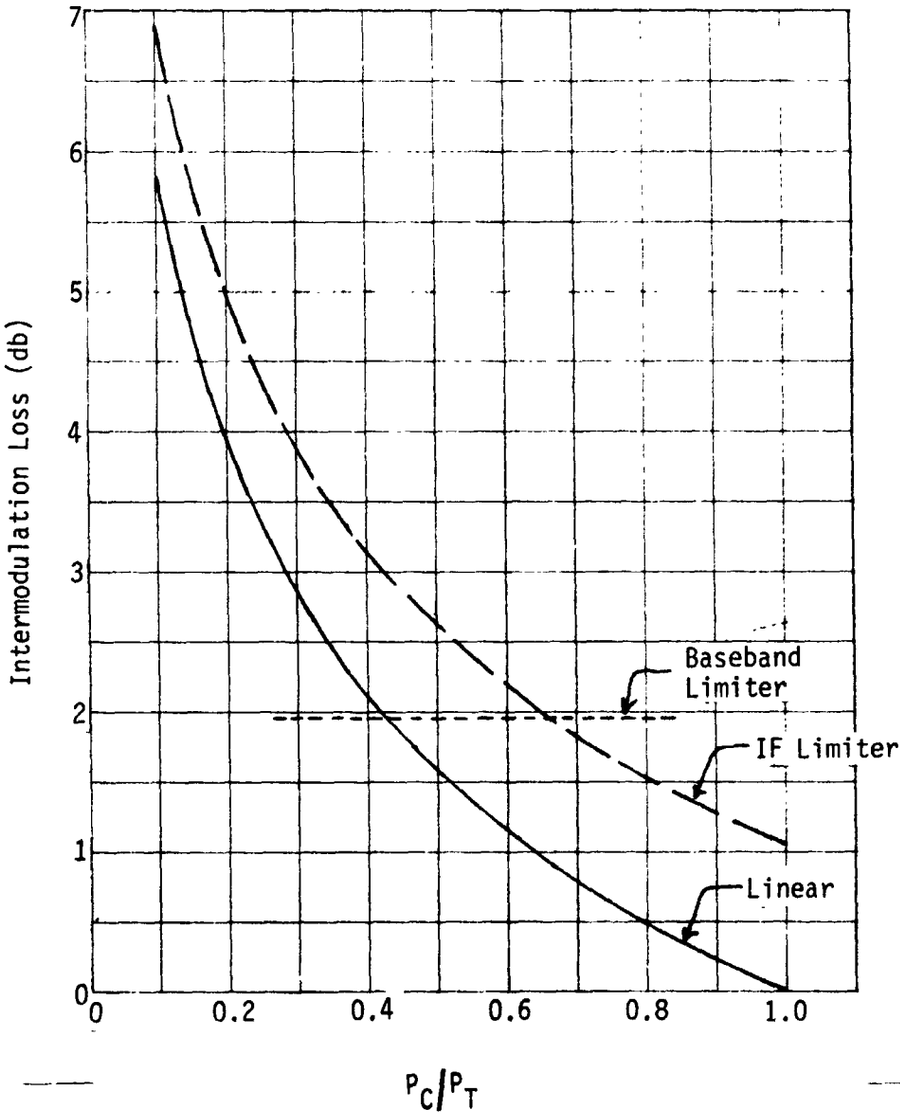


Fig. VII-20 Intermodulation Loss, Weak Signals in Gaussian Noise

in the linear case. Therefore for $\frac{P_C}{P_T}$ giving an intermodulation loss in the linear case greater than 1.96 db, baseband limiting would be preferred. From Fig. VII-20, this occurs for downlink $P_C/P_T < 0.43$. If we compare baseband limiting with IF limiting, the former would be preferred for $P_C/P_T < 0.66$. Since some kind of limiting would generally be used, and since P_C/P_T will generally be less than 0.66, this implies that baseband limiting would generally be preferred.

These results should be valid for $\frac{S_M}{N_M}$ less than -10 db. For higher SNRs, losses will be less. Let us consider an example at $\frac{S_M}{N_M} = 1.0$. Consider first the linear case. At this SNR we can no longer use the central limit theorem assumption giving Eq [31] and [32], and neither Eq [28] nor [29] are accurate for filtered waveforms. All of them will give the same results for weak signals, where results are determined by signal power and are independent of signal waveforms.

Results given by Eq [28] and [29] do not differ greatly at SNRs up to 0 db. The exact results depend on the statistics of the filtered waveforms, which are difficult to determine. A reasonably good approximation can be constructed as follows. Assume that the waveform is similar to that sketched in Fig. VII-21, having flat tops and sinusoidal-shaped transitions, with the duty cycle of the transition regions adjusted to account for the energy lost in the filtering. This will have the same RMS value as the actual waveform (and thus will give a correct result for weak signals), and should be sufficiently close to the actual waveform in statistics to give a reasonably good approximation for stronger signals. Decreasing SNR would improve the approximation. Thus, for example, F = 0.7 MHz gives a filter loss of 0.878. A duty

cycle of 24.4% sinewave and 75.6% square wave would give a mean-square value of 1 x 0.756 + ½ x 0.244 = 0.878 as desired. $\frac{P_S}{P_T}$ would then be the duty-cycle weighted average of the results given by Eq [28] and [29].

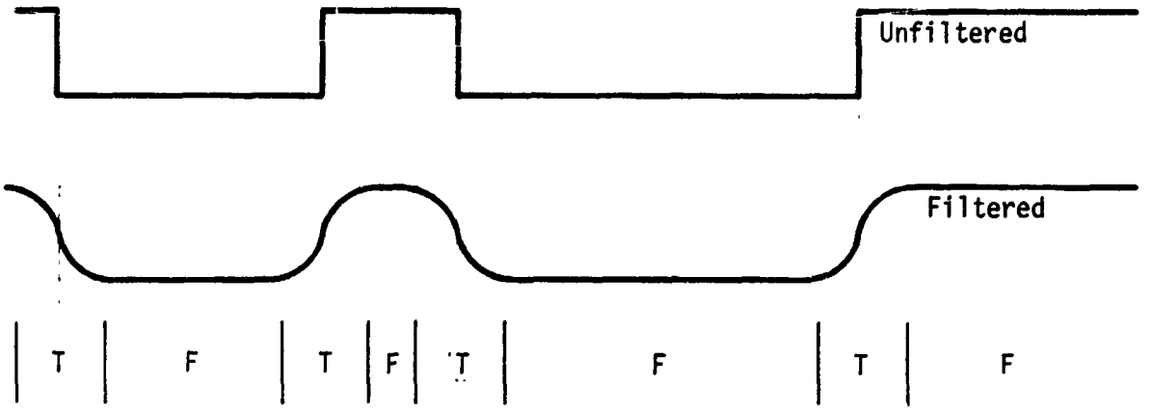


Fig. VII-21 Filtered and Unfiltered Waveforms

Using this approach, and setting $\frac{S_M}{N_M} = 1$, F = 0.7 MHz, a plot of intermodulation loss vs $\frac{P_C}{P_T}$ is shown in Fig. VII-22. Losses with an IF limiter are also shown on Fig. VII-22. Since SNR on the much wider IF bandwidth will be low even for a modulator SNR of 1, the weak signal limiter loss of 1.05 db is used.

Values for the other losses are the same as given above. Note that Eq [28] and [29] will not directly give results with inputs in the form of $\frac{S_M}{N_M}$ and $\frac{P_C}{P_T}$. An iterative solution is necessary. This was programed into the computations giving the curve of Fig. VII-22.

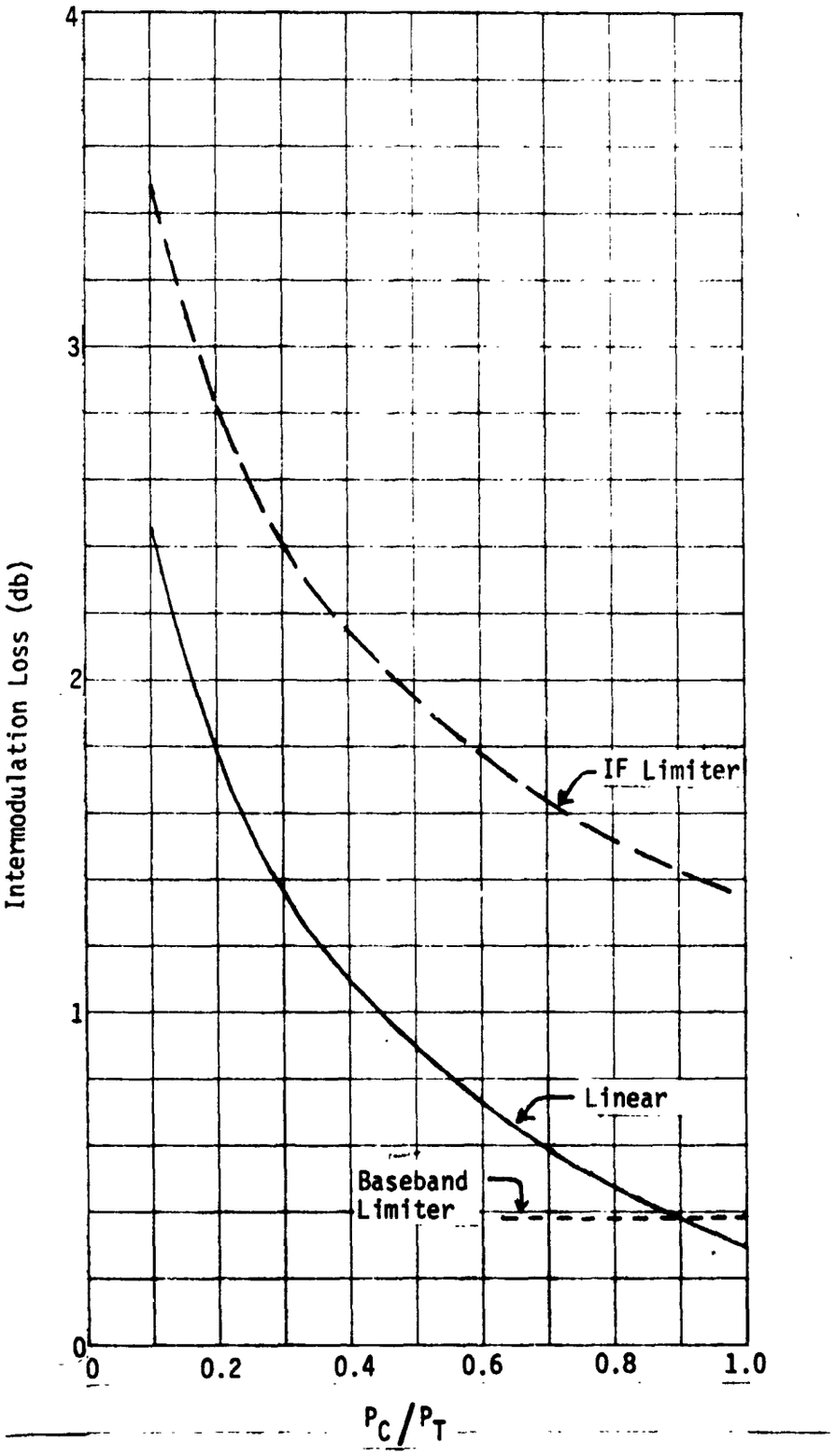


Fig. VII-22 Intermodulation Loss, SNR = 1.0

In the baseband limiter case, the limiter loss decreases for stronger SNR, as shown in Fig VII-23 (Ref VII-17). This limiter loss curve is nonlinear, decreasing rapidly in the vicinity of unity SNR. The result of this nonlinearity is that for a given SNR the loss corresponding to a square-transition waveform is always worse than that corresponding to a filtered waveform with finite rise times. Therefore, we will use this loss as a conservative bound on the actual loss.

At unity SNR the limiter loss is 0.7 db = 0.85. However, in the case of nonweak signals the effect of limiter loss is not exactly the same as that of intermodulation loss. For the linear case we have:

$$\frac{P_S}{P_T} = \left(1 - \frac{P_C}{P_T}\right)\frac{S_M}{S_M + N_M} \cdot L_{IM} \qquad [34a]$$

$$\simeq \left(1 - \frac{P_C}{P_T}\right)\frac{S_M}{N_M} \cdot L_{IM} \qquad \text{(weak signal)} \qquad [34b]$$

$$\simeq \left(1 - \frac{P_C}{P_T}\right) \cdot L_{IM} \qquad \text{(very strong signals)} \qquad [34c]$$

For baseband limiting we have:

$$\frac{P_S}{P_T} = \left(1 - \frac{P_C}{P_T}\right)\frac{S_M L_L}{S_M L_L + N_M} \qquad [35a]$$

$$\simeq \left(1 - \frac{P_C}{P_T}\right)\frac{S_M}{N_M} \cdot L_L \qquad \text{(weak signals)} \qquad [35b]$$

$$\simeq \left(1 - \frac{P_C}{P_T}\right) \qquad \text{(very strong signals)} \qquad [35c]$$

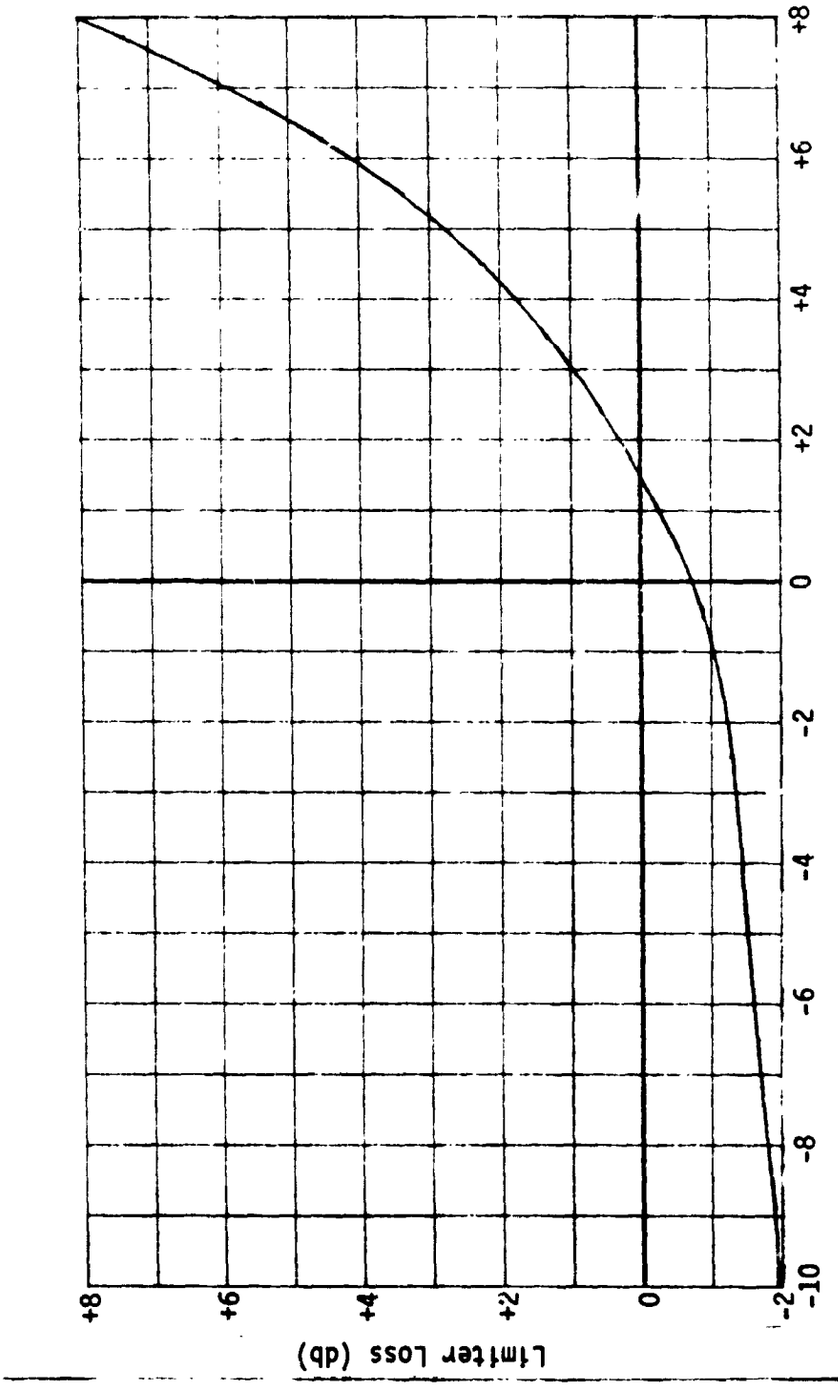


Fig. VII-23 Limiter Loss, Baseband Limiting

from Eq [34] and [35] we have

$$\frac{P_S \text{ (Baseband Limiter)}}{P_S \text{ (Linear)}} = \frac{L_L}{L_{IM}} \cdot \frac{S_M + N_M}{S_M L_L + N_M} \qquad [36a]$$

$$\simeq \frac{L_L}{L_{IM}} \qquad \text{(weak signals)} \qquad [36b]$$

$$\simeq \frac{1}{L_{IM}} \qquad \text{(very strong signals)} \qquad [36c]$$

It should be noted that for very strong signals and little filtering $L_{IM} \to 1$, so either system gives relaying without loss.

Substituting $\frac{S_M}{N_M} = 1$ into Eq [36a] gives

$$\frac{P_S \text{ (Baseband Limiter)}}{P_S \text{ (Linear)}} = \frac{0.918}{L_{IM}} = -0.38 \text{ db} - L_{IM} \text{ (db)}$$

This implies that baseband limiting would be preferred whenever $L_{IM} > 0.38$ db. Referring to Fig. VII-22, this occurs for $\frac{P_C}{P_T} < 0.9$ in the linear case, and for all $\frac{P_C}{P_T}$ in the IF limiter case. We can conclude that baseband limiting will be preferred for virtually all cases of interest.

Optimization of F for higher SNRs is also of interest. This was examined for baseband limiting. Plots of performance losses versus the transponder bandwidth F were made for numerous values of S/N_o, the ratio of unfiltered signal power received at the transponder to the transponder noise in a 1 MHz bandwidth. For $S/N_o < 7$ db these plots had a rather narrow minimum around F = 0.7 MHz. Above this S/N_o a broader second minimum appeared at a larger F, which became lower than the first minimum at $S/N_o = 8.3$ db. Therefore, the plot of best F versus S/N_o shown

in Fig. VII-24 has a discontinuity at this point. The region between these minima was not significantly higher than the minima. The dashed curves in Fig. VII-24 are upper and lower bounds on F giving performance within 0.1 db of the optimum F at the indicated S/N_o. Any F within this region will give performance virtually indistinguishable from the optimum. It is clear from this figure that the conventional choice of F = 1.5 MHz is satisfactory for $S/N_o > 7.5$ db but rather poor for $S/N_o < 6.5$ db, a more typical operating region for probes having low-gain antennas. For S/N_o greater than about 8 db and for F > 1.5 the limiter will regenerate the unfiltered binary waveform, so the receiver mismatch and correlator losses will vanish for these strong signals. For weaker signals the exact effect of the limiting is hard to assess. It is conservative to use the values in Fig. VII-19. These become more accurate as S/N_o decreases.

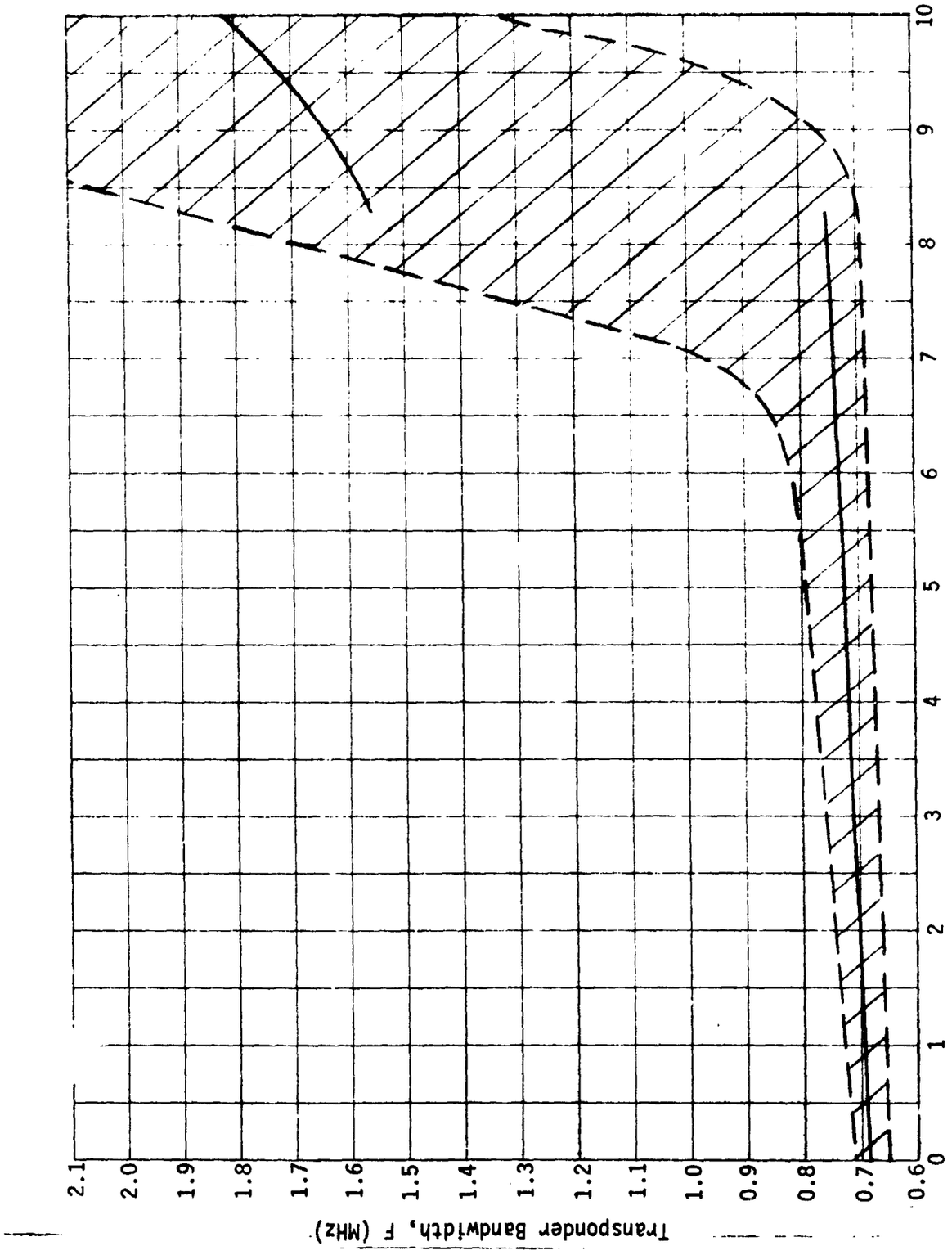


Fig. VII-24 Optimum Transponder Bandwidth

D. POSITION DETERMINATION, BALLOON PROBES

It is desired to get a position fix on the balloon probes each time a communication contact is made with them. Several possible approaches to making this position fix have been considered. Two will be described here.

1. Ranging - Polarization Fix

One coordinate of the desired fix can be gotten from a conventional two-way ranging measurement. Link calculations indicate an unacceptably long transmission period requirement to achieve lockon of a conventional 1 megabit/sec ranging code, so a 10 kb/sec code will be used. This will give a range measurement accurate to 1.5 km.

Range, in conjunction with altitude, gives the angular distance ϕ away from subearth, which fixes the probe on a circle about the subearth point. This circle is actually a belt whose width is determined by the uncertainties in the range and altitude measurements. Accuracy is considered later in this section.

The other coordinate of the fix will be derived from the balloon antenna polarization. A two-antenna system is proposed for the balloon. The antenna system radiation patterns are shown in Fig. VII-25. The cavity helix, which looks upward, is circularly polarized, and the annular slot, which looks out near the horizon, is vertically polarized. This two-antenna system is proposed primarily because it is simple and it gives good coverage over the whole hemisphere. Data transmission and ranging would be done over the antenna providing the most gain, determined by observing a signal transmitted from Earth. The cavity helix would be used out to 45° away from the subearth point and the annular slot would be used from there out to the limbs. The annular slot, which is vertically polarized, aligned by gravity with local vertical, can

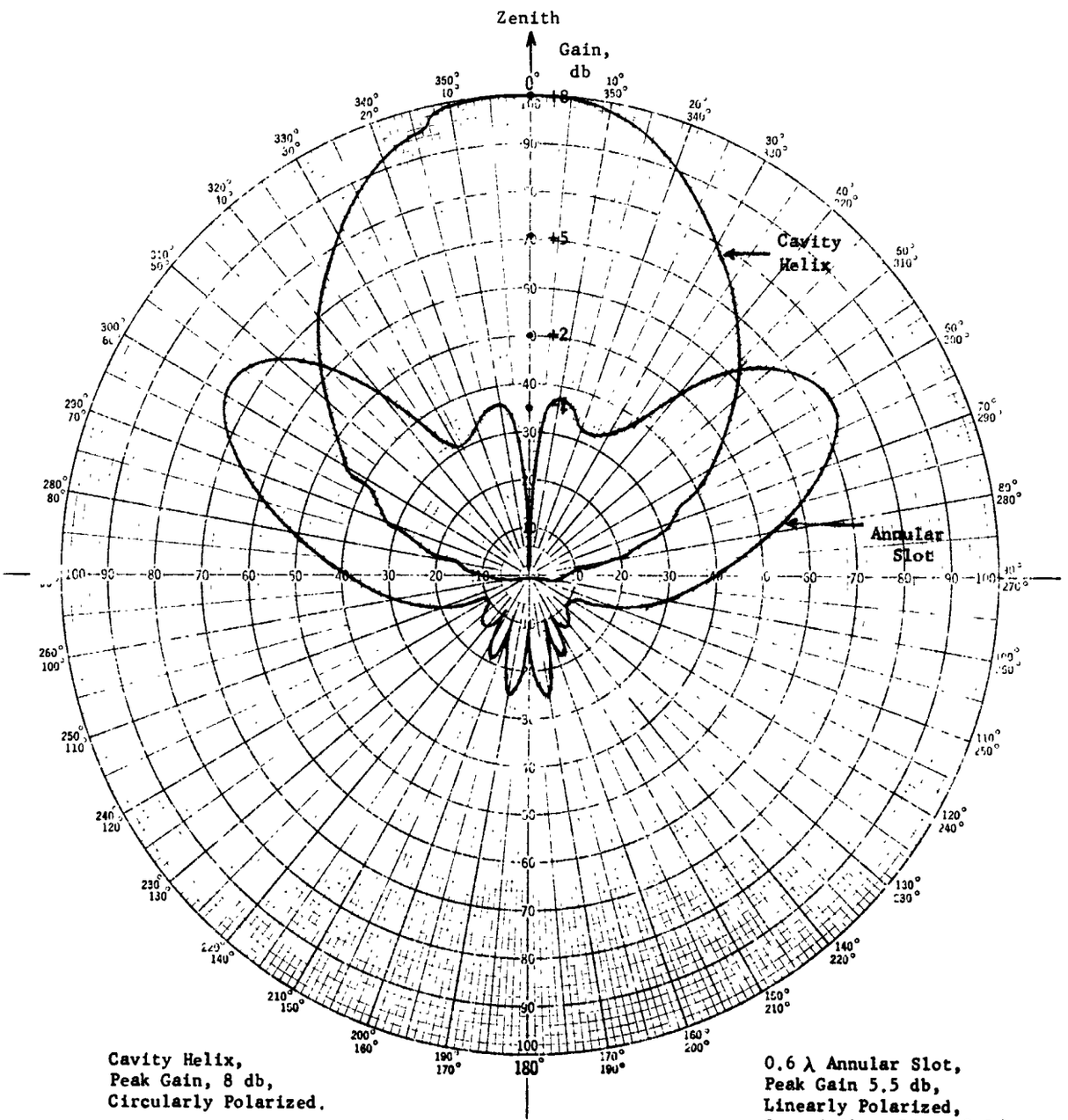


Fig. VII-25 Radiation Pattern, Balloon Antenna System

also be used to provide the remaining coordinate in the location fix. It would be used for this purpose, sending carrier only, after the data transmission was completed and regardless of which antenna was used for data transmission. Referring to Fig. VII-26, if this polarization is aligned with local vertical, the direction of the linear polarization, as observed on Earth, is that of a line passing through the subearth point and the probe. The point at which this line intersects the circle defined by the range measurement is the location of the probe. As shown in Fig. VII-27, there will be an ambiguous location on the opposite side of the circle. However, knowledge of the initial placement of the probe together with subsequent fixes should permit selection of the correct location under most circumstances. It would be desirable to observe and record the polarization direction for several minutes to average out any effects caused by a swinging motion of the gondola. The operating sequence now specifies a 2-minute duration for this measurement. The balloon-gondola combination has a well-damped oscillation period of 3.4 sec (500 mb balloon) and 5 sec (50 mb balloon), so 2 minutes should give more than adequate averaging unless a substantial steady-state wind shear is present, which is unlikely.

The gondola and antenna should be rotationally symmetric, however, there could be a very small rotational dependency in the polarization. This will also average out as the balloon rotates. The balloon is expected to rotate at about 1 rpm, based on observations on Earth. It can be designed so that its seams are shaped to favor one direction of rotation. If this is done, it is expected to rotate at a somewhat higher rate, perhaps 5 rpm. Either rate should be sufficient to average out most of the rotation-dependent errors, though the higher rate would be preferable.

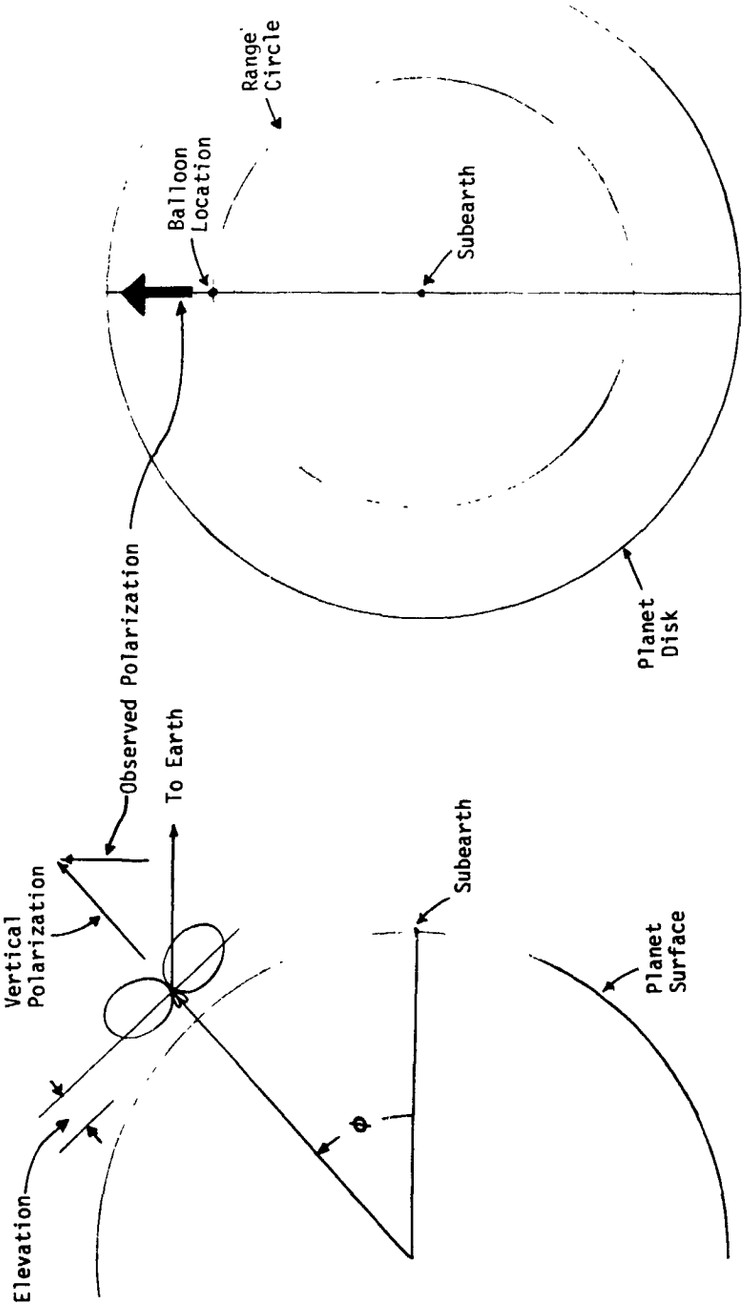


Fig. VII-26 Position Determination by Ranging and Polarization

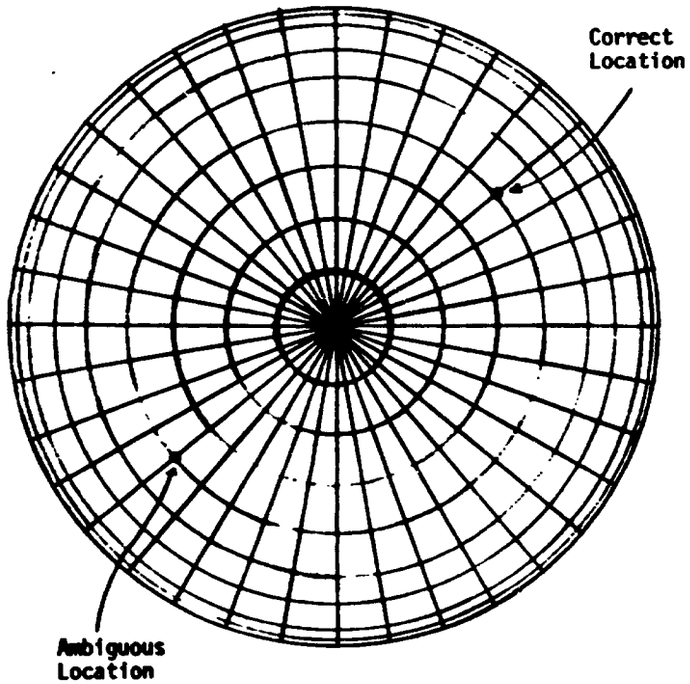


Fig. VII-27 Range-Polarization Coordinates Centered on the Subearth Point

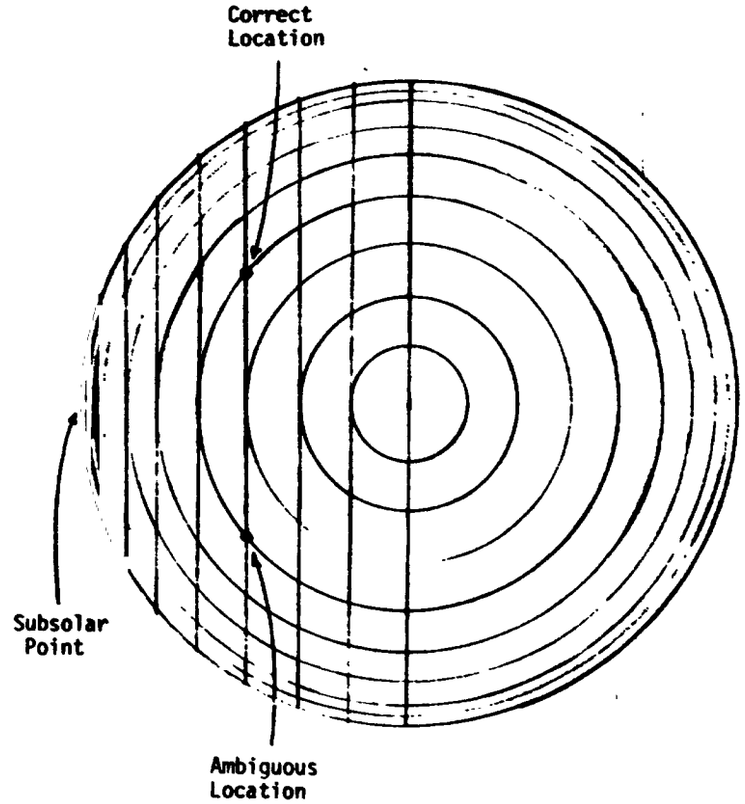


Fig. VII-28 Range-Sun Zenith Angle Coordinates

The coordinate set furnished by the polarization, radial lines emanating from the subearth point, has the desirable feature that it is orthogonal to the set furnished by the ranging, thus giving a more precise fix. The range circle-sun angle sets shown in Fig. VII-28, for example, has a region near the equator where the two sets are almost parallel to each other for substantial distances.

The annular slot radiation pattern shown in Fig. VII-25 is that measured using an 0.6 λ diameter annulus, flush-mounted on a 3.8 λ diameter (20 in.) circular ground plane. This was selected to minimize the width of the null at zenith. As shown, it is 10° wide at the -2 db gain points. The antenna actually used on the balloon probe may not be this good, and might go to 20° width at the -2 db gain points.

This is important because, for balloon locations very near to the subearth point, the antenna gain in this null region might not be great enough to provide a usable signal for polarization determination at the ground station. It has been calculated that for our assumed balloon transmitter (8 watts), carrier lock can be reliably maintained down to a probe antenna gain of -2 db if carrier only is transmitted.

One of the available DSIF feed cones is linearly polarized and capable of being mechanically tracked with a polarization-tracking servo. Tracking rate capability should be adequate to permit tracking of the gondola swings due to wind turbulence, allowing the averaging necessary to minimize errors due to this source.

If the polarization experiment is carried out close to the subearth point (zenith angle $\phi < 10°$) the signal will be weak because of the null in the antenna pattern at $\phi = 0$. Weak-signal techniques could be used. This would require a dual-polarization feed, two low-noise (maser) front ends, two receiver channels, and two-channel predetection recording, with subsequent processing of the recordings to recover the desired information. A similar setup has been made before at the DSN on an experimental basis, but it is not and will not be a part of the routine capability of the DSN. If this were used, measurements could be made into perhaps 2.5° from subearth with usable data. Without it, the limit would be around 10°. This latter value would leave a circle about 2000 km in diameter around the subearth point where one coordinate of the fix would be unreliable or nonexistent. The balloon's initial placement will be outside this circle, and it may never enter it. If it did, and particularly if it later emerged from it, a reasonably reliable guess at its path could be inferred from a projection based on the ranging coordinate (whose accuracy would be unimpaired) together with the history of its path outside this circle. Also, crossing of the terminator, which is within this circle, would be detected by the balloon solar radiometer. This event, together with the ranging, will give a position fix inside this circle. Accordingly, if the weak-signal mode is not available, the mission will not be seriously affected.

Position errors arise from a number of sources. The ϕ coordinate will have errors due to the ranging measurement uncertainty and the altitude measurement uncertainty. The former is 1.5 km in earth-directed distance. It is planned to use pressure as a measure of altitude. A pressure verus altitude calibration will

have been made earlier by a ballistic probe. However, the uncertainty in the relationship between local altitude at the ballistic probe impact point and radius will be (conservatively) on the order of 10 km. Using these values, uncertainty in location on the planet due to the range uncertainty is 1.5 csc ϕ km and that due to radius uncertainty is 10 cot ϕ km. Clearly, except for ϕ very near 90°, the radius uncertainty will dominate. Over virtually all the planet ($\phi > 6°$) this error will be less than 100 km.

Figure VII-25 shows that the ratio of the power received from the two antennas can also be used to infer ϕ. This is inherently a much less precise measurement than the ranging measurement, but it is independent of the altitude uncertainty. This offers a method to reduce the altitude uncertainty. Recursive filtering techniques could be used to evaluate the correlation between the ϕ's determined by the two methods over the whole mission, and select an altitude-pressure relationship that maximizes this correlation. However, it is estimated that a fairly long mission, on the order of 100 to 300 observations (33 to 100 days), would be required to give a significant improvement in the altitude uncertainty by this method. The 10 cot ϕ + 1.5 csc ϕ formulation for this component of the error breaks down for very small ϕ ($\phi < 3°$) because of curvature of the planet surface. The error reaches a maximum at $\phi = 0$ where it equals (nominal float radius assumed to be 6120 km) $(2 \times 6120 \times 11.5)^{\frac{1}{2}} = 375$ km. This component of the error is plotted vs ϕ in Fig. VII-29.

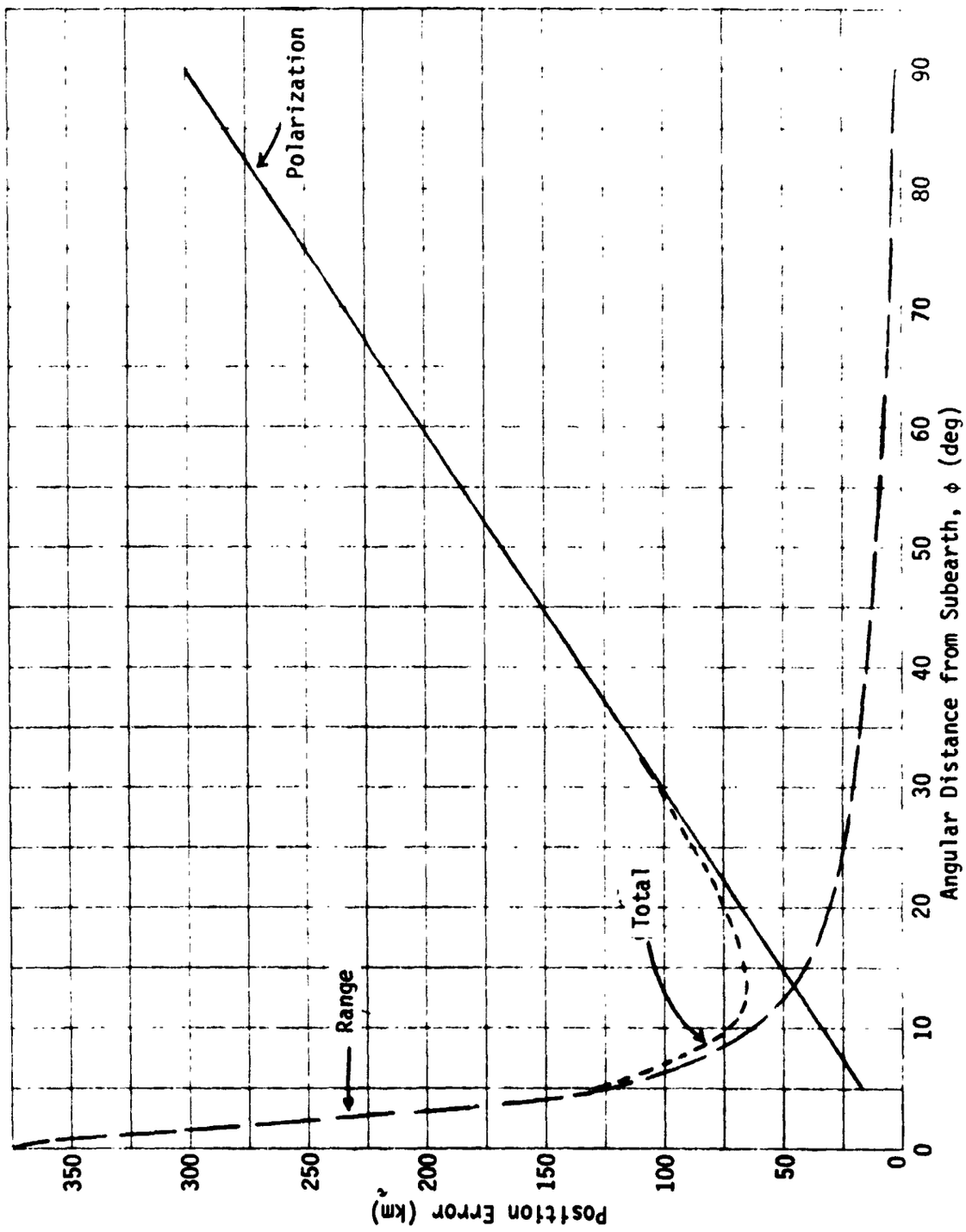


Fig. VII-29 Position Error, Range-Polarization Fix

Errors in the polarization measurement include those due to:

1) Imperfect averaging of gondola swings from wind turbulence;
2) Imperfect averaging of rotational dependencies in the radiation pattern;
3) Tracking servo readout and calibration;
4) Noisy signals;
5) Faraday rotation;
6) Steady-state wind shears.

As noted earlier, the 2-minute averaging time should reduce 1) and 2) above to negligible levels, a small fraction of a degree. The DSIF polarization-tracking head is specified to have a readout precision of 1°. The readout error would also be reduced to a negligible value by averaging over the 2-minute experiment period. Readout is provided in a manner similar to the rest of the antenna tracking data, on tape. A moderately strong signal, sufficient for carrier lock, is required. Some degradation will occur close to the subearth point, just outside the point at which lock cannot be maintained at all. Again, averaging should reduce this to a small fraction of a degree providing loop lock is maintained.

Polarization can be altered during signal propagation by Faraday rotation. Because Venus has no significant magnetic field, it is nonexistent in the Venusian ionosphere.

Rotation in the Earth's ionosphere at the 2.3 GHz DSN frequency is not negligible. Under normal conditions it may be as high as 2.5° at night to 10° at midday (Ref VII-18). However, the error introduced by this effect is not the magnitude of the rotation, but the uncertainty in this magnitude. Modern ionospheric sounding techniques permit the construction of accurate ionization profiles (Ref VII-19). Since the rotation does not depend significantly on the details of the profile, but only on the total

integrated ionization (which would be determined with greater accuracy than the details) the expected rotation should be predictable within a small fraction of a degree, providing full use is made of available ionospheric sounding data.

Rotation in interplanetary space must also be considered. There will be some ionization along this path due to the solar plasma. The total integrated ionization along a path similar to the Earth-Venus path has been estimated by Brenran to be commensurate with that along a zenith path through the Earth's ionosphere (Ref VII-20). However, since the magnetic field in this region is orders of magnitude weaker than that in the Earth's ionosphere, the total rotation would be much less than that occurring in the Earth's ionosphere, less than 0.1°.

It can be concluded that error sources 1) thru 5) are quite small, probably not exceeding 1° total. Error source 6), steady-state (i.e., longer than 2-minute duration) wind shear, is difficult to estimate. Our balloon design mounts the gondola immediately below the balloon, which minimizes this source of error. One way to eliminate this error would be by the use of a two-axis "departure from vertical" instrument inside the gondola. Correlation of the variations in attitude observed by this instrument with polarization angle variations observed on Earth would give sufficient data to determine the average wind shear error in the polarization record.

This instrument is not included in our balloon design, but it could be added if the problem were considered sufficiently serious.

We estimate, somewhat arbitrarily, that the total uncertainty will not exceed 3°. No detailed analysis of expected wind shears has been made. This error is equivalent to a location uncertainty of about 300 km at the limbs, decreasing linearly with ϕ to zero as the subearth point is approached. This component dominates the

total error except near the subearth point. If a careful analysis of expected wind shears indicates that this is optimistic, a departure from vertical sensor would be recommended.

Error due to this source is shown vs ϕ in Fig. VII-29. This is not plotted for $\phi < 5°$, since it is assumed that no polarization fix is possible in this region because of the null in the annular slot antenna pattern. The RMS sum of the errors in the two coordinate sets gives the total error. This is also plotted in Fig. VII-29.

The ranging-polarization fix is our baseline approach to the problem, primarily because it can be done without the addition of any special instruments to the probe.

2. Ranging - Microwave Radiometer Fix

This has little advantage over the ranging-polarization fix, though it would be better for locations very close to the subearth point. It might be considered if there were some other (scientific) justification for the radiometer, or for use on a planet with a strong magnetic field.

The ranging fix would be the same as described above. The second coordinate would be derived in some cases from the sun-zenith angle. This gives the coordinate set shown in Fig. VII-28.

A microwave radiometer is suggested rather than a visual light radiometer for two reasons. First, it would not be affected by a cloud cover, and second, it can be used to find an alternative target, the galatic center, when the probe is on the dark side of the planet. This will give a coordinate set similar to that in Fig. VII-28. There are conditions under which neither the Sun nor the galatic center are visible, but the ability to sense either one gives a substantial increase in the effective coverage of the system.

Although the Sun is much hotter than the galatic center, the temperatures seen by a moderately directive antenna are commensurate at the lower microwave frequencies because the galaxy is a distributed source. A radiometer sees the temperature averaged over its antenna beam, and the average of the Sun (which occupies a 0.7° sector viewed from Venus) and the surrounding cool sky may not be much hotter than the average over the sector of the galaxy seen by the radiometer antenna beam. Figure VII-30 shows the temperature of the Sun and the galactic center as seen from Venus using a 20° beamwidth antenna, plotted versus frequency. It is practical to detect temperatures as low as 5°K with a reasonably simple radiometer, assuming an integration time of around 5 sec. A frequency around 1.5 GHz could be used. THis would require an aperture about 3 ft in diameter, either electronically or mechanically steered, so the device would not be a trivial add-on. Resolution would probably not be better than about ±10°. If it were desired just to detect the Sun and not the galactic center, the antenna could be smaller and/or the resolution better, but operation would be limited to the light side of the planet.

In summary, although this approach has not been exhaustively studied, it appears that the size and complexity of the device, coupled with its poor resolution, makes it less attractive than the ranging-polarization approach.

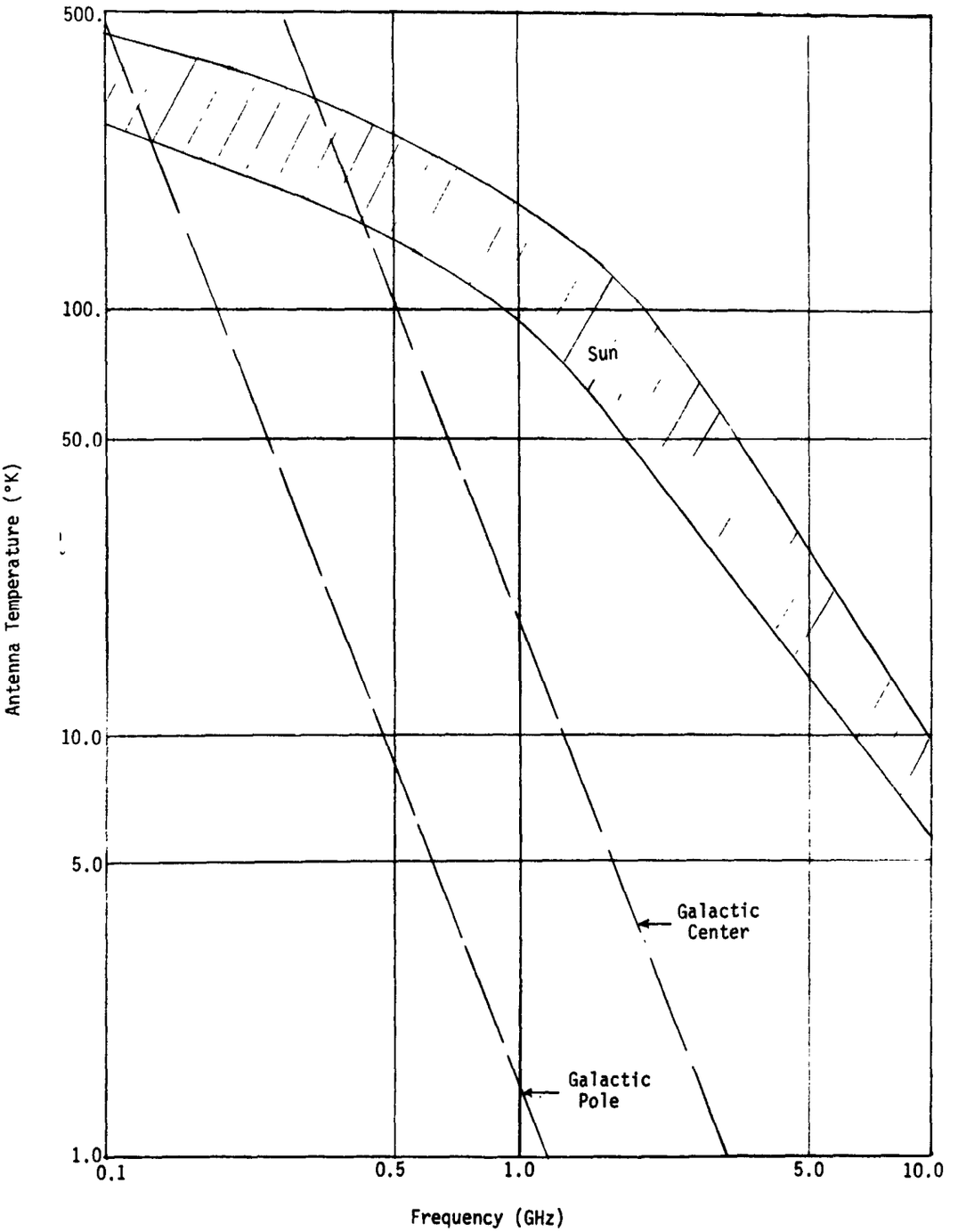


Fig. VII-30 Antenna Temperature, Sun and Galaxy, as Seen from Venus, 20° Beamwidth

E. PROBE ANTENNA SELECTION

Possible target sites considered in this program range from near the limbs to near the subearth point, and the balloon probes must be capable of operating over the whole visible hemisphere. A communications mask angle of 70° is imposed on the descent probes because of atmospheric effects, but this is relaxed to approach 90° if desired for the balloon and high cloud probes that do not enter the lower atmosphere.

The ideal antenna for near-limb probes would have a conical pattern looking near the horizon, with a null in the zenith direction, and with peak gain in the direction toward Earth. For entry angles of 70° from subearth, for example, this peak should ideally be at 70° from zenith in the upper atmosphere, decreasing to about 65° at the surface due to ray-bending effects in the atmosphere. The surface conditions are more severe because of atmospheric losses, so the latter angle should be used as a basis for the antenna design.

Relatively low-gain antennas (5 to 8 db) are selected for two reasons. First, they are smaller and lighter than higher-gain antennas, and second, their wider beamwidth allows more tolerance for targeting errors and probe attitude perturbations due to wind gusts.

Our selected antenna type for limb probes is an annular slot, flush-mounted on the top surface of the probes, as sketched in Fig. VII-31. With the possible expection of a monopole, this is the simplest antenna giving the desired near-horizontal conical pattern. It is selected in preference to a monopole primarily because it is flush-mounted.

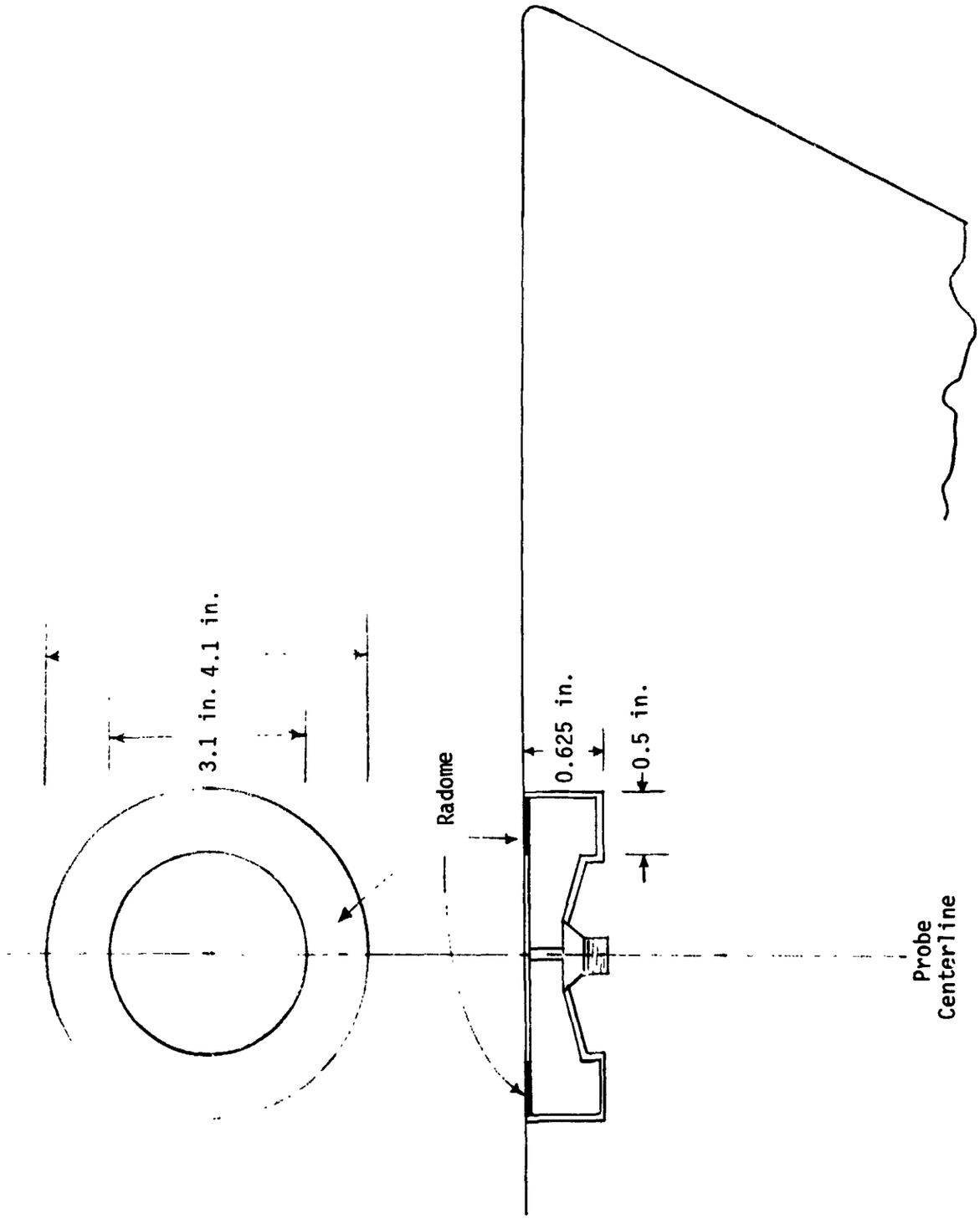


Fig. VII-31 0.6λ Annular Slot Antenna

Both the annular slot and the monopole give vertically-polarized radiation. This is contrary to the usual practice of using circularly polarized antennas on deep-space probes. This has several consequences, listed blow:

1) As discussed in Section B of this chapter, vertical polarization gives a marked advantage in reducing multipath signal strength for near-limb probes. This advantage decreases as the look angle is moved away from horizontal toward zenith, becoming negligible above about 45°.
2) As discussed in Section D of this chapter, the vertical polarization provides vital position fixing information for the balloon probes. This could also be used to refine the position fix of the other probes, though we hve not indicated this as a requirement.
3) Circular polarization is difficult to achieve in a near-horizontal conical pattern, and cannot be achieved at all with a flush-mounted antenna on the top of the probe because of the null induced in the horizontally polarized component by the top ground plane. An aperture of some vertical extent, either raised above the probe top or in a belt (which would have to be continuous to avoid lobing problems) around the probe body, is required. One possible antenna, the four-arm equiangular spiral on a cone, is sketched in Fig. VII-32. Height is that required for the large probe. This is clearly undesirable because of its height above the probe top surface, but any other antenna giving a pattern with good circularity near the horizon would be equally undesirable. For look angles some distance above the horizon, 45° or more, the problem is not so severe. This will be considered later.

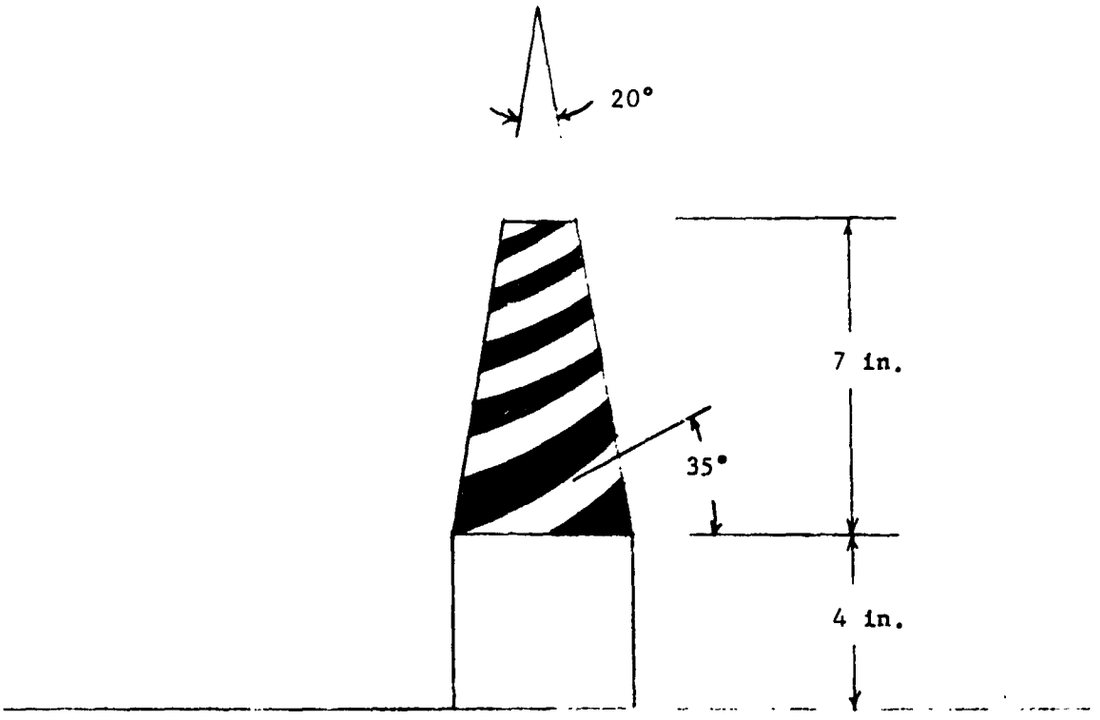


Fig. VII-32 Four-Arm Equiangle Spiral on a Cone Antenna

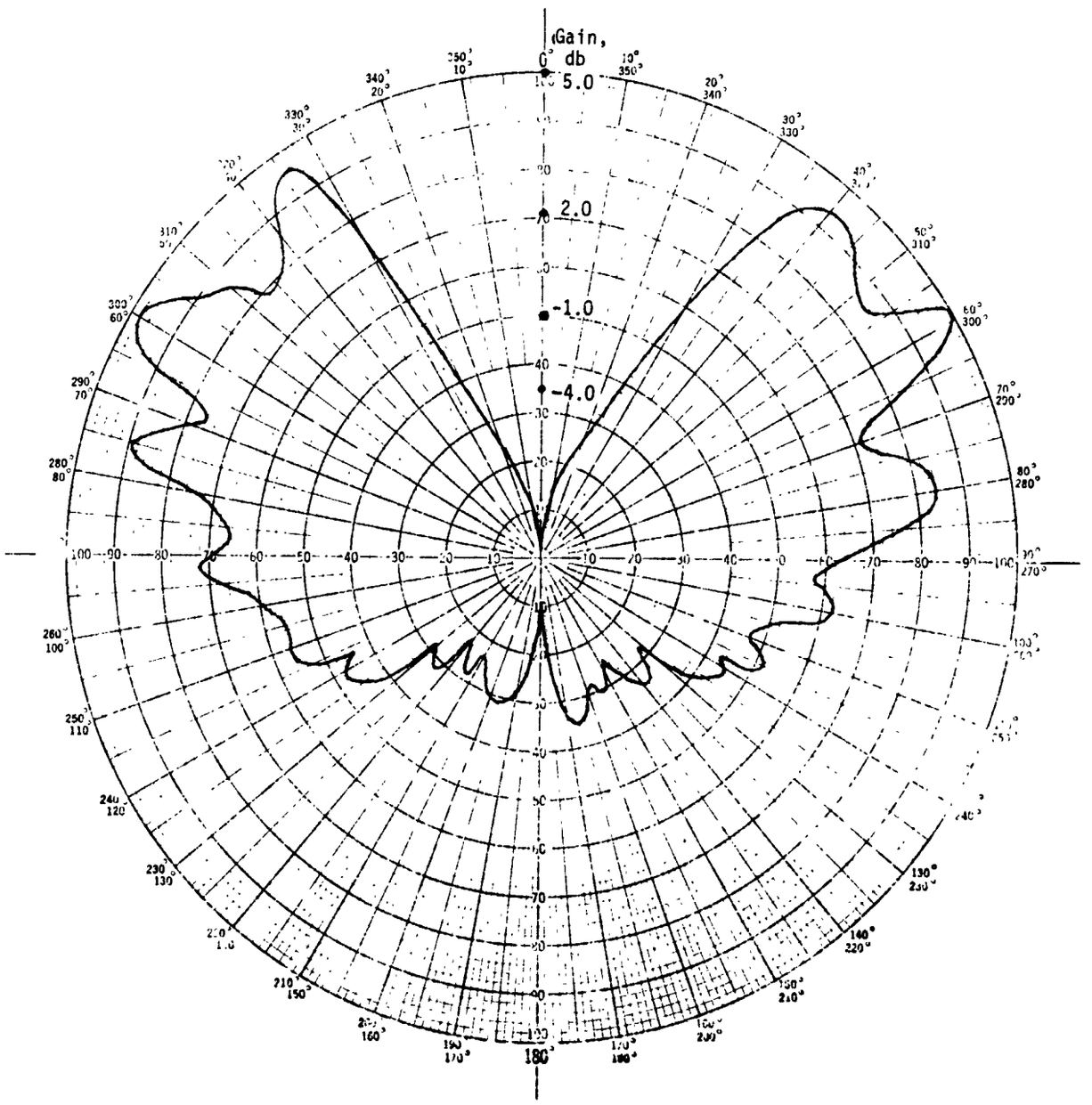
4) As discussed in the DSN capabilities document (Ref VII-21), the DSN antennas can be configured to receive vertical polarization with no more polarization loss than that normally suffered using circular polarization. However, it cannot simultaneously receive linear and circular or linear in two different directions without polarization losses. This has some awkward consequences for a multiprobe mission, because the polarization observed on Earth from a vertically polarized antenna, aligned with probe local vertical, is a function of target location. Therefore, unless the probes are targeted to the same point they cannot be received simultaneously without significant losses. We are proposing to solve this problem by staggering the probe entry times so that overlaps can be avoided or confined to probes going to the same targets. Changeover of the DSN antennas from one polarization to another can be done rapidly (~10 min) by switching between feed cones.

It is concluded that vertical polarization is preferred for near-horizon look angles, with circular polarization preferred for near-zenith look angles. The zenith angle at which the recommended polarization is changed from one type to the other is around 40° to 45°.

The radiation pattern of an annular slot on a finite circular ground plane is of course influenced by the size of the ground plane. Figure VII-33 shows this effect for a 0.6 λ diameter annular slot. The principal effect is on the beamwidth, with little change in the direction of the beam maximum, which stays around $\phi = 65°$. The 5 λ ground plane corresponds approximately to the size of the small and high-cloud probes, and the 8 λ pattern corresponds approximately to the large probe. The 3.85 λ ground plane pattern is of particular interest because of the narrowness of its zenith null. This is important for the balloon probe because it permits the polarization experiment described in Section D of this chapter to be carried out even though the balloon is quite close to the subearth point. While this does not exactly match the size of the balloon probe as presently configured, it is expected that adjustments in probe size and shape and annular slot diameter through model studies can be made to give a pattern with a null in the zenith region about as narrow as that shown in the 3.85 λ ground plane pattern.

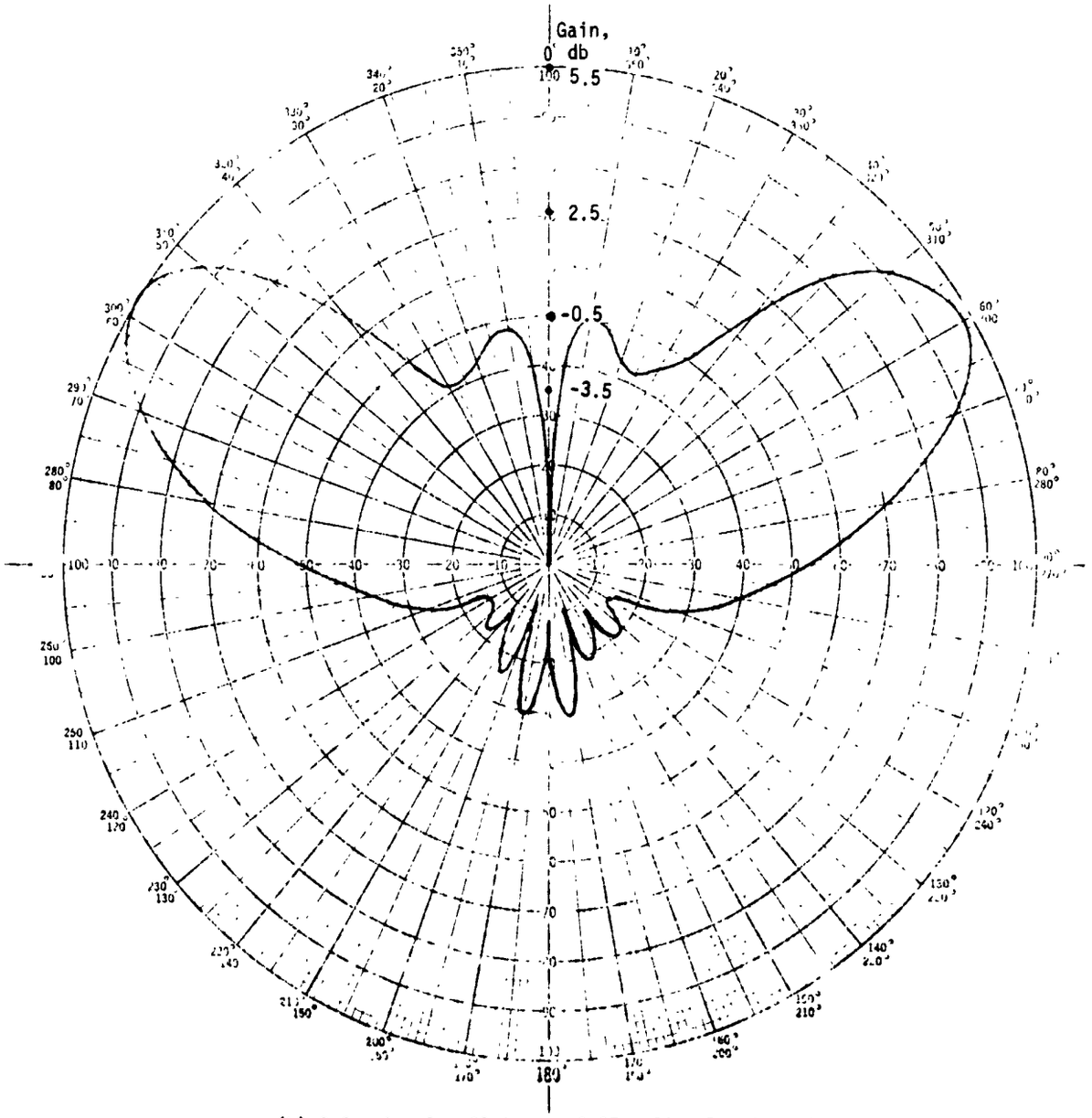
Reducing the diameter of an annular slot below about 0.6 λ is analogous to reducing a monopole length below 0.25 λ; it has little effect on the pattern, but simply makes an impedance match more difficult to achieve. Therefore, for entry angles greater than 70°, some other antenna type might be recommended. However, since none of our entries are beyond 70°, this has not been given further consideration.

Increasing the annular slot diameter moves the pattern peak upward toward zenith, and also makes it less affected by ground plane size. For any zenith angle between 40° and 70°, a slot diameter can be selected to give a beam maximum at the desired angle. Figure VII-34 shows a pattern for a 1.2 λ diameter slot, which has a peak gain at $\phi = 40°$, and a null at the horizon, $\phi = 90°$.



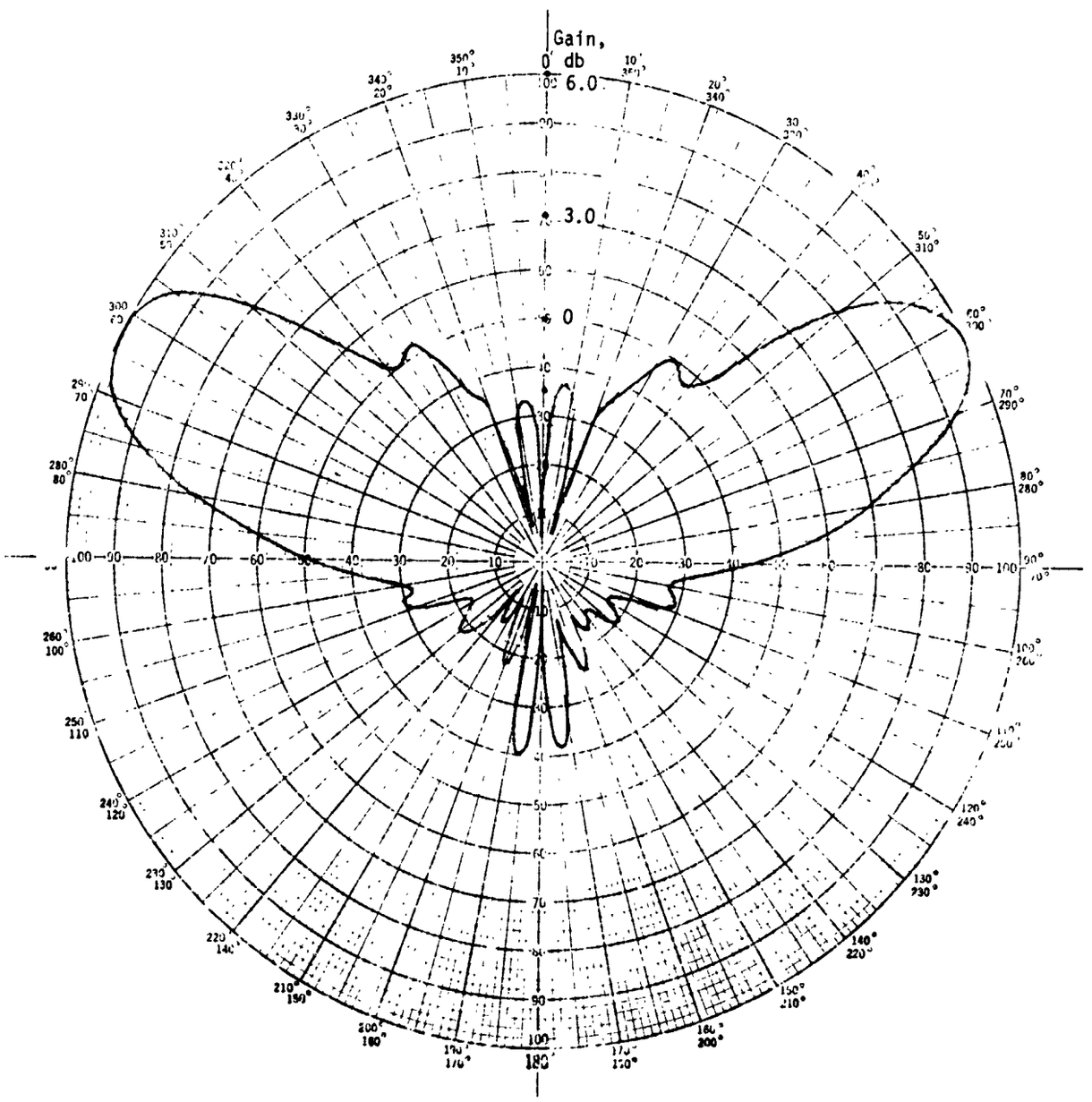
(a) 0.6 λ Annular Slot on a 0.94 λ Circular Ground Plane; Peak Gain, 5.0 db

Fig. VII-33 Radiation Pattern



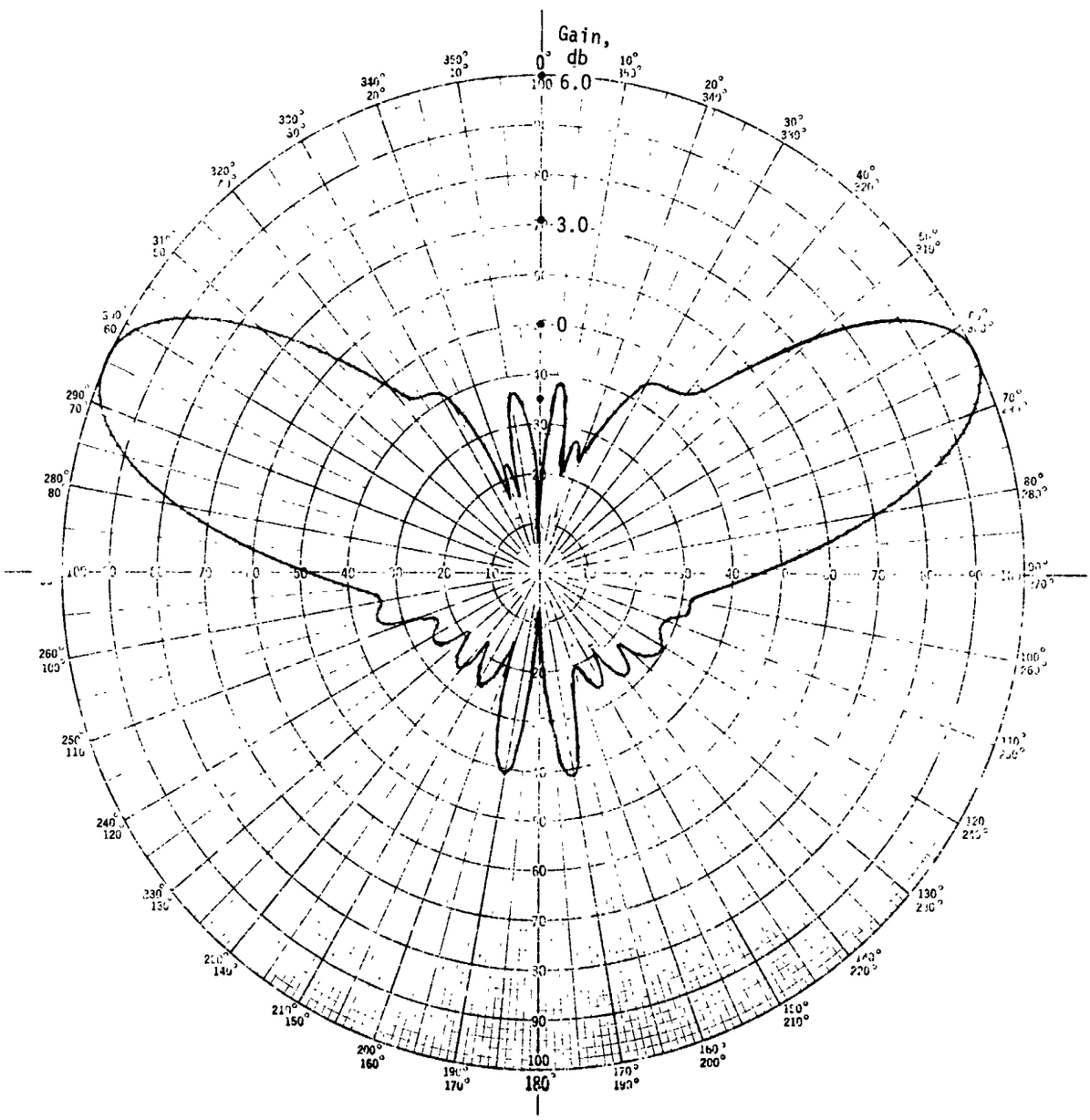
(b) 0.6 λ Annular Slot on a 3.85 λ Circular Ground Plan; Peak Gain, 5.5 db

Fig. VII-33 (cont)



(c) 0.6 λ Annular Slot on a 5.0 λ Circular Ground Plane; Peak Gain, 6.0 db

Fig. VII-33 (cont)



(d) 0.6 λ Annular Slot on a 8.0 λ Circular Ground Plane; Peak Gain, 6.0 db

Fig. VII-33 (concl)

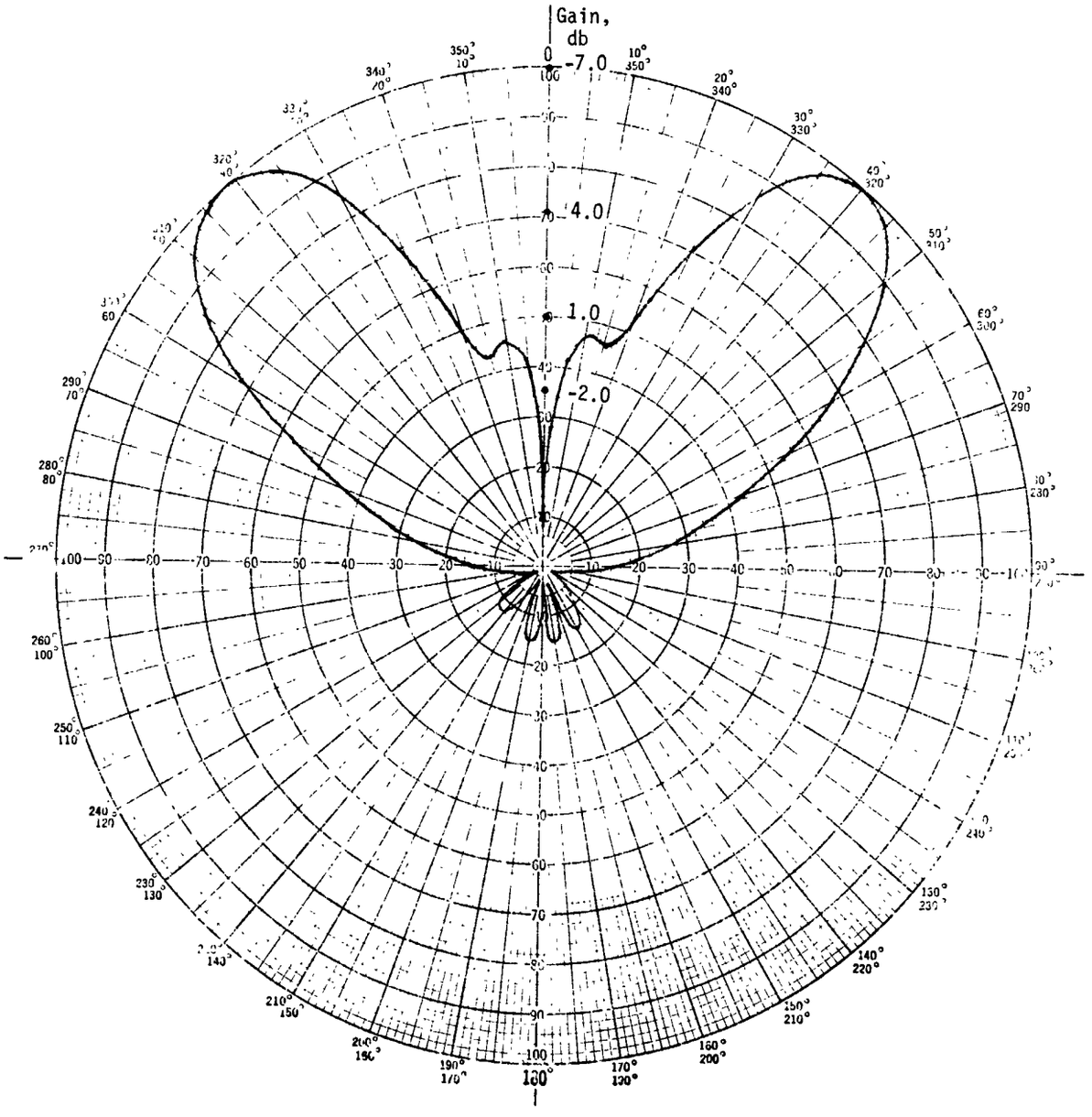


Fig. VII-34 Radiation Pattern, 1.2 λ Annular Slot on an 8.0 Circular Ground Plane; Peak Gain, 7.0 db

Increasing the slot diameter above 1.2 λ would move the beam further upward toward zenith, but a second lobe would begin to appear on the horizon, an undesirable feature. Also, most of the advantages of linear polarization vanish for $\phi < 40°$. Simple circularly polarized antennas are available, and the multipath problem is much reduced by antenna directivity.

One possible antenna for this region is the four-arm cavity-backed planar spiral. Fed in the difference mode it give a circularly polarized conical beam pattern with a maximum around $\phi = 40°$. A pattern is shown in Fig. VII-35. Cavity-backed spirals have rather low efficiency, 60% being a typical value. A more efficient antenna can be constructed from a ring array of linearly polarized elements. Such an array, fed in the proper phase rotation will give a circularly polarized conical beam. The array sketched in Fig. VII-36 will give a pattern similar to that shown for the 1.2 λ annular slot, except that it will be circularly polarized. Increasing element gain and ring diameter will give a pattern having a higher gain and a smaller cone angle. For example, a ring of six 0.5 λ Yagis, on a 1.7 λ circle will give a conical pattern without sidelobes having a beam maximum near 30° and a gain of about 8 db. This antenna is somewhat larger than desired, and decreasing the cone angle further would further increase antenna size and weight.

For ϕ smaller than about 30°, a conical pattern becomes less desirable and practical than an axial lobe pattern. There are many circularly polarized antennas that will give a pattern of this type. Perhaps the simplest is a crossed slot, which gives a gain of about 5 db. We are recommending a short helix in a cavity for somewhat higher gain. The antenna sketched in Fig. VII-39 has a gain of 8 db. Its radiation pattern, shown in Fig. VII-37, is virtually independent of ground plane size.

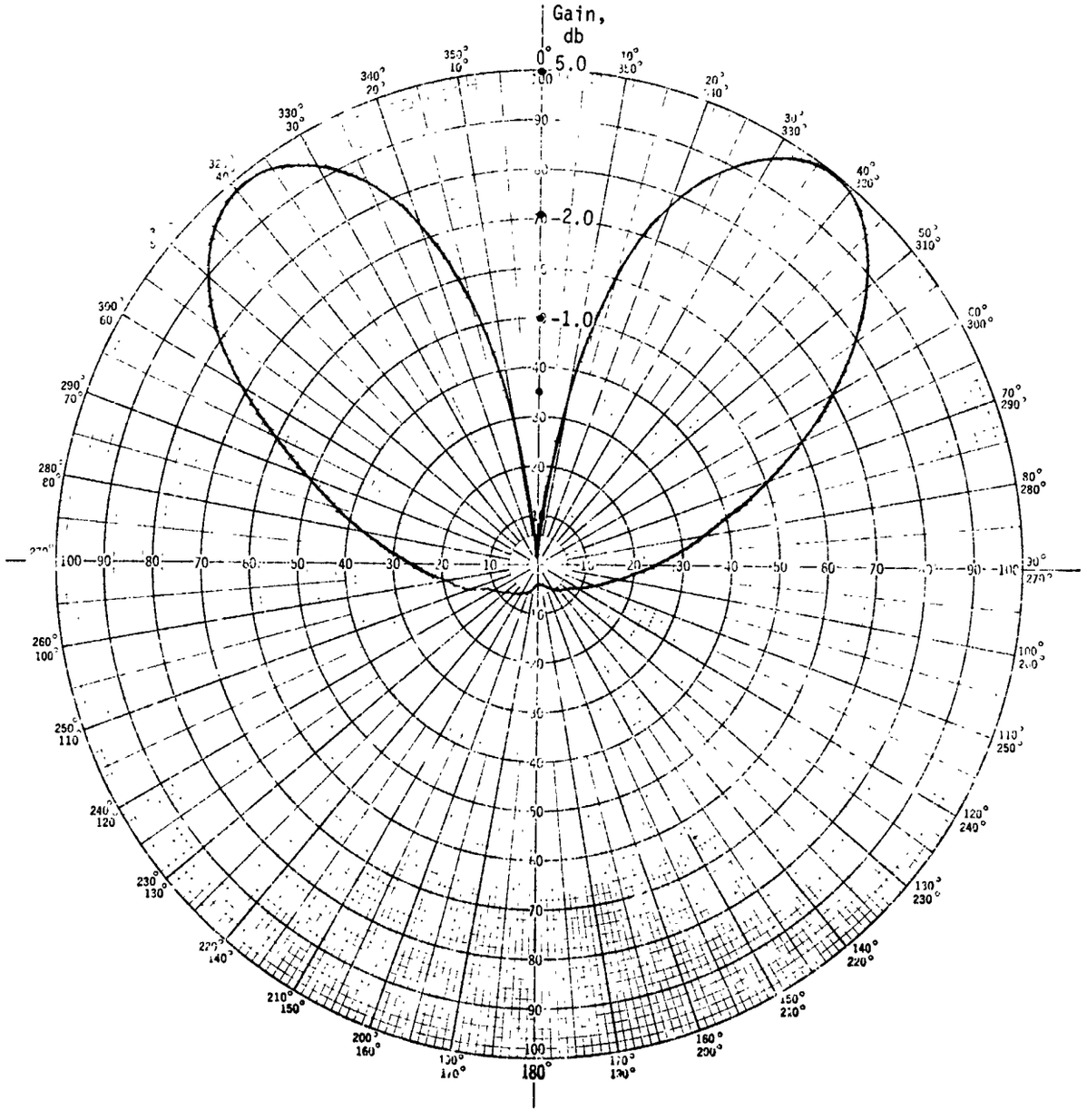
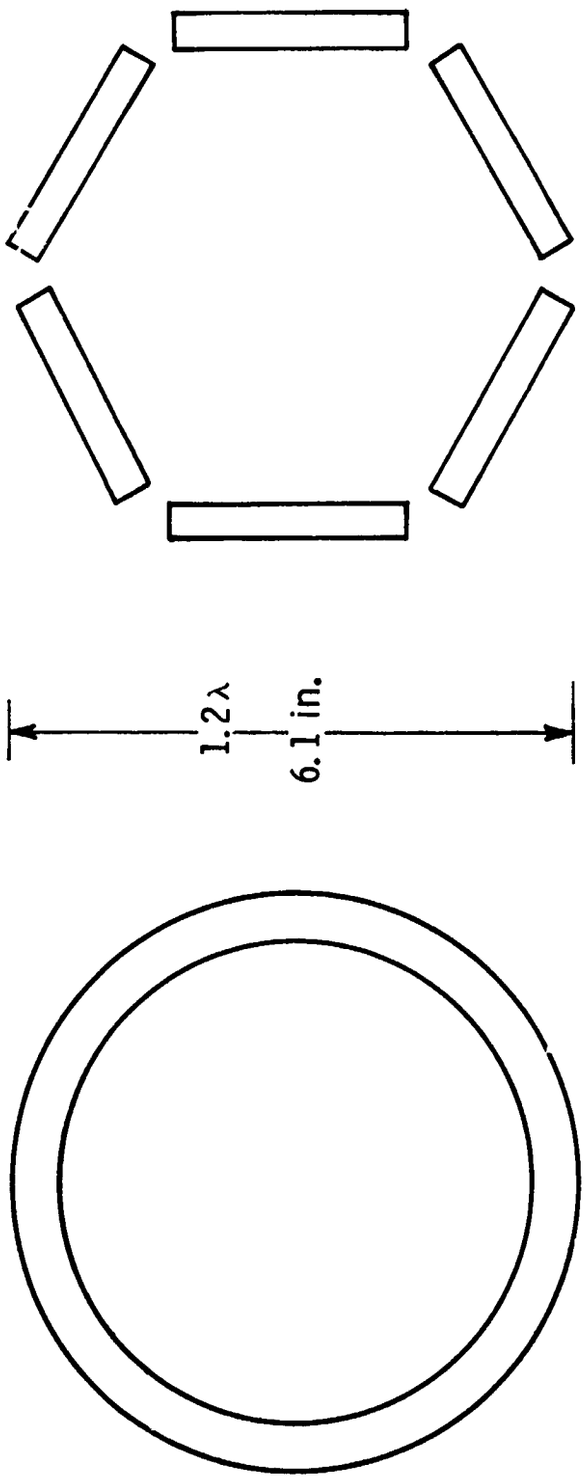


Fig. VII-35 Radiation Pattern, Four-Arm Cavity-Backed Spiral, Difference Mode, Peak Gain, 5.0 db



F'g. VII-36 Annular Slot and Ring Array of 0.5 λ Slots, 1.2 λ Diameter

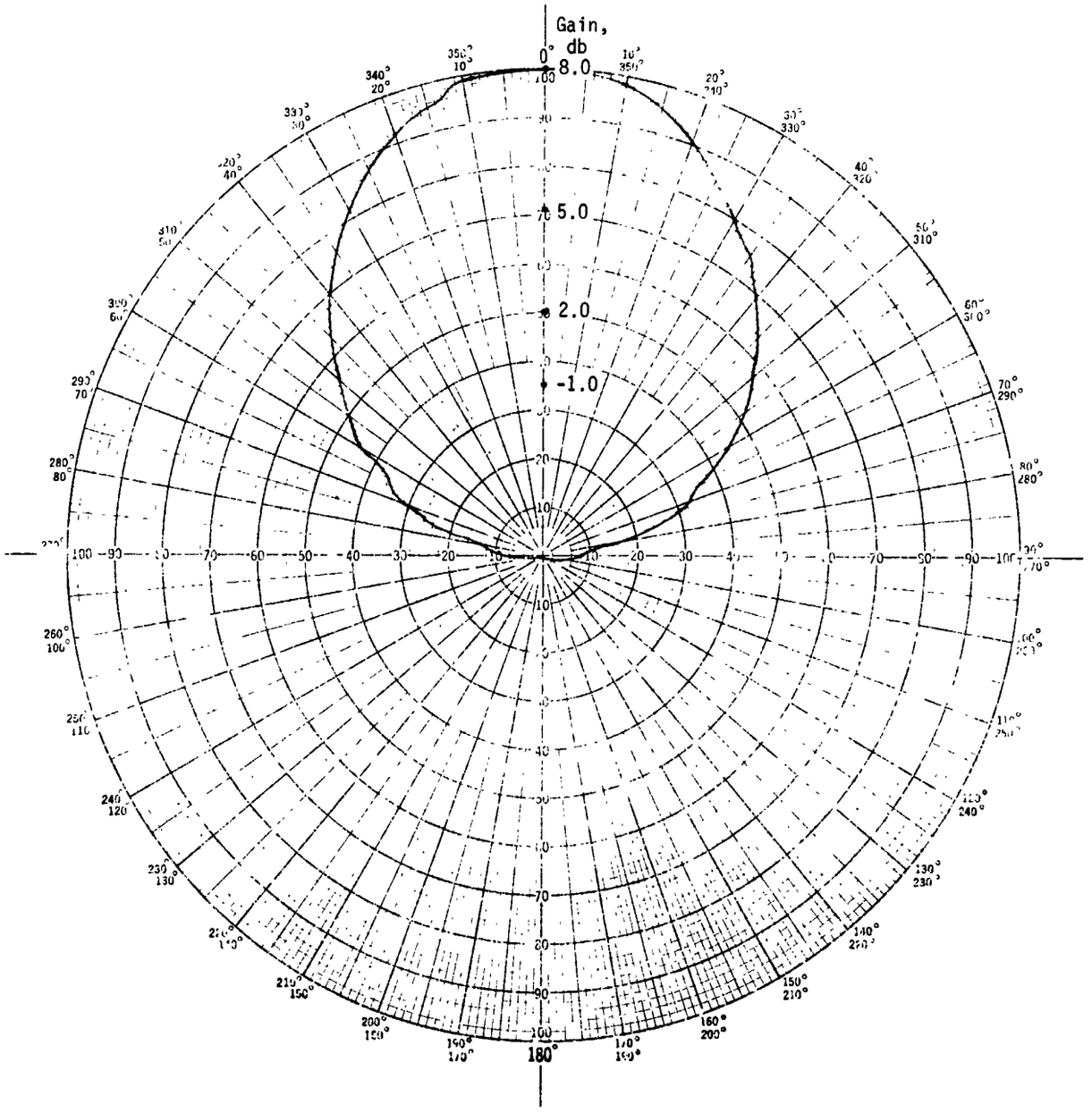


Fig. VII-37 Radiation Pattern, 0.5 λ Cavity Helix; Peak Gain, 8 db

The above survey is intended to span the whole range of possible entry angles. Entry points actually selected on the various mission options are confined to limb probes (ϕ = 70°), LSMT probes (ϕ = 24° on the option No. 2 mission, now eliminated, and ϕ = 40° on the trial mission) and balloon probes. We are proposing 0.6 λ annular slots for the limb probes, 1.2 λ annular slots for the ϕ = 40° probes, and a cavity helix for the 24° probe. A two-antenna system is recommended for the balloon probes, a cavity helix for coverage over ϕ < 45° and a 0.6 λ annular slot for coverage over ϕ > 45° and for the polarization experiment. The antenna is shown in Fig. VII-39 and the combined pattern is shown in Fig. VII-38.

One more probe must be considered. In the flyby spacecraft option, the high-altitude science will be put into the large probe, and these data will be transmitted before entry. The preentry attitude of this vehicle will give a look angle back to Earth 20° off vehicle zenith, and the postentry look angle will be 70° off zenith. The two antenna system used on the balloon cannot be used without accepting some polarization loss either before or after entry, because there would not be time to switch from circular to linear polarization in the interim between the two transmissions. The four-arm equiangular spiral on a cone antenna, sketched in Fig. VII-32, could be used. Fed in the sum mode, it gives an axial beam which would be used prior to entry. After entry the difference mode would be used, giving a conical pattern. The spiral pitch angle controls the look angle of this conical beam. A 35° pitch angle gives a beam maximum at the desired 65°. Radiation patterns are shown in Fig. VII-40. Polarization is circular in both modes. This appears to be preferable to the polarization loss even though this antenna will be an 11-in. protrusion on the top of the probe. This is simply another penalty associated with the flyby spacecraft option.

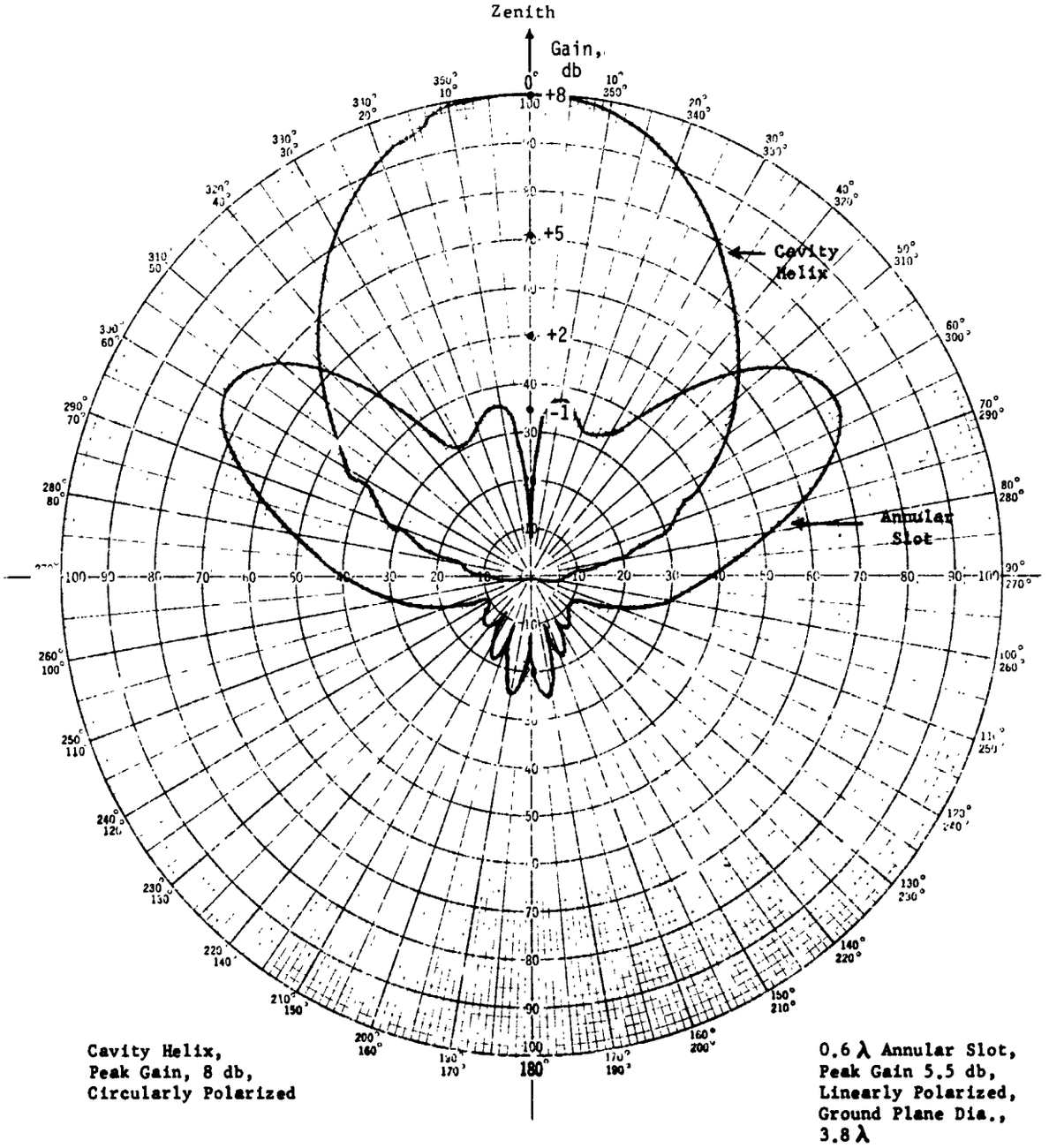


Fig. VII-38 Radiation Pattern, Balloon Antenna System

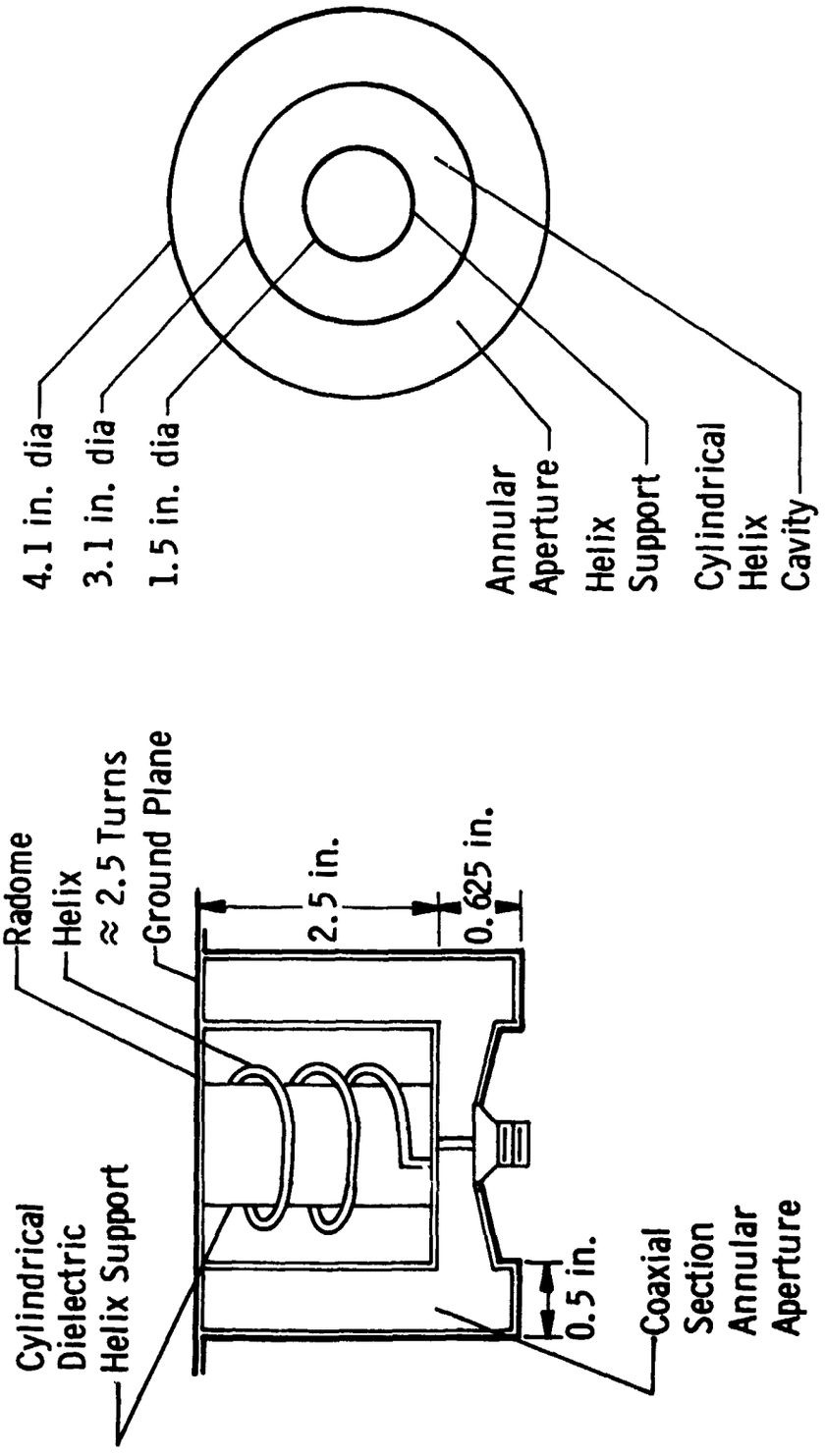


Fig. VII-39 Cavity Helix-Annular Slot Antenna Combination

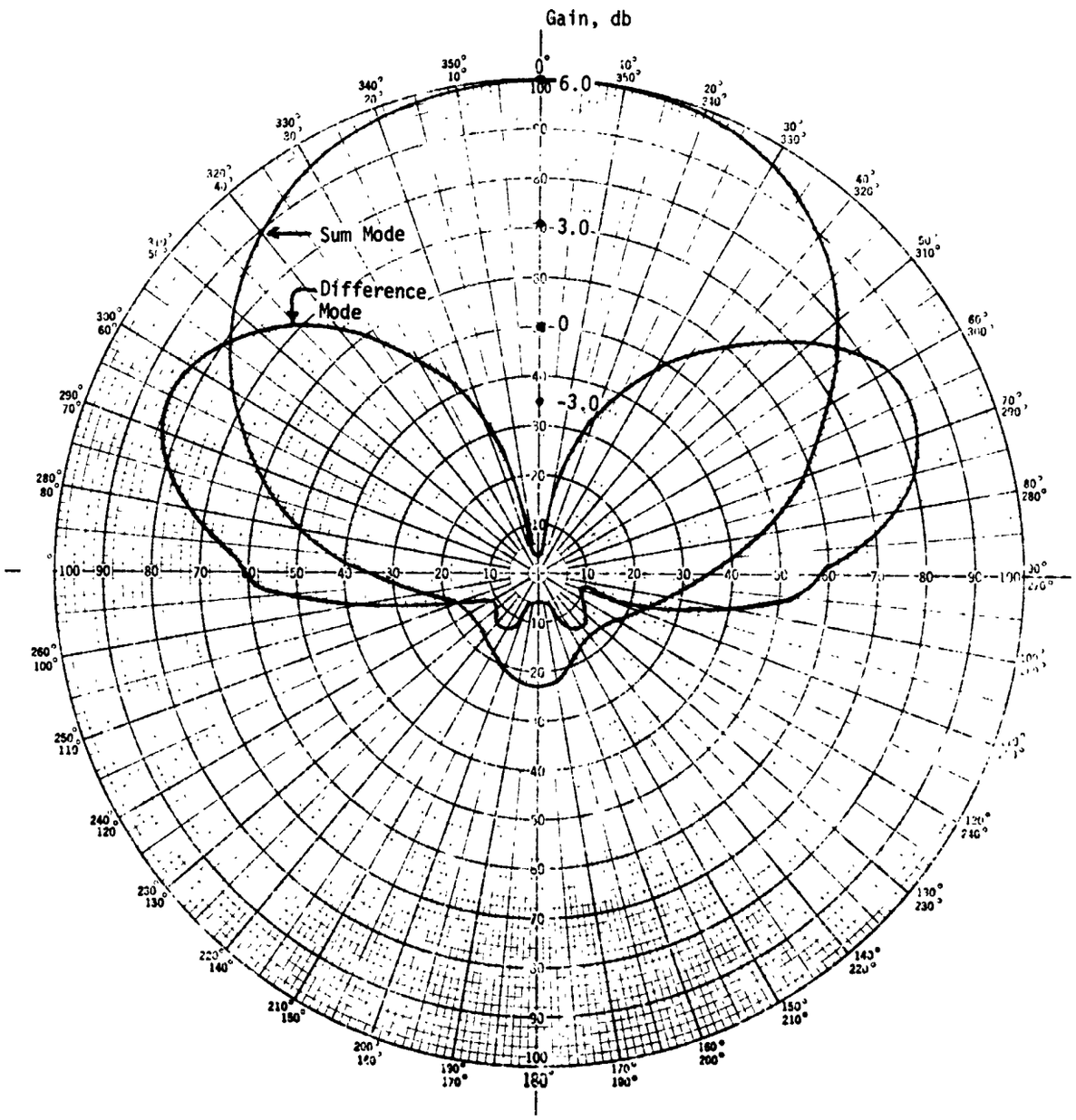


Fig. VII-40 Radiation Patterns, Equiangular Spiral on a Cone Antenna

The link calculations for all of these probes generally assume a pointing loss of 3 db. This means that attitude swings due to atmospheric turbulence of ±15° on the limb probes, and somewhat more on the other probes, can be tolerated. It should be noted, however, that all of these links have some additional unused margins. In particular, when the probes are high in the atmosphere where the more severe turbulence is expected, the margin allocated to atmospheric losses is not required. Deep in the atmosphere, where atmospheric losses are high, turbulence is expected to be low. Therefore, it is expected that the link could handle swings of 20° to 25° high in the atmosphere without loss of contact, though the data error rate might be increased somewhat during these large excursions. The possibility of a temporary loss of signal due to a very large swing cannot be avoided, but these should damp out rapidly. Loss of contact should not persist more than a few minutes at most.

These antennas would have to be designed to handle high temperatures, up to 1000°F. Dielectric windows and supports would be of fused quartz or high-temperature ceramics. The antenna structure could be fabricated from stainless steel, silver plated to improve electrical surface conductivity. High-pressure coaxial feedthroughs would have to be used to bring the input cable from inside the pressure vessel out to the antenna.

Specifications for these antennas are given in Tables VII-3 thru VII-6.

Table VII-3 Annular Slot (0.6 λ diameter) Antenna Specification

Radiation Pattern	Conical, beam peak at 65°
Frequency	2.3 GHz
Gain	6 db
Halfpower Beamwidth	30 - 35°
Power	50 watts average
Polarization	Vertical
Efficiency	90%
VSWR	1.15 relative to 50 Ω
Temperature	-65° to 1000°F
Weight	12 ounces

Table VII-4 Cavity Helix Antenna Specification

Radiation Pattern	Axial Beam
Frequency	2.3 GHz
Gain	8 db
Halfpower Beamwidth	80°
Power	50 watts average
Polarization	R. H. circular
Axial Ratio	2 db
Efficiency	90%
VSWR	1.15 relative to 50 Ω
Temperature	-65°F to 1000°F
Weight	12 ounces

Table VII-5 Annular Slot (1.2 λ diameter) Antenna Specification

Radiation Pattern	Conical, beam peak at 40°
Frequency	2.3 GHz
Gain	7 db
Halfpower Beamwidth	30°
Power	50 watts average
Polarization	Vertical
Efficiency	90%
VSWR	1.15 relative to 50 Ω
Temperature	-65°F to 1000°F
Weight	2 lb

Table VII-6 Four-Arm Spiral on a Cone Antenna Specification

Spiral Pitch Angle	35°
Cone Angle	20°
Radiation Pattern	
Sum Mode	Axial Beam
Difference Mode	Conical, Beam Peak at 65°
Frequency	2.3 GHz
Gain	
Sum Mode	6.0 db
Difference Mode	4.5 db
Halfpower Beamwidth	
Sum Mode	120°
Difference Mode	50°
Power	50 watts average
Polarization (both modes)	R.H. Circular
Efficiency	85%
VSWR	1.20 relative to 50 ohms
Temperature	-65° to 1000°F
Weight	1.6 lb

F. ELECTRICAL POWER SYSTEM

Each of the probes has a battery power supply to provide all the power for the scientific mission, data collection, and transmission. The batteries are charged before launch and are maintained in a charged condition through flight to probe separation by connection to a regulated power source in the Common Capsule Adapter.

Silver-zinc cells are chosen to make up the batteries for these missions because they offer the optimum stored energy-to-weight ratio and have a capability of maintaining a charge for the duration of the earth to Venus flight with a minimum charge power expenditure during the flight.

A voltage of 28 volts is specified as nominal for the system. Silver-zinc batteries have a large difference between open circuit voltage, nominal operating voltage, and discharged voltage. These voltages are defined below together with resulting system voltages for batteries of 18, 19, and 20 cells.

Voltage	Per Cell	18 Cell	19 Cell	20 Cell
Open Circuit	1.86	33.5	35.3	37.2
Nominal Operating	1.49	26.8	28.3	29.8
Discharged	1.4	25.2	26.6	28

Based on these values a 19-cell battery is chosen for the application.

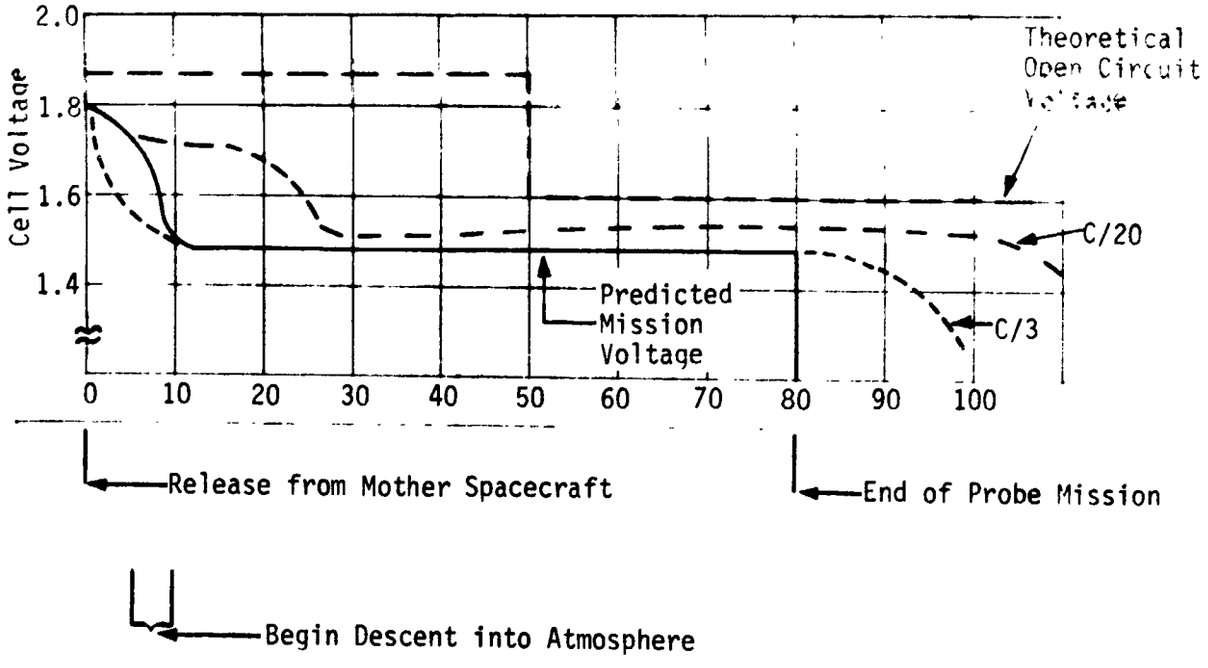
Energy requirements, the product of the (power required) times (time duration of operation), were summed for each load. This gave the minimum watt-hours required for operation. Maximum currents for any period of operation were then determined. Comparison of the maximum current required to the battery ampere-hour rating (C factor), derived from the watt-hour requirement, indicated maximum loads are of the order of C/3. Because of this relatively

heavy current drain occurring at the end of the mission, an 80% depth of discharge is used to ensure voltages do not drop off before the end of the mission. The same derating is used for the balloon, although in this case the decision was based on the continued low temperature operation of the probe. Typical voltage curves are shown in Fig. VII-41.

Weights of each battery were determined by using the total watt-hour capacity and the energy density shown in Fig. VII-42. The two surface impacting probes are considered to not require dry heat sterilization because the bioshield will remain intact until impact at which time temperatures will exceed those at which biota can live. Dry heat sterilization is assumed to be a requirement for the high cloud and balloon probes as these may disperse in the upper atmosphere of the planet.

A considerable amount of research and development is being done in the industry today to develop heat sterilizable Ag-Zn batteries; however, very limited data are presently available. The curves shown in Fig. VII-42 of sterilizable vs nonsterilizable silver-zinc batteries have been generated by the Martin Marietta Corporation and used for comparative purposes. These curves represent estimated energy densities for specific battery designs and include cells, battery case, potting, wiring, and connectors for a 30-v nominal battery with the following constraints:

1) Sealed silver-zinc cells;
2) Thin plate construction to allow good high current drain performance;
3) Shock (ordnance type): 2400 g peak response with the peak occurring at 200 cps (equivalent to 1500 g, 0.4 msec, half sine pulse input);
4) Vibration: Random, overall 11.7 g RMS with input flat 100 to 200 cps at 0.3 g^2/cps, rolloff below 100 cps at 6 db/octave, rolloff above 200 cps at 4 db/octave.



Note: Typical Venus probe mission times are indicated.

Fig. VII-41 Cell Voltage vs Percent Capacity, Ag-Zn Battery

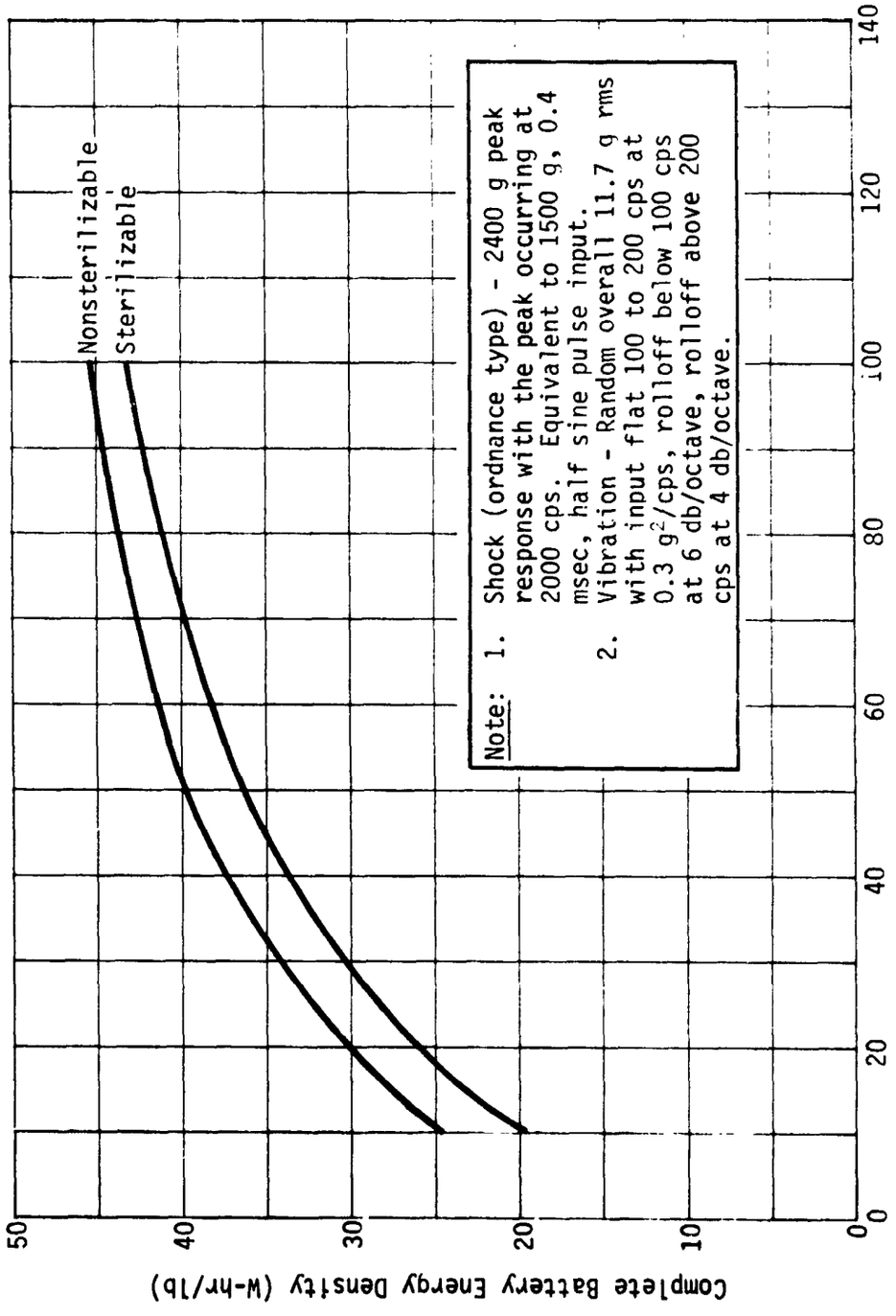


Fig. VII-42 Typical Battery Energy Densities for Ag-Zn Batteries

The nonsterilizable battery curve is based on Electric Storage Battery (ESB) Company sealed silver-zinc cells packaged in a battery to meet the above requirements. Data from the JPL sterilizable battery contract with ESB was then used to extrapolate the sterilizable battery curve allowing for the relatively less severe ordnance shock specified above. These curves are based on very limited data and should be used accordingly. They are being continuously revised as more data become available from the JPL-ESB contract and Martin Marietta in-house test programs on sterilizable silver-zinc cells. The watt-hour per pound calculations are based on the following formula:

$$\text{W-hr/lb} = \frac{\text{(Specified amp-hr) (average battery voltage)}}{\text{Total Battery Weight}}$$

As the vehicle configuration becomes firm, battery weight calculations should be based on more specific cell, environmental, and load profile data.

Battery volumes were based on dimensions of a 25 amp-hr sealed battery packaged in a 2x2x5 cell orientation. This was considered the maximum packing that could achieve adequate thermal transfer to the containing atmosphere. A factor of 1.72 W-hr/in.^{3} was determined. This was derated to 1.6 for sterilizable cells to permit extra strength case material. This same packing factor, reduced by 10%, was used for the batteries of less than 10 amp-hr as case and interconnections become a major portion of the volume for low capacity batteries.

Thermal heat rejection was based upon the assumption that the battery would be fully charged at the initiation of load. The thermal heat generated is the product of the voltage drop in the battery and the current flowing. Figure VII-41 shows the theoretical open circuit voltage of the battery cells as the upper curve. The voltage difference between the upper curve and the

lower curve defined by the load on the battery is the voltage drop at that load. The open circuit voltage step at 50% discharge is theoretical and yet reasonably representative. Open circuit voltage will recover after rest to almost full value on a 90% discharged battery. If, however, the battery is loaded for a few minutes and then checked on open circuit, the lower value will be observed.

The design of the battery has been based upon the following criteria of operation. The battery will be received in a charged condition from the vendor with electrolyte installed and cells sealed. Before launch, the battery will be recharged by the application of 1.93 v per cell until the current drops to a value of approximately C/200. With the battery in this condition, the voltage may be dropped to 1.89 volts per cell. This voltage will cause only a few milliamps of current to flow, but will maintain the full charge condition on the battery. Launch may now occur. A charging voltage of 1.89 v/cell shall be maintained during the complete flight. Charging currents will be zero to a few milliamperes. Present available data indicate a charging voltage tolerance of ±0.01 v/cell should be maintained. If the voltage is too high, the battery will overcharge and develop both excess heat and pressure. If the voltage is too low, the charge may not be maintained and the formation of dendritic crystals in and through the porous separators is more likely to occur.

Battery temperatures are critical. The following limits represent the best information currently available. The electrolyte shall not get below 0°F. Below this temperature there is increased possibility of crystallization and the possible puncture of separator material.

When the probe is deployed it is desirable to have the battery at about 40°F before applying load. Light loads could be applied as low as 20°F, however heavy loads (around C/3) should not be applied below 40°F. Voltage, and consequently power, will increase with temperature; however, the total available energy will decrease. A voltage increase of 0.1 v/cell from a temperature of 40°F to 130°F is characteristic. Storage at 130°F could typically result in a 10% loss in available energy per month.

The maximum temperature at the end of mission should not exceed 140°F.

A summation of the power system descriptive data is shown in Table VII-7.

A solar array is added to both balloon probe power systems to permit extended float time for little additional weight. The array may be sized to provide enough energy to operate the probe as well as to maintain the charge in the battery while receiving direct and reflected solar radiation. The battery is sized to power the probe when in the dark. Battery size and weight will be the only parameters affected by changing the length of operation in the dark. Changes in battery energy density with power are shown in Fig. VII-42.

To determine array area, a reasonable value of cell performance at expected illumination intensity (Fig. VII-43) and cell temperature (Fig. VII-44) must be established. Cell temperature is governed primarily by properties of the substrate on which cells are mounted. Equilibrium temperature values for typical substrate materials at earth orbit conditions (i.e.: 1 astronomical unit at air mass zero) range from 40°C for aluminum plates with thermal coating to 70°C for 3/8-in.-thick honeycomb.

Table VII-7 Ag-Zn Battery Power System

Probe Type	Cruise Power (W)/ Time (hr)	Descent Power (W)/ Time (hr)	Battery Energy (W-hr)	Battery Size (amp-hr)	Battery Weight (lb)	Battery Volume (cu in.)	Battery Average Descent Heat (W)
Large Probe (Impacting Spacecraft)	0.1/264	234.8/2.175	674	24	21.6	391	60.2
Small Probe	0.1/264	100.7/1.7	254	9.1	10.6	162	23
High Cloud Probe	0.1/264	96.7/1.5	216	7.7	12 Steri-lized	148	22.5
Balloon Probe	0.1/264	30/245 Active 1.8/165.5 Rest	497	17.7	21.6 Steri-lized	311	0.52
Large Probe (fly-by spacecraft)	0.1/263.6	111/0.368 Approach 234.8/2.175 Descent	722	25.8	22.6	420	51 includes Approach
Balloon Probe (low elevation)	0.1/264	30/2.46 Active 0.1/165.5 Rest	146	5.2	9.1 Steri-lized	100	0.122

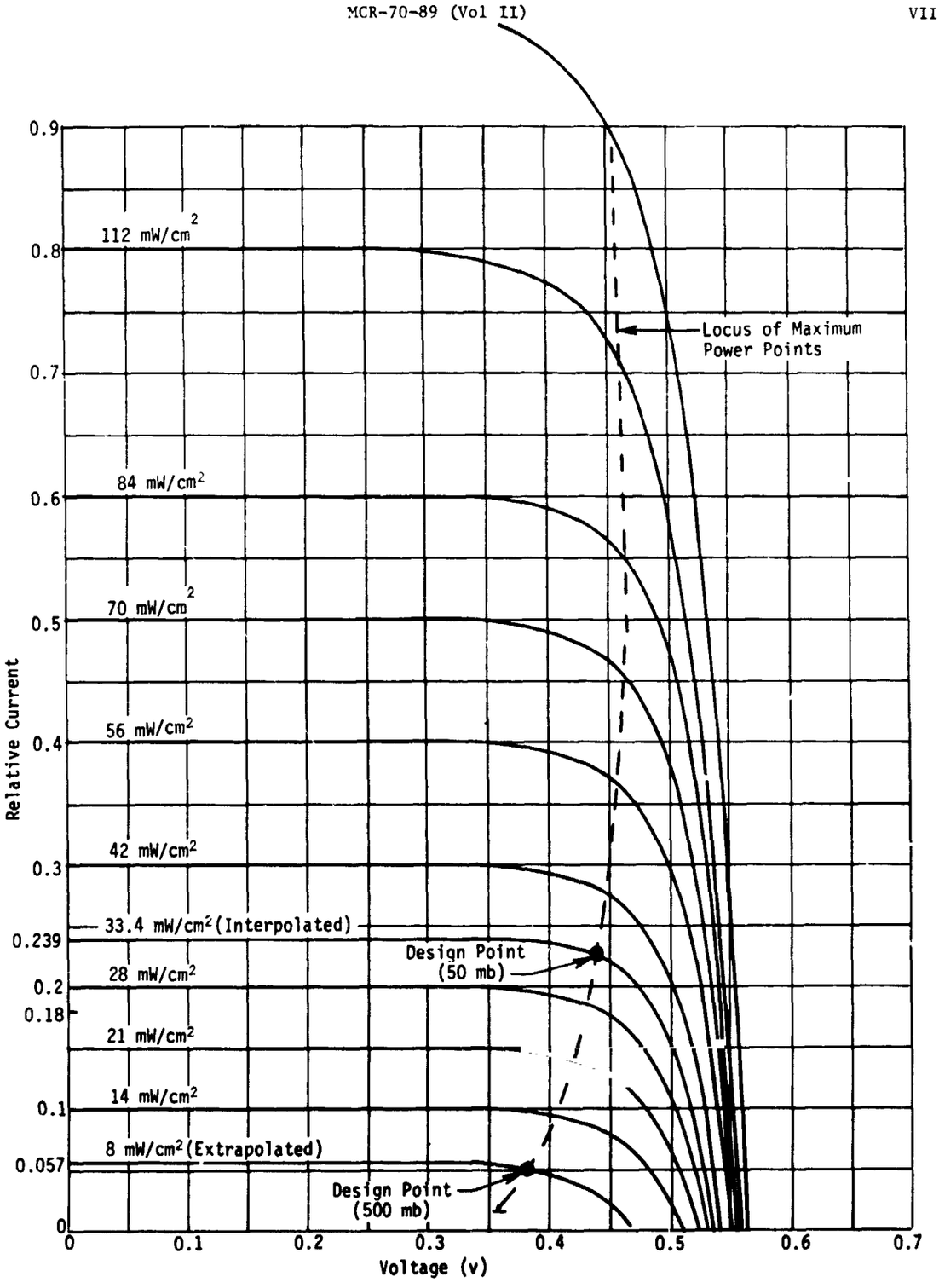


Fig. VII-43 Typical I-V Characteristics as a Function of Solar Irradiance at Constant Temperature

Note: 1. 2x2 cm 10 ohms cm N/P solar cell.
2. Silicon thickness 0.012 in., active area 3.9 cm^2.
3. Sunlight simulator 140 mW/cm^2.
4. Balloon calibration.

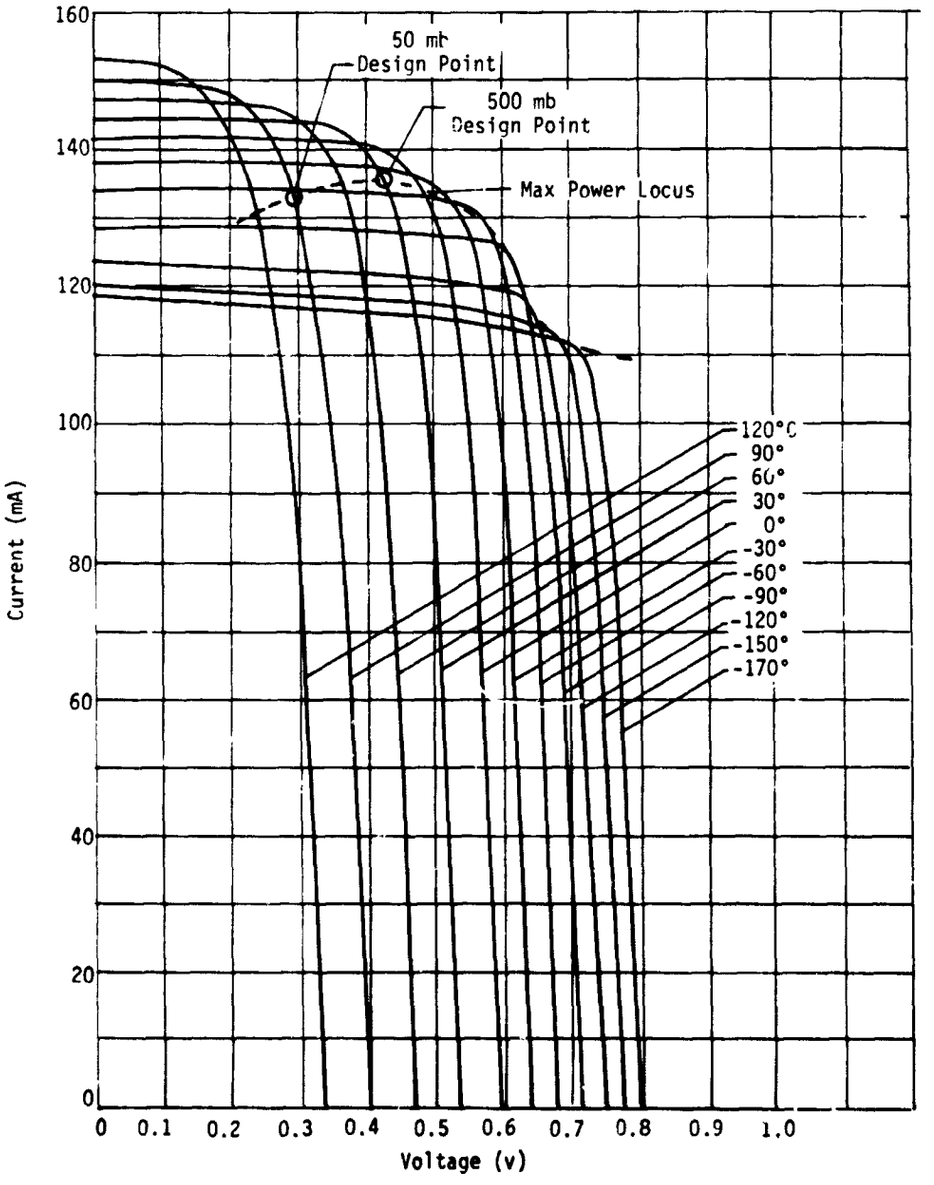


Fig. VII-44 Voltage-Current Characteristics vs Cell Temperature

Direct illumination intensities outside the Venus cloud (F_o) are approximately equal to two earth suns. It will tend to increase temperatures over values expected near earth.

However, the dense atmosphere in which the probe will be floating may tend to stabilize the array temperature at a lower temperature. The ambient temperature at 50 mb is approximately -23°C; at 500 mb, +17°C. A thermal model would have to be analyzed in detail to determine the array equilibrium temperature to refine the array design. The 90°C temperature curve is chosen from Fig. VII-44 for the 50 mb probe; 30°C curve for the 500 mb probe.

Figure VII-45 shows the three expected possibilities of the balloon float altitude-cloud relationships. Directions of the flux (F) components are shown in Fig. VII-46. Because of uncertainty in the cloud-top elevation, the 50 mb balloon may be either in or above the clouds. The 500 mb balloon will be below the clouds.

F_A is the solar flux from above the balloon, F_S is the sum of the direct side flux and the scattered flux from the side (at some level from all sides), and F_B is the flux from the underlying atmosphere and/or cloud. Solar flux F, as used here, is equivalent to intensity in usual solar array design parlance.

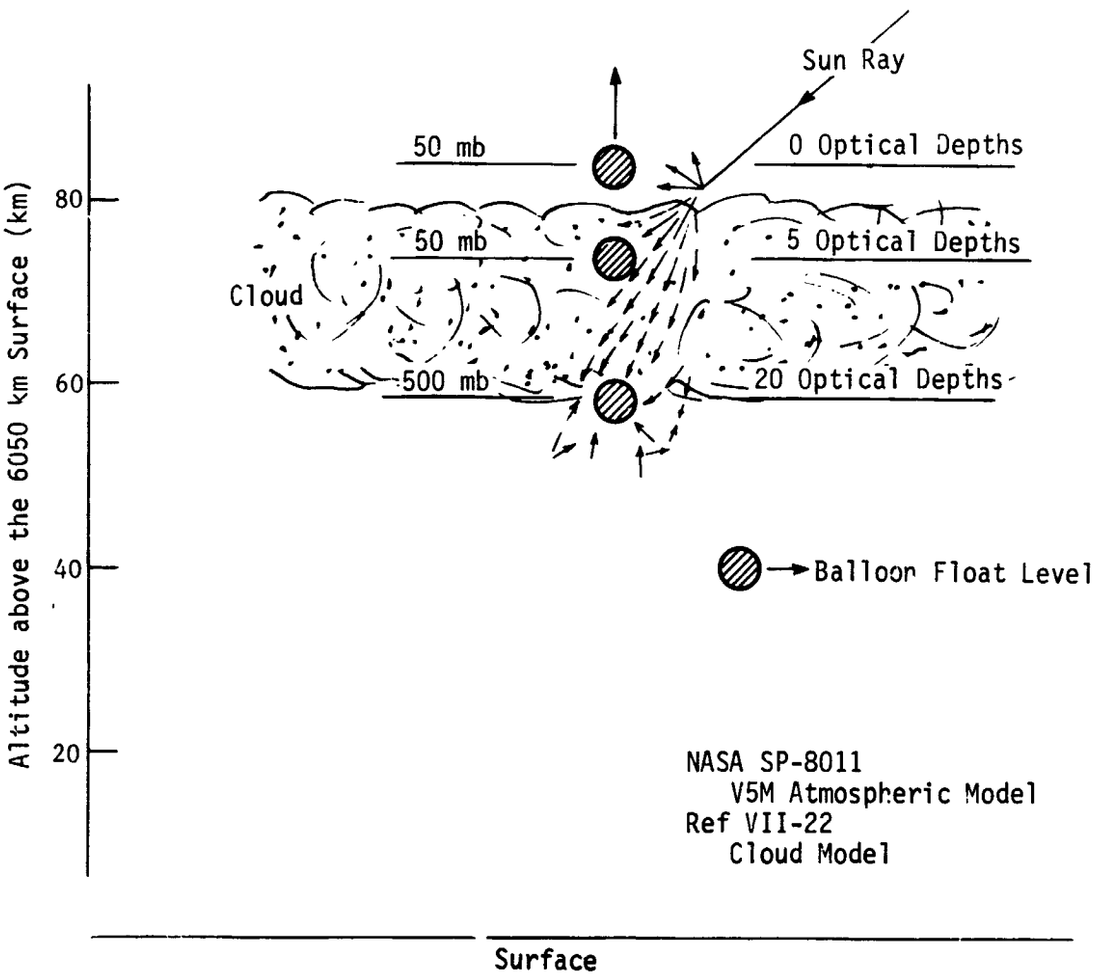


Fig. VII-45 Venus Probe Solar Radiation Environment

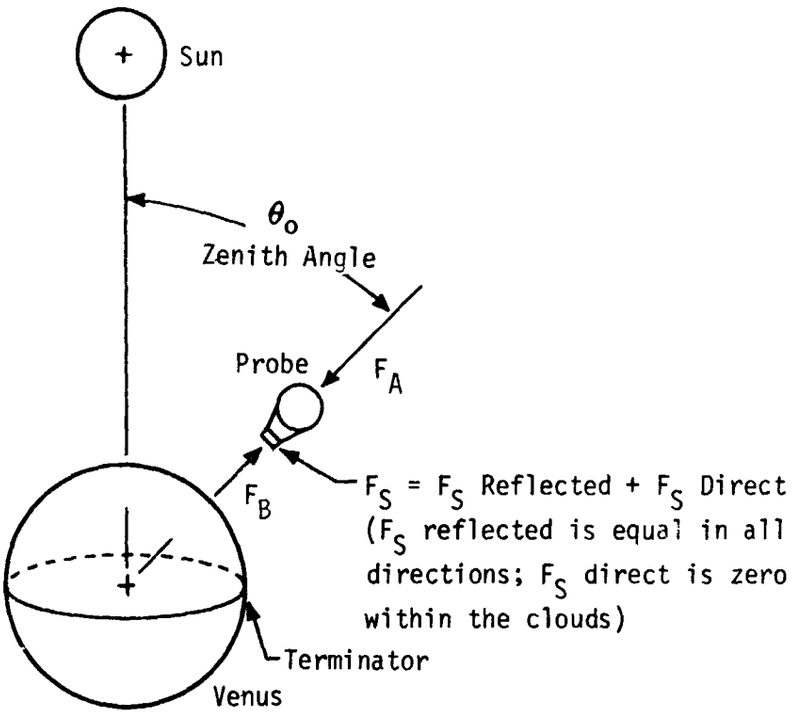


Fig. VII-46 Coordinate Nomenclature

From diffusion theory (Ref VII-23) the diffuse light transmission through an Earth-type cloud can be estimated by

$$T = \frac{0.57 + 1.12 \cos \theta_0}{t/2V + 1.42} \qquad [37]$$

where T is the fractional transmission, t is the geometrical thickness of the cloud, θ_0 is the solar zenith angle, and V is the visibility. For the Venus cloud, the mean free scattering path, λ, has been estimated to be 1 km (Ref VII-22). The optical depth, τ, is related to λ by

$$\tau = t/\lambda$$

hence the optical depth for such a cloud is

$$\tau = t/1.0 \qquad (t \text{ in km})$$

Hence, in Eq [37],

$$T = \frac{0.57 + 1.12 \cos \theta_0}{\tau/2V + 1.42}$$

the visibility, V, is related to λ by

$$V = 4 \lambda$$

hence

$$T = \frac{4.56 + 8.96 \cos \theta_0}{\tau + 11.36}$$

Since F_A is related to the incident solar flux an additional $\cos \theta_0$ is needed, giving

$$F_A = \frac{4.56 + 8.96 \cos \theta_0}{\tau + 11.36} F_o \cos \theta_0 \qquad [38]$$

The following cases will be considered: (1) 50 mb balloon above cloud layer; (2) 50 mb balloon in cloud layer (at five optical depths); and (3) 500 mb balloon (at 20 optical depths).

Case (1): 50 mb Balloon above Clouds - Illumination on top of probe (F_A) is:

$$F_A = F_0 \cos \theta_0 \quad [39]$$

where F_0 (280 mW/cm^2) is the solar flux at Venus (molecular atmospheric attenuation between Sun and the 50 mb probe is ignored).

Side illumination on the probe F_S (total side radiation) is equal to the sum of the diffuse and direct components. For the proposed cylindrical array the proportion of effective area is 0.2 with unidirectional parallel illumination.

$$F_S = F_S \text{ direct} + F_S \text{ diffuse} \quad [40]$$

where F_S direct = 0.2 F_o sin θ_0, and F_S diffuse = 0.2 F_o cos θ_0.

Illumination on the bottom is:

$$F_B = (0.8)\ F_0 \cos \theta_0 \quad [41]$$

The 0.2 factor in Eq [40] and the 0.8 factor in Eq [41] were obtained from Ref VII-24.

Case (2): 50 mb Balloon (at 5 optical depths) (Fig. VII-47)

$$F_A = \frac{\left(4.56 + 8.96 \cos \theta_0\right)}{16.36} F_0 \cos \theta_0 \quad [42]$$

$$F_S = 0.7\ F_A \left(F_S \text{ direct} = 0 \text{ within cloud layer}\right) \quad [43]$$

$$F_B = 0.4\ F_A \quad [44]$$

The factors 0.7 and 0.4 were obtained from Ref VII-24.

Case (3): 500 mb Balloon (at 20 optical depths) (Fig. VII-48)

$$F_A = \frac{\left(4.56 + 8.96 \cos \theta_0\right)}{31.36} F_0 \cos \theta_0 \quad [45]$$

$$F_S = 0.2\ F_A \quad [46]$$

$$F_B = 0.1\ F_A \quad [47]$$

The 0.2 factor was obtained from Ref VII-24 and the 0.1 factor is the assumed albedo of the lower Venus atmosphere.

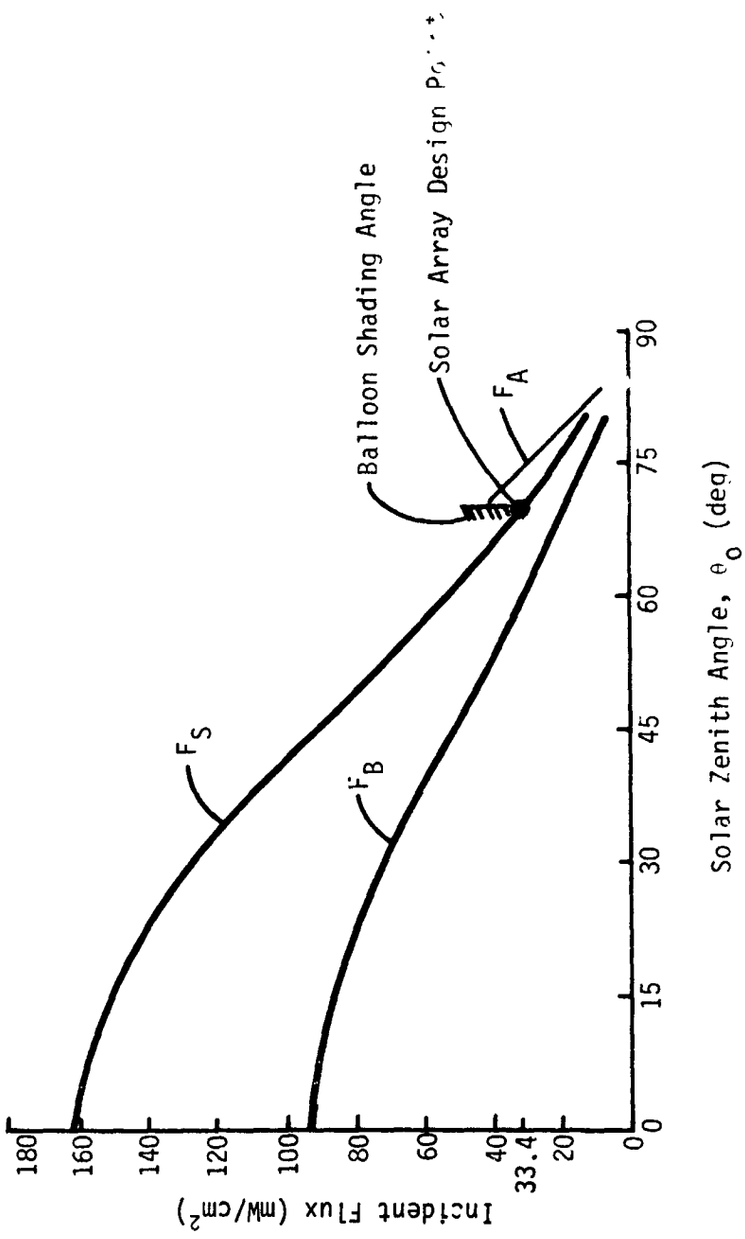


Fig. VII-47 50 mb Incident Flus vs Zenith Angle (at 5 Optical Depths)

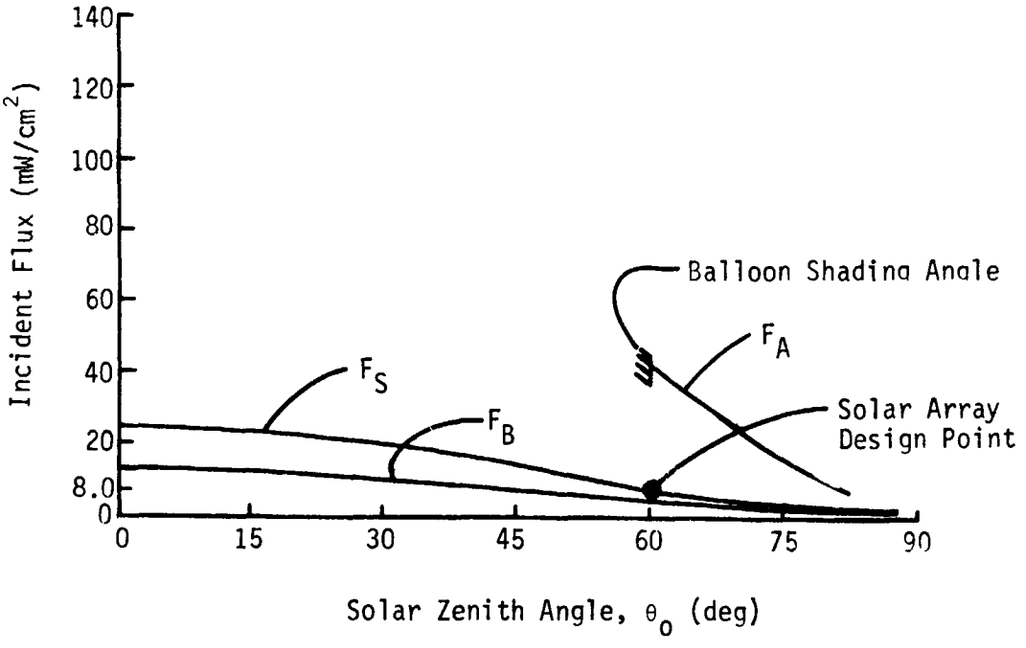


Fig. VII-48 500 mb Incident Flux vs Zenith Angle (at 20 Optical Depths)

Power conditioning equipment includes voltage regulation, power distribution, bus bars, battery charging, etc. For 28 v at 4.15 W the unit will weigh approximately 0.6 lb; for 1.5 W, approximately 0.3 lb.

The 50 mb probe is located in the area where it is uncertain whether it is in or out of the clouds. Consequently the array has to be sized for the condition giving the lesser intensity. This occurs when the probe is within the clouds at a depth of about five optical units.

A cylindrical array can be manufactured and mounted easily to the spherical gondola of the 50 mb probe. The side flux F_S at $\theta_0 = 69°$ (see Fig. VII-48) is used for sizing the array because it is equal from all sides and is less affected by zenith angle than F_A and F_B. The 69° zenith angle is used as a reasonable design point because the probability of the probe being within the region bounded by a 69° zenith angle is 78%. After application of suitable design factors such as redundancy and additional cell area, adequate power will be obtained for larger zenith angles.

Figure VII-43 shows relative power output at several illumination intensities. From Fig. VII-47 the 50 mb balloon will see a side flux F_S of 33.4 mW/cm^2 at $\theta_0 = 69°$. The 90°C curve from Fig. VII-44 gives 133 ma @ 0.29 v. From Fig. VII-43 at 33.4 mW/cm^2 the current will be reduced by factor of 0.22. Individual cell output p_c (milliwatts) becomes approximately:

$$P_{c_{50\ mb}} = 29.3 \text{ ma @ } 0.29 \text{ v} = \text{mW/cell}$$

For a typical panel with approximately 200 cells/ft^2:

$$P_{50\ mb} = 1.7 \text{ W/ft}^2.$$

From the balloon probe discussion in Chapter III.E, 2.30 watts of array power is required. Therefore, the approximate array area required is $2.30/1.7 = 1.28$ ft^2. One hundred cells in series are required to achieve 28 v or more. Three cells in parallel will provide current to give adequate power output from array.

Similarly, the required area for the 500 mb probe is calculated at $\theta_0 = 60°$ (i.e., the balloon shading angle):

From Fig. VII-49: $F_S = 8$ W/cm^2, proportional;
Current = 0.05;
From 30°C curve in Fig. VII-44: $P_{c_{140}}$ = 135 ma @ 0.43 v.

Individual cell power $P_{c_{500\ mb}}$ becomes approximately:

$$P_{c_{500\ mb}} = 6.75 \text{ ma @ } 0.43 \text{ v} = 2.9 \text{ mW/cell}$$

for 200 cells/ft^2

$$P_{500\ mb} = 0.58 \text{ W/ft}^2$$

Required power, from Chapter III.E, is 1.70 W. Approximate panel area is therefore $\frac{1.70}{0.58} = 2.93$ ft^2.

Sixty-five cells in series and 9 cells in parallel are required to achieve desired power at 28 v.

Weight estimates for array and power conditioning components are shown in Table VII-8.

The 50 mb probe requires that a cylindrical extension be added to the gondola for solar array support (Fig. VII-49). On the 500 mb probe the solar array would be body mounted to the existing gondola over a 1-mil kapton substrata (Fig. VII-50).

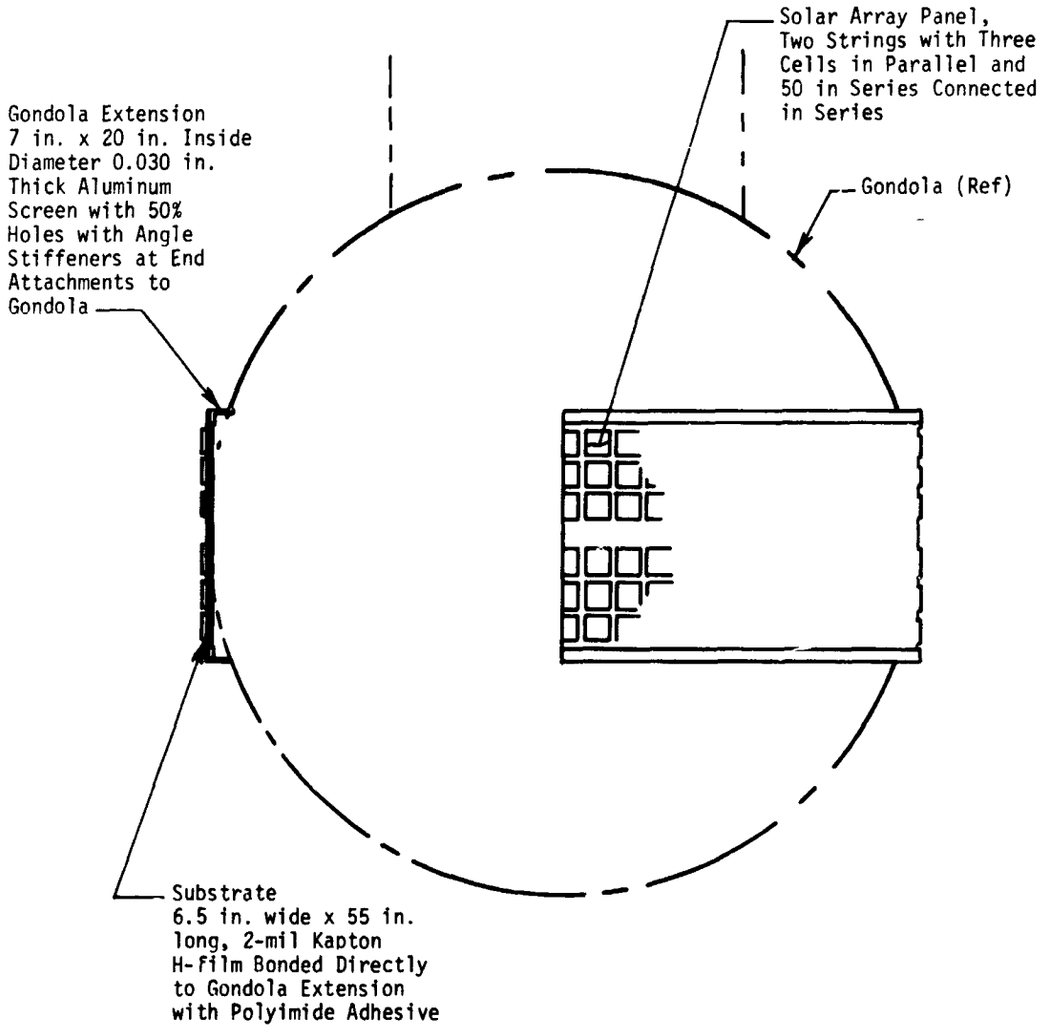


Fig. VII-49 50 mb Probe Solar Array

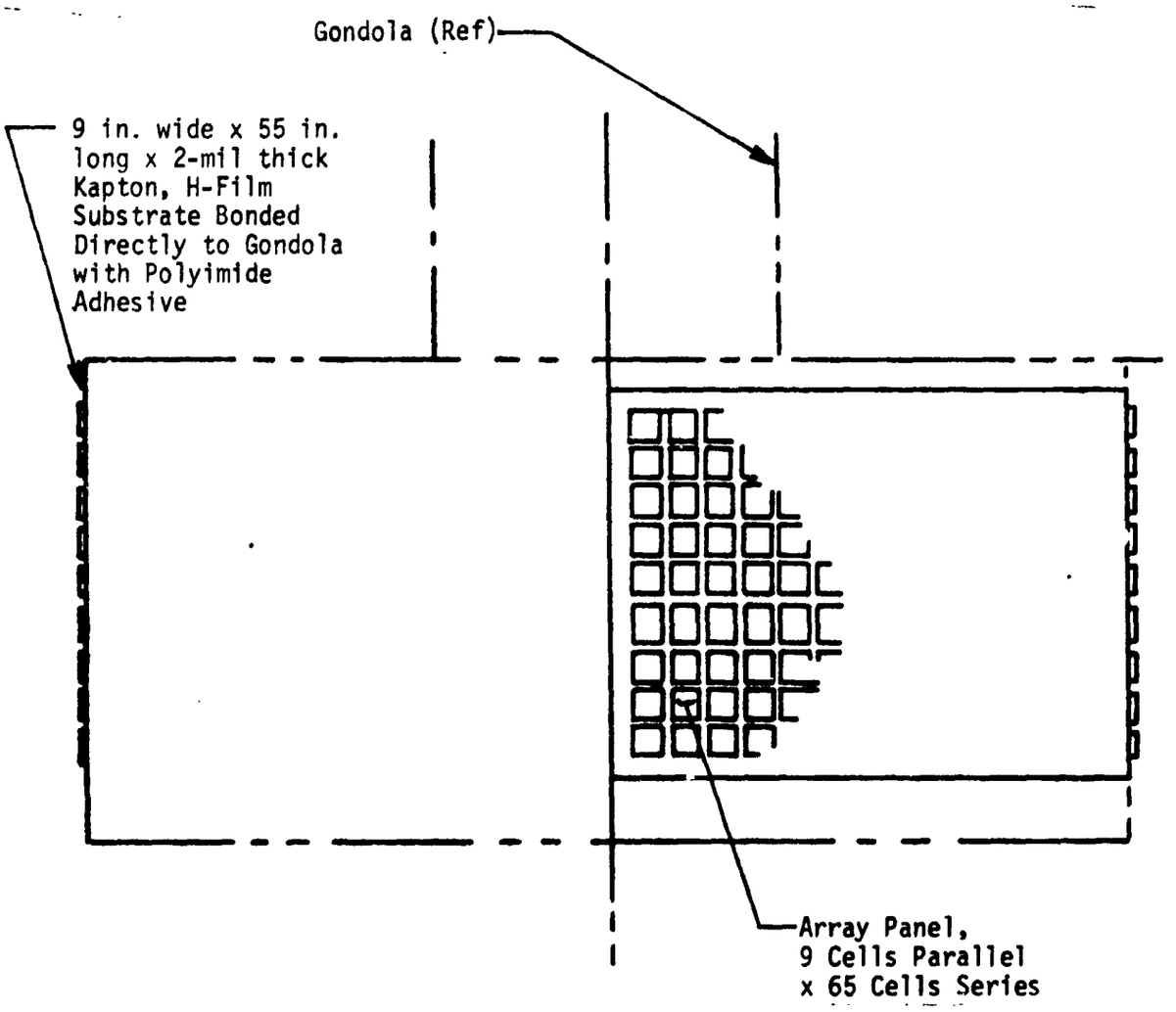


Fig. VII-50 500 mb Probe Solar Array

Table VII-8 Solar Array Weight Estimates

Item	50 mb	500 mb
Cells, 12-mil 10 Ω-cm Silicon	0.27	0.45
Covers 6-mil Microsheet Glass	0.09	0.18
Cover Adhesive	0.03	0.05
Cell Adhesive	0.02	0.03
Solder	0.01	0.02
Interconnects	0.01	0.02
Substrate	0.04	0.06
Substrate Adhesive	0.03	0.06
Bus Bar and Connectors	0.01	0.02
	0.51	0.89
Mounting Structure	1.23	0
Subtotal	1.74	0.89
Power Conditioning and Distribution	0.60	0.30
Total	2.34	1.19

As noted above, battery weight is the only parameter which is affected by changing the probe life on the planet dark side. It can be estimated for 5- and 10-day dark probe periods by scaling battery weight with the use of Fig. VII-42. The balloon probes will enter on the light side. Power taken from battery during postseparation cruise and initial postdeployment contact is assumed to be recharged during light before the probe enters the dark side.

The method of calculations and values obtained are shown in Table VII-9 for both 5 and 10 days of operation in dark at 50 mb and 500 mb.

Sketches of the proposed array are shown in Fig. VII-49 for the 50 mb probe and Fig. VII-50 for the 500 mb probe.

Table VII-9 Battery Weight Determination

Parameter	500 mb		50 mb	
Dark Time ⟶	5 Days	10 Days	5 Days	10 Days
Active Float Power (W)	41	41	41	41
Total Active Time (minutes)	112	224	112	224
Inactive Float Power (W)	0.1	0.1	1.7	1.7
Total Inactive Time (minutes)	7,088	14,176	7,088	14,176
Battery Watt-hr (80% Discharge)	110	220	360	720
Amp-hr (@ 28 v)	3.95	7.90	12.9	25.8
Energy Density (W-hr/lb) (from Fig. VII-42, Sterilizable Batteries)	14	17	22	28
Battery Weight (lb)	7.5	12.3	16.4	25.7

The optical depths shown in Fig. VII-45 are based on the cloud model given in Ref VII-22, as stated earlier. Sizing of the solar panels is based on these assumed optical depths, with reasonable margins. However, this cloud model could be substantially in error, and uncertainty about the light levels can only be dispelled by measurements made by an entry probe. Unless this is done before the multiprobe mission, the solar panel sizing must be considered to be a major uncertainty in the balloon probe design.

G. PYRO SUBSYSTEM

The function of the pyro subsystem is to initiate explosive reactions that in turn cause mechanical reactions, such as the release of restraining mechanisms, or propulsive forces. The initial element of the pyro subsystem is the initiator containing a bridgewire embedded in a compressed explosive. When heated by an electrical impulse the bridgewire causes a localized explosive reaction. The explosive reaction is propagated, in some cases through pairs of donor and receptor charges, until sufficient energy is available to accomplish the desired end result. The end result may include actuation of such devices as pin pullers or cable cutters. These are referred to as pyromechanical devices.

For reasons of both safety and reliability associated with initiator operating characteristics it is necessary to provide functions of arming and safing in addition to delivery of the firing impulse. This group of functions is normally provided under the control of the sequencer.

1. Pyro Subsystems Functions

Functions designated to be performed by the pyro system for the Venus 1975 mission are divided into Planetary Vehicle functions and capsule system functions.

a. Planetary Vehicle - The Planetary Vehicle functions are:

1) Separation of the Planetary Vehicle biocanister for the impacting spacecraft mission. (The biocanister will remain with the launch vehicle final stage);

2) Separation of the individual biocanisters of the individual capsules. (This will be accomplished for all capsules before separation of the first capsule from Planetary Vehicle);

3) Separation of the individual capsules from the Planetary Vehicle.

b. Capsule System - The capsule system functions are:

1) Capsule spin-up;
2) Deflection propulsion initiate;
3) Deflection propulsion terminate;
4) Deflection propulsion module jettison;
5) Despin weight deployment;
6) Despin weight jettison;
7) Entry science deployment;
8) Initiate decelerator mortar;
9) Aeroshell separation;
10) Decelerator reefing or jettison;*
11) Descent science deployment;*
12) Balloon extension;*
13) Balloon inflation;*
14) Separate parachute;†
15) Balloon inflation termination;†
16) Balloon inflation system jettison;†
17) Balloon science deployment.†

2. Pyro Subsystem Design Criteria

Pyro subsystem design is based upon use of the standard initiator, under development for the Viking Program. This initiator is in turn similar to the standard Apollo initiator defined in NASA specification SKB-26100053 (Ref VII-25).

*Not applicable to balloon probes.

†Balloon probes only.

The Viking standard initiator is in two versions with the following major characteristics:

Maximum diameter or Maximum hexagon*	0.850 in. or 0.625 in.
Maximum length	0.950 in.
No fire current	$\geq$ 1.0 amp ($\bar{3}$) (0.9995 reliability)
No fire power	$\geq$ 1.0 W ($\bar{3}$) (0.9995 reliability)
Minimum fire voltage (MFV)	25 v
Normal fire energy (at MFV)	210 joules
All fire energy (at MFV)	105 joules (0.9995 reliability)
Checkout current	0.020 amp

Dual initiators will be used for each pyro function. Pyromechanical units will be used singly. Separate firing circuits of twisted, shielded, pairs will be provided for each initiator. Firing energy will be supplied by the power system and will be stored in each of two capacitor assemblies. The same capacitor assemblies may be used for successive firings provided that sufficient recharging time (approximately 12 sec) is allowed between firings. Each initiator circuit will also contain a safe/arm switch. Operation of the safe/arm switch and charging of the capacitor assembly will be under the control of the respective sequencer in the Common Capsule Adapter or in the Entry Capsules, as applicable. Operation of the firing circuit will be initiated either by the sequencer or by other sensors. In the latter case sequencer backup may be provided.

*The hexagonal unit is designed to be used when no auxiliary charges are involved. The diametral unit is designed to be welded to pyromechanical units containing auxiliary charges.

H. REFERENCES

VII-1 A. J. Stratton: "Optical and Radio Refraction on Venus." *Journal of Atmospheric Science.* Vol 25, No. 4, pp 666-667.

VII-2 R. K. Luneberg: *Mathematical Theory of Optics.* U. of California Press. Berkeley, 1964.

VII-3 O. P. Yakolev, *et al.*: *Propagation of Ultra Short Waves in the Atmosphere of Venus.* English Translation, NASA-Goddard Document N69-24128, 5 May 1969.

VII-4 R. P. Ingalls and J. V. Evans: "Scattering Properties of Venus at 3.8 cm." *The Astronomical Journal.* March 1969.

VII-5 Final Report, "1972 Venus Flyby/Entry Probe Mission Study." Contract JPL 951-964 (AVCO), p 3-302.

VII-6 *Study of a 1973 Venus-Mercury Mission with a Venus Entry Probe.* JPL Report 760,1, Vol II, Appendix A, *Planetary Effects of Venus.* August 18, 1967.

VII-7 *Selected Studies of VHF/UHF Communications for Planetary (Mars/Venus) Relay Links.* Final Report, Contract NAS2-3772, RCA.

VII-8 *Study and Analysis of Multipath and Modulation Selection for Relay Radio Links.* (RCA input to the Voyager Contract.) RCA Report 100032-A (VCB-155).

VII-9 Harold Staras: "Rough Surface Scattering on a Communication Link." *Radio Science.* June 1968.

VII-10 A. B. Glenn: "Fading from Irregular Surfaces for Line-of-Sight Communications." *IEE Transactions on Aerospace and Electronic Systems.* March 1968.

VII-11 D. O. Muhleman, *et al.*: "A Review of Radar Astronomy - Part 2." *IEEE Spectrum.* November 1965.

VII-12 P. Beckman and A. Spizzichino: *The Scattering of Electromagnetic Waves from Rough Surfaces.* Pergamon, 1963, p 94.

VII-13 A. Kliore, *et al.:* "Atmosphere and Ionosphere of Venus from the Mariner 5 S-Band Radio Occultation Measurement." *Science*, Vol 158, 1967, p 1683.

VII-14 G. Fjeldbo and V. R. Eshleman: "Atmosphere of Venus as Studied with the Mariner 5 Dual RF Occultation Experiments." *Radio Science.* October 1969.

VII-15 C. C. Watterson, *et al.: SHF Bandwidth Study, Phases I, II, & III.* NBS Reports 8839 and 8842, 1965.

VII-16 JPL Document 831-1, Rev A, 1 October 1968, pp 2-9.

VII-17 M. Easterling: *Analysis of the Effects of a Limiter on a Square-Wave Signal Plus Additive Gaussian Noise.* JPL Research Summary 36-14, May 1, 1962.

VII-18 K. C. Yeh and G. W. Swenson: "Ionospheric Electron Content and Its Variations Deduced from Satellite Observations." *J. Geophys. Research*, 66, 1967, pp 1060-1067.

VII-19 T. W. Wright and G. H. Smith: "Review of Current Methods for Obtaining Electron-Density Profiles from Ionograms." *Radio Science.* October 1967.

VII-20 *Space Communications*, McGraw-Hill, 1963, p 65. (A. V. Balakrishnan, Ed)

VII-21 *Tracking and Data System Estimated Capabilities for the Mars 1973 Mission.* JPL Document 611-1, December 1, 1968.

VII-22 Goody, Belton, and Hunt: *Quantitative Spectroscopy of Venus in the Region 8,000 - 11,000 Å.* Gordon and Beach Science Publishers Inc., 1968, pp 69-97. (edited by Brandt and McElroy)

VII-23 R. L. Hulstrom: "Optical Properties of the Venus Atmosphere." Paper given at the Joint National Meeting of AAS and ORSA, June 17-20, 1969.

VII-24 Van de Hulst, *et al.:* "Transfer of Visible Radiation through Clouds." *Journ. of Atm. Sci.*, Vol 26, No. 5, Part 2, 1969, pp 1078-1087.

VII-25 *Procurement Specification for Single Bridgewire Apollo Standard Initiator.* NASA Specification SKB-26100053.

VIII. ENGINEERING MECHANICS SUPPORTING STUDIES

A. THERMAL CONTROL

The emphasis in the thermal control portion of the study was placed on designing the thermal/structural configuration of the descent probes, and to a lesser extent, determining the requirements for the earth-to-Venus cruise phase. Entry convective and shock layer radiation heat inputs are accommodated by an ablative heat shield that is staged at M $\sim$ 0.9 before heat transfer to the descent probes takes place. The entry heat shield designs are based on JPL heat shield data and are discussed in Section B of this chapter, Chapter II, Section I, and Chapter III, Section B. The cruise and descent phase thermal control analyses that can thus be performed independently of the heat shield design are discussed in the following paragraphs.

Although the mission environments vary over a wide range, the resulting thermal control provisions are all passive or semi-passive.

The baseline design of the descent probes provides insulation to limit heat transfer from the environment, and phase change material (PCM) that acts as an internal heat sink. Cruise phase thermal control is accomplished by providing insulation on the outside of the biocanisters, with a thermal control coating yielding acceptable payload temperatures both near earth and near Venus. The component temperature limits are shown in Table VIII-1.

Upon ejection from the Mariner spacecraft, the probe aeroshells are exposed to the sun, and a surface coating is provided so that the payloads will achieve a steady-state temperature close to the minimum of the allowable range. Low payload temperatures at the beginning of the descent phase are desirable because this allows the maximum temperature increase during descent to the surface.

Table VIII-1 Component Temperature Limits

Component	Operating (°F)	Nonoperating (°F)
Electronics*	40 to 120	-35 to 160
Batteries†	40 to 130	0 to 100
Balloons§	-40 to 155	-40 to 120
Inflation Gas§	30 to 90	-60 to 120
Decelerators§		
Deployment	-65 to 275	-40 to 275
Postdeployment	-65 to 450	-40 to 275

*Standard limits for most electronics.
†Temperatures discussed in Chapter VII.F.
§Manufacturers' data.

The overall thermal control problem was broken down into a number of essentially independent parts. Each of these parts were analyzed separately with computational techniques chosen to best suit each particular situation.

The sizing of the large and small probes represents a complex problem involving many coupled effects. The heat transfer through the insulation, the internal power dissipation, the instrument weight and packaging density, the descent profile, and the structural requirements are all interrelated. This situation suggested the development of a computer program so that these coupled effects could be treated effectively and efficiently. Accordingly, a descent probe thermal/structural program was developed for the IBM 1130 computer.

The thermal control of the high-cloud and balloon probes presented a relatively simple problem because these probes are not designed to function to the planet surface and are not subjected to a severe environment. Therefore, satisfactory analyses were carried out by hand calculations.

The cruise phase was investigated using a radiation analyzer program (MTRAP) and a thermal analyzer program (CINDA). The radiation analyzer program was used to establish the internal view factors and this information was, in turn, used as input to thermal models that were analyzed with CINDA.

A number of the science instruments were given individual attention relative to their thermal design. Both CINDA and hand calculations were used in this area.

CINDA was also used to investigate an alternative approach to the double-walled probe configuration.

A number of auxiliary studies were performed during the course of this effort. These include the development of a CINDA subroutine for the thermal modeling of PCM, an investigation of pressure canister temperature gradients, and an investigation of the thermophysical properties of the Venus atmosphere.

1. Cruise Phase

Prior to descent into the Venusian atmosphere the probes are subjected to two distinctly different environments. During the cruise to the planet, prior to deflection, the probes are located in individual biocanisters attached to the truss structure. The probe payloads must be maintained between 40° and 120°F while the solar constant increases by a factor of nearly two.

The second environment occurs after the probes are deflected toward their targets. They are ejected from their biocanisters and are exposed directly to the sun before starting descent.

Since the first environment is variable over a long time period and the second is essentially constant and lasts for a relatively short time, the thermal control requirements for each was considered separately.

a. Preseparation - The preseparation cruise configuration, shown in Fig. VIII-1, has the forward end of the large probe pointing at the sun. The three other probes are mounted 90° from the large probe roll axis, and thus receive solar impingement on one side of their biocanisters. The probe interiors must be maintained between 40° and 120°F while the solar constant increases from 442 Btu/hr/ft^2 near earth to 850 Btu/hr/ft^2 near Venus. It was decided to analyze this phase on a steady-state basis (with CINDA) for two conditions -- near earth and near Venus. Midcourse correction attitudes were neglected, which is a valid assumption given the thermal control system dictated by the nominal attitude.

Constrained by the Planetary Vehicle configuration and attitude and the environmental requirements, the indicated approach was to determine if some combination of insulation and thermal control coatings could keep the probes warm enough at earth and cool enough at Venus. The Venus requirement dictated the design, and the analysis provided for heaters to be added to the near-earth condition, if required. Because the three inboard probes have essentially the same environment, only one small probe was analyzed, along with the large probe.

The first step in the analysis was to determine the probe's internal black-body view factors. The MIRAP computer program was used, and a plot used to check the input data is shown in Fig. VIII-2. The Mariner bus and the solar panels are included. The external view factors were computed by hand because many simplifying assumptions could be made. Although the backs of the probes "see" each other, the Mariner bus, and to a small extent, the solar panels, no heat transfer paths were provided other than conduction through the insulation and radiation to space. The probe's backsides and the +Z end of the bus should be at nearly the same temperature, and the solar panels, although relatively hot, have very small view factors to the probes.

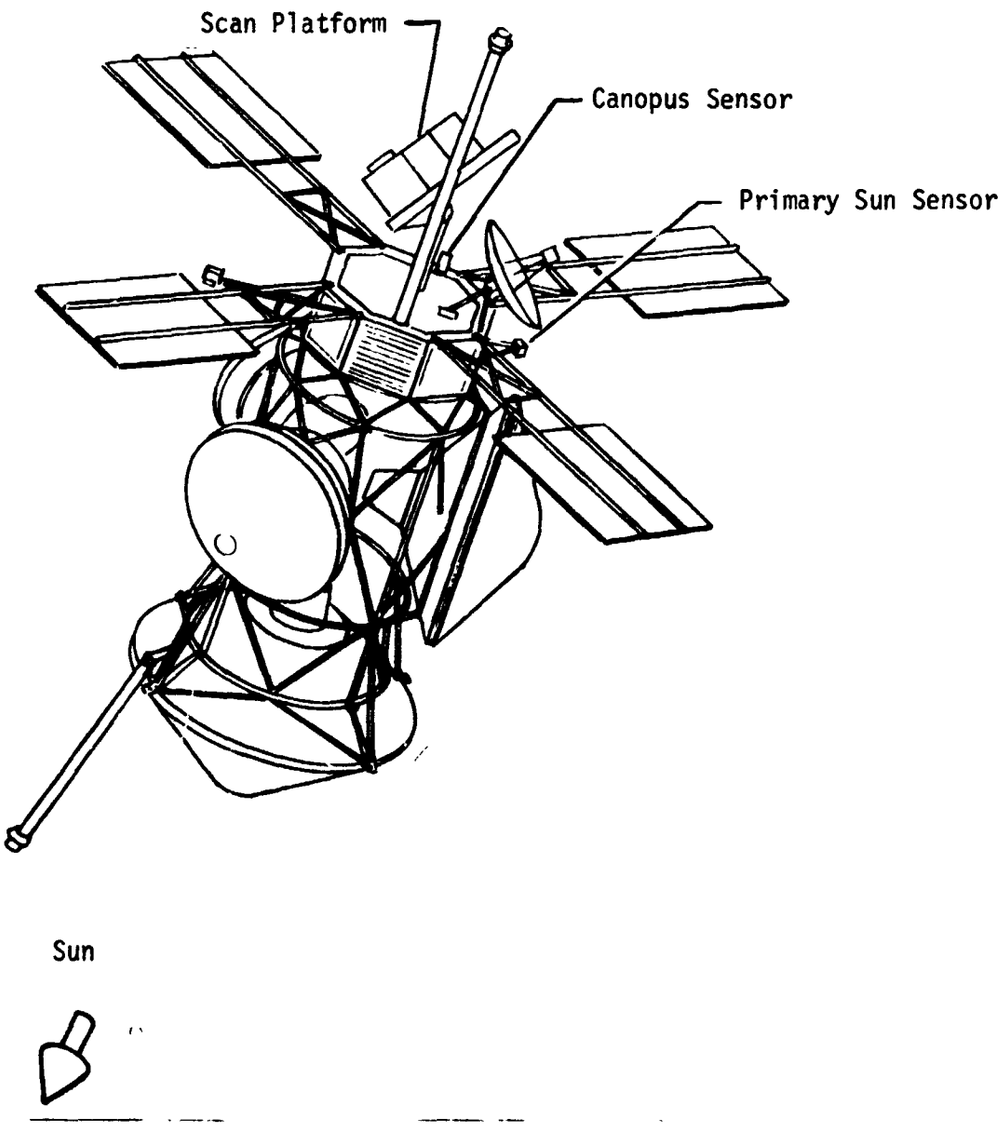


Fig. VIII-1 Planetary Vehicle Characteristics

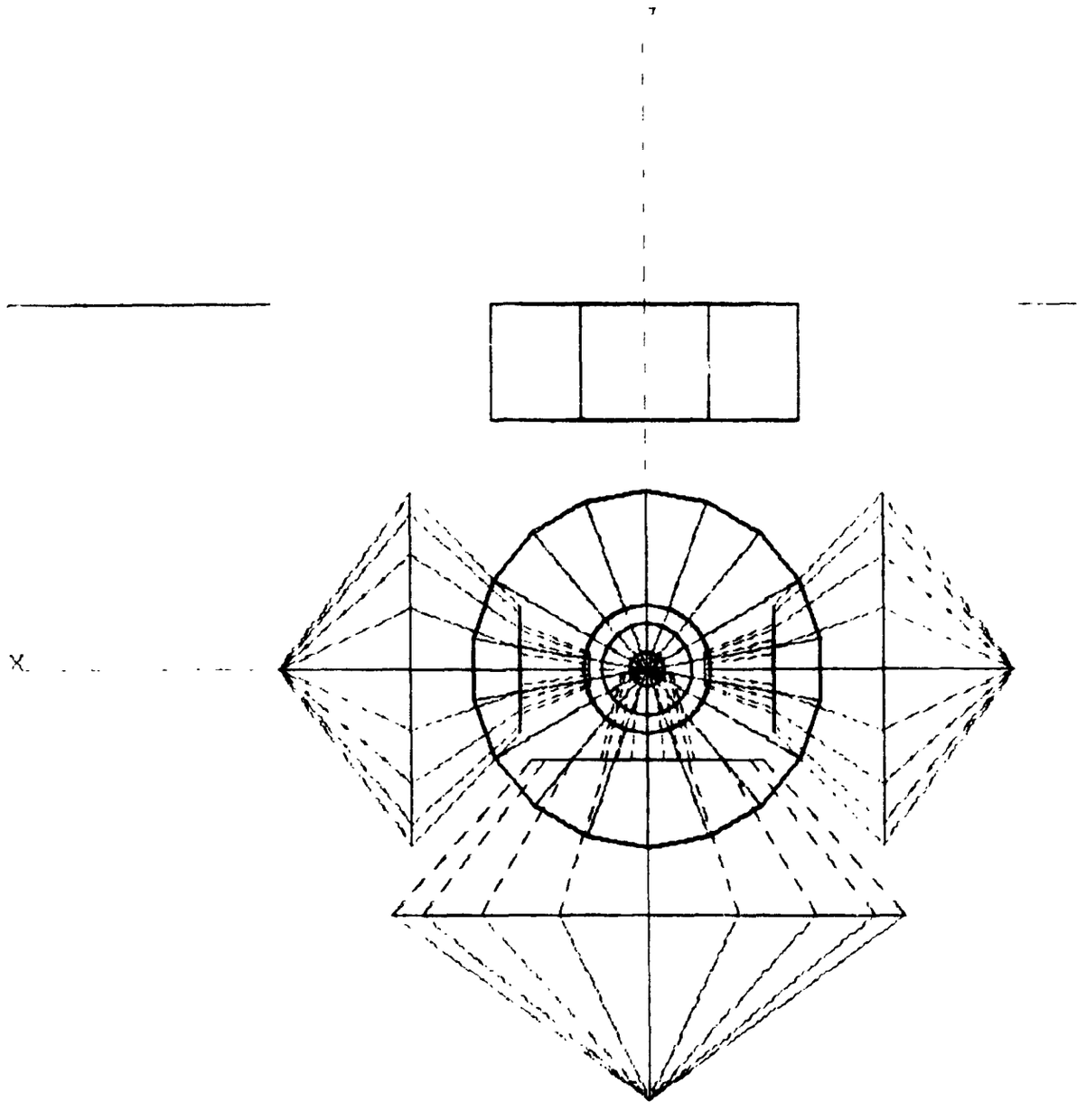


Fig. VIII-2 Computer Plot of Planetary Vehicle Surfaces

The insulation was placed on the outboard side of the biocanisters, and properties for 20 layers of 1/4-mil crinkled goldized Kapton were used. Properties for the thermal control coating were then parameterized to determine the corresponding probe equilibrium temperatures at earth and Venus. The insulation was so efficient that everything inside it reached the same temperature, allowing use of a relatively simple thermal model. With insulation on the outside, the midcourse correction becomes an insignificant transient effect. The cases that were run are plotted in Fig. VIII-3, showing the effect of solar absorptance/infrared emittance (α/ε) on the probe's internal temperature. An α/ε near 2.75 can maintain both probes within their temperature limits both near earth and near Venus with no additional heating or cooling requirements. Keep in mind that this analysis was based on many estimates, and that a more detailed analysis may result in a configuration that requires power from the bus to maintain minimum temperatures near earth.

In conclusion, the recommended thermal control configuration for the preseparation cruise phase consists of 20 layers of 1/4-mil goldized Kapton on the outside of all the biocanisters, with an outside cover having a coating with $\alpha/\varepsilon = 2.75$. This value is typical of several polished metals, such as Rene 41, 347 stainless, and Mg-Li alloy 9-1.

Spacecraft Interface - As described in Chapter IV.A, the probes are to be located on the sunlit side of the Mariner spacecraft, along the +Z axis. Addition of the probes to the Mariner '69 20a configuration could possibly affect the thermal radiative environment of the louvers on the bus. The present bus design provides for minimal influence on the louvers from the remainder of the spacecraft, and to retain this degree of isolation might require moving the solar panels to the +Z edge of the bus and inverting the louvers. This should be investigated.

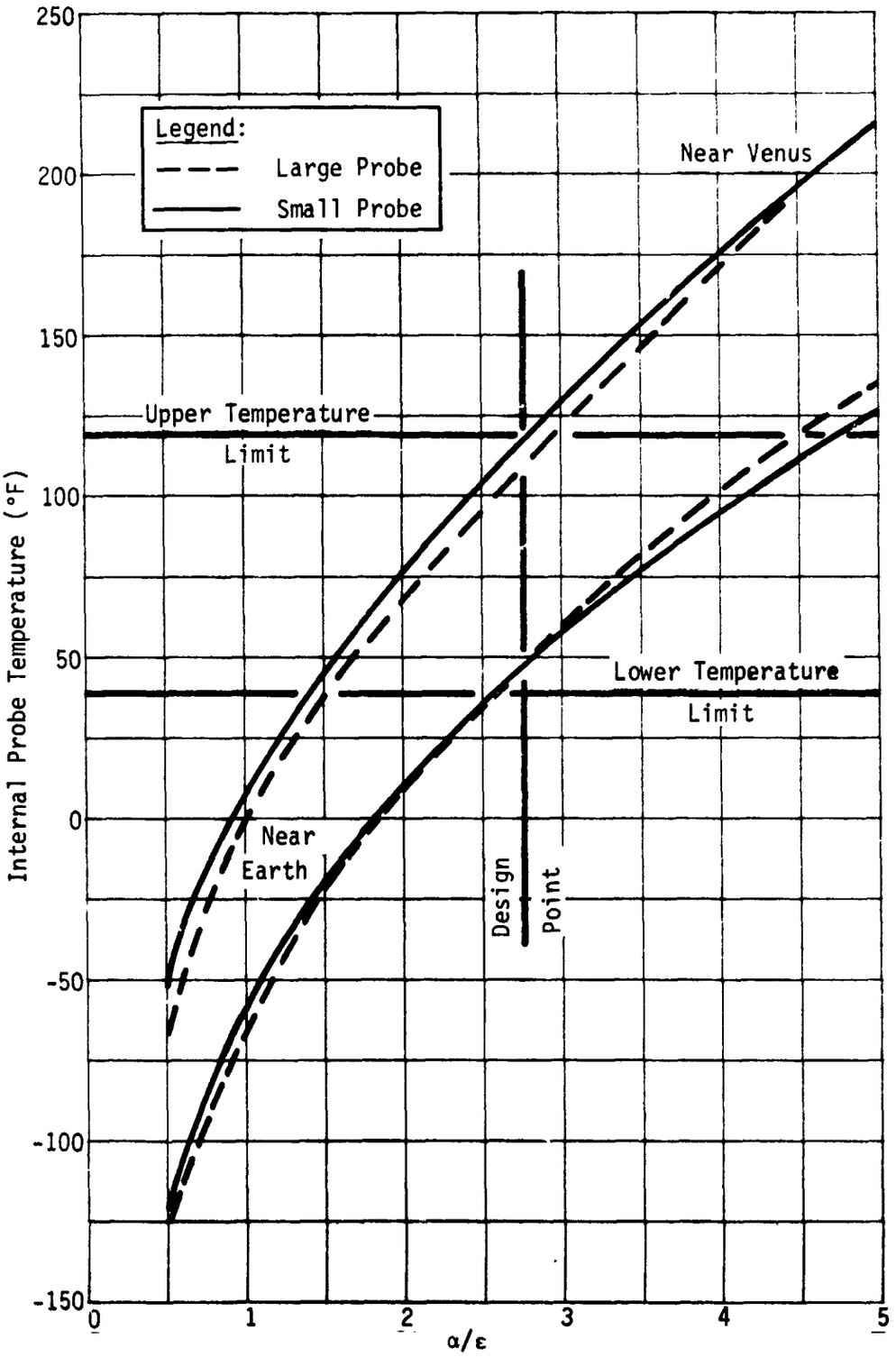


Fig. VIII-3 Probe Cruise Temperature vs α/ε

Another factor that might affect the louver performance is the deflection sequence, described in Chapter V.C. The Planetary Vehicle attitude during the sequence is such that the louvers will receive some solar exposure in excess of their design value. The solar constant at the location of the maneuver is 1.9 suns, although no bay faces are normal to the sun except instantaneously during pitch turns. Out of a total sequence time of 2.08 hr, most of the initial time is spent at pitch angles of 17° and 9° while rolling, which means the exposure per louver is very small. A subsequent 500 sec pitch maneuver goes through 90° and holds at 15° off normal for about 10 minutes, before rolling for about 17 minutes. The final pitch turn goes back through 90°. The 10-minute attitude hold is the worst-case condition. Although it is felt that this condition is short enough that it will not affect the Mariner design, it should be verified.

2. Postseparation Phase

At separation the probes are ejected from their protective biocanisters and are directly exposed to the sun during their approach to the planet.

It was found that the internal temperature of each probe could be brought to and maintained at the lower operating temperature limit (40 to 50°F range) before entry regardless of its temperature at separation through the proper selection of thermal coatings. A low initial temperature for atmospheric entry is desirable, because the thermal control system relies on the thermal capacitance of the probe to limit the temperature rise of the internal electronics.

A thermal model of the large probe in the postseparation configuration (with aeroshell) was constructed to determine how long it would take the probe to cool from a maximum initial temperature of 120°F. This temperature, which corresponds to the maximum

operating temperature limit, may be attained as the probe nears Venus in the cruise phase before separation. A diagram of the thermal model is shown in Figure VIII-4. Only the large probe was considered, because it had the largest time constant.

Coating properties were selected that would give the probe a steady-state temperature of about 48°F. The nominal orientation for all the entry probes has the solar vector about 80° off the V_{HE} vector. To bracket this condition two orientations were considered: the solar vector normal to the deflection motor and the solar vector 90° from the deflection motor. These orientations required respective α/ε ratios of 0.30/0.85 and 0.75/0.85 because the cross sectional area presented to the sun changes with orientation as does the influence of internal thermal coupling. Although these orientations do not represent actual orientations they do represent extreme cases. Since the α/ε ratios required for these cases can be obtained with available coatings or combinations of coatings, the selection of coatings will not be a problem. Coating degradation should not be a problem either, because the probe will only be exposed to the sun for about 300 hr.

Figure VIII-5 shows the transient response of the large probe after separation as it cools to its equilibrium temperature determined by its solar orientation and aeroshell coating properties. The response is essentially the same for both orientations, since the thermal time constant of the probe is the dominating factor. The step in the curve is caused by the freezing of the PCM. The curve shows that the probe essentially reaches steady-state in the 300 hr (nominal) between separation and entry. The temperature of the probe just before entry thus can be set at any reasonable desired temperature independent of the temperature at separation.

Although the effects of planetary albedo and emission were not included they would have some effect on the α/ε combination chosen, but would not change the basic approach.

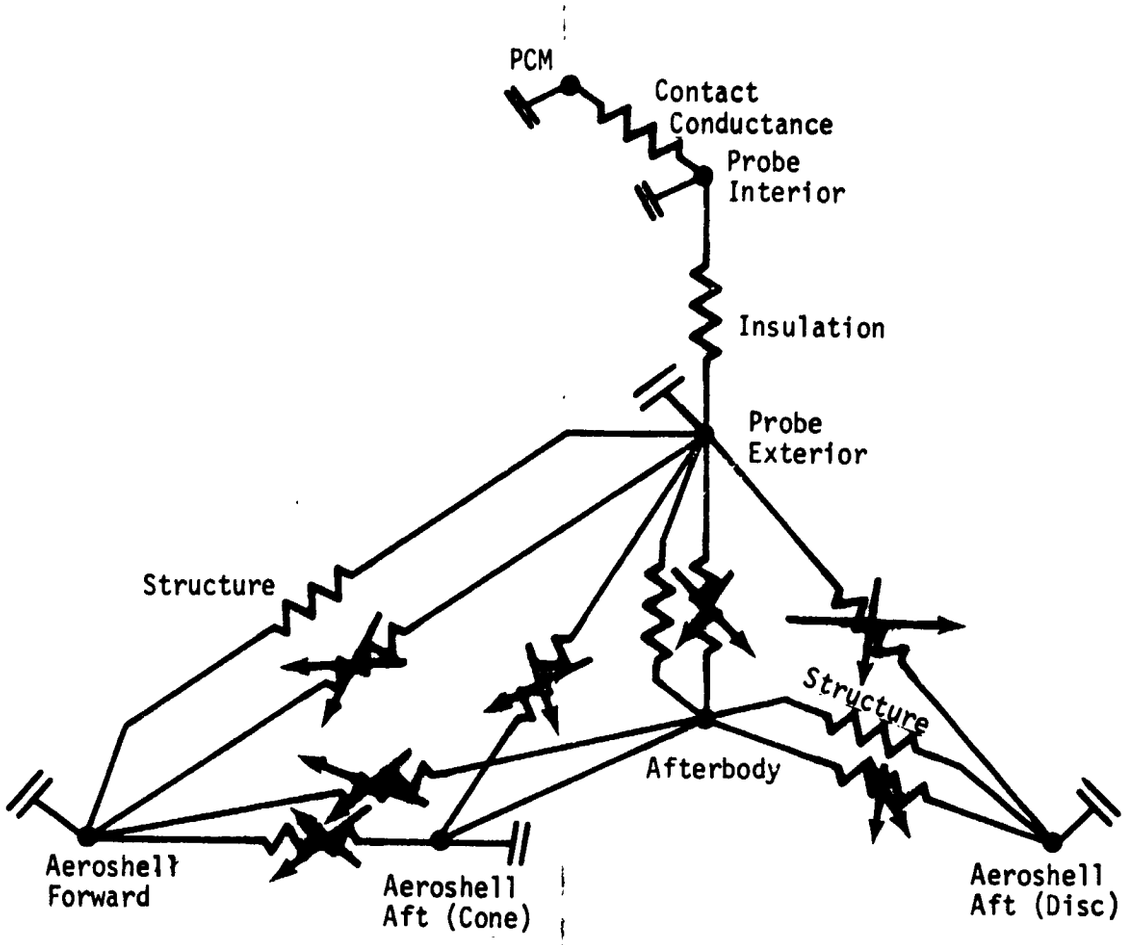


Fig. VIII-4 Large Probe Postseparation Thermal Model

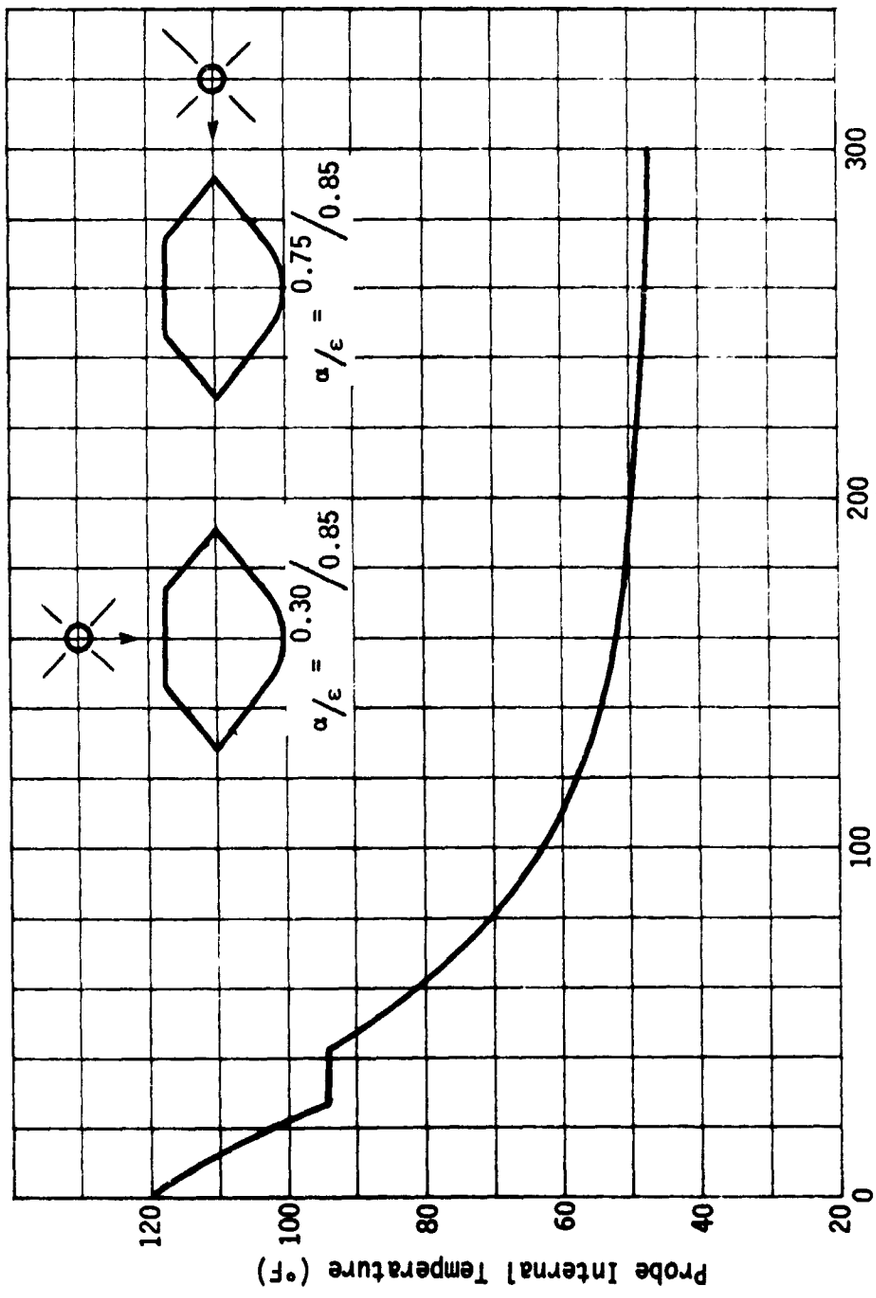


Fig. III-5 Postseparation Cooling of Large Probe

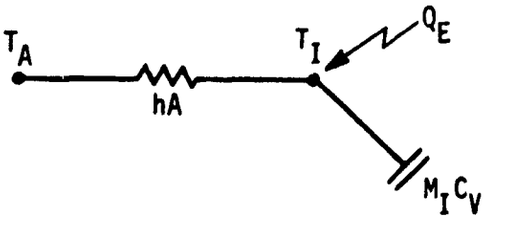
3. Descent Phase

a. High-Cloud and Balloon Probes

High-Cloud Probe - The high-cloud probe is designed to begin its terminal descent at a radius of 6127 km and function from this altitude to a radius of 6105 km. Assuming a V5M atmosphere, the descent time is 68 minutes, while the ambient temperatures corresponding to the beginning and end of the descent are -39°F and 72°F, respectively. The mass of science instruments and communication equipment is 69.9 lb_m. Electrical power dissipation was assumed constant at 123.2 W.

A thermal analysis of this probe was performed assuming that the atmospheric temperature varies linearly and that the film coefficient between the atmosphere and probe surface was constant with a value of 2 Btu/(hr-ft^2-°F). Also, it was assumed that no provision is made for thermal control, such as insulation or PCM.

The thermal network which represents this problem is given in Fig. VIII-6.



Q_E = electrical dissipation

h = film coefficient

A = probe surface area

M_I = mass of instruments and communication equipment

C_V = average specific heat of instruments and communication equipment

T_A = atmospheric temperature, assumed linear with time

T_I = temperature of payload

Fig. VIII-6 High-Cloud Probe Thermal Network

Applying a heat balance results in the equation:

$$hA\left(T_A - T_I\right) + Q_E = M_I C_V \frac{dT_I}{d\tau}$$

where τ is time.

The solution of this equation is given by:

$$T_I' = T_{I_i}' \frac{-hA\tau}{eM_I C_V} + \frac{Q_E}{hA}\left(1 - \frac{-hA}{eM_I C_V}\right) + \frac{M_I C_V \alpha}{hA}\left(\frac{-hA\tau}{eM_I C_V} + \frac{hA\tau}{M_I C_V} - 1\right)$$

where

T_{I_i}' = scaled initial payload temperature = $T_{I_i} - T_{A_i}$,

T_{A_i} = initial atmospheric temperature,

T_I' = scaled payload temperature = $T_I - T_{A_i}$,

T_A = scaled payload temperature = $\alpha\tau$,

τ = time,

α = slope of assumed atmospheric temperature-time curve.

Using this equation and assuming that T_{I_i} is 60°F, one finds that the payload temperatures will remain within limits during the probe descent. A plot of the payload temperature vs time is given in Fig. VIII-7. Note that a temperature of 60°F is certainly realizable for an initial payload temperature. This is achieved by selecting a thermal control coating on the aeroshell which yields this temperature as the equilibrium temperature during coast to the planet following separation. This is discussed in Section A.1 of this chapter, Cruise Phase Thermal Control.

Balloon Probes - Option 1 and Option 2 of the proposed mission call for a 500 mb and 50 mb balloon, respectively. The environments which these balloons will experience are given in Table VIII-2.

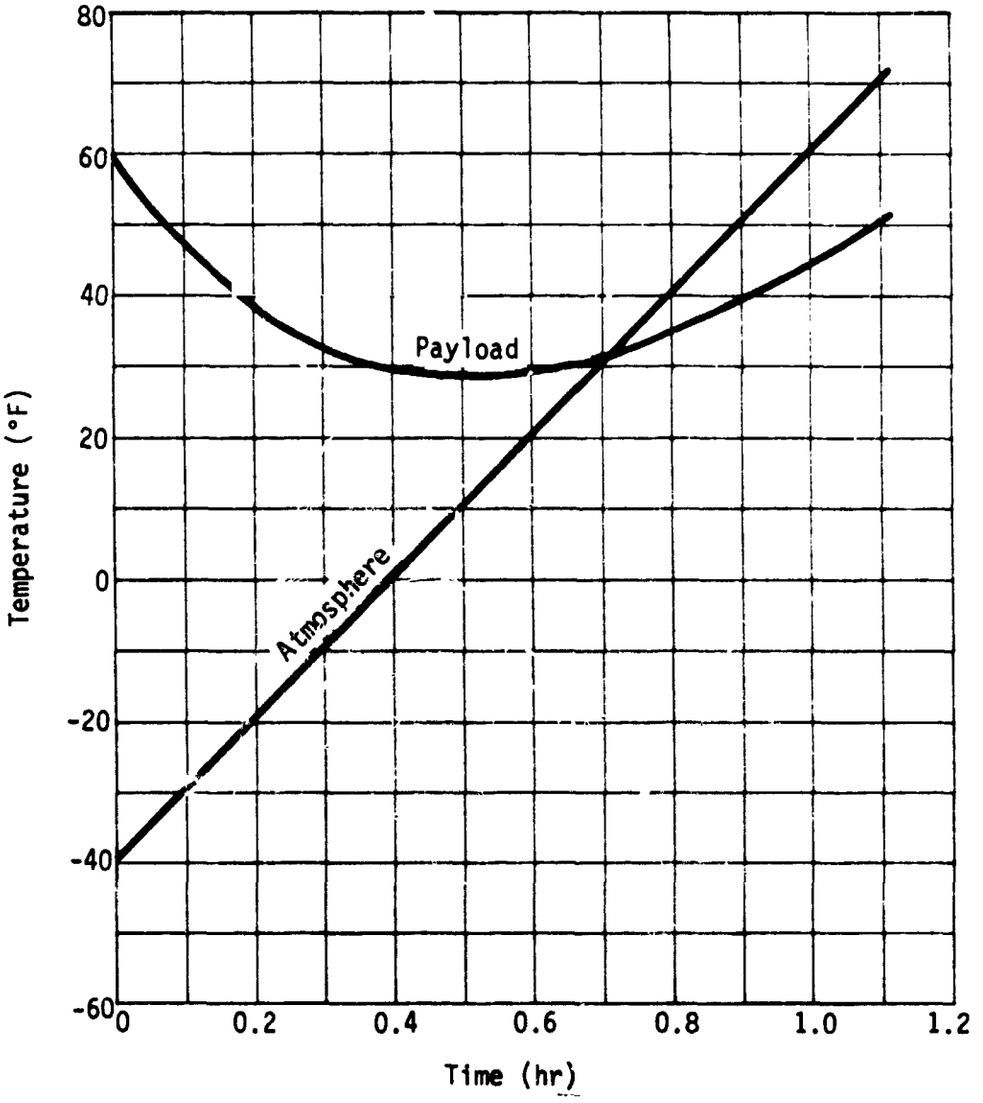


Fig. VIII-7 High-Cloud Probe Temperature History

Table VIII-2 Balloon Probe Environments

	MMC-Lower		V5M	
Balloon	Planet Radius (km)	Temperature (°F)	Planet Radius (km)	Temperature (°F)
50 mb	6120	-33	6123	-20
500 mb	6107	64	6110	26

The range of temperatures the 500 mb balloon will experience are such that no special thermal control provisions are required. It is recommended, however, that the exterior surfaces of the instrument package have low solar absorptivity, low IR emissivity values so that the convection with the local environment dominates radiation. Even though this radiation coating would probably have little effect on equilibrium temperatures it is recommended, because the radiation environment is unknown under the clouds.

Both the 50 and 500 mb balloons transmit data at relatively high-power levels over short time periods. The instrument temperature rise during the 7-minute data transmission period is on the order of 1°F and consequently no thermal control is required for these transient conditions.

The nominal float altitude of the 50 mb balloon places it in the range of the anticipated cloud tops. Because of this, the balloon might be above or below the cloud tops. Further, if the balloon is relatively far beneath the clouds it will be subjected to an unknown radiation environment. Because of these unknowns a relatively conservative approach was taken in providing thermal control for the 50 mb balloon. Accordingly, two extreme steady-state design conditions were chosen that will result in a system design of high confidence.

First, the balloon was considered above the clouds with direct solar heating, albedo from the planet, and surface emission from the top half only of the instrument package. For this situation convection from the ambient gases is neglected. This situation corresponds to a worst-case condition relative to high temperatures. Assuming the instrument package is spherical, the radiation energy balance is:

$$T = \left(\frac{\alpha}{\varepsilon}\right)^{\frac{1}{4}} \left(\frac{G_S + G_A}{2\sigma}\right)^{\frac{1}{4}}$$

where

T = surface temperature (°R),

α = solar absorbtivity,

ε = IR emissivity,

G_S = solar flux,

G_A = albedo flux,

σ = Stephen-Boltzmann constant.

For an $\alpha/\varepsilon = 0.2$ the previous equation yields a surface temperature of 70°F. Since convection from the cold environment is neglected, this represents a maximum temperature. Also, note that the α/ε of 0.2 is certainly realizable with existing coatings.

With a high-side limit on temperature established, the other extreme was now investigated. For the low temperature condition, imagine the instrument package beneath the clouds with no radiation exchange and with the ambient temperature imposed on the outer surface of the package. For this situation the steady-state heat transfer through the insulation is calculated to determine the electrical heating required to maintain the instrument temperature within the operating range. Here, preliminary calculations indicated the necessity of providing a vacuum insulation system. Therefore, a double-walled instrument package is required. The steady-state heat transfer equation for this condition is given by:

$$Q = \left[\left(\frac{KA}{\Delta X}\right)_P + \left(\frac{KA}{\Delta X}\right)_I\right] \Delta T$$

where

$\left(\frac{KA}{\Delta X}\right)_P$ = conductance of penetrations,

$\left(\frac{KA}{\Delta X}\right)_I$ = conductance of insulation,

ΔT = temperature difference between inside and outside of insulation.

Estimating the penetration conductance as 0.06 Btu/(hr-°F) and assuming an insulation conductivity of 0.0004 Btu/(hr-ft-°F) (multilayer insulation), 1 in. of insulation yields a heat loss of 1.64 W. This value corresponds to a temperature difference of 63°F, and assumes the amplifier is operating.

In summary, the thermal control requirements for the 50 mb balloon probe consist of a surface coating with an α/ε of 0.2, 1 in. of multilayer insulation and a 2.2 W thermostatically controlled heater, to maintain temperatures between 30° and 70°F.

b. Large and Small Descent Probes - The basic approach relative to the thermal/structural design of the large and small probes is a double-walled canister. The inner canister houses the communications equipment and most of the science instruments, while thermal insulation is located in the evacuated region between the inner and outer canister walls. An environment of sulfur hexafluoride (SF_6) is maintained in the instrument canister at one atmosphere of pressure. This gas provides an excellent environment relative to the electronics and also offers a heat transfer path between the various instruments. Coupling the instruments thermally with a conducting/convecting environment will tend to suppress local hot spots.

The double-walled canister approach provides a vacuum region that allows the use of extremely effective multilayer thermal insulation. However, the manufacture and assembly of the double-walled canister arrangement would certainly present problems. Also this approach causes the outside canister wall to be subjected to both high temperatures and high pressures. An alternative approach uses insulation outside a single-walled canister, and although the insulation performance is degraded by the atmosphere, the pressure canister operates at relatively low temperatures. This outside insulation approach is discussed in subsection 8 of this section.

Probe Weight Program - Because of the lengthy calculations involved in sizing the descent probes, a computer program was devised to handle these computations. The digital program provided a means of rapid response to changes in basic parameters and, also, allowed sensitivity studies to be easily performed. The program was written in Fortran II and was run on an IBM 1130 computer.

A flow chart of the Descent Probe Thermal and Structural Design Program is given in Appendix J. In general, the program takes as input the characteristics and properties of the planet atmosphere, the mass of instruments to be carried, the aerodynamic characteristics of the probe, thermal and structural material properties, and then computes the overall descent probe weight.

The first step in the program is the computation of the descent profile. This computation is carried out beginning with the chute deployment at a given arbitrary altitude and ballistic coefficient. The program allows, then, a step change in ballistic coefficient at any altitude between chute deployment and the planet surface. This feature simulates release from the chute.

The next step in the program is the computation of the probe internal volume and outside diameter. Basic input data required for these calculations are the payload mass, payload packaging density, insulation thickness and probe length/diameter (L/D) ratio. (The probe is assumed to be made up of two spherical ends joined together by a cylindrical center section which gives accurate enough estimates for the pressure shell. An L/D of unity represents a spherical probe.) The program is designed so that for a given run the insulation thickness and L/D can be varied from initial values, stepping in even increments to maximum values. This allows total probe weights to be computed as a function of both insulation thickness and L/D with a single computer run. Having a value for D allows the specification of outside surface area and effective insulation area. Also, at this point the program determines the weight of the pressure vessel by applying hoop stress and buckling equations, basing the weight on the criteria that require the maximum wall thickness (see Section B of this chapter).

With the descent profile (altitude vs time), probe geometry, and insulation configuration specified, a heat transfer analysis is carried out in order to determine the heat transfer through the insulation. The thermal model used for this analysis is given in Fig. VIII-8. The computational method used is a backward-differencing or implicit technique.

The main features of the heat transfer analysis include provisions for solar heating, probe surface emission to deep space, and radiation from the cloud tops during the descent above the clouds. Once below the cloud tops, black body radiation is assumed from the local ambient atmosphere. Throughout the entire descent, convective heat transfer is calculated between the probe surface and the local atmospheric gases. At each computation step an average exterior film coefficient is calculated using the equation:

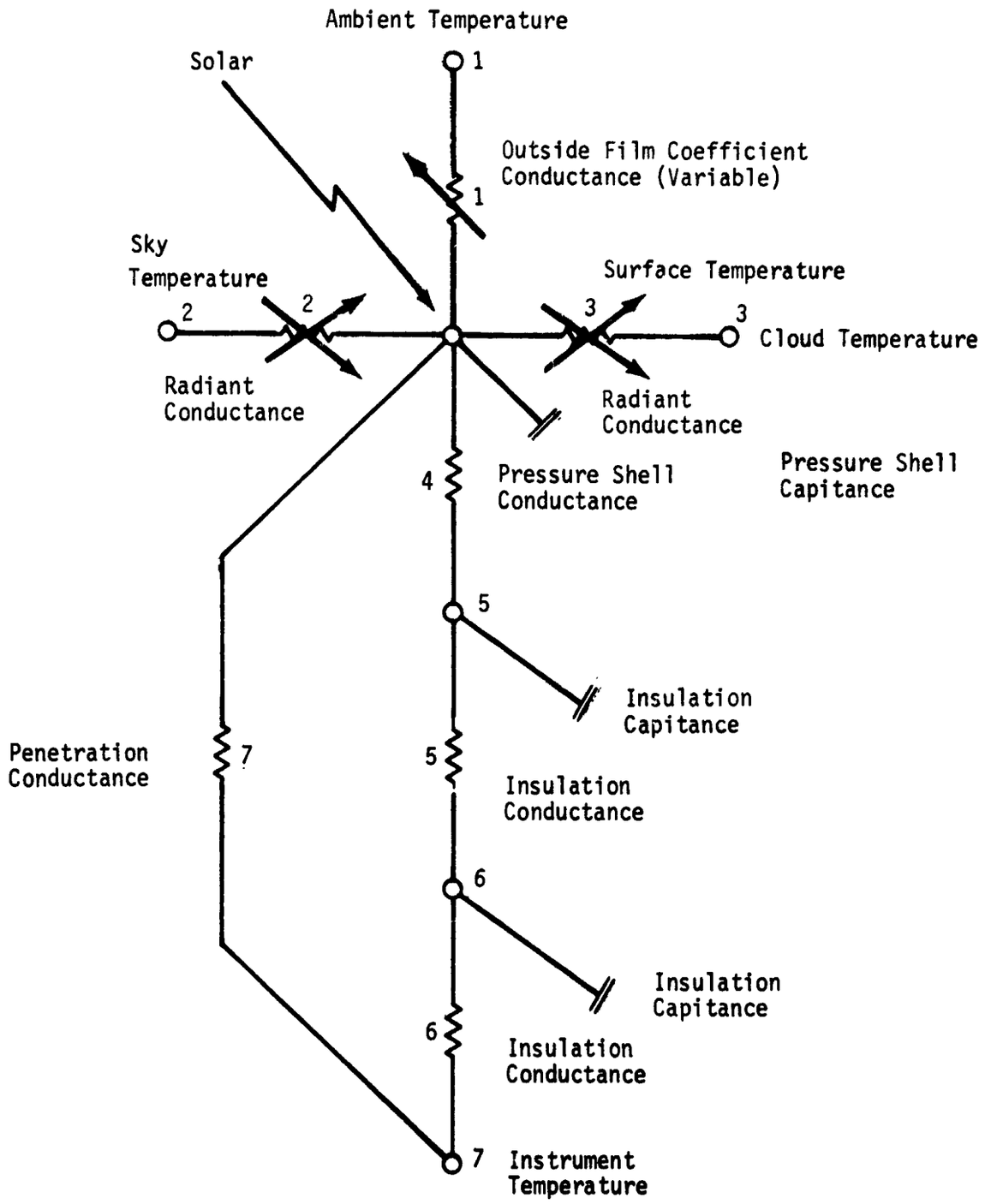


Fig. VIII-8 Thermal Model Used in Descent Probe Thermal and Structural Design Program

$$h = \frac{k}{D}\left(2. + 0.6\ Re^{1/2}\ Pr^{1/3}\right)$$

where

Re = Reynolds Number, $\rho VD/\mu$,

Pr = Prandtl Number, $\mu C_p/k$,

h = Film coefficient,

D = Probe diameter,

k = Thermal conductivity of the atmosphere,

ρ = Density of the atmosphere,

μ = Viscosity of the atmosphere,

C_p = Specific heat of the atmosphere,

V = Probe velocity.

Forced convection aspects of the descent phase are discussed in detail in subsection 6, following. The radiation properties chosen for this study represent approximate values; however, since the heat transfer is dominated by convection, a more accurate evaluation of radiation properties was not warranted.

The effective conductivity of the multilayer insulation is strongly affected by the number and nature of penetrations made through it. The effect of these penetrations has been accounted for by providing conduction paths for the penetrations (lumped together) in the thermal model. For example, the large probe provided paths for the strap and lateral supports, the antenna coax, electrical leads, and six science instruments. The lumped conductance for the penetrations for the large probe is approximately ten times as large as the conductance through the insulation. The penetration conductances are listed in Append. J (Vol III).

Once the heat transfer through the insulation is determined, a heat balance is applied to establish the mass of PCM required to limit the payload to a prescribed temperature increase. For both the large and small probes an independent heat balance was applied to each payload component that dissipates electrical energy. This was done to determine the required location of PCM and to supplement the gross calculation performed in the program. For the baseline design, the results of the calculations for individual instruments for the large probe matched the results of the program, since the heat transfer through the insulation was not included in the individual calculations. However, the program indicated no PCM requirement for the small probe, while the computation based on individual instruments resulted in 2.5 lb. These results would have agreed if a more detailed thermal model had been analyzed by the program. The 2.5 lb was used in the weight statement in Chapter III.B.

Sensitivity Studies - The probe weight program was used throughout the study to investigate many aspects of the thermal/structural design problem. The sensitivity of probe weight relative to changes in L/D and insulation thickness is illustrated in Fig. VIII-9. For an L/D of 1.5, Fig. VIII-10 shows the variation in structure, PCM, and insulation weights as functions of insulation thickness. Figure VIII-11 shows the sensitivity of probe weight relative to the effective conductivity, allowable temperature rise, and equipment packaging density. This curve illustrates that packaging density has a relatively large influence on total probe weight because it establishes the diameter of the heavy pressure vessel. It can also be seen that permitting a greater temperature rise of the equipment than the design value of 60°F used for the trial mission would not significantly reduce the capsule weight, however, attempting to hold a much smaller ΔT would cause

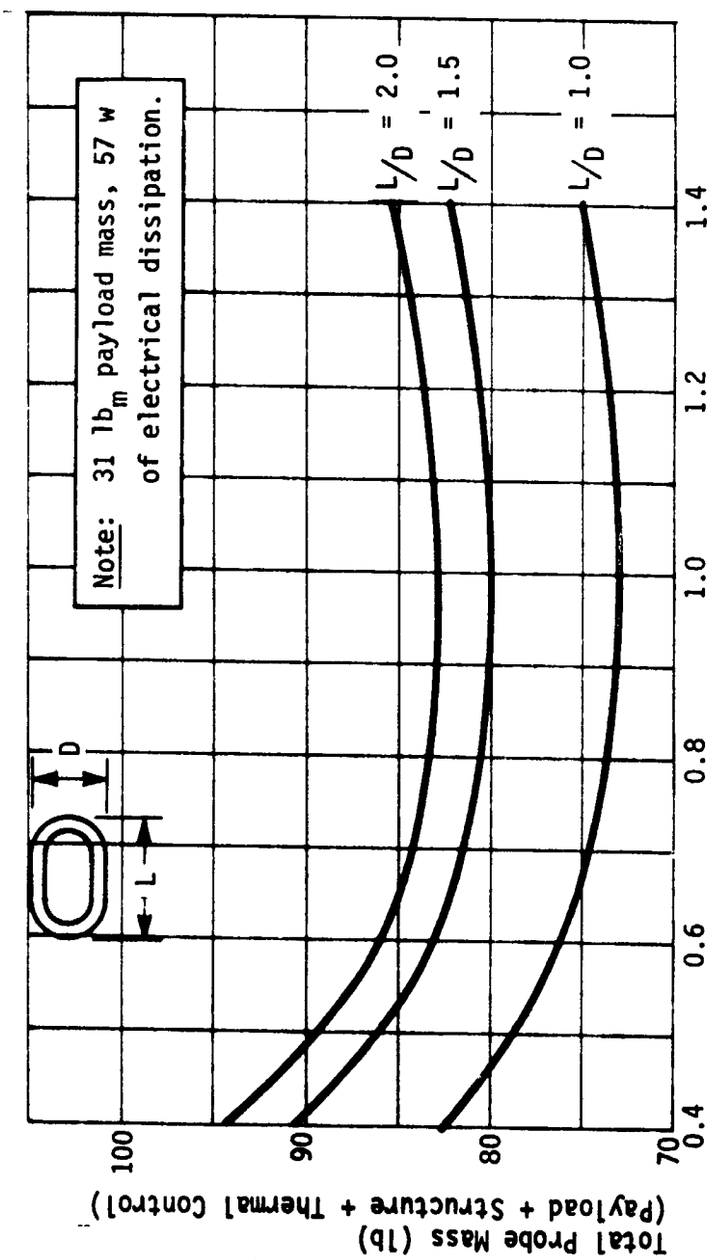


Fig. VIII-9 Influence of Probe Geometry and Insulation Thickess on Probe Weight

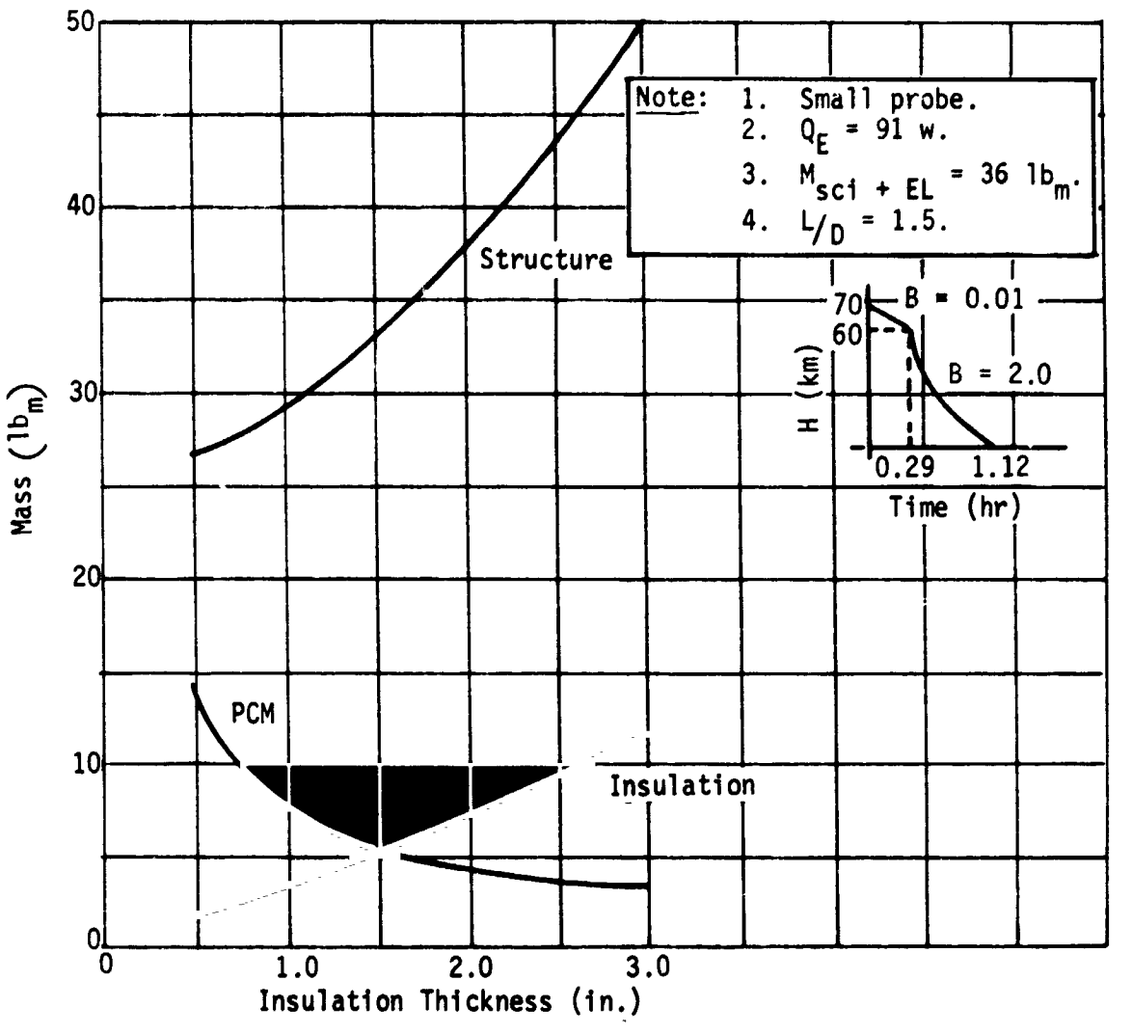


Fig. VIII-10 Variation in Thermal Structural Weights with Insulation Thickness

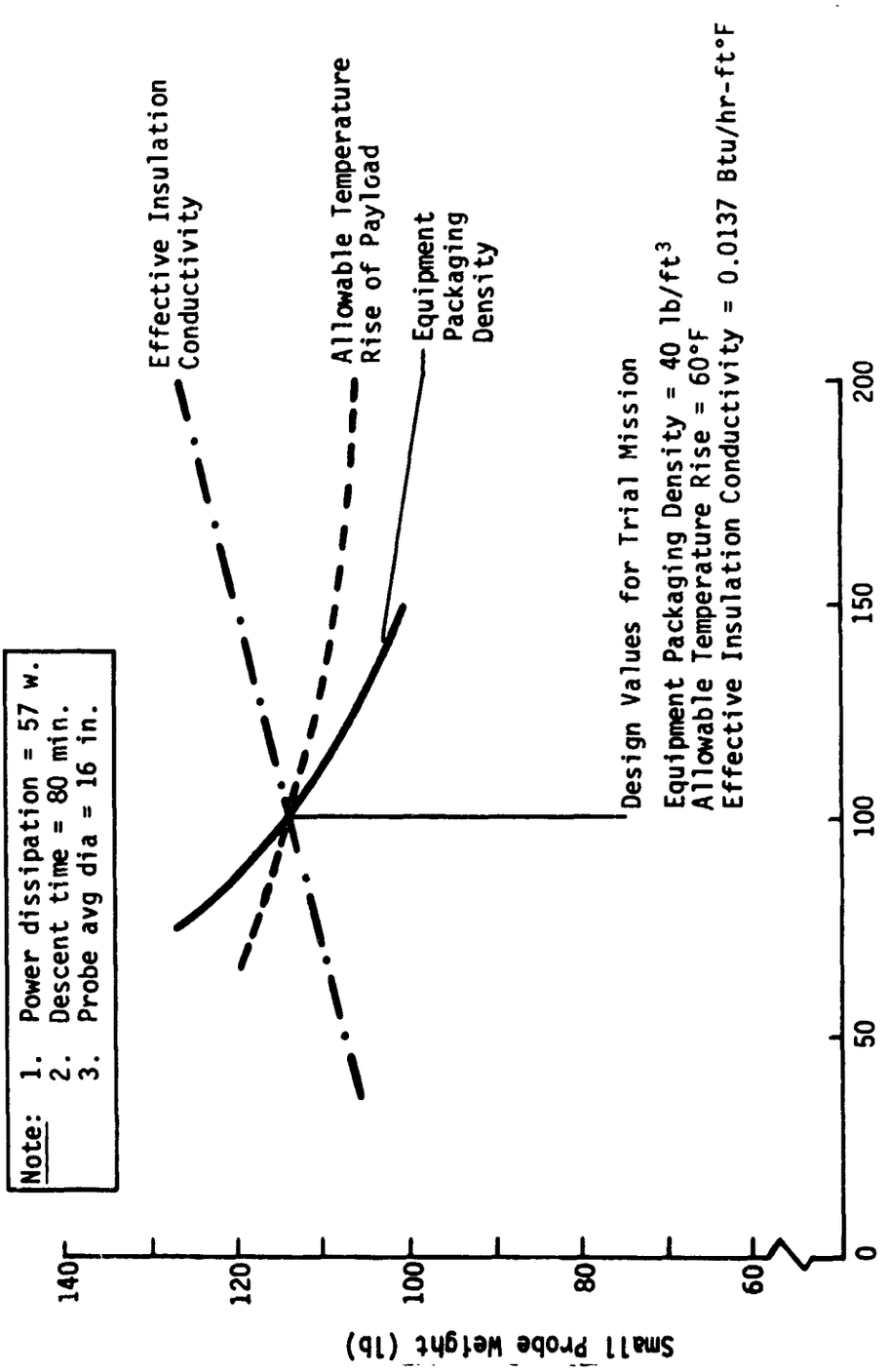


Fig. VIII-11 Sensitivity of Descent Probe Weight to Design Parameter Variation

a substantial weight increase. The effective insulation conductivity is difficult to estimate at this time since this quantity is strongly affected by insulation penetrations. Such penetrations must be minimized or designed to provide poor conduction paths. Figure VIII-12 shows the effect of various descent profiles on probe weight. The decrease in weight achieved by increasing the ballistic coefficient of the descent probes levels off at a value of about 2.0 slug/ft^2. Note that the difference in probe weight corresponding to the V5M and MMC-Lower atmospheres is approximately 13%.

Baseline Design - The input and output data for the computer program corresponding to the final configuration is given in Appendix J. Also included in the appendix is a program listing and additional details about the program.

4. Thermal Control of Individual Science Instruments

Thermal control analyses were performed on a gross payload basis, although three instruments on the large probe required special attention. The instruments were the evaporimeter/condensimeter, the solar and thermal radiometer, and the radar altimeter.

a. Evaporimeter-Condensimeter - The evaporimeter-condensimeter is used to measure the temperature at which various atmospheric constituents condense. This is accomplished by directing a small atmospheric flow past a thermoelectrically cooled mirror. Since any condensation that might occur on the walls (upstream from the mirror) or windows of the instrument would cause errors, they must be maintained above the ambient temperature. Three watts of power would be sufficient to maintain the windows and walls 25°C above ambient.

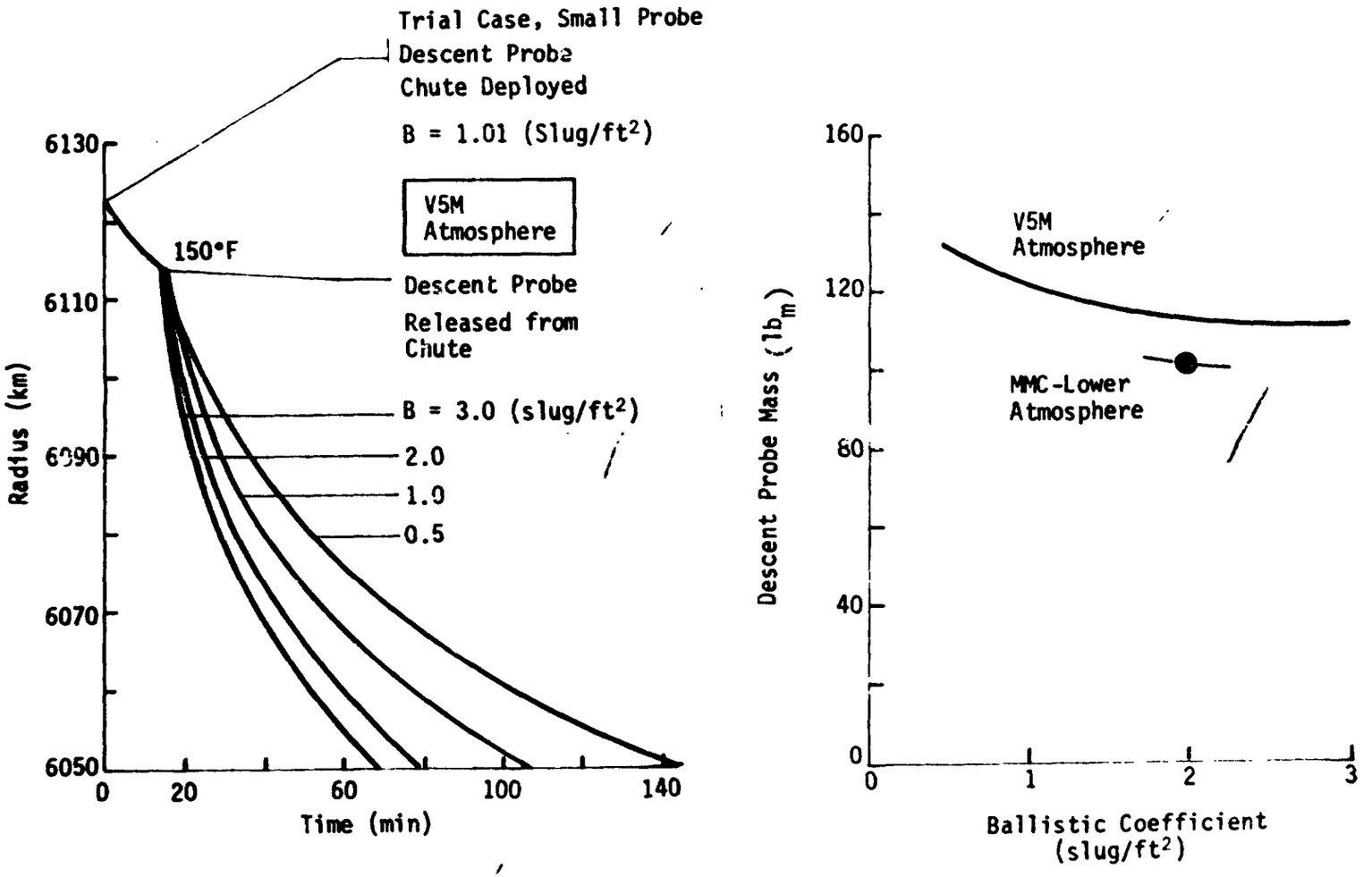


Fig. VIII-12 Sensitivity of Descent Probe Weight to Subsonic Descent Profile

The thermoelectric device used to cool and heat the mirror has a low coefficient of performance (heat removed/power required) at low temperatures. At high altitudes, where low temperatures are incurred, 0.25 W would be required to maintain the mirror 25°C below ambient (allowing 0.5 W for transient cooling). As the ambient temperature increases, the coefficient of performance improves considerably, resulting in perhaps an order of magnitude reduction in the power required. The thermoelectric device can also be used to heat the mirror by reversing the flow of current.

b. Solar Radiometer and Thermal Radiometer - The solar radiometer and the thermal radiometer are contained in a spherical pressure vessel (mounted external to the probe) with six windows and a window-wiping mechanism. The pressure vessel will contain sensing elements and their associated preamplifiers, with the remaining electronics located inside the probe.

The radiometer will be evacuated so that multilayer insulation can be used to insulate the internal components from the instrument walls. One-third pound of PCM will be required to maintain internal temperatures within acceptable limits. The sensors can be maintained at a constant temperature (below 300°K) with thermoelectric devices using PCM as a heat sink. A maximum power of 1 W will be required for these devices.

c. Radar Altimeter - The radar altimeter is mounted in the nose of the probe separate from the bulk of internal equipment; therefore it must be provided with its own means for thermal control. A thermal model of the probe nose was constructed to determine the amount of PCM that would be required to hold the altimeter temperature below its maximum operating limit of 240°F. A diagram of the thermal network is shown in Fig. VIII-13.

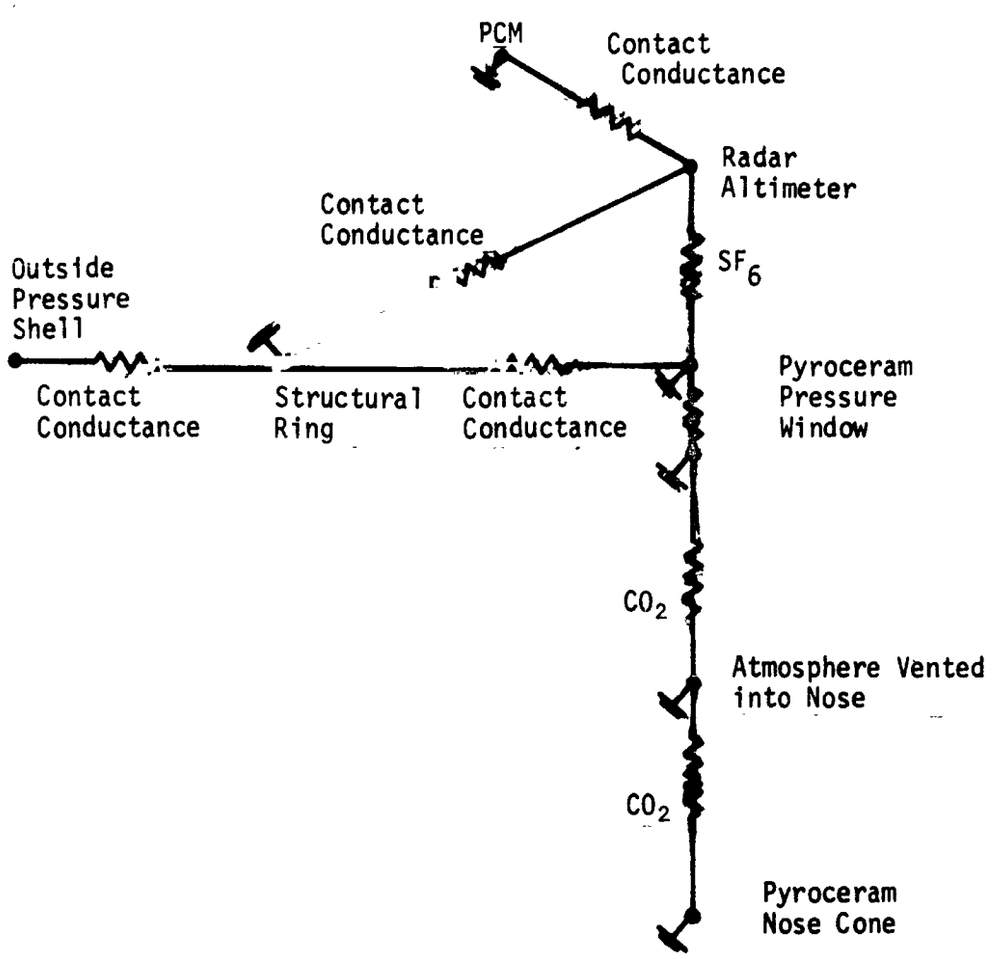


Fig. VIII-13 Radar Altimeter Thermal Model

Radar altimeter temperature histories were generated parametrically for various amounts of PCM. These data are shown in Fig. VIII-14. figure indicates that 0.6 lb of PCM is sufficient for maintaining the temperature of the altimeter below 240°F during the mission.

It was assumed that the PCM was packaged integral with the antenna electronics and that RF-transparent insulation was used to reduce convective heat flow between the Pyroceram windows.

The present configuration differs from the configuration the analysis was based on. The Pyroceram nose cone of the present configuration is now pressurized. In the earlier configuration the nose cone was vented to ambient and the pressure load was carried by a second Pyroceram window directly in front of the radar altimeter. Because the present configuration is less severe thermally than the earlier one, the data presented can be considered conservative.

5. Atmospheric Thermophysical Properties

In the entry phase, the atmospheric temperature varies over such a broad range that it was necessary to take into account the temperature dependence of the thermophysical properties. How the properties are used is shown below:

$$v \propto \rho^{-1/2}$$

$$h \propto k^{2/3}, \rho^{1/4}, C_p^{1/3}, \mu^{-1/6}$$

where

v = Velocity,

h = Heat transfer coefficient,

ρ = Density,

k = Conductivity,

C_p = Specific heat,

μ = Viscosity.

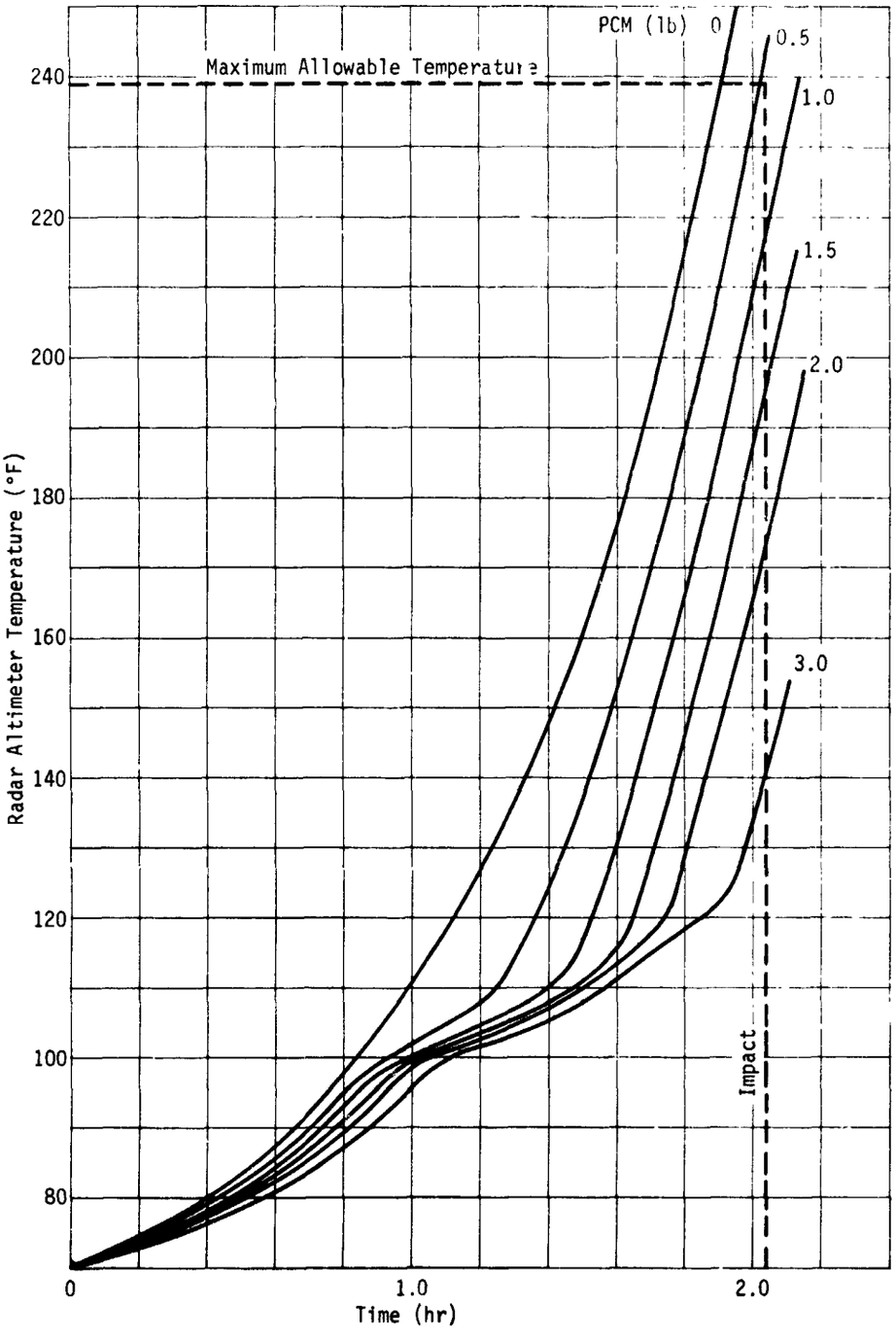


Fig. VIII-14 Radar Altimeter Temperature History

For simplicity the atmospheric properties were assumed to be those of pure carbon dioxide. An examination of the compressibility factor showed a variation of less than 3% over the applicable temperature and pressure ranges, so ideal gas behavior was assumed. Accordingly, specific heat was taken to be a function of temperature only, pressure effects being neglected. In addition, viscosities of gases have a very slight dependence on pressure so this effect was ignored.

Thermal conductivity, however, was possibly somewhat dependent on pressure but no data were readily available. Late in the study period some conductivity data as a function of both temperature and pressure were obtained, and the effect of these new data on the probe temperatures was evaluated against data at one atmosphere (from the same source). This comparison was run on the single wall, outside insulation configuration (refer to subsection 8 following) because the pressure effects would be more drastic for this situation than for the double wall configuration. This is because the data show the greatest variance from one atmosphere data when the pressure is relatively high and the temperature is relatively low, and this condition exists at the lower altitudes inside the insulation surfaces. As explained above, the gas conductivity was used in place of the insulation conductivity and the conductances corresponding to the insulation were evaluated at the *mean* temperatures and the *atmospheric* pressure. The results are shown in Fig. VIII-15. It is seen that, although the temperatures at the center of the insulation are comparable, the high pressure, low temperature conductivities cause the temperature on the inside of the insulation to differ significantly.

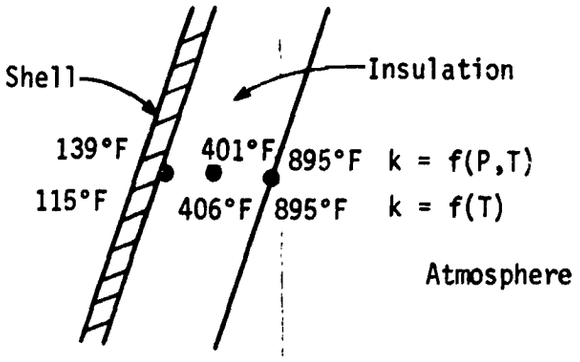


Fig. VIII-15 Exterior Insulation Temperatures

6. Convective Heat Transfer Coefficients

The heat transfer during terminal descent is dominated by convection from the atmosphere to the probe, and the entry velocity and atmospheric properties are such that the probe surface temperature follows the atmospheric temperature rather closely. The correlation used for prediction of the heat transfer coefficient was

$$h = \frac{k}{D}\left[2. + 0.6\ Re^{1/2}\ Pr^{1/3}\right],$$

which is for forced convection for a submerged sphere in an infinite fluid (previously described in subsection 3). This correlation predicts the *average* coefficient over the entire surface, and although the probe shape is nonspherical, the predictions are felt to be adequate for the scope of this study.

A more detailed look at the structural design, however, pointed out that thermal stresses in the pressure shell were being ignored and, if present, would have to be allowed for in the design. Thermal stresses might occur if the structure is directly exposed to the atmosphere (as in the baseline design), and the flow field is such that local heat transfer coefficients vary significantly along the probe body and cause temperature gradients along the shell.

The severity of the problem was examined for a typical small probe configuration, with ballistic coefficients of 0.01 and 2. and the V5M model atmosphere. The significant parameters were probe velocity, probe shape, and atmospheric temperature and density. The probe velocity profile is shown in Fig. VIII-16 and the resulting Mach and Reynolds numbers are shown in Fig. VIII-17. Since the Mach numbers are low (less than 0.3) the problem can be treated as incompressible.

To determine if there is a large variance in the heat transfer coefficient, it is necessary to determine if the flow trips from laminar to turbulent. The probe's terminal descent configuration is a blunt nosed cone, with a hemispherical nose and a 21° half angle. Figure VIII-18 shows the location on a spherical body where the flow would trip as a function of the log of the Reynolds number. The cone flare causes the point at which the flow trips (at the Reynolds numbers shown in Fig. VIII-18) to move aft. In this laminar region the coefficient would decrease from a maximum at the stagnation point to the point at which the flow trips to turbulent. The coefficient in the turbulent region would be much higher, of course. To define the laminar and turbulent coefficients as a function of position along the body would require either an extensive analysis, literature search, or a test. However, the stagnation point coefficient can be predicted from an available correlation.

From the Mangler transformation of the flat plate case,

$$Nu_x = 0.76\ Re_x^{0.5}\ Pr^{0.4}.$$

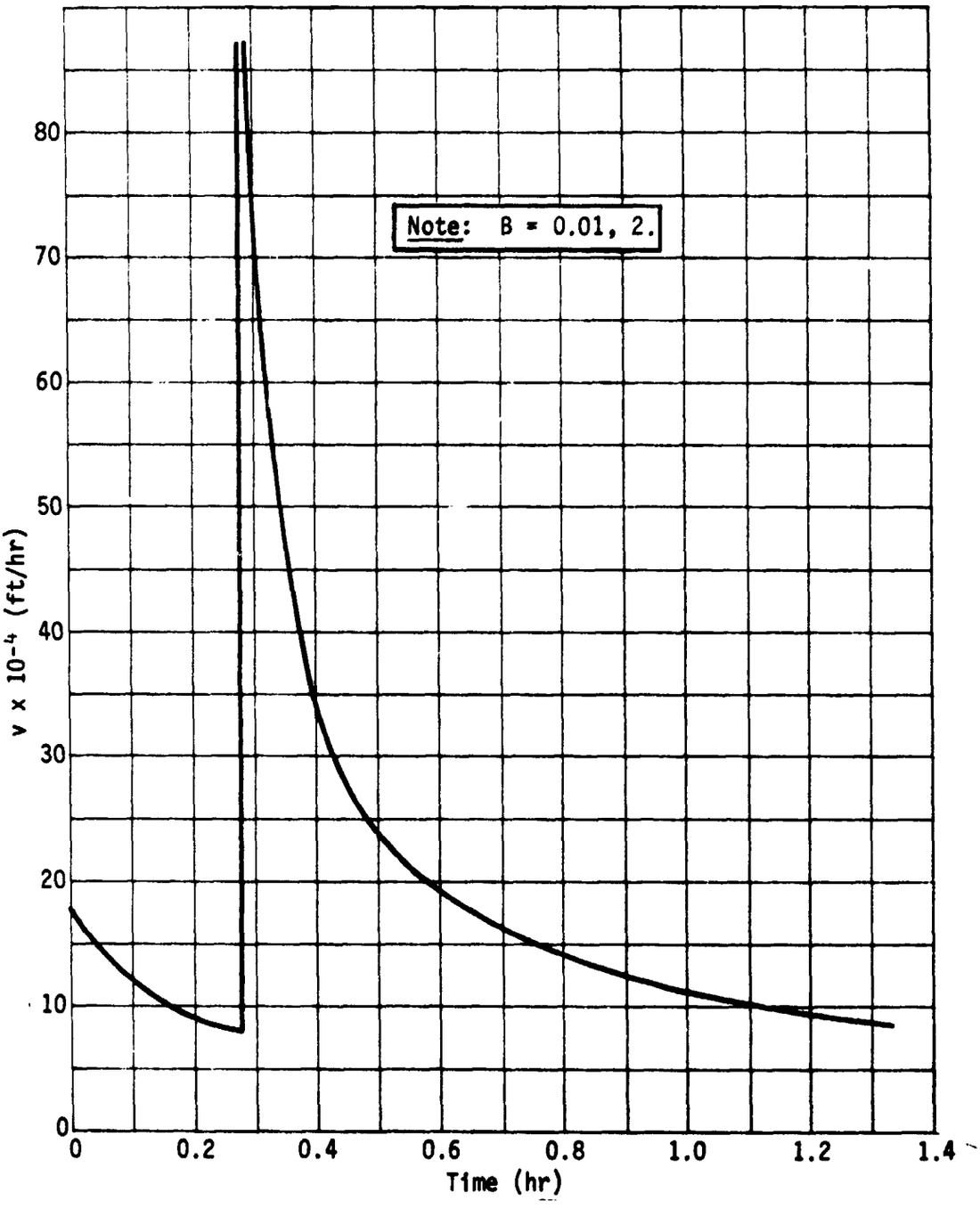


Fig. VIII-16 Small Probe Descent Velocity Profile

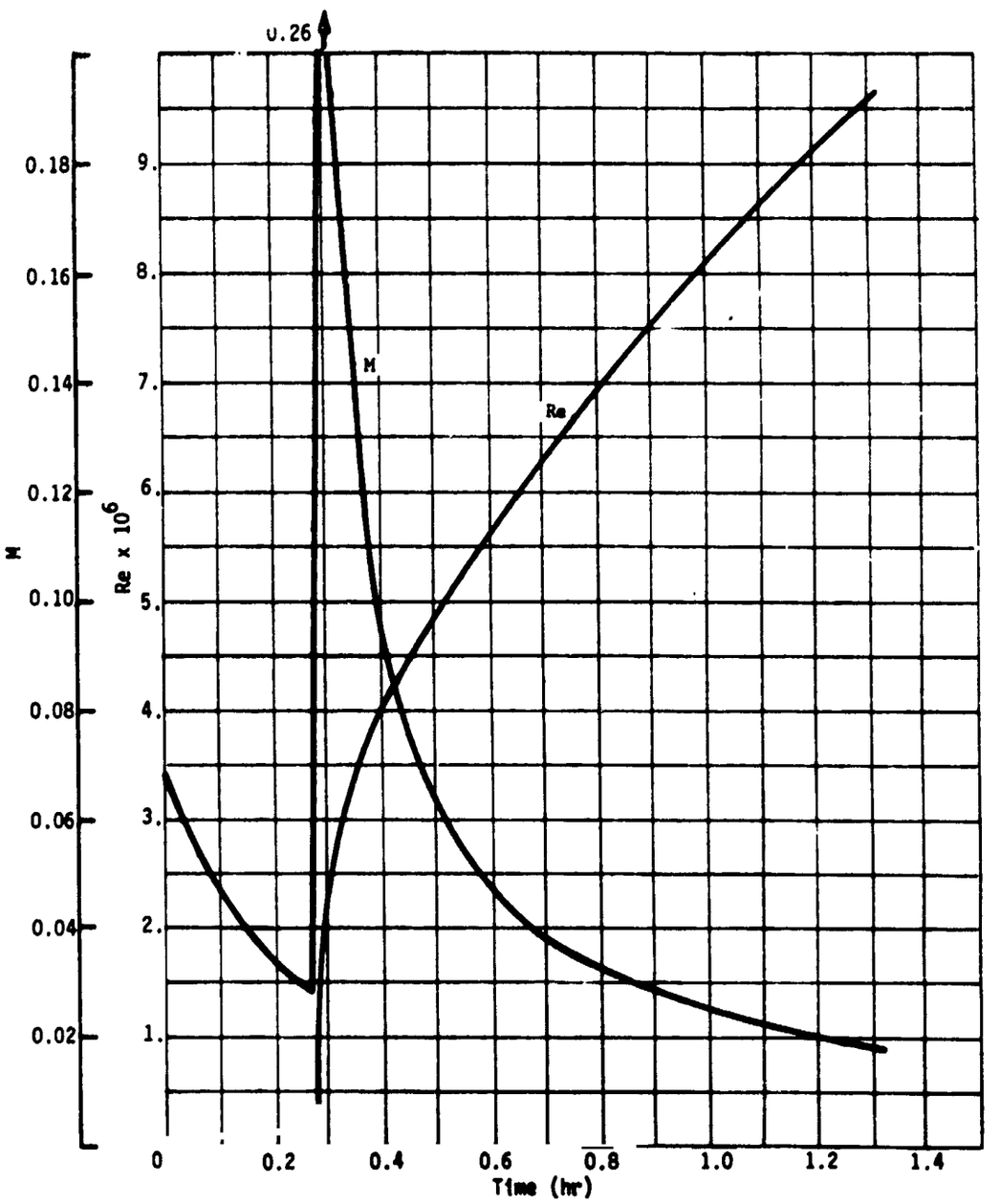


Fig. VIII-17 Small Probe Descent Conditions

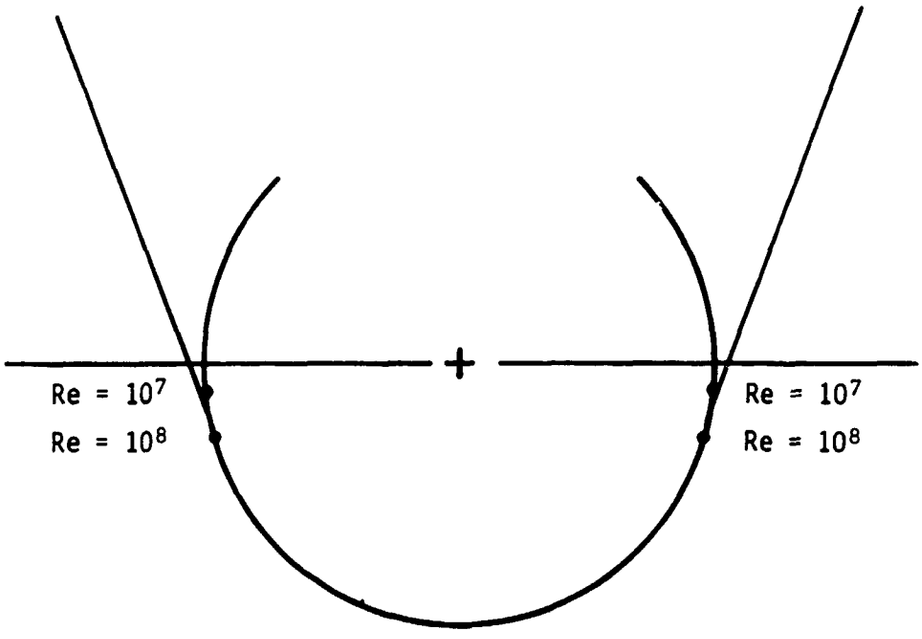


Fig. VIII-18 Location and Reynolds Number at which Flow Becomes Turbulent on the Small Probe

Substituting the potential flow solution for flow normal to a sphere,

$$u_\infty = \frac{3V}{2R} x \text{ for small } x/R$$

yields

$$Nu_R = 0.93\ Re_R^{0.5}\ Pr^{0.4}$$

or

$$h = 0.93\ \frac{2k}{D}\ (0.5)^{0.5}\ Re^{0.5}\ Pr^{0.4}$$

where

Nu = Nusselt number,
Re = Reynolds number,
Pr = Prandtl number,
h = Convective heat transfer coefficient,
k = Thermal conductivity,
u_∞ = Free stream velocity along body,
V = Free stream velocity,
R = Radius of sphere,
D = 2R,
x = Displacement along body.

Lacking the availability of firm estimates for the local coefficient variation, a transient analysis was performed using a simplified model of the small probe's outer shell, and assumed coefficients. As a starting point it was assumed that the coefficient at the stagnation point was as shown in Fig. VIII-19, varying with time. The variation of local coefficients along the probe was assumed to occur as discussed above, choosing the point at which the flow trips to turbulent at 90° from the stagnation point. The magnitude of the coefficients was estimated by extrapolating data for flow past a sphere at a lower Reynolds number,

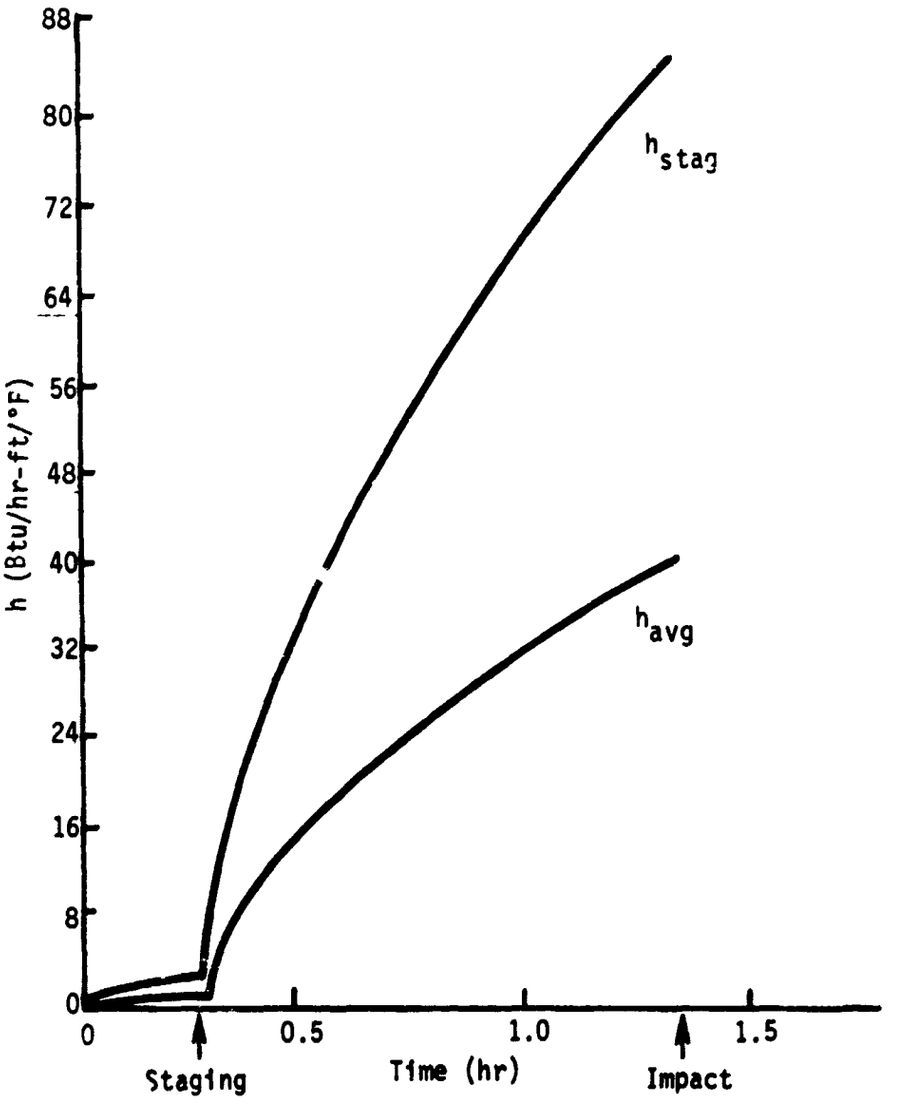


Fig. VIII-19 Small Probe Heat Transfer Coefficients

ratioed to the value at the stagnation point. The local coefficients also varied with time, and a set is shown in Fig. VIII-20. The thermal model included only the probe outer shell, lumped with the stiffeners. The most severe temperature gradient occurred about a third of the way through the descent. This is also shown in Fig. VIII-20.

Two gradients are observable: the one on the right is caused by the step change in film coefficient and the one on the left is caused by a step change in the wall thickness used in the thermal model. The lumped wall thickness changes at the point where the cone flare intersects the hemispherical cap, and causes a temperature gradient because of the resulting difference in thermal response across the intersection. However, this gradient is caused more by the assumptions in the thermal model than by the design.

In any case, neither temperature gradient is significant enough to affect the structural design, even with the conservative assumptions used. If a detailed design were performed, this problem would have to be reexamined.

7. Phase Change Material Mechanization

The use of PCM to add to the entry probe's thermal capacitance, and thus limit temperature excursions, was selected as part of the baseline thermal control configuration at the beginning of the study. Mechanizing the PCM requires the selection of a material, a packaging configuration, a determination of the thermal "efficiency" of the PCM, and an analytical technique for thermal modeling the PCM. In this study the effort was limited to a development of an analytical technique.

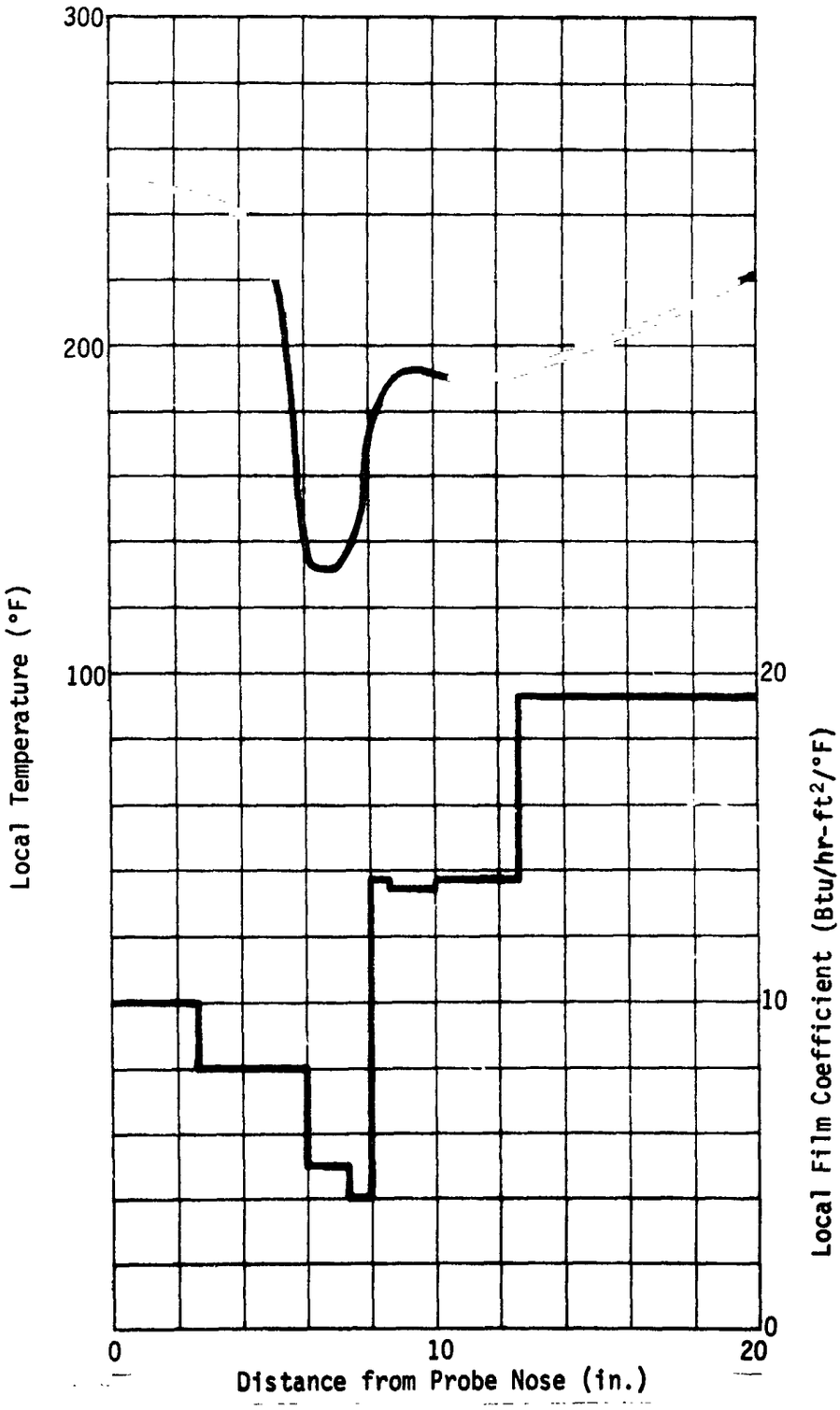


Fig. VIII-20 Small Probe Outer Pressure Shell Temperature Profile and Film Coefficient Distribution

The most common of the PCMs in the literature are the n-paraffins, having melting temperatures in the 50-130°F range and heats of fusion in the 80 to 110 Btu/lb range. For purposes of this evaluation, PCM properties were assumed to be as follows: heat of fusion = 80 Btu/lb and density = 50 lb/ft^3. The heat of fusion was chosen conservatively because no penalty was included for packaging weight, and the choice of melting temperature is not important as long as it is within the equipment operating limits.

The PCM naturally must be contained as close to the heat sources as practical, and would probably be designed integral to the unit requiring thermal control. As mentioned above, no weight was assigned to the container, but a preliminary estimate indicates that the allowance should be about 15 to 20% of the PCM weight.

The design of the container determines the effectiveness of the PCM in limiting the temperature rise of the equipment. A problem incurred with organics is that, since their conductivity is so low in both the solid and liquid phases, it is difficult to transfer heat into the material unless it is packaged in a thin layer. For this reason PCM is commonly packaged in aluminum honeycomb, which provides heat transfer paths into the material. As melting progresses from the hot surface, estimating the heat flow from the equipment to the PCM becomes very difficult and therefore was not taken into account in this study.

The descent phase thermal analysis was performed using CINDA, although in order to properly simulate the PCM it was necessary to write a special subroutine. In addition to being used to establish temperatures inside the probes, the subroutine was used to establish the sensitivity of the payload temperature to the thermal conductance between the payload and the PCM. This sensitivity is shown in Fig. VIII-21. The curves show that the conductive coupling between the payload and the PCM should be made very high to limit the payload temperature.

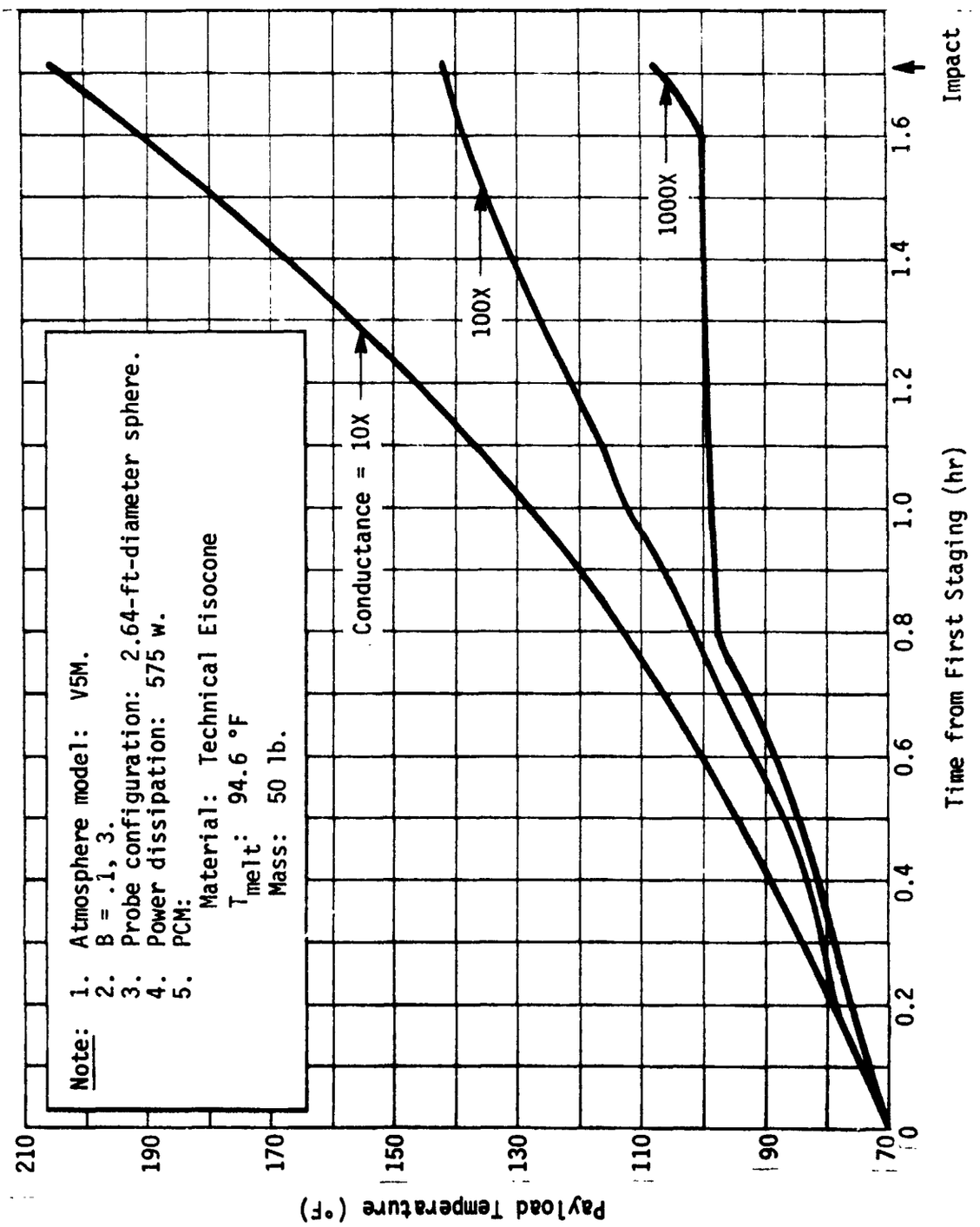


Fig. VIII-21 Sensitivity of Payload Temperatures to PCM Coupling

8. Alternative Design Approaches

a. Single Wall-Outside Insulation Design - An alternative thermal/structural concept that has been evaluated is one where the pressure vessel is protected from the high atmospheric temperature by insulation. This concept has many advantages over the baseline design, which employs a double-walled pressure vessel containing multilayer insulation in an evacuated space between the walls. With insulation outside the shell, the need for the inner wall is eliminated and correspondingly the outer wall dimensions and weight decrease. The primary advantage results from the fact that reducing the maximum temperature of the titanium shell from the present design temperature of 900°F to temperatures compatible with the payload allows the shell to be much lighter due to improved material properties. The shell can now also contribute to the thermal capacitance of the payload. The weight of the outside insulation is a penalty particularly since it is dense, but the net difference is a weight savings. Further weight savings may result from a change to an aluminum shell, which is possible at the temperatures achieved by this concept. The shell specific heat would also increase by a factor of 1.5.

The comparison was made using a transient thermal model of a large probe configuration, entering into a V5M atmosphere with ballistic coefficients of 0.1 and 3., before and after staging. The entry time from 73 km was 1.7 hr. A significant unknown in the analysis was the performance of the insulation when exposed to the Venusian atmosphere. A dense, compressed powder (Min-K) with no external cover was used, and the only data available were for vacuum and one atmosphere air as a function of temperature. The presence of CO_2 at high pressures certainly raises the effective conductivity of the insulation, as might the mass transfer associated with the flow of atmospheric gases into the pores of

the insulation. In an attempt to be conservative the conductivity used was that of pure CO_2. For comparative purposes a run was made using the conductivity data of the insulation in one atmosphere air. Both of these results are shown in Table VIII-3.

Table VIII-3 Summary of Cases Run for Single-Wall Concept

	T_{Shell} (°F)
2 in. Min-K, CO_2 conductivity, evaluated at mean temperatures	54
2 in. Min-K, bivariate* CO_2 conductivity evaluated at atmospheric temperature	78
2 in. Min-K, bivariate* CO_2 conductivity evaluated at mean temperatures through insulation	61
1 in. Min-K, bivariate* CO_2 conductivity evaluated at mean temperatures through insulation	139
1 in. Min-K, conductivity from bivariate* CO_2 data at 1 atmosphere, evaluated at mean temperatures through insulation	115
1 in. Min-K, vendor Min-K data in 1 atmosphere air, evaluated at mean temperatures	158

*A function of pressure and temperature, discussed in subsection 5.

The thermal analysis took into account the external convective heat transfer coefficient based on the probe velocity and temperature-dependent atmospheric transport properties, and radiation from the atmosphere to the probe. The payload and internal supporting structure were considered isolated from the titanium shell and PCM was used to add to the internal capacitance to absorb the power dissipation.

For the mission and configuration analyzed, 1 in. of external insulation limited the shell temperature to 140°F, which is compatible with the shell design and the payload requirements. The weight comparison is shown in the following tabulation.

Component	Double Wall, Insulation Inside (lb)	Single Wall, Insulation Outside (lb)
Science	75	75
Power, Communications	55	55
Outer Shell	80	55
Inner Shell	13	0
Supporting Structure	19	19
Insulation	8	24
PCM	4	0
Antenna	3	3
Cone Flare	9	9
Total	266	240

This comparison and resul[illegible]t weight savings is subject to some qualifications, although th[illegible] weight estimates are felt to be conservative in both cases.

Some other advantages to the single-wall concept in the areas of producibility, reliability, and thermal stress are discussed in the following paragraphs.

Producibility - The high temperature, high pressure requirements in the double-wall concept necessitate a highly stiffened titanium outer shell. The strength-to-weight ratio of 6Aℓ-4V titanium alloy at elevated temperatures dictates its preference in a ring-stiffened shell in the conical portion and waffle arrangement in the spherical bulkheads. Both arrangements require close tolerance machining and chem-milling to achieve a minimum weight design. However, limiting the structural temperature to a low level may allow the use of an aluminum alloy. Although it may have a slightly lower strength-to-weight ratio than titanium, it will be inherently stiffer because of the larger sections required and less additional material would be needed at junctures, penetrations, etc, which may result in a small weight penalty or possibly even a weight advantage. Disregarding the weight aspect, aluminum construction is preferred because of the ease of producing

aluminum, in either a ring-stiffened or waffle construction. A detailed design and analysis is required to establish a weight advantage with either material, which is not justifiable in this study.

Another major problem is the design of seals at all the structural assembly joints and at the penetrations required to integrate and mechanize the science instruments. The entry and descent phase imposes on both designs the requirement of maintaining the interior at one atmosphere of pressure while the exterior pressure reaches a maximum of 150 atmospheres. The double-wall design requires maintaining a vacuum in the annular space between the walls as well as containing the one atmosphere within the inner wall during the 5-month cruise.

A third problem is that of installation of the multilayer insulation in a complex annular cavity, while attempting to minimize heat shorts at seams and the numerous penetrations. The insulation proposed on the outside would be much easier to install and less sensitive to penetrations.

Reliability - In reference to the seals mentioned above, the more seals a design contains, the lower its reliability. The time factor in containing the atmosphere in the inner canister also reflects in reliability. Although a failure modes analysis is required to weigh the relative reliabilities, a seal failure is likely to be catastrophic in either design.

Thermal Stress - One factor that might influence the outer shell design is thermal stresses induced by varying heat transfer coefficients along the probe surface as a result of the boundary layer profile. With the insulation on the outside, the thermal gradient is on the insulation rather than the metallic skin and causes no problems.

The insulation design has an impact on the science mechanization, the communication subsystem, and of course the design of the structure. The insulation must be penetrated by many of the science instruments and by the antenna leads but the design of the components themselves will need little change. The penetrations degrade the multilayer performance more significantly than the Min-K. Structural penetrations are required to attach the cone afterbody and, for both designs, an attachment to the aeroshell.

b. Pressure Equalized Design - A possible third design concept is one in which the ambient pressure is transmitted to the interior of the probe, eliminating the need for the heavy pressure shell. As in the concept discussed above, insulation would still have to be applied to the exterior of the probe to reduce the heat transfer from the atmosphere. The pressure could be transmitted by some kind of bellows device to the interior which would contain, in addition to the payload, a material (possibly PCM) to distribute the pressure and add to the thermal capacitance of the payload. This concept has not been evaluated and therefore its potential weight advantage has not been established for this pressure range. Some of its characteristics are listed below:

- No high-pressure seals required;
- The payload can be packaged in any convenient shape;
- Low structure weight;
- Small pressure canisters would still be required for some individual instruments;
- Remainder of components must be compatible with the high pressure and the pressure-distributing medium.*

*A small, feasibility test to explore this possibility was run at Martin Marietta on a previous proposal effort. Several representative electronic components were tested and shown to operate, virtually without change in performance when exposed to a pressure environment of 1000 atmospheres. The maximum Venusian pressure is 159 atmospheres.

B. STRUCTURAL/MECHANICAL SYSTEM

1. Entry Aeroshell Structural Design

The aeroshell structural weights for all configurations were taken from curves (Fig. VIII-22) that show weight as a function of stagnation pressure, aerodynamic shape, base diameter, for a ring-stiffened aluminum monocoque shell design. These data were generated for previous Martin Marietta studies and represent a single structural configuration that results in consistency across the wide range of pressure, body cone angles, and diameters of interest in the multiprobe study. Where smaller diameters than shown were evaluated in trade studies, weights were scaled down from the 4.0 ft diameter. A small difference results between the 45° and 60° cone half angles. The weights for an intermediate cone angle of 55° results in approximately the same as for 60° and were taken as being the same. For a 50° cone angle the weights are proportioned midway between the 60° and 45° data.

Use of parametric aeroshell data from Ref VIII-1 was considered but it was concluded that some inconsistencies would result if they were used, e.g., the Ref VIII-1 data for 6.0-ft-diameter aeroshell plotted in Fig. VIII-23 illustrate the spread of aeroshell weights available for any given pressure. If a 15-lb allowance for a base cover and internal structure is added to the Ref VIII-1 data, some consistency is found to exist between the Martin Marietta ring stiffened aluminum curves and the midrange data of the Ref VIII-1 60° (optimized) stainless steel honeycomb. The computer program used in developing the ring stiffened data was also used extensively in Mars mission studies and results of the current detailed design phase of the Viking program have confirmed the validity of the aeroshell weight data derived from the computer program.

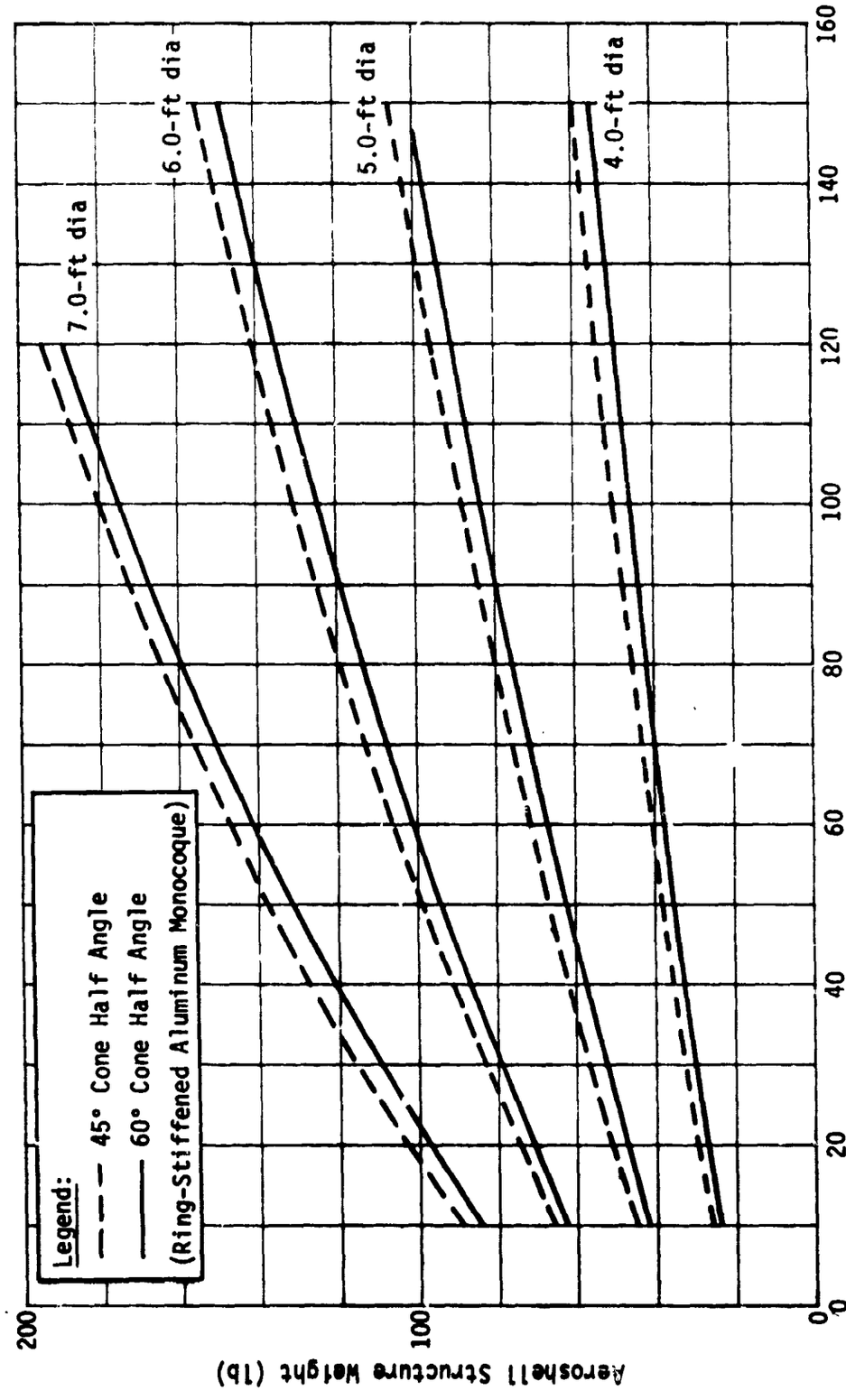


Fig. VIII-22 Aeroshell Parametric Weights

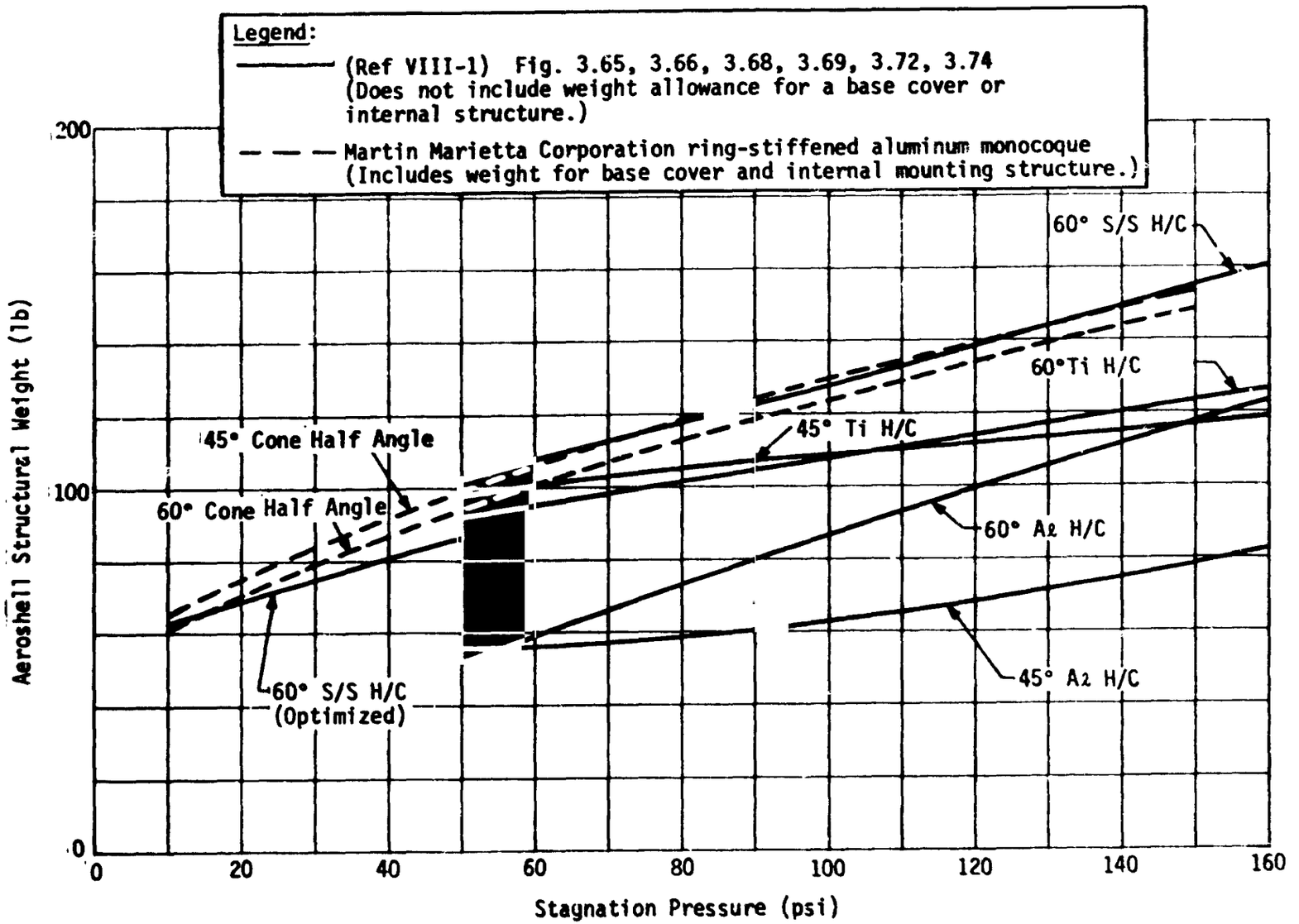


Fig. VIII-23 Comparative Aeroshell Structure Weights for 6.0-ft Diameter

The entry aeroshell is assumed to support the entry pressure loads at a backface (structural) temperature of 300°F. The aeroshell body is considered vented, but to be covered over the base. In all probe configurations the science and equipment payloads require staging out of the aeroshell before descent after entry. Although the aeroshell structure temperature will ultimately increase to 600°F due to soak through from the heat shield after the high beat pulse, this occurs well after peak aerodynamic pressures when pressure loads are low, and in most cases after aeroshell jettison. Therefore an aluminum aeroshell is capable of providing the structural integrity for a Venus mission.

The aluminum shell structure is compatible with both the carbon phenolic ablator that is selected for most of the probe entries and the AVCOAT 5026 ablator selected for the high-cloud probe to achieve a low entry m/C_DA.

2. Heat Shield

Heat shield data have been provided by JPL for use in this study. JPL Section Document 131-05, *Venus Entry Heat Shield Design Requirements and Technology Limits*, which contains the specified information is included as Appendix G of Volume III of this report. Summary curves from this document and their application to the baseline probes are presented in the probe synthesis sections of Chapter III of this volume.

The two heat shield materials specified, carbon phenolic and AVCOAT 5026-39/Hc-G, were found to provide acceptable weight fractions (10 to 15% of entry weight for the forebody protection), but neither material was found to be optimum for the whole range of entry probe conditions, i.e., the high-cloud probe required a low density material (AVCOAT 5026 was used) to achieve a low m/C_DA while the ballistic coefficients and nose radii required for the descent probe types precluded use of the low density material because of shear and pressure gradient limitations.

NASA test conditions specified in Document 131-05 were not used as constraints in selecting the missions, per JPL instruction; however, the final baseline probe peak entry heating rate and pressure conditions do not appear to exceed the test capability values listed (see Chapter III, Section B).

3. Pressure Vessel Analysis

The impact of electrical connections through the vessel is to create the need for structural beef-up around the penetrations, to require special designs for sealing the connectors against the pressure, and to provide a locally high conductivity path for heat flow into the interior. The weight provisions for the bosses and pressure resistant connectors and feedthroughs is considered to be included in the 20% contingency factor utilized on weight since specific designs of these details are outside the scope of this study. The heat flow through the wires and structural attachments is, however, accounted for in the thermal analysis as described in Section A of this chapter and Appendix D of Volume III.

A spherical capsule canister although most optimum weight-wise, does not provide the ballistic coefficient desired in the final descent phase. For this reason, and others discussed in Section C of this chapter, a sphere/cone/sphere design with a fixed flare was selected. The actual shapes of probe canisters required for a particular descent profile were not definable until the late stages of the baseline mission evaluation and were subject to change. Consequently formulas pertinent to a hemispherically domed cylinder equivalent in volume to the sphere/cone/sphere were selected to input to the structural/thermal program (Section A of this chapter) to establish the structural shell weights. This section defines the simple formulas used in the program and compares the resulting weight for an equivalent cylinder with that of an actual sphere/cone/sphere canister.

The critical design condition for the structural/thermal concept is based on the V5M atmosphere. The ambient pressure is 150 earth atmospheres while the temperature is 900°F. The 150 atmosphere constitutes a 2210 psi external collapsing pressure.

The design concept for the equipment compartment of a subsonic descent capsule is a pressure sustaining outer shell at ambient temperature; a hermetically sealed inner canister that contains one atmosphere of sulphur hexafluoride gas; and an annulus between the canisters that is evacuated to vacuum throughout the operational modes. The structural design arrangement for the outer canister in the simplified equivalent cylinder model consists of monocoque domes and ring stiffened walls, while for the actual design the arrangement is waffle stiffened domes and an integrally ring-stiffened cone frustum. The inner canister is a monocoque shell whose weight is lumped with internal support structure in the program and calculated as a percentage of the payload weight (25%).

The material selected for the outer pressure canister is the 6Aℓ-4V titanium alloy because of its high strength to weight at elevated temperature; it is readily machinable, weldable, and can be formed into dome shapes and can be chem-milled. The inner canister is also fabricated of 6Aℓ-4V titanium alloy.

The formulas used in the structural/thermal design program are as follows:

Cylinder - Based on buckling criteria,

$$t^{5/2} = \frac{P \times l \times r^{3/2} \times 1.10}{0.736 \times E}$$

or

$$t = 0.075\ D^{3/5}$$

where:

P = external pressure (2210 psi),

l = length of cylinder between stiffeners (in this case ring stiffeners at 1.0 in. spacing were used),

R = radius of the cylinder outside envelope,

E = modulus of elasticity,

E = 16×10^6 lb/in.^{2} for titanium @ room temperature (RT) reduced to 60% of E @ RT to allow for the ambient condition of 900°F,

Factor of safety = 1.10.

Accounting for the frame weight is achieved by inputting a 50% increase to the monocoque shell weight calculated with the above formula.

The resulting shell thickness with the 1.5 factor for frame section is then compared with the shell thickness required to support hoop compression loads by use of the following formula:

$$t = \frac{P \times R}{F_c}$$

where:

F_c = compressive allowable of the titanium material (taken as 80,000 psi at 900°F),

P and R are same as above.

The greater shell thickness is then used to calculate the total volume (weight) of the material in the cylindrical structure.

The ring stiffeners are spaced at 1.0-in. intervals along the cylinder length. The 1.0-in. spacing was established as an optimum for this type of pressure vessel in this range of diameters from previous in-house studies. The frame depth that determines the structural envelope in the cylindrical portion is nominally inputted to be variant with the diameter at a rate of 5% of D.

Sphere - Based on buckling criteria,

$$t^2 = \frac{P\ R^2\ 3(1 - \nu^2)}{2\ E}$$

or

$$t = 0.00915\ D$$

where:

P = external pressure (psi),

R = radius of the sphere,

ν = Poissons ratio (0.30 for titanium),

E = modulus of elasticity 16.0 x 10^6 lb/in.^{2} at room temperature (degraded to 60% due to 900°F temperature).

The structural envelope assigned for the dome is 2.5% of the body diameter to account for the conversion to waffle construction in the actual design. No accounting for thermal stress effects is included in the program.

The above formulas are optimistic for monocoque shell thicknesses as has been proven by tests at STL and reported in STL Report No. TR-59-0000-09959, December 1959. However, when the resulting thicknesses of material are resolved into the more efficient waffled and ring-stiffened types of construction indicated, the results are only slightly optimistic and probably achievable if all excess material is removed by machining and chem-milling.

An analysis of the baseline small probe design was performed to check the correlation of its structural weight as determined by the simple program formulas (spherical capped cylinder) with that determined by a more exact analysis of a spherically capped cone frustum. The program results based on a ballistic coefficient of 2.0 descent profile and a cylinder L/D of 1.5 resulted in a diameter of 16.4 in. and a pressure canister weight of 38.6 lb

(outer shell only). An allowance of approximately 4.0 lb is included in the total structural weight output of the program (54.2 lb) for penetrations and assembly joints. The weight calculated for the small probe pressure canister outer shell from the analysis shown in the following paragraphs for a sphere/cone/sphere is 39.5 lb.

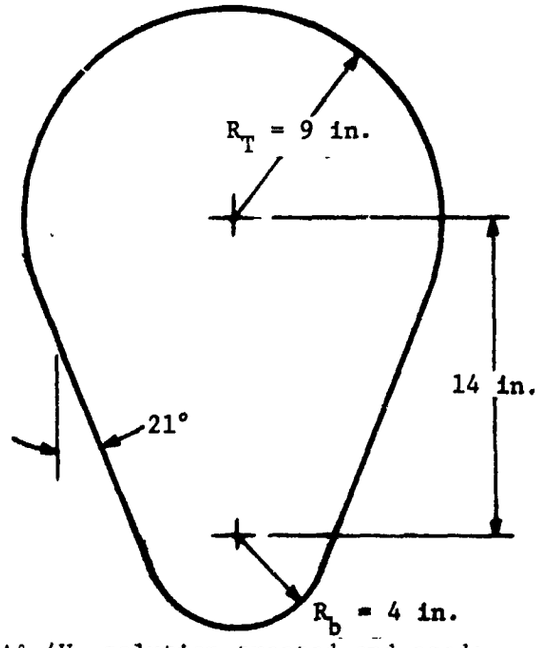
STRESS ANALYSIS OF SMALL DESCENT PROBE, SPHERE/ CORE/SPHERE CONFIGURATION

The critical design condition for the small descent probe is the condition just before impact.

Structural temperature = 867°F (lags ambient temperature slightly);

Design collapse pressure = 150 atm or 2210 psi;

Ultimate Factor of safety = 1.10;



Material = titanium Ti-6Al-4V, solution treated and aged;

Modulus E = 16,400,000 psi (RT),
12,400,000 psi (867°F);

Allowable Compression Yield Stress, F_{CY} = 152,000 psi (RT),
84,300 psi (867°F).

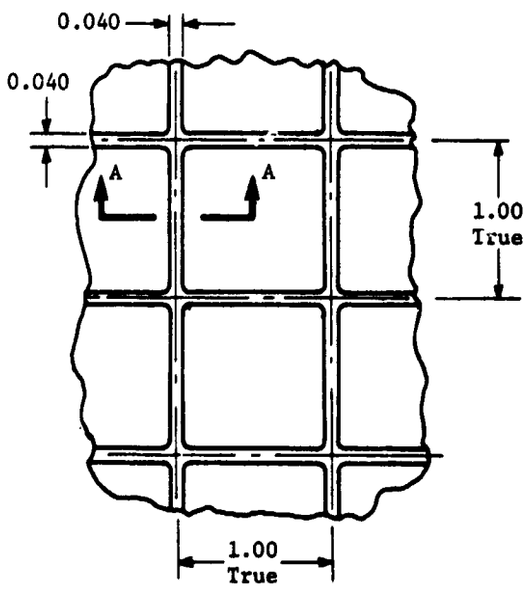
Information on Modulus and Allowable Compression Yield Stress is taken from MIL-HDBK-5A, February 8, 1966.

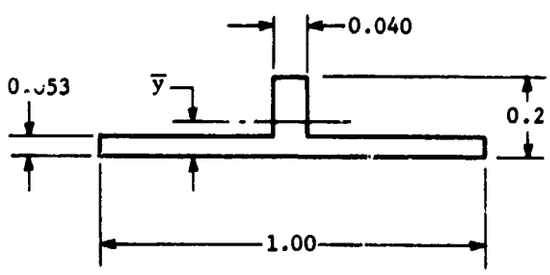
The pressure vessel is divided into three segments: small hemisphere, large hemisphere, and cone frustum.

Small Hemisphere

Waffle construction was found to be the most efficient structure for the small hemisphere,

R = 4.0 in.





Section A-A

$\bar{y}$ = 0.0364 in.

I_w = 0.000075 in.^{4}

t_{sm} (smear thickness) = 0.0588 in.

Determine the thickness of the monocoque equivalent having the same moment of inertia.

$I_w = I_m = \frac{1}{12} t_m^3$ I_m = moment of inertia of monocoque

t_m = 0.0965 in. t_m = thickness of monocoque

Check spherical plate stability due to external collapse pressure using the equivalent monocoque.

Use Fig. 47, p 146 of NACA TN 3783 to check stability. The empirical curves are based on test data for externally pressurized spherical plates.

$$Z_d = \frac{d^2(1 - \mu^2)^{\frac{1}{2}}}{rt}$$

$$\sigma_{CR} = \frac{K_P \pi^2 E t^2}{12(1 - \mu^2) d^2}$$

$$Z_d = \frac{(8)^2 (0.91)^{\frac{1}{2}}}{4(0.0965)} = 159$$

d = diameter, 8 in.
μ = Poisson's ratio, 0.3
r = radius, 4 in.
t = thickness
K_P = function of Z_d and r/t
E = modulus, 12,400,000 psi
σ_{CR} = allowable buckling stress

K_P = 53, from Fig. 47 of NACA TN 3783

$$\sigma_{CR} = \frac{53 \pi^2 (12.4) (10)^6 (0.0965)^2}{12 (0.91) (8)^2} = 86,300 \text{ psi}$$

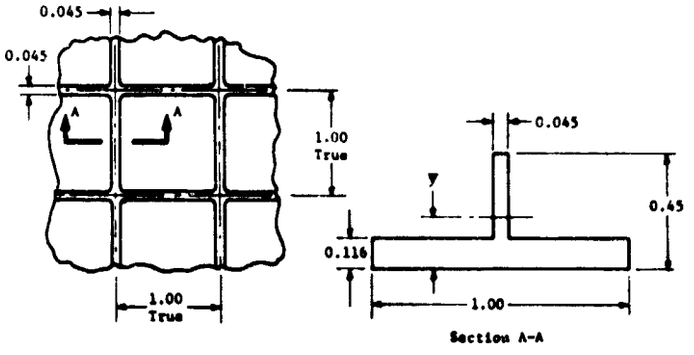
Compressive stress on sphere using smear thickness,

$$f_c = \frac{PR}{2t_{sm}} = \frac{2210(1.1) (4)}{2(0.0588)} = 82,700 \text{ psi}$$

$$M.S. = \frac{84,300}{82,700} - 1 = \underline{+0.02}$$

Large Hemisphere (same procedure as small)

Waffle construction was found to be the most efficient structure for the large hemisphere. The equations used are the same as for the small hemisphere.



t_{sm} = 0.131 in.

$\bar{y} = \frac{0.01097}{0.131} = 0.0837$

I_w = 0.000945 in.^{4}

Determine the thickness of the monocoque equivalent having the same moment of inertia.

$I_w = I_m = \frac{1}{12} t_m^3$ I_m = moment of inertia of monocoque

$t_m = 0.224$ in. t_m = thickness of monocoque

$$Z_d = \frac{(18)^2 (0.91)^{\frac{1}{2}}}{9(0.224)} = 153$$

$K_p = 51$, from Fig. 47 of NACA TN 3783

$$\sigma_{CR} = \frac{51 \pi^2 (12.4) (10)^6 (0.224)^2}{12(0.91) (18)^2} = 90{,}800 \text{ psi}$$

Compressive stress on sphere using smear thickness,

$$f_c = \frac{PR}{2t_{sm}} = \frac{2210(1.1) (9)}{2(0.131)} = 83{,}500 \text{ psi}$$

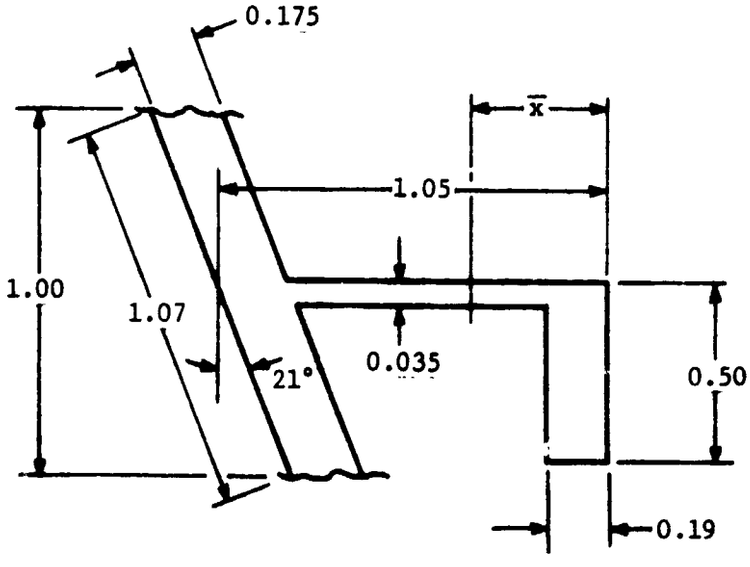
$$\text{M.S.} = \frac{84{,}300}{83{,}500} - 1 = \underline{+0.01}$$

Cone Frustum

The ring stiffened cone is found to be the most efficient structure. The ring frames are to be spaced at one-inch centers along the vertical axis. The depth of the ring frames and the basic cone wall thickness shall vary along the length of the cone frustum. Calculations will only be shown at the aft and forward sections.

Aft Cone Section

1. Check Ring Frame Stability:



R = 9.0 in.

Use Formula 12 in Table XV from "Roark" for stability check.

$p' = \frac{3EI}{R^3}$

Moment of inertia and area.

Area = 0.3065 in.^{2}

t_{sm} = 0.286 in.

x = 0.658 in.

L = 0.0521 in.^{4}

p' = 2660 lb/in.

M.S. = $\frac{2660}{2430} - 1 = \underline{+0.09}$

2. Check Hoop Compression Stress:

$$f_c = \frac{PR}{t_{sm} \cos \theta}$$

$$f_c = \frac{2430(9)}{0.286\ (0.934)} = 81{,}800 \text{ psi}$$

$$\text{M.S.} = \frac{84{,}300}{81{,}800} - 1 = \underline{+0.03}$$

3. Check the 0.175 Wall for Stability:

A. Due to external collapse pressure:

$$P_{CR} = \frac{0.736\ E\ t^{5/2}\ \cos^{5/2} \theta}{\ell\ R^{3/2}}$$

This equation is taken from STL Report No. TR-59-0000-09959, December 1959 "Semiannual Report on Development of Design Criteria for Elastic Stability of Thin Shell Structures" by P. Seide, and reduced by 20%, therefore, including all test points shown on Fig. 8 of the report.

P_{CR} = critical external pressure,

E = modulus of elasticity,

t = wall thickness,

θ = cone slant angle,

ℓ = cone height, measured along vertical axis,

R = radius of circumference.

$$P_{CR} = \frac{0.736(12.4)\ (10)^6\ (0.175)^{5/2}\ (0.934)^{5/2}}{1(9)^{3/2}}$$

$$= \frac{0.736(12.4)\ (10)^6\ (0.0128)\ (0.843)}{27}$$

$$= 3650 \text{ psi}$$

Stress ratio due to external pressure = $R_p = \frac{2430}{3650} = \underline{0.666}$

B. Due to axial compression load:

Design curves in Fig. 3.3.1-1 of Martin Marietta's Structural Analysis Manual are used.

$$L/r = \frac{1}{9} = 0.11$$

$$r/t = \frac{9}{0.175} = 51.3$$

$$\frac{F_{CR}}{E} = 18.5(10)^{-3}$$

$$F_{CR} = 18.5(10)^{-3}\ (12.4)\ (10)^6 = 229{,}000 \text{ psi (for cylinder)}$$

$$F_{CR} \text{ (cone)} = F_{CR} \text{ (cylinder)} \cos^2 \theta$$

$$F_{CR} \text{ (cone)} = 229{,}000\ (0.892) = 204{,}000 \text{ psi}$$

of magnitude force and acceleration in the lateral direction.

A direct comparison of launch loads induced in the spacecraft by the Titan IIIC of this study and those induced by the Atlas/Centaur launch vehicle (ref VIII-1) is not a simple matter because the influence of the truss and adapter structural stiffness on the magnitude of the dynamic amplification of loads at the spacecraft/launch vehicle interface. Although no dynamic analysis of the proposed structural system was performed, the weights based on the peak accelerations at booster burnout were increased to account

$$f_c = \frac{PR}{2t \cos \theta}$$

$$= \frac{2430(9)}{2(0.175)\ (0.934)} = 67{,}000 \text{ psi}$$

Stress ratio due to axial compression load $R_c = \frac{67{,}000}{204{,}000}$

$$= \underline{0.329}$$

$$R_c + R_p = 0.329 + 0.666 = \underline{0.995} < 1.0$$

O.K.

Forward cone section checked by same procedure and yields similar results.

4. Planetary Vehicle Structure

The payload adapter probe support truss structure, and modifications required for the spacecraft structure are discussed in Chapter IV, Planetary Vehicle Synthesis. For these systems, the prelaunch and launch phases result in the maximum lateral as well as longitudinal inertia loads. These loads are due to the acoustic and structural vibration environment as well as the thrust/weight factors experienced during launch. Subsequent to launch, firing the midcourse propulsion system imparts a much lower order of magnitude force and acceleration in the lateral direction.

A direct comparison of launch loads induced in the spacecraft by the Titan IIIC of this study and those induced by the Atlas/Centaur launch vehicle (Ref VIII-1) is not a simple matter because the influence of the truss and adapter structural stiffness on the magnitude of the dynamic amplification of loads at the spacecraft/launch vehicle interface. Although no dynamic analysis of the proposed structural system was performed, the weights based on the peak accelerations at booster burnout were increased to account

for dynamic magnification. In the final design, adapter and truss stiffnesses and attachment compliances would be adjusted to limit the accelerations experienced by the spacecraft itself to avoid modifications to the Ref VIII-1 configuration 20a spacecraft structure, other than those required by the relocation and increased impulse of the propulsion system and the ACS propellant storage systems as discussed in Chapter IV.

C. DECELERATOR DESIGN

Conventional-type parachutes were used in all decelerator applications for the baseline mission probe designs. The deployment conditions were all high or medium subsonic Mach numbers and the dynamic pressures were relatively low ($q \leq 40$ psf) as compared to conventional parachute design. The main chute designs incorporate pilot chutes for extraction and reefing to control opening shock loads. Early in the study, a high-cloud probe design required auxiliary deceleration at supersonic speeds and high dynamic pressure ($q = 205$ psf, $M = 4.0$). A supersonic ballute was designed for this application and the design data are given in this section.

1. Decelerator Design Criteria

The decelerator applications of the study fall into three main groups: (1) main parachutes; (2) staging or drogue parachutes; and (3) supersonic decelerators. The design criteria for each type of decelerator is as follows:

1) The main parachutes for terminal descent control have ballistic coefficients varying from $B = 0.005$ slug/ft^2 to $B = 0.035$ slug/ft^2 as required to satisfy the descent rates imposed by the science instrument sampling requirements. A subsonic deployment Mach number

was required, although at low dynamic pressures this is not necessary. A margin of altitude of 300 m was used for the dereefing sequence before main chute deployment;

2) For staging parachutes or drogues for separation and extraction purposes, a separation deceleration of 32 ft/sec^2 was used as the basic design criterion for sizing. This criterion is based on Viking system design experience;
3) The ballute decelerator is used for high dynamic pressure, supersonic deceleration control. Deployment Mach number is restricted to M = 4.0 or less to avoid any significant aerodynamic heating environment. A combined payload plus ballute ballistic coefficient of B = 0.077 $slug/ft^2$ is required for the application studied.

2. Decelerator Flight Test Experience

The decelerator applications of this study fall within the current decelerator flight test experience, as depicted in Fig. VIII-24. The figure, based on Ref VIII-2 illustrates general flight test experience in terms of dynamic pressure and Mach number regions. Sounding rockets have produced the extremely low dynamic pressure and Mach number test points. Sled tests, as well as special payload applications, have produced the dynamic pressures over 1000 psf. Aerospace flight experience includes both supersonic Mach numbers and fairly high dynamic pressures. The Mars Planetary Entry Parachute Program (PEPP) deployed parachutes from 30 to 84 ft in diameter at supersonic speeds. The PRIME lifting body flight tests deployed a ballute of about 4.5 ft in diameter at a dynamic pressure of nearly 200 psf, and a Mach number of about 3.0.

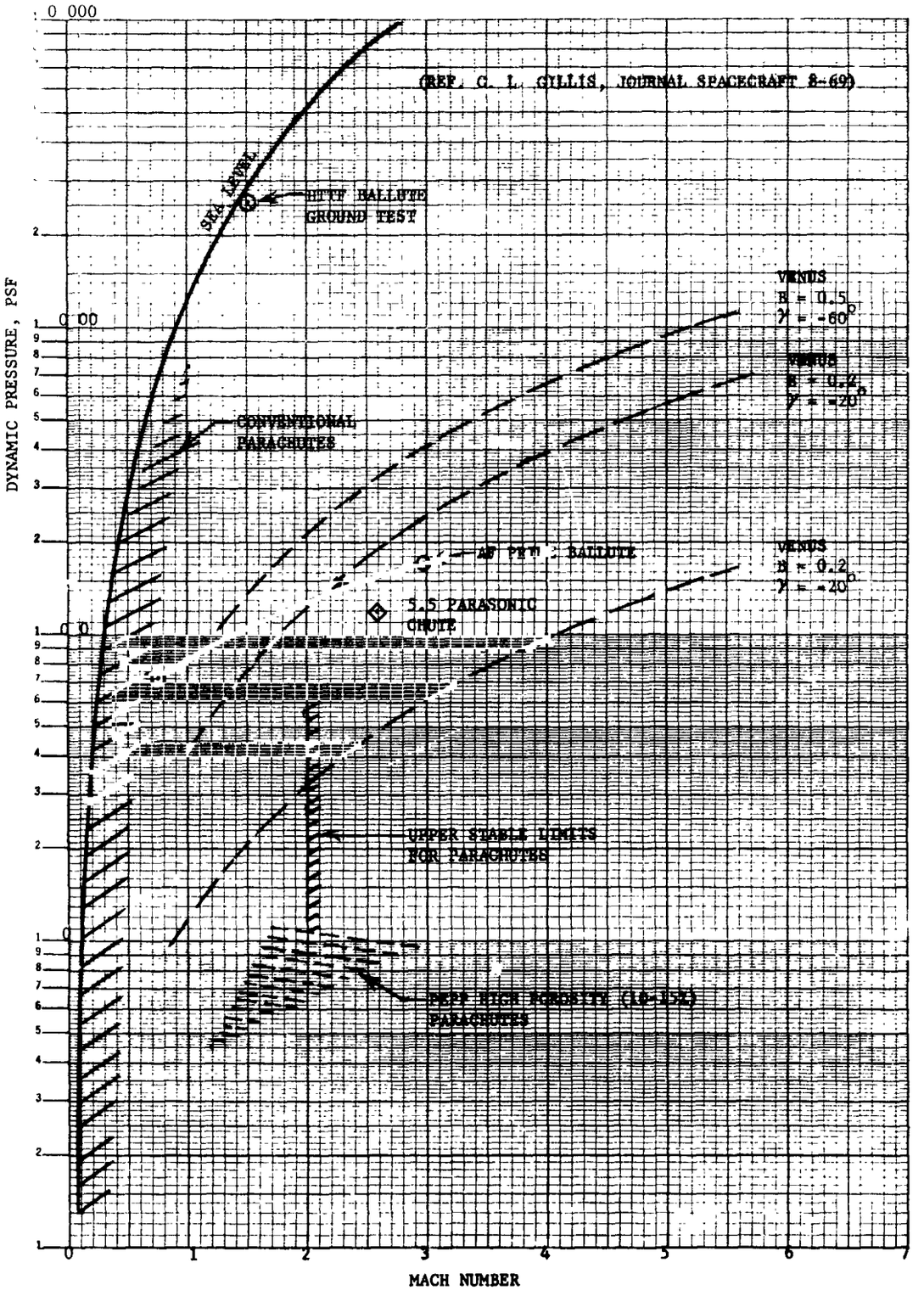


Fig. VIII-24 Decelerator Flight Test Experience

Although the baseline probe designs incorporate conventional parachutes deployed at subsonic speeds and low dynamic pressures, an alternative design requires a supersonic decelerator with a deployment Mach number of 4.0 and dynamic pressure of 205 psf. A ballute design was chosen since the deployment conditions closely match those experienced in the PRIME ballute tests.

3. Decelerator Design Trade Studies

The terminal descent phase parachute sizing and weight estimation for this study is based on the design curves of Fig. VIII-25 thru VIII-28.

Figure VIII-25 presents terminal velocity versus m/C_DA for various altitudes near the surface. The reference terminal velocities at $m/C_DA = 1.0$ were computed for the MMC-Lower density atmosphere.

Each probe type has different terminal descent velocity requirements based on the particular scientific instruments on board. A compromise m/C_DA has been chosen for each probe type so that a close match of the optimum descent velocity versus altitude is obtained. For parachute sizing, the required m/C_DA values are as follows:

Probe Type	m/C_DA (slug/ft^2)
Large	0.035
Small	0.015
High Cloud	0.005
Balloon	0.032

All main parachutes used in this study are of the disk-gap-band type developed by the G. T. Schjeldahl Company. The disk-gap-band (DGB) parachute has a drag coefficient of $C_{D_o} = 0.53$ based on the total constructed diameter, D_o, including the band (see accompanying sketch). Although the drag coefficient is reduced from that of solid parachute designs, the DGB parachute

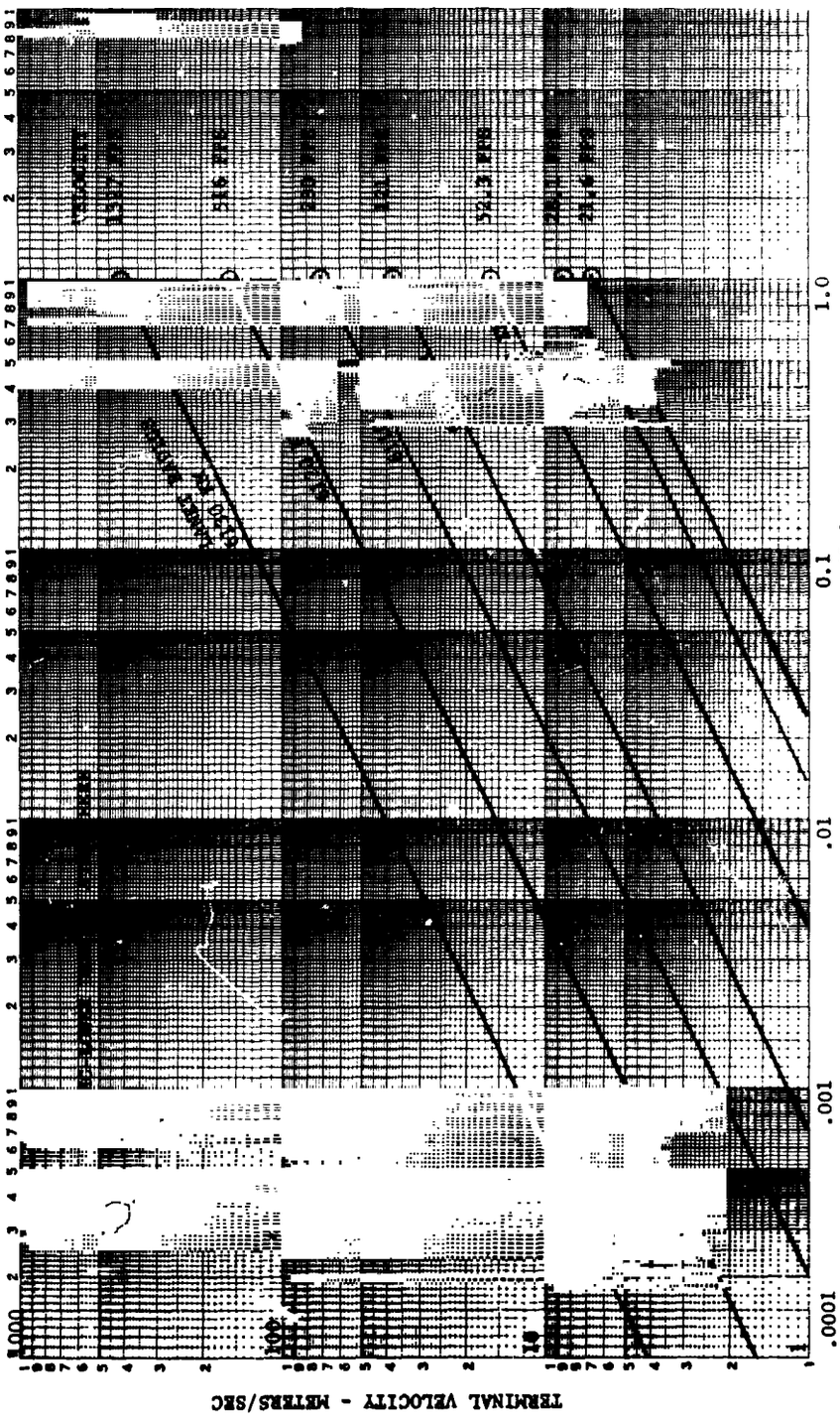


Fig. VIII-25 Terminal Velocity vs m/C_DA

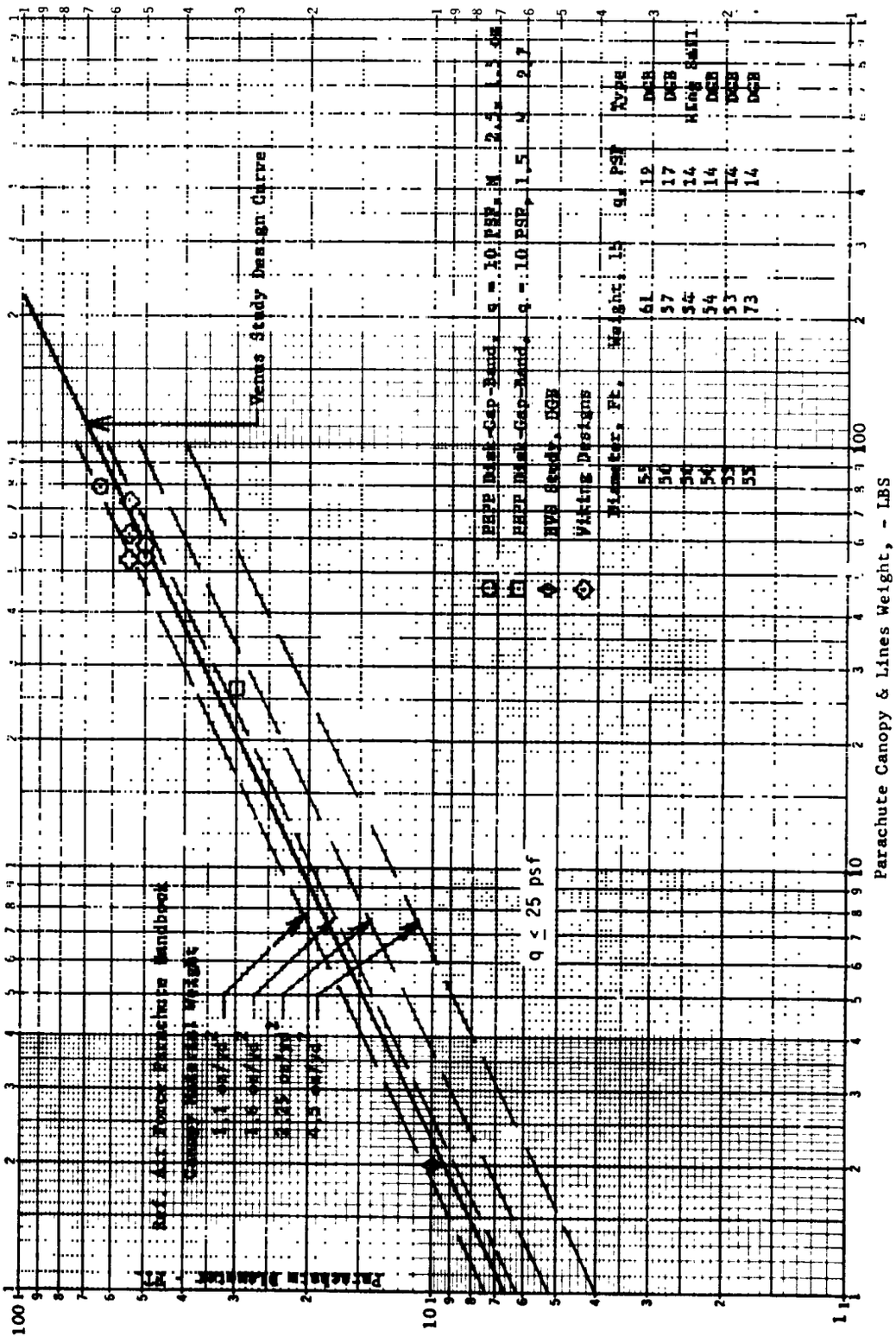


Fig. VIII-26 Parachute Weight

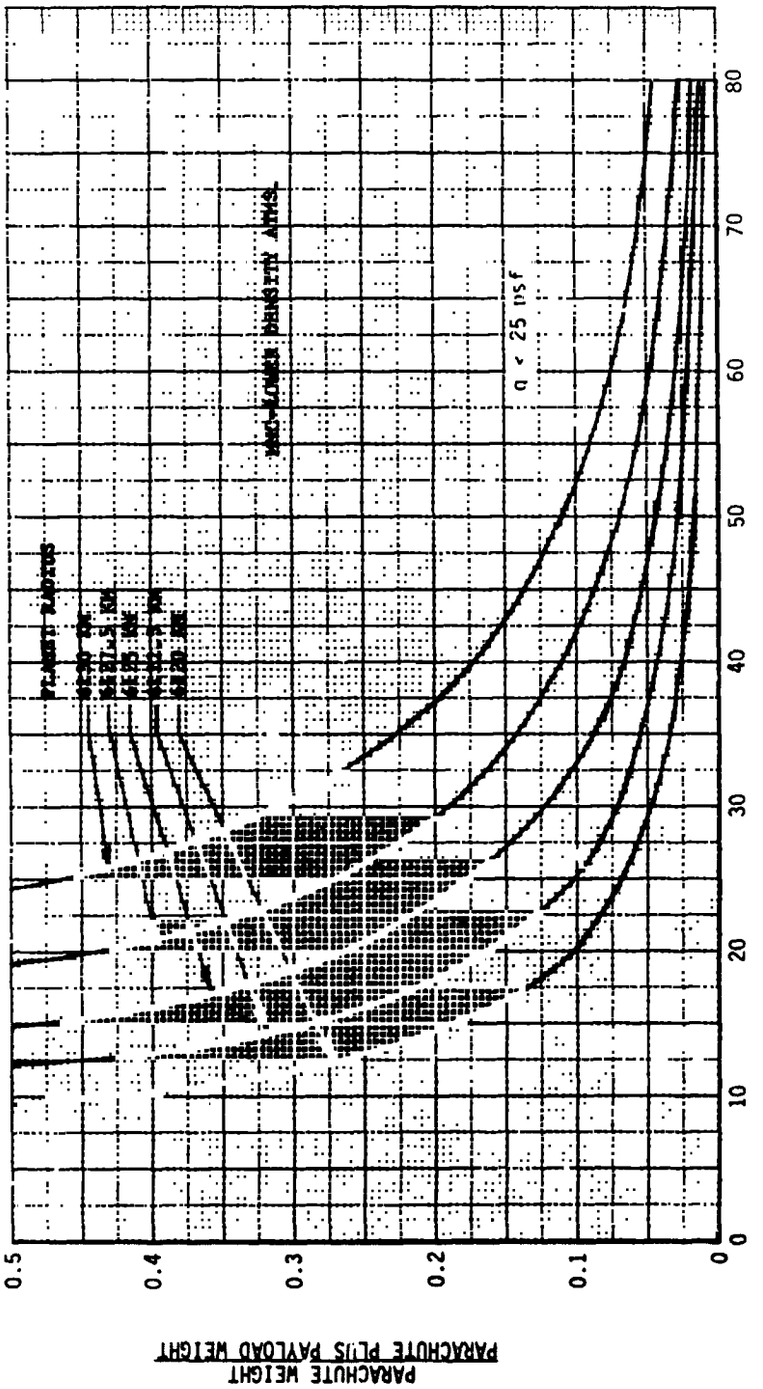


Fig. VIII-27 Parachute Weight Penalty vs Terminal Velocity

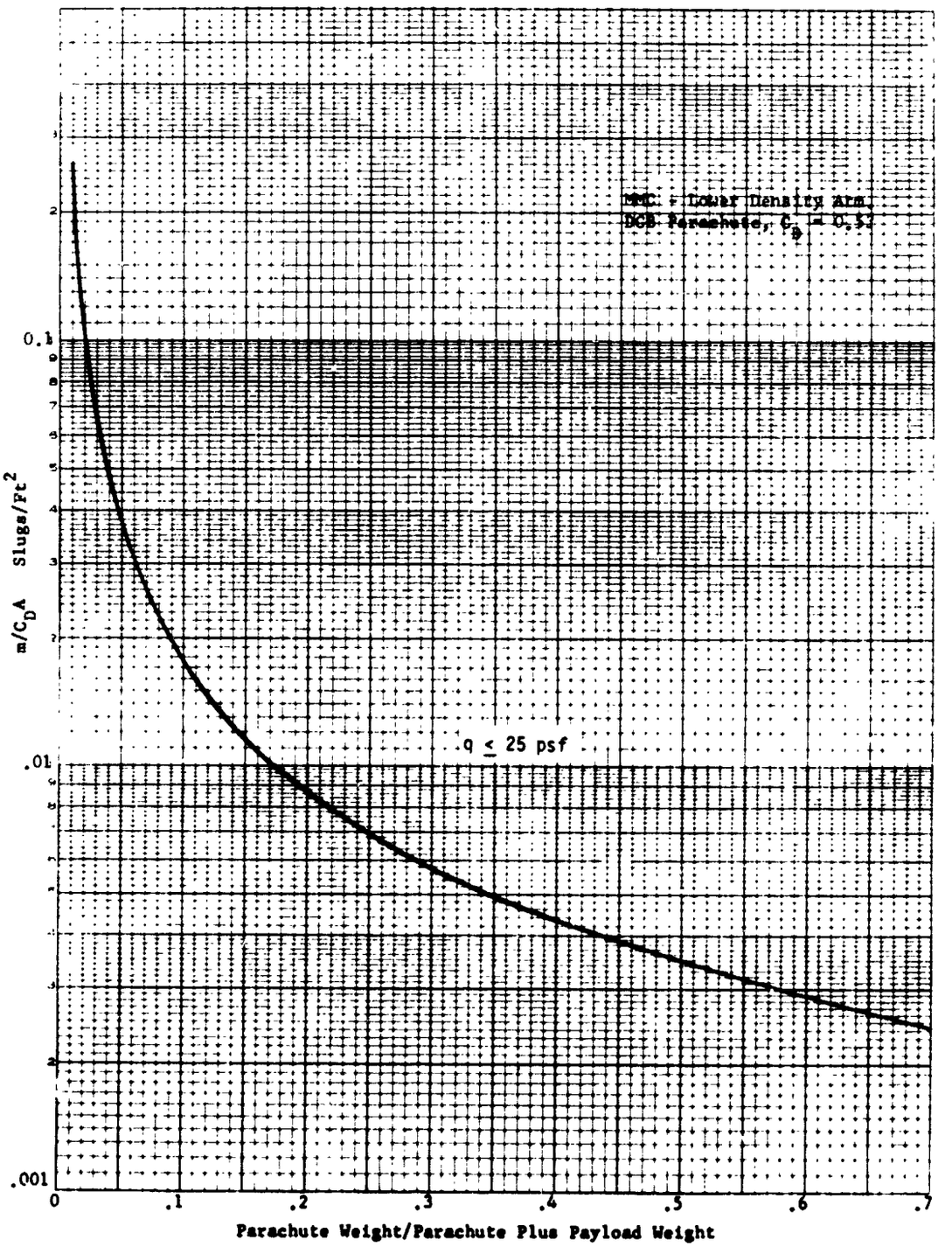
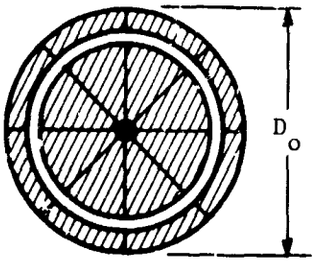


Fig. VIII-28 m/C_DA vs Parachute Weight Penalty



provides a very stable descent with rapid damping from angular disturbances. Figure VIII-26 presents DGB parachute weight versus diameter and this weight includes only the canopy and lines. Weights for parachutes of this type flight tested in the PEPP correlate well with the basic data from the Air Force Parachute Handbook. In addition, weights for proposed hardware designs for disk-gap-band parachutes in the current Mars Viking Program correlate very well with the design curve. The data points are shown in Fig. VIII-26.

For the high dynamic pressure conditions, the parachute weights must be increased to account for the increased airloads. A correction in weight due to dynamic pressures above q > 25 psf has been used in this study and the equation is as follows:

$$\Delta \text{ Weight}_{q > 25 \text{ psf}} = 6.2 \times 10^{-5} (C_D A)^{1.5} (q-25)$$

This factor is based on an equation suggested by C. L. Gillis (Ref VIII-2). Figure VIII-29 illustrates the effect of dynamic pressure on parachute weight based on the above equation for the large probe design.

Figure VIII-27 shows the ratio of the parachute weight to the parachute plus payload weight as a function of terminal velocity and planet radius.

A summary design curve is presented in Fig. VIII-28. For a given parachute design $m/C_D A$ the weight penalty is shown directly as the ratio of parachute weight to parachute plus payload weight. The $m/C_D A$ consists of only physical characteristics of the payload and parachute mass and the parachute diameter and drag coefficient. Therefore, the $m/C_D A$ as well as the parachute weight are independent of altitude.

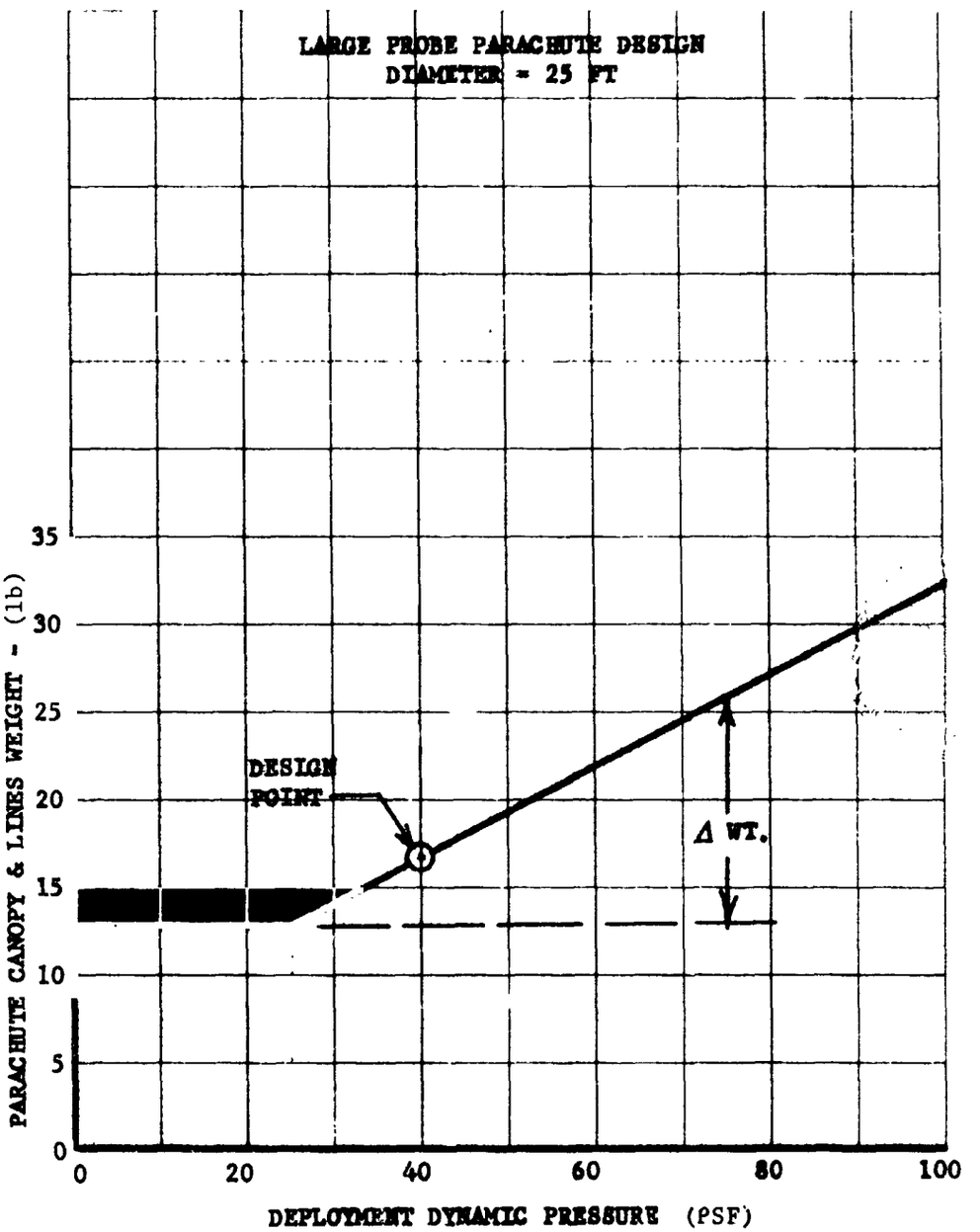


Fig. VIII-29 Effect of Dynamic Pressure on Parachute Weight

A device for reducing the parachute drag during descent might find application in tailoring the descent profile more precisely to the varying sampling interval desired by the science instruments. Such a system, postreefing, was applied with success in the PEPP flight tests to reduce wind drift effects. The payload weight is used to provide the required force to draw in the canopy skirt after the riser line is cut by an explosive device. The payload drops the required distance with respect to the canopy to accomplish the postreefing and a secondary riser arrests the falling payload and performs the reefing function.

4. Supersonic Decelerator Design

Design data are presented here for a ballute-type supersonic decelerator. A supersonic decelerator was required for a possible high-cloud probe targeting option to the subsolar point. This probe and target option resulted in an entry ballistic coefficient of $B = 0.2$ slug/ft^2 and entry angle, $\gamma_E = -45°$. To meet the desired deployment radius of 6127.0 km with the main parachute deployed ($m/C_DA = 0.005$ parachute), auxiliary supersonic deceleration was required. Design tradeoffs showed that a decelerator providing total aeroshell and decelerator $m/C_DA = 0.077$ slug/ft^2 at a radius of 6128.4 km, would slow the entry vehicle down to $M = 0.7$ and a dynamic pressure of about 10 psf just above the deployment radius of 6127.0 km. At this time the pilot and main parachute can be safely deployed and inflated at 6127.0 km radius.

The supersonic deployment conditions described above occur at $M = 4.0$ and a maximum dynamic pressure of 205 psf. The ballute size is calculated from the expression:

$$A_{Ballute} = \frac{m - B(C_DA)_{P/L}}{B\, C_{D_{Ballute}}}$$

where:

m = mass, total (8.45 slugs),

B = total ballistic coefficient, $m/C_D A$,

$(C_D A)_{P/L}$ = payload drag area (37.0 ft^2),

$C_{D_{Ballute}}$ = ballute drag coefficient (0.9),

which gives, $A_{Ballute}$ = 80.75 ft,

$Diameter_{Ballute}$ = 10 ft.

The drag coefficient variation with Mach number is presented in Fig. VIII-30. This figure includes the effects of the aeroshell wake on the ballute drag. For this design case, the ratio of ballute to aeroshell diameter is greater than 1.5 so that the wake effects are not large. A drag coefficient of 0.9 was chosen as an average value from the figure.

For weight estimation, data obtained from the Goodyear Aerospace Corporation for the Viking Mars Lander ballute design were used. The following equation includes ballute component weights designed for Mach 4.0 pressure distributions. These components include ballute front section, burble fence, center section, base, meridians, riser, and inlets. The weight terms combine to form the following equation:

$$\text{Ballute weight} = 12.36 \times 10^{-4} (q) (R^3) + 0.0475 R^3 + 4.8 \times 10^{-3} (q) (R^2)$$

where:

q = deployment max dynamic pressure (psf),

R = radius of ballute (ft).

The ballute weight is 64 lb for a ballute diameter of 10 ft, dynamic pressure of 205 psf, and Mach number of 4.0.

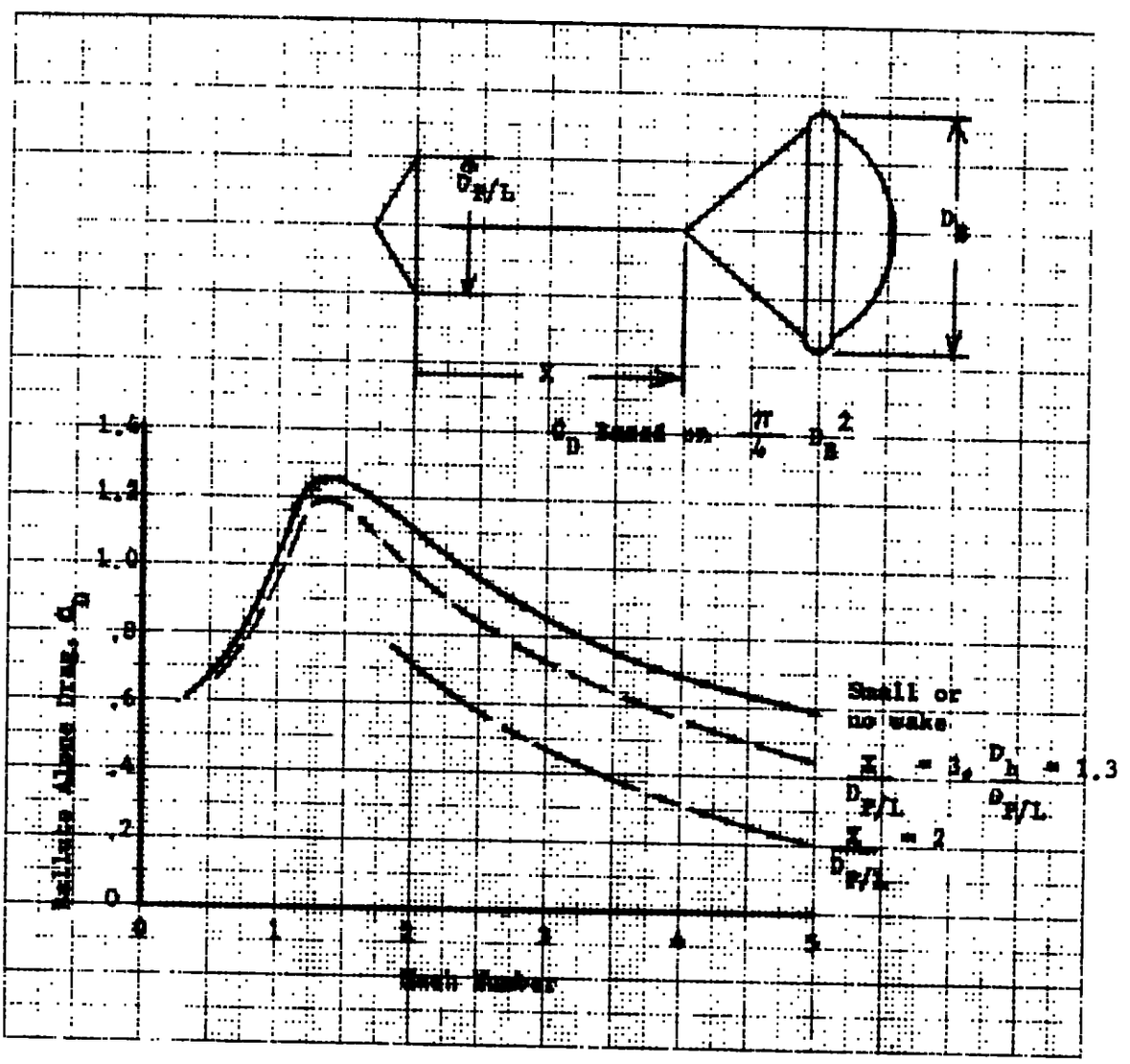


Fig. VIII-30 Characteristic Ballute Drag

D. ATTITUDE CONTROL SYSTEM STUDIES

1. Probe ACS

Spin stabilization of the entry probes was selected because of its simplicity and light weight, and to take advantage of subsystem design information developed in the previous JPL/AVCO Venus Study. In that study (Ref VIII-1) spin rocket motor characteristics were established that provided impulse and thrust levels used in pairs that were appropriate to achieving 3 rad/sec with probes in the range of 252 lb to 286 lb and spin moments of inertia of 8.7 to 11.9 slug-ft^2. These are adaptable to the current study probes, whose characteristics are shown in the following tabulation, providing four motors are used on the large descent probe. Weight of the motors is 0.49 lb each.

The despin is accomplished by similar motors, canted slightly, or by despin yo-yos at somewhat higher weights of 2.8 lb per system for the 250 lb probes vs 0.98 lb for the rocket motor system.

Probe	Large Descent Probe	Small Descent Probe	High-Cloud Probe	Balloon Probe 500 mb
Entry Weight (lb)	498	252	255	234
Spin Moment of Inertia (slug-ft^2)	62	14.2	14.5	14.3

2. Spacecraft Attitude Control System

Because the inertia of the Planetary Vehicle for this study is much greater than that for configuration 20a of Ref VIII-1 (see Chapter IV, Section A), it is desirable to increase thrust levels to bring the accelerations more closely in line with the normal operation of the Mariner as discussed in Chapter IV. In fact a lower limit on accelerations of 0.2 mrad/sec^2 has been recommended by JPL.

As a first approach, a study was made of the propellant usage required if the $\sim$0.8 mrad/sec^2 of configuration 20a was maintained. This study is described in Appendix G and summarized in the following subsection.

The relatively small increase in propellant weight required, 9.36 minus 6.0 or 3.36 lb (from Table VIII-4), indicates that increasing thrust levels to the values indicated -- 0.043 lb in pitch and 0.025 lb in roll -- would be acceptable from a weight standpoint. However, the maximum accelerations after all probes are released would be over twice the 0.8 mrad/sec^2 value. This might be undesirable since it is important to return the spacecraft to its initial orientation to align the upper atmosphere science instruments with the impacting spacecraft velocity vector. Therefore thrust levels that produce 0.8 mrad/sec^2 after probe release, 0.018 lb in pitch and 0.009 lb in roll, were calculated. These levels result in accelerations of 0.33 and 0.30 mrad/sec^2, respectively, during the times when all probes are in place, which does not significantly change the time required to complete the ejection maneuvers. The effect of changes in thrust level on propellant usage are described in the following paragraphs.

a. ACS Propellant Usage Study - Planetary Vehicle - The parameters given below were used to calculate the propellant usage for the ACS, assuming both sets of nozzles are operable:

Thrust (pitch/yaw) = 43 x 10^{-3} lb;
Thrust (roll) = 25 x 10^{-3} lb;
Control moment arm = 9.5 ft;
Moment of inertia (pitch/yaw) = 1030 slug-ft^2;
Moment of inertia (roll) = 570 slug-ft^2;
Initial tipoff rates = 50 x 10^{-3} rad/sec;
Angular acceleration (pitch/yaw) = 0.80 x 10^{-3} rad/sec^2;

Table VIII-4 ACS Propellant Usage Summary

Description	Channel	Usage (10^3 lb)
A. Stabilize Initial Tipoff Rates	P	107.5
	Y	107.5
	R	60.2
B. Orient to Sun Reference	P	13.2
	Y	13.5
C. Orient to Canopus	R	7.6
D. Limit Cycle Operation	P	326.0
	Y	326.0
	R	184.0
E. Midcourse		
1. Orient for Main Engine Burn	P	13.5
	Y	13.5
	R	7.6
2. Null Main Engine Offsets*	P or Y	915.0
	R	915.0
F. Probe Ejection		
1. 10 Maneuvers	P	135.0
	R	76.0
2. 1st Probe	P	0.6
	R	0.6
3. 2nd and 3rd Probes	P	1.5
	R	1.5
4. 4th Probe	P	1.4
	R	1.4
		Total = 3.23 lb†
		For cross coupling take 1.2 x Total = 3.80 †

*Under normal circumstances, the autopilot (jet vanes) will perform this function.

†Based on dual jet operation. For the case of only one set of valves (single jet) in operation, the limit cycle requirement is reduced to ¼ the values shown which makes the total 2.6 or 3.12 with cross coupling. The total gas to be carried on the mission is calculated as three times the system usage with only one set of valves operable: 3 x 3.12 = 9.36 lb. The existing capability is 6.0 lb.

Angular acceleration (roll) = 0.835×10^{-3} rad/sec^2;

Commanded rate = 3.1416×10^{-3} rad/sec;

Limit cycles -

Dead band (pitch/yaw) = $\pm 4 \times 10^{-3}$ rad,

Dead band (roll) = $\pm 4.3 \times 10^{-3}$ rad,

Minimum on-time - 20 msec;

Mission length = 153 days;

I_{sp} of N_2 Gas = 70 sec;

Main engine ΔV = 27 m/sec;

Main engine thrust vector misalignment = $\pm 1°$;

Center of gravity uncertainty = ± 0.1 in.;*

Probe eject mechanism misalignment = $\pm 1°$;

Probe separation ΔV = 1 ft/sec.

Using these parameters and the equations given in Appendix G, the propellant usage table (Table VIII-4) was developed. Note that a factor of 1.2 was applied to the final usage value to account for inertia cross-coupling.

*The 0.1 in. may be optimistic, however a larger value will not significantly impact the gas requirements, i.e., during probe ejection the 1° angular misalignment assumption overshadows the cg uncertainty, and for midcourse correction the jet vanes of the propulsion unit will normally provide control.

The influence of thrust level selection is as follows:

Tipoff Rates - assuming identical initial tipoff rates, the time required to null out these rates is inversely proportional to the thrust level, and the attitude angles developed during this time are proportional to the square of the required time. However, the propellant used is independent of thrust level, so no savings in propellant is available with lower thrust levels;

Orientation Maneuvers - assuming identical commanded rates, the on-time is inversely proportional to thrust, but, again, propellant usage is unchanged for a lower thrust level;

Limit Cycles - assuming a minimum on-time of 20 msec, the normal limit cycle rate will be reduced directly with the thrust level, hence the number of cycles will be almost directly proportional to the thrust, and the propellant usage will be proportional to the square of the thrust level;

Offsets and Misalignments - assuming the same offsets and misalignments, no propellant changes result from reduced thrust levels.

b. Accuracy Considerations - Probe Deflection - Four sources of error contribution to deviations in thrust application angle (other than navigational position errors) are identified on page 3-468 of Ref VIII-1.

These are: (1) initial alignment of the spacecraft to the inertial reference frame; (2) the separation tip off errors; (3) probe spin-up error; and (4) deflection motor thrust misalignment error.

The latter three are functions of the probe geometry, inertia, spin rate, spring system misalignment, and rocket motor burn time. Values for these quantities for the probes of the current study are quite similar except for the large descent probe. An item-by-item comparison reveals the errors due to these three sources will be equal to or slightly less than those of the referenced study "Best Entry Probe," which are respectively 0.12°, 0.19°, and 0.21°.

The initial alignment errors are made up primarily of two sources, limit cycle dead band and gyro drift rate, which are 0.458° and 0.24°/hr, respectively (these values are conservative if one assumes the errors have uniform distribution). Thus for any probe, the error standard deviation is given by:

$$\sigma^2 = (0.458)^2 + (0.24t)^2 + (0.12)^2 + (0.19)^2 + (0.21)^2$$

which for a 2-hr sequence would result in a 0.75° error at the end of the period.

E. PROBE DEFLECTION PROPULSION

Solid rocket motors are used for probe deflection impulse. The range of total impulse of interest is 1140 lb-sec to 2850 lb-sec. Motors in the near lower range were defined in Ref VIII-1 and are shown as the square points in the system weight plot of Fig. VIII-31. Several motors with impulse and burn time appropriate to the higher values of this study have been defined and shown as the circled points. Further descriptions are given in Chapter III.

It is concluded that the maximum system weight required for deflection will be 20 lb.

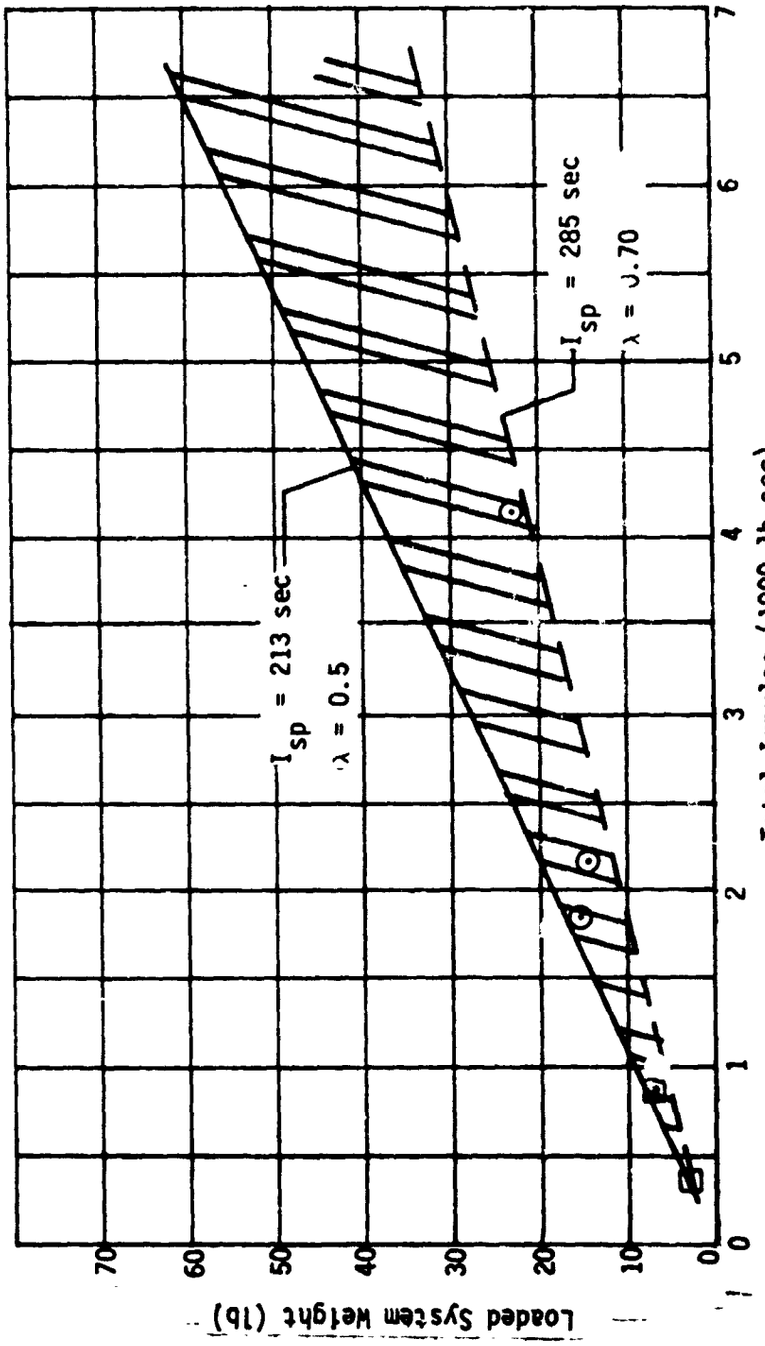


Fig. VIII-31 Solid Rocket Motor Performance

F. PLANETARY VEHICLE PROPULSION SYSTEM

Significant changes are required for the spacecraft midcourse propulsion system because of the increased mass and relocation of center of gravity. These are discussed in Chapter IV, Section D.

G. TERMINAL DESCENT DYNAMICS AND ANTENNA POINTING ANGLE

1. Terminal Descent Dynamics Criteria

The descent capsule must provide a stable orientation for both the science instruments and the data link antenna. Section H that follows discusses the aerodynamic static stability requirements in terms of center of gravity and center of pressure locations. This section discusses the dynamic stability characteristics as affected by configuration.

The most critical problem affected by descent capsule dynamics is the maintenance of the data link during large capsule oscillations. Since both the large and small descent capsules are targeted near the limbs they have fairly flat conical beam antenna patterns, as depicted in Fig. VIII-32.

The figure illustrates a probe descending to the planet on a vertical trajectory that is near the limit of the communications angle of 70° from subearth. A typical antenna pattern is shown that is designed to provide high gain toward subearth for the nominal attitude. If the probe pitch angle is disturbed in the plane of the earth due to turbulence, there will be a loss in the antenna gain in the subearth direction. For pitch angles below about 15° to 20° the signal loss is still below the design margins. For large pitch disturbances a temporary loss in signal will result.

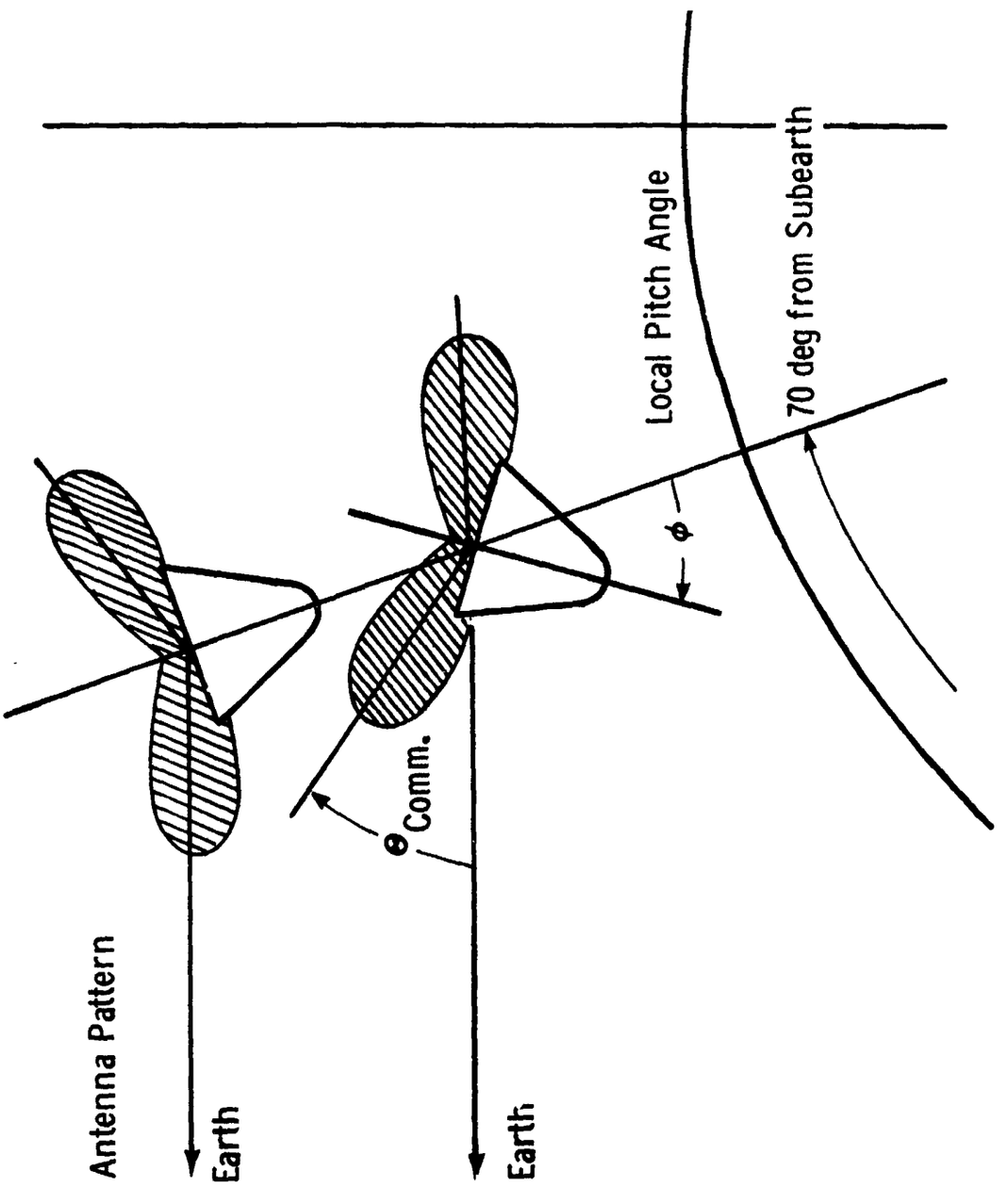


Fig. VIII-32 Antenna Pattern and Communications Angle

The major difficulty in this investigation is in attempting to set a realistic criterion for the atmospheric turbulence on Venus. Atmospheric scientists have postulated various models that define possible circulation patterns over the entire planet; however, there apparently is insufficient data to predict the severity of atmospheric anomalies such as local weather effects and possible jet stream phenomena.

Because of the uncertainty in predicting gust criteria, this section focuses attention on the relative effects of gusts in general on a range of configurations at various mission conditions. As discussed in Section H, the general cone shape was chosen for the baseline large and small descent capsules. For this investigation of dynamics and gust response, the primary configuration variable is cone half angle ($20° \leq \vartheta \leq 60°$).

In the typical mission, the probe descends part way down on a parachute, and is then released to descend to the surface at terminal velocity. With no requirement for a spin rate above about 15°/sec (and spin destabilizes at these conditions), it is reasonable to use the linear analytical solutions to the pitch equations of motion. Under these conditions the solutions are within 10% or less of the full six-degree-of-freedom solutions. The solutions of the equations of motion pertinent to this study are as follows:

$$\omega_n^2 = -\frac{\rho V^2 AD}{2 Iy}\left[C_{m_\alpha} + \frac{\rho AD}{2 m} C_{m_q} C_{L_\alpha}\right]$$

where:

ω_n = natural pitch frequency (rad/sec),

ρ = atmosphere density slug/ft^3),

V = terminal velocity (fps),

A = base area of cone (ft^2),

D = base diameter of cone (ft),

Iy = pitch moment of inertia (slug-ft^2),

m = vehicle mass (slugs),

$C_{m_q} = \frac{\partial C_m}{\partial \frac{qD}{V}}$, pitch damping,

C_{m_α} = pitching moment coefficient change with angle of attack, 1/rad,

$C_{L_\alpha} = C_{N_\alpha} - C_A$, lift curve slope, 1/rad.

The damping characteristics are expressed by the quantity time to damp to half amplitude.

$$T_{\frac{1}{2}} = \frac{0.693}{\frac{\rho V A}{4 m}\left[C_{N_\alpha} - C_A - \left(C_{m_q} + C_{m_{\dot\alpha}}\right)\left(\frac{D}{\sigma}\right)^2\right]}$$

where:

$T_{\frac{1}{2}}$ = time to damp to half amplitude (sec),

ρ = atmosphere density (slug/ft^3),

V = terminal velocity (fps),

A = base area of cone (ft^2),

m = vehicle mass (slugs),

C_{N_α} = normal force coefficient slope, 1/rad,

C_A = axial force coefficient,

$C_{m_q} = \frac{\partial C_m}{\partial \frac{qD}{V}}$, pitch damping (q),

$C_{m_{\dot\alpha}} = \frac{\partial C_m}{\partial \dot\alpha \frac{D}{V}}$, pitch damping ($\dot\alpha$),

D = base diameter of cone (ft),

$\sigma = \sqrt{\frac{Iy}{m}}$ = radius of gyration (ft).

The bracket term is the conventional stability parameter, K. When K is positive the vehicle is dynamically stable. Figure VIII-33 presents the cone normal force slope and axial force coefficients as a function of cone half angle. From the stability parameter,

$$K = C_{N_\alpha} - C_A - \left(C_{m_q} + C_{m_{\dot\alpha}}\right)\left(\frac{D}{\sigma}\right)^2$$

it can be seen that even for $C_{m_q} + C_{m_{\dot\alpha}}$ equal to zero, probes with cone angles below about 35° are stable. But subsonic cones have positive damping [negative values of $\left(C_{m_q} + C_{m_{\dot\alpha}}\right)$], as shown in Fig. VIII-34. Using typical inertia and diameter values generated for various probe designs, the time to damp to half amplitude versus cone angle and altitude was calculated and is presented in Fig. VIII-35.

This indicates that lower cone angles exhibit higher damping. The time to damp to half amplitude is strongly influenced by the terminal velocity and density of the atmosphere and improves as the probe approaches the surface. This result is greatly affected by the moment of inertia in pitch, and in roll for the spinning case. However, these results are based on typical designs from both the present Martin Marietta study and from the AVCO study (Ref VIII-1).

Figure VIII-36 shows schematic time histories of the probe characteristic response to an angle of attack disturbance. The 20° cone has a higher static stability. It also illustrates a more rapid damping rate for the 20° cone. A previous figure indicated that the damping varied with altitude; however, the natural frequency is about constant with altitude for a probe descending at terminal velocity.

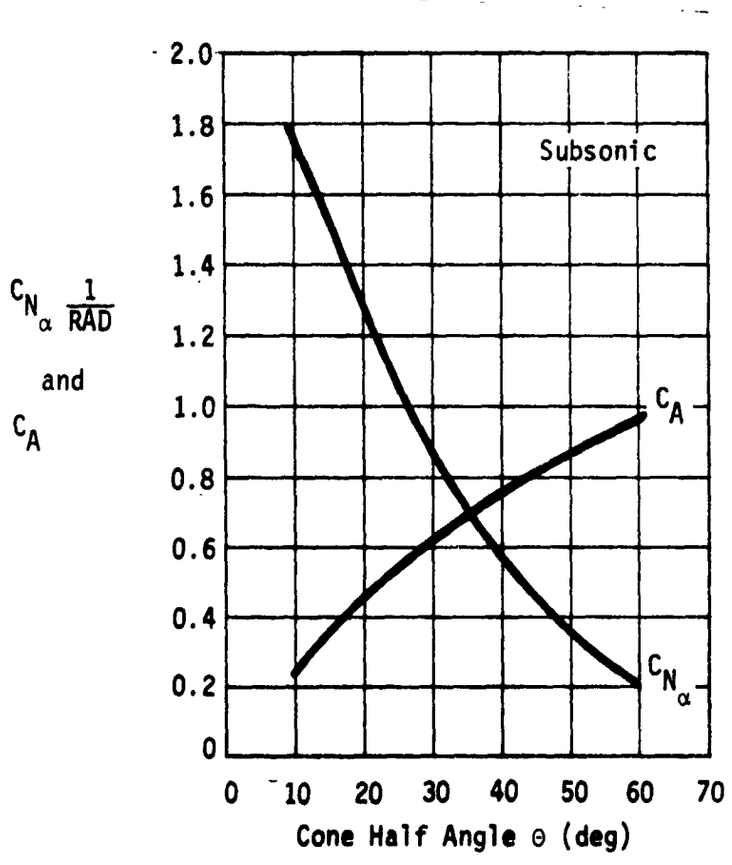


Fig. VIII-33 Normal and Axial Force Coefficients for Cones

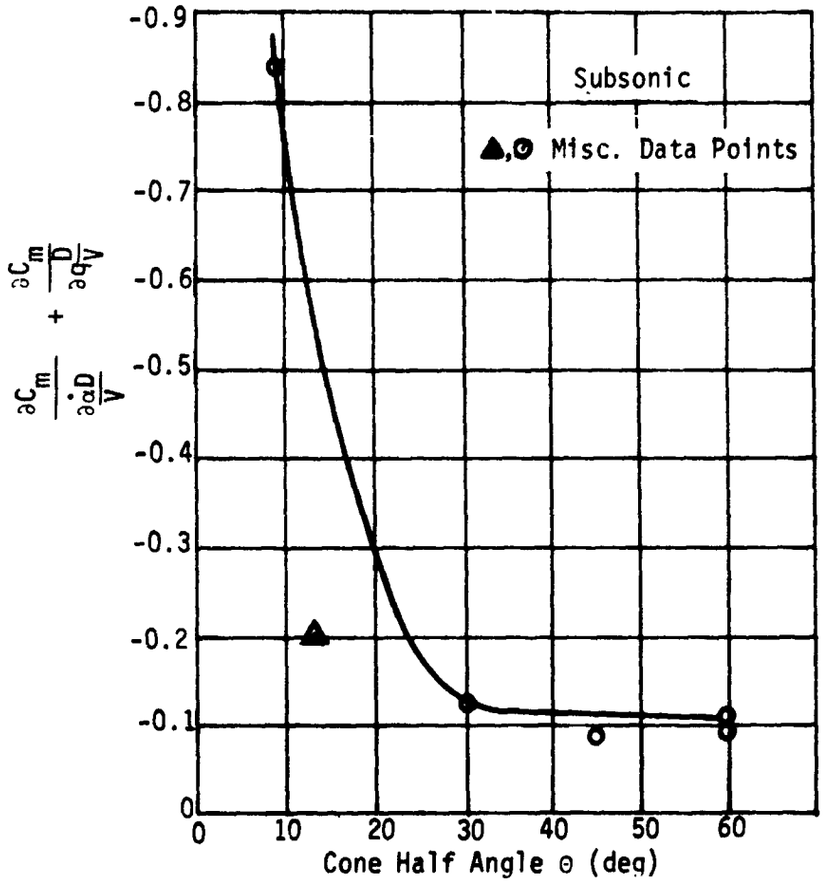


Fig. VIII-34 Cone Pitch Damping Coefficients

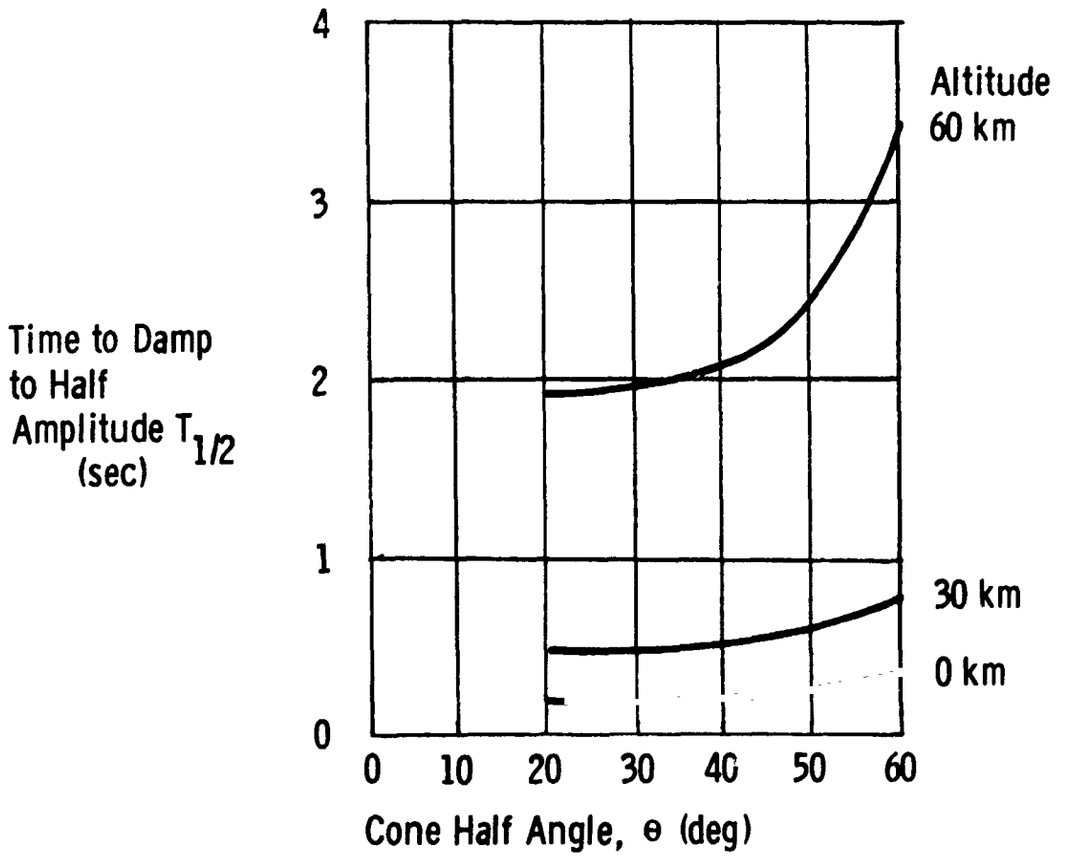


Fig. VIII-35 Cone Damping Characteristics

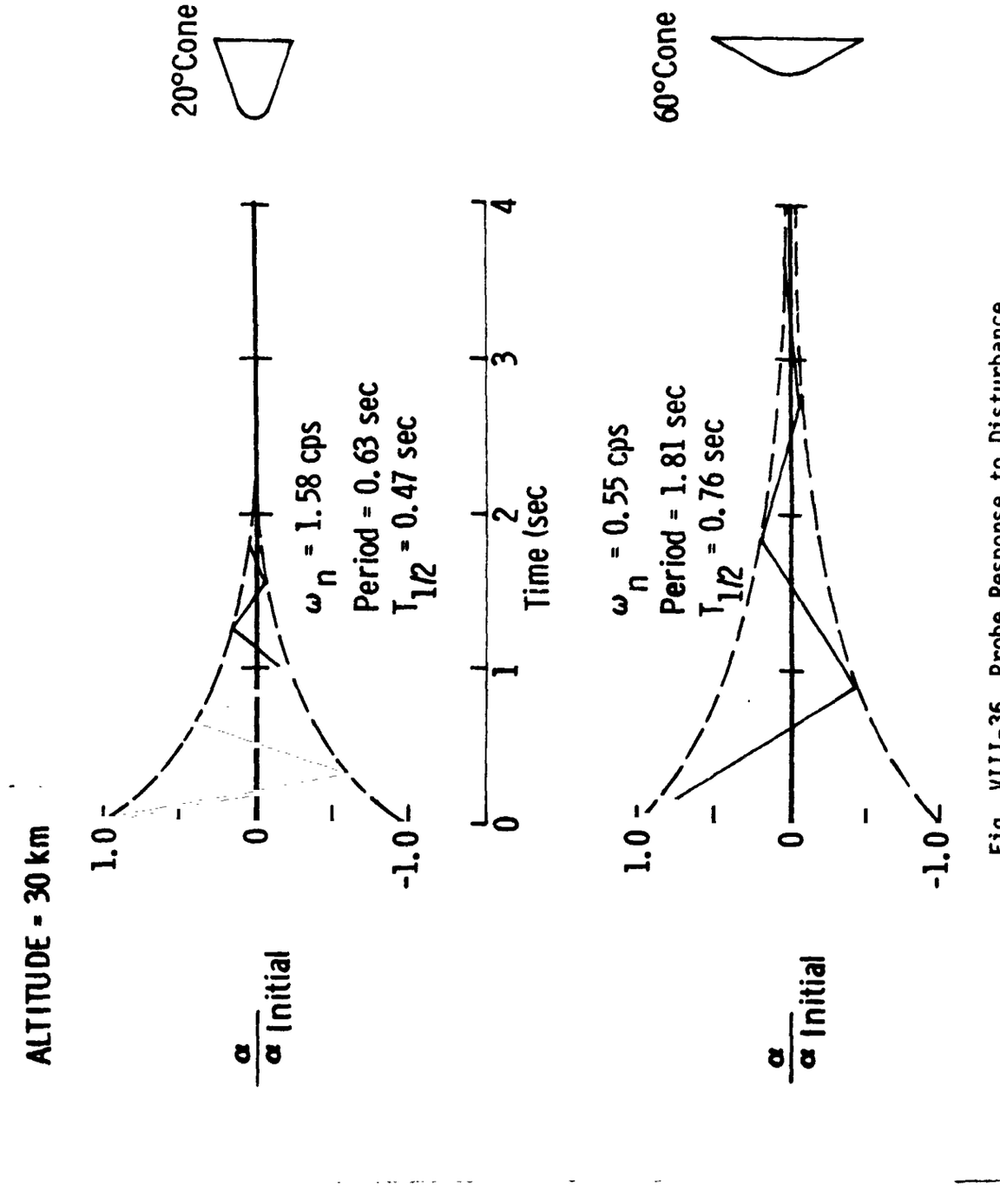


Fig. VIII-36 Probe Response to Disturbance

The previous figures showed the relative damping of cone configurations as a function of the cone angle. The damping establishes how rapidly the capsule recovers from a disturbance. However, for a given gust or shear the ballistic coefficient and, therefore, the terminal descent velocity establishes the magnitude of the angle of attack and pitch disturbance. This is graphically shown in Fig. VIII-37. This figure illustrates the resulting initial angle of attack disturbance due to horizontal gusts at a 30 km altitude. Here the effect of terminal velocity and ballistic coefficient are apparent. The 60° cone with its low terminal velocity experiences nearly twice the angle of attack disturbance as that of the 20° cone at lower gust velocities.

Figure VIII-38 illustrates the initial angle of attack resulting from various horizontal, sharp edge gusts at various altitudes. From the small diagram of the velocity vectors it is apparent that the angle of attack disturbance is directly related to the terminal velocity and, therefore, the ballistic coefficient. The values shown are for the 20° cone probe with a ballistic coefficient, B, of 2.0.

The result of probe dynamics and response to turbulence is reflected in the communications pitch angle or antenna pointing angle. For the case of a horizontal gust that sustains its velocity for a few seconds, the probes respond in pitch toward the relative wind velocity vector and oscillate in angle of attack about this new reference. This response is depicted in the vector diagram (Fig. VIII-39). The maximum communications pitch angle is obtained during the initial overshoot in angle of attack. For a given horizontal gust the 60° cone experiences a pitch angle of about 1.8 times that of the 20° cone.

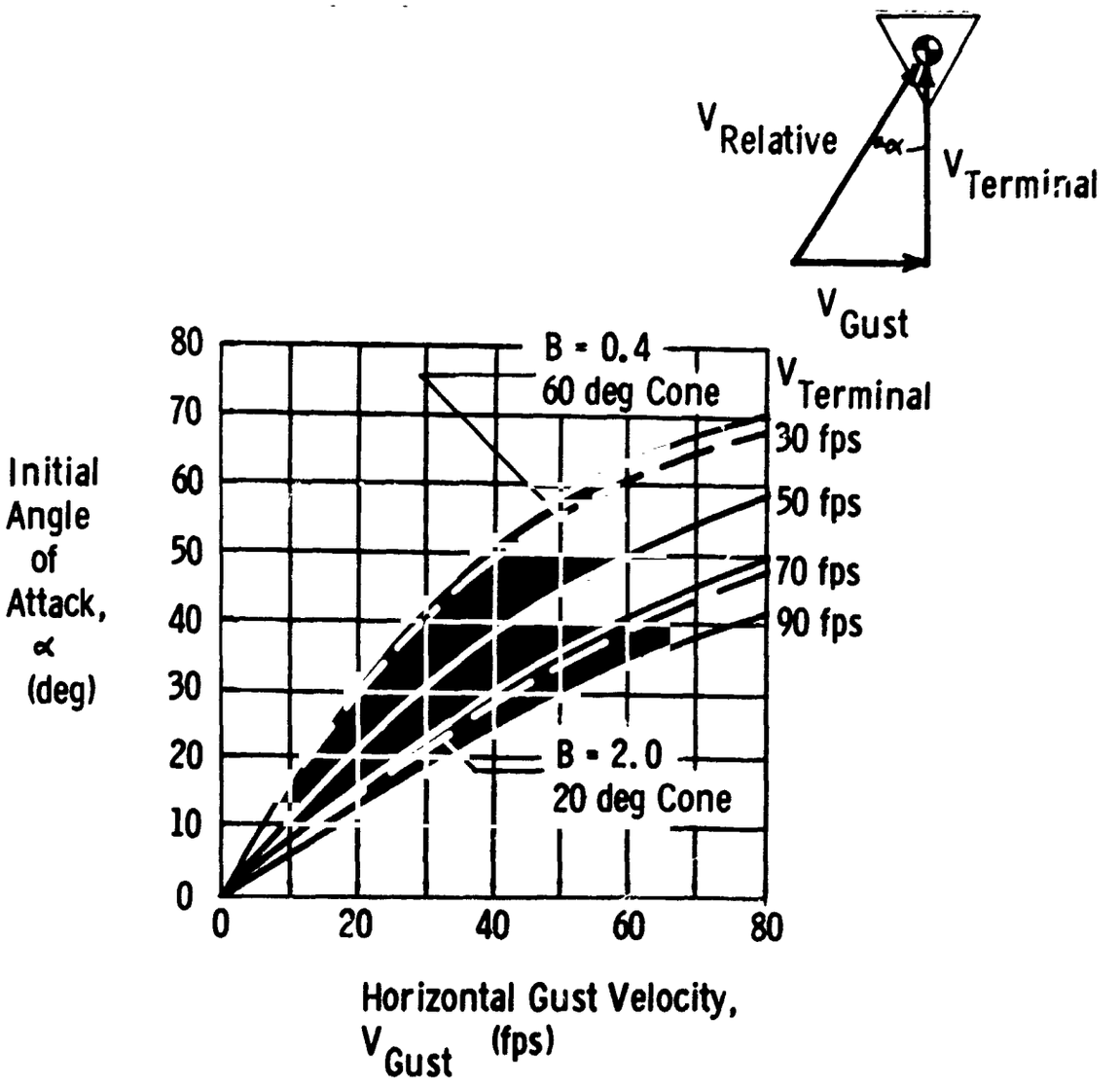


Fig. VIII-37 Horizontal Gust Effects at 30 km Altitude

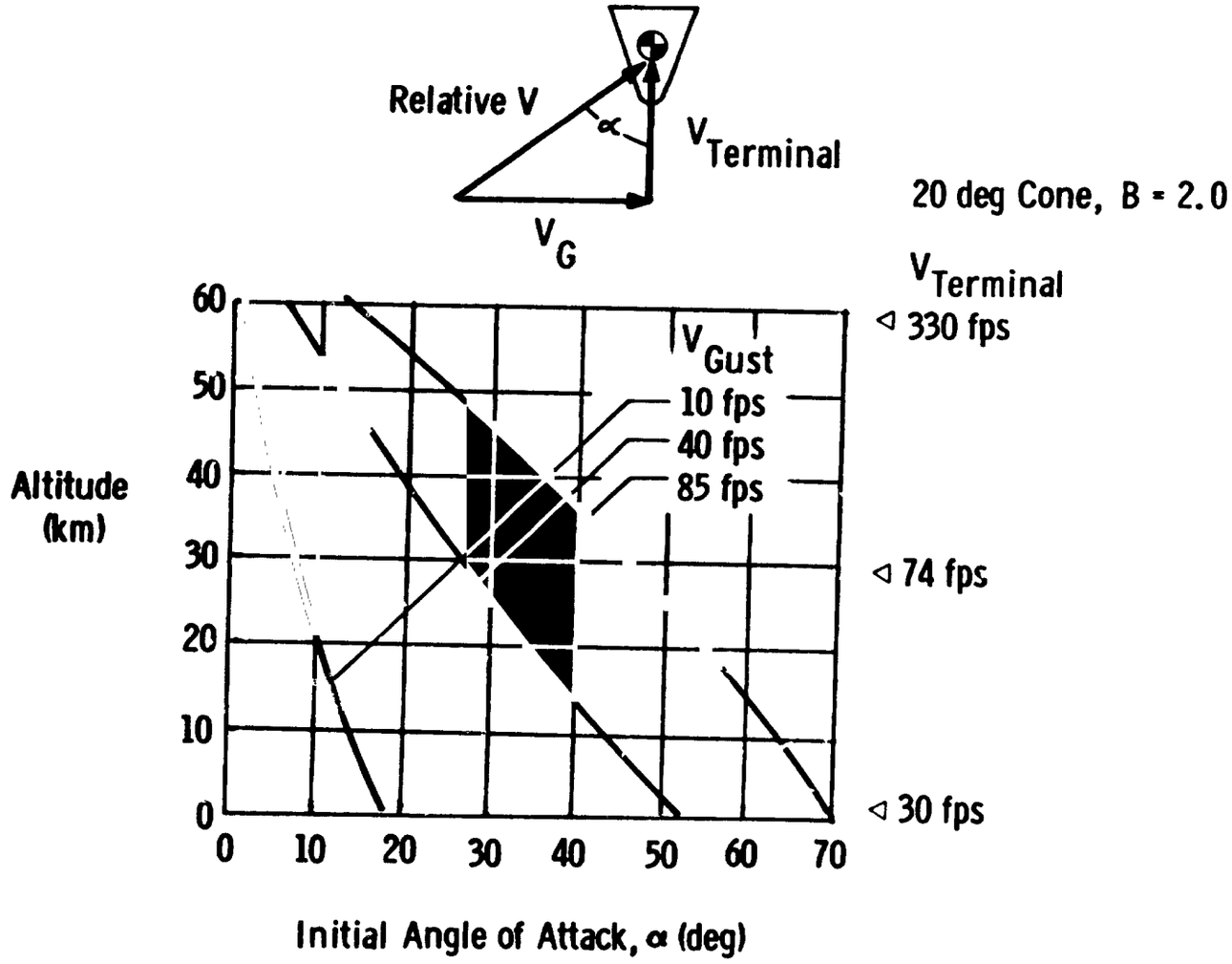


Fig. VIII-38 Horizontal Gust Effects at Various Altitudes

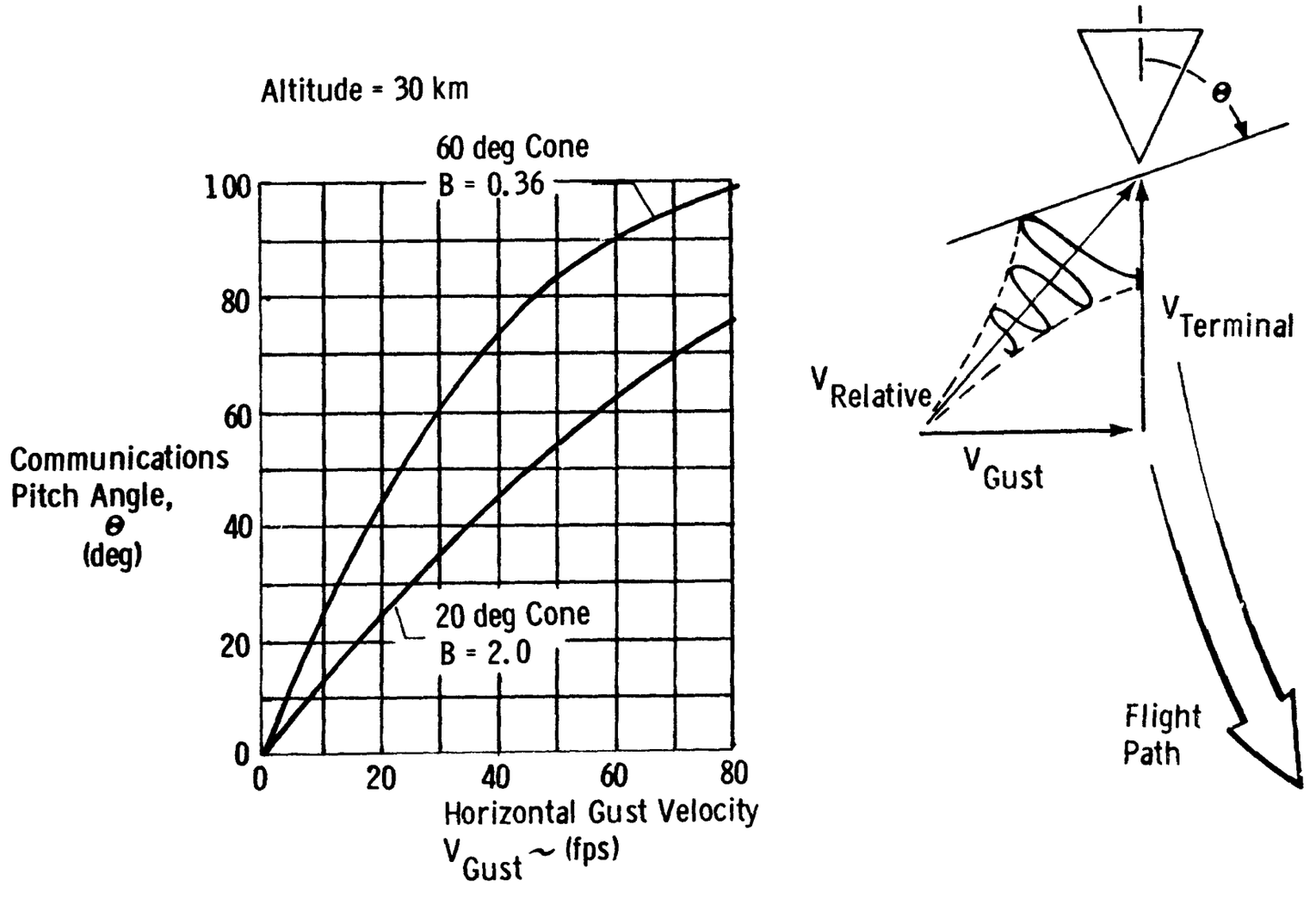


Fig. VIII-39 Communications Angle Disturbance

As discussed earlier, a reasonable turbulence level is difficult to establish. NASA SP-8011 describes a possible Venus atmosphere circulation model, which includes a maximum wind shear of 0.05 ft/sec/ft. However, this circulation model in no way accounts or attempts to predict the local weather anomalies. Some fairly severe turbulence might be expected near the tropopause (near 500 mb ambient pressure).

Angle of attack disturbances based on the low shear rate of 0.05 ft/sec/ft are small ($\alpha \leq 6°$) for the altitudes and descent rates within the area of interest of this study. Since the antenna designs can handle communications angle disturbances of 15° to 20° and still be within their design margins, it can be concluded that the range of designs meet the circulation model wind shear criteria. For more severe disturbances the data link may be temporarily lost, and the lower cone angle configurations will recover more rapidly.

2. Spin Requirements

It is desirable to have a positive roll rate to satisfy the science instrument requirements. However, it is also desirable from a stability standpoint to limit the maximum roll rate to less than 1 rad/sec. This requirement suggests a built-in roll device such as fins. For fin roll control, the roll rate, p, is proportional to the terminal descent velocity:

$$p = kV_T$$

The large probe has a diameter of 6.25 ft, a ballistic coefficient of 2.0 slug/ft^2, and an initial radius after chute staging of 6085 km. The roll rate, p, to achieve one revolution in 1 km at these conditions is 10.8°/sec. A set of fins would require a fixed deflection angle of 0.35° to obtain the roll rate (neglecting damping). Although this angle is small, a careful wind tunnel test

program could be used to determine final size and alignment of the fins. By designing relatively large fins, the effects of wakes produced from the science instrument sampling ports would be minimized.

For the case of probe descent on a parachute, the roll rate can be obtained by appropriate design of a few gore vents. The roll rate will again be proportional to the descent velocity; however, if a step change in roll rate is desirable it could be obtained by modifying the gore vent shape (e.g., releasing a vent line).

H. SUBSONIC DESCENT CAPSULE AERODYNAMICS DESIGN DATA

The terminal descent capsule configuration must provide the necessary drag area to control descent velocity and it must provide a stable orientation for the science instruments and data link antenna. Various configurations were considered including cones, cone-cylinder-flare, and sphere shapes. Cone-cylinder-flare and cone-flare shapes were eliminated because of possible limit cycle oscillations and packaging difficulties. The sphere provides an excellent structural and thermal control configuration, but it tends to have erratic aerodynamic forces. A burble fence will stabilize the wake; however, sufficient aerodynamic design data to size the fence and evaluate the dynamic stability was not available for the study. The configuration center of gravity and center of pressure are inherently close coupled, and as the burble fence becomes large the effective aerodynamic shape begins to approach that of a cone or cone-flare shape. In addition, a sphere will have a very high ballistic coefficient ($B \geq 8$ to 12 slug/ft^2) and, therefore, its descent velocities are too high to satisfy the science instrument velocity requirements.

An interesting configuration alternative would consist of a sphere with a small drogue parachute to provide drag and stability. This is somewhat less reliable than a fixed configuration, but might be lighter in weight.

A cone shape provides an inherently stable, highly reliable configuration with predictable performance. Therefore, based on the above considerations and design considerations discussed elsewhere, the cone shape was chosen for the terminal descent capsule configuration for the large and small probes.

Figure VIII-40 presents the subsonic aerodynamic drag coefficient versus cone half angle. Figure VIII-41 presents the center of pressure locations as a function of both cone angle and bluntness. Note that bluntness has very little effect on the center of pressure location. For the designer, Fig. VIII-42 provides the center of gravity location in terms of required distance the center of gravity must be ahead of the center of pressure obtained in Fig. VIII-41. All configurations considered in this study were constrained in equipment layout by this cg criteria.

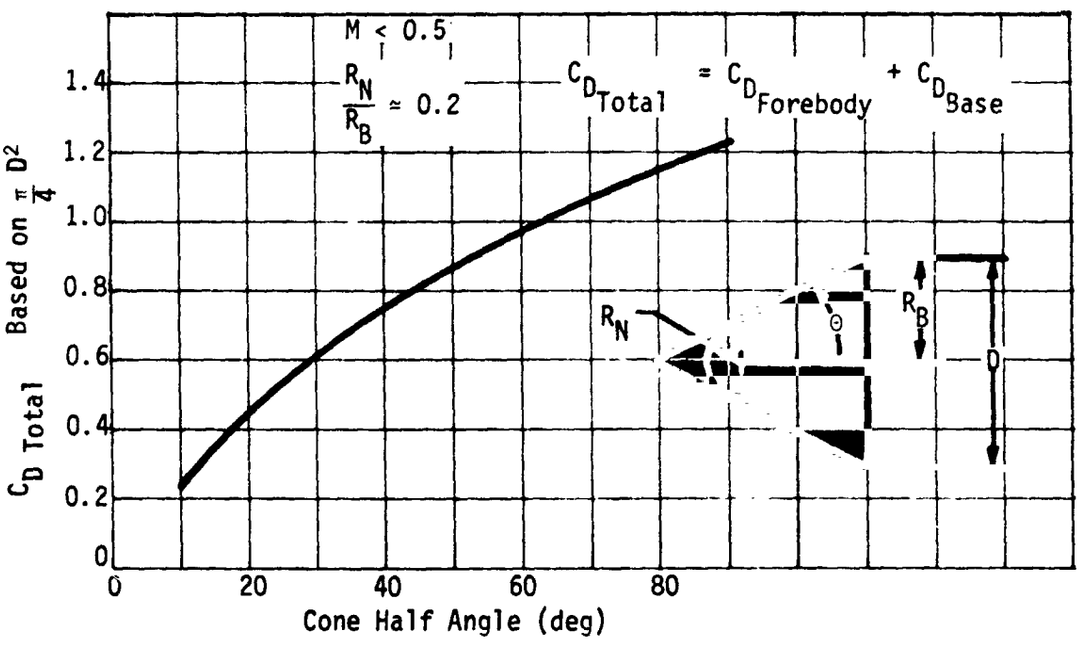


Fig. VIII-40 Cone Total Drag Coefficient

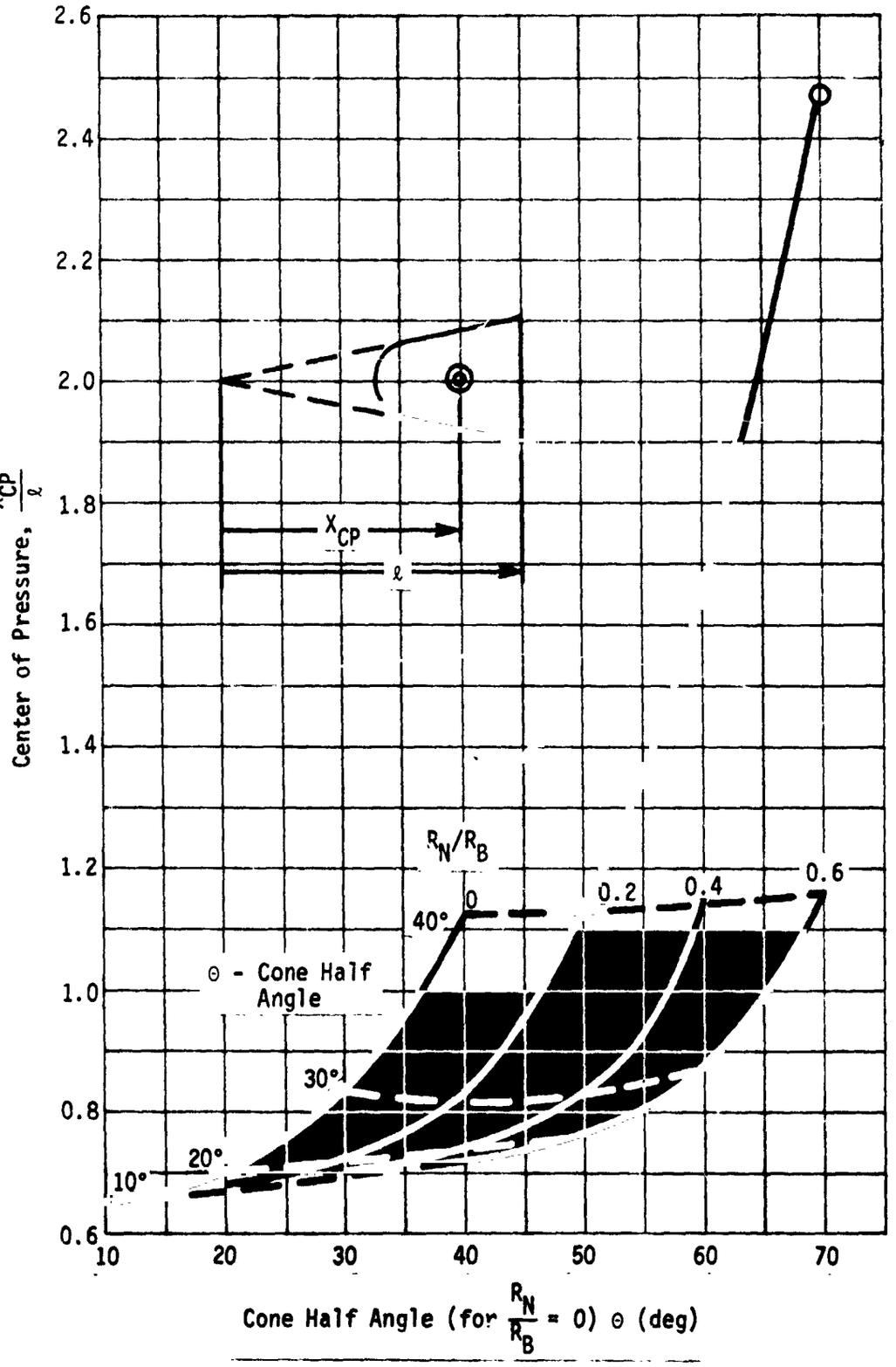


Fig. VIII-41 Cone Subsonic Center of Pressure

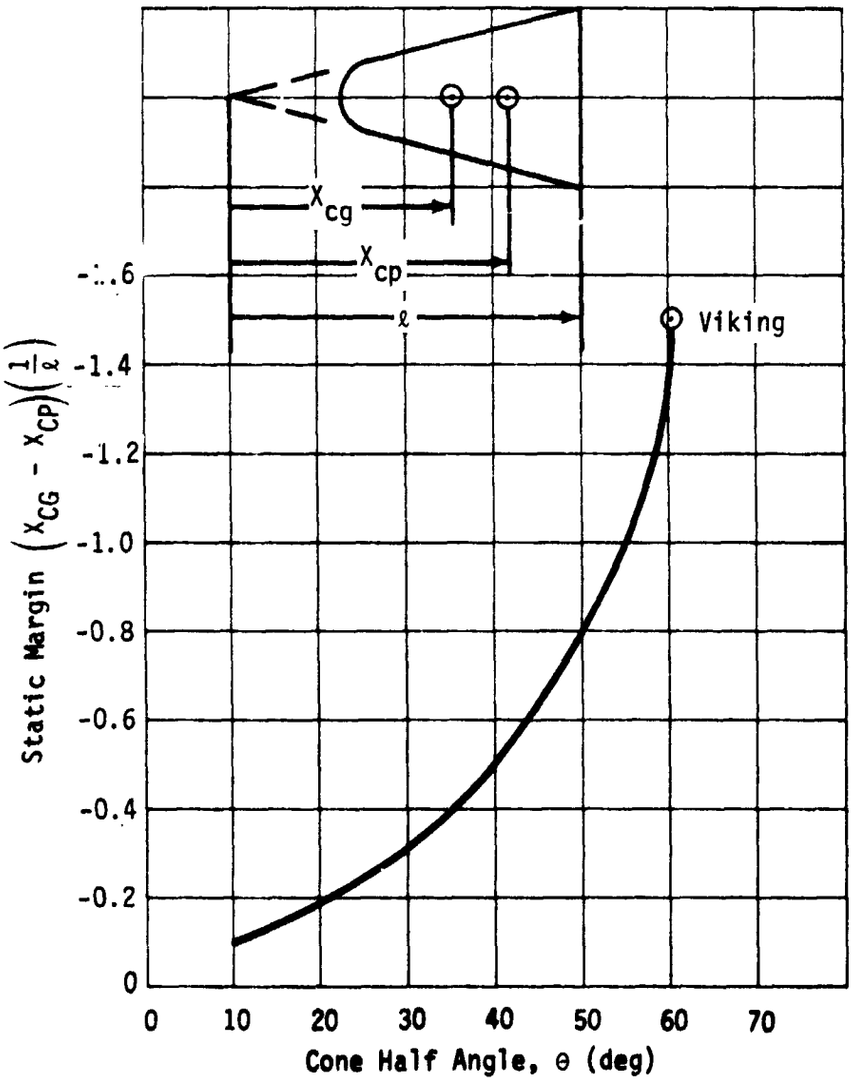


Fig. VIII-42 Longitudinal Static Stability Margin

I. BALLOON DESIGN

1. Balloon Design Criteria

Based on the mission requirements of this study, balloon design trade studies performed under NASA contracts NAS1-6607, NAS1-7590, and Martin Marietta inhouse efforts (Ref VIII-3 thru VIII-6), and general balloon industry experience (Ref VIII-7 thru VIII-9), the following design criteria were established for the balloon design:

1) Spherical, superpressure balloon;
2) Design float ambient pressure -
   500 mb low-altitude balloon;
   50 mb high-altitude balloon;
3) Science payload of 11.0 lb;
4) Minimum lifetime of 7 days;
5) Flotation system will be sterilizable;
6) Inflation system will use gaseous hydrogen;
7) Balloon will inflate within 45 sec;
8) Balloon will be capable of deployment and inflation in a 1 psf external dynamic pressure while descending on a parachute;
9) Balloon must have sufficient superpressure to survive crossing the terminator from sunlight to dark and return.

2. Balloon Design Data

A superpressure balloon, that is a balloon whose internal pressure is higher than ambient pressure, was chosen for this application because of some distinct advantages over the typical zero-pressure meteorological balloon. The superpressure balloon seeks a predetermined density altitude and, within its design limits,

will remain at that altitude. It is stable and will return to the design altitude after disturbances due to turbulence. Balloon flight mechanics are governed by the gas law, which may be written as follows:

$$\rho_A V = M_g \left(\frac{W_A}{W_g}\right)\left(\frac{T_A + \Delta T}{T_A}\right)\left(\frac{P_A}{P_A + \Delta P}\right) = \text{mass floated}$$

ρ_A = ambient density,

P_A = ambient pressure,

T_A = ambient temperature,

ΔP = superpressure (above ambient),

ΔT = supertemperature (above ambient),

V = balloon volume,

M_g = mass of gas in balloon,

W_A = molecular weight of atmosphere,

W_g = molecular weight of balloon gas.

The physical characteristics that determine the balloon supertemperature, ΔT, are as follows:

Atmosphere transmissibility;

Atmosphere emissivity;

Albedo for clouds (above only);

Cloud optical thickness;

Surface temperature (below only);

Effective surface emissivity;

Solar reflectance of surface (below only);

Composition of atmosphere;

Sun angle;

Balloon material optical properties.

The superpressure physical characteristics are:

Supertemperature extremes;

Vertical winds;

Balloon design.

Martin Marietta inhouse studies performed to complement NASA Contract NAS1-7590 (Buoyant Venus Station Studies) investigated the available Venus atmosphere data and postulated nominal and extreme variations for the values of the above atmospheric quantities. Based on that study, a nominal variation in supertemperature, of 50°K (90°F) was obtained. This variation includes the effects of sun angle from subsolar to the dark side with and without clouds. Figure VIII-43 presents the resultant balloon design superpressure required to meet the 50°K variation in supertemperature. Balloons are then sized by use of the gas law, material strength characteristics, and the expression:

$$\rho_A V = \text{weight lofted} = W_{Payload} + W_{Balloon} + W_{Gas}$$

By expressing the balloon and gas weights in terms of density times volume the expression becomes:

$$\rho_A V = W_{P/L} + \rho_B V + \rho_{Gas} V$$

$$W_{P/L} = V\left(\rho_A - \rho_B - \rho_{Gas}\right)$$

$$\text{Balloon volume, } V = \frac{W_{P/L}}{\rho_A - \rho_B - \rho_{Gas}}$$

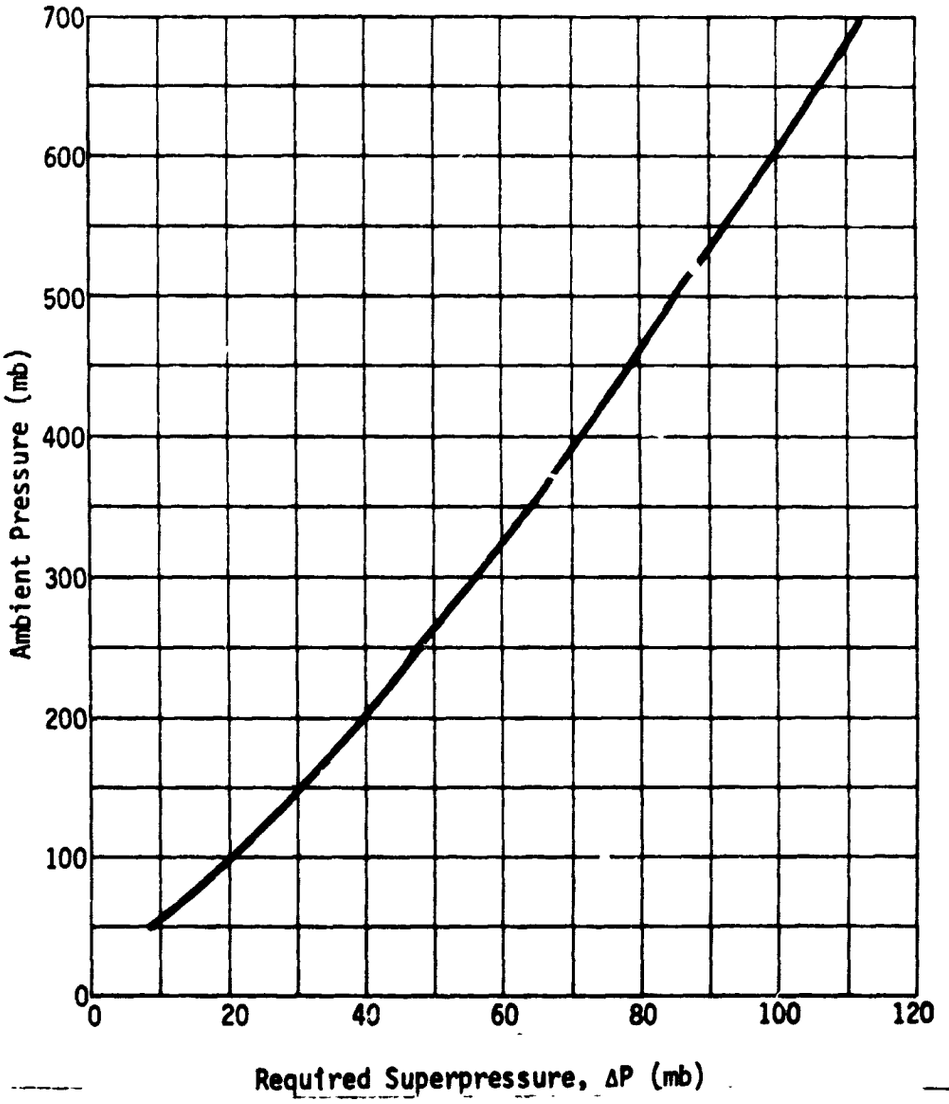


Fig. VIII-43 Balloon Probe Design Superpressure

J. REFERENCES

VIII-1 *1972 Venus Entry/Flyby Probe Mission Study.* JPL/AVCO Study.

VIII-2 C. L. Gillis: "Deployable Aerodynamic Decelerators for Space Missions." *Journal of Spacecraft.* August 1969.

VIII-3 *Final Report, Buoyant Venus Station Feasibility Study.* NASA CR-66404 thru CR-66409. Prepared by Martin Marietta Corporation, Denver, Colorado for NASA Langley Research Center. Contract NAS1-6607.

VIII-4 *Buoyant Venus Station Mission Feasibility Study for 1972-1973 Launch Opportunities.* NASA CR-66725 (Vol I thru III). Prepared by Martin Marietta Corporation, Denver, Colorado, for Langley Research Center. Contract NAS1-7590.

VIII-5 *Wind Tunnel Test Results of the Deployment/Inflation Characteristics of a Model Balloon (Buoyant Venus Station Concept).* MCR-69-23. Prepared by Martin Marietta Corporation, Denver, Colorado for Langley Research Center. Contract NAS1-7590.

VIII-6 *Materials Feasibility Tests (Buoyant Venus Station Concept).* PR-22-69-17. Prepared by Martin Marietta Corporation, Denver, Colorado for Langley Research Center. Contract NAS1-7590.

VIII-7 Louis A. Teichman: *The Fabrication and Testing of PAGEOS I.* NASA TN D-4596. Langley Research Center, Langley Station, Hampton, Virginia, June 1968.

VIII-8 Vincent E. Lally: *Superpressure Balloons for Horizontal Soundings of the Atmosphere.* NCAR-TN-28. National Center for Atmospheric Research, Boulder, Colorado. June 1967.

VIII-9 Vincent E. Lally: *The Use of Superpressure (GHOST) Balloons for the GARP Experiments.* COSPARj-17. XIth Assembly of COSPAR, Tokyo. May 1968.